Geochemical Insights into Crustal Melting in the Bhutan Himalaya

Thesis

Geochemical insights into crustal melting in the Bhutan Himalaya

---

Thomas Neil Hopkinson

MSci Hons. (University of Bristol) 2012

This thesis is submitted for the degree of Doctor of Philosophy

School of Environment, Earth and Ecosystems Sciences,

The Open University, United Kingdom

30th June 2016

Abstract

Crustal melting and granitic intrusions are characteristics of many continental collision zones. The processes, sources and timing of melt generation in collision zones are critical to understanding crustal and tectonic evolution. In the Himalaya, multiple Oligocene-Miocene leucogranite bodies intrude the Greater Himalayan Series (GHS), a lithotectonic package of high-grade metamorphosed sediments. This package is underthrust by a chemically distinct metasedimentary package, the Lesser Himalayan Series (LHS).

Multiple elemental and isotopic techniques provide insight into leucogranite source and petrogenesis in central Bhutan (eastern Himalaya). Whole-rock major and trace elemental abundances confirm that all studied leucogranites are the product of muscovite breakdown between 640 and 760°C. Sr-Nd signatures suggest that most samples were sourced from the GHS; however several samples yield signatures more comparable with those from the LHS, an observation that currently appears unique to Bhutan.

O, U-Pb, Hf isotopes in zircon confirm previous whole-rock findings that melting in the eastern Himalaya took place over 20 Myr, from 31 to 11 Ma. Increasingly radiogenic Nd and Hf isotope signatures are observed in younger leucogranites, which suggest a deeper source, and potentially more contribution from melting LHS. Importantly, O-Hf isotopic signatures indicate that there is no mantle input into eastern Himalayan melting, a finding important for heat budget calculations and for crustal growth models in orogenic belts.

Stable Rb and Sr isotopic analyses from both whole-rock leucogranites and mineral separates establish, for the first time, that mass-dependent isotopic fractionation occurs during the formation of highly evolved crustal melts. Consistent Sr fractionation of up to 2.51‰ is

observed between plagioclase, K-feldspar and micas. These observations have implications for the application of stable isotopes as petrogenetic indicators and for Rb-Sr geochronology.

Together, the findings of this study provide new insights into both Himalayan and global tectonic evolution and the geochemical nature of melt generation.

Acknowledgements

This thesis is the product of three-and-a-half years of work, in which time I have been helped and encouraged by a great many people, without whom I may well not have finished this PhD.

First and foremost I must thank my wonderful supervisory team – Clare Warren, Nigel Harris, Sam Hammond and Randy Parrish – for their support, ideas and encouragement. You were always happy to listen to my ideas and questions (no matter how stupid), and give advice and guidance. I would recommend supervisory dog-walking meetings to everyone, as chats with Nigel while walking Tashi have proved some of the most useful of all! I would also like to thank other members of the HiT team (past and present) – Tom Argles, Daniele Regis, Catherine Mottram and Lucy Greenwood – for providing ideas and support over the years too.

Special thanks must go to Bruce Charlier. While not an official supervisor, he devoted an enormous amount of time and effort in helping me out and training me in the labs and on instruments, and provided a guiding light during the stable isotope side of my project. Sam Hammond deserves enormous praise for managing to keep most labs running while simultaneously being a great supervisor. I would also like to thank Andy Tindle, Michelle Higgins, Kaye Green and Gordon Imlach for lab support at the Open University. I also have huge thanks for the late John Watson for all his assistance and friendly chats while preparing samples for XRF.

At NIGL and the British Geological Survey, I would like to thank Nick Roberts, Matt Horstwood and Chris Spencer for all their technical support, as well as suggesting ideas for the evolution of the project. I would also like to thank Adrian Wood for providing help in sample preparation, as well as long and enjoyable conversations about heavy metal and politics. Also, John Craven deserves my gratitude for assistance on the ion probe at Edinburgh.

In the field I would like to thank Orgyen and the team for making our trip through Bhutan an easy, interesting and incredibly enjoyable experience. I would also like to thank Namsey Tours for all their logistical assistance (and for upgrading me to business class). For my Canadian fieldwork, which has unfortunately proved fruitless for this project, I would also like to thank Jamie Puffer for being an indispensable field assistant.

I would also like to express my gratitude to anyone who I've met at the many conferences I've attended throughout my PhD, especially those who offered advice at any level. Of particular mention are the Himalayan team from Oxford – Mike Searle, Dave Waters and Brendan Dyck – who have provided many friendly discussions over the years.

I would to thank Sam, Bethan, Fliss, Pete, Frazer, Hayley, Adele, Kerry and Anouk for being fantastic office-mates, and for the daily rounds of University Challenge questions. I spent two fun years of my PhD living at the Broughton Hotel, and would like to thank Peter, Catherine, Lucy, Guillermo, Marcus, Bertie, Chris, Leanne and Sophie for being great house-mates over the years! Huge thanks must go to me amazing family, for all their unending love, support and encouragement over the years. Finally, my biggest thanks must go to Lara, for being an incredible partner and companion and for providing support and fun times over the past seven years. I could not have done this without you!

Contents

List of figures

List of tables

Chapter 1

Introduction

Melting of the crust is a crucial process in global tectonics; it weakens specific layers within the Earth and facilitates movement of whole crustal blocks. This thesis is a study of crustal melting in the Himalaya, one of the Earth's youngest mountain ranges, and applies geochemical techniques to unravel the history of Himalayan granites, the products of anatexis, to investigate problems relating to tectonic evolution. In the following sections I review firstly the nature of granites, particularly as representatives of crustal melting, and secondly the Himalayan orogeny which provided the context within which the granites studied in this thesis have formed.

1.1. Granites

1.1.1. Granite descriptions and classifications

Granites have been a subject of intense study throughout the history of igneous geology, especially in recent decades with advancements in trace element and isotope geochemistry and geochronology. Granites are a common type of intrusive felsic igneous rock, found in many tectonic settings worldwide. Their colour is predominantly white, grey or pink, which reflects their bulk mineralogy. They are dominated by quartz, alkali feldspar and plagioclase, and commonly contain other darker minerals such as biotite, muscovite or hornblende. Granites with very few dark minerals are known as leucogranites.

Although small volumes of granite magmas have been generated in oceanic settings from fractional crystallisation of mafic magma, the vast majority of granites are derived from some combination of mantle-derived melts and the assimilation of re-melted deep crustal, igneous rocks often undergoing associated fractional crystallization, which renders the remaining melt enriched in felsic minerals. Typically these are found in subduction zone continental margins. However certain granites, such as those found in the High Himalaya, are considered to be the direct result of melting of crustal material (typically (meta)sediments), producing melts with similar major element chemistry and mineralogy, but potentially very different trace element and isotopic content.

1.1.2. Geochemical fingerprinting of granite source

The primary method to assess the source of a granite is by its geochemistry. The first granite classification system was developed by Chappell and White (1974), which sought to divide granites into I-type (those with an igneous source) and S-type (those with a sedimentary protolith) based on their bulk geochemistry and mineralogy. The system was developed using granites from the Lachlan Fold Belt of southeastern Australia, and it was here that end-member type localities were assigned for both categories. The main major element geochemical differences observed between the groups were that the I-types contained higher concentrations of Na_2O and CaO than the S-type granites. The depletion in Na_2O and CaO typically leads S-type granites to yield higher aluminium saturation index values (ASI = Al_2O_3 / Na_2O + K_2O + CaO) than I-type granites, with 1.1 quoted as the divide between the two granite types.

Isotope geochemistry plays a more dominant role in distinguishing between granite types, and between potential individual sources contributing to a granite magma. Initial Sr and Nd isotopic compositions of S-type granites are typically more radiogenic than I-type granites, owing to the older, more evolved, nature of their source (Compston and Chappell, 1979; McCulloch and Chappell, 1982; Chappell and White, 1992). However, the observed range of isotopic ratios (for either Sr or Nd) is large for both granite types, with overlap observed between the groups. Indeed isotopes can conceal the contribution of crustal melting in arc systems where the crust is

juvenile as in the Arabian Shield (Duyverman et al., 1982). On the other hand, given contrasting isotopic characteristics of potential crustal sources, isotope geochemistry may be successful in linking melts to specific crustal sources, as has been demonstrated with Himalayan leucogranites (e.g. Deniel et al., 1987; Guillot and Le Fort, 1995).

Such studies have been performed using bulk-rock geochemical data, which provides averaged information of all mineral phases within a rock, and therefore may fail to resolve specific contributions from individual sources. In addition, bulk-rock geochemistry may fail to reflect the true composition of the melt for a variety of reasons, such as incomplete separation of melt from restite, or the effects of post-magmatic processes, such as hydrothermal alteration.

In more recent years, advances in micro-analysis techniques (e.g. laser ablation or ion probe) have allowed for the measurement of geochemical compositions of accessory phases. One common accessory mineral is zircon, which is known for its ability to act as a geochronometer through the isotopic decay of U (which is present in measurable quantities on the Zr site) to Pb. As zircons crystallise with negligible amounts of Pb in their crystal lattice, an assumption can be made that the vast majority of Pb present will originate from the radioactive decay of U, and therefore an age for the zircon may be calculated. Zircons may also be analysed for their Lu-Hf and O isotopic compositions, which may be used to identify the potential sources of a granitic melt. Examples of this combined isotopic approach to investigating zircons are in Kemp et al. (2006, 2007). In these studies, zircons from Lachlan Fold Belt S-type granites were shown, by their O and Hf isotopic signatures, to contain up to 75% mantle derived material. This finding is in stark contrast to previous whole rock trace element and isotopic investigations of these rocks, which classified them as the type-example of sediment derived granites. The findings of this study demonstrate the huge potential in microanalytical techniques to not only accurately determine the age of samples, but also to obtain more detailed information on their sources than whole-rock data can provide.

1.2. The Himalayan orogeny and the significance of leucogranites

The most active and dynamic parts of the Earth's crust are found at plate boundaries, where crust is created, deformed, and destroyed. When plates collide, rocks are buried, metamorphosed and melted by the extreme forces at work. The resultant expressions of these processes on the planet's surface are mountain belts. One of the tallest, longest and youngest of these is the Himalaya, situated at the eastern end of the Alpine-Himalayan orogenic belt, which forms the southern margin of the Eurasian plate. The Himalaya began to form during the collision of Asia and India ~55-50 million years ago (Klootwijk et al., 1992; de Sigoyer et al., 2000; Najman et al., 2010). As uplift continues, the region remains tectonically active, with seismic activity relating to the orogen affecting areas from Afghanistan to eastern China. Devastating earthquakes in Sichuan province in 2010, and most recently in central Nepal in 2015, have increased scrutiny of the mountain belt from a seismic point of view.

The geological youth of the Himalayan mountain belt means that it provides a perfect natural laboratory for studying processes occurring within collision zones, such as metamorphism, folding, faulting and melting. Recent advances in in-situ geochronological techniques have allowed highly precise ages to be obtained from accessory phases such as zircon or monazite that grow distinct rims during different episodes of magmatism or metamorphism. The relative youth of the Himalaya compared to other mountain belts also means that ages may be dated with a higher degree of analytical precision than in older orogens. Attempting to link ages to tectonic events in a young orogenic system such as the Himalaya will therefore result in a greater understanding of processes and timescales involved and hence inform our understanding of the Earth's older orogenic belts.

One further element of Himalayan geology that lends itself to detailed study is the presence of leucogranites across the orogen. These are of Himalayan (largely Miocene) age and are widely believed to result from melting of the sedimentary lithologies in the core of the orogen. Thus they provide an ideal context for investigating both the thermal history of orogenesis and the

mechanical constraints imposed by melting core lithologies and hence lowering bulk viscosities which carries crucial implications for tectonic evolution.

Figure 1.1: *Satellite view of Indian subcontinent bounded to the north by the Himalayan orogeny (courtesy of Google).*

1.3. Geology of the Himalaya

The Himalaya is divided into four main geological units, striking roughly parallel along the length of the orogeny (see Figure 1.2). Furthest to the south, and structurally lowest, is the sub-Himalayan or Siwalik group, above which lies the Lesser Himalayan Series (LHS), the Greater Himalayan Series (GHS), and the Tethyan Himalayan Series (THS) (also known in the literature

as the Tethyan Sedimentary Sequence, or TSS). North of the THS is the Indus-Tsangpo suture zone, marking the boundary between the Indian and Asian continents.

See Figure 1.2 for a simplified geological map and generalised cross-section of the eastern and central areas of the orogen.

The Siwalik group is made up of Miocene to Pleistocene sandstones and siltstones eroded off the Himalayan orogen (Parkash et al., 1980; Cerveny et al., 1988). After deposition, this group was underthrust by the Indian craton along the Main Frontal Thrust (MFT), the southernmost major thrust fault of the Himalayan orogen. The top of the Siwalik group is marked by the Main Boundary Thrust (MBT), separating the unit from the overlying LHS.

The LHS is a unit of (meta)-sedimentary limestones, sandstones, quartzites, siltstones, slates and schists, with metamorphic grade varying from lower amphibolite facies to no observable metamorphism (Gansser, 1983; McQuarrie et al., 2008; Mottram, 2014). In the Eastern Himalaya, the unit is sub-divided into two distinct groups – the lower Baxa group is characterized by younger Neoproterozoic-Palaeozoic sediments, and the higher Daling-Shumar group, which is Paleoproterozoic in age and intruded with ~1.8 Ga granites (Gansser, 1983).

The top of the LHS is marked by the Main Central Thrust (MCT). This thrust, along with the MBT and MFT, are thought to be expressions of the Main Himalayan Thrust (MHT), the main fault along which movement has been focussed during the collision, and underlying the entire span of the Himalayan orogen (Larson et al., 1999). The GHS, a high-grade metamorphic package of metapelites and orthogneisses, overlies the LHS along the MCT (Gansser, 1983). Partial melting has affected much of the unit, increasingly so at higher structural levels, to create migmatites and leucogranite bodies (Gansser, 1983; Long and McQuarrie, 2010; Greenwood, 2013).

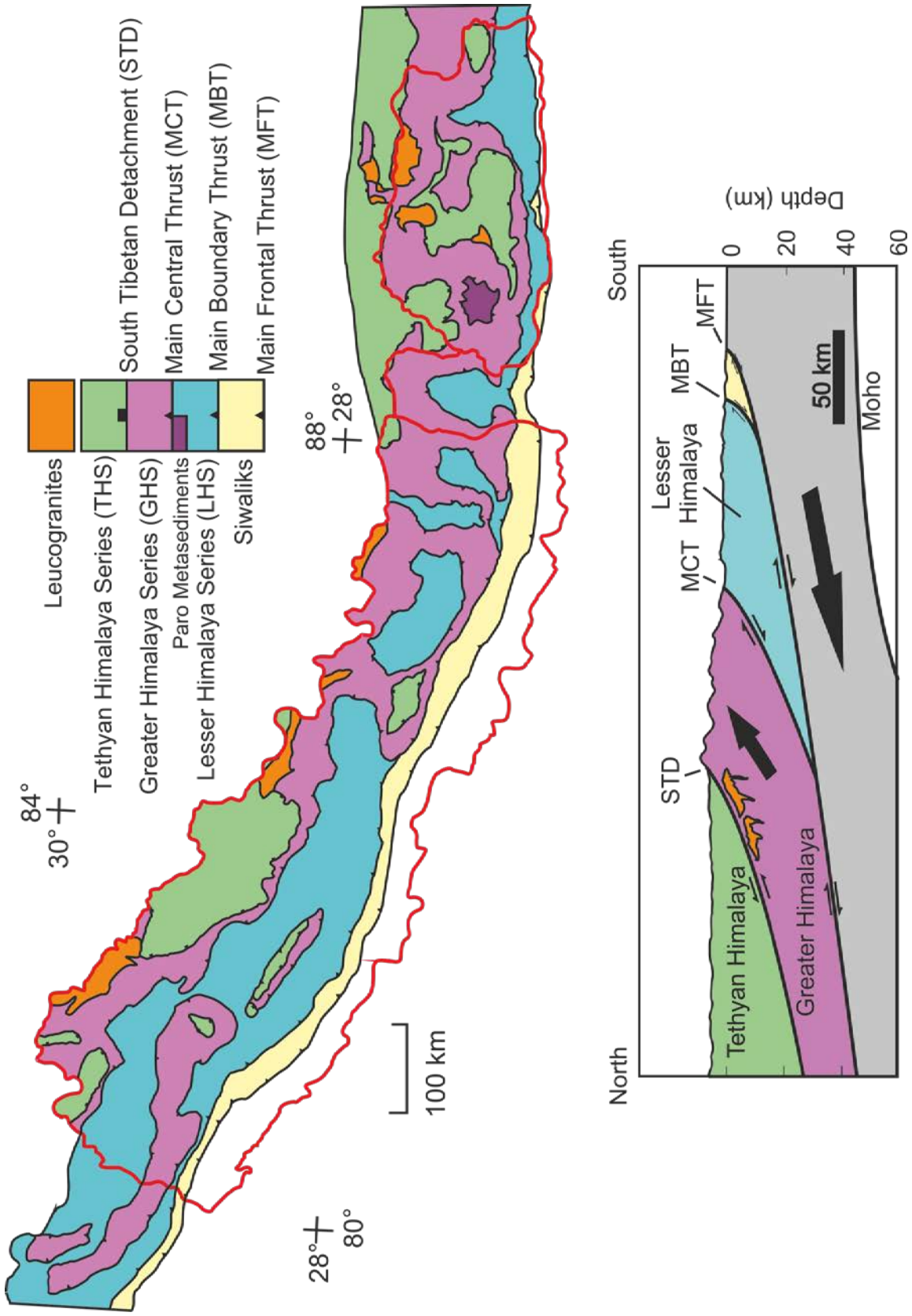

Figure 1.2: *Simplified geological map of the central and eastern parts of the Himalayan orogen. (Adapted from Mottram et al., 2014).*

The exhumation of the GHS from depth is understood to have been facilitated by the South Tibetan Detachment (STD) normal fault, which bounds the top of the GHS, as it is at this fault that the majority of shear deformation appears to have affected the GHS and where the majority of leucogranites are found (Burchfiel et al., 1992). The THS, a (meta)-sedimentary unit of siltstones, quartzites, limestones and schists, displaying metamorphism up to middle-greenschist facies overlies the STD. These sediments were thought to have been deposited in the Tethyan Ocean prior to its closure, which were then uplifted during the India-Asia collision (Najman, 2006).

More detail can be found in Chapter 2 of this thesis (specifically relating to Bhutan) or in such papers as Heim and Gansser (1939), Gansser (1964), Hodges (2000), and Guo and Wilson (2012).

1.4. Himalayan tectonic models

Several tectonic models have been invoked to explain the current geological structure of the Himalaya. Two models have proved the most popular – and divisive – of those conceived to explain the mountain belt: the channel flow model and the critical taper model.

1.4.1. Channel flow

The channel flow model suggests that the exhumation of the GHS initiated as the unit began to partially melt, while being pressured from above by the weight of a more rigid thickened crust (the Tibetan plateau). Due to the pressure contrast between the Tibetan plateau and the Indian foreland, the channel is forced to move southwards, before turning upwards due to concentrated erosion on the Himalayan front, which leads to a rapid removal of material and the ultimate exposure of the GHS channel (Beaumont et al., 2004; Jamieson et al., 2004; Harris, 2007; Jamieson et al., 2011).

The model was first suggested and described by numerical modelling in 2001 by Beaumont et al., after geophysical research discovered significant quantities of partially molten material in the mid crust beneath the Tibetan plateau, inferred to have been melted during the Himalayan orogeny (Nelson et al., 1996).

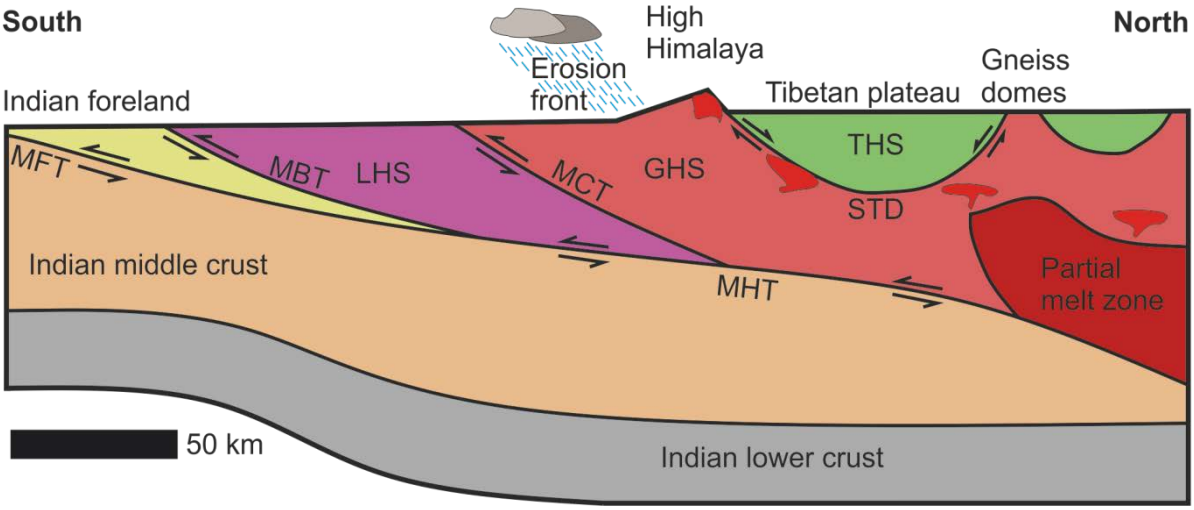

Figure 1.3: *Cross section of the Himalaya demonstrating the channel flow model. The formation of a partial melt zone beneath the Tibetan plateau causes a dramatic drop on viscosity, which then flows and is exhumed southwards towards the High Himalaya as material is removed at the erosion front. Adapted from Beaumont et al. (2001).*

Critical to the model is the presence of melt, a small fraction of which (up to 8% melt volume) significantly reduces rock viscosity (Rosenberg and Handy, 2005). The model suggests that the presence of a partially melted layer in the thickened mid-orogenic crust triggered the creation of a low-viscosity channel. Controversy focuses on whether partial melting in the Himalaya caused the initiation of exhumation or was a consequence of exhumation (due to the crossing of the solidus following a decrease in pressure).

1.4.2. Critical taper

Critical taper, also known as critical wedge, models have been invoked as a relatively simple explanation of the geometry observed in a variety of collisional orogens (Davis et al., 1983; Dahlen et al., 1990; Dahlen, 1990). An orogenic wedge forms as a strong underthrusting plate

(e.g. Indian crust) carrying weaker material (e.g. sediment) encounters a strong hanging wall (e.g. Tibetan crust). Further material is added to the wedge at its tip and thickening occurs as the material is redistributed by thrusting, until a critical angle of the wedge is met and Coloumb failure occurs (Platt, 1993). At this point, extensional faulting must result (Dahlen et al., 1984).

In Himalayan critical taper models, the entire Himalaya is considered an orogenic wedge subject to the mechanics described above (e.g. Burchfiel and Royden, 1985; Burchfiel et al., 1992; Grujic et al., 1996; Kohn, 2008). The STD, a large-scale extensional structure, is considered the upper boundary to the wedge, initially forming due to gravitational collapse in the Miocene in order to restore the wedge's critical angle (Burchfiel and Royden, 1985; Burchfiel et al., 1992). The thrust faults (MCT, MBT, MFT) indicate periods of accretionary underthrusting, adding material and thickening the wedge (Harrison et al., 1998). Although the critical taper model essentially assumes the wedge behaves as a rigid block, flow within the wedge may be allowed as described by Harris and Massey (1994).

1.5. Leucogranites in Himalayan evolution

The Himalaya contains two east-west trending belts of leucogranite bodies. The North Himalayan leucogranites of southern Tibet are believed to be associated with gneiss dome uplift (King et al., 2011; Guo and Wilson, 2012). Further south are the High Himalayan leucogranites, intruding the uppermost lithologies of the GHS. It is these leucogranites that shall form the focus of this study, and any subsequent reference to leucogranites shall be referring to these, unless otherwise stated.

Leucogranites are found throughout the GHS, increasing in prevalence upwards through the sequence towards the THS, often culminating in large leucogranite bodies at the STD (Gansser, 1983; Guo and Wilson, 2012; Greenwood, 2013). Due to the intrinsic links thought to exist between melting and tectonic history of the GHS as outlined above, they have been the subject

of intense study, with particular impetus on understanding their source, age and petrogenetic conditions.

The High Himalayan leucogranites have been divided into two main categories based on their bulk mineralogy. The majority of leucogranites are two-mica leucogranites, notable for containing both biotite and muscovite in addition to quartz and feldspars. Tourmaline leucogranites, which form the second group, significantly contain tourmaline, in addition to one or both micas, quartz and feldspar (e.g. Le Fort et al., 1987; Harris et al., 1995). In addition, pegmatites are also recorded as having intruded across the orogen, characterized by their larger grainsize.

Numerous geochemical studies have been conducted, both using isotopes (Sr and Nd on whole rock, U-Pb in zircons) and trace elements (e.g. Rb, Sr, Ba, REEs) to determine the source, petrogenesis and timing of these melts (e.g. Inger and Harris, 1993; Guillot and Le Fort, 1995; Harris et al., 1995; Guo and Wilson, 2012). Through bulk rock Sr and Nd isotopic studies, it appears that the source of the leucogranites was the GHS, due to similar isotopic signatures shared by both GHS and leucogranite (e.g. Le Fort et al., 1987). Within the GHS it is thought that different sources have contributed to the formation of two-mica and tourmaline leucogranites, due to subtle differences in Rb/Sr ratios, Sr isotopic signatures and, crucial to tourmaline crystallization, boron abundances (Guillot and Le Fort, 1995). That the GHS might provide the lone source of these melts is not surprising, as the leucogranites are found solely within the sequence, with no field evidence yet observed for mantle-derived, mafic igneous bodies. In addition, the LHS and THS, other potential candidates for the source material, show no evidence for partial melting, whereas the GHS records extensive evidence. The suggestion that the mantle has played no part in producing widespread melting is possibly unique to the Himalaya. Many granite bodies in mountain belts around the world (e.g. Caledonides, North American Cordillera) are at least partially sourced from mantle material, which implies that advective heating has been added to these orogens through mantle magmas (e.g. Atherton and Ghani, 2002; Vigneresse, 2004). If it can be confirmed that the Himalayan leucogranites

contain no record of mantle input, this would imply that all heating within the orogeny was a product of burial, as a combination of conductive heat transfer and radioactive production of heat, with implications for our understanding of the thermal history of the orogen.

Should it be proven that the High Himalayan leucogranites represent pure crustal melts, it would open one further line of enquiry. Without the influence of the mantle, Himalayan melts would represent some of the lowest temperature and lowest batch volume melts on Earth, perfect conditions for stable isotope fractionation. In a recent study of stable Sr isotopic ratios ($^{88}Sr/^{86}Sr$) published by Charlier et al. (2012), variations in stable Sr ratios were detected in some felsic compositions. Given the correlation between $^{88}Sr/^{86}Sr$ and Eu anomaly, it was suggested that crystallization of feldspar causes mass-dependent fractionation of Sr. Without mantle input, the Himalaya represents a perfect natural laboratory for testing this hypothesis and investigating stable isotope fractionation during melting and crystallization.

Petrogenetic conditions of crustal melting to generate granite magmas are typically determined by trace element studies, in particular Rb, Sr and Ba which form the large ion lithophile elements (LILEs) and are sited in major phases in the protolith that drive the melt reactions. The most fusible rocks in the GHS are the metapelites, due in part to their mica-rich assemblages, and as such the most likely mineral phases to be involved in the melt reaction are biotite or muscovite. This melting may then occur under vapour-present or vapour-absent conditions, depending on the availability of H_2O during melting. Each of these different modes of melting will involve a different melt reaction, with each reaction producing and consuming different minerals and therefore leaving different geochemical signatures in the resultant rock, particularly in the LILEs. In the Himalaya, the Rb/Sr ratio of most leucogranites appears to increase as Ba decreases; a trend most suggestive of alkali feldspar being accumulated (e.g. Inger and Harris, 1993) (Fig. 1.4). This could be due either to fractional crystallization or the production of alkali feldspar as part of the melt reaction. As there is little density difference between feldspar and magma, and the lack of field evidence for cumulates, fractional crystallization seems unlikely, therefore suggesting alkali feldspar is produced as a peritectic

phase by the melt reaction. One possible melt reaction would be the breakdown of muscovite in vapour-absent conditions: muscovite + quartz + plagioclase = melt + K-feldspar + sillimanite. This evidence in combination with calculated crystallization temperatures of the leucogranites (typically ~700°C; Ayres and Harris, 1997; Greenwood, 2013) identifies the melt reaction as vapour-absent muscovite breakdown (e.g. Harris and Massey, 1994; Greenwood, 2013).

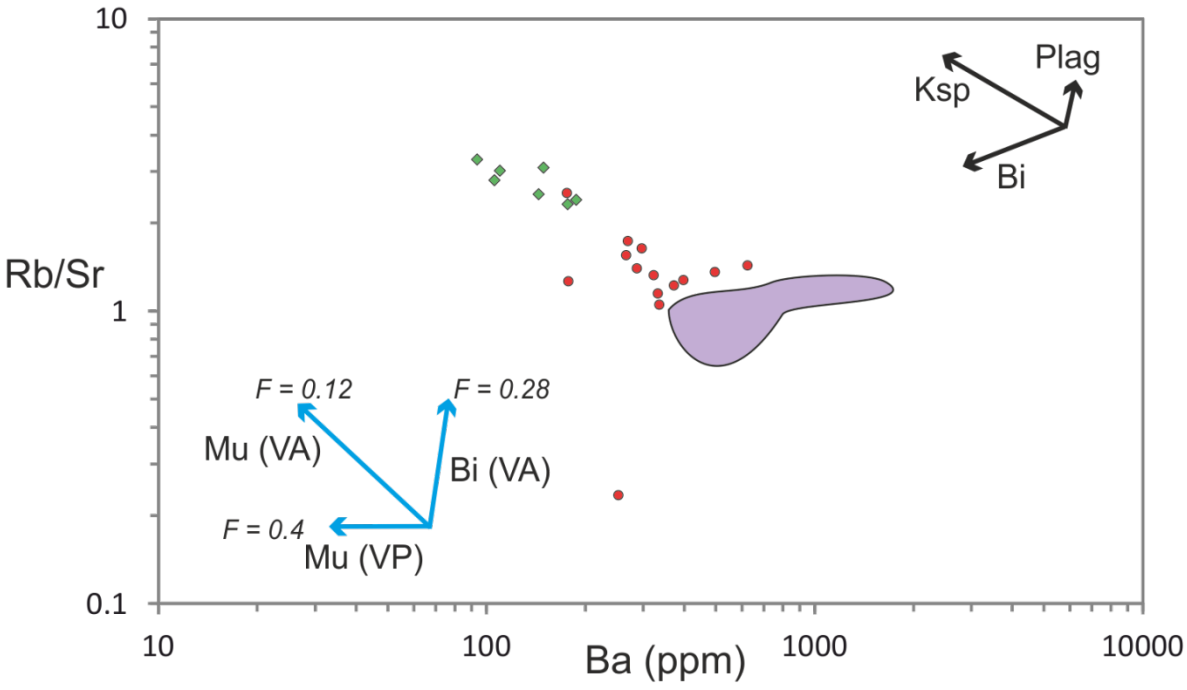

Figure 1.4: *Plot of Rb/Sr against Ba concentration for Langtang leucogranites (Nepalese Himalaya). Purple field represents GHS composition. Red circles indicate two-mica granites, while green diamonds represent tourmaline granites. Black vectors represent 10% crystallization of phases indicated. Blue vectors represent change caused by different partial melting reactions of muscovite (Mu) and biotite (Bi) melting under vapour-absent (VA) and vapour present (VP) conditions. Melt fraction extracted from each melt reaction is also indicated. Adapted from Inger and Harris (1993).*

Timing of crystallization has most often been constrained by U-Pb studies of either zircon or monazite, typically by LA-ICP-MS. Ages obtained from leucogranites throughout the Himalaya are shown in Figure 1.5, with data for High Himalayan leucogranites shown as crosses (references in figure caption). Across the orogen, the oldest ages obtained are fairly

constant – typically around 24 Ma (Harrison et al., 1997; Searle et al., 1997, 2003). The minimum ages appear to get younger eastwards through the orogen, with some samples from Bhutan as young as 12 Ma (Daniel et al., 2003; Greenwood 2013).

Due to the linked nature of the melts with the GHS, leucogranite crystallisation ages may be compared to metamorphic ages of the surrounding GHS. Prograde metamorphism is thought to have begun at ~30 Ma (Rubatto et al., 2012; Greenwood, 2013), reaching peak P-T conditions at ~23-20 Ma (Kellett et al., 2010; Rubatto et al., 2012; Greenwood, 2013), before decompressing at a relatively constant temperature between ~23-20 Ma and 20-13 Ma (Kellett et al., 2010; Rubatto et al., 2012; Greenwood, 2013). As leucogranite crystallization ages (with the exception of the Leo Pargil dome) are recorded between 24 and 12 Ma, these data imply that the majority of leucogranites appeared to form during decompression and exhumation.

One problem of this implication is the question of what caused exhumation to begin in the first place. The channel flow model requires partial melting to have occurred by the time that extrusion was initiated, in order to create a low viscosity channel that exhumes. However, it appears that all Miocene leucogranites analysed so far are products of exhumation, rather than the cause of it. The lack of any major High Himalayan leucogranite body crystallizing during prograde metamorphism is a major problem for the channel flow model.

However, a study of North Himalayan leucogranites found that certain melts ("anastomosing, equigranular granites") were typically older than those found in the main belt of the Himalaya, crystallizing between 28 and 24 Ma (King et al., 2011). These melts also appear to be formed by biotite breakdown, due to the presence of igneous garnet and the associated increase in HREE/LREE ratios and Y abundances. These early forming AEGs were suggested to have been the initial melts to reduce the viscosity of the GHS and induce exhumation. If similar Oligocene-aged prograde leucogranite bodies can be found in the High Himalaya, these may well provide additional further evidence for the initial reduction in viscosity and the onset of channel flow.

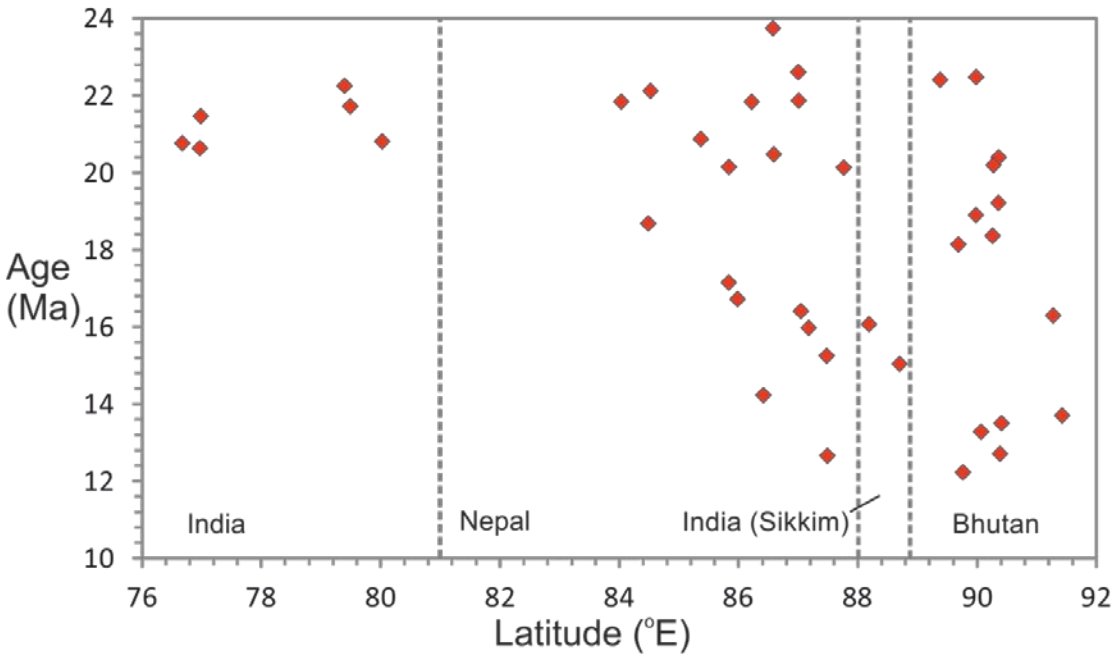

Figure 1.5: *Plot of leucogranite age versus latitude. Dashed lines roughly represent national borders. Data from Scharer et al. (1986), Searle et al. (1997, 2003), Simpson et al. (2000), Daniel et al. (2003) and Greenwood (2013).*

The long duration of melting recorded by regional studies (between 24 and 12 Ma in Bhutan) requires further comment. The ~11 million years of igneous history recorded at the Leo Pargil dome was thought to be comprised of distinct pulses rather than protracted of melting (Lederer et al., 2013), although no similar studies have been attempted in the High Himalayan leucogranites. It is therefore unknown whether melts in Bhutan were being constantly generated between 24 and 12 Ma, or whether there were also distinct pulses of melting, which could then in turn be linked to specific tectonic events recorded in metamorphic rocks. Furthermore, few attempts have been made to detect whether either the source of melting or the petrogenetic conditions have changed during this timeframe. More detailed studies of how the source and mode of melting changes over time may well be critical to our further understanding of the tectonics of the Himalaya.

1.6. Thesis objectives

This study aims to determine the geochemical characteristics of a suite of leucogranites intruded into the High Himalaya of Bhutan. Their geochemistry shall then be used to answer a range of problems relating to the role of crustal melts and granites in both Himalayan and global contexts:

- What units of the Himalaya are the primary source for melting, what was the primary melt reaction, and at what temperature did they form?
- Over what time-period has melting in the Himalaya occurred? And in the duration of leucogranite genesis has there been any change in either the source or the mode of melting?
- Can High Himalayan leucogranites be demonstrated, from their zircon geochemistry, to represent pure crustal melts (without any input from mantle-derived sources)? If so, what implications does this have for the heat budget of the Himalayan orogeny?
- By analysing a suite of whole-rock leucogranites and mineral separates, can stable isotope fractionation be demonstrated to occur during the generation and crystallisation of granite magma?

1.7. Thesis structure

Chapter 2: The Bhutan Himalaya

In this chapter I give a more detailed overview of the regional geology encountered in Bhutan, as well as describing the fieldwork undertaken in the autumn of 2012. I also provide both hand sample and thin section sample descriptions for each category of leucogranite and GHS samples.

Chapter 3: Major and trace element geochemistry

In this chapter I describe the various methods that previous studies have employed in order to generate major and trace element geochemistry data, and evaluate which method suits my samples the best. I then show and describe major and trace element data for all leucogranite samples, first using aluminium saturation indices and europium anomalies to determine whether leucogranite samples likely represent pure melt signatures, or whether it is possible they have incorporated restitic phases. Trace element data is then used to perform modelling of temperatures and melt reactions, in order to understand the petrogenetic conditions surrounding the formation of Bhutan leucogranites.

Chapter 4: Whole-rock isotope geochemistry

Whole rock Sr, Nd and Pb radiogenic isotope geochemistry data is presented for 19 Bhutan leucogranite samples. Isotope ratios are compared to previous data reported from potential source regions (i.e. the GHS, LHS and THS) in order to evaluate the likely sources of melting to produce leucogranites.

Chapter 5: The identification and significance of pure sediment-derived granites

The High Himalayan leucogranites are thought to be derived from the GHS in which they are now found, based on whole-rock Sr and Nd isotope studies (e.g. Le Fort et al., 1987) which is limited in providing averaged information that may mask contributions from specific sources. In this study, I show how a combined Hf, U-Pb, O isotopic approach, similar to that of Kemp et al. (2006, 2007), proves that these leucogranites contain no mantle component and therefore that they provide an exemplary end-member for S-type granites. This chapter is adapted from a manuscript submitted to the journal Geology.

Chapter 6: Zircon isotope geochemistry and geochronology

Several problems related to the formation and emplacement of leucogranites in the Himalaya are investigated in this study. Few studies have attempted to make detailed links between

changes in source and age of the High Himalayan leucogranites. In this chapter I describe through an isotopic study of zircons how the source of melting changes over the igneous history of the Bhutan Himalaya, and compare findings in zircon isotope geochemistry to those from whole-rock isotopic data.

Chapter 7: Stable Sr and Rb isotope fractionation during melting

High Himalaya leucogranites are examples of crustal melting formed under the lowest magmatic temperatures that are possible. Hence they are ideal for studying disequilibrium isotopic behaviour that might not be apparent in the evolution of higher-temperature magmas.

In this chapter I present the stable Sr ratios of a selection of whole rocks and mineral separates from High Himalayan leucogranites by using both MC-ICP-MS and a double-spike TIMS technique. The TIMS method allows for far higher precision compared to plasma instruments and will also provide data for ^{84}Sr. The leucogranites of the Himalaya provide excellent candidates for investigating potential stable isotope fractionation, due to the low temperatures and low volumes of melting involved in their formation. I demonstrate that Sr fractionation occurs during melting and crystallization, and by analysing mineral separates I show that there is systematic fractionation between feldspars that could lead to the variations seen by Charlier et al. (2012).

I also present stable Rb ratios and show that while variations outside of analytical uncertainty can be recorded, there is little consistency to the nature of this fractionation between mineral phases or samples.

Chapter 8: Synthesis and conclusions

In this final chapter I summarise the findings and conclusions reached in this study, and attempt to answer the fundamental research questions as documented above. Suggestions for future work are then proposed.

Chapter 2

The Bhutan Himalaya

Bhutan lies to the north of the Bay of Bengal, in the eastern Himalaya (Figure 2.1). The majority of the bedrock is formed of high-grade metamorphic Greater Himalaya Sequence (GHS) rocks (Figure 2.2), though a somewhat unique feature of Bhutan's geology is the presence of several tectonic klippen (isolated portions of a tectonic nappe that have resisted erosion) of Tethyan Himalaya Sequence (THS) rocks. These klippen allow the fault that separates the two units, the South Tibetan Detachment (STD), to be readily accessible at low elevations, permitting improved sampling and investigation of rocks from the fault zone. Associated with this fault, but also found throughout the upper GHS, are large volumes of leucogranites. The large volume of easily accessible leucogranite in the Bhutan Himalaya is the reason this area was chosen for fieldwork.

2.1. Geography

Bhutan is a small country roughly comparable in both size and geography to Switzerland. Located in the east of the Himalayan mountain belt, Bhutan is bordered to the west by the Indian state of Sikkim and to the east by the Indian state of Arunachal Pradesh (Fig. 2.1). The low-level (less than one hundred metres above sea level) plains of Indian Assam border to the south, and elevations rise northwards towards the 5000 m-high Tibetan plateau at the northern border with China.

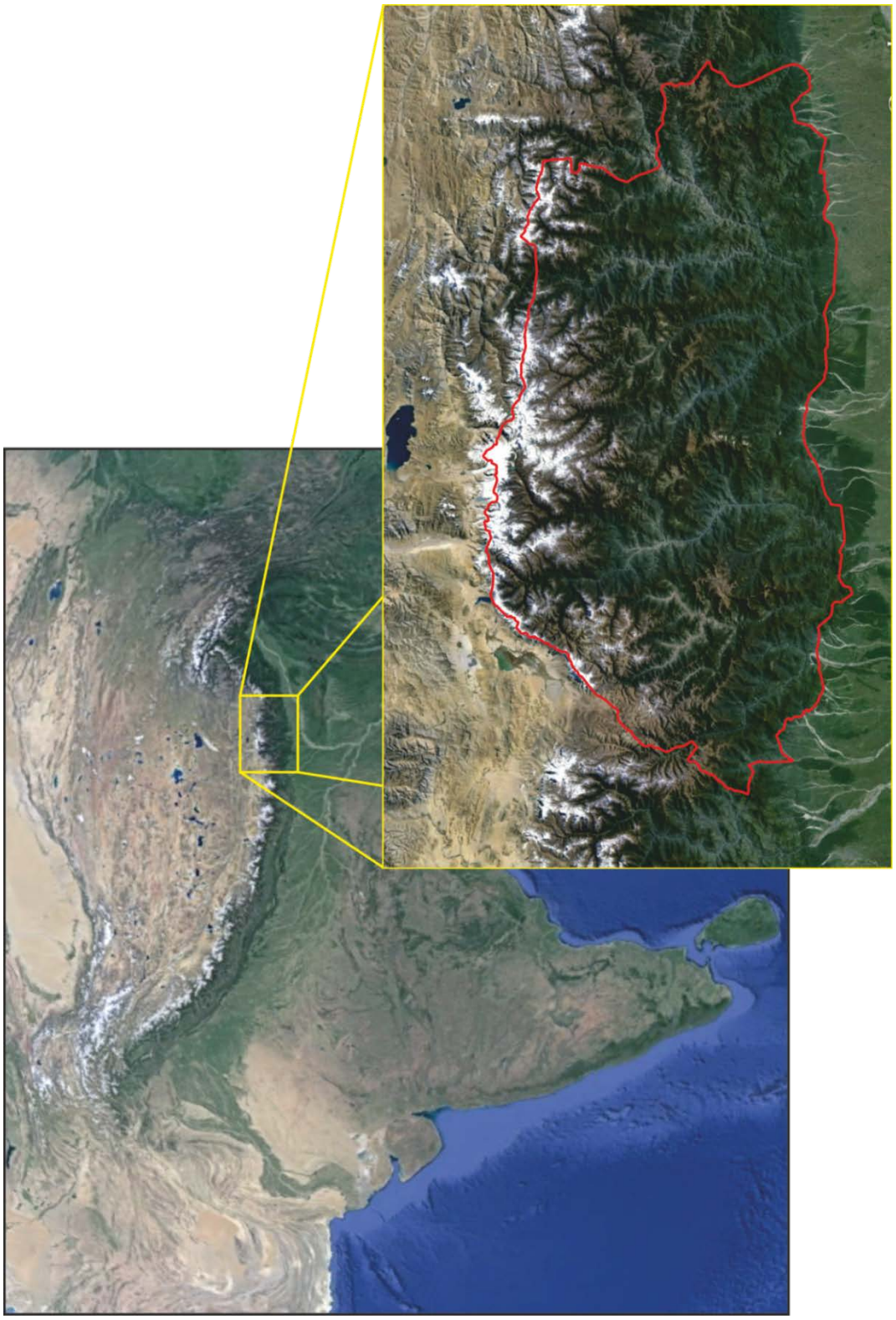

Figure 2.1: *Satellite view of India, south-western China and the Himalayan orogeny, with Bhutan highlighted in inset (Images courtesy of Google).*

Warm summer temperatures and very high precipitation (up to 1000 mm per year) mean that 70% of Bhutan is covered in forest. The bedrock is therefore not always exposed. However, due to recent improvements in infrastructure, road cuts are common, and provide readily accessible sites for fieldwork.

2.2. Geology

2.2.1. Lesser Himalayan Series

The LHS outcrops in the south of the country (Figure 2.2) and comprises a series of limestones, quartzites, siltstones and slates (Gansser, 1983; McQuarrie et al., 2008). There is very little exposure of the LHS in western and central parts of Bhutan, and the majority of studies have focussed on a section along the Kuru Chu river valley in eastern Bhutan (e.g. McQuarrie et al., 2008).

The LHS in Bhutan is divided into four main units: the Daling-Shumar Group, the Baxa Group, the Diuri Formation and the Gondwana Sequence (Gansser, 1983). The Daling-Shumar Group is the structurally highest unit of the sequence and is composed primarily of quartzites with occasional bands of phyllite or schist. Detrital U-Pb zircon and monazite dating suggest protolith ages of 1.84 – 1.76 Ga (Daniel et al., 2003). Its thickness varies across the strike of the Bhutan Himalaya, but peaks at roughly 10 km in the Kuru Chu area (McQuarrie et al., 2008). The Baxa Group, composed of quartzite, siltstone and slate with occasional lenses of dolomite and limestone, underlies the Daling-Shumar Group (Gansser, 1983; Tangri, 1995; McQuarrie et al., 2008). Field observations suggest the group is 2.5 km thick, while thrusting has also caused thickening up to 11 km in the Kuru Chu region (McQuarrie et al., 2008). The Diuri Formation, a 2.5km thick unit of slates, shales and diamictites, underlies the Baxa group. The structurally lowest LHS group is the Gondwana Sequence, comprised of sandstones, siltstones and shales, with coal lenses and Permian-aged plant fossils (Lakshminarayana, 1995).

2.2.2. Greater Himalayan Series

The GHS in Bhutan forms the majority of the bedrock in the country (Figure 2.2), and predominantly consists of metapelites, with minor orthogneisses, calc-silicates, quartzites, and mafic rocks (Gansser, 1983). Leucogranites intrude throughout the higher structural levels, particularly around the STD zone.

GHS metamorphism in Bhutan has generally reached upper amphibolite facies and partial melting is common, producing migmatites (Hodges, 2000). Rare occurrences of granulitised eclogites are exposed within the northern reaches of the GHS in northwest Bhutan (Swapp and Hollister, 1991; Cottle et al., 2009, Warren et al., 2011). Peak metamorphic conditions are 650°C and 9-13 kbar at the base of the GHS near the Main Central Thrust, rising up to 750-800°C and 10-14 kbar at higher structural levels, where partial melting and migmatization have occurred (Daniel et al., 2003). Zircon and monazite geochronology from the GHS have revealed a history of partial melting at upper amphibolite facies conditions stretching from 36-17 Ma (Rubatto et al., 2013; Greenwood, 2013).

In Bhutan the thickness of the GHS has been greatly increased due to the action of two thrust faults (Figure 2.2): the Kakhtang Thrust in central and eastern Bhutan and the Laya Thrust in the north west (Grujic et al., 2002; Long et al., 2011). It has been postulated that these thrusts are part of the same fault system, though this remains unconfirmed (Grujic et al., 2011).

The top of the unit is bound by the South Tibetan detachment (STD), with the Tethyan Sedimentary Sequence above. In Bhutan specifically, the STD is separated into two sections. The inner STD is exposed along the northern border at the highest structural levels, and the outer STD exposed further south, bounding a large klippen of TSS material in the centre of the country (Long and McQuarrie, 2010; Greenwood, et al., 2015).

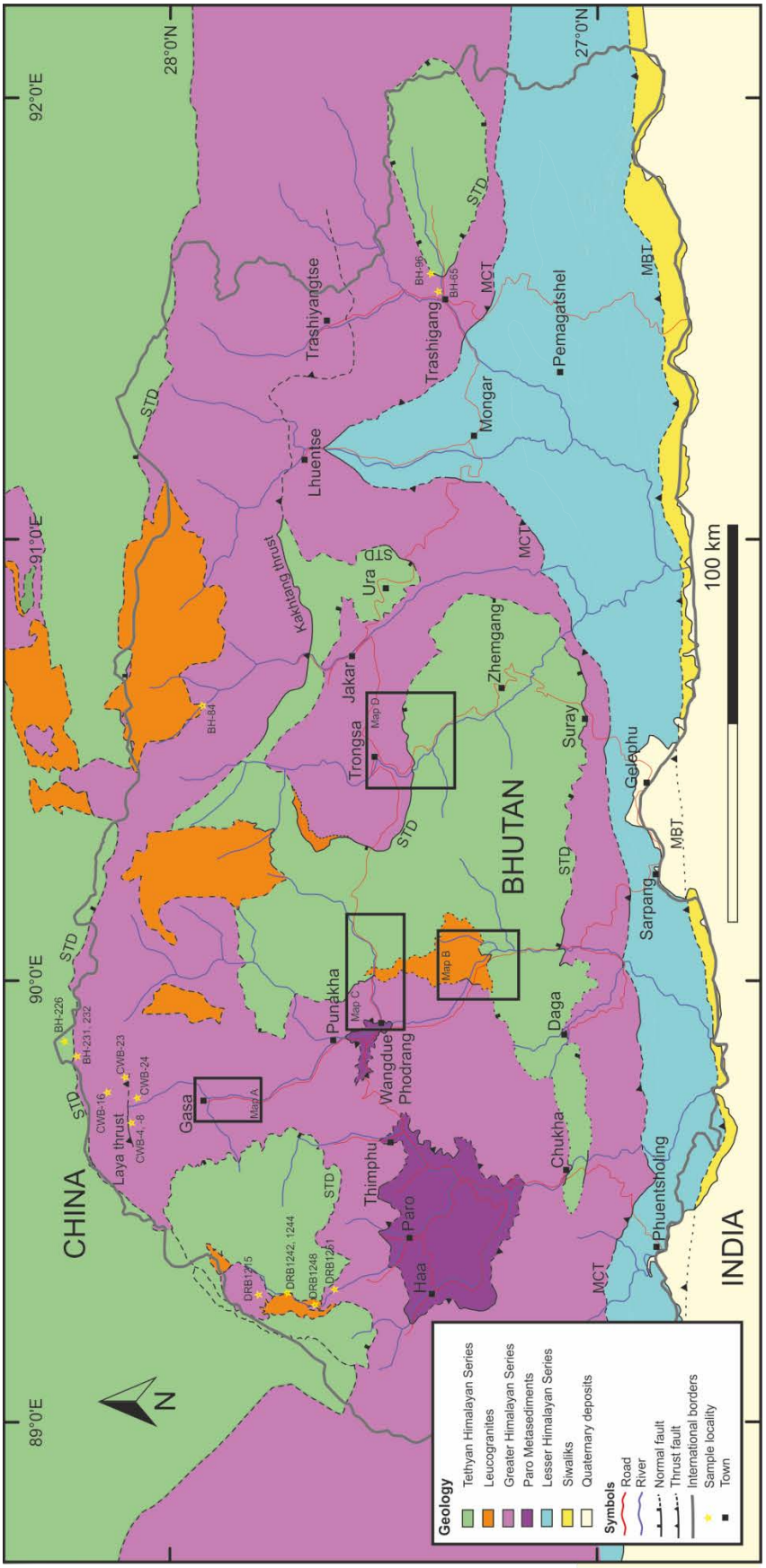

Figure 2.2: *Geological map of Bhutan adapted from Greenwood (2013) and Greenwood et al. (2015). Selected sample localities are shown. Boxes indicating areas covered in local maps are also shown.*

2.2.3. Tethyan Himalaya Series

The THS lies directly above the STD (Figure 2.2) and is formed of sediments (occasionally showing low-grade metamorphism) deposited in the Tethyan Ocean. Occasional volcanic units are also present.

At the base of the THS is a unit of greenschist-facies metasediments known as the Chekha Formation, mostly containing quartzites and mica schists. The base of the Chekha, and therefore the exact location of the STD, has been interpreted and mapped differently by various authors. Gansser (1983), Grujic et al. (2002) and Greenwood (2013) have interpreted it as the base of a garnet-staurolite-muscovite schist, whereas Long and McQuarrie (2010) identified a structurally-higher tan coloured quartzite unit as the basal unit.

The THS in Bhutan is most easily accessed where exposed in the tectonic klippen found at relatively low elevations. As many as five klippen have previously been mapped in Bhutan termed, from west to east, the Lingshi, Dang Chu, Black Mountain, Ura and Sakteng klippen (e.g. Grujic et al. 2002, Long et al. 2011). However, more recent mapping has suggested that the central three klippen – the Dang Chu, Black Mountain and Ura klippen – may instead form one large klippe that extends across the centre of the country (Figure 2.2, Greenwood et al., 2015).

2.2.4. Leucogranites

In Bhutan, leucogranite bodies are found throughout the upper regions of the GHS. Their abundance increases upwards towards the STD, with kilometre-scale plutons occurring either immediately below, or cross-cutting, the detachment. Rare intrusions into the lowest units of the TSS are also recorded (Guo and Wilson, 2012; Greenwood et al., 2015). At outcrop scale, these leucogranites can occur as either layer-parallel sheets, cross-cutting dykes, or larger plutons.

There are three compositional categories of leucogranite; two-mica granites, tourmaline leucogranites and pegmatites. All types may form small veins or larger plutons, although the

majority of examples are found as centimetre to metre scale sills and dykes (Gansser, 1983; Greenwood, 2013). Many larger leucogranite intrusions form layer-parallel bodies close to the STD, with some dykes intruding upwards into the overlying Chekha formation.

2.3. Sampling localities

2.3.1. Gasa section

Samples collected along the Punakha-Gasa transect (Figures 2.3 and 2.4) represent the lowest sampled structural levels of the GHS. Granite sills and dykes were typically small scale, rarely exceeding 50 cm thickness (Figure 2.4a). The mineralogical composition of individual leucogranite bodies was highly varied, with all leucogranite types exposed. One locality (1G, Figure 2.4b) displayed cross-cutting relationships with a pegmatite sharply cross-cut by a tourmaline leucogranite sill, which appeared to be coeval with a two-mica leucogranite, inferred from slight mixing at the boundary between the two (Figure 2.4b). The conclusion that the pegmatites were the earliest emplaced melt at this locality is in contrast with other regional observations that suggest the pegmatites were the most recent melts to crystallize (e.g. Greenwood, 2013; and references therein).

The GHS in this area contains metapelites with varying degrees of migmatization. The metapelites mostly occur as either schists (muscovite + biotite + quartz + feldspar ± garnet ± sillimanite), or as gneisses with quartz and feldspar in the leucosomes, and biotite dominating the melanosome. These gneisses may also contain garnets, sillimanite, or rarely kyanite. The kyanite is commonly rimmed with sillimanite. Unique to this area is the occurrence of bountiful calc-silicate units, composed predominantly of quartzites containing varying quantities of calcium-bearing mineral phases (in particular calcite and titanite). Augen-gneiss bodies are also present, though these are far less common than the metapelites (Figure 2.4c).

There is abundant evidence for boudinage and shear thinning (Figure 2.4d), and occasional examples of garnet pressure shadows in both leucogranites and host rocks. Sense of shear is top-to-the-south, consistent with previous findings in Bhutan (Grujic et al., 2002). Parasitic folds are commonly present in calcite layers, and centimetre to metre scale S- and Z-shaped folds are present in the metapelites and quartzites.

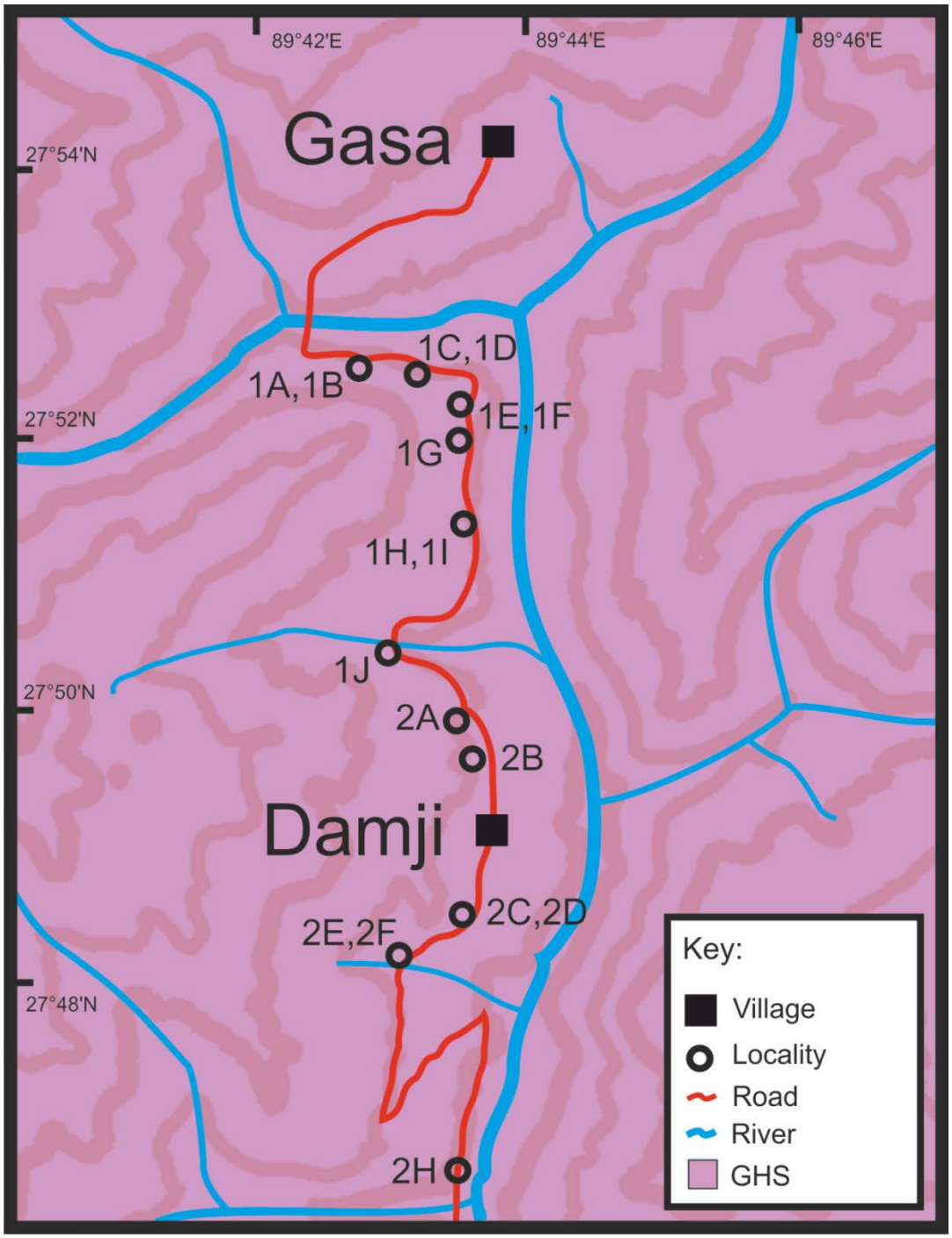

Figure 2.3: *Map A. Local map of the Gasa area with individual localities indicated.*

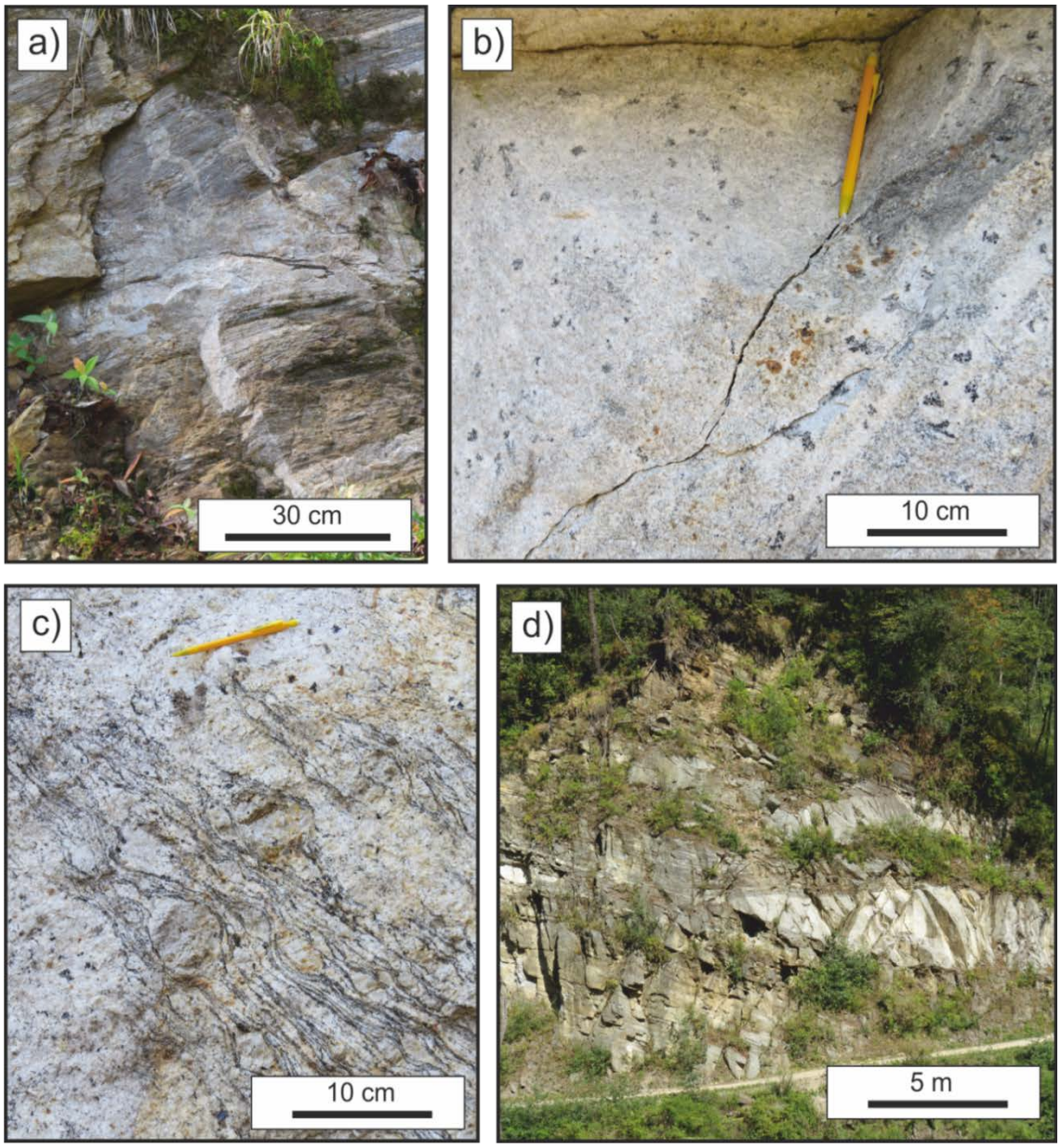

Figure 2.4: *a) Granite dyke cross cutting an earlier sill and GHS schist (Locality 1A). b) Mingling of two-mica and tourmaline magmas at locality 1G. Tourmalines appear as centimetre-sized radial crystals. c) Schlieren of augen-gneiss engulfed by leucogranite at locality 2G. d) Leucogranite sill tapering from a thickness of ~3 m to ~10 cm, showing evidence for post-magmatism deformation.*

2.3.2. South of Wangdue-Phodrang

The road south of Wangdue provides a transect through the upper levels of the GHS into the Black Mountain klippe (Figure 2.5). The basal Chekha Formation of the THS was the host for

all of the leucogranite samples collected along this transect. Closest to the STD (locality 3A) the host rocks are middle-greenschist facies metapelitic schists, composed of biotite + muscovite + quartz + plagioclase ± garnet. Rare bands of quartzite intersperse the unit. At structurally higher levels, the THS comprises lower-greenschist facies phyllites with rarer intrusions of granite. The phyllites are highly micaceous and sedimentary structures are preserved. At locality 3B a fining-upwards sequence suggested that the unit has not been overturned. In addition, sedimentary bedding is common, and at locality 3C cleavage replaces bedding as the dominant foliation. Evidence of shear is also present, in the forms of boudinage and shear thinning, as shown in Figure 2.6b.

The leucogranite bodies exposed along this transect are more plentiful and larger in scale, ranging from metre-scale dykes (Figure 2.6c) to cliff-forming bodies with a large kilometre-scale unit of leucogranite cross-cutting the STD. Structurally upwards towards the STD, increasing quantities of leucogranite with two-mica, tourmaline and pegmatitic facies all observed, commonly displaying cross-cutting relationships.

Localities 3A and 3D lie within the major leucogranite body mapped by Greenwood et al. (2015). Rather than being a continuous unit of homogenous leucogranite, this unit appeared to represent an area where leucogranite sills, dykes and plutons forms the majority (>50%) of outcrop. The individual intrusions display abundant mineralogical variety. Two-mica, tourmaline, garnet and muscovite leucogranites and pegmatites were observed. At locality 3A, a two-mica leucogranite and a garnet leucogranite appear to be coeval (Figure 2.6a); these are both cross-cut by a tourmaline leucogranite, which is in turn cross-cut by a pegmatite. A similar sequence of crystallization and intrusion is commonly reported across the Himalaya (e.g. Guillot and Le Fort, 1995, Greenwood, 2013).

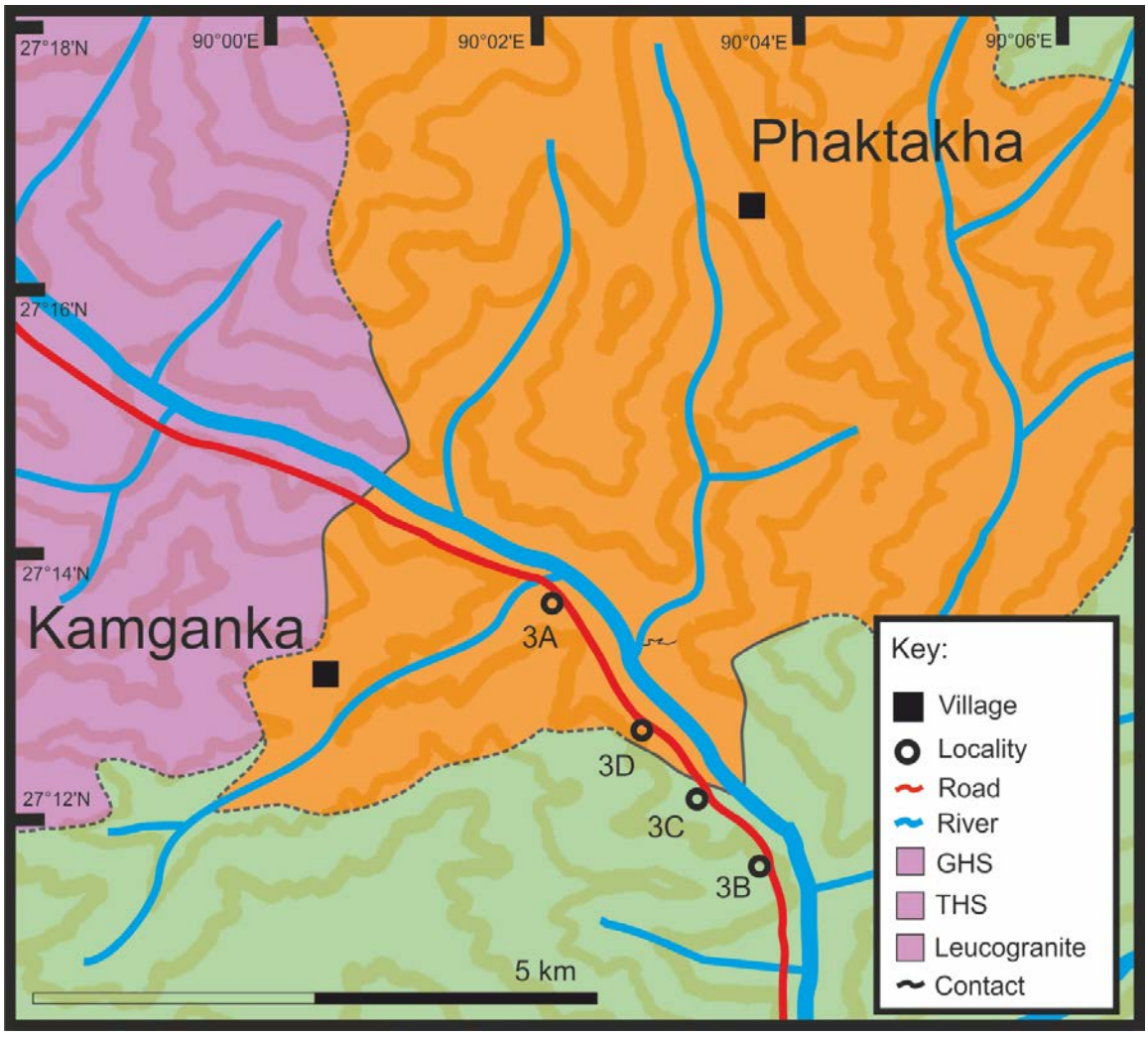

Figure 2.5: *Map B. Local map of transect south of Wangdue-Phodrang with individual localities indicated.*

2.3.3. Wangdue to Pele La

The road east of Wangdue provides a transect through the upper levels of the GHS, into the THS, crossing the STD (Figure 2.7). Leucogranite bodies are less abundant than south of Wangdue, and sills and dykes are typically no thicker than 60 cm (Figure 2.6d). Pegmatite intrusions are more common and typically thicker, often forming sills and dykes reaching 2-3 m in thickness (Figure 2.6d), with one major unit of tourmaline pegmatite (locality 4G) reaching at least 30 m by 20 m in size, located within the STD zone. The smaller leucogranite dykes are

largely two-mica leucogranites in this area, with some bearing garnets. They were commonly cross-cut by pegmatites.

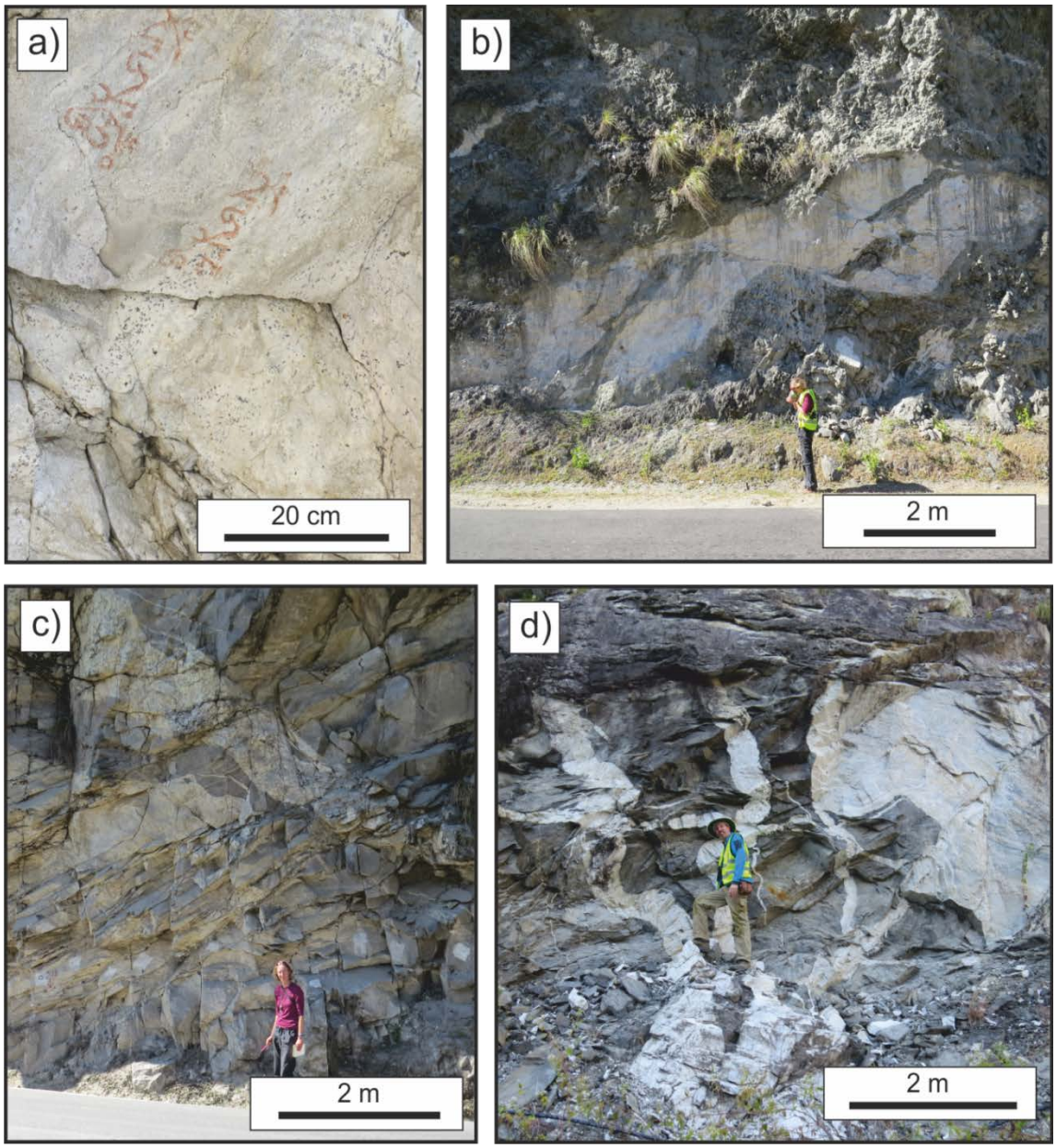

Figure 2.6: *a) Mingling of different granitic magmas at locality 3A. b) Top-to-the-north sheared leucogranite dyke (Locality 3A). c) Cross cutting leucogranites at locality 3A. d) Three generations of cross-cutting magmatism at locality 4H.*

The upper GHS in this region is dominated by metapelitic gneisses, with common migmatization. Leucosome layers are typically dominated by quartz and plagioclase, with some

garnet, whereas melanosome layers are dominated by biotite, sillimanite and rare tourmaline. Structural evidence of shearing increases structurally upwards towards the STD zone in this transect, with shear foliation, boudinage and parasitic folding increasingly common.

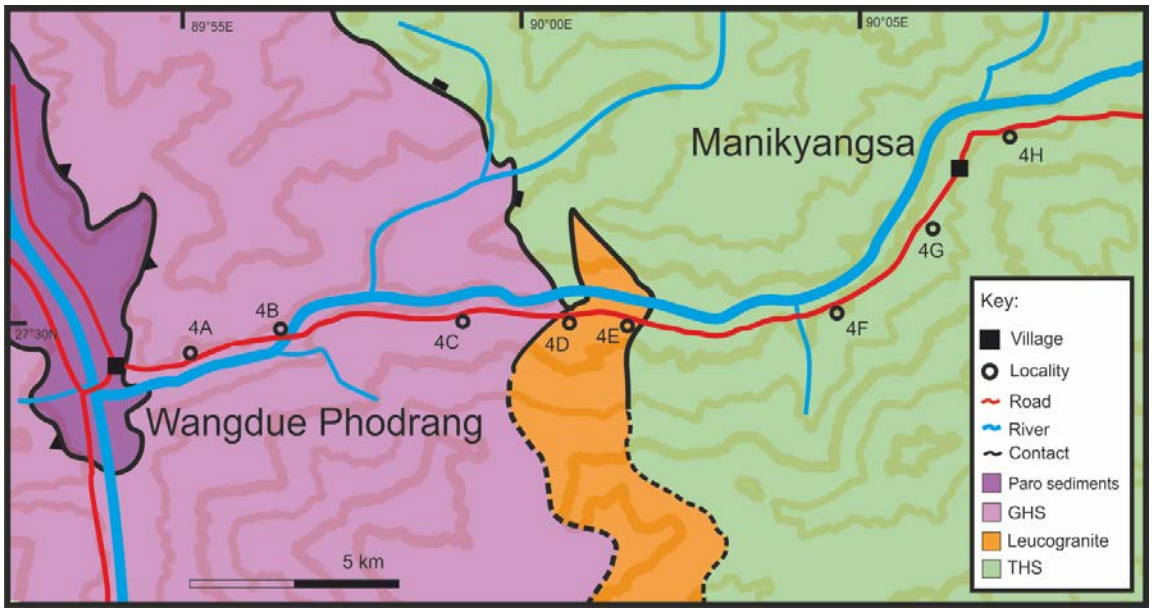

Figure 2.7: *Map C. Local map of transect east of Wangdue-Phodrang with individual localities indicated.*

The THS immediately above the STD is dominated by middle-greenschist facies phyllites containing biotite, muscovite, quartz, plagioclase and rare garnet, interbedded with quartzites. The THS is occasionally intruded by leucogranite and pegmatite dykes.

2.3.4. South of Trongsa

The outcrops exposed along the road south of Trongsa towards Zhemgang increase in structural level from the GHS into the Black Mountain klippe of THS material (Figure 2.9). Melt units are less common along this transect, with no body exceeding 2 m in width, and no cross-cutting relationships observed (Figures 2.8c and 2.8d). Leucogranite bodies in this area are typically tourmaline-bearing, with fewer examples of two-mica varieties. One example of a muscovite granite was also collected (locality 5M). Both two-mica and tourmaline pegmatites are also common.

The GHS in this area is more varied than in the other sampled regions. The sequence includes metapelitic gneisses and schists, orthogneisses and rare mafic amphibolite blocks. The metapelitic gneisses typically exhibit migmatization, with leucosomes containing quartz and plagioclase, and melanosomes containing biotite, feldspar and rare tourmaline, sillimanite and hornblende. The schists share a similar mineralogy, but are richer in mica, and also contain chlorite and staurolite. Rare orthogneiss bodies are typically more leucocratic than the metapelites, and are dominated by quartz, plagioclase and biotite, with rare garnet.

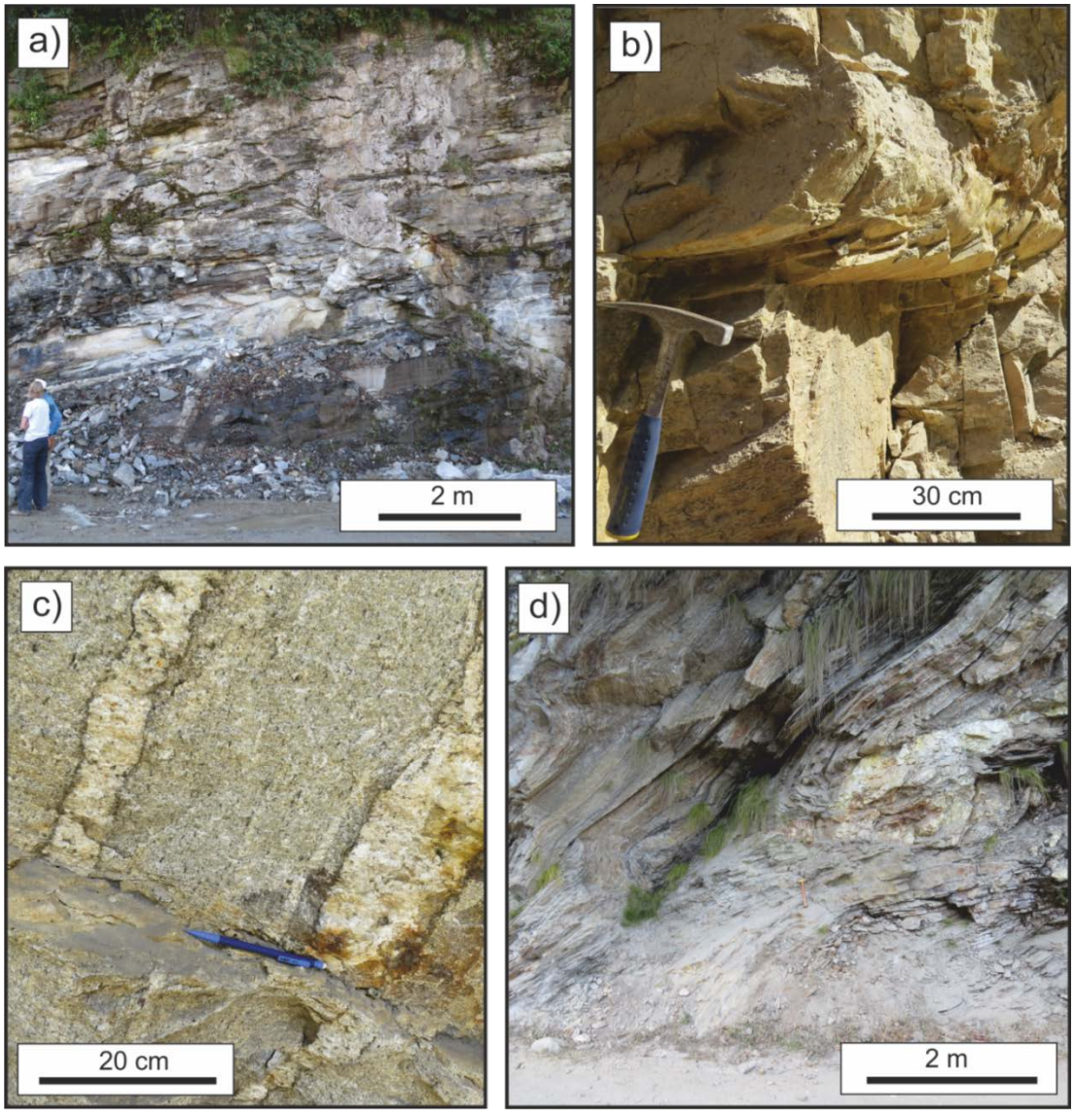

Figure 2.8: *a) Cross-cutting leucogranite intrusions at locality 4H. b) Cross bedding in the Tan quartzite of the THS observed at locality 5A. c) Leucogranite veins cut by brittle faulting at locality 6F. d) Metasediments folding around leucogranite pod at locality 6B.*

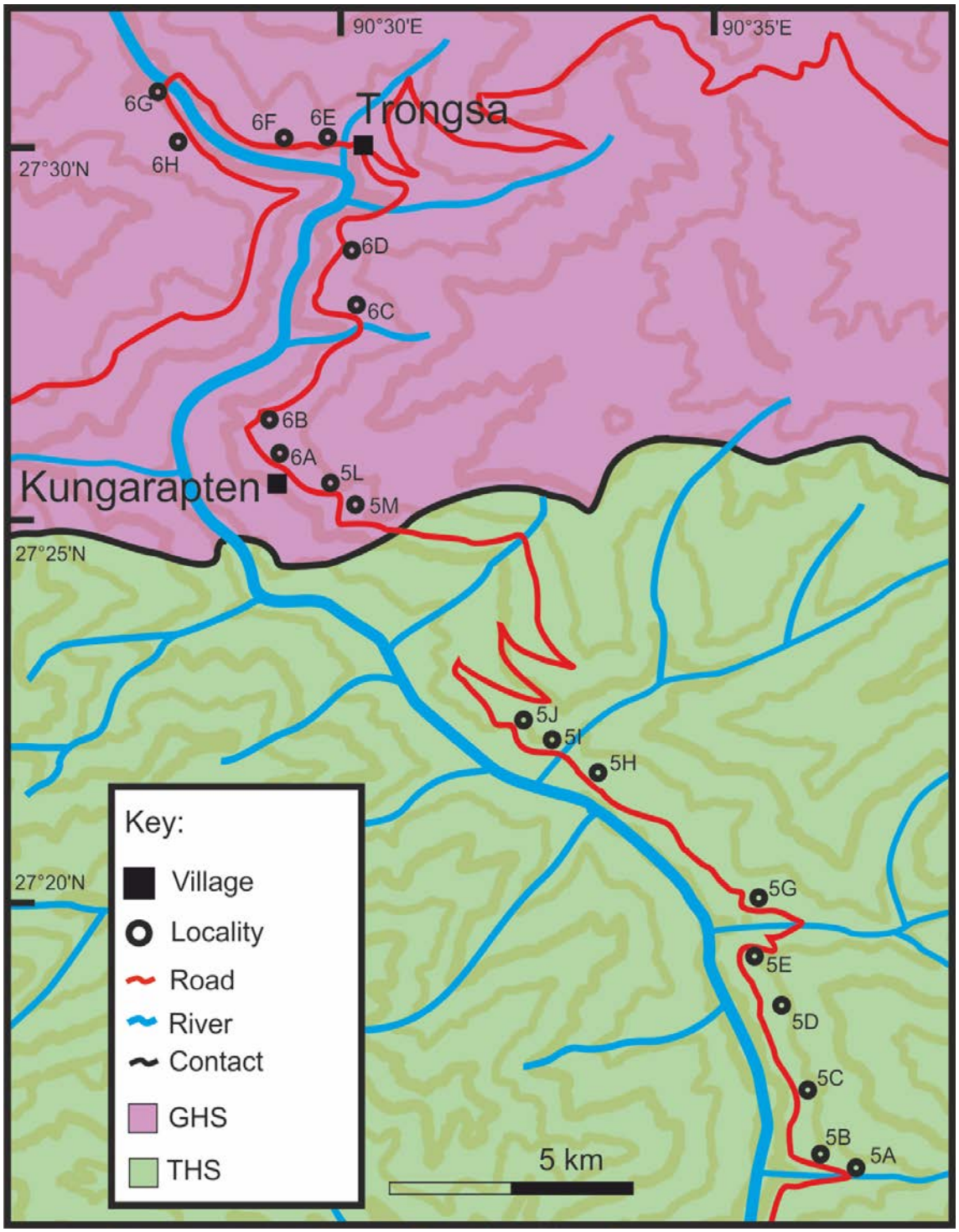

Figure 2.9: *Map D. Local map of the area around Trongsa, with individual localities indicated.*

The Chekha formation here is dominated by phyllites and quartzites, metamorphosed to middle-greenschist facies at the base of the unit and to lower-greenschist facies at the top. At locality

5A a unit of tan quartzite, immediately above the Chekha formation, represents a structural level into which the leucogranites did not intrude. This unit is characterized by sandy-coloured quartzites and (meta)psammites, which have only experienced weak metamorphism. Cross-bedding indicates a fluvial depositional environment for these sediments (Figure 2.8b). The psammites contain quartz, plagioclase, biotite and muscovite. Some units also contain chlorite, suggesting low-grade metamorphism.

2.4. Other samples

Several samples documented in this thesis were collected by others from areas not covered in this field season. Samples with a DRB- prefix were collected from the Jhomolari Massif, north-west Bhutan, by Daniele Regis (Geological Survey of Canada); CWB- prefixed samples were collected by Clare Warren (Open University) from the Laya area of north-west Bhutan, and samples with a BH- prefix were collected by Djordje Grujic (Dalhousie University) from a range of localities within Bhutan.

2.4.1. Jomolhari Massif

The Jomolhari massif is a dome of GHS material, bound to the west by the Yadong graben and by the Lingshi fault to its east, juxtaposing the unit against the THS (Regis et al., 2014, Gansser, 1983). To the south of the massif is a large leucogranite body outcropping at the STD and intruding into the THS above. DRB1215 was sampled from within the massif, as a layer-parallel sill of leucogranite. Samples DRB1242, DRB1244, DRB1247 and DRB1248 were sourced from within the large leucogranite body south of the massif. Finally DRB1251 was collected from within the GHS to the south of the pluton. For discussion in later chapters, the DRB- prefix is dropped.

2.4.2. Laya

Laya is located to the north of Gasa, and is situated close to the Laya Thrust. The Laya Thrust is an out-of-sequence thrust within the GHS, placing deeper GHS to the north on top of more shallow rocks to the south (Warren et al., 2011). Samples CWB-16 and CWB-23 were collected from the hanging wall to the north of this thrust, with the remaining samples taken from the footwall.

2.4.3. BH- Samples

Samples with the prefix BH were collected by Djordje Grujic from three different locations around Bhutan. Samples BH226, BH231A, BH231B and BH232 were collected from the area north of Laya at the border with Tibet. At these latitudes and elevations the structurally higher STD is exposed (as opposed to the structurally lower STD associated with klippen further south). These leucogranites are therefore associated with the structurally highest levels of the GHS. Samples BH65 and BH96 were collected from around Trashigang in the east of the country, along a transect crossing the STD between the GHS and the Sakteng klippe. Finally sample BH84 was collected from the Chura Kang leucogranite body, the largest in Bhutan, in the north-east of the country.

2.5. Sample descriptions and petrography

2.5.1. Leucogranites

The two main categories of leucogranites found across the Himalaya are the two-mica and the tourmaline leucogranites (Guillot and Le Fort, 1995; Harris et al., 1995; Greenwood, 2013). In Bhutan, ‘garnet leucogranites’ are also common, and these are similar to the two-mica and tourmaline leucogranites but also contain up to 10% garnet. Two examples of muscovite leucogranites were also found, distinct from other leucogranites in that they contain neither biotite nor tourmaline.

2.5.1.1. Two-mica leucogranites

The two-mica leucogranites are the most common form of leucogranite described from the Himalaya (Guillot and Le Fort, 1995), and form the majority of samples collected for this study. They contain quartz (20-25%), plagioclase (10-35%), K-feldspar (10-35%) and mica (5-25%). Euhedral quartz and plagioclase are typically up to 10 mm in length, while K-feldspar grains are mostly subhedral and generally up to 15 mm in length. The ratio of biotite to muscovite varies between samples, with some samples containing only rare examples of the less abundant mica. Biotite blades are typically up to 15 mm long, while muscovites are often smaller, typically no longer than 8 mm.

Micas are typically good indicators of whether a rock has experienced either stress or fluid interaction. In many samples the biotite has been partially or wholly replaced by chlorite, suggesting post-crystallization fluid-interaction. In some samples, distorted or cracked micas record evidence of post-crystallization stress.

In the field, the two-mica leucogranite bodies outcrop in a variety of volumes, from small, 5-20 cm in-situ melt pods, to cross-cutting dykes (up to 5 m in width) and even as large cliff-forming bodies. Unlike previous studies, which have suggested that two-mica leucogranites are often cross-cut by (and therefore are older than) tourmaline leucogranites (e.g Guillot and Le Fort, 1995) no consistent correlation between mineralogy and field-relationship age was observed in this study. Two-mica and tourmaline leucogranites commonly cross-cut each other at different localities, and even show mingling upon contact in some places.

Order of crystallization can be inferred from thin sections. Plagioclase and biotite typically form euhedral grains and rarely contain inclusions, suggesting that they were the first phases to crystallize. Quartz is generally subhedral, although some crystals engulf plagioclase, thereby suggesting relatively early crystallisation. K-feldspar and muscovite crystals are subhedral to anhedral, and form most of the matrix, suggesting that they are the last phases to crystallise. These K-feldspars commonly contain inclusions of quartz or plagioclase. In some samples, rare

K-feldspar crystals are euhedral, suggesting that the melt has entrained K-feldspar probably formed during the melt reaction.

Numerous accessory phases can also be observed in thin section. The most prevalent of these is zircon, found in the majority of samples. Other common phases include rutile, titanite (sphene), apatite, monazite and ilmenite. Samples also contain rare xenotime, pyrochlore and euxenite.

There is some evidence for mild deformation in some samples. Undulose extinction of quartz is common, and micas are often sheared and deformed. Biotite is sometimes converted to chlorite (either partially or wholly), indicating retrograde fluid activity.

2.5.1.2. Tourmaline leucogranites

Tourmaline leucogranites are the second-most prevalent type of leucogranite found in the orogen, comprising ~30% of all leucogranites. They are dominated by quartz (20-25%), plagioclase (10-35%) and K-feldspar (10-35%) and contain up to 15% schorl tourmaline. Tourmaline forms two main textures: large prismatic cylinders and radiating skeletal crystals (Figures 2.4b, 2.10a). Prismatic tourmaline forms lathes up to 15 mm in length, while the radiant variety forms patches up to 10 mm in diameter. Tourmaline leucogranites also commonly contain muscovite (up to 5%), occasionally up to 5% biotite and rare sillimanite.

In thin section tourmaline appears equant, occasionally displaying radial symmetry that represents their 3-dimensional appearance in hand specimen. Their colour varies between black, blue and yellow, confirming that tourmaline is the schorl variety. Occasional crystals display pleochroism between yellow and blue. One sample, DRB1215, contains the elongated, prismatic form of tourmaline. This sample also contains sillimanite, forming clusters of fine grained needles, comprising 5% of the rock.

2.5.1.3. Garnet leucogranites

This variety of leucogranite is distinguished by the presence of garnet, comprising no more than 10% of the rock. In many other aspects garnet leucogranites are similar to the two-mica and

tourmaline varieties. Quartz, plagioclase and K-feldspar form the majority of the rock, while muscovite, biotite, tourmaline and sillimanite are commonly present in varying quantities. The one notable exception to this is sample 1D01, which contains ~5% sillimanite but no tourmaline or mica. This sample also contains 40% quartz, as well as plagioclase and K-feldspar.

The grainsize of garnet leucogranites is typically smaller than other varieties; garnets rarely exceed 5 mm in diameter, with quartz and feldspar no larger than 8 mm. 1D01 is exceptional in that garnets reach 15mm in diameter. Sillimanite occurs as clusters of fine needles, only individually distinguishable in thin section. Needles are individually no longer than 2mm long, while the clusters can be up to 20mm in length.

In thin section, garnets are euhedral and free of inclusions, indicating an igneous origin and that they crystallised early. In 1D01 the garnets are somewhat corroded, suggesting garnet breakdown through resorption (Figure 2.10b). This in turn suggests this particular sample crystallized early in the history of the orogen, perhaps during prograde metamorphism, and has experienced the same metamorphic history as that of its host rock. This could also explain the presence of sillimanite in this sample. The order of crystallization is otherwise similar to that of other leucogranite varieties.

2.5.1.4. Muscovite leucogranites

Three samples contain no tourmaline, biotite or garnet, but instead contain abundant (up to 30%) muscovite (Figure 2.10c). In hand specimen they are entirely white. Quartz and plagioclase generally comprise 25-35% of the rock and K-feldspar ~15%. The grainsize is relatively small, with quartz and feldspar minerals up to 8 mm in diameter, while muscovite blades are typically no longer than 5 mm.

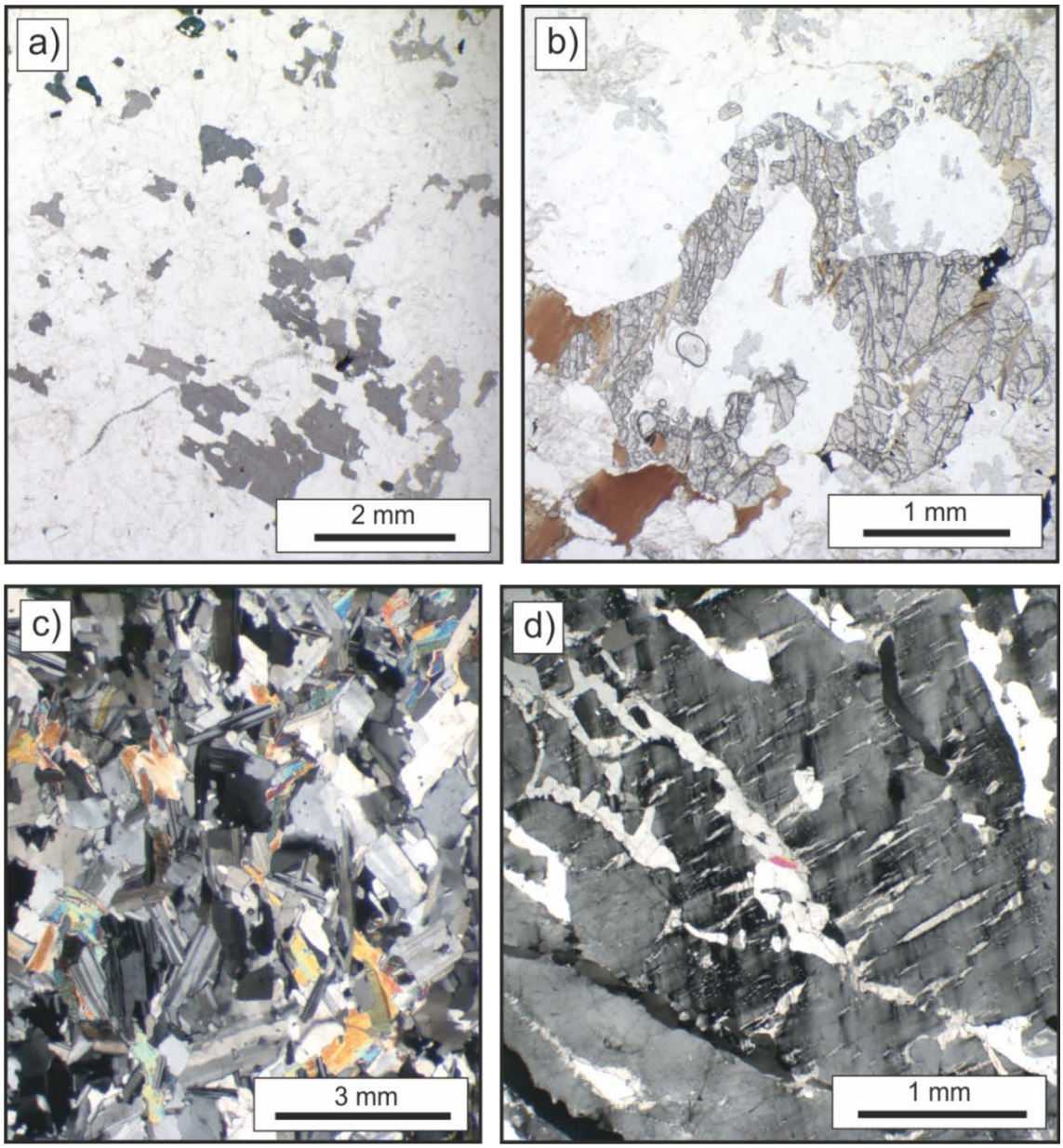

Figure 2.10: *a) Typical appearance of radial tourmaline in tourmaline leucogranite samples. b) Degraded appearance of garnet in sample 1D01, suggesting resorption has occurred between early-formed phenocryst and remaining melt. c) Typical appearance of muscovite leucogranites, with short blades of plagioclase and muscovite. d) Indications of fluid interaction in pegmatite 1G01. K-feldspar shows perthitisation, and quartz veins have formed.*

Samples 3D02 and 5M01 contain roughly equal quantities of plagioclase and K-feldspar. Sample 4H01 contains 55% plagioclase, often as small interlocking blades displaying strong albite and pericline twinning. Muscovite leucogranites contain no zircon, instead monazite and apatite are the most common accessory phases. One sample, 4H01, also contains cassiterite.

2.5.2. Pegmatites

Pegmatites are most readily distinguished from leucogranites by their coarse grain size. However, the mineralogy of an individual pegmatite can be similar to that of either a two-mica or of a tourmaline leucogranite. Grain size of all minerals can be up to 50 mm with some tourmaline or biotite crystals reaching 100 mm in length. Field observations indicate that pegmatite intrusions were the latest igneous event, and pegmatites often cross cut other leucogranite bodies. The main exception is at locality 1G, where the pegmatite (sample 1G01) is the earliest of three melt intrusions.

In thin section, biotite is commonly partially or wholly converted to chlorite, and feldspars commonly perthitised (Figure 2.10d). Small-scale veins can also be observed. This suggests that the majority of minerals have experienced some degree of fluid interaction since crystallization.

2.5.3. Greater Himalayan Series

2.5.3.1. Metapelitic gneisses

The metapelitic gneisses of the Bhutan Himalaya exhibit a range of textures and mineralogies. The most common variety comprises of leucocratic layers, dominated by quartz and feldspar, and melanocratic layers of biotite. Many samples also contain sillimanite and garnet. Muscovite and chlorite are also occasionally present, and accessory phases such as rutile, titanite, zircon and monazite are common.

Signs of shear deformation can be seen in many thin sections of gneisses. Garnet is one of the most informative minerals to record deformation, and is best exemplified by sample 6B01 (Figures 2.11a and 2.11b). 3-8 mm garnets contain S-shape trails of inclusions, indicating where they have been rolled and rotated during shear deformation. Layers of mica have also flowed around these garnets as they are rotated. Garnets can also appear to be smeared along foliation (such as in 3A06), possibly indicating garnet breakdown.

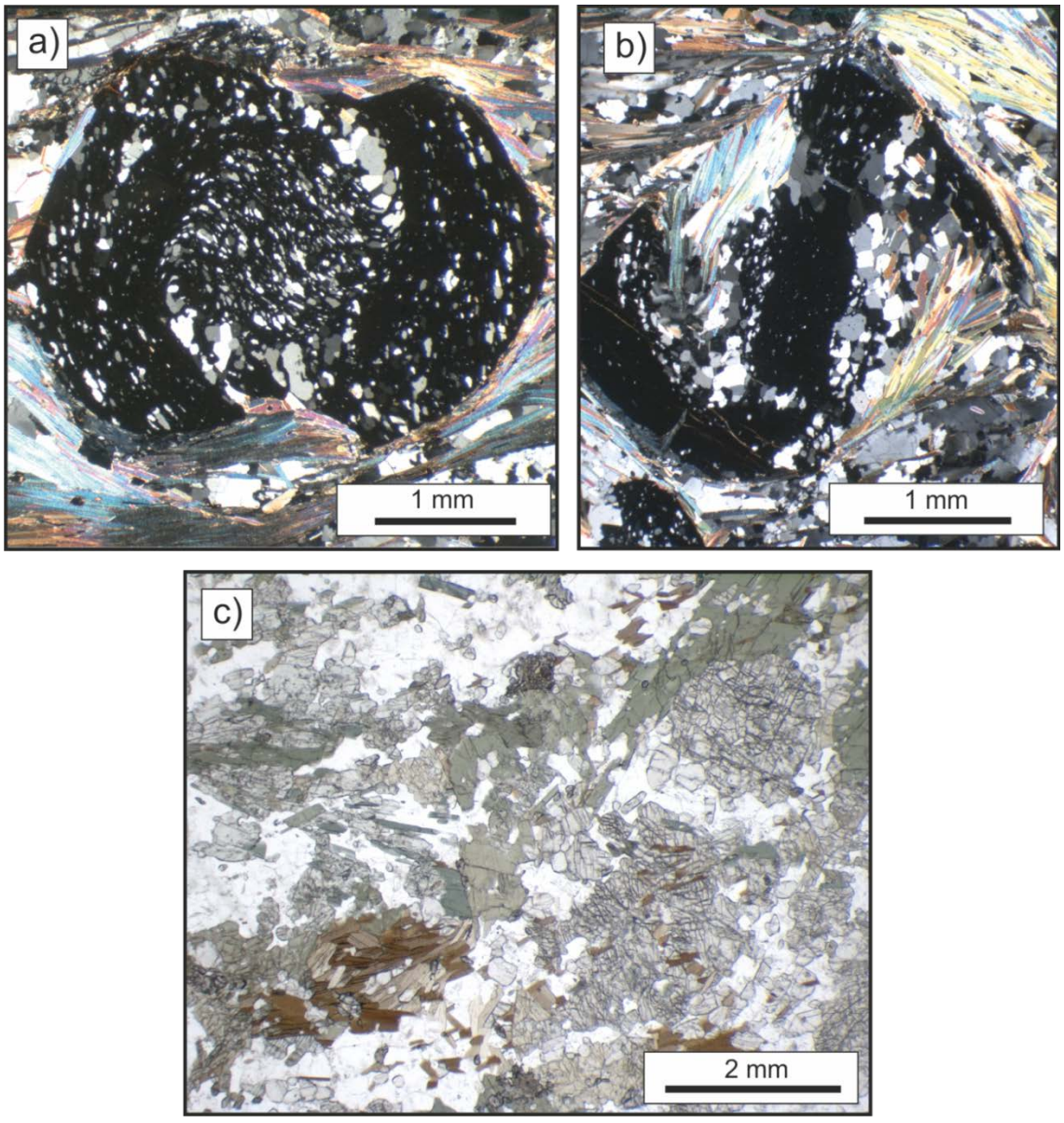

Figure 2.11: *a) and b) Rolled garnets in sample 6B01, indicating a history of shearing. c) Sample 5M03, amphibolite containing pyroxene (high relief, colourless), amphiboles (green) and biotite (brown).*

2.5.3.2. Metapelitic schists

The metapelitic schists are similar in composition to the gneisses, but are distinguished by higher quantities of fine-grained mica, which define the foliation. They uniformly contain feldspar and quartz, with occasional tourmaline, staurolite, sillimanite, rutile, titanite, zircon and monazite. Garnet commonly forms porphyroblasts, with foliation wrapping around them.

In one sample (5M03) hornblende and clinopyroxene are present as major phases, in addition to biotite (sometimes replaced by chlorite), feldspar and quartz (Figure 2.11c). Hornblende appears as elongated prismatic minerals, often aligned. The foliation is defined by biotite, and displays strong pleochroism between light and dark green. Clinopyroxene forms clusters of anhedral, rounded grains, often between layers of mica-amphibole.

2.5.3.3. Orthogneisses

The orthogneisses in the GHS are less voluminous than the metapelites, however they form an integral part of the sequence. They are mesocratic, with leucosomal layers of quartz and feldspar and melanosomal layers of biotite, an indication of their granitic protolith (Spencer et al., 2012). Augen of K-feldspar are occasionally present. Foliation is commonly observed, if biotite and/or muscovite are present. Zircon and monazite form common accessory phases.

Chapter 3

Major and trace element geochemistry

3.1. Introduction

3.1.1. Elemental geochemistry

Geochemical analysis can be a powerful tool for providing insight into the history of a rock. The field of geochemistry has been studied and improved upon throughout the 20th century, based on the early ground-breaking work of Clarke (1924) and Goldschmidt (1954), as well as many others. Understanding the elemental and isotopic composition of igneous rocks has become an essential practice in order to understand their source(s), age and igneous evolution.

For leucogranites, which are sourced primarily from metasedimentary rocks, geochemistry may be used to determine a sample's petrogenetic conditions, such as the mineral reactions involved to form a melt, and the temperature at which the melt crystallized. In addition, as many leucogranites have migrated away from their source rocks, geochemistry may be the only method by which melt can be linked to source. However, such investigations of source are best suited to isotope geochemistry, and are dealt with in later chapters. In this chapter, major and trace element abundances are presented and discussed for all leucogranite samples. Geochemical data is used here to determine whether samples represent pure melts, or whether they have incorporated restitic phases during their crystallization. Trace element data is then

used to model the petrogenetic conditions under which samples formed, and to determine melt reactions and temperatures involved in the formation of the Himalayan leucogranites.

3.1.2. Dissolution and analysis of granitic rocks

The insolubility of minerals such as zircon presents problems in the interpretation of bulk-rock analyses of granitic rocks. Zircons are one of the primary residences for Zr, Hf and heavy REEs, so if fully representative data for these elements is required it is essential that samples are fully dissolved. An additional issue for Himalayan leucogranites is that the majority of zircons in the leucogranites include pre-existing detrital cores so that up to 90% of the zircon in the granite did not crystallize from Miocene melts. It is therefore arguable that it would be preferable to exclude such cores from geochemical studies where the composition of the granitic magma is being inferred from whole-rock granite samples.

Traditionally, high-pressure bomb dissolution is the standard technique for dissolving rock samples containing zircon, as it is only under the high pressures generated within the bomb that zircon completely dissolves. While the method ensures complete dissolution of zircon, it is both time-consuming and risky in its acid usage when compared to other methods. Additionally, low quantities of powder (0.02 g) are used in each dissolution, therefore allowing for sample powder heterogeneity, or the "nugget effect" to potentially be a problem. High-pressure bombs may also be more susceptible to contamination, due to the high strain rates endured by the Teflon and the small volumes of sample involved in a dissolution. Hand-cranked beaker dissolutions are moderately quicker and safer, however one previous study comparing high-pressure bomb and hand-cranked beaker methods to dissolve zircon found that, while the hand-cranked beakers did not fully dissolve zircon (based on Zr and Hf abundances), this made little difference to REE profiles obtained, which were similar for both methods (King, 2007). A third potential methodology is the analysis of fluxed glass discs by laser-ablation. This method is safer for the user, as it avoids the need for acids, and is quicker, as fluxed glass

discs used to analyse major elements by XRF may be recycled. However, it is untested in its ability to fully dissolve zircon and other insoluble phases.

In order to determine the best method for analysing the bulk-rock geochemistry of granitic rocks I used a small selection of samples to compare the trace element and REE data obtained from the two acid-digestion methods (high-pressure bomb and hand-cranked beaker) and laser ablation analysis of fluxed glass discs. Full results, discussion and conclusions of this technique comparison can be found in Appendix B, and a summary of the conclusions is provided in Section 3.3.

3.2. Methods

All samples were crushed by standard techniques (jaw crushing and TEMA agate milling) at the Open University. Major and certain trace elements were determined by X-ray fluorescence (XRF), for which pressed powder pellets and glass discs were prepared from sample powders.

Seven samples (1D01, 1G02, 1G03, 3A01, 3A02, 3A03 and 3A04) were chosen for the technique comparison comparing hand-cranked beaker and high-pressure bomb acid digestions, and LA-ICP-MS analysis of fluxed glass discs.

Two techniques employed the use of acid digestion. Powders were dissolved in a HF/HNO_3 mix in either high-pressure bombs or in PTFE Teflon beakers for several days, before being dried down and re-dissolved in HCl in PTFE Teflon beakers. Solutions were dried down once more, and redissolved in 2% HNO_3. Solutions were doped with a multi-element dope (Be, In, Rh, Tm, Re, Bi) prior to ICP-MS analysis. For both techniques, four samples (1D01, 3A01, 3A02 and 3A03) were repeated across analytical sessions, and two (1D01 and 3A02) were repeated with different dissolutions.

For the laser ablation technique, fragments of XRF fused glass disc were embedded in an epoxy mount prior to analysis by laser ablation (LA) ICP-MS at the University of Leicester. Glass discs were examined by SEM prior to analysis in order to confirm complete dissolution of accessory phases into the flux.

Full methods are supplied in Appendix A (Analytical methods).

3.3. Technique comparison conclusions

Full results and discussion of the technique comparison are provided in Appendix B (Comparison of techniques for the dissolution of granitic material).

After comparing data from the three techniques, it was determined that LA-ICP-MS analysis of fluxed glass discs provided the best method for this study. The technique was chosen on the basis of data reliability, the technique's ability to fully dissolve accessory phases by fusion into glass discs, and the speed by which data could be acquired, as glass discs can be recycled for laser ablation following major element analysis by XRF.

Hand-cranked beaker dissolutions yielded Zr and Hf concentrations typically 90% lower than high-pressure bomb dissolutions and glass discs of the same sample, suggesting incomplete dissolution of zircons in hand-cranked beakers. However, this had little effect on the REE abundances yielded, as hand-cranked beakers yielded similar concentrations to glass discs. The REE abundances of high-pressure bomb dissolutions were typically far higher than in either of the two other techniques, and also generally more erratic, with different dissolutions of certain samples yielding different REE concentrations. The reason for this was assigned to sample heterogeneity, as only 0.02 g of sample is used in each high-pressure bomb dissolution, meaning that the "nugget effect", or the inclusion of small quantities of accessory phases, could drastically alter the resultant REE data.

3.4. Results

Full major and trace element data (by LA-ICP-MS analysis of glass discs) for all leucogranites are tabulated in Table 3.1.

Table 3.1. Major and trace element geochemistry for Bhutanese leucogranites
Major element oxides in %, trace element abundances in ppm

	1C01	1D01	1G01	1G02	1G03	3A01	3A02	3A03	3A04	3C01	3D02	4CO1	4D01	4G01	4H01	5H01	5J01	5M01	
	Tm	Grt	Peg	Tm	2M	Peg	Grt	2M	Tm	Peg	Musc	Peg	2M	Tm	Musc	Tm	Tm	Musc	
SiO_2	73.65	77.54	70.42	73.79	73.76	72.94	74.75	73.15	74.25	70.43	75.70	76.00	75.73	73.98	75.37	73.83	74.02	74.37	SiO_2
TiO_2	0.09	0.05	0.11	0.07	0.07	0.01	0.01	0.04	0.02	0.01	0.04	0.08	0.02	0.02	0.02	0.01	0.01	0.02	TiO_2
Al_2O_3	14.39	11.95	14.96	14.15	14.21	14.96	14.37	14.81	14.61	16.54	14.75	13.03	13.74	14.68	14.42	15.03	14.80	14.58	Al_2O_3
Fe_2O_3	1.07	1.04	1.19	0.77	0.66	0.33	0.66	0.78	0.90	0.36	0.41	0.53	0.12	0.48	0.40	0.52	0.78	0.50	Fe_2O_3
MnO	0.02	0.06	0.02	0.01	0.01	0.02	0.09	0.02	0.05	0.19	0.01	0.01	0.01	0.02	0.06	0.04	0.23	0.03	MnO
MgO	0.40	0.11	0.27	0.16	0.16	0.04	0.05	0.10	0.07	0.03	0.13	0.21	0.05	0.07	0.03	0.05	0.03	0.07	MgO
CaO	2.16	0.42	0.97	0.82	0.95	0.30	0.63	0.61	0.56	0.26	0.69	0.92	1.00	0.62	0.22	0.43	0.33	0.62	CaO
Na_2O	6.19	2.63	2.41	3.67	3.97	4.83	5.63	4.77	4.83	6.23	5.33	2.77	5.01	5.18	5.11	6.20	7.47	5.61	Na_2O
K_2O	0.79	5.80	8.48	5.29	5.25	6.95	2.88	3.95	3.37	5.87	1.89	4.83	4.36	3.99	3.68	3.85	2.07	1.90	K_2O
P_2O_5	0.09	0.18	0.13	0.12	0.11	0.07	0.08	0.12	0.08	0.05	0.06	0.06	0.06	0.08	0.02	0.10	0.09	0.02	P_2O_5
Sc	2.65	3.66	1.29	3.53	5.65	0.643	0.743	0.905	0.879	0.237	0.846	3.35	0.620	1.03	0.334	0.966	0.363	0.827	Sc
Ti	646	334	738	458	460	52.3	48.5	235	98.3	28.3	229	546	138	138	125	39.7	22.3	114	Ti
V	9.50	2.98	5.57	3.58	3.02	1.17	1.39	1.87	1.13	2.62	4.87	14.9	1.55	1.60	3.01	1.45	1.55	1.59	V
Cr	11.4	11.4	5.70	13.8	9.18	4.45	17.0	6.97	10.6	6.24	9.50	15.5	13.9	12.4	20.4	5.68	9.80	5.54	Cr
Mn	169	418	92.5	71.4	87.3	133	691	124	373	1428	36.8	55.1	42.0	195	454	277	1638	185	Mn
Co	1.87	0.594	3.04	1.35	0.774	0.0880	0.205	0.183	0.185	0.145	0.479	1.07	0.231	0.577	0.201	0.0745	0.0217	6.58	Co
Ni	6.25	2.77	2.26	2.99	2.67	2.09	2.22	1.28	2.79	1.79	3.48	3.97	2.24	2.00	2.25	1.80	2.25	16.7	Ni
Cu	8.47	5.65	35.7	26.9	6.24	3.80	8.34	4.72	8.24	20.9	3.42	4.16	4.62	3.24	4.75	4.23	5.29	31.5	Cu
Zn	23.5	9.97	26.0	23.1	27.8	27.0	24.5	55.8	62.2	9.12	18.6	13.0	7.64	43.6	37.6	45.2	47.4	117	Zn
Ga	15.0	14.3	16.4	18.4	20.9	17.5	23.2	22.0	22.1	29.9	21.4	14.3	11.7	25.4	31.9	19.4	20.1	25.5	Ga
Rb	48.3	254	330	322	277	572	251	323	296	1041	168	162	143	453	547	352	273	241	Rb
Sr	89.6	62.1	181	61.0	54.6	11.4	11.5	44.1	10.2	14.1	64.0	116	121	20.2	8.80	8.50	0	12.8	Sr
Y	12.4	20.2	33.0	24.2	32.1	6.60	15.7	12.1	15.4	4.10	5.70	6.20	9.20	15.3	9.10	9.40	5.00	5.70	Y
Zr	38.5	40.9	20.5	46.3	54.3	12.5	37.8	36.4	18.6	27.0	26.3	37.3	30.1	32.4	38.6	30.8	38.6	14.6	Zr
Nb	4.90	5.00	7.40	12.9	16.1	7.90	12.4	14.5	10.4	28.7	22.6	4.40	3.00	19.2	89.6	11.3	12.7	39.3	Nb
Sn	4.39	3.09	3.77	3.80	4.58	8.74	13.63	11.9	10.7	26.3	39.2	4.31	4.92	26.9	1860	7.73	5.66	24.4	Sn
Cs	2.03	2.60	9.59	14.5	15.3	54.2	12.5	18.4	11.1	111	11.7	2.62	4.44	50.5	200	20.0	20.5	14.6	Cs
Ba	54.0	132	803	188	114	29.6	41.2	143	17.7	80.3	181	777	498	37.1	28.9	10.2	5.63	13.0	Ba
La	5.06	5.46	21.7	11.0	11.8	1.21	3.60	4.98	4.33	1.18	2.00	5.93	5.06	5.14	1.79	2.28	1.51	3.25	La
Ce	10.4	13.3	46.0	22.6	25.8	1.68	6.53	9.64	8.79	1.12	3.40	11.7	10.6	10.8	2.72	3.83	2.41	6.27	Ce
Pr	1.09	1.54	4.81	2.45	2.75	0.170	0.635	1.08	0.905	0.0734	0.364	1.23	1.09	1.20	0.242	0.336	0.295	0.564	Pr
Nd	3.84	5.55	17.67	9.21	9.70	0.637	2.17	3.99	2.76	0.181	1.09	4.00	3.87	4.09	0.995	1.07	0.53	1.70	Nd
Sm	0.999	1.87	4.31	2.42	2.97	0.224	0.862	1.26	0.868	0.0726	0.34	0.963	1.19	1.40	0.304	0.454	0.184	0.592	Sm
Eu	0.383	0.258	0.929	0.393	0.321	0.0465	0.0491	0.245	0.0560	0.0135	0.239	0.702	0.86	0.103	0.189	0.0433	0.0545	0.0802	Eu
Gd	1.12	2.48	4.78	2.85	3.09	0.527	1.24	1.77	1.31	0.0419	0.56	1.21	1.27	1.55	0.440	0.878	0.304	0.480	Gd
Tb	0.210	0.527	0.716	0.539	0.608	0.0867	0.318	0.326	0.282	0.0112	0.107	0.181	0.199	0.384	0.114	0.146	0.113	0.172	Tb
Dy	1.43	3.79	4.96	3.49	4.47	0.670	2.36	1.97	2.14	0.0709	0.666	1.40	1.02	2.47	1.11	1.01	0.539	0.597	Dy
Ho	0.242	0.631	0.909	0.747	0.843	0.0980	0.446	0.288	0.377	0.0601	0.116	0.275	0.213	0.365	0.194	0.185	0.0902	0.111	Ho
Er	0.736	1.65	2.78	2.14	2.44	0.263	1.45	0.633	1.02	0.0581	0.433	0.971	0.568	1.13	0.639	0.764	0.407	0.310	Er
Tm	0.103	0.227	0.349	0.316	0.335	0.0576	0.217	0.102	0.276	0.0104	0.0611	0.136	0.197	0.176	0.107	0.148	0.0791	0.0791	Tm
Yb	0.700	1.43	2.55	2.15	2.44	0.362	1.70	0.590	1.07	0.0780	0.426	0.805	0.450	0.876	0.923	1.06	0.560	0.260	Yb
Lu	0.0734	0.215	0.365	0.328	0.345	0.0428	0.213	0.0820	0.180	0.0121	0.0580	0.122	0.0999	0.102	0.120	0.288	0.146	0.0462	Lu
Hf	1.19	1.88	0.65	1.54	1.78	0.337	1.87	1.27	0.644	3.33	0.947	1.05	1.07	1.85	3.35	1.36	2.23	0.657	Hf
Ta	0.402	0.297	1.10	3.81	2.90	4.45	1.76	3.51	1.69	255	11.37	0.475	0.352	7.43	260	7.12	9.76	17.0	Ta
W	1.11	0.457	1.28	0.860	1.01	0.875	2.98	3.20	2.24	1.53	2.43	5.40	1.37	2.93	4.27	1.10	0.361	3.02	W
Pb	46.4	51.2	127	155	127	113	83.5	107	79.7	71.7	58.5	62.0	87.4	65.6	66.3	126	60.0	78.9	Pb
Th	4.44	7.28	15.0	10.1	8.26	0.815	2.97	3.21	4.84	4.76	1.55	3.48	2.75	5.93	6.49	20.4	1.45	4.23	Th
U	1.90	3.17	5.07	6.48	6.37	1.35	2.79	3.04	2.65	8.38	3.84	1.57	1.42	9.52	10.1	3.12	10.3	7.29	U

Table 3.1. Major and trace element geochemistry for Bhutanese leucogranites

Major element oxides in %, trace element abundances in ppm

	6A01	6FO2	DRB-1215	DRB-1242	DRB-1244	DRB-1247	DRB-1251	CWB-10-4	CWB-10-8A	CWB-10-16	CWB-10-23	BH-65C	BH-84	BH-96	BH-226	BH-231A	BH-231B	BH-232	
	2M	Peg	Tm	2M	2M	2M	2M	2M	Tm	2M	2M	Grt	2M	Musc	2M	2M	2M	2M	
SiO_2	72.19	72.01	72.35	74.47	69.29	72.49	73.53	74.58	75.31	75.23	76.64	74.49	71.27	71.97	74.46	73.23	72.88	73.29	SiO_2
TiO_2	0.08	0.08	0.03	0.03	0.02	0.05	0.07	0.03	0.03	0.08	0.05	0.18	0.34	0.01	0.11	0.21	0.21	0.14	TiO_2
Al_2O_3	14.91	15.27	14.94	14.87	16.86	15.26	14.32	14.66	14.39	14.18	13.42	13.88	14.85	16.73	14.63	14.82	15.21	15.04	Al_2O_3
Fe_2O_3	0.72	0.63	0.43	0.49	0.17	0.72	0.85	0.40	0.41	0.93	0.78	1.86	2.95	0.08	1.14	1.62	1.67	1.32	Fe_2O_3
MnO	0.01	0.01	0.01	0.04	0.01	0.01	0.02	0.01	0.01	0.02	0.02	0.04	0.04	0.02	0.03	0.04	0.04	0.03	MnO
MgO	0.17	0.20	0.13	0.05	0.06	0.17	0.18	0.10	0.09	0.19	0.11	0.33	0.81	0.02	0.20	0.55	0.57	0.29	MgO
CaO	0.78	0.90	0.99	0.48	1.40	0.55	0.89	0.76	0.75	0.61	0.77	0.96	2.25	0.38	0.79	1.37	1.42	0.88	CaO
Na_2O	4.67	3.39	6.86	1.99	5.54	5.68	4.42	3.96	3.90	3.12	3.44	3.01	4.51	8.30	3.58	3.61	3.68	3.87	Na_2O
K_2O	4.74	6.62	3.55	7.10	6.53	4.80	5.97	5.98	5.89	5.99	5.05	4.83	2.12	2.17	4.74	4.13	3.96	4.56	K_2O
P_2O_5	0.14	0.10	0.15	0.08	0.03	0.21	0.11	0.12	0.12	0.10	0.09	0.19	0.10	0.02	0.15	0.11	0.11	0.12	P_2O_5
Sc	2.51	3.86	0.836	0.554	0.802	0.655	3.46	1.33	1.67	2.52	1.96	2.75	4.94	0.809	3.01	3.19	3.49	2.87	Sc
Ti	550	573	198	167	130	331	432	139	147	490	301	991	1948	50.5	594	1216	1217	850	Ti
V	2.61	10.9	1.63	1.88	2.96	1.90	3.59	3.22	3.56	3.72	2.26	10.6	23.4	1.63	5.31	22.7	23.6	11.7	V
Cr	8.93	5.66	9.28	6.82	7.01	28.8	9.52	9.68	17.7	12.5	18.6	14.5	24.7	6.96	9.73	35.0	35.8	17.8	Cr
Mn	88.9	51.9	49.8	319	25.1	83.8	107	63.7	77.4	175	178	232	273	104	221	272	284	191	Mn
Co	0.507	0.814	0.289	0.267	1.29	0.828	1.74	0.868	0.961	1.59	0.982	2.20	4.54	0.236	1.03	3.50	3.29	1.62	Co
Ni	3.21	1.54	1.03	1.72	4.68	7.62	2.97	4.05	6.79	7.12	3.70	2.65	5.19	5.96	3.26	12.0	9.32	5.43	Ni
Cu	6.03	5.32	3.74	6.59	21.9	6.51	18.6	6.98	7.24	15.6	8.97	2.97	3.63	4.10	2.10	3.96	4.95	4.06	Cu
Zn	46.6	15.0	44.2	27.2	6.90	69.7	12.5	15.6	20.8	34.4	29.1	32.2	33.9	8.13	43.5	62.5	58.8	45.8	Zn
Ga	20.6	15.9	20.4	26.6	19.5	23.1	17.1	18.8	20.7	17.4	15.2	19.9	18.6	26.8	21.9	22.1	22.4	21.9	Ga
Rb	311	318	209	387	182	407	231	274	268	262	236	347	163	188	334	216	219	296	Rb
Sr	80.3	87.3	54.0	57.4	404	49.6	75.9	36.6	32.5	93.4	69.4	39.0	130	66.9	94.7	199	209	210	Sr
Y	12.5	13.5	5.20	5.40	7.30	14.8	26.3	7.90	8.70	21.2	31.9	16.2	22.9	1.90	15.5	11.8	11.8	11.2	Y
Zr	48.2	58.9	26.8	20.9	20.3	32.7	40.9	23.4	24.8	41.6	34.1	73.2	154	17.7	43.8	65.1	67.1	59.9	Zr
Nb	12.4	7.50	1.90	18.0	12.9	4.10	11.3	22.6	15.6	11.2	13.6	14.6	16.0	50.6	16.4	9.04	9.08	13.3	Nb
Sn	9.88	9.39	7.29	56.9	1.04	9.57	1.96	4.55	4.95	8.96	5.15	7.01	5.73	843	12.9	4.43	7.43	10.1	Sn
Cs	11.3	7.95	8.56	25.1	16.7	52.5	4.02	5.95	5.86	10.5	7.23	11.8	10.4	36.0	37.2	11.3	18.5	32.9	Cs
Ba	261	186	89.4	114	593	129	288	79.0	75.5	380	127	183	345	138	233	376	408	526	Ba
La	7.84	7.93	3.66	1.93	3.30	4.53	10.0	2.62	2.35	8.83	9.51	20.5	33.5	0.686	12.7	19.5	18.5	16.1	La
Ce	17.2	17.3	6.59	2.93	6.14	9.53	22.2	5.09	4.70	20.9	20.5	46.6	67.8	0.442	26.6	41.3	40.6	33.4	Ce
Pr	1.81	1.83	0.654	0.295	0.583	1.19	2.33	0.506	0.535	1.72	2.24	5.03	7.34	0.0354	2.97	4.41	4.31	3.69	Pr
Nd	7.24	6.93	1.92	1.26	1.99	4.12	7.65	1.61	2.14	6.47	8.20	19.1	25.0	0.298	11.3	17.0	17.1	13.9	Nd
Sm	1.92	1.94	0.703	0.313	0.453	1.61	2.22	0.773	0.789	1.52	2.51	4.10	4.70	0.0933	2.63	3.54	3.43	3.01	Sm
Eu	0.480	0.394	0.236	0.140	0.534	0.282	0.620	0.0885	0.0794	0.509	0.366	0.479	0.692	0.110	0.376	0.620	0.603	0.526	Eu
Gd	2.12	1.86	0.611	0.444	0.534	2.06	2.29	0.915	0.930	1.83	3.60	3.75	4.04	0.213	2.49	2.66	2.59	2.63	Gd
Tb	0.343	0.361	0.135	0.206	0.142	0.414	0.409	0.174	0.215	0.521	0.830	0.607	0.631	0.0434	0.395	0.441	0.390	0.332	Tb
Dy	2.01	2.29	0.656	0.635	1.02	2.34	3.41	1.22	1.17	2.60	4.83	2.87	3.86	0.229	2.45	2.01	1.98	1.90	Dy
Ho	0.298	0.435	0.129	0.115	0.196	0.392	0.694	0.187	0.221	0.606	0.972	0.483	0.762	0.0450	0.449	0.337	0.346	0.414	Ho
Er	0.769	1.17	0.244	0.324	0.714	0.948	2.15	0.649	0.732	1.67	2.74	1.57	2.21	0.249	1.18	1.04	0.956	0.892	Er
Tm	0.0825	0.170	0.0374	0.0692	0.135	0.186	0.377	0.209	0.0987	0.483	0.397	0.201	0.320	0.0270	0.170	0.137	0.142	0.162	Tm
Yb	0.490	0.992	0.256	0.371	0.913	0.743	2.31	0.725	0.588	2.18	2.31	1.10	2.18	0.298	1.14	0.850	0.842	0.871	Yb
Lu	0.078	0.130	0.0403	0.0551	0.115	0.099	0.355	0.0797	0.0932	0.257	0.363	0.160	0.355	0.0443	0.194	0.115	0.202	0.138	Lu
Hf	1.33	2.11	0.911	0.961	1.74	1.02	1.19	0.856	1.04	1.05	1.07	2.44	4.48	2.16	1.67	2.18	2.17	2.05	Hf
Ta	0.921	0.909	0.311	7.93	15.8	0.679	2.16	10.7	5.40	2.06	2.93	2.03	1.89	145	3.06	1.00	1.02	3.01	Ta
W	3.32	5.76	0.349	2.93	0.663	1.31	0.948	2.64	2.20	1.65	2.95	1.05	1.64	1.83	5.92	0.828	1.12	3.87	W
Pb	90.5	69.8	64.3	70.1	63.5	63.9	78.6	82.2	92.1	93.0	103	32.8	18.2	20.7	59.6	62.2	58.1	88.3	Pb
Th	4.60	6.73	2.35	3.61	4.06	2.72	8.39	1.64	1.54	7.90	6.18	19.2	18.2	4.77	73.0	10.3	10.2	9.50	Th
U	3.94	1.97	7.92	10.8	10.0	5.13	3.81	8.27	6.70	3.90	14.4	4.03	3.70	8.28	10.3	5.87	5.77	8.43	U

Major-element data show that the two-mica leucogranites, the majority (12 out of 16) are peraluminous (as shown in Figure 3.1), indicating their chemistry is similar to other leucogranites from the Himalaya (e.g. Ayres and Harris, 1997; Guo and Wilson, 2012; Greenwood, 2013). In addition, two-mica leucogranite trace element compositions most closely resemble other leucogranites, as indicated in the multi-element diagrams (Figure 3.2a), where samples are normalised to an 'average' Himalayan leucogranite (from Ayres and Harris, 1997), hereafter referred to as AH97. Maximum deviation from the average leucogranite composition is generally smaller than one order-of-magnitude, with most variation recorded in the REE compositions (Figure 3.3a). The majority of two-mica samples from this study are similar to AH97, with negative Eu anomalies between 0.2 and 0.9. In contrast, three samples, 4D01, DRB1244 and CWB-10-16, show positive Eu anomalies, ranging between 1.2 and 2.9. A few samples have HREE anomalies, particularly Tm.

The tourmaline leucogranites yield a wider range of major and trace element compositions than the two-mica leucogranites. Tourmaline leucogranites lie in all three fields of the aluminium saturation index diagram, with 4 peraluminous, 3 metaluminous and 1 peralkaline sample (Figure 3.1). Tourmaline leucogranites also vary more widely than the two-mica group in their trace element compositions (Figure 3.2b), with some samples recording large negative anomalies in Ba, Sr and Eu. REE abundances in all tourmaline-bearing samples are lower than in the two-mica leucogranites, with only one sample (1G02) containing higher concentrations of REEs than AH97 (Figure 3.3b). Five samples record negative Eu anomalies between 0.1 and 0.6, while three contain small positive Eu anomalies between 1 and 1.3. HREE profiles are largely flat, compared to the reference composition in contrast to the two-mica samples, which are progressively depleted towards Lu.

The three garnet leucogranites are broadly similar to the average Himalayan leucogranite in major and trace element compositions. All three samples lie in the peraluminous field (Figure 3.1), and record trace element abundances similar to those found in AH97 (Figure 3.2c). Sample 3A02 records a large negative Ba anomaly, while BH-65 is enriched in Th (Figure

3.2c). REE profiles (Figure 3.3c) are also broadly similar to AH97, with all three samples containing large negative Eu anomalies of between 0.1 and 0.4.

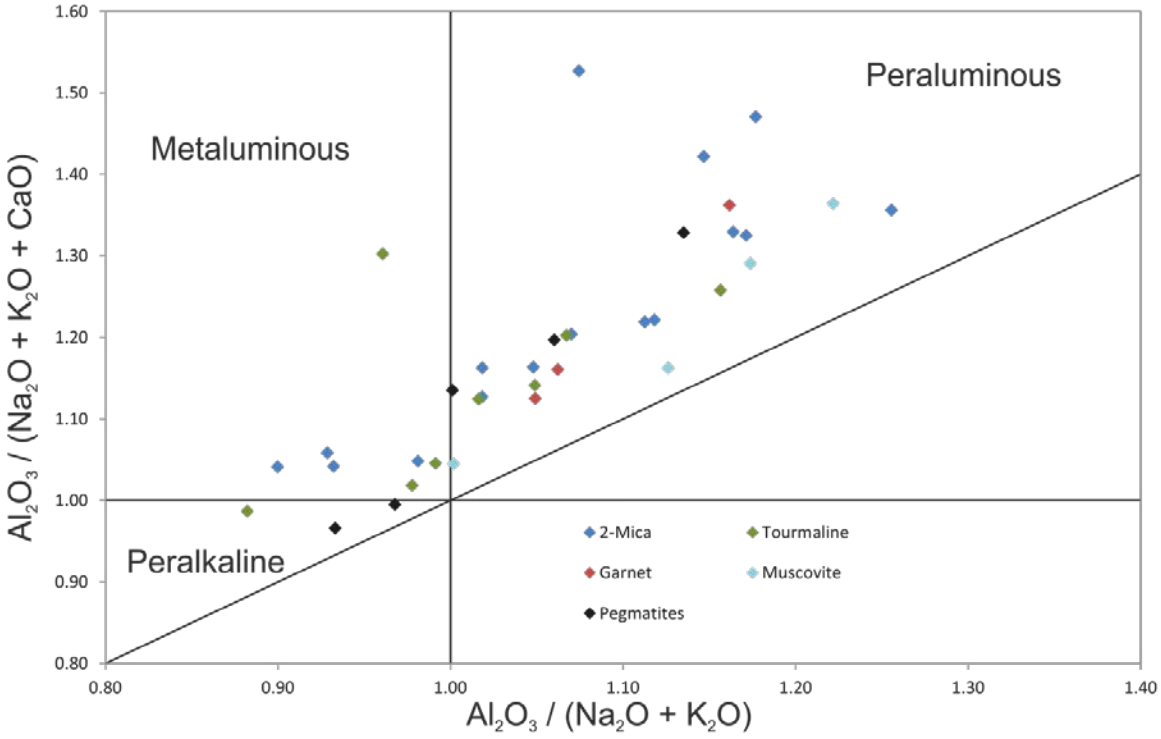

Figure 3.1: *Plot of aluminium saturation index for all samples.*

Muscovite leucogranites are all peraluminous (Figure 3.1). However, their trace element abundances differ largely from AH97 (Figure 3.2c) in that all four samples contain a large positive Nb anomaly, and two samples are depleted in Ba. REE abundances for muscovite leucogranites are universally lower than AH97, up to two orders-of-magnitude for some elements. Eu anomalies vary between 0.8 and 2.2, with the majority of samples containing a positive anomaly. Muscovite leucogranites also have unusually high concentrations of Sn, Nb and Ta. Sn concentrations of between 20 and 2000 ppm and Ta concentrations of 10-260 ppm set these samples apart from other leucogranites, possibly reflecting the activity of late pneumatolytic fluids.

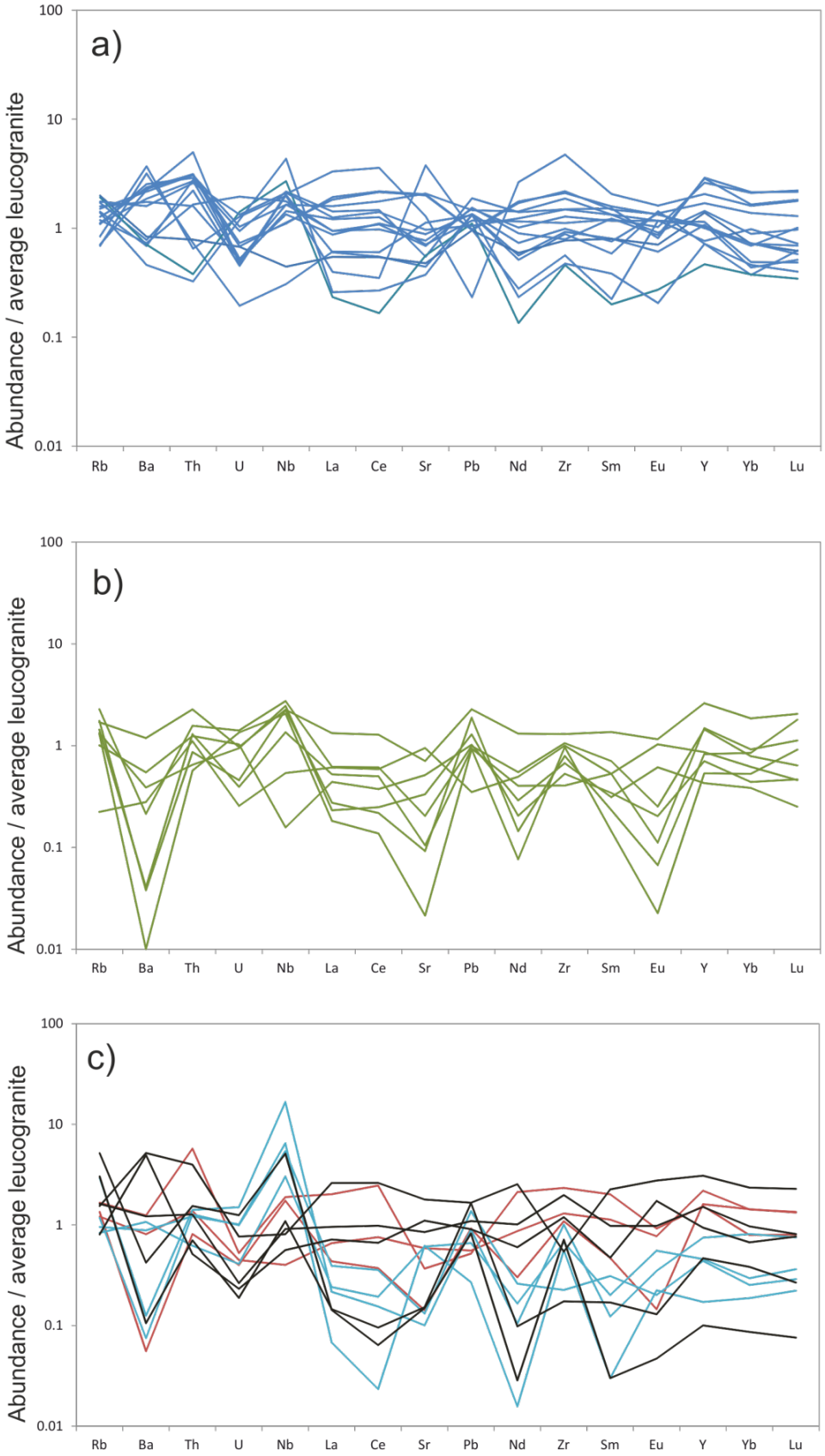

Figure 3.2: *Trace element diagrams for a) 2-mica leucogranites, b) tourmaline leucogranites, c) garnet (red) and muscovite (light blue) leucogranites and pegmatites (black). Data are normalised to an average Himalayan leucogranite composition (Ayres and Harris, 1997).*

The pegmatites provide the largest variety in major-element and trace-element compositions. Of the five samples, three lie in the peraluminous field while two are peralkaline (Figure 3.1). The trace element chemistry of these samples is also highly variable, with wide deviations (up to two orders-of-magnitude) from the reference leucogranite (Figure 3.2c). This is also reflected in the REE abundances. One sample, 1G01, has higher REE abundances than the average leucogranite, while the remaining four samples are all depleted.

3.5. Discussion

3.5.1. Major and trace element geochemistry

The majority (26 out of 36) of samples record peraluminous compositions, with seven metaluminous and three peralkaline samples. Previously recorded Himalayan leucogranites have almost universally been peraluminous in composition (e.g. Harris et al., 1995; Guo and Wilson, 2012), making it likely that metaluminous or peralkaline samples from this study represent impure leucogranite compositions. Samples falling outside this field may have incorporated pre-existing minerals from source or have been affected by metasomatism of post-crystallizational fluids. The former option is possible for metaluminous samples, as the entrainment of residual plagioclase may produce a whole-rock metaluminous signature. However, no peralkaline minerals are observed in Himalayan leucogranites, and for the three samples in this category the most likely option is that they have experienced fluid alteration after crystallization. As two of the three samples are pegmatites, this is a likely explanation.

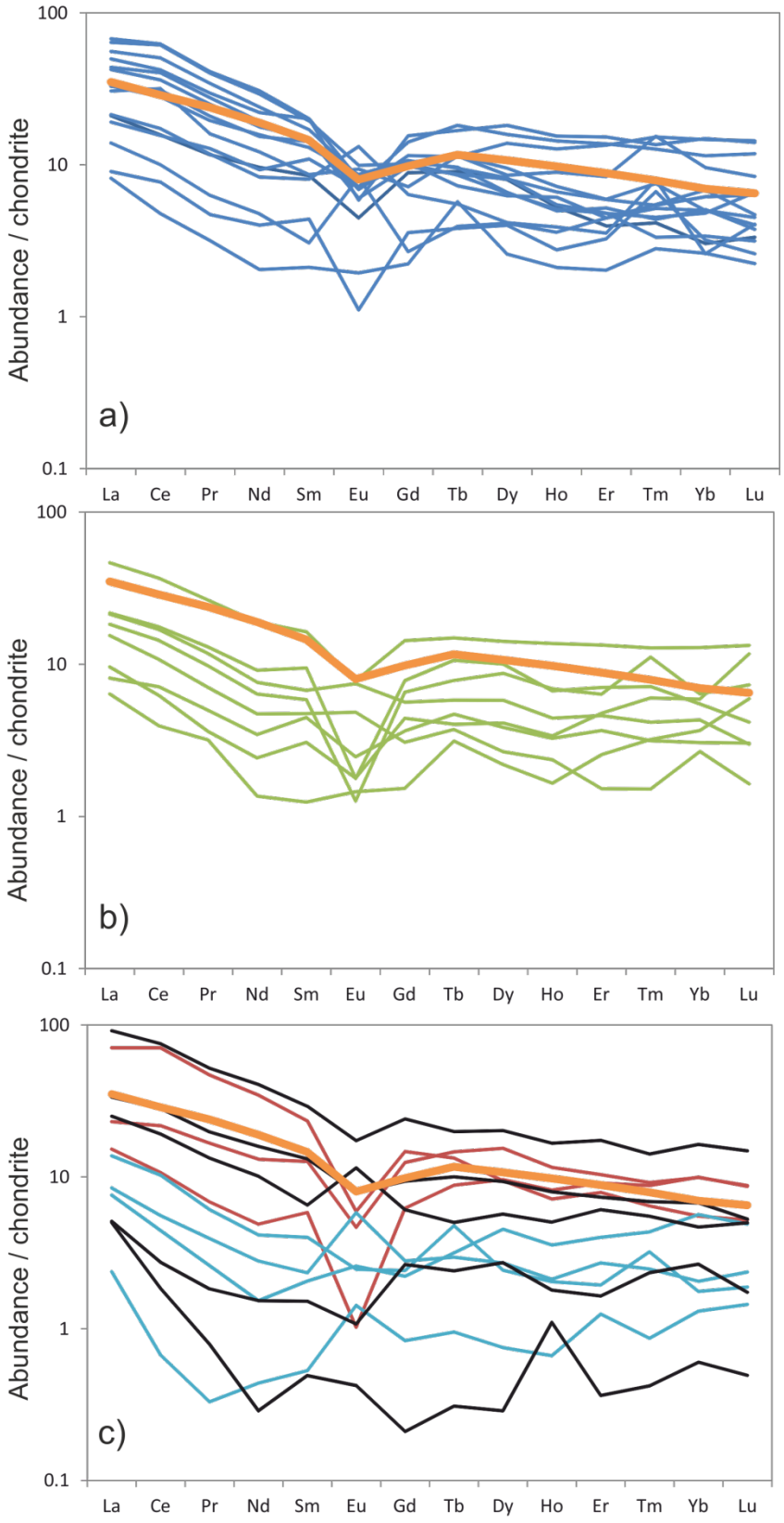

Figure 3.3: *Chondrite-normalised REE plots for a) two-mica leucogranites, b) tourmaline leucogranites, c) garnet (red) and muscovite (light blue) leucogranites and pegmatites (black). Thick orange line indicates average leucogranite composition (Ayres and Harris, 1997).*

All two-mica (Figure 3.2a) and the majority of tourmaline leucogranites (Figure 3.2b) record trace element abundances within an order-of-magnitude of an average Himalayan leucogranite composition (of Ayres and Harris, 1997). The only elements for which tourmaline leucogranites have larger negative deviations are Ba, Sr and Eu, probably due the removal of anatectic feldspar during melting and crystallization.

Figure 3.2c shows trace element data plotted relative to AH97 for garnet and muscovite leucogranites and pegmatites. Garnet leucogranites are very similar in composition to AH97; however, far larger variations are seen in both muscovite leucogranites and pegmatites, suggesting either that these samples do not represent pure melts or that these samples have been affected by pneumatolytic fluid activity during or after crystallization. The latter possibility is most likely, as while there is no obvious evidence for non-igneous xenocrysts being present in thin section for either leucogranite type, there is ample evidence for fluid alteration (see Chapter 2.5). There is also chemical evidence for such alteration, with muscovite leucogranites containing the highest concentrations of Sn (up to 2000 ppm) observed in all samples, which could imply that tin mineralisation by metasomatism has occurred (Haapala, 1997).

Two-mica (Figure 3.3a) and tourmaline (Figure 3.3b) leucogranites record REE concentrations similar to AH97, though typically depleted, especially in the case of tourmaline leucogranites. The majority of samples record negative Eu anomalies, consistent with the majority of Himalayan leucogranites. However, certain samples record positive anomalies, indicating that they have incorporated cumulate feldspar, therefore these samples do not represent pure melts.

Garnet leucogranites also have REE patterns similar to the average leucogranite value, all with negative Eu anomalies. Muscovite leucogranites and pegmatites have highly variable REE contents, many severely depleted relative to the average leucogranite. This could also be a result of the fluid alteration that muscovite leucogranites may have experienced, as discussed above. While REE elements are not typically fluid mobile, they may be removed or added to an igneous system by the presence of pneumatolytic fluids during the final stages of crystallization. REEs and metallic elements (such as Sn) may bond to anions contained within the fluid,

particularly halogens (Harris, 1981), which can lead to such cations being removed or enriched in particular leucogranites.

Several samples from all leucogranite types have individual anomalies in specific HREE elements, commonly Tm or Yb. Given that no minerals are able to cause variations in individual HREEs, these anomalies are difficult to explain.

3.5.2. Petrogenetic modelling

Bulk-rock major and trace element geochemistry can provide crucial insights into the nature of the conditions that led to melting, and also the nature of the melt reaction. It is important to only use samples with compositions that are likely to resemble pure granitic melts and to exclude those which show evidence of contamination, either through fluid alteration or mineral entrainment. Consequently only samples which are peraluminous and have negative Eu anomalies were used in the modelling. All pegmatites were also excluded due to petrographic and chemical evidence for fluid interaction, and that their coarse grain size prevents representative sampling. Additionally, muscovite leucogranites were excluded due to their highly variable trace element geochemistry. All samples selected are broadly similar in composition (within one order-of-magnitude for most elements) to AH97 (Figures 3.2 and 3.3).

3.5.2.1. Melt reactions and P-T conditions

During crustal melting, the most fertile lithologies of continental crust are of pelitic composition (e.g. Patiño Douce and Johnson, 1991; Patiño Douce and Harris, 1998). Melting is the result of the breakdown of mica and is likely to involve one of the following three melt reactions (Figure 3.4):

1) Vapour-absent muscovite breakdown:

   $Mu + 0.18Pl + 0.18Q \rightarrow 0.6L + 0.38Ksp + 0.35Sil$

2) Vapour-absent biotite breakdown:

   $Bi + 0.61Pl + 0.5Q + 0.15Sil \rightarrow 1.65L + 0.08Ksp + 0.6Grt + 0.05Ilm$

3) Vapour-present muscovite breakdown:

$Mu + 0.62Pl + 0.46Q + 0.12H_2O \rightarrow 1.99L + 0.29Sil$

Mineral abbreviations: Mu = muscovite, Pl = plagioclase, Q = quartz, Ksp = K-feldspar, Sil = Sillimanite, Bi = biotite, Grt = garnet, Ilm = ilmenite, L = liquid (from Whitney and Evans, 2010).

GHS melting is thought to have taken place in the mid-crust between depths of 15 and 30 km, at pressures of ~4-8 kbar (grey bar, Figure 3.4. Searle et al., 2010; Streule et al., 2010). At these depths, hydrous melting of muscovite takes place between 630 and 650°C, fluid absent muscovite melting between ~680 and ~790°C, and vapour-absent biotite breakdown (for a typical biotite composition found in GHS pelites) between ~760 and ~790°C, as shown in Figure 3.4 (Zhang et al., 2004).

Determining the nature of the melt reaction is crucial to understanding of Himalayan tectonics. Previous studies have indicated melting is most likely to have taken place during decompression of the crust at fairly constant temperature (e.g. Harris et al., 1994). This finding suggests that the only two possible melt reactions are vapour-absent muscovite or biotite breakdown, due to the positive gradient of their melt reaction lines which may be crossed by isothermal decompression. In contrast, the hydrous melt reaction curve with its negative slope may only be crossed by heating, the most likely source of which would be advective heating in the form of mantle derived melts.

3.5.2.2. Melt temperature

Trace elements are commonly concentrated in accessory phases in felsic rocks. This is particularly true for Zr and the LREEs, where nearly 100% of their total abundances are hosted by zircon and monazite, respectively. As such, it is possible to calculate modal abundances of these minerals in the bulk rock using whole-rock trace element data in order to assess melt temperature.

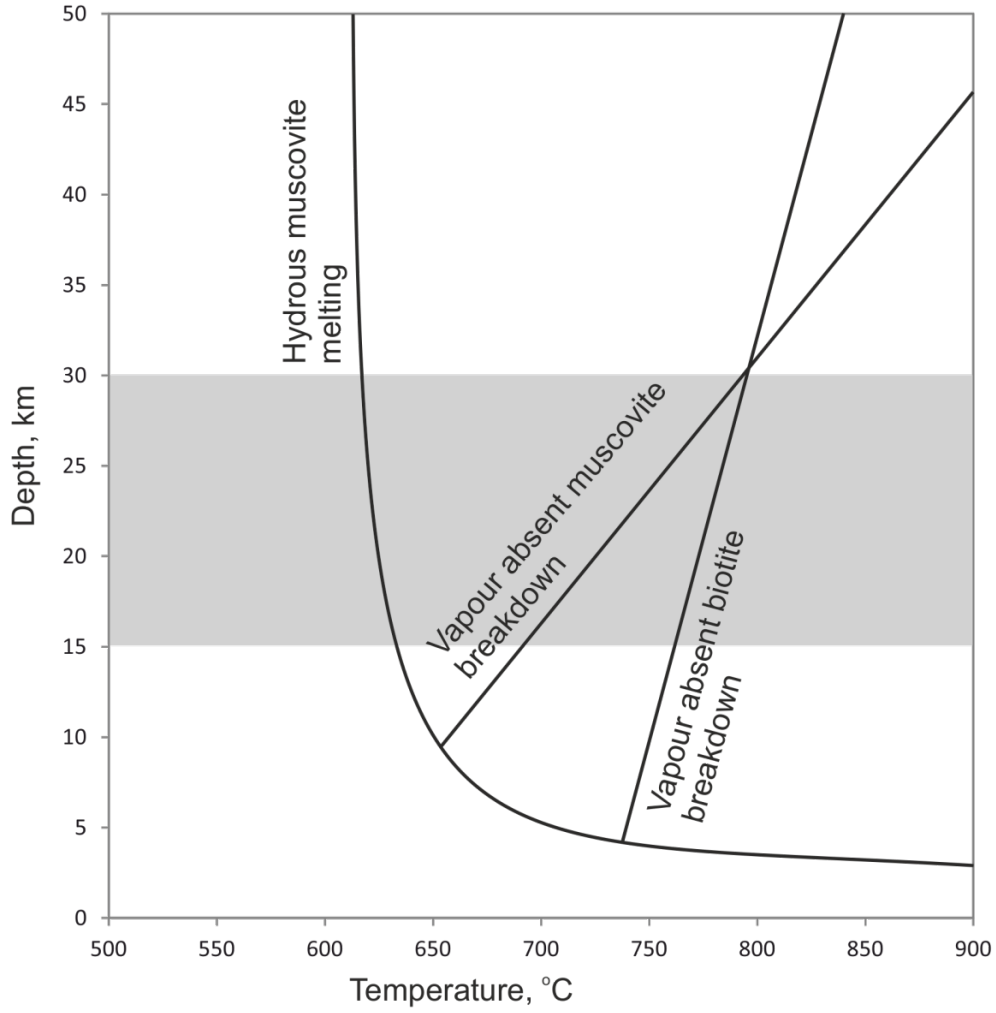

Figure 3.4: *Schematic pressure-temperature diagram showing geometry of melt reactions. Shaded area indicates depths where melting is thought to have occurred in the Himalaya (Searle et al., 2010; Streule et al., 2010). Plot adapted from Zhang et al., 2004.*

The solubility of accessory phases such as zircon and monazite in granitic melts has been experimentally investigated at a variety of temperatures, melt compositions and, for monazite, H_2O contents (Watson and Harrison, 1983; Montel, 1993). Abundances of Zr and LREEs can therefore be used as independent proxies for the solidus temperatures, assuming that the melt is saturated in the dissolved trace element and that insignificant quantities of monazite or zircon are inherited (i.e. the granite sample represents a granitic melt rather than a mix of melt and residual, entrained phases). The latter caveat is of particular concern as a source of uncertainty, since zircon cores are typically inherited by Himalayan leucogranites. A second source of error

lies within the LREE monazite thermometer, as the H_2O content of the melt must be input into the model, which can significantly affect the resultant temperature (increasing water contents from 6% to 10% corresponds to a drop in REE temperature of ~25°C). For this project, an H_2O content of 6% has been used, comparable to that of other fluid-undersaturated leucogranite melts (Montel, 1993; Harris et al., 1995); however, the water contents of individual granite melts may vary.

Temperatures obtained by both thermometers are shown in Figure 3.5 (pure melts shown as solid diamonds, 'excluded' samples shown as hollow circles). The majority of samples lie within uncertainty of the 1:1 reference line. Two tourmaline leucogranites and one two-mica leucogranite lie above the line, with higher LREE temperatures than Zr. In addition, three two-mica, one tourmaline and one garnet leucogranite lie beneath the line, with lower LREE temperatures than Zr.

The most likely explanation for the three samples lying above the line is an underestimation of the water content of the melts involved. By increasing the assumed water content to 9%, the LREE monazite temperature is brought in line with that given by the Zr. Two possibilities exist to account for the samples lying beneath the reference line. It is possible that water content has been overestimated for these samples, as decreasing that input factor to a value of 3% raises the LREE monazite temperature to that of the Zr thermometer. Alternatively, these samples could contain particularly large quantities of inherited zircon, which would cause a rise in the temperature recorded by the Zr thermometer. However, the only one of these samples for which zircons were extracted and analysed (3A02) contained no evidence for any zircon cores (see Chapter 6 for details of zircon geochemistry). As many samples lying on the 1:1 line do contain zircon cores, it is unlikely that such cores are an issue in the thermometry of these Himalayan leucogranites. The most likely explanation is that the H_2O content has been overestimated, leading to a lower LREE monazite temperature.

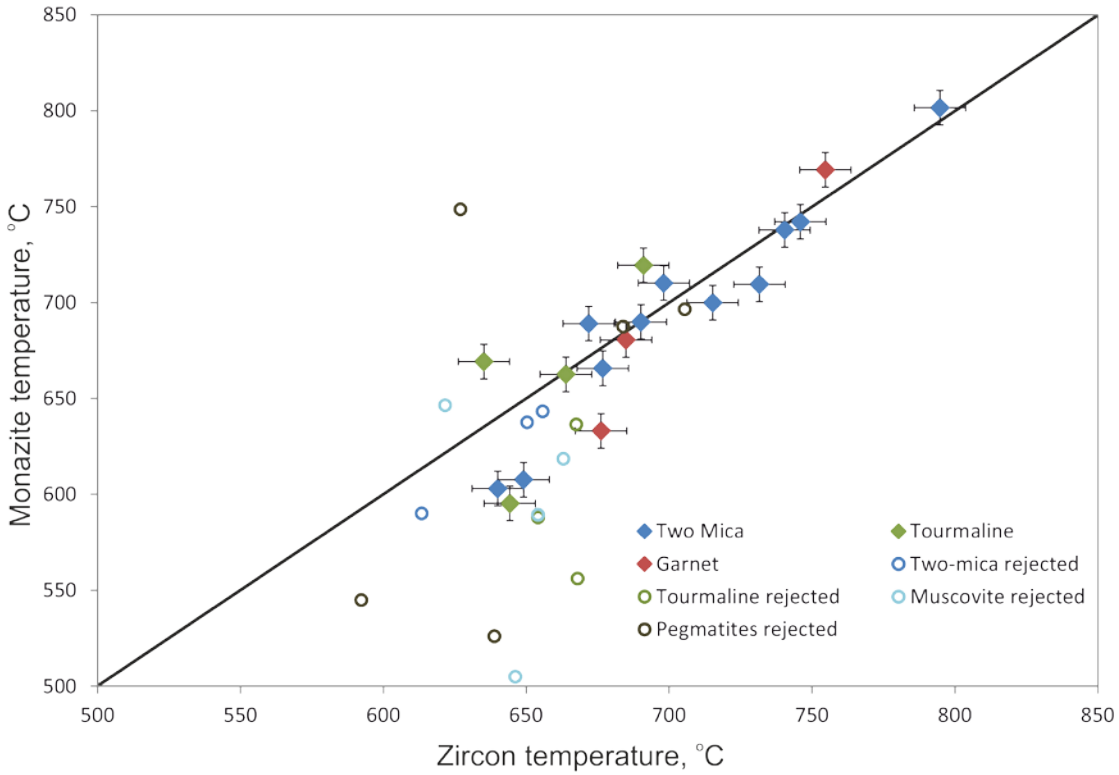

Figure 3.5: *Temperatures obtained by zircon and REE in monazite thermometers for all pure leucogranites. Excluded leucogranites are also shown as unfilled circles (criteria for rejection outlined in Section 3.4.2). Black line represents the 1:1 reference line along which both thermometers yield the same temperature. Error bars are calculated using uncertainties in Zr and REE concentrations and are represented at the 2σ level. They do not take into account uncertainties in quantities of inherited zircon or estimated H_2O contents.*

Temperatures obtained from pure High Himalayan leucogranite melts vary between 640°C and 760°C. This temperature range covers all three possible melt reactions as detailed in Figure 3.4, although the vast majority lie in the temperature range appropriate for vapour-absent muscovite melting.

3.5.2.3. Large-ion-lithophile modelling of melt reactions

Rb, Sr and Ba (all large ion lithophile elements, or LILEs) commonly reside in major phases such as feldspars and micas, occupying sites of other alkali or alkali-earth elements (such as K or Ca). As such, their relative abundances in the melt and reactant source are used to track

changes in mineralogy between source and melt, and also help identify the melt reaction (e.g. Harris and Inger, 1992; Inger and Harris, 1993).

All samples are enriched in Rb/Sr and depleted in Ba relative to GHS metapelites (Figure 3.6). This trend is characteristic of alkali feldspar being formed during the melting process, with the result that Sr and Ba are preferentially taken up by the alkali feldspar, and therefore depleted in the melt. Alternatively, alkali feldspar may be removed from the melt by fractional crystallization. However, as there is no field or petrographic evidence for cumulates from feldspar removal through fractionation, fractional crystallization is considered unlikely. Therefore the trend suggests that the melt reaction involved alkali feldspar being a product of the melt reaction; an observation that eliminates hydrous muscovite melting as a possible melt reaction.

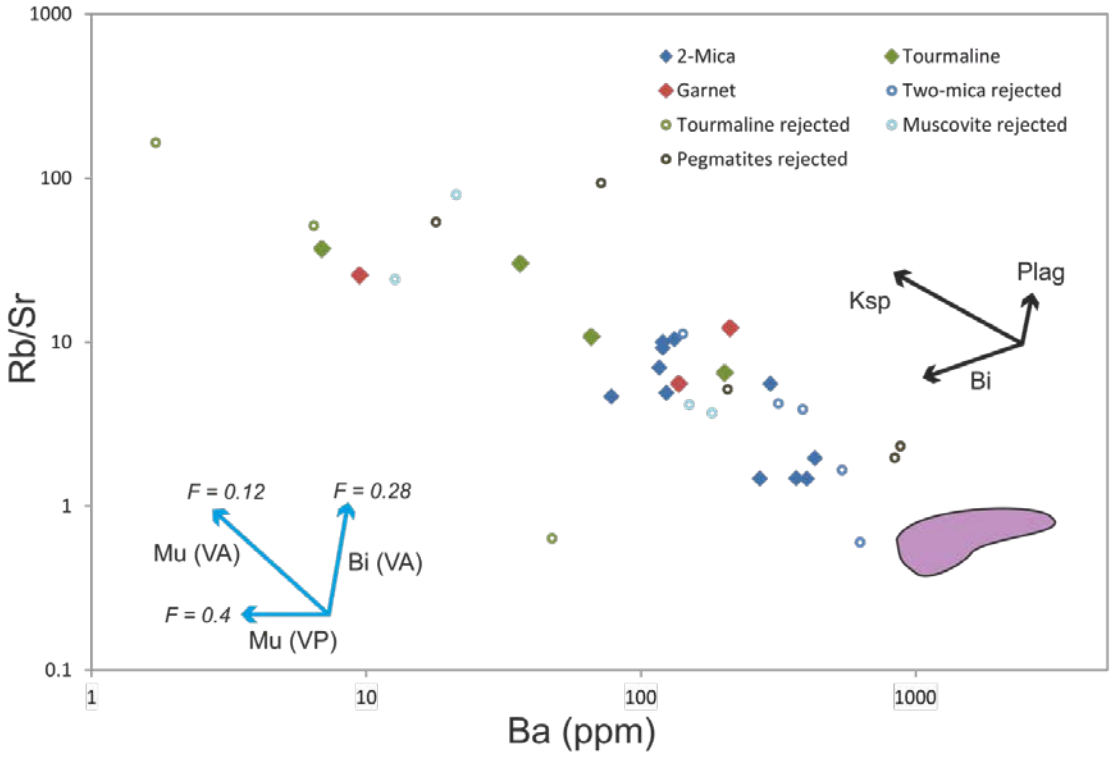

Figure 3.6: *Rb/Sr against Ba for all studied Bhutan leucogranites. Purple field represents GHS composition (Inger and Harris, 1993). Black vectors represent 10% crystallization of phases indicated. Blue vectors represent change caused by different partial melting reactions of muscovite (Mu) and biotite (Bi) under vapour-absent (VA) and vapour present (VP) conditions. Melt fraction extracted from each reaction is also indicated. GHS data and vectors adapted from Inger and Harris (1993).*

The depletion of Ba in conjunction with a rise in Rb/Sr further precludes the possibility that the leucogranites formed by the vapour-absent biotite melting reaction. Biotite commonly contains large quantities of Ba and breakdown of biotite would cause the melt to become enriched in Ba, with only small quantities of peritectic K-feldspar being produced into which Ba would be partitioned. Conversely, vapour-absent muscovite breakdown causes a decrease in Ba due to larger quantities of peritectic K-feldspar being generated, into which Ba is partitioned.

Figure 3.6 shows a single trend in LILE data which most closely resembles that predicted for muscovite breakdown under vapour-absent conditions, strongly suggesting that the High Himalayan leucogranites formed by this reaction.

3.6. Conclusions

Trace element data were used to model both melt reaction and the temperature at which leucogranites crystallized. Zircon and LREE in monazite temperatures vary between 640 and 760°C, consistent with temperatures recorded in other leucogranite studies (e.g. Harris et al., 1995).

The increase in Rb/Sr and corresponding decrease in Ba compared to the GHS in all samples is strongly indicative of muscovite breakdown in vapour-absent melting in all samples regardless of mineralogical type, consistent with the temperatures obtained. Tourmaline leucogranites appear to have more extreme Rb/Sr and lower Ba abundances compared to other leucogranites, suggesting a more evolved melt consistent with a lower melt fraction.

Chapter 4

Whole-rock isotope geochemistry

4.1. Introduction

Since the discovery in the early 1900s that lead is the final decay product of uranium, radiogenic isotopes have been employed for use in geochemistry and geochronology (Boltwood, 1907; Holmes, 1911, 1913; Soddy, 1913). Radiogenic isotope systems rely on the radioactive decay of one parent isotope to produce a daughter isotope at a known rate. These systems can be used to determine the timing of crystallization or original melt formation of a given rock or mineral. In addition, as isotopic fractionation between source and melt is minor (e.g. Richter et al., 2003), the initial isotope ratios of any given igneous rock may represent those of its source(s), thereby potentially allowing the source to be identified.

Radiogenic isotopes have, in recent decades, led to increasingly sophisticated insights, as advancements in thermal ionization mass spectrometry (TIMS) and multi-collector inductively coupled plasma mass spectrometry (MC-ICP-MS) have allowed increasingly precise measurements to be made (e.g. Horstwood et al., 2003; Parrish and Noble, 2003). These advances, along with the advance of higher spatial precision techniques including laser ablation, have led to the ability to target micrometre-scale crystallisation episodes in mineral phases such as zircon or monazite. The ability to target individual growth rims, as well as to determine between igneous rim and inherited core, has vastly improved the detail to which igneous events can be dated, and their geochemistry understood.

For a particular radiogenic isotope system to be useful across any particular part of the geological time scale, the half-life must be appropriate such that the abundances of both the remaining parent isotope and the daughter isotope are in sufficient quantities to be precisely measured. In total, six isotope systems are commonly employed in geochemical and geochronological studies. These are uranium/thorium-lead (^{238}U to ^{206}Pb, ^{235}U to ^{207}Pb and ^{232}Th to ^{208}Pb), samarium-neodymium (^{147}Sm to ^{143}Nd), rubidium-strontium (^{87}Rb to ^{87}Sr), potassium-argon (^{40}K to ^{40}Ar), lutetium-hafnium (^{176}Lu to ^{176}Hf) and rhenium-osmium (^{187}Re to ^{187}Os). Of these, U/Th-Pb, Sm-Nd, Rb-Sr and Lu-Hf were analysed this study; Rb-Sr, Sm-Nd and U/Th-Pb on whole rock, and U/Th-Pb and Lu-Hf on zircons.

The most common isotope systems to be used for granite whole-rock studies are U-Pb, Rb-Sr and Sm-Nd, as all elements involved are incompatible and as such their abundances are concentrated in more evolved melt compositions, like granite, during fractional crystallization. Fractional crystallisation also commonly causes a systematic increase in the Rb/Sr ratio as a melt becomes more felsic, and this increase in parent-daughter ratio often causes the ^{87}Sr/^{86}Sr of crustal rocks to be highly divergent from mantle values, allowing for relative contributions from crust and mantle to be readily assessed. Sm and Nd are rarely fractionated by crustal processes, and therefore variations in the ^{143}Nd/^{144}Nd ratio are more dependent on the model age of mantle extraction.

U-Pb is most commonly used for geochronological purposes, due to the presence of two 'parallel' decay chains. ^{238}U decays to ^{206}Pb, while ^{235}U decays to ^{207}Pb, and by coupling parent-daughter isotope ratios of both decay chains it is possible to obtain highly accurate ages. One of the most commonly dated accessory phases is zircon, due to its omnipresence in a wide variety of silicate rocks and up to percent levels of U, but only trace levels of Pb at the time of crystallisation. As such, the majority of analysed Pb is likely to be the product of radioactive decay, and any corrections to account for pre-existing, or 'common', Pb are minor. For minerals which also contain large quantities of Th (such as monazite), a third decay chain of ^{232}Th to ^{208}Pb may also be coupled to the U-Pb decay chains.

4.2. Methods

All samples were crushed by standard techniques (jaw crushing, followed by TEMA agate milling) at the Open University. Powders were dissolved in a HF/HNO_3 solution in PTFE beakers at 120˚C on a hotplate for >12 hours. Dissolved samples were evaporated down, re-dissolved in HCl under the same conditions and further evaporated down to dryness.

Samples were then passed through AG50W-X8 (Biorad) cation exchange resin columns in order to separate the majority of matrix elements from those of interest. Samples were subsequently split into three cuts for separate Pb, Nd and Sr analysis.

For Pb, samples were dried down and dissolved in 1M HBr before being passed through Biorad AG1-X8 anion exchange resin columns in order to separate out Pb. Pb cuts were then dried down before being dissolved in concentrated HNO_3 in order to remove any remaining HBr from the samples. Samples were then split into natural and double-spike aliquots prior to loading on filaments, assuming 1000 ng Pb in each aliquot. Double-spike aliquots were mixed with a ^{207}Pb-^{204}Pb double spike identical in composition to that described in Thirlwall (2000). Natural and double-spike aliquots were then loading onto tungsten filaments and analysed by TIMS. NBS981 standard was used to ensure within-run reproducibility.

For Nd, column cuts were dried down and dissolved in 4M HNO_3 before being passed through Eichrom LN-specific resin REE columns in order to separate out Nd. Samples were dried down and redissolved in 3% HNO_3 to a concentration of 100 ppb Nd. Samples were then analysed by MC-ICP-MS, using the J+M standard to ensure reproducibility.

For Sr, column cuts were dried down and dissolved in 7M HNO_3 before being passed through Eichrom Sr-specific resin to separate out Sr. Samples were then dried down and redissolved in 3% HNO_3 to a concentration of 100 ppb Sr. Samples were then analysed by MC-ICP-MS, using the NBS987 standard to ensure reproducibility.

Full details are provided in Appendix A.

4.3. Results

Full isotopic data are shown in Table 4.1. Initial ratios for all data were calculated by correcting to an age of 20 Ma, an average age for leucogranite generation in the Himalaya (e.g. Guo and Wilson, 2012). An assumed age was required because precise geochronological data are not available for all samples. In addition, isotope data for all potential source rocks are age-corrected to 20 Ma and as such using different correction ages for individual leucogranites may skew interpretation of source. The differences in isotopic ratios corrected to 20 Ma and those corrected to any specific known age lies within uncertainty for all samples and isotope systems. For more discussion on geochronology, see Chapter 6.

Uncertainties are presented as 2 σ, which refers to an uncertainty of two standard deviations.

Neodymium isotope data are commonly represented in epsilon notation, which refers to a variation in parts per ten thousand relative to a standard:

$$\varepsilon^{143}Nd = \left(\frac{{}^{143}Nd/_{144}Nd_{\text{sample}}}{{}^{143}Nd/_{144}Nd_{\text{standard}}} - 1 \right) * 10000$$

Table 4.1: Whole-rock isotope data for Bhutanese leucogranites

	1D01	1G01	1G02	1G03	3A01	3A02	3A03	3A04	4D01	
	Grt	Peg	Tm	2M	Peg	Grt	2M	Tm	2M	
Sr method	TIMS	MC-ICP-MS	MC-ICP-MS	MC-ICP-MS	TIMS	TIMS	TIMS	TIMS	MC-ICP-MS	Sr method
$^{87}Sr/^{86}Sr$	0.978210	0.766658	0.824239	0.809263	0.807666	0.787705	0.777162	0.793745	0.768719	$^{87}Sr/^{86}Sr$
2 σ	0.000022	0.000083	0.000065	0.000066	0.000020	0.000020	0.000020	0.000020	0.000083	2 σ
$^{87}Sr/^{86}Sr_i$	0.974755	0.765154	0.819859	0.805058	0.766035	0.769610	0.771099	0.769732	0.767737	$^{87}Sr/^{86}Sr_i$
$^{143}Nd/^{144}Nd$	0.512259	0.511803	0.511616	0.511591	0.511981	0.511955	0.511896	0.511979	0.511961	$^{143}Nd/^{144}Nd$
2 σ	0.000018	0.000019	0.000019	0.000018	0.000025	0.000018	0.000018	0.000019	0.000018	2 σ
$^{143}Nd/^{144}Nd_i$	0.512234	0.511785	0.511594	0.511568	0.511956	0.511925	0.511873	0.511955	0.511936	$^{143}Nd/^{144}Nd_i$
εNd_i	-7.88	-16.65	-20.36	-20.87	-13.30	-13.91	-14.91	-13.32	-13.69	εNd_i
2 σ	0.35	0.38	0.38	0.36	0.49	0.35	0.36	0.37	0.36	2 σ
$^{206}Pb/^{204}Pb$	20.9357	19.0653		18.9813	18.9063	18.9336	18.8560	18.9507	18.9125	$^{206}Pb/^{204}Pb$
2 σ	0.0034	0.0033		0.0027	0.0032	0.0029	0.0028	0.0030	0.0033	2 σ
$^{207}Pb/^{204}Pb$	15.8922	15.7937		15.7806	15.7899	15.7945	15.7941	15.7942	15.7885	$^{207}Pb/^{204}Pb$
2 σ	0.0030	0.0030		0.0045	0.0029	0.0046	0.0046	0.0049	0.0030	2 σ
$^{208}Pb/^{204}Pb$	39.5820	39.5150		39.4232	39.5763	39.5779	39.5592	39.5714	39.6890	$^{208}Pb/^{204}Pb$
2 σ	0.0086	0.0083		0.0109	0.0082	0.0114	0.0110	0.0126	0.0083	2 σ
$^{207}Pb/^{206}Pb$	0.7591	0.8284		0.8314	0.8352	0.8342	0.8376	0.8334	0.8348	$^{207}Pb/^{206}Pb$
2 σ	0.0003	0.0003		0.0004	0.0003	0.0004	0.0004	0.0004	0.0003	2 σ
$^{206}Pb/^{204}Pb_i$	20.9156	19.0598		18.9750	18.9039	18.9269	18.8509	18.9440	18.9096	$^{206}Pb/^{204}Pb_i$
$^{207}Pb/^{204}Pb_i$	15.8920	15.7937		15.7805	15.7899	15.7944	15.7941	15.7941	15.7885	$^{207}Pb/^{204}Pb_i$
$^{208}Pb/^{204}Pb_i$	39.5669	39.5096		39.4205	39.5758	39.5755	39.5574	39.5674	39.6872	$^{208}Pb/^{204}Pb_i$
$^{207}Pb/^{206}Pb_i$	0.7598	0.8286		0.8316	0.8353	0.8345	0.8378	0.8337	0.8349	$^{207}Pb/^{206}Pb_i$

Table 4.1: Whole-rock isotope data for Bhutanese leucogranites

	5M01	DRB1215	DRB1247	DRB1251	CW-10-16	CW-10-23	BH-65C	BH-84	BH-226	BH-231B	
	Musc	Tm	2M	2M	2M	2M	Grt	2M	2M	2M	
Sr method	MC-ICP-MS	TIMS	TIMS	TIMS	MC-ICP-MS	MC-ICP-MS	MC-ICP-MS	TIMS	MC-ICP-MS	TIMS	Sr method
$^{87}Sr/^{86}Sr$	0.795758	0.760098	0.762264	0.829544	0.830595	0.797008	0.911392	0.740317	0.770572	0.730144	$^{87}Sr/^{86}Sr$
2 σ	0.000083	0.000020	0.000020	0.000020	0.000066	0.000066	0.000083	0.000020	0.000083	0.000020	2 σ
$^{87}Sr/^{86}Sr_i$	0.780168	0.756902	0.755492	0.827016	0.828259	0.794189	0.903944	0.739281	0.767654	0.729281	$^{87}Sr/^{86}Sr_i$
$^{143}Nd/^{144}Nd$	0.511961	0.511935	0.511907	0.511758	0.511688	0.511566	0.511984	0.512021	0.511728	0.511933	$^{143}Nd/^{144}Nd$
2 σ	0.000020	0.000018	0.000018	0.000019	0.000019	0.000018	0.000045	0.000045	0.000045	0.000046	2 σ
$^{143}Nd/^{144}Nd_i$	0.511936	0.511909	0.511877	0.511736	0.511670	0.511543	0.511967	0.512005	0.511709	0.511916	$^{143}Nd/^{144}Nd_i$
εNd_i	-13.69	-14.22	-14.85	-17.59	-18.88	-21.36	-13.09	-12.35	-18.13	-14.09	εNd_i
2 σ	0.40	0.35	0.36	0.37	0.36	0.35	0.88	0.89	0.87	0.89	2 σ
$^{206}Pb/^{204}Pb$	18.5091	19.0240	18.7204	20.4498	19.8869	19.6754	19.5722	19.5125	19.4626	18.8100	$^{206}Pb/^{204}Pb$
2 σ	0.0035	0.0028	0.0027	0.0035	0.0030	0.0027	0.0038	0.0033	0.0037	0.0033	2 σ
$^{207}Pb/^{204}Pb$	15.7729	15.8034	15.7856	15.9241	15.8707	15.8583	15.8245	15.7997	15.8249	15.7617	$^{207}Pb/^{204}Pb$
2 σ	0.0034	0.0045	0.0045	0.0050	0.0046	0.0045	0.0038	0.0030	0.0036	0.0030	2 σ
$^{208}Pb/^{204}Pb$	39.0877	39.5970	39.4095	40.7662	39.8627	40.0873	39.3321	40.3560	39.8509	39.2416	$^{208}Pb/^{204}Pb$
2 σ	0.0099	0.0110	0.0109	0.0127	0.0115	0.0109	0.0114	0.0083	0.0110	0.0085	2 σ
$^{207}Pb/^{206}Pb$	0.8522	0.8307	0.8432	0.7787	0.7981	0.8060	0.8085	0.8097	0.8131	0.8379	$^{207}Pb/^{206}Pb$
2 σ	0.0003	0.0004	0.0004	0.0004	0.0004	0.0003	0.0004	0.0003	0.0003	0.0003	2 σ
$^{206}Pb/^{204}Pb_i$	18.4906	19.0064	18.7046	20.4426	19.8818	19.6468	19.5471	19.4705	19.4273	18.7900	$^{206}Pb/^{204}Pb_i$
$^{207}Pb/^{204}Pb_i$	15.7727	15.8032	15.7854	15.9241	15.8706	15.8580	15.8243	15.7993	15.8245	15.7615	$^{207}Pb/^{204}Pb_i$
$^{208}Pb/^{204}Pb_i$	39.0842	39.5953	39.4067	40.7611	39.8593	40.0833	39.2931	40.2883	39.7687	39.2300	$^{208}Pb/^{204}Pb_i$
$^{207}Pb/^{206}Pb_i$	0.8530	0.8315	0.8439	0.7790	0.7982	0.8072	0.8095	0.8114	0.8146	0.8388	$^{207}Pb/^{206}Pb_i$

4.3.1. Strontium – neodymium isotopes

$^{87}Sr/^{86}Sr_i$ and εNd_i for all analysed leucogranites are plotted in Figure 4.1, together with potential source fields for the GHS, THS and LHS (data from Guo and Wilson, 2012, and references therein). $^{87}Sr/^{86}Sr_i$ varies from 0.729 to 0.975, while εNd_i varies from -7.8 to -21.4. The majority of samples (15 out of 19) record $^{87}Sr/^{86}Sr_i$ ratios between 0.756 and 0.829 and εNd_i values between -12.3 and -21.4. However there are four notable outliers. Samples BH-84 and BH-231B record particularly low $^{87}Sr/^{86}Sr_i$ ratios of 0.74 and 0.73, respectively, and plot in an area covered by both the GHS and THS fields. BH-65 and 1D01 both have more radiogenic $^{87}Sr/^{86}Sr_i$ ratios than the majority of samples, with ratios of 0.904 and 0.975, respectively, and lies in the GHS orthogneiss field. The latter, 1D01, is the only sample to record an anomalous εNd_i value of -7.9, a less radiogenic value than other samples, and also falls outside of any potential source fields.

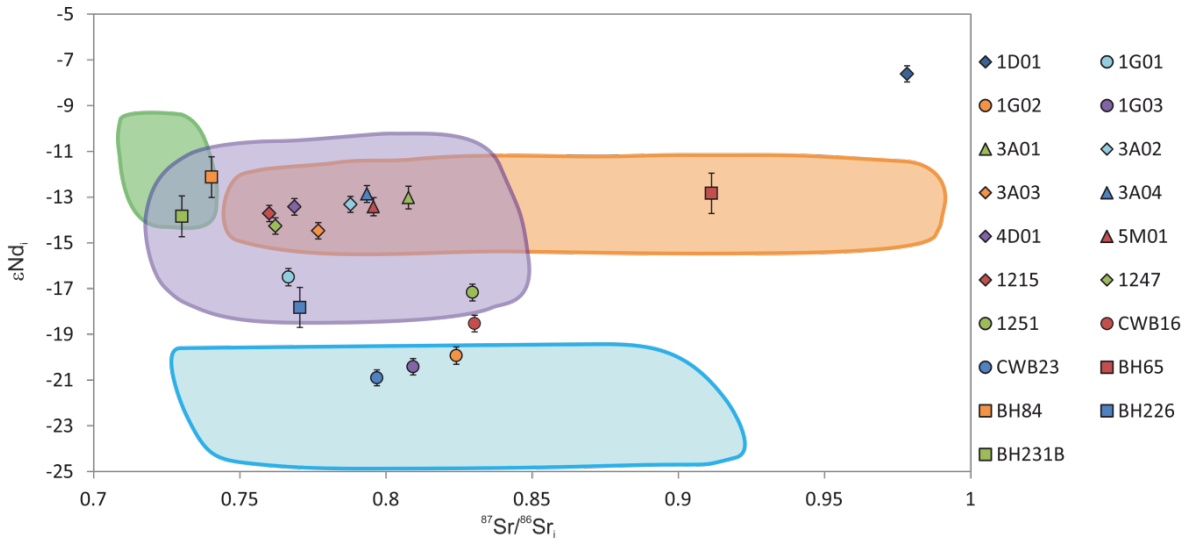

Figure 4.1: *Plot of Sr-Nd isotopic data for all leucogranites. Generalised potential source fields are shown: GHS metapelites (purple), GHS orthogneisses (orange), THS (green), LHS (blue); data from Guo and Wilson, 2012, and references therein. Error bars are 2 s.d. and for Sr are covered by the data symbol.*

4.3.2. Lead isotopes

Whole-rock Pb isotope data were collected from 18 leucogranite samples; data are plotted in Figure 4.2. $^{206}Pb/^{204}Pb$ ratios for all samples vary between 18.50 and 20.94, $^{207}Pb/^{204}Pb$ between 15.76 and 15.76 and 15.93, and $^{208}Pb/^{204}Pb$ ratios between 39.08 and 40.77.

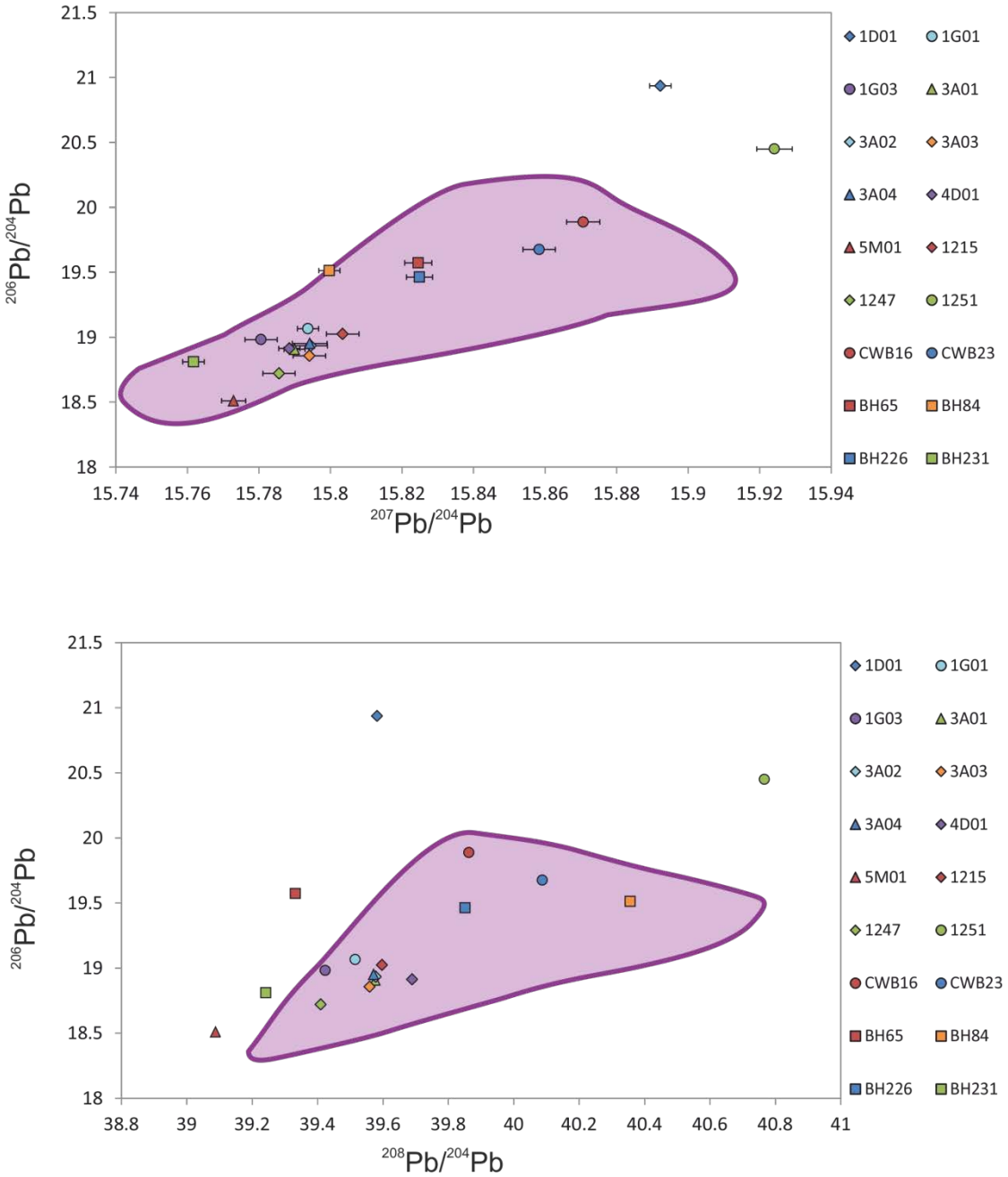

Figure 4.2: *Pb data for all Himalayan leucogranite samples. GHS metapelite fields shown in purple (Vidal et al., 1982; Gariepy et al., 1985). Error bars are 2 s.d., however are smaller than the symbols for $^{206}Pb/^{204}Pb$ and $^{208}Pb/^{204}Pb$.*

4.4. Discussion

4.4.1. Strontium – neodymium isotopes

The wide variability in Sr-Nd radiogenic isotope data reflect the heterogeneity of the source materials, as can be seen in the size of the fields representing the GHS and LHS. It should be noted that both lithotectonic units comprise a wide range of crustal materials, including semi-pelites, pelites, granitic gneisses and calc-silicates so that this variability is expected. Thirteen of the 19 samples record Sr-Nd values that overlap the GHS metapelite field, as would be expected if this unit were the source of these melts. Two of these, BH-84 and BH-231B, have sufficiently low $^{87}Sr/^{86}Sr_i$ ratios so that they also plot within the THS field, although there is no field evidence for THS melting, and therefore it is unlikely that these samples involve any THS material. Eight samples also overlap with the GHS orthogneiss field, however it is more likely that metapelites formed the major source for these samples, due to the abundance of fusible micaceous phases.

Three samples (1G02, 1G03 and CWB-23) yield εNd_i isotope ratios that are more radiogenic than any known to date from the GHS, and only observed in LHS metasediments (Guo and Wilson, 2012). We therefore suggest that these three samples (in addition to CWB-16, which plots between the GHS and LHS fields) have incorporated at least some LHS material during melting. However it is difficult to evaluate how much material must have been incorporated simply from Sr-Nd systematics, as the LHS Sr-Nd field is particularly large and poorly constrained, and even a small contribution (e.g. 5%) of LHS-sourced material to a GHS-dominated melt system may be sufficient to move the resultant granite geochemistry into the LHS field.

Sample BH-65 plots within the GHS orthogneiss field, with a $^{87}Sr/^{86}Sr_i$ ratio that is more radiogenic than those seen in the GHS metapelites. This suggests that the dominant source of this granite is the orthogneiss.

Sample 1D01 is characterized by the most radiogenic $^{87}Sr/^{86}Sr_i$ ratio of all granites, although the εNd_i value is the highest observed (and therefore the least radiogenic). It therefore does not plot in any potential source field, nor can it easily be explained by mixing two potential sources. The elevated $^{87}Sr/^{86}Sr_i$ ratios may indicate that orthogneiss is likely to be the dominant source of this sample, although the εNd_i is not observed in any potential source materials. As the orthogneiss field is constrained entirely from data from north-western India (Miller et al., 2001), it is possible that Bhutanese orthogneisses may record higher εNd_i. However, no analyses have been performed on such samples during this study. The most likely explanation for the origin of this sample is that it formed from melting of orthogneisses, based on its $^{87}Sr/^{86}Sr_i$ ratio.

4.4.2. Lead isotopes

Whole-rock Pb isotope data were collected from 18 leucogranite samples (Figure 4.2). Published Pb isotope work in the Himalaya is limited to two studies that analysed leucogranites and GHS metapelites in Nepal (Vidal et al., 1982; Gariepy et al., 1985). No data are available from other potential source materials – GHS orthogneisses, LHS or THS.

Pb isotope ratios for Bhutan leucogranites cover a wide range of compositions, roughly covering the field of GHS metapelites, and plotting similarly to other previously reported leucogranite chemistry (Vidal et al., 1982; Gariepy et al., 1985). The $^{206}Pb/^{204}Pb$ vs $^{207}Pb/^{204}Pb$ plot shows that 17 of the 18 samples lie within the GHS metapelite field (see Figure 4.2a), including those identified, from Sr-Nd data, to be at least partly sourced from the LHS. Two exceptions are 1D01 and 1251, which yield more extreme $^{206}Pb/^{204}Pb$ and $^{207}Pb/^{204}Pb$ ratios than the known range of GHS metapelites. For 1D01, this implies that the GHS orthogneisses, the suspected source based on Sr-Nd, have a more radiogenic Pb composition than the metapelites.

Figure 4.2b plots $^{206}Pb/^{204}Pb$ vs $^{208}Pb/^{204}Pb$, where 13 out of 18 samples plot within the GHS metapelite field. 1D01 once again yields ratios that plot outside the metapelite field, with a $^{208}Pb/^{204}Pb$ ratio lower than the majority of metapelites. Three additional samples (5M01, BH-65 and BH-231) plot outside the GHS field, all yielding low $^{208}Pb/^{204}Pb$ ratios. BH-65 and

1D01 are the two samples thought to be derived from GHS orthogneisses based on their Sr-Nd geochemistry, which raises the possibility that the orthogneisses could be characterized by low $^{208}Pb/^{204}Pb$ ratios. This in turn makes it possible for both samples 5M01 and BH-231 to be also derived from orthogneiss material, though it is impossible to be conclusive without knowing the Pb isotope ratios of the GHS orthogneiss itself. Sample 1251 once again plots outside the GHS field, yielding higher $^{206}Pb/^{204}Pb$ and $^{208}Pb/^{204}Pb$ ratios than the GHS metapelites.

4.5. Conclusions

$^{87}Sr/^{86}Sr_i$ and εNd_i vary significantly across all samples, between 0.729 and 0.978 and between -7.8 and -21.4, respectively. Eight of the 19 samples plot within the area covered by both the GHS orthogneiss and the GHS metapelite field, with the latter being the most likely source of melting due to the abundance of fusible mica (muscovite). However, several samples plot in two other different source fields, with two samples (1D01 and BH-96) sourced predominantly from orthogneisses due to their extreme $^{87}Sr/^{86}Sr_i$ ratios. Additionally, four samples (1G02, 1G03, CWB16 and CWB23) yield εNd_i values lower than any found in the GHS, with samples 1G02, 1G03 and CWB23 plotting within the LHS field. These four samples must therefore have incorporated at least some portion of LHS material during their genesis, in order to explain their low εNd_i values. The implications of such findings shall be discussed in full in Chapter 8.

13 out of 18 samples lie within the GHS field across all three Pb isotope ratios. Those which fall outside the field may be at least partially sourced from other potential source materials. 1D01 is the only sample that is separate from the GHS metapelite field across all isotope systems, making it possible that this sample is sourced of different material. However the four samples (5M01, 1251, BH-86, BH-231) which yield Pb ratios outside of the GHS metapelite field all fall into that field in Sr-Nd space. This may provide evidence for mixed sources for these samples, however given the lack of previous Pb isotope work on other potential source regions, few conclusions can be reached.

Chapter 5

The identification and significance of pure sediment-derived granites

The following chapter is adapted from a manuscript which has been submitted for publication to the journal Geology. I performed all data gathering and analysis, with technical assistance from co-authors, and wrote the majority of the manuscript. Co-authors provided edits and constructive comments to the final version.

The identification and significance of pure sediment-derived granites

Thomas N. Hopkinson[1]*, Nigel B.W. Harris[1], Clare J. Warren[1], Christopher J. Spencer[2,3], Nick M.W. Roberts[2], Matthew S.A. Horstwood[2], Randall R. Parrish[2], EIMF[4]

1. Department of Environment, Earth and Ecosystems, Open University, Milton Keynes, MK7 6AA, UK.
2. NERC Isotope Geosciences Laboratory, British Geological Survey, Keyworth, NG12 5GG, UK.
3. Department of Applied Geology, Curtin University, Bentley, 6102, WA, Australia.
4. Edinburgh Ion Microprobe Facility, University of Edinburgh, Edinburgh, EH9 3FE, UK.

*thomas.hopkinson@open.ac.uk

5.1. Abstract

Our understanding of the evolution of the Earth's continental crust depends on the characterization of the constituent geochemical reservoirs (Kemp et al., 2007). One of the major issues in such models is obtaining representative upper and lower crustal compositions. The development of the I- and S-type granite classification initially suggested that these categories would directly reflect the compositions of their igneous and sedimentary source regions (Chappell and White, 1974; Teng et al., 2004; Bea et al., 2007; Savage et al., 2012). More recently, detailed studies have shown that most granites are mixtures of melts extracted from the mantle and melts derived from the continental crust. A recent granitic zircon Hf-O data from widely recognised S-type granites (including the type area in Australia) have shown that these S-type 'end-members' include a significant (20 to 75 %) mantle-derived component (Kemp et al., 2006, 2007), consistent with the inference that all granites are partially sourced from the mantle and thus that granite formation always contributes to crustal growth. Here we demonstrate that the Himalayan leucogranites are derived solely from metamorphosed upper crustal sediments, and fail to show any component of a mantle contribution, therefore representing a more suitable 'S-type' type locality. Importantly they provide an excellent insight into the radiogenic and stable isotope compositions of continental sediments and the melts that are sourced from these sediments.

5.2. Introduction

The formation of granitic magmas is a key process in crustal evolution, facilitating heat transfer within the crust and contributing to mechanical weakening of the crust throughout episodes of mountain building. Granites are particularly associated with crustal melting at convergent plate margins where crustal rocks are thickened, heated and deformed. Whilst individual granite bodies may have multiple melt sources, it has become well-established that most granites can be classified as either 'I-type' (those with mainly igneous, including mantle, sources), or 'S-type'

(those with mainly sedimentary sources) as first described formally in the Lachlan Fold Belt of south-east Australia (Kemp et al., 2007), and supported by early bulk-rock Sr-Nd isotope studies (McCulloch and Chappell, 1982). This simple chemical classification, later extended to include further categories such as A-type (Loiselle and Wones, 1979), has arguably become the most widely used scheme for granite classification.

Since the initial study, further bulk-rock isotope results showed that the S-types granites from the Lachlan fold belt have significant mafic input and thus are not 'pure' crustal melts (Collins, 1996; Healy et al., 2004). Nevertheless, Lachlan granites classified as 'S-type' continue to be taken as a paragon of sediment-sourced magmas (Teng et al., 2004; Bea et al., 2007; Savage et al., 2012). A misunderstanding of the nature of 'S-type' granites may lead to misleading conclusions in interpreting the role of granite petrogenesis or geochemical behaviour during crustal melting. For example, based on the assumption that 'S-type' granites represent the crustal end-member of granitic rocks, minor differences in the bulk-rock Si isotope composition of 'I-type' and 'S-type' granites led researchers to conclude that Si isotopes are not sensitive to sedimentary input. A further study documenting the similarity between bulk-rock Li isotopes from Lachlan S-type granites and their associated sedimentary rocks suggested that Li isotope fractionation during crustal melting was negligible (Teng et al., 2004). Neither conclusion is valid if the S-type samples are in fact mixtures of both mantle and crustal melt sources.

As yet there is no conclusive chemical evidence that coherent granite bodies, as opposed to the leucosome component in migmatites, may be derived entirely from melting sediments. The recognition of such bodies will provide representative compositions of pure crustal melts for future geochemical studies. The establishment of the total volume of pure crustal melts of different ages are critical for calculating the global magmatic budget, as these magmas have not contributed to net crustal growth.

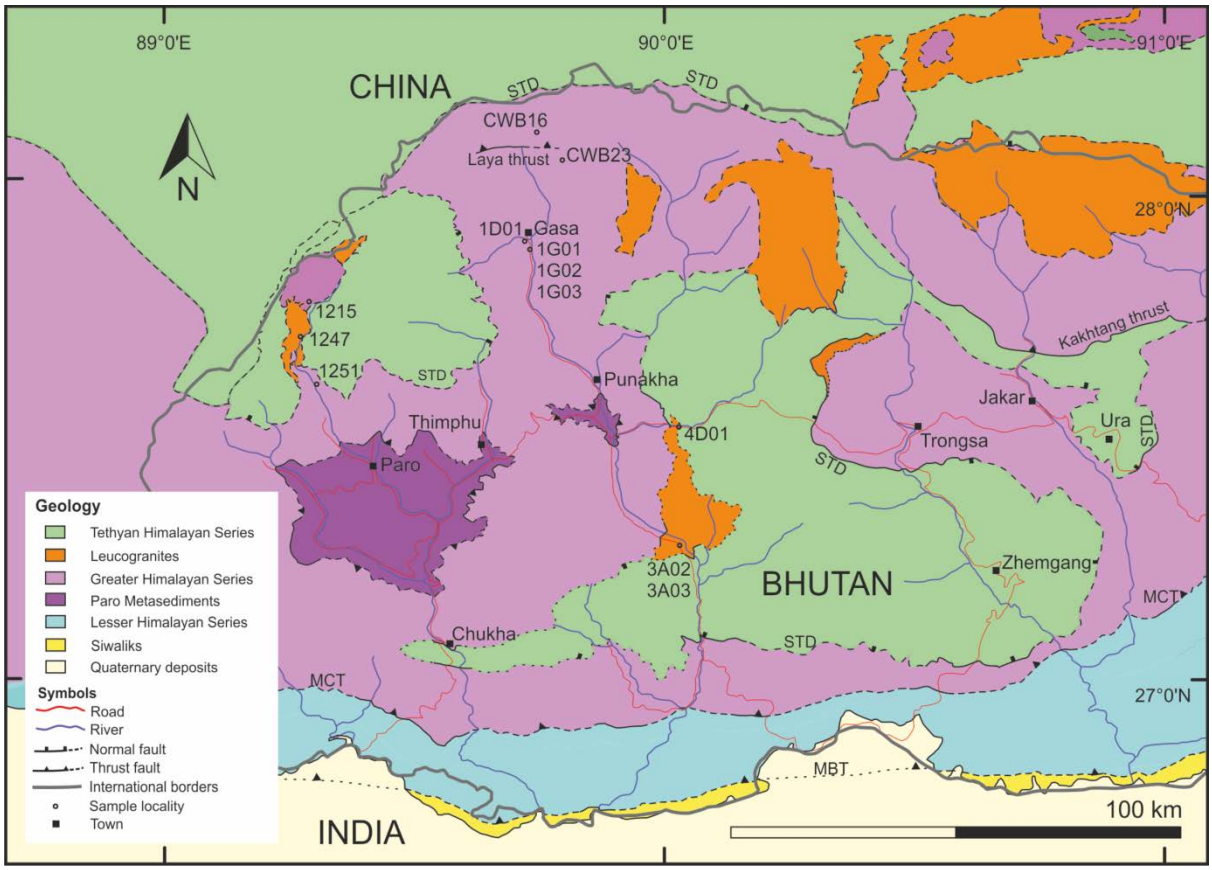

Figure 5.1: *Geological map of western Bhutan, adapted from Greenwood et al. (2016) showing sample localities. STD = South Tibetan Detachment, MCT = Main Central Thrust, MBT = Main Boundary Thrust, MFT = Main Frontal Thrust.*

The recognition of pure crustal melts also carries implications for the thermal and tectonic evolution of orogenic belts. Two processes can control magma generation in mountain belts. The first process is that during collision hot mantle material is directly entrained into the lower crust, which will ultimately cause advective heating to produce large amounts of crustal melts with mantle material present. This is a more likely explanation for a slow collision during which some element of lateral extension may be present. In contrast, during a rapid, major collision melting results when a thick pile of pelitic to semi-pelitic sedimentary rocks is tectonically buried deep enough to allow them to melt extensively without external influence.

The distribution and timing of melting depends on the heat production of the sediments (abundances of radioactive elements U, Th and K), the distribution and thickness of fertile

lithologies, and to some extent, the geometry of the collision (Patiño-Douce et al., 1990). The origin of the High Himalayan leucogranites is therefore intrinsically associated with the geodynamic and thermal evolution of the India-Asia collision. Although collision and crustal thickening is widely held to have occurred at 50-55 Ma (Najman et al., 2010) and may have begun as early as 59 ± 1 Ma (Hu et al., 2015), an alternative view for major collision at ~34 Ma has also been proposed (Aitchison et al., 2007). Given that the High Himalayan leucogranite bodies formed at ~20 Ma, the competing models allow timespans varying from >30 million years (for early Eocene collision) and ~14 million years (for collision on the Eocene-Oligocene boundary). For widespread melting to occur in the mid crust, temperatures must reach values of at least ~700°C (Harris et al., 1995). Thermal models for orogenic evolution require a time period of at least 20 to 30 million years between collision and melting for all realistic values of heat production and sedimentary thicknesses (England et al., 1992; Medvedev et al., 2006). To accelerate this process, additional heat sources would be required, potentially including advection, provided by rising melts from the lower crust or mantle, or shear heating along discrete thrusts, for which there is little to no evidence (Royden, 1993; Harris and Massey, 1995). Hence the 'young' collision model requires a widespread mantle melt component to provide advective heating to accelerate the rate of Miocene magmatism. The absence of any recognized intermediate or mafic intrusions across the High Himalaya therefore suggests an early collision, unless a mantle component can be identified in the leucogranite melts themselves.

Traditionally, granite geochemical studies have been based on bulk-rock data that provide averaged information of all component mineral phases and therefore fail to resolve contributions from discrete individual sources. Furthermore, bulk-rock samples may not reflect the original composition of the crystallised melt for a variety of reasons, ranging from incomplete separation of magma from restitic or peritectic phases (due to the high viscosity of granite magmas and to the small density contrast between such melts and silicate phases), or to the modification of the crystallised granite by post-magmatic processes such as hydrothermal activity and weathering.

Advances in *in-situ* micro-analysis techniques for the determination of e.g. U-Pb, Lu-Hf and O isotopic compositions in accessory minerals have revolutionized approaches to assessing the evolution of the continental crust, and granite petrogenesis (Kemp et al., 2007, 2012; Appleby et al., 2010; Roberts and Spencer, 2014). Zircon is a common accessory mineral in granitic rocks and retains geochemical information about the evolution of its host melt. For typical peraluminous melt, <100 ppm zirconium is needed to saturate the melt and crystallize zircon (Hanchar and Watson, 2003). Therefore Zr saturation is likely reached early in the magmatic evolution of such granites, the time at which it is most likely to retain the record of its source.

The three isotope systems combine to inform both timing and melt source. U-Pb is a well-documented geochronometer that records the timing of zircon crystallization, while the Lu-Hf and O systems together combine to record the geochemical characteristics of the source. Lu-Hf is a radiogenic isotope system that records the average age of mantle extraction of the melt source. In general, samples with more negative εHf values were extracted from the mantle further back in time (a deviation in $^{176}Hf/^{177}Hf$ from the chondritic uniform reservoir (CHUR) value in parts per ten thousand). The behaviour of oxygen isotopes in rocks and minerals provides a stable-isotope proxy for the extent of sedimentary recycling in the sample source. Oxygen isotopes are fractionated during low-temperature processes such as subaerial weathering. Magmas that incorporate this supracrustal material will inherit a heavier $\delta^{18}O$ signature (or greater $^{18}O/^{16}O$ value) with respect to the Vienna Standard Mean Ocean Water (VSMOW; in parts per thousand).

Hf-O measurements of zircon from granitic rocks from the Lachlan type area have suggested that 'S-type' granitic and volcanic rocks cannot be derived from a single protolith and instead incorporate between 20 and 75% of material from a mantle source (Kemp et al., 2007, 2012). A more recent Hf-O isotopic study of zircons in 'S-type' granites from the Caledonian orogeny report a range of zircon compositions including those with typical 'mantle-like' O isotope signatures (Appleby et al., 2010). Thus on the basis of published studies it appears that many

granites, including those traditionally classified as 'S-type', are derived from mixed evolved and juvenile sources, generally interpreted as crustal and mantle-sources respectively.

We have analysed the chemical composition of zircons from peraluminous Oligocene to Miocene-aged leucogranites exposed in the Himalayan orogen in Bhutan (Figure 5.1). These leucogranites intrude amphibolite-facies metasediments of Neoproterozoic source age, the Greater Himalayan Sequence (GHS) (Ahmad et al., 2000). Structurally below the GHS is the Lesser Himalayan Sequence (LHS), a Paleoproterozoic-sourced stack of metasediments (Ahmad et al., 2000). Both sequences comprise a mix of orthogneiss, carbonate and quartzite compositions with a minor pelite component. The pelitic assemblages are significantly more fusible and therefore provide appropriate source materials for anatectic melts where temperatures are relatively low (<750 °C, Patiño Douce and Johnston, 1991). Bulk-rock isotope geochemical data from similar High Himalayan leucogranites exposed elsewhere in the Himalaya suggest that they formed by partial melting of the GHS pelitic lithologies into which they now intrude (Deniel et al., 1987; Le Fort et al., 1987; Harris et al., 1995). The granites are therefore appropriate for testing the hypothesis that they represent pure crustal melts, and that these melts provide geochemical signatures that characterise their sedimentary source.

5.3. Results

In-situ secondary ion mass spectrometry (SIMS) and laser ablation MC-ICP-MS analyses comprising 260 O, Hf and U-Pb isotopic analyses were conducted on 232 individual zircons recovered from 12 samples of Himalayan leucogranite. Of these, 80 spots yielded pre-Himalayan or mixed ages (1900-400 Ma), identifying inherited cores where $\delta^{18}O$ and εHf compositions predate partial melting during the Himalayan orogeny. The remaining 180 spots yielded Himalayan ages between 33-11 Ma; full data are supplied in Appendix D.

Age-corrected (to 20 Ma) εHf_{20} of all Himalayan-aged samples varies between -8.7 and -29.8, and $\delta^{18}O$ between 6.9‰ and 12.5‰ (Figure 5.2). Of these analyses, 97% lie within uncertainty of the previously defined GHS O-Hf compositional range (Massey et al., 1994; Harris and Massey, 1995; Vervoort and Blichert-Toft, 1999; Lackey et al., 2005). Zircon data from some samples cluster densely (e.g. 1D01, 3A03). Samples 1G02 and CWB16 show variations in zircon εHf_{20} that are greater than analytical uncertainty, but $\delta^{18}O$ values conversely show little variation. In contrast, zircons in other samples, including 1G01, 4D01, 1215 and 1247, show variation in $\delta^{18}O$ while εHf_{20} values remain relatively constant. Only one sample, 1G03, contained zircons that yielded significant variation in both isotope systems, with εHf_{20} varying between -30 and -15 and $\delta^{18}O$ between 7.1‰ and 8.1‰.

Zircons in samples 1G02 and 1G03 yielded slightly lower $\delta^{18}O$ values than have previously been reported from bulk-rock GHS data. One zircon from 1G03 also yielded somewhat more negative εHf_{20} than has previously been reported for the GHS.

Two main age groups are observed in the pre-Himalayan zircon core data (Figure 5.3); 550-450 Ma and 900-800 Ma. There is also a smaller group of Paleoproterozoic cores of ~1800 Ma found in only four samples – 1G02, 1G03, 1247 and CWB16. In addition, several zircons yield ages between these main groups, representing either a mixed age or another, smaller source contribution. The majority of zircons within the 550-450 Ma group have an εHf_t composition of

+2.5 to -8, with outliers at +9.5 and -15.5. The majority of zircons in the 900-800 Ma population lie between -7 and -15. The smaller ~1800 Ma group records εHf_t between +8 and -10.

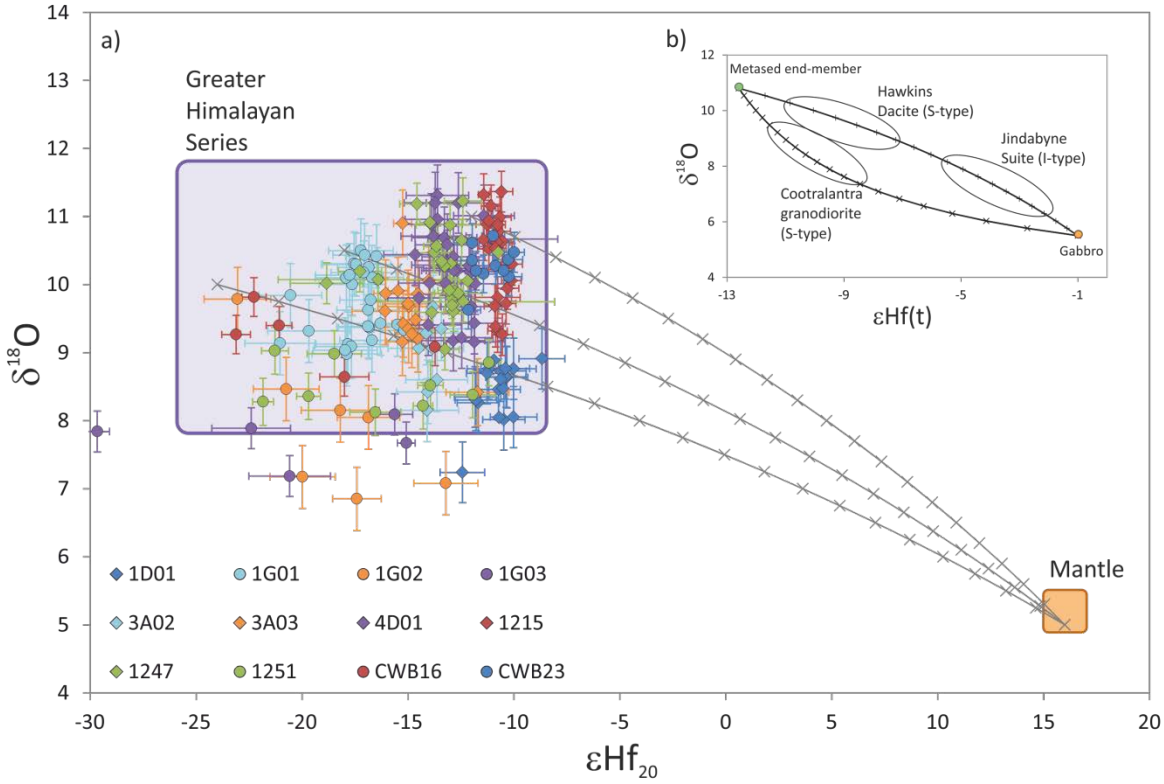

Figure 5.2: *a) $\delta^{18}O$-εHf_{20} isotope arrays for Oligocene to Miocene-aged zircons and zircon rims compared to possible mixing lines generated by binary mixing between potential GHS sources and the mantle (ticks show mixing at 5% intervals). The range of isotopic values from bulk rock GHS analyses (the likely source of melting) and the depleted mantle have also been plotted for reference. The GHS whole-rock εHf range is calculated from whole rock εNd (Harris and Massey, 1994) using the correlation of Vervoort and Blichert-Toft (1999). Whole-rock GHS $\delta^{18}O$ values are taken from Massey et al. (1994), and recalculated using the fractionation equation of Lackey et al. (2005) assuming 74% SiO_2 in the melt. For the mixing lines, mantle-like oxygen and hafnium isotopic values were used (Valley, 2003; Bouvier et al., 2008). The Xigaze ophiolite of southern Tibet was chosen to provide bulk-rock Hf abundances for a mantle-derived end-member of appropriate age (2.1 ppm, Pearce and Wanming, 1988; Malpas et al., 2003). There is no correlation between samples with the same symbol or colour. Error bars are 2σ for Hf and 2 s.d. for O.*

(b) Plot adapted from Kemp et al. (2006) highlighting one I-type and two S-type granites from the Lachlan fold belt, and mixing lines between potential metasedimentary and gabbroic end-members.

5.4. Discussion

Of the Oligocene-Miocene aged zircon rims, 97% lie within uncertainty of the GHS metasedimentary Hf-O isotopic field, confirming that the main source of these melts was the GHS material into which they are now emplaced (Figure 5.2). Potential mixing lines drawn between possible GHS compositions and a mantle-derived end-member (Vervoort and Blichert-Toft, 1999; Vallley, 2003) show that, in comparison with the Lachlan fold belt data (Figure 5.2 inset), zircon arrays from individual granites do not define mixing lines, but most instead vary in $\delta^{18}O$ at relatively constant εHf_{20}. Thus, whilst the GHS field is relatively large so that granite zircon compositions lying within it might represent mixtures between sediment of more extreme crustal signature (higher $\delta^{18}O$ and lower εHf_t) and mantle, evidence from individual granites argue against any such mixing.

Zircons in four samples, 1G02, 1G03, 1251, and CWB16, show significant variations in εHf_{20} consistent with the interpretation that the melt in these samples has been derived from multiple sources. Of these, data from samples 1251 and CWB16 lie within the GHS field, suggesting they reflect mixing between two different crustal sources within the GHS. For example the most fusible lithologies in the GHS are likely to be pelitic or semi-pelitic in composition, reflecting mudstone and greywacke protoliths respectively, that are likely to have slightly differing isotopic characteristics. One zircon in 1G03 records more negative εHf_{20} values than the bulk GHS, which could suggest mixing between the GHS and an older source. This source could potentially be the Lesser Himalayan Series (LHS) which underthrusts the GHS and is characterised by older (Paleoproterozoic) sedimentary protoliths and significantly older Nd model ages (Ahmad et al., 2000). Furthermore, the presence of Paleoproterozoic zircon cores in samples 1G02, 1G03 and CWB16 suggest that some LHS material has been entrained into these leucogranites, although the majority of their source is the GHS.

Zircons from 1G02 and one zircon each from samples 1D01 and 1G03 also yield lower $\delta^{18}O$ values than the GHS field. These three samples were all collected south of the village of Gasa (Figure 5.1), where numerous epidote-bearing calc-silicate lenses are exposed (Gansser, 1983). Epidote-bearing calc-silicates in the Himalaya yield an overall lower bulk-rock $\delta^{18}O$ than the dominant metapelites (Massey et al., 1994), hence a small contribution from calc-silicate material in the source melt could explain the reduced $\delta^{18}O$ compared to the granites from other areas.

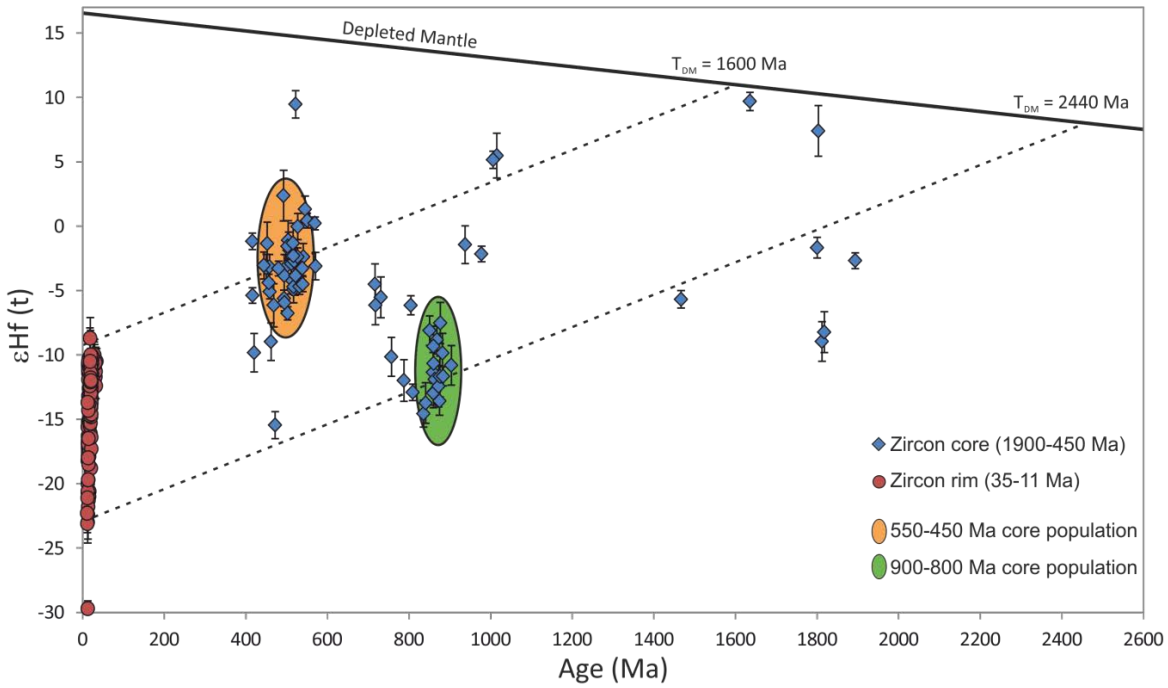

Figure 5.3: *Plot of εHf_t and U-Pb crystallization age for core and rim zircon data. Core data plot in two main groups, at 550-450 Ma and 900-800 Ma, with additional zircons plotting at ~1800 Ma and between these groups. Evolution line for the depleted is shown. Evolution lines from core populations are also plotted, assuming a $^{176}Lu/^{177}Hf$ ratio of 0.015. Himalayan-age zircon rim data is bound by these evolution lines, with no positive deviation to a mantle value. Error bars are 2σ uncertainty.*

Pre-Himalayan zircon core data may also be employed to assess the relationship between source and melt. Figure 5.3 displays the relationship between Himalayan rim and pre-Himalayan core data, with Hf evolution lines based on a $^{176}Lu/^{177}Hf$ ratio of 0.015 (typical of upper continental crust, Griffin et al., 2002). The range of Himalayan-aged zircon εHf_{20} values is entirely

constrained by the evolution lines derived from the two most abundant source fields – the 550-450 Ma and 900-800 Ma groups. This suggests that the Himalayan-aged rims derive their Hf isotopic composition solely from these two sources. Furthermore, as there is no positive deviation in the Himalayan-aged rim εHf_{20} data towards a mantle value, it provides additional evidence against the possibility that the mantle contributed to the formation of these zircon rims, and to their host leucogranites.

5.5. Conclusions

Overall, the data show that Oligocene-Miocene aged zircons and zircon rims from granites that intrude the high metamorphic grade Greater Himalayan Sequence in Bhutan show little isotopic variation within individual rock samples, and lie within the field defined by isotopic variability in the GHS. Some zircon populations display isotope trends that are consistent with mixing between two or more metasedimentary sources, but none show trends that are consistent with mixing with a mantle source. Furthermore, εHf_t data from zircon cores suggests the Himalayan-aged rims derived solely from Cambrian and Proterozoic sources, with no positive deviation in rim data towards a mantle value. In addition, no field evidence exists for xenoliths of mafic composition in the Himalayan leucogranites.

The lack of Miocene mantle interaction significantly affects our understanding of the Himalayan orogen. As this removes the possibility of additional heat sources being involved in the melt process, it fails to support the possibility of the 'young' collision model at ~34 Ma (Aitchison et al., 2007). The most likely scenario is that a single collision (albeit with diachroneity along strike) occurred to form the Himalayan orogeny at ~55-50 Ma (Najman et al., 2010).

Unlike granitic zircon O-Hf studies from other regions, we find no evidence for source contributions from melting of igneous sources, or mixing with mantle-derived or more juvenile melts. We therefore conclude that they are true crustal melts from metasedimentary sources, a conclusion consistent with their bulk geochemical signatures (Deniel et al., 1987; Le Fort et al.,

1987; Harris et al., 1995). The Himalayan leucogranites therefore provide clear evidence that syn-collision S-type granites need not contribute to crustal growth, and further that the presence of such granites within orogenic belts does not require an advective heat source in thermal models for orogenic evolution. We also propose that an 'end-member' S-type granite may be defined as a rock whose zircon Hf-O isotopic signatures lie entirely within error of those of its probable source, and where no trajectories to mantle values are observed. These leucogranites are also a more appropriate 'type-locality' for S-type granites than the Lachlan Fold Belt of Australia. This finding has implications for the formation of granites in general, for crustal growth estimates within orogenic belts and for the thermal and mechanical modelling of the Himalayan orogen.

Chapter 6

Zircon isotope geochemistry and geochronology

6.1. Introduction

Zircons are particularly useful accessory mineral phases for investigating both the geochronology and the geochemical history of a sample. This is primarily due to the significant concentrations of U, Lu and Hf that are incorporated into crystal lattices, allowing for analysis of both the U-Pb and Lu-Hf isotope systems. The mineral is exceptionally useful for geochronology, as minimal quantities of Pb are incorporated into the zircon crystal lattice during crystallization. Therefore the vast majority of the Pb present is the product of radioactive decay from U and Th since the mineral crystallized, and any additional non-radiogenic lead can be corrected for. The Hf isotope signature of zircon is better used as a geochemical tracer. The $^{176}Lu/^{177}Hf$ ratio within zircon is typically very low (< 0.0005; Kinny and Maas, 2003), meaning the radiogenic accumulation of ^{176}Hf within the zircon occurs at virtually negligible rates. As such, zircons better preserve the $^{176}Hf/^{177}Hf$ ratio of the magmatic source at the time of their crystallization. Hf isotopic ratios can be used to distinguish different source inputs to the host magma, and to determine model ages, i.e. mantle extraction ages of the magmatic source.

Zircons are also highly resistant to weathering, ensuring that they are passed down the geological record through sedimentary recycling. Zircon has a high solidus temperature, and therefore crystals can survive multiple igneous or metamorphic events, but may crystallise new

rims or growth zones that record each of these later events. In the case of the High Himalayan leucogranites, the outermost zircon rims record information relating to the formation and crystallization of the leucogranites. Zircon cores formed in previous magmatic episodes are also present, and provide additional information about the leucogranite source.

In the Himalaya, the age and source of leucogranite intrusions is critical to understanding the history of Himalayan tectonics. Previous studies of Bhutanese High Himalayan leucogranites have recorded that melting took place over a 12 million year period, between 24 Ma and 12 Ma (Guo and Wilson, 2012; Greenwood, 2013, and references therein). However, it is unknown whether this represents continuous granite formation or whether melting occurs in pulses. Additionally, few attempts have been made to link age to geochemistry, and therefore it is unknown whether there is any change over time in the source or the petrogenetic conditions involved in leucogranite formation. Previous studies into source have only utilised whole rock Sr and Nd analyses (e.g. Le Fort et al., 1987; Guillot and Le Fort, 1995; Harris et al., 1995), while no studies have analysed the Hf isotopic content of leucogranite zircons. In this study, leucogranite zircon U-Pb and Lu-Hf compositions shall be compared to whole rock Sr and Nd isotopic contents in order to determine how leucogranite genesis has changed over the history of melting in the Bhutanese Himalaya.

U-Pb and Hf isotope data were collected from zircons from 12 leucogranites (8 of which contain core populations), data for which are fully tabulated in Chapter 5. Samples were chosen based on providing geographical coverage and sampling the complete range of mineralogical leucogranite types. Methods are summarised in Chapter 5 and detailed in full in Appendix A.

6.2. Results

6.2.1. U-Pb geochronology

Zircon U-Pb data from the Himalayan-aged rims are plotted on Tera-Wasserburg diagrams ($^{238}U/^{206}Pb$ vs $^{207}Pb/^{206}Pb$). Tera-Wasserburg diagrams are used for younger material in order to easily determine quantities of common Pb within a zircon. Lower intercept ages are used when the data are discordant, in these cases, the regression is anchored to a common Pb composition ($^{207}Pb/^{206}Pb_i$) as recorded by whole rock Pb isotope geochemistry (see Chapter 4, Table 4.1). For those samples not analysed for Pb isotope contents, a value of 0.83 ± 0.02 is used (Stacey and Kramers, 1975). Where available, U-Pb data from pre-Himalayan cores are plotted on conventional Wetherill Concordia diagrams ($^{207}Pb/^{235}U$ vs $^{206}Pb/^{238}U$).

Also calculated alongside each age is a mean square weighted deviation (MSWD), which is a measure of goodness of fit of the age population distribution, taking into account both internal and external reproducibility. Where MSWD = 1, all age data fit along a normal distribution. For MSWD values less than 1, the observed scatter in the data is less than predicted, and therefore the data are underdispersed. In this case, uncertainties are overestimated. When MSWD > 1, the scatter in the data is greater than that predicted for a single age population, the data are therefore overdispersed and uncertainties are overestimated. The range of acceptable MSWD values varies depending on the number of data comprising the age calculation (Spencer et al., 2016), however for the purposes of this study any MSWD values less than 2.5 are deemed to be acceptable. Calculated ages with greater MSWD values are deemed to be overdispersed, and therefore assigning a single age calculation is inappropriate. In these instances, an approximate value is provided as the assigned age.

Alongside plots are cathodoluminescence (CL) images of typical zircons from each sample, showing locality of analyses within them.

Sample 1D01 yielded 19 Himalayan-aged zircon rim and 15 inherited core analyses (Figure 6.1a). All but four of the rim analyses lie on concordia, with ages varying from 34 Ma to 18.5 Ma, with a dense cluster of 8 zircon rim data providing an age of 31.18 ± 0.22 Ma.

Core data for this sample (Figure 6.1b) are uniformly discordant, falling on a regression representing mixing with an older age, determined from the upper intercept as c. 537 Ma, when anchored to the zircon rim age.

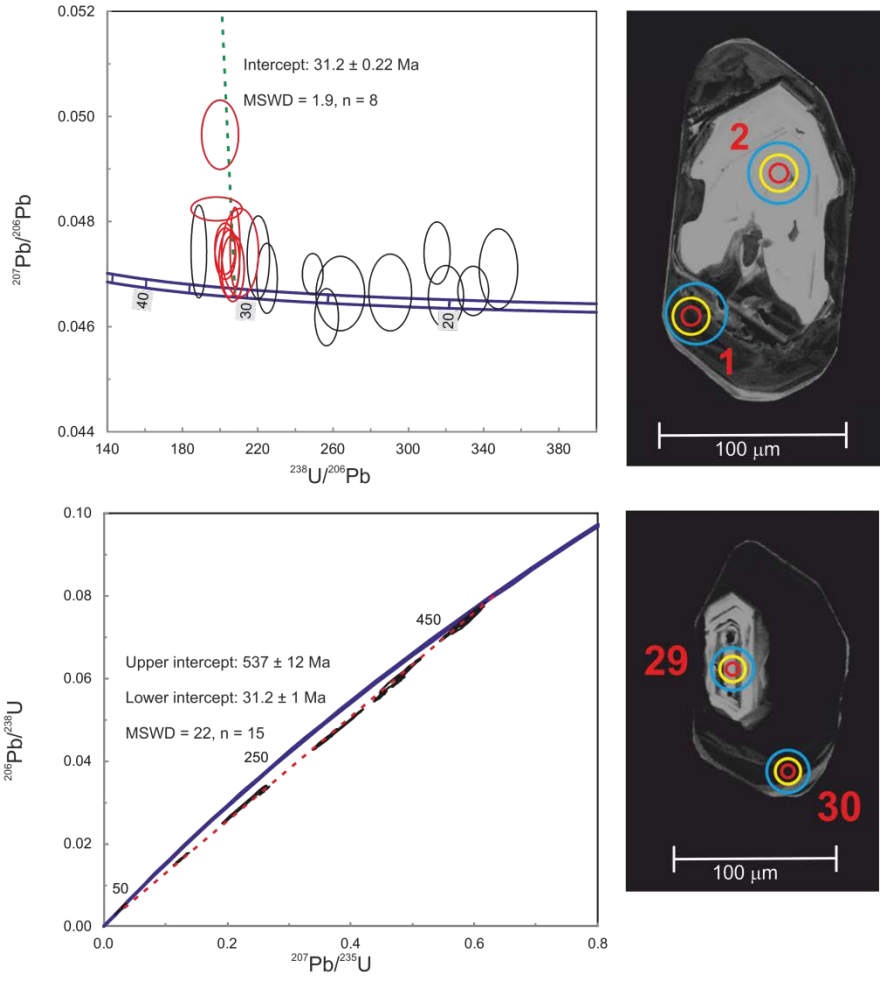

Figure 6.1: *U-Pb Tera-Wasserburg and Concordia diagrams for zircon rims (above) and cores (below) of sample 1D01. Mixing lines are plotted as red dashed lines, while lines regressing to a common Pb composition are shown as green dashed lines. Red rim data represent those used in age calculation. For CL images, red circles indicate O-isotope pits, yellow circles indicate U-Pb pits and blue circles represent Hf isotope pits. Numbers indicate analysis number for all data in the same spot.*

Sample 1G01 yielded 27 Himalayan-aged rim and 4 inherited core analyses (Figures 6.2a and 6.2b). The majority (23 out of 27) of data points form a dense cluster, with an age of 13.67 ± 0.14 Ma when anchored to common Pb (with c. 13.7 Ma as the assigned crystallization age of, due to the high MSWD). Four samples lie discordantly above the concordia. An additional 4 samples yield slightly older ages than the main population.

Core data for this sample are all discordant, with two points forming a mixing line that intercepts concordia at 520 ± 20 Ma. Two additional core analyses yield upper intercept ages of 731 ± 8 Ma and 1015 ± 13 Ma, when anchored to the rim age.

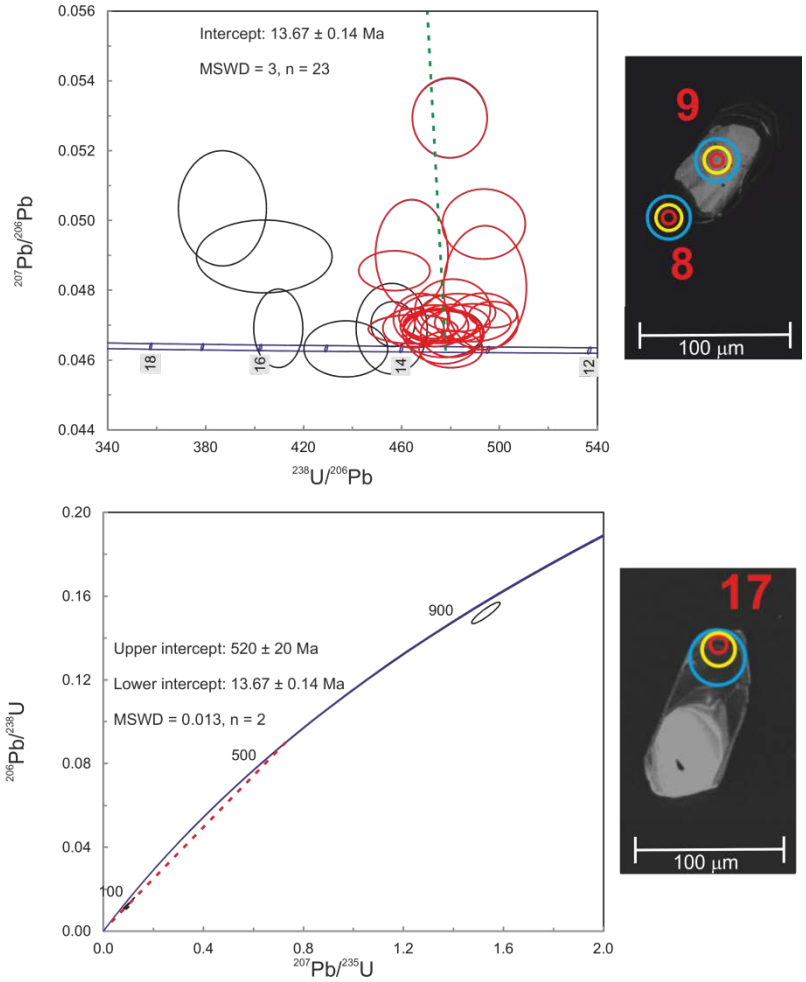

Figure 6.2: *U-Pb Tera-Wasserburg and Concordia diagrams for zircon rims (above) and cores (below) of sample 1G01. Mixing lines are plotted as red dashed lines, while lines regressing to a common Pb composition are shown as green dashed lines. Red rim data represent those used in age calculation. For CL images, red circles indicate O-isotope pits, yellow circles indicate U-Pb pits and blue circles represent Hf isotope pits. Numbers indicate analysis number for all data in the same spot.*

Sample 1G02 yielded 7 rim analyses of Himalayan age and 26 inherited cores (Figures 6.3a and 6.3b). Four of the rim data points for this sample appear to form a cluster close to concordia, yielding an age of 12.46 ± 0.13 Ma, when anchored to common Pb. Three additional rim points appear to plot on a mixing line when anchored with the youngest zircon core age (496 ± 19 Ma), intercepting the concordia at 12.54 ± 0.37 Ma.

Core ages lie on three apparent mixing lines that intercept concordia at 1814 ± 11 Ma, c. 866 Ma, and c. 496 Ma.

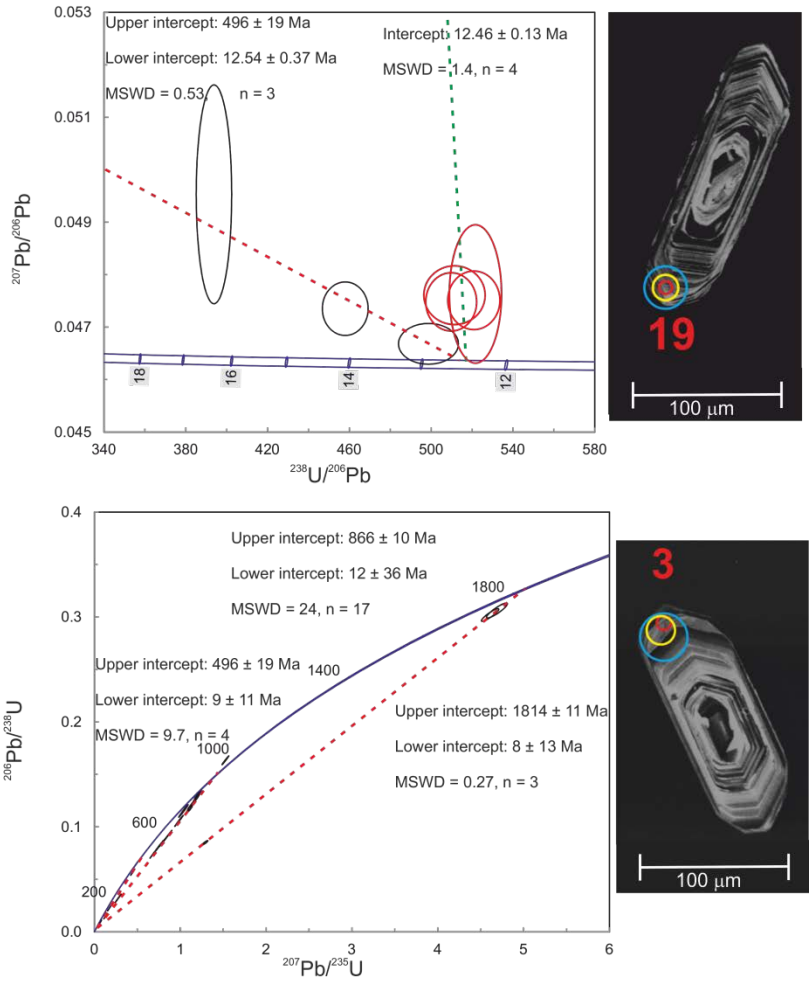

Figure 6.3: *U-Pb Tera-Wasserburg and Concordia diagrams for zircon rims (above) and cores (below) of sample 1G02. Mixing lines are plotted as red dashed lines, while lines regressing to a common Pb composition are shown as green dashed lines. Red rim data represent those used in age calculation. For CL images, red circles indicate O-isotope pits, yellow circles indicate U-Pb pits and blue circles represent Hf isotope pits. Numbers indicate analysis number for all data in the same spot.*

Sample 1G03 yielded 5 Himalayan-aged zircon rim and 3 inherited core analyses (Figures 6.4a and 6.4b). Four of the five rim analyses form a concordant cluster at 12.52 ± 0.19 Ma, with one concordant analysis providing an age of ~17 Ma.

One core plots concordantly with an age of 472 ± 8 Ma. The other two core analyses fall on mixing lines that suggest crystallisation at 810 ± 23 Ma, and 1800 ± 16 Ma.

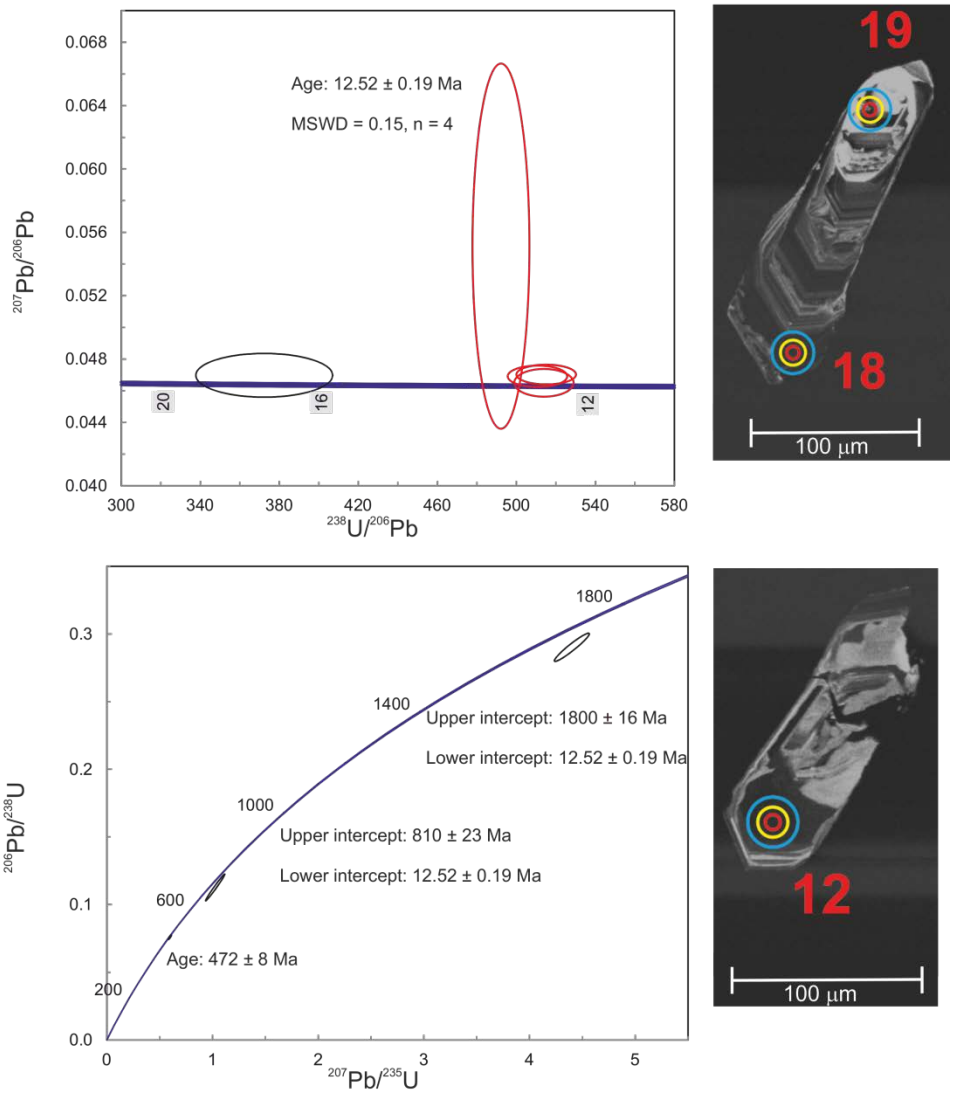

Figure 6.4: *U-Pb Tera-Wasserburg and Concordia diagrams for zircon rims (above) and cores (below) of sample 1G03. Red rim data represent those used in age calculation. For CL images, red circles indicate O-isotope pits, yellow circles indicate U-Pb pits and blue circles represent Hf isotope pits. Numbers indicate analysis number for all data in the same spot.*

Sample 3A02 provided 8 Himalayan rim ages but no older core ages (Figure 6.5). All data points are slightly discordant, with six lying on a single mixing line to a common Pb component that yields an age of 19.68 ± 0.30 Ma.

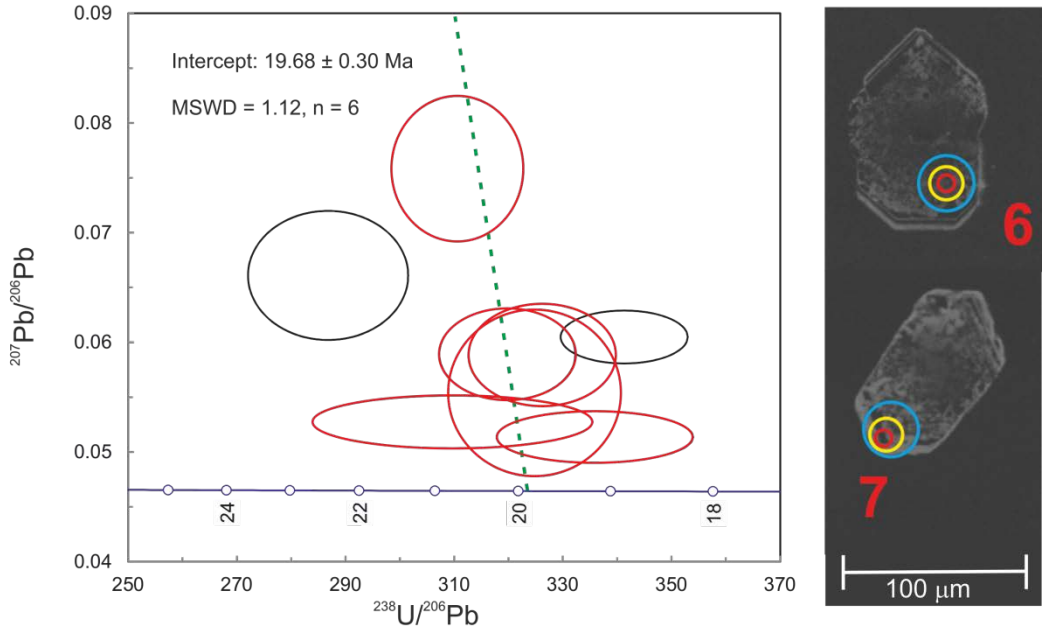

Figure 6.5: *U-Pb Tera-Wasserburg diagram for zircon rims of sample 3A02. Lines anchored at a common Pb composition are shown as green dashed lines. Red rim data represent those used in age calculation. For CL images, red circles indicate O-isotope pits, yellow circles indicate U-Pb pits and blue circles represent Hf isotope pits. Numbers indicate analysis number for all data in the same spot.*

Sample 3A03 yielded 14 rim and 5 core analyses (Figures 6.6a and 6.6b). Individual zircons record scattered ages between 16 and 21 Ma, all but one of which are discordant. One dense cluster of zircon rims yield a crystallization age of 18.0 ± 0.9 Ma when anchored to common Pb. Due to the high MSWD of this age, the sample is assigned a crystallization age of c. 18 Ma.

Core data, when anchored at 18 Ma, form two arrays that intercept concordia at 501 ± 15 Ma and c. 983 Ma.

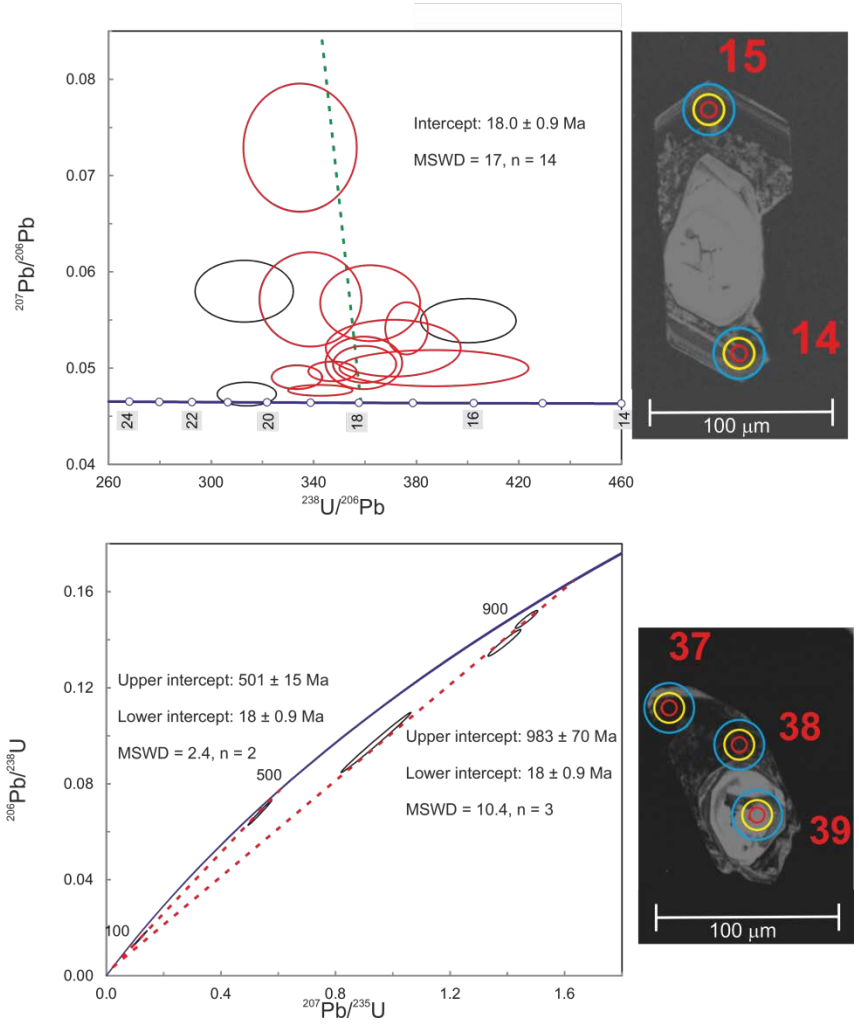

Figure 6.6: *U-Pb Tera-Wasserburg and Concordia diagrams for zircon rims (above) and cores (below) of sample 3A03. Mixing lines are plotted as red dashed lines, while lines regressing to a common Pb composition are shown as green dashed lines. Red rim data represent those used in age calculation. For CL images, red circles indicate O-isotope pits, yellow circles indicate U-Pb pits and blue circles represent Hf isotope pits. Numbers indicate analysis number for all data in the same spot.*

Sample 4D01 yielded 29 Himalayan-aged analyses (Figure 6.7). Twelve of these data form a tight cluster of concordant ages at 17.92 ± 0.13 Ma, when anchored to common Pb. Three grains yielded younger ages that are outside of uncertainty of the main cluster. Twelve grains yielded slightly older ages, with some slightly discordant.

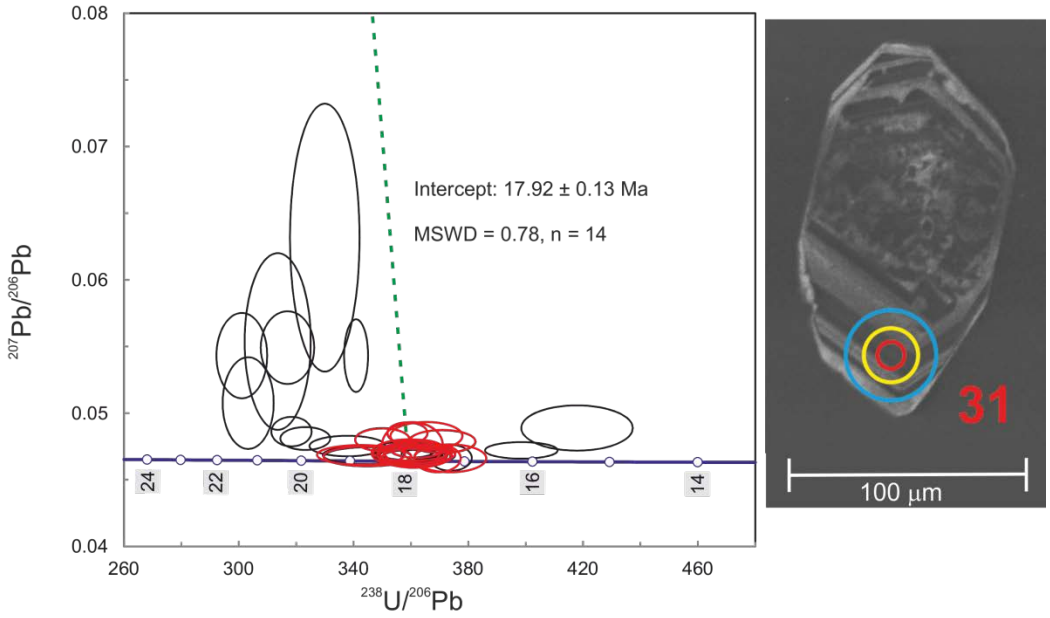

Figure 6.7: *U-Pb Tera-Wasserburg diagram for zircon rims of sample 4D01. Lines regressing to a common Pb composition are shown as green dashed lines. Red rim data represent those used in age calculation. For CL images, red circles indicate O-isotope pits, yellow circles indicate U-Pb pits and blue circles represent Hf isotope pits. Numbers indicate analysis number for all data in the same spot.*

Sample 1215 yielded 22 Himalayan-aged rims (Figure 6.8). The data form two distinct age populations, with each group containing both concordant analyses and some discordant. Five data points record an older age of 23.06 ± 0.26 Ma, while 15 data points yield a younger age of 14.06 ± 0.22 Ma, with both ages being anchored to common Pb. Due to the high MSWD on the younger age, this population is assigned an age of c. 14.1 Ma. Two data plot between the two age populations.

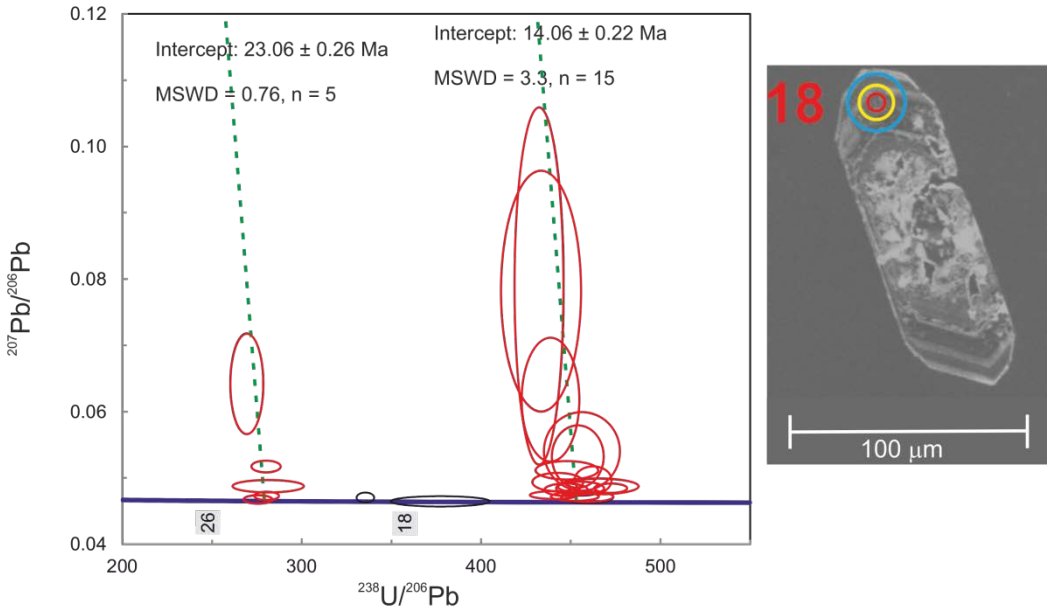

Figure 6.8: *U-Pb Tera-Wasserburg diagram for zircon rims of sample 1215. Lines regressing to a common Pb composition are shown as green dashed lines. Red rim data represent those used in age calculation. For CL images, red circles indicate O-isotope pits, yellow circles indicate U-Pb pits and blue circles represent Hf isotope pits. Numbers indicate analysis number for all data in the same spot.*

Sample 1247 yielded 24 Himalayan-aged zircon rims and 6 inherited cores (Figures 6.9a and 6.9b). 18 of the young rims form a tight concordant cluster that yields an age of 21.01 ± 0.21 Ma. An additional six rims record a younger age of 19.6 ± 0.68 Ma; however these analyses are more uncertain and contain small quantities of common Pb, and are assigned an age of c. 19.6 Ma due to the high MSWD of the population.

Five core analyses lie on a mixing line that intercepts concordia at 498 ± 11 Ma when anchored at the older rim age of 21.01 Ma. A sixth core also plots on a mixing line to 1733 ± 81 Ma.

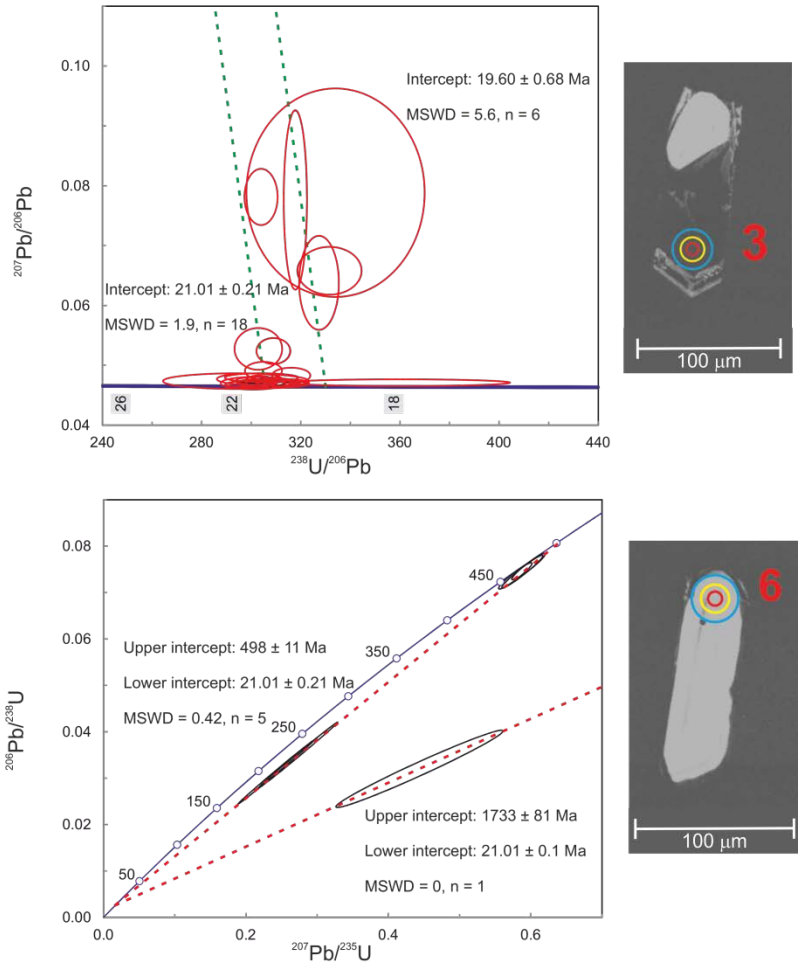

Figure 6.9: *U-Pb Tera-Wasserburg and Concordia diagrams for zircon rims (above) and cores (below) of sample 1247. Mixing lines are plotted as red dashed lines, while lines regressing to a common Pb composition are shown as green dashed lines. Red rim data represent those used in age calculation. For CL images, red circles indicate O-isotope pits, yellow circles indicate U-Pb pits and blue circles represent Hf isotope pits. Numbers indicate analysis number for all data in the same spot.*

Sample 1251 yielded 9 rim and 14 inherited core analyses (Figures 6.10a and 6.10b). Eight rim analyses form a concordant cluster at 13.98 ± 0.30 Ma, with an assigned age of c. 14.0 Ma due to the high MSWD.

Twelve cores form a mixing line that intercepts concordia at 526 ± 20 Ma, when anchored at the Himalayan crystallization age of 14.10 Ma. Two core analyses form a second array yielding an upper intercept age of 868 ± 270 Ma.

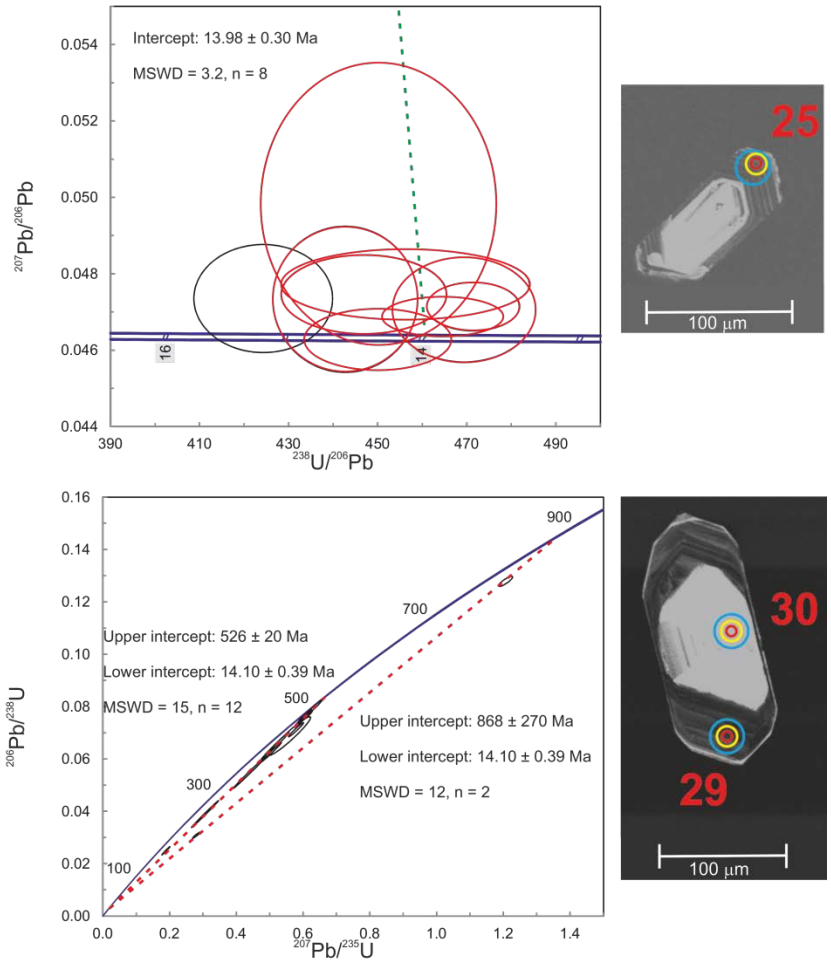

Figure 6.10: *U-Pb Tera-Wasserburg and Concordia diagrams for zircon rims (above) and cores (below) of sample 1251. Mixing lines are plotted as red dashed lines, while lines regressing to a common Pb composition are shown as green dashed lines. Red rim data represent those used in age calculation. For CL images, red circles indicate O-isotope pits, yellow circles indicate U-Pb pits and blue circles represent Hf isotope pits. Numbers indicate analysis number for all data in the same spot.*

Sample CWB16 yielded 5 rim and 6 core analyses (Figures 6.11a and 6.11b). The 5 rims yielded an age of 11.74 ± 0.81 Ma, though with a high MSWD of 11. A crystallization age of c. 11.7 Ma is therefore assigned.

Three core points form a mixing line intercepting concordia at 534 ± 11 Ma, with three additional core analyses yielding upper intercept ages of 717 ± 17 Ma, 1467 ± 21 Ma and 1894 ± 6 Ma, all when anchored to the crystallization age of 11.74 Ma.

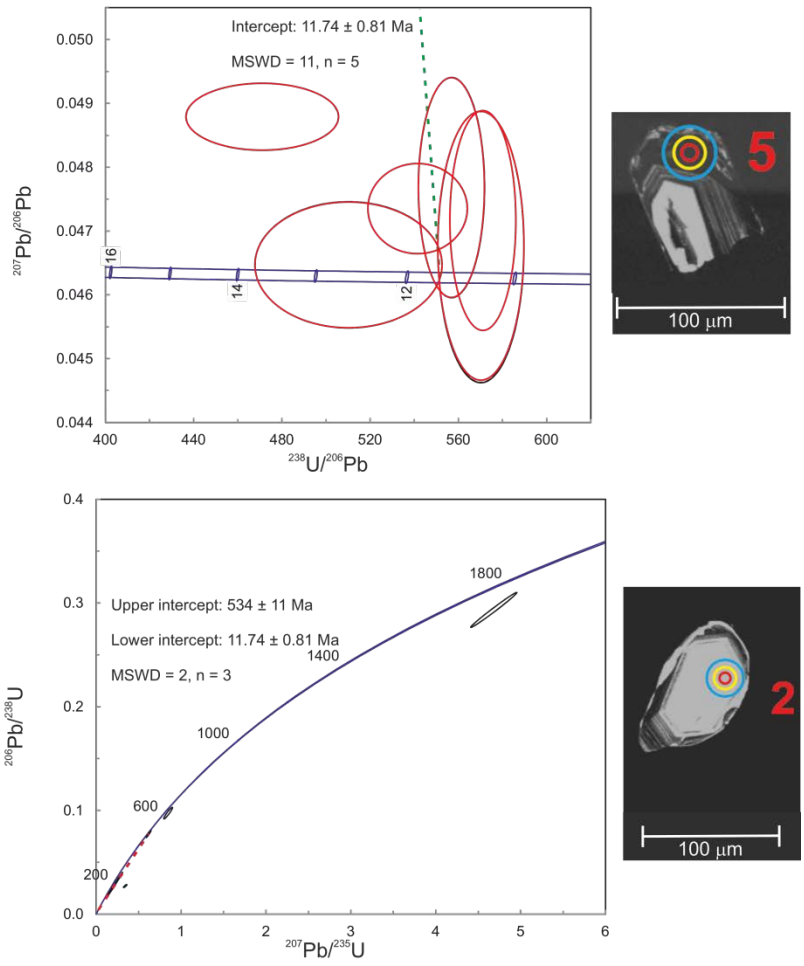

Figure 6.11: *U-Pb Tera-Wasserburg and Concordia diagrams for zircon rims (above) and cores (below) of sample CWB16. Mixing lines are plotted as red dashed lines, while lines regressing to a common Pb composition are shown as green dashed lines. Red rim data represent those used in age calculation. For CL images, red circles indicate O-isotope pits, yellow circles indicate U-Pb pits and blue circles represent Hf isotope pits. Numbers indicate analysis number for all data in the same spot.*

Sample CWB23 yielded 11 Himalayan-aged rims (Figure 6.12). Eight rims form a mostly concordant cluster at 19.94 ± 0.19 Ma, while three zircons record younger ages.

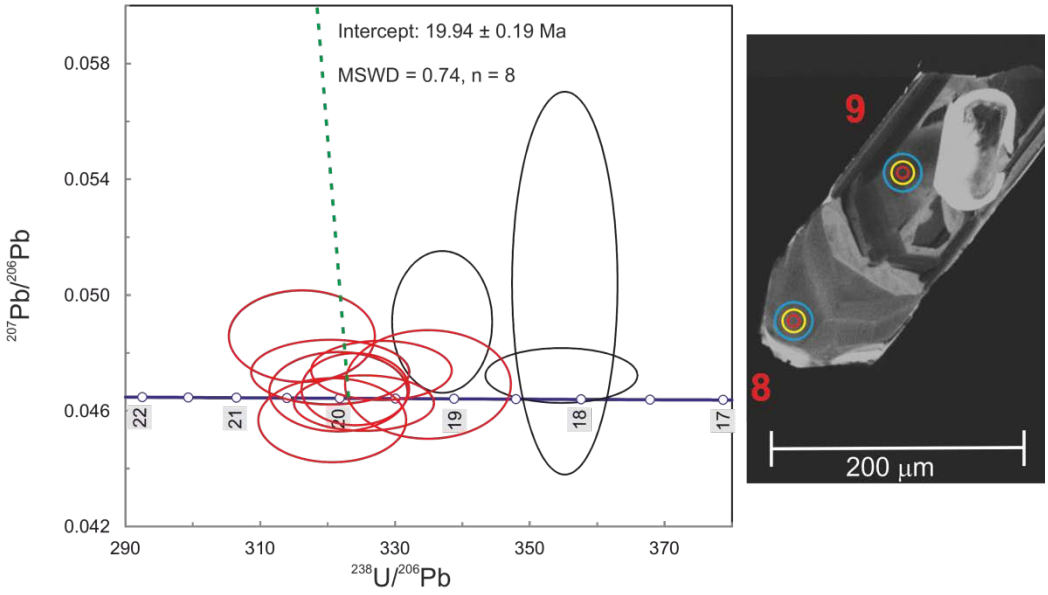

Figure 6.12: *U-Pb Tera-Wasserburg diagram for zircon rims of sample CWB23. Lines regressing to a common Pb composition are shown as green dashed lines. Red rim data represent those used in age calculation. For CL images, red circles indicate O-isotope pits, yellow circles indicate U-Pb pits and blue circles represent Hf isotope pits. Numbers indicate analysis number for all data in the same spot.*

6.2.2. U-Pb age summary

Individual zircon rims record Himalayan crystallization ages between 34.0 and 11.5 Ma, with the crystallization ages of samples determined to be between 31.2 and 11.7 Ma.

Pre-Himalayan cores are present in the majority of samples, and across all samples form three dominant groups. 45 of the 80 zircon cores analysed fall in the 550 – 450 Ma population, while 23 cores form a smaller group between 900 – 800 Ma. The third group is comprised of seven zircons, with ages ~1800 Ma.

Table 6.1: Summary of sample geochronology data

Sample	Population	Calculated age	No. zircons	MSWD	Assigned age
1D01	Himalayan rims	31.18 ± 0.22 Ma	8	1.9	31.18 ± 0.22 Ma
	Cores	537 ± 12 Ma	15	22	c. 537 Ma
1G01	Himalayan rims	13.67 ± 0.14 Ma	23	3	c. 13.7 Ma
	Cores	520 ± 20 Ma	2	0.013	520 ± 20 Ma
1G02	Himalayan rims	12.46 ± 0.13 Ma	4	1.4	12.46 ± 0.13 Ma
	Cores 1	866 ± 10 Ma	17	24	c. 866 Ma
	Cores 2	496 ± 19 Ma	4	9.7	c. 496 Ma
	Cores 3	1814 ± 11 Ma	3	0.27	1814 ± 11 Ma
1G03	Himalayan rims	12.52 ± 0.19 Ma	4	0.15	12.52 ± 0.19 Ma
3A02	Himalayan rims	19.68 ± 0.30 Ma	6	1.12	19.68 ± 0.30 Ma
3A03	Himalayan rims	18.0 ± 0.9 Ma	14	17	c. 18 Ma
	Cores 1	987 ± 70 Ma	3	10.4	c. 980 Ma
	Cores 2	501 ± 15 Ma	2	2.4	501 ± 15 Ma
4D01	Himalayan rims	17.92 ± 0.13 Ma	14	0.78	17.92 ± 0.13 Ma
1215	Himalayan rims 1	14.06 ± 0.22 Ma	15	3.3	c. 14.1 Ma
	Himalayan rims 2	23.06 ± 0.26 Ma	5	0.76	23.06 ± 0.26 Ma
1247	Himalayan rims 1	21.01 ± 0.21 Ma	18	1.9	21.01 ± 0.21 Ma
	Himalayan rims 2	19.60 ± 0.68 Ma	6	5.6	c. 19.6 Ma
	Cores	498 ± 11 Ma	5	0.42	498 ± 11 Ma
1251	Himalayan rims	13.98 ± 0.30 Ma	8	3.2	c. 14.0 Ma
	Cores 1	526 ± 20 Ma	12	15	c. 526 Ma
	Cores 2	868 ± 270 Ma	2	12	c. 870 Ma
CWB16	Himalayan rims	11.74 ± 0.81 Ma	11	5	c. 11.7 Ma
	Cores	534 ± 11 Ma	3	2	534 ± 11 Ma
CWB23	Himalayan rims	19.94 ± 0.19 Ma	8	0.74	19.94 ± 0.19 Ma

Table 6.1: *Summary of geochronology data for all samples. MSWDs in red indicate where they are too high and therefore underestimate uncertainties. In these instances, approximate ages are assigned.*

6.2.3. Hafnium isotopes

6.2.3.1. Zircon rims

Hf isotope ratios for Himalayan-age zircon rims were age-corrected to 20 Ma, an average age for Himalayan leucogranite samples, rather than their precise ages as recorded by the U-Pb data

(between 33-11 Ma). Any age-scatter caused by Pb-loss is difficult to detect at such a young age, and therefore to avoid problems in Hf age correction caused by incorrect ages it was considered more prudent to correct all the data to a single age. The difference between εHf_t and εHf_{20} for any given analysis lies within the quoted uncertainty.

Hf isotope data from all Himalayan-aged zircon rims are displayed on the εHf_{20} vs age plot in Figure 6.13. εHf_{20} of all zircons varies between -10.0 and -23.1, with one anomalous zircon from sample 1G03 yielding a value of -29.7 and one zircon from sample 1D01 yielding a value of -8.7.

Zircon rims from sample 1D01 yield εHf_{20} values between -8.7 and -12.4, with 18 out of 19 samples yielding values lower than -10. There is no correlation between age and εHf_{20}.

The εHf_{20} values of 25 zircons from sample 1G01 range between -15.2 and -21.0. Most analyses yielded εHf_{20} values between -15.2 and -19.7. Two zircons yielded apparently anomalous values of -20.6 and -21.0 which also recorded the oldest zircon rim ages.

6 zircons from sample 1G02 yielded highly variable εHf_{20} values from-13.2 and -23.0.

5 zircons from sample 1G03 yielded εHf_{20} values generally varying between -15.1 and -22.4, with one rim yielding value of -29.7.

8 zircon rims from sample 3A02 yielded a tight group of εHf_{20} values between -13.4 and -14.5.

13 zircon rims from sample 3A03 yielded εHf_{20} values between -14.5 to -16.1, with one outlier at -11.7.

Sample 4D01 yielded 29 zircon rims with εHf_{20} values between -11.0 and -14.7.

22 zircons from sample 1215 yielded εHf_{20} values between -10.1 to -11.4. No variation in εHf_{20} values was noted between the two age populations.

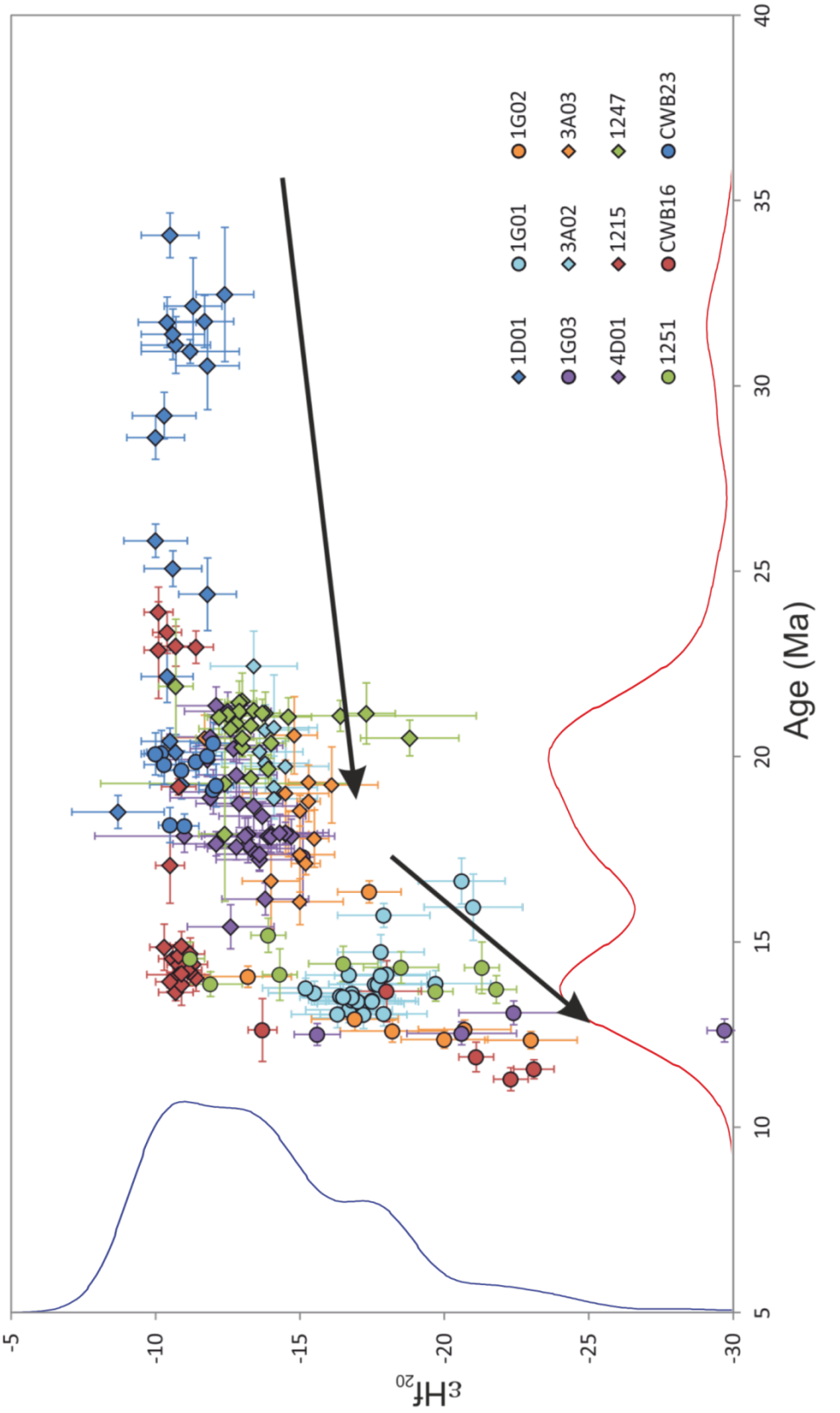

Figure 6.13: *Plot of age versus εHf_{20} values for young zircon rims. Red line indicates a cumulative frequency plot for ages, while blue line indicates cumulative frequency plot for* **ε***Hf data.*

20 out of 24 zircon rims from sample 1247 yielded εHf_{20} values between -12.2 and -14.6. One zircon yielded a more positive εHf_{20} value of -10.7. In addition, three rims recorded more negative εHf_{20}, with values of -16.4, -17.3 and -18.8.

9 zircon rims from sample 1251 yielded highly variable εHf_{20} compositions from -11.2 to -21.8.

5 zircon rims from sample CWB16 yielded highly variable εHf_{20} values, between -13.7 to -22.

Sample CWB23 yielded the narrowest range of εHf_{20} values, with 11 analyses between -10.0 and -12.0.

6.2.3.2. Zircon cores

Zircon core εHf_t data are plotted against age in Figure 6.14. The cores yield three main age populations: 550 – 400 Ma, 900 – 800 Ma, and ~1800 Ma. A few additional zircon cores yield ages between these age populations.

The 550-400 Ma population derives predominantly from samples 1D01 and 1251, with a small number of cores from all other samples. εHf_t for this age population predominantly range between +2.4 and -6.8, with apparently anomalous values of +9.5, -9.0, -9.8 and -15.5.

The 900-800 Ma population is dominated by cores from sample 1G02, with additional data points from 1G03 and 1251. εHf_t for this group range between -7.5 and -14.6. An additional 4 zircon cores from samples 1G01 and 3A03 yielded slightly older ages compared to the main age group, between 937 and 1015 Ma, which yield significantly higher εHf_t values, ranging from +5.5 to -2.2.

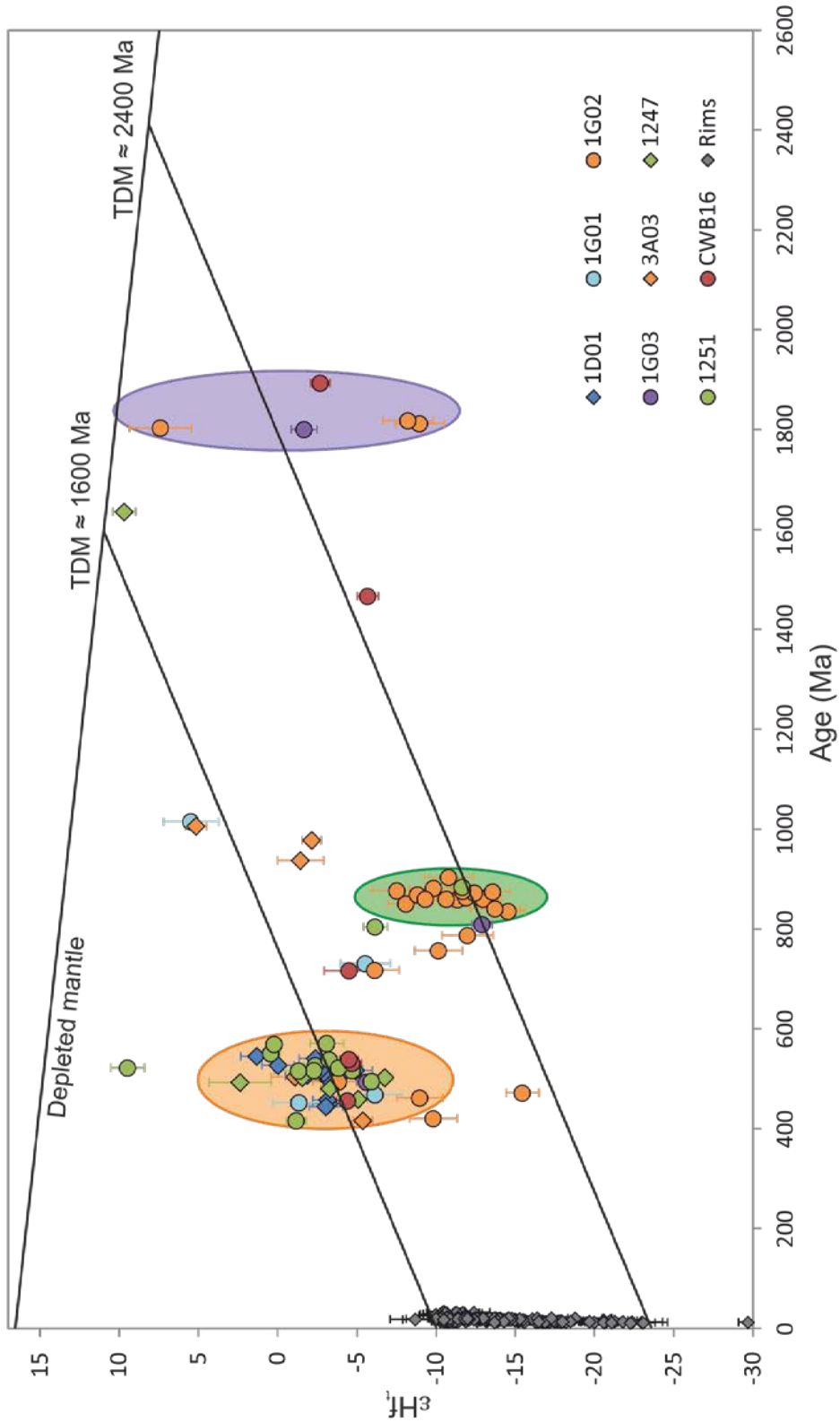

Figure 6.14: *Plot of age and εHf_t values for zircon core data, with regression lines from the minimum and maximum rim εHf_t values.*

These data could either represent outliers from the main 900-800 Ma age population (which would suggest a general decrease in source εHf_t values through time) or a separate population from a different source material.

Five zircon cores yielded ~1800 Ma ages in samples 1G02, 1G03 and CWB16. εHf_t values for these cores ranged from +7.4 to -9.0.

6.3. Discussion

6.3.1. Significance of crystallization ages

The timing of leucogranite crystallization of 12 samples were constrained by their zircon rim U-Pb ages, ranging from 31.2 to 11.7 Ma. This range, spanning 19.5 million years, is larger than any previous range published from High Himalayan leucogranites. Similar ages to the youngest samples at ~12 Ma have previously been documented in Bhutanese leucogranites (Daniel et al., 2003; Greenwood, 2013) although High Himalayan leucogranites as old as 31.18 Ma (such as sample 1D01) have not previously been recorded in Bhutan. Zircons from anatectic gneisses in Sikkim, however, have yielded similar Oligocene ages (Mottram, 2014). Zircon rim ages from all samples appear to form two main clusters of ages, one centred at ~20 Ma and one at ~14 Ma, as illustrated by the cumulative frequency plot in Figure 6.13. Relatively few zircons appear to have crystallized between 16 and 17 Ma. This could indicate two distinct episodes of melting and granite crystallization within the Himalaya.

Only one sample (1215) contains clear evidence for two discrete phases of igneous activity. Other samples yielding a wide age range are less well constrained in terms of separate crystallisation "events". For example, 1D01 yields 19 zircon rim ages recording crystallization ages between 34.0 and 18.5 Ma. This apparent 15.5 million year spread in ages may represent continuous melting and crystallization throughout this time frame. Leucogranites from north-western India were identified as representing melting across the timespan from 30 to 18 Ma

(Lederer et al., 2013), a similar period to that recorded by zircons in 1D01. However, this age range was established in many different leucogranite samples rather than one single body, and 15.5 million years of continuous magmatism in a single leucogranite has not been previously recorded. 8 of the 19 rim analyses form a cluster at 31.18 ± 0.22 Ma, and this age is likely to represent the true crystallization age of the rock. Zircon rims which are ostensibly younger may be the result of Pb-loss, which would result in a zircon yielding an apparent age that is younger than its actual age.

Sample 1247 also contains an apparently younger age population (c. 19.6 Ma), although the zircon data that make up this population typically have high common Pb levels and large uncertainties. As the younger zircons all form one population, it is unlikely that Pb loss is their cause. It is more likely this population represents either a second, more minor, period of crystallization, or an influx of fluids at this time.

6.3.2. Significance of core ages

Zircon core data fall into three dominant age populations, 550 – 450 Ma, 900 – 800 Ma and ~1800 Ma. These populations match those found in previous detrital zircon studies of the Himalayan orogen (both GHS and LHS, e.g. Spencer et al., 2012) and identify 3 periods of orogenesis in the likely source rocks from which the melts have been derived. The GHS metapelites in Bhutan are dominated by two main age populations, one at 550 – 450 Ma, and another at ~900 Ma (McQuarrie et al., 2008; Long and McQuarrie, 2010; Spencer et al., 2012). In addition to these dominant GHS populations, small quantities of ~1800 Ma zircons are found throughout the GHS metapelites (e.g. Chakungal et al., 2010). However this age population is most commonly associated with the LHS, in which ~1800 Ma is the dominant age population (Long and McQuarrie, 2010). The orthogneisses of the GHS formed in one specific igneous event and therefore only contain one zircon age population, at 500-450 Ma (Spencer et al., 2012). As this age population overlaps with that of the GHS metapelites, it is difficult to identify which lithology provided the potential source from zircon studies alone.

In leucogranite samples of this study, the 550-400 Ma population is the most dominant, comprising 45 core analyses across all samples; and all samples for which core data are available have at least one core falling into this category. A Cambro-Ordovician 'Pan-African' event is widely recognised from metamorphic and isotopic studies of the GHS across the Himalaya (Islam et al., 1999; Cawood et al., 2007; Spencer et al., 2012).

Those samples with younger crystallization ages appear to have an increased level of inheritance from the 900-800 Ma and ~1800 Ma age populations, as exemplified by 1G02 and 1G03. This may represent a change of source, or a change in the balance between contributing sources, over the period of Himalayan magmatism.

6.3.3. Discussion of hafnium isotope data

The maximum value of εHf_{20} over the ~23 Ma period of Himalayan igneous activity is -10 (with the exception of one zircon with a value of -8.7, Figure 6.13). The constancy of this maximum value suggests that over the period of melting, no additional sources with higher εHf values, such as the mantle, were sampled.

The minimum value of εHf_{20} decreases throughout the period of magmatism. The younger zircons yielded increasingly negative εHf_{20} compositions, to a minimum of -23.1 (with one anomalously low value of -29.7). This suggests that throughout the evolution of the orogen, increasing amounts of material of older model age material became involved in melting.

All samples younger than 17 Ma, with the exception of sample 1215, also show greater variability in their εHf_{20} values, suggesting these samples are the products of more than one source. Older samples have a much tighter array of εHf_{20} values, suggesting a single source.

This trend is illustrated on Figure 6.14, where regression lines are plotted from the maximum and minimum zircon rim εHf_{20} values, in order to constrain their model age and examine potential source contributions based on zircon core data. Regression lines are calculated using a $^{176}Lu/^{177}Hf$ ratio of 0.015, an average value for the continental crust (Griffin et al., 2002). A

regression line taken from the maximum zircon rim εHf_{20} value reveals a lower model age of ~ 1600 Ma, and intersects the centre of the 550 – 400 Ma field. A second regression line from the minimum εHf_{20} composition of the zircon rims reveals an upper model age of ~2400 Ma, while intersecting the centre of the 900 – 800 Ma population, and also crossing the ~1800 Ma field.

17 Ma appears to mark a change in zircon core populations inherited by leucogranites, with the majority of > 17 Ma leucogranites containing source populations where relatively young zircon cores, usually 550-400 Ma, predominate. These leucogranites are therefore most likely the product of melting of GHS orthogneisses and/or younger metapelites. Older zircon core populations are increasingly observed in leucogranites younger than 17 Ma, which exhibit a lower and more mixed range of εHf_{20} values. Younger leucogranites may also incorporate a small portion of LHS material although since ~1800 Ma zircons are found in both the GHS and LHS, it is impossible to be certain from zircon studies alone.

6.3.4. Source of melting

Zircon Hf and U-Pb data appear to indicate that the source of the High Himalayan leucogranites changes over the duration of melting in the orogen. Younger samples appear to have increasingly lower εHf_{20} values, suggesting an increase in older source materials becoming involved in the melt over time. This is also observed in whole-rock isotope data (see Chapter 4), specifically Nd, as displayed in Figure 6.15. Figure 6.15a shows the correlation between εNd_i and average zircon εHf_{20} values, while Figure 6.15b the decrease of εNd_i in progressively younger samples. The strong positive correlation (excepting CWB23) between bulk-rock Nd and zircon Hf isotopes confirms that the bulk-rock isotopes provide a valid indication of source characteristics despite the averaging effects of using bulk-rock samples.

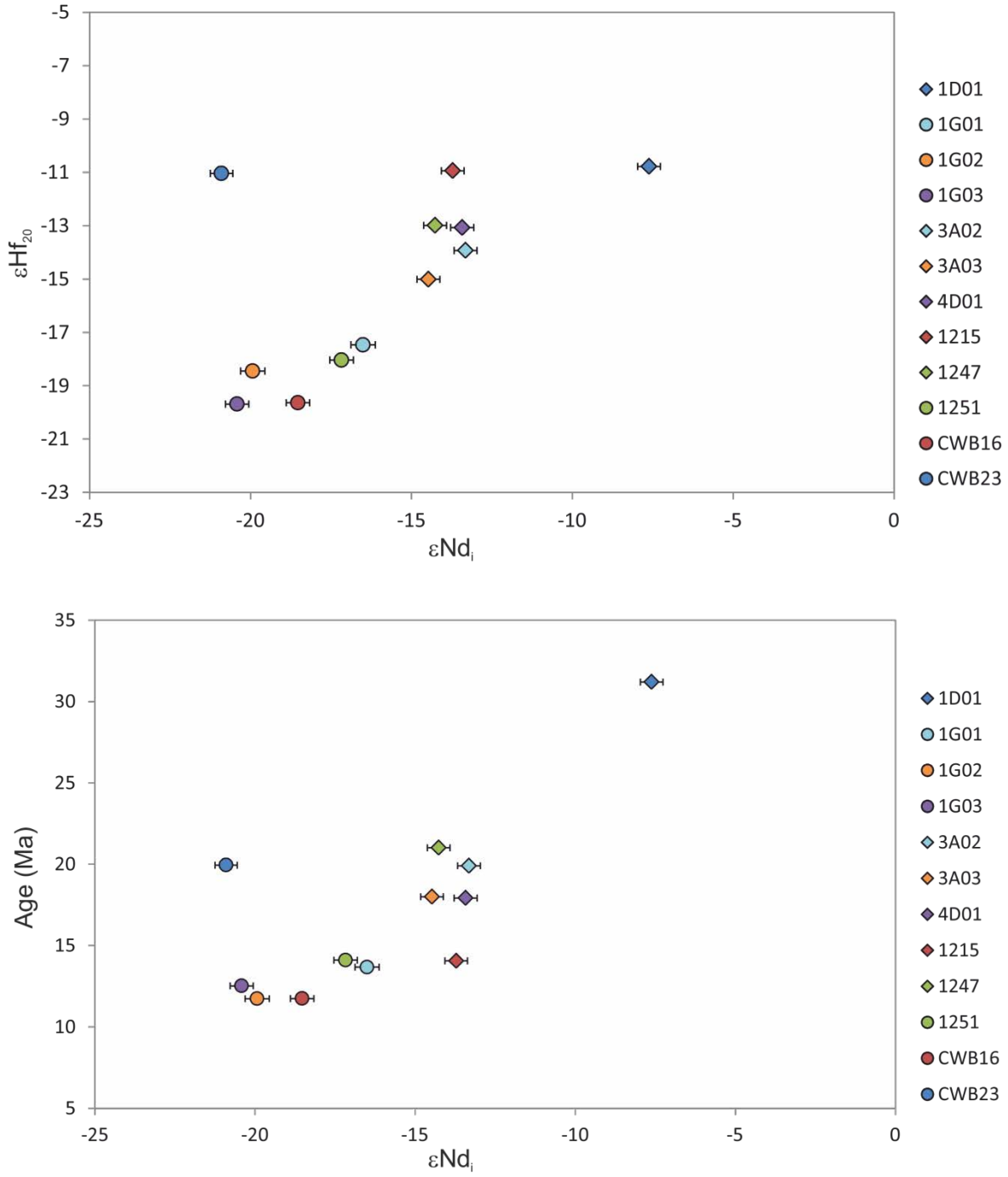

Figure 6.15: *Whole-rock Nd isotope change plotted against a) average zircon Hf and b) crystallization ages.*

A change in source chemistry of High Himalayan leucogranites in Bhutan is therefore indicated at ~17 Ma. Six samples (1D01, 3A02, 3A03, 4D01, 1247 and CWB23) that are older than 17 Ma yield zircons with higher εHf_{20} values (between -10 and -14) with very little variation. Core

populations for these samples, where available, also tend to be part of the 550-400 Ma group, suggesting an orthogneiss or younger GHS metasediment source, with few zircon cores falling into other age groups. Sample 3A03 is an exception, with two 550-400 Ma cores and 3 cores aged between 930 and 1015 Ma. However these have εHf_t values that are higher than the similarly-aged 900-800 Ma group, and probably represent a different source material.

Sample 1D01, the oldest sample analysed, yields Sr-Nd isotope values that suggest a predominant orthogneiss source (see Chapter 4). However, samples 3A02, 3A03, 4D01 and 1247 all have whole-rock isotope ratios that fall within both the GHS metapelite and orthogneiss fields, and therefore their specific source cannot be uniquely identified. CWB23 is the only sample that lies off the correlations observed in Figures 6.15a and 6.15b, with much more radiogenic εNd_i than the εHf_{20} observed in zircons. Assessing the source of this sample is therefore difficult, due to the contrasting conclusions that can be reached from the decoupled isotope systems.

Samples younger than 17 Ma include 1G01, 1G02, 1G03, 1215, 1251 and CWB16. These samples are characterized by lower εHf_{20} values which vary more widely across multiple zircon rims. The one exception to this is sample 1215, that provides zircon rims which record little variation in εHf_{20} and an average value of -10.94, comparable to >17 Ma samples. Sr-Nd isotopic values suggest affinity with the GHS metapelite field, rendering this as the likely sole source to sample 1215. The remaining samples in this younger group all produce low εHf_{20} with correspondingly low εNd_i values (Figure 6.15). These trends suggest that increasing amounts of older-model-age material are being involved in melting, as confirmed by an increase in the quantity of 900-800 Ma and ~1800 Ma zircon cores found in younger leucogranites. Core populations are also varied, with samples commonly yielding cores from all three dominant age populations. This is testament to the increasing mixing of sources involved in melting, with leucogranite magmas sampling increasing amounts of older 900-800 Ma GHS metapelites, as well as younger metapelites or orthogneisses, and possibly LHS material.

Samples 1G02, 1G03 and CWB16 are the three youngest samples analysed and all yield the most radiogenic εHf_{20} and εNd_i values (with the exception of CWB23 in the latter case), as shown in Figure 6.15. The εNd_i values for these three samples are all lower than those found in the GHS, with samples 1G02 and 1G03 containing Sr and Nd isotopic ratios found only in the LHS. These three samples are also the only samples from which ~1800 Ma cores were extracted, a zircon age population most commonly associated with the LHS (McQuarrie et al., 2008). This therefore suggests that small quantities of LHS material were involved in producing the youngest leucogranites in the Bhutan Himalaya. This has tectonic implications for Himalayan orogeny since the LHS is a structurally deeper lithotectonic unit (it forms the footwall of the MCT) so implying that the melt source extended to deeper levels in younger Miocene melts.

6.4. Conclusions

U-Pb analyses of Himalayan-aged leucogranite zircon rims have revealed a history of melting in the Bhutan Himalaya from 31.2 Ma, to 11.7 Ma, a longer period than has previously been observed in the region.

At least three main age populations contribute to the source of Himalayan melting, with the majority of zircon cores falling into 550 – 400 Ma, 900 – 800 Ma, and ~1800 Ma groups. These age populations may be linked to different portions of potential source material, with a tendency for older leucogranites (>17 Ma) to inherit more 550-400 Ma cores, and for younger (<17 Ma) leucogranites to inherit more cores from the two older age populations.

Together, whole-rock isotope geochemistry, zircon Hf isotopic ratios and age data show that the source of leucogranite generation in Bhutan changes over time. Two main groups of ages are seen in a cumulative frequency plot of age data, and Hf isotopic data suggests a significant change at 17 Ma, with samples older than this containing relatively stable εHf_{20} values between

-10 and -14. Younger than 17 Ma, samples contain increasingly more negative and more radiogenic εHf_{20} values, down to -23.1, with the lowest εHf_{20} values recorded in the youngest samples. A change is also seen in the age and Hf isotope composition of zircon cores found in samples, with older samples typically containing more ~550-400 Ma cores with εHf_t values between -10 and +5, and younger samples containing more 900-800 Ma cores with εHf_t values between -15 and -5.

Zircon age, Hf isotopic data and whole rock εNd_i values show a clear positive correlation between εNd_i and average zircon εHf_{20} values, and younger samples show increasingly lower εNd_i values. As lower εNd_i values are found only in LHS material as opposed to the GHS (Figure 4.1, Chapter 4), this could indicate an increasing amount of LHS material melting or becoming entrained in melts over the course of melting in the Bhutan Himalaya. Full tectonic implications of this finding are discussed in Chapter 8.

Chapter 7

Stable strontium and rubidium isotope geochemistry

This chapter presents a study of stable isotope fractionation within leucogranites and their mineral separates. Firstly, the variations in stable isotope fractionation of both strontium and rubidium in individual leucogranites are described. These data are then used to constrain sources and the conditions under which they formed. In later sections the significance of stable isotope fractionation and the implications this has for Rb-Sr geochronology are evaluated.

7.1. Introduction to stable isotope geochemistry

Variations in the isotopic composition of different elements within a rock can be generated through a variety of mechanisms, with each revealing different information about timescales and processes. The most commonly investigated process in isotope geochemistry involves the radioactive decay of unstable nuclides and the subsequent radiogenic build-up of their daughter isotopes over geologically-useful timescales. This approach has been used extensively throughout this study to investigate the geochronological and source relationships among a suite of Himalayan leucogranites (see Chapters 4 – 6). However, isotopic variations or fractionation of selected elements can be induced by processes other than radioactive decay. The physical fractionation of isotopes can occur in nature in two ways, through either mass-dependent or mass-independent processes. The study of such variations in high temperature systems has

produced new avenues of research in the general field of 'non-traditional' stable isotopes, leading to new understandings about geological processes in both terrestrial and extra-terrestrial materials. Developments in this area has in part been fuelled by recent advances in techniques and methods, and has led to the challenging of long-held basic assumptions; where once stable isotope ratios were thought to be invariant in nature, fractionation has been measured for a number of elements (see Albarede, 2004; Albarede and Beard, 2004; Johnson et al., 2004 for overviews).

Mass-dependent fractionation of a given isotopic system occurs as a function of the difference in mass between the isotopes involved, usually indirectly through variations in bond strengths, diffusivities or molecular velocities. Several general principles govern stable isotope fractionations. Firstly, the total magnitude of fractionation decreases significantly as temperature increases, roughly in proportion to $1/T^2$. Secondly, fractionation is typically larger where relative differences in masses of the different isotopes of a given element are largest. As such, it is expected that lighter elements, i.e., those with larger percentage mass difference between isotopes, are more readily affected by stable isotope fractionation than those with smaller mass differences for a given temperature (cf. Li; Parkinson et al., 2007; and U; Hiess et al., 2012). A third principle is that the heavier isotopes of an element will tend to become more concentrated in substances where they can form stronger bonds, with the magnitude of fractionation proportional to any differences in bond strength between substances. Where the element in question has multiple redox states the resulting isotopic fractionations can be used to interrogate environmentally relevant processes; e.g. Zn (Kavner et al., 2008).

Mass-independent fractionation, on the other hand, is rare; and occurs when the total fractionation between two isotopes is not proportional to their masses. For the purposes of isotope geochemistry these are most commonly associated with initial heterogeneities produced by nucleosynthetic processes, for example those associated with star formation (Burbidge et al., 1957). The origins of such heterogeneities form the basis of robust ongoing debate in

addressing the nature and relative proportions of the fundamental building blocks of the planets (e.g. Taylor, 1964; Davies, 1981; Boyet and Carlson, 2006).

In general, the natural processes involved in mass-dependent fractionation are identical to those occurring in a mass spectrometer during analysis. For example, in a thermal ionisation mass spectrometer (TIMS), a finite reservoir of sample exists on the filament. As the sample is progressively consumed, lighter isotopes are ionised preferentially, leaving the residual analyte on the filament increasingly enriched in the heavier isotopes. This Rayleigh-type distillation process is generally known as instrumental mass fractionation (IMF) and changes throughout an analysis run. IMF requires correction, and is most often corrected by normalising all ratios of interest to one assumed to be invariant in the sample using power- or exponential-law fractionation corrections (Cavazzini, 2012). In contrast, the fractionation occurring in a MC-ICP-MS instrument produces a constant offset or fractionation from the true value or accepted value for the 'invariant' ratio through small differences in ionisation efficiency between isotopes, and complex space-charging effects in the plasma-vacuum interface. This effect is generally known as mass bias (MB) and it implies a constant offset from a true value, rather than one which evolves through time.

In principle, MC-ICP-MS derived ratios can be corrected in the same fashion as for TIMS analysis, but the exact method of correction for either case - using power-law or exponential-law - has long been debated (e.g., Meija et al., 2009). However, the key point is that so-called internal normalisation to a fixed value for a particular isotope ratio erases possible stable isotope variations produced in nature, and so a potential source of additional information relating to process is lost. Disentangling the natural versus laboratory-induced fractionation is the aim of non-traditional stable isotope studies (Albarede and Beard, 2004).

7.1.1. Stable isotopic fractionation of strontium

Strontium (Z = 38, A_r = 87.62) exists in only the 2+ redox state and has four naturally occurring isotopes (^{84}Sr, ^{86}Sr, ^{87}Sr and ^{88}Sr) with ^{88}Sr being the most abundant (82.58%). The Rb-Sr, or

radiogenic strontium isotope system ($^{87}Sr/^{86}Sr$ or $\delta^{87/86}Sr$) which is based on the decay of ^{87}Rb to ^{87}Sr (with a ~49 billion year half-life, Rotenberg et al., 2012) is a long-established tool in isotope geochemistry and geochronology, and is routinely used to investigate high temperature magmatic systems and the igneous origin of minerals and rocks. Conventional radiogenic Sr isotope measurements (using TIMS or MC-ICP-MS) are corrected for IMF or MB respectively by normalising to an assumed value for the $^{86}Sr/^{88}Sr$ ratio of 0.1194 (Steiger and Jager, 1977). This internal normalisation permits the measurement of $^{87}Sr/^{86}Sr$ ratios to a very high precision (sometimes to the 6^{th} decimal place). However, implicit in the use of a fixed value is the assumption that this ratio remains invariant.

The majority of studies involving stable strontium isotope geochemistry have focussed on low-temperature systems. Strontium is known to fractionate during the precipitation of carbonates for coral (e.g. Fietzke and Eisenhauer, 2006), foraminifera (Bohm et al., 2012) and coccolithophores (Stevenson et al., 2014). The first study to identify possible stable Sr fractionation in high-temperature geological material used TIMS double spiking techniques and highlighted variations in the $^{86}Sr/^{88}Sr$ ratio of up to 1.5‰ recorded in calcium-aluminium-rich inclusions (CAIs) and chondrules from the Allende meteorite (Patchett, 1980a; Patchett, 1980b). Consistent with this early work, similar deviations in $^{86}Sr/^{88}Sr$ in CAI were found using external element doping and MC-ICP-MS (Moynier et al., 2010; Charlier et al., 2012).

Moynier et al. (2010) and Charlier et al. (2012) both investigated the stable Sr composition of a range of high temperature (i.e., magmatic) terrestrial samples and found that the majority have heavy $\delta^{88/86}Sr$ values relative to the standard NBS-987 (by definition zero) and a fairly uniform composition of 0.30 ± 0.07‰ (2 s.d.). Most of these magmatic rocks are basaltic to andesitic in composition suggesting that mantle melting delivers melts to the Earth's surface that have a restricted range in stable Sr isotopic ratios, and that fractionation of olivine and clinopyroxene have little effect on $\delta^{88/86}Sr$. In contrast, the highly evolved melts analysed by Charlier et al. (2012), ranging in composition from andesites to high-silica rhyolites, have $\delta^{88/86}Sr$ values that extend from +0.19 to –0.19‰, and represent the only terrestrial silicates to have light (i.e. more

negative) $\delta^{88/86}$Sr values. These melts are characterised by decreasing Sr and increasing Rb with increasing SiO_2, consistent with extensive crystal fractionation, with $\delta^{88/86}$Sr correlating negatively with Rb/Sr ratios. Additionally, Charlier et al. (2012) also found that $\delta^{88/86}$Sr correlated negatively with Eu/Eu* and therefore suggested that plagioclase preferentially partitions heavy Sr isotopes, producing melts with increasing light δ^{88}Sr with increasing degrees of crystal fractionation. An additional implication from this work was that isotopic fractionation may be coupled with crustal assimilation, by some form of assimilation fractional crystallisation (AFC) process, such that the melts assimilate progressively more crust with light $\delta^{88/86}$Sr.

The primary issue with these conclusions is that they were reached using a sample suite encompassing a range of petrogenetically unrelated samples, rather than a single consanguineous suite. Therefore there have been no direct observations of a reduction in $\delta^{88/86}$Sr as feldspar fractionation occurs within a single suite. In addition, no mineral separates were analysed in order to confirm their assertion that stable strontium fractionation in evolved rocks was caused by feldspar fractionation. If systematic fractionation of stable Sr isotopes can be recorded between coexisting mineral phases, this would be conclusive proof that the variations observed by Charlier et al. (2012) were caused by feldspar fractionation.

Since stable isotope fractionation should be of greater magnitude at lower temperatures and in lower volume melting environments, the Himalayan leucogranitic melts are well-suited to investigate such fractionation. Also, because these rocks represent wholesale crustal melts, they allow for the disentanglement of the effects of crystal fractionation versus inheritance of the isotopic composition from the protolith.

7.1.2. Stable isotope fractionation of rubidium

Rubidium (Z = 37, A_r = 85.47) has two naturally occurring isotopes (^{85}Rb and ^{87}Rb) with ^{85}Rb being the most abundant (72.17%) and the only stable isotope.

Traditionally, Rb (and Sr) sample concentrations are usually calculated using isotope dilution (ID) via the addition of mixed ^{87}Rb-^{84}Sr spike (Faure and Mensing, 2005). The limitation on the

accuracy of the Rb content using this approach derives from the fact that Rb only has two isotopes and thus has no normalising ratio. In a conventional TIMS Rb analysis, runs are conducted for samples and standards under identical conditions (filament temperature, vacuum pressure, load size etc.) and a fractionation factor determined from the standard data which is then applied to the unknowns. Typical precisions using this approach are in the region 1 to 2 % at best. A more recent approach used admixed Zr to account for mass bias during analysis by MC-ICP-MS, the result being a significant improvement (up to a precision of 0.05%, 2 s.d.) in the determination of $^{87}Rb/^{86}Sr$ (Waight et al., 2002). Whichever method for Rb isotope analysis is used, it is assumed that no variation exists in an $^{87}Rb/^{85}Rb$ ratio of 0.38540 ± 0.00019 (value for standard NBS-984, Waight et al., 2002), which is used to calculate the concentration of ^{87}Rb in the ID calculations, and in turn the $^{87}Rb/^{86}Sr$ ratio.

Only one previous study has sought to investigate stable isotope fractionation of Rb (Nebel et al., 2005). Their study showed no departure of the $^{87}Rb/^{85}Rb$ ratio from the accepted value of NBS-984 ($^{87}Rb/^{85}Rb$ = 0.38540 ± 19). Due to the potential of Himalayan leucogranites to have experienced stable isotope fractionation and given their very high Rb contents, we also test the conclusion reached by Nebel et al. (2005) that Rb isotope ratios are invariant.

7.1.3. Previous techniques for analysing stable Sr isotopes

Conventional radiogenic Sr isotopic analyses traditionally seek only to ascertain the $^{87}Sr/^{86}Sr$ ratio of a sample, and use the measured $^{88}Sr/^{86}Sr$ ratio to correct for fractionation using exponential law fractionation (Thirlwall, 1991). In the case of measuring stable Sr isotope variations by MC-ICP-MS this can only realistically be achieved by Zr doping (Waight et al., 2002; Charlier et al., 2006). The external element doping approach is similar to that used for Pb (using Tl; Thirlwall, 2002), where the $^{90}Zr/^{91}Zr$ is measured at the same time as the Strontium isotopes. The assumed invariant Zr isotope ratio is then used to correct the Sr (or Rb) isotope ratios. This method has significant drawbacks, however. Firstly, mass bias does not necessarily affect all elements equally, and therefore it is impossible to be certain that mass bias corrections have been performed correctly when using Zr (a high field-strength element) to correct for Sr

(an alkaline earth metal; see analogous literature for Pb and Tl –Thirlwall, 2002). Secondly, it is difficult to account for any change in mass bias between samples and standards, where the addition of any residual unseparated matrix to a plasma instrument may cause a shift in the internal fractionation factor between elements. One further problem specific to the measurement of Sr by MC-ICP-MS is the isobaric interference of ^{84}Kr (a common contaminant of Ar gas) with ^{84}Sr, rendering the latter isotope impossible to measure without an interfering element correction (and further possibility for inter-element fractionation).

Although double spike methods have been in use for a long time (e.g., Pb – Compston and Oversby, 1969; Sr – Patchett 1980a, 1980b), their usage has recently become more popular (e.g. Thirlwall, 2000; Siebert et al., 2001; Baker et al., 2004; Rudge et al., 2009). One recent study saw the reinvigoration of a double-spike (DS) TIMS technique for Sr (Neymark et al., 2014), and this technique has several significant advantages compared to the MC-ICP-MS method. The only drawback is the increased amount of time required to prepare samples and acquire data. TIMS data can be more precise than MC-ICP-MS, and accuracy is also improved over external element correction methods since mass- and elemental- fractionation is less likely to be influenced by matrix effects. In addition, the absence of any isobaric Kr interference on mass 84 allows the full suite of Sr isotopes to be measured, including ^{84}Sr.

7.2. Methods

Nineteen samples were selected to be analysed for stable Sr and Rb analysis. For Sr, 15 samples were analysed by MC-ICP-MS and 10 by TIMS, with 6 samples repeated across both methods for comparison. As Rb has only two isotopes – ^{85}Rb and ^{87}Rb – double spike techniques are impossible, and therefore all (natural, unspiked) Rb analyses were conducted using MC-ICP-MS and the Zr doping technique (Charlier et al., 2006). In addition, 4 samples were selected from which mineral separates were extracted. These were chosen on the basis that they covered a wide variety of whole rock $\delta^{88/86}$Sr ratios. K-feldspar, plagioclase,

muscovite and biotite separated from these samples were also analysed for their stable Sr and Rb compositions in order to investigate whether systematic variations between minerals exists, and whether this might drive isotopic fractionation observed at the bulk rock scale.

In addition to investigating the stable Rb and Sr isotopic systematics of leucogranites and their mineral separates, isotope dilution measurements of the Rb and Sr were also carried out on aliquots to which a mixed Rb-Sr spike had been added to each in order to determine Rb and Sr concentrations and so calculate the $^{87}Rb/^{86}Sr$ for use in isochron studies. This will be discussed in the second part of this chapter.

7.2.1. Sample preparation

To help illustrate the full analytical protocol, Figure 7.1 shows a flow chart illustrating how one sample dissolution provides material for a total of five different analyses: Rb and Sr natural analyses, double spike Sr, and Sr and Rb concentrations via ID.

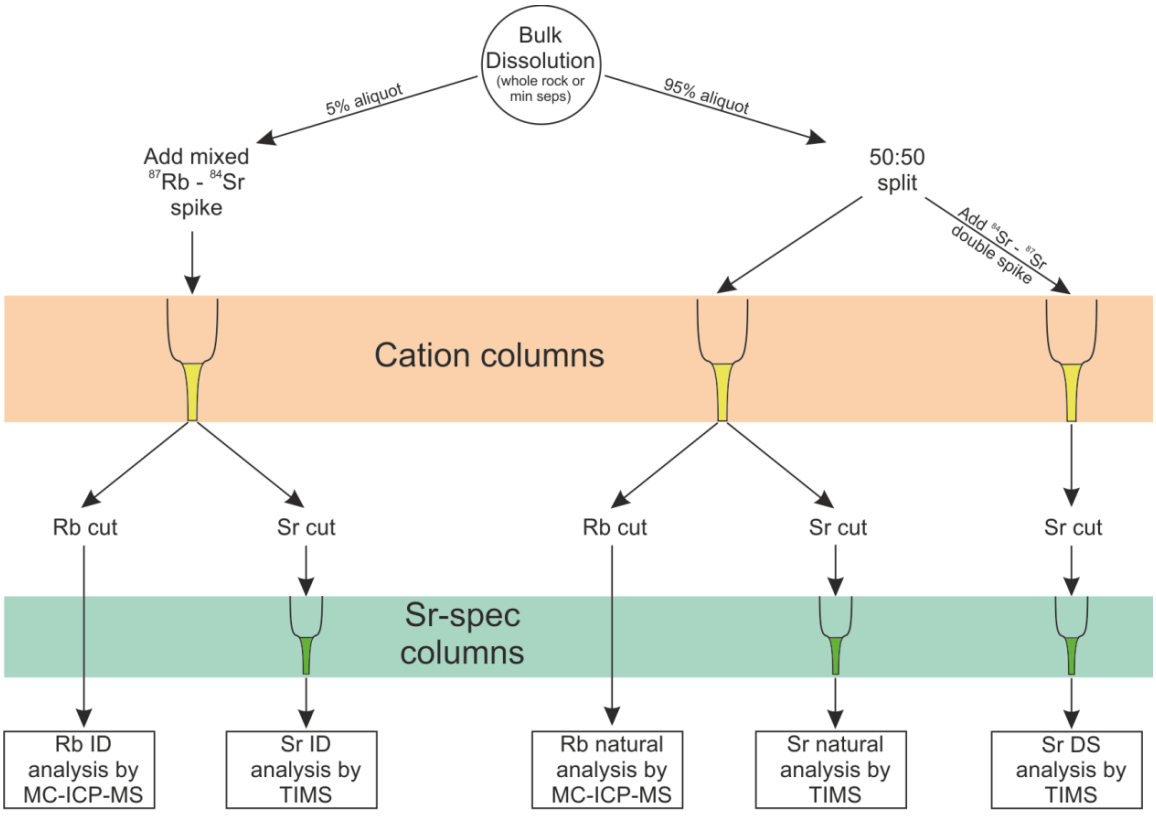

Figure 7.1: *Flow chart illustrating sample preparation and column procedures used in this study.*

Whole rock samples were crushed by standard techniques (jaw crusher, Tema agate mill). For mineral separates, samples were crushed by disc mill and feldspar and mica separated by hand. To separate plagioclase from K-feldspar, picked feldspars were mounted on a SEM stub and analysed on a Zeiss Supra 55V SEM at the Open University in order to easily differentiate the two classes of feldspar. Grains were removed from the stub and then cleaned using acetone prior to dissolution.

Samples were then dissolved in a HF/HNO_3 mixture in closed Teflon beakers at 120°C for several days. For all dissolutions except mica separates, enough material was dissolved in order to provide at least 2100 ng Sr. Following drying-down, samples were re-dissolved in HCl to ensure complete removal of fluorides, and dried down once more.

Prior to column chemistry mineral separate solutions were split into two aliquots. 5% of each sample was separated for ID measurements, in order to calculate Rb and Sr concentrations. Based on the predicted Rb/Sr ratios, samples were doped with one of two dope solutions. Rb and Sr concentrations for whole rock samples are known from XRF analysis.

The remaining 95% of each mineral separate sample and the entire whole rock solutions were then split into two aliquots in preparation for analysis by TIMS, one of which was spiked with a Sr (^{84}Sr-^{87}Sr) double spike. Both aliquots were then treated identically in order to remove the possibility of differential blank issues.

All samples were then re-dissolved in 2.5M HCl and passed through Biorad AG50W-X8 cation resin columns containing 2 ml resin, in order to remove the majority of matrix elements and to provide Rb and Sr cuts. Using techniques detailed by Charlier et al. (2006), all Sr aliquots (Sr ID, Sr natural, Sr DS) were then dissolved in 7M HNO_3 and passed through Sr specific resin columns to remove any remaining Rb and Ca and ensure clean separation of Sr.

7.2.2. Strontium by TIMS

Following column chemistry, samples were dried down, then taken up again in 1 µl of 16M HNO_3 and dried onto Re filaments with the Ta_2F_5 activator prior to being analysed on a

Thermo-Fisher Triton TIMS at the Open University. Data were collected in 54 blocks of 10 cycles with a 16 second integration. Faraday cups were positioned to collect masses 84, 85, 86, 87, 88, and a sixth cup collected a 'dummy' mass 89. Identical protocols were used for both spiked and unspiked aliquots and were performed in static mode using six amplifiers in rotation. Baselines were measured by source deflection after a 30 second pre-baseline wait time for 2 minutes after each step in the amplifier rotation. The amplifiers were cycled through the 'dummy' mass in both cases in order to fully discharge the amplifier used for ^{88}Sr collection back to baseline values before then collecting the smaller ^{84}Sr beam. Without this additional step in the rotation sequence we found from earlier work that an incorrect baseline was measured prior to measuring the small ^{84}Sr peak, resulting in inaccurate $^{84}Sr/^{86}Sr$ data. The magnitude of this effect was found to be proportional to the size of the preceding ^{88}Sr beam. Six amplifiers and 54 blocks of data permitted nine complete rotations of each amplifier.

Deconvolution of the natural and spiked samples was carried out offline using equations outlined by Neymark et al. (2014) which involve an iterative solution using a Newton-Raphson technique. A 5000 iteration Monte-Carlo simulation (Rudge et al., 2009) was used to calculate the uncertainties for the deconvolved data.

For this study, within-run Monte-Carlo-derived uncertainties for individual samples were quadratically added to the external reproducibility of the deconvolved standards run with each batch of samples.

7.2.3. Rubidium by MC-ICP-MS

Rb cuts were then dissolved to a concentration of 100 ppb in 3% HNO_3 and doped with 600 ppb Zr, before being analysed on a Thermo Fisher Neptune Plus at the Open University. Faraday cups were positioned to collect masses 83, 84, 85, 86, 87, 88, 90, 91, 92. Data were thereafter processed offline for interfering element and mass bias correction. ^{88}Sr was used to correct for ^{87}Sr interference on ^{87}Rb. Following interfering element corrections, the calculated $^{87}Rb/^{85}Rb$ was used to determine the mass bias correction for $^{90}Zr/^{91}Zr$ in a set of NBS-984 Rb standard

solutions doped with Zr. The mass bias corrected $^{90}Zr/^{91}Zr$ for a given analytical session was then used to correct unknown samples, also doped with Zr at the identical concentration.

7.2.4. Strontium by MC-ICP-MS

Whole-rock samples only analysed for stable Sr isotopes by MC-ICP-MS were dissolved separately. Dissolution and column procedures are identical to those described above (Section 7.2.1), though the entire samples were treated as Sr natural aliquots.

For analysis by MC-ICP-MS, samples were dissolved in a 3% HNO_3 solution and doped with 600 ppb Zr, before being analysed on a Thermo Fisher Neptune Plus at the Open University. Analyses were performed at a concentration of 100 ppb Sr. The Faraday cup configuration was identical to that used for Rb analysis. Data were thereafter processed offline for interfering element and mass bias correction. ^{83}Kr was used to monitor ^{86}Kr interference on ^{86}Sr, and ^{85}Rb was used to correct ^{87}Rb interference on mass ^{87}Sr. Following interfering element corrections, the calculated $^{88}Sr/^{86}Sr$ was used to determine the mass bias correction for $^{90}Zr/^{91}Zr$ in a set of NBS-987 Sr standard solutions doped with Zr. The mass bias corrected $^{90}Zr/^{91}Zr$ for a given analytical session was then used to correct unknown samples, also doped with Zr at the identical concentration.

Full details for all methods are provided in the Supplementary Methods.

7.3. Results

Stable isotopic fractionation is commonly presented in delta notation, which refers to a variation in parts per thousand relative to a standard (NBS-987 for strontium, and NBS-984 for Rb).

For example:

$$\delta^{88}Sr\ (‰) = \left(\frac{{}^{88}Sr/{}^{86}Sr_{\text{sample}}}{{}^{88}Sr/{}^{86}Sr_{\text{standard}}} - 1 \right) * 1000$$

Table 7.1: Stable Sr isotope data for whole rock samples

	1D 01	1G 01	1G 02	1G 03	3A 01	3A 02	3A 03	3A 04	4D 01	5M 01	
Rb ppm	254	330	322	277	572	251	323	296	143	241	Rb ppm
Sr ppm	62	181	61	55	11	12	44	10	121	13	Sr ppm
Rb/Sr	4.1	1.8	5.3	5.1	50	22	7.3	29	1.2	19	Rb/Sr
Sr method	TIMS	MC-ICP-MS	MC-ICP-MS	MC-ICP-MS	TIMS	TIMS	TIMS	TIMS	MC-ICP-MS	MC-ICP-MS	Sr method
$^{84}Sr/^{86}Sr$	0.056529	-	-	-	0.056496	0.056503	0.056457	0.056460	-	-	$^{84}Sr/^{86}Sr$
2 s.d.	0.000005	-	-	-	0.000005	0.000004	0.000004	0.000004	-	-	2 s.d.
$^{87}Sr/^{86}Sr$	0.978210	0.766658	0.824239	0.809263	0.807679	0.787705	0.777162	0.793745	0.768719	0.795758	$^{87}Sr/^{86}Sr$
2 s.d.	0.000022	0.000083	0.000065	0.000066	0.000021	0.000020	0.000020	0.000020	0.000083	0.000083	2 s.d.
$^{88}Sr/^{86}Sr$	8.36949	8.37660	8.37704	8.37605	8.37452	8.37308	8.38008	8.37964	8.37770	8.37839	$^{88}Sr/^{86}Sr$
2 s.d.	0.00044	0.00111	0.00044	0.00044	0.00044	0.00041	0.00041	0.00041	0.00111	0.00112	2 s.d.
$\delta^{84}Sr$	0.67	-	-	-	0.08	0.21	-0.60	-0.54	-	-	$\delta^{84}Sr$
2 s.d.	0.08	-	-	-	0.08	0.08	0.08	0.08	-	-	2 s.d.
$\delta^{88}Sr$	-0.68	0.17	0.22	0.10	-0.08	-0.25	0.58	0.53	0.30	0.38	$\delta^{88}Sr$
2 s.d.	0.05	0.13	0.05	0.05	0.05	0.05	0.05	0.05	0.13	0.13	2 s.d.

Table 7.1: Stable Sr isotope data for whole rock samples

	1215	1247	1251	CWB 16	CWB 23	BH 65	BH 84	BH226	BH231	
Rb ppm	209	407	231	262	236	347	163	334	216	Rb ppm
Sr ppm	54	50	76	93	69	39	130	95	199	Sr ppm
Rb/Sr	3.9	8.2	3.0	2.8	3.4	8.9	1.3	3.5	1.1	Rb/Sr
Sr method	TIMS	TIMS	TIMS	MC-ICP-MS	MC-ICP-MS	MC-ICP-MS	TIMS	MC-ICP-MS	TIMS	Sr method
$^{84}Sr/^{86}Sr$	0.056492	0.056488	0.056507	-	-	-	0.056461	-	0.056473	$^{84}Sr/^{86}Sr$
2 s.d.	0.000004	0.000005	0.000005	-	-	-	0.000005	-	0.000005	2 s.d.
$^{87}Sr/^{86}Sr$	0.760098	0.762264	0.829544	0.830595	0.797008	0.911392	0.740317	0.770572	0.730144	$^{87}Sr/^{86}Sr$
2 s.d.	0.000020	0.000020	0.000020	0.000066	0.000066	0.000083	0.000020	0.000083	0.000020	2 s.d.
$^{88}Sr/^{86}Sr$	8.37498	8.37498	8.37248	8.37637	8.37839	8.37885	8.37927	8.37971	8.37734	$^{88}Sr/^{86}Sr$
2 s.d.	0.00041	0.00041	0.00041	0.00043	0.00043	0.00111	0.00041	0.00111	0.00041	2 s.d.
$\delta^{84}Sr$	0.01	-0.06	0.29	-	-	-	-0.53	-	-0.32	$\delta^{84}Sr$
2 s.d.	0.08	0.08	0.08	-	-	-	0.09	-	0.09	2 s.d.
$\delta^{88}Sr$	-0.03	-0.03	-0.33	0.14	0.38	0.43	0.48	0.54	0.25	$\delta^{88}Sr$
2 s.d.	0.05	0.05	0.05	0.05	0.05	0.13	0.05	0.13	0.05	2 s.d.

Sr isotopic data for whole rocks are provided in Table 7.1. Rb/Sr ratios for the majority of granite samples are between 1 and 8, although 3A02, 3A04 and 3A01 have higher ratios of 21.9, 29.0 and 50.2, respectively.

Variations in $\delta^{88/86}$Sr of samples repeated across methods are shown in Figure 7.2. Three samples (3A02, 3A03 and 1247) out of the six lie within error of a 1:1 line (note; this is not a mass fractionation line, but a measure of the equivalence of data between double spike and Zr-normalisation for the same samples), the remaining three are ~0.1 per mil lighter as measured by MC-ICP-MS analysis.

Stable isotope data are typically plotted on three-isotope plots, in this case plotting $\delta^{88/86}$Sr against $\delta^{84/86}$Sr. If isotopic fractionation is controlled only by mass-dependent processes, all isotopes should be fractionated in proportion to the differences in isotopic mass and lie along a mass fractionation line, with $\delta^{84/86}$Sr values being almost the inverse of $\delta^{88/86}$Sr. Any deviation from this line indicates a component of mass-independent fractionation. The equation for such a kinetic fractionation line is as follows (equations from Young et al., 2002):

$$\delta^{84/86}Sr = \left(10^3 + \delta^{84/86}_{ref}Sr\right)\left(\frac{10^3 + \delta^{88/86}Sr}{10^3 + \delta^{88/86}_{ref}Sr}\right)^{\beta} - 10^3$$

Where

$$\beta = \frac{\ln\left(\frac{m^{86}Sr}{m^{84}Sr}\right)}{\ln\left(\frac{m^{86}Sr}{m^{88}Sr}\right)}$$

In these equations *m* refers to the absolute masses of the isotopes in question (IUPAC values from Berglund and Wieser, 2011). Reference values of $\delta^{84/86}$Sr and $\delta^{88/86}$Sr refer to the values of the standard NBS-987, by definition zero. The gradient of this line is -0.976.

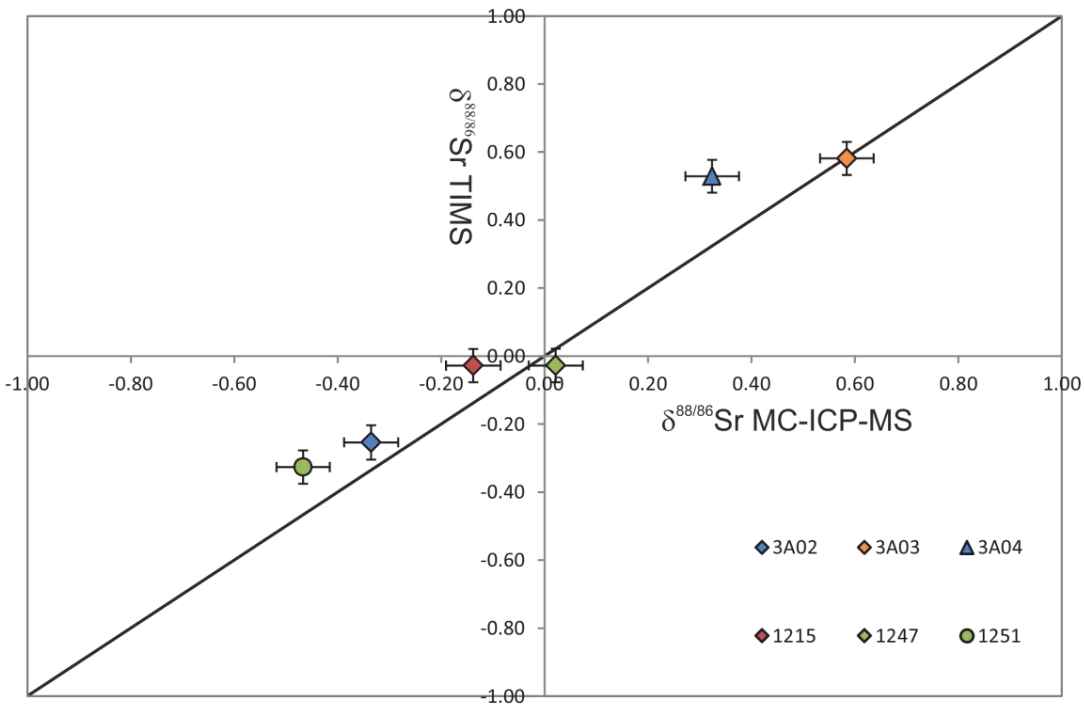

Figure 7.2: *Plot of whole rock $\delta^{88/86}$Sr via TIMS vs $\delta^{88/86}$Sr via MC-ICP-MS for samples that have been analysed by both techniques. Three samples lie within error of the line – 3A02, 3A03, and 1247. The remaining samples lie away from the 1:1 line. R^2 = 0.9325 for the overall correlation.*

Figure 7.3 displays a three-isotope plot of $\delta^{88/86}$Sr vs $\delta^{84/86}$Sr for whole-rock data obtained by TIMS. All samples lie within uncertainty of the mass-dependent fractionation line. Total variation is 1.26‰, varying from -0.68 to 0.58. Also plotted for comparison are the four samples only analysed by MC-ICP-MS. Since there is no $\delta^{84/86}$Sr available for these samples, they are plotted as lying on the mass fractionation line (and without error bars in the x-axis).

Rb and Sr concentrations and isotopic data for mineral separates are provided in Table 7.2. Plagioclase from all samples contain Rb/Sr ratios that vary between 0.6 and 1.6, while K-feldspars are characterised by ratios between 1.3 and 2.2. Muscovite samples from 3A03 and 1247 yield Rb/Sr ratios of 134 and 116, respectively. Biotite from 1251 yields a Rb/Sr ratio of 114.

Table 7.2: Stable Sr and Rb isotope data for mineral separate samples

	1G03			3A03				1247				1251				
	Plag	K-spar	Whole-rock	Plag	K-spar	Musc	Whole-rock	Plag	K-spar	Musc	Whole-rock	Plag	K-spar	Biotite	Whole-rock	
Rb ppm	77	208	277	124	135	626	323	83	169	613	407	84	142	560	231	Rb ppm
Sr ppm	99	100	55	78	75	5	44	63	80	5	50	134	103	5	76	Sr ppm
Rb/Sr	0.8	2.1	5.1	1.6	1.8	134	7.3	1.3	2.1	116	8.2	0.6	1.4	114	3.0	
Sr method	TIMS	TIMS	MC-ICP-MS	TIMS	TIMS	TIMS	TIMS	TIMS	TIMS	-	TIMS	TIMS	TIMS	TIMS	TIMS	Sr method
$^{84}Sr/^{86}Sr$	0.056479	0.056487	-	0.056443	0.056465	0.056449	0.056457	0.056481	0.056485	-	0.056488	0.056470	0.056525	0.056385	0.056507	$^{84}Sr/^{86}Sr$
2 s.d.	0.000004	0.000004	-	0.000004	0.000004	0.000004	0.000004	0.000004	0.000004	-	0.000005	0.000004	0.000004	0.000005	0.000005	2 s.d.
$^{87}Sr/^{86}Sr$	0.806676	0.811537	0.809263	0.774141	0.777100	0.868988	0.777162	0.758335	0.764530	-	0.762264	0.827008	0.830912	0.864035	0.829544	$^{87}Sr/^{86}Sr$
2 s.d.	0.000020	0.000020	0.000066	0.000020	0.000020	0.000021	0.000020	0.000020	0.000020	-	0.000020	0.000020	0.000020	0.000023	0.000020	2 s.d.
$^{88}Sr/^{86}Sr$	8.376877	8.375151	8.376051	8.381870	8.378857	8.382128	8.380078	8.376386	8.376252	-	8.374978	8.378186	8.369790	8.390836	8.372478	$^{88}Sr/^{86}Sr$
2 s.d.	0.000392	0.000392	0.000441	0.000392	0.000392	0.000405	0.000408	0.000392	0.000392	-	0.000410	0.000391	0.000391	0.000405	0.000409	2 s.d.
$\delta^{84}Sr$	-0.21	-0.07	-	-0.86	-0.45	-0.74	-0.60	-0.18	-0.11	-	-0.06	-0.38	0.60	-1.87	0.29	$\delta^{84}Sr$
2 s.d.	0.07	0.07	-	0.07	0.07	0.08	0.08	0.07	0.07	-	0.08	0.07	0.07	0.09	0.08	2 s.d.
$\delta^{88}Sr$	0.20	-0.10	0.10	0.80	0.44	0.83	0.58	0.14	0.12	-	-0.03	0.36	-0.65	1.87	-0.33	$\delta^{88}Sr$
2 s.d.	0.05	0.05	0.05	0.05	0.05	0.05	0.05	0.05	0.05	-	0.05	0.05	0.05	0.05	0.05	2 s.d.
$^{87}Rb/^{85}Rb$	0.385952	0.385871	0.385971	0.385914	0.385878	0.385872	0.385875	0.385876	0.385873	0.385988	0.385920	0.386024	0.386026	0.386064	0.386016	$^{87}Rb/^{85}Rb$
2 s.d.	0.000018	0.000018	0.000017	0.000018	0.000018	0.000018	0.000017	0.000018	0.000018	0.000018	0.000017	0.000018	0.000018	0.000019	0.000017	2 s.d.
$\delta^{87}Rb$	-0.18	-0.39	-0.13	-0.28	-0.37	-0.39	-0.38	-0.38	-0.38	-0.09	-0.26	0.01	0.01	0.11	-0.01	$\delta^{87}Rb$
2 s.d.	0.05	0.05	0.04	0.05	0.05	0.05	0.04	0.05	0.05	0.05	0.04	0.05	0.05	0.05	0.04	2 s.d.

Figure 7.4 shows a three-isotope plot of $\delta^{88/86}$Sr vs $\delta^{84/86}$Sr for mineral separate data. All samples lie within uncertainty of the mass-dependant fractionation line. Total variation is 2.51‰, varying from -0.65 to 1.87. Figure 7.5 shows the $\delta^{88/86}$Sr values for the same mineral separates with a dimensionless x-axis, allowing comparison between data points.

Figure 7.6 shows $\delta^{88/86}$Sr for samples with zircon core populations as described in Chapter 5. Data are separated based on their zircon core age population.

Total variation of $\delta^{87/85}$Rb is 0.50‰, varying from -0.39 to 0.11, as plotted in Figure 7.7. Largest variation within samples is found in 1G03 and 1247, in which mineral separates and whole rock values differ by 0.4‰. Data for samples 3A03 and 1251 are indistinguishable across all mineral separates and whole rock values.

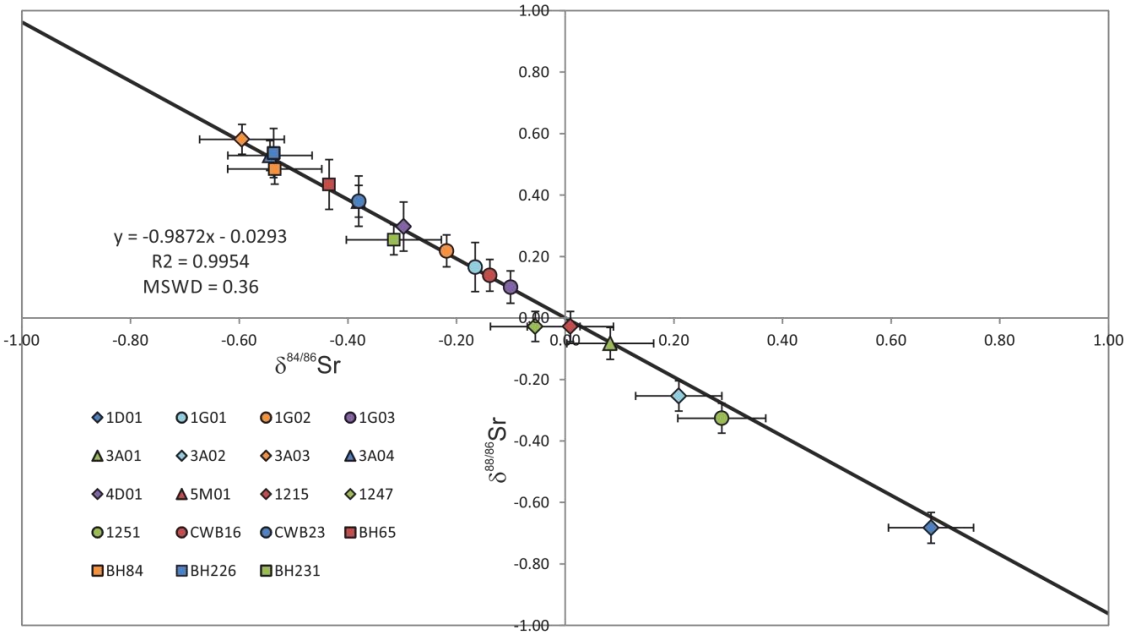

Figure 7.3: *Whole-rock Sr isotope data for Himalayan leucogranites. Red circles indicate data obtained by TIMS (for which both $\delta^{88/86}$Sr and $\delta^{84/86}$Sr are available), green circles represent samples only measured by MC-ICP-MS. As no $\delta^{84/86}$Sr ratios are available for these samples, they are represented as lying on the mas-fractionation line. All data obtained by TIMS lie within error of this line.*

Radiogenic Rb-Sr data and isochrons ages for the four samples from which mineral separates were extracted are documented in Table 7.3. Of all mineral separates, plagioclase samples contain the lowest $^{87}Rb/^{86}Sr$ and $^{87}Sr/^{86}Sr$. K-feldspar samples yield higher $^{87}Rb/^{86}Sr$ ratios, and also more radiogenic $^{87}Sr/^{86}Sr$ ratios which are typically similar to the whole rock values from the same sample. Mica samples contain the highest $^{87}Rb/^{86}Sr$ ratios of between 329 and 387, and as such yield the most radiogenic $^{87}Sr/^{86}Sr$ ratios. 1G03, without a high Rb/Sr mica analysis, yields an imprecise age of 21 ± 62 Ma, within uncertainty of the zircon crystallization age of 12.52 ± 0.19 Ma. An isochron of all phases from 3A03 yields an Rb-Sr age of 17.66 ± 0.31 Ma, within uncertainty of the zircon crystallization age of 18.00 ± 0.90 Ma. All phases from 1247 yield an Rb-Sr isochron age of 21.84 ± 0.45 Ma, similar (though outside of uncertainty) of the zircon crystallization age of 21.01 ± 0.21 Ma. The Rb-Sr isochron of all phases from 1251 yields an age of 7.80 ± 1.30 Ma, significantly different from the zircon crystallization age of c. 14.0 Ma.

7.4. Discussion of stable Sr data

7.4.1. Comparison between techniques

Figure 7.2 compares $\delta^{88/86}Sr$ data for the same samples measured by both TIMS double spiking and MC-ICP-MS Zr-doping methodologies. The variation from the 1:1 line is most likely caused by a difference in mass bias during analysis of samples by MC-ICP-MS and suggest that data gathered by this method have the potential to be less accurate. Both precision and accuracy for TIMS measurements are generally better by virtue of the very long count times employed, and the predictability of the mass fractionation behaviour of samples and standards run at the same load size.

7.4.2. Strontium stable isotope variations in whole-rock Himalayan leucogranites

Data for whole rock samples are displayed on Figure 7.3, a three-isotope plot of $\delta^{88/86}$Sr vs $\delta^{84/86}$Sr. The kinetic mass-fractionation line is also added for reference, and as all TIMS samples (red circles) lie within uncertainty of this line, it is clear that fractionation is caused by mass-dependent processes. Also plotted on Figure 7.3 are data obtained by MC-ICP-MS (green circles), though since only $\delta^{88/86}$Sr data are available for these samples, they are plotted as lying on the mass fractionation line for comparison purposes. Total variation across all samples is 1.26‰, far larger than previously recorded terrestrial data (total variation observed by Charlier et al., 2012, is 0.5‰). Also unlike previous terrestrial data published by Charlier et al. (2012), whole rock data obtained in this study appear to fractionate to both heavier and lighter $\delta^{88/86}$Sr values than the bulk silicate Earth (BSE) value of 0.3‰. This suggests that feldspar fractionation and removal of heavier Sr cannot solely be responsible for the $\delta^{88/86}$Sr signatures observed and other processes need to be invoked.

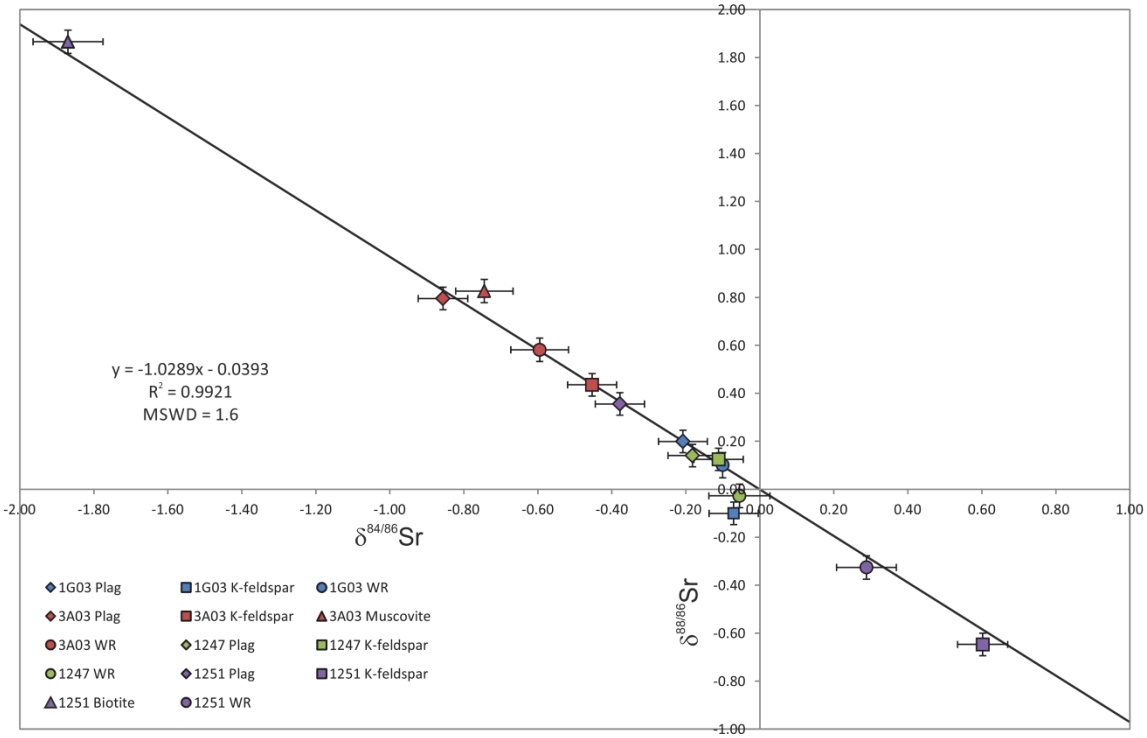

Figure 7.4: *Stable Sr data for mineral separates and whole rocks from which they were extracted. All samples except for 1G03 K-feldspar lie within error of the kinetic mass-fractionation line.*

7.4.3. Stable isotope fractionation during crystallization

In order to gain insight into the factors causing the $\delta^{88/86}$Sr variations seen in whole rocks, the Sr isotopic compositions of mineral separates were determined using the TIMS and double spike techniques. A second three-isotope plot (Figure 7.4) shows mineral separate and whole rock data for four samples, and displays variations larger than those observed in whole rock data. It is again clear that mass-dependent fraction is driving variation, and the data are better compared in Figure 7.5. In three of the four samples, the pattern of fractionation between minerals is consistent, the exception being sample 1247, where plagioclase, K-feldspar and whole rock are virtually indistinguishable. In the three other samples, plagioclase appears to be enriched in heavier Sr, relative to whole-rock, whereas K-feldspar is universally lighter. Muscovite and biotite were only available in sufficient quantity in one sample each, and in both cases display enrichment in heavier Sr isotopes. In sample 3A03, muscovite records a similar $\delta^{88/86}$Sr as plagioclase whereas biotite in sample 1251 records a $\delta^{88/86}$Sr = 1.87, an enrichment of 2.20‰ relative to the sample's whole-rock signature.

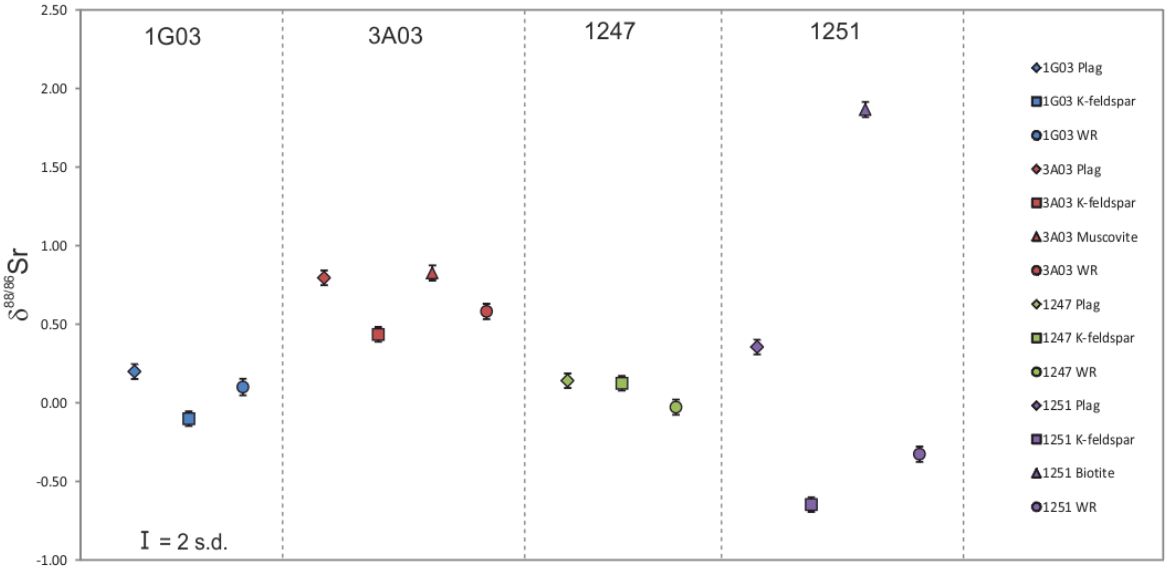

Figure 7.5: *Whole rock and mineral separate $\delta^{88/86}$Sr data for the four samples from which mineral separates were extracted. Significant variation occurs within all samples with the exception of 1247. In 1G03, 3A03 and 1251, plagioclase and micas are always isotopically heavier than the whole rock value, whereas K-feldspar is always isotopically lighter.*

The consistent pattern observed between plagioclase and K-feldspar relative to whole-rock suggest that it is crystallization that drives the variations observed in Sr isotopes. This finding is therefore consistent with the conclusion inferred from other igneous rocks that $\delta^{88/86}$Sr is reduced by feldspar fractionation (Charlier et al., 2012). As plagioclase crystallizes it preferentially takes in heavier Sr, and thus if it is removed from an igneous system then the resultant felsic rock will be isotopically lighter.

This theory, however, cannot entirely explain the $\delta^{88/86}$Sr signatures recorded by whole-rock Himalayan leucogranites. Pure feldspar fractionation would imply that those samples which are heavier than BSE are enriched in plagioclase, for which there is no evidence from the Eu anomalies of these rocks (see Chapter 3, and also Figure 7.6). It is more likely that the variations observed in whole-rock data are representative of either variations in the source or in the conditions of formation of these leucogranites, or a combination of both effects. The Greater Himalayan Series (GHS), from which they are entirely sourced, is a heterogeneous body made of up metasediments derived from a variety of sources, and also orthogneisses derived from granites. Little mafic material is observed, rendering it unlikely the GHS itself records a BSE signature of Sr isotopes. The mode of origin of these leucogranites may also cause variations in $\delta^{88/86}$Sr, even if the source does reflect BSE. Previous studies on the leucogranites of the Himalaya have concluded they most likely formed as vapour-absent melting of either muscovite or biotite during decompression, and may incorporate other minerals from the GHS during melting. Therefore a small-scale melt with little incorporation of other phases would likely be enriched in heavier isotopes of Sr, but should the source be rich in K-feldspar which also enters the melt, then a lighter $\delta^{88/86}$Sr signature would result.

7.4.4. The use of the stable Sr system as a tracer of igneous events.

The evidence that Sr experiences mass-dependent isotopic fractionation during melting and crystallization highlights the possibility that the stable Sr isotopic content of a sample can reveal information about its igneous history. Two main factors are important in determining the Sr composition of a rock: source and petrogenetic history.

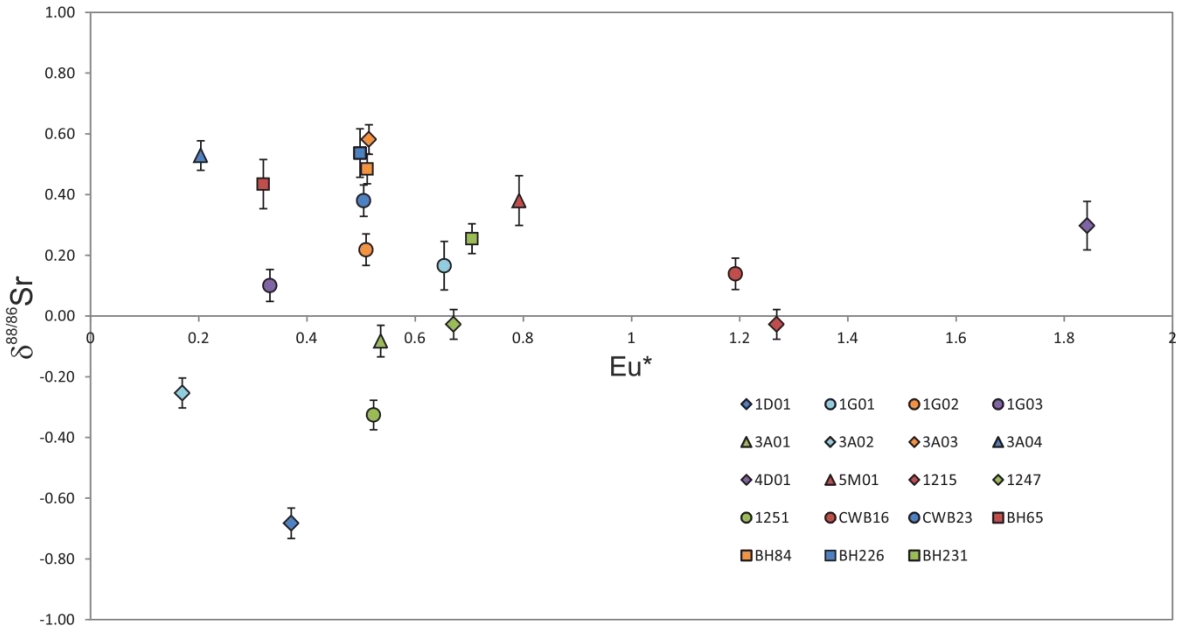

Figure 6: *$\delta^{88/86}$Sr plotted against europium anomaly. Note the absence of correlation.*

Within the GHS there are two main lithologies from which melts may be derived – metasediments and orthogneisses. Orthogneisses are metamorphosed from granites that intruded the proto-GHS at ~500 Ma. The metasediments are of sedimentary origin, derived from a variety of sources based on their detrital zircon core populations. They are derived in part from granites of the same igneous event as the orthogneisses (at ~500 Ma), with other core populations at ~900 Ma and ~1800 Ma. The orthogneisses of the GHS typically have significant Eu anomalies (0.2 – 0.5, Zhang et al., 2004), indicating that they have undergone feldspar fractionation at some point in their history. As such, their bulk rock stable Sr isotopic signatures are likely to be lighter than surrounding metasediments, and therefore any leucogranites derived from them will also inherit this light signature.

It may be possible, therefore, to observe a correlation between whole-rock leucogranite stable Sr signatures and zircon core population. Such a plot is shown in Figure 7.7, for those samples for which both stable Sr and zircon core analyses have been performed. There is some correlation apparent, with the four lightest samples yielding predominantly 550 – 450 Ma core populations, while the zircon cores from the two heaviest samples yield a majority ~900 Ma population.

However, more ages from zircon cores are required to substantiate this correlation - samples 3A03, 1247 and CWB16 yielded only 5, 6 and 6 zircon core analyses, respectively. Of the two heavier samples (i.e., with a bulk rock $\delta^{88/86}$Sr greater than +0.2) the heaviest (3A03) yielded only 5 core analyses, of which 3 (60%) were ~900 Ma. For 1G03, the second heaviest sample, 19 of the 26 (73%) cores were ~900 Ma in age, a greater proportion than for 3A03. These problems are caused, in part, by sampling strategy. During data acquisition, zircon core analysis was accidental and only a secondary consideration to the main objective of zircon rim geochronology. For this reason, more core analyses were performed on certain samples than for others.

However, petrogenesis adds another factor to whole-rock leucogranite stable Sr signatures, one that is largely unquantifiable without further study. All High Himalayan leucogranites analysed in this study were determined to have formed by vapour-absent muscovite breakdown, with the equation:

$$Mu + 0.18Pl + 0.18Q \rightarrow 0.6L + 0.38Ksp + 0.35Sil$$

Where Mu = muscovite, Pl = plagioclase, Ksp = K-feldspar, Sil = sillimanite, and L = liquid (from Whitney and Evans, 2010). In this reaction, muscovite and plagioclase are consumed to form melt, both of which tend to harbour isotopically-heavy Sr. Additionally, a bi-product of the reaction is K-feldspar, an isotopically-light mineral. Therefore the melt reaction on its own will tend to produce melts which are isotopically heavy for Sr. However it is probable that many High Himalayan leucogranites have incorporated at least some anatectic K-feldspar that formed in the melt reaction. This process will then lead to a reduction in the $\delta^{88/86}$Sr of the leucogranite. Quantifying such incorporation is difficult, as Eu anomaly is also affected by the specific source the leucogranite melted from as much as by feldspar fractionation or incorporation.

To summarise, leucogranite whole-rock stable Sr ratios are controlled by source, melt reaction and incorporation of restitic phases. The processes by which these factors affect the resultant

$\delta^{88/86}$Sr of a leucogranite are described above, and allow for the possible use of stable Sr ratios as a tracer of igneous processes. However, further work is needed to understand the isotopic composition of the specific sources of melting (GHS and LHS metasediment, and orthogneiss) and the mineral phases therein before further conclusions can be reached.

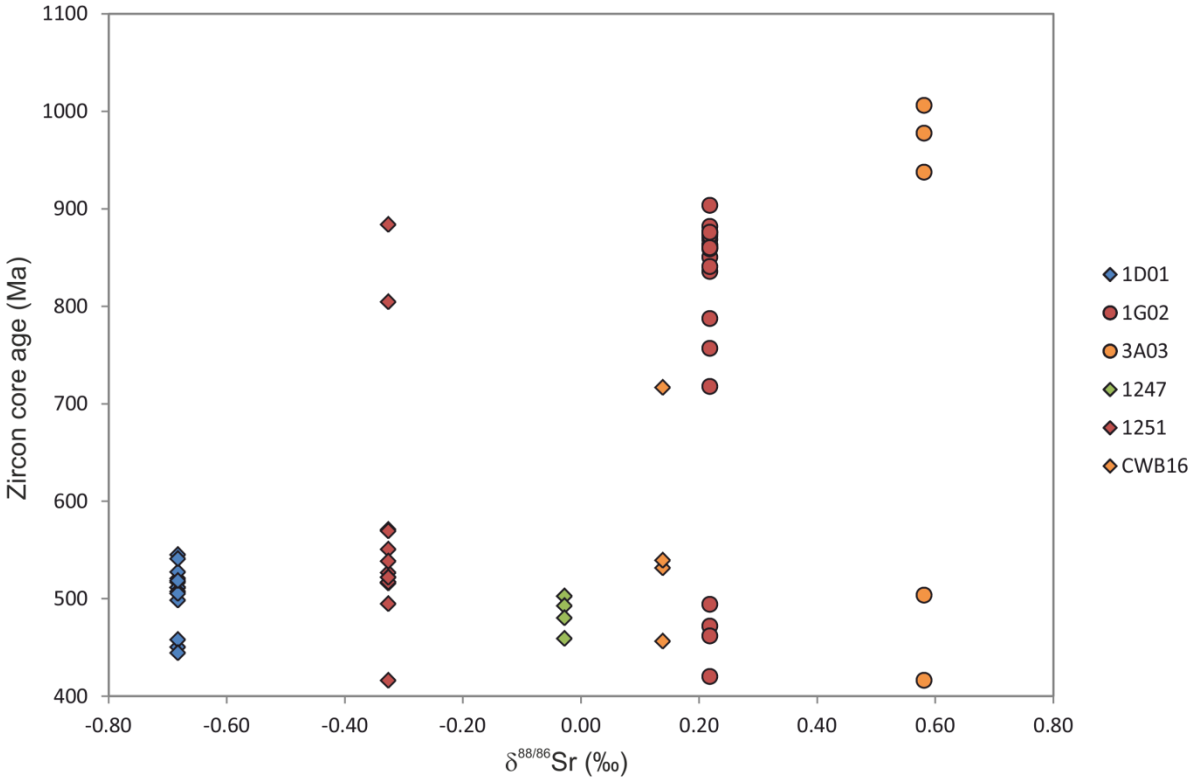

Figure 7.7: *$\delta^{88/86}$Sr for whole rock samples for which zircon core data is available. Those samples with predominantly 550-400 Ma zircon cores record lighter Sr isotopic values, while the two samples with a majority of 900-800 Ma cores yield the heaviest $\delta^{88/86}$Sr values.*

7.5. Implications of Rb isotope data

Stable Rb variations are shown in Figure 7.8. The total variation in $\delta^{87/85}$Rb is 0.5‰, from -0.39 to +0.11. While consistent patterns were discernible between mineral phases in the Sr data, no such patterns can be observed in the Rb data. Two samples, 3A03 and 1251, yield indistinguishable $\delta^{87/85}$Rb values across all mineral phases. 1251 is also the only sample for which isotopic values are heavier than BSE, while all other samples and mineral separates are lighter by between 0.1 and 0.4‰. In sample 1G03, plagioclase and whole rock $\delta^{87/85}$Rb values

are indistinguishable, while K-feldspar is 0.2‰ lighter. The lightest phases in sample 1247 are plagioclase and K-feldspar, which both yield $\delta^{87/85}$Rb values of -0.38. The whole rock $\delta^{87/85}$Rb value is 0.12‰ heavier, while muscovites from this sample yield $\delta^{87/85}$Rb values of -0.09.

While no consistent patterns can be seen in stable Rb data to suggest a systematic fractionation of heavier Rb into specific minerals (as observed in stable Sr data), the individual data obtained in this part of the study are precise enough (0.05% 2 s.d.) to suggest stable Rb variations up to a magnitude of 0.5‰ can be observed in nature. This variation could have implications for Rb-Sr geochronological studies, where any deviation in the stable Rb ratio of a sample could have a large impact on ages calculated from the decay of Rb.

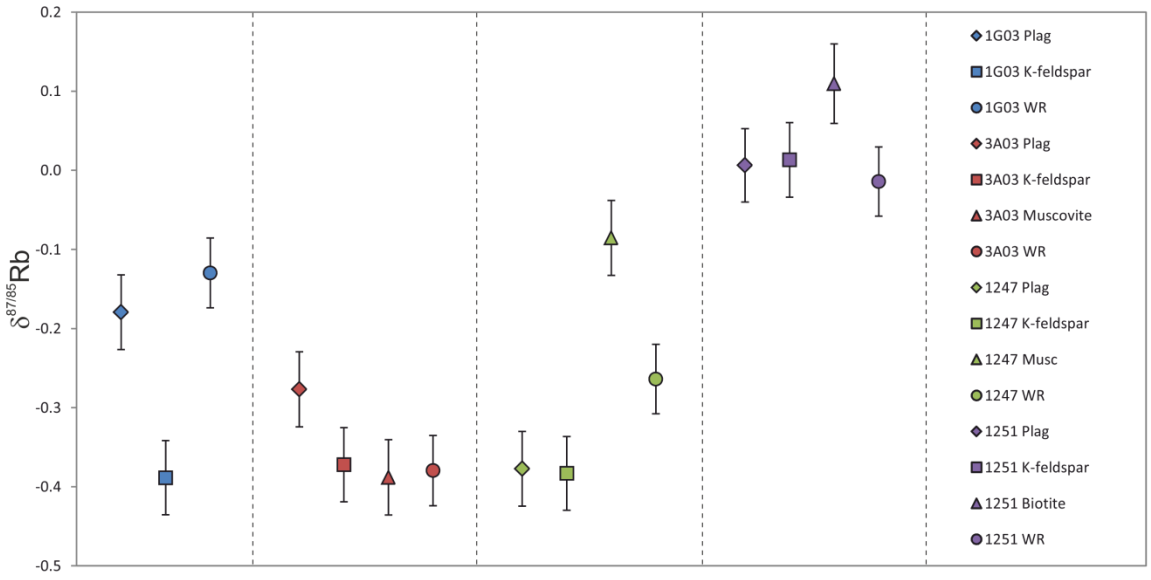

Figure 8: *Plot of stable Rb data of all mineral separate and whole rock samples. Uncertainties are quoted at 2 standard deviations.*

Table 7.3: Rb-Sr geochronology data

		1G03			3A03				1247				1251				
		Plag	K-spar	Whole-rock	Plag	K-spar	Musc	Whole-rock	Plag	K-spar	Musc	Whole-rock	Plag	K-spar	Biotite	Whole-rock	
	$^{87}Rb/^{86}Sr$	3.0679	17.0944	14.8063	7.4771	218279	387.07	213545	5.0616	33.0998	335.76	23.8396	2.3133	1149	329.40	8.8950	$^{87}Rb/^{86}Sr$
	2 s.d.	0.0920	0.5128	0.4442	0.2243	0.6548	0.0271	0.6406	0.1518	0.9930	0.0319	0.7152	0.0694	0.3448	0.0368	0.2669	2 s.d.
	$^{87}Sr/^{86}Sr$	0.806676	0.811537	0.809259	0.774141	0.777100	0.868988	0.777162	0.758335	0.764530	0.860772	0.762264	0.827008	0.830912	0.864035	0.829544	$^{87}Sr/^{86}Sr$
	2 s.d.	0.000020	0.000020	0.000035	0.000020	0.000020	0.000021	0.000035	0.000020	0.000020	0.000035	0.000035	0.000020	0.000020	0.000023	0.000035	2 s.d.
	Age	-	-	-	17.59	17.72	-	17.68	21.81	22.39	-	22.24	7.91	7.34	-	7.58	Age
Two-point	2 s.d.	-	-	-	0.01	0.03	-	0.03	0.01	0.07	-	0.05	0.01	0.00	-	0.01	2 s.d.
with	$^{87}Sr/^{86}Sr_i$	-	-	-	0.772273	0.771610	-	0.771800	0.756767	0.754000	-	0.754730	0.826746	0.829714	-	0.828586	$^{87}Sr/^{86}Sr_i$
mica	2 s.d.	-	-	-	0.000060	0.000170	-	0.000170	0.000051	0.000340	-	0.000240	0.000021	0.000042	-	0.000046	2 s.d.
	Age	-	-	2100	-	-	-	17.66	-	-	-	21.84	-	-	-	7.80	Age
All	2 s.d.	-	-	62.00	-	-	-	0.31	-	-	-	0.45	-	-	-	1.30	2 s.d.
phases	$^{87}Sr/^{86}Sr_i$	-	-	0.805700	-	-	-	0.771910	-	-	-	0.756600	-	-	-	0.827500	$^{87}Sr/^{86}Sr_i$
	2 s.d.	-	-	0.005000	-	-	-	0.000870	-	-	-	0.001700	-	-	-	0.003600	2 s.d.
Zircon	Age	-	-	12.52	-	-	-	c. 18 Ma	-	-	-	21.01	-	-	-	c. 14.0 Ma	Age
U-Pb	2 s.d.	-	-	0.19	-	-	-		-	-	-	0.21	-	-	-		2 s.d.

7.6. Discussion of Rb-Sr geochronology data

Rb-Sr isochron and zircon U-Pb ages are presented in Table 7.3, together with zircon U-Pb crystallization ages for samples 1G03, 3A03, 1247 and 1251. Isochrons are shown in Figure 7.9. Two-point isochron ages are given when anchoring feldspar or whole rock data with mica, due to the extreme $^{87}Rb/^{86}Sr$ and $^{87}Sr/^{86}Sr$ ratios of muscovite and biotite. Additionally, ages calculated using all phases are also presented. Due to the similarity in parent-daughter ratio, and therefore the resultant unreliability in calculating ages, two-point isochrons using feldspars and whole rocks only have not been calculated. However, 1G03 has only one calculated age using all phases, which is highly imprecise (21 ± 62 Ma) due to the lack of an analysed mica phase. In contrast, all isochrons involving mica (samples 3A03, 1247 and 1251) yield higher precision than for 1G03, and ages for 3A03 and 1247 are all within uncertainty of the zircon U-Pb age.

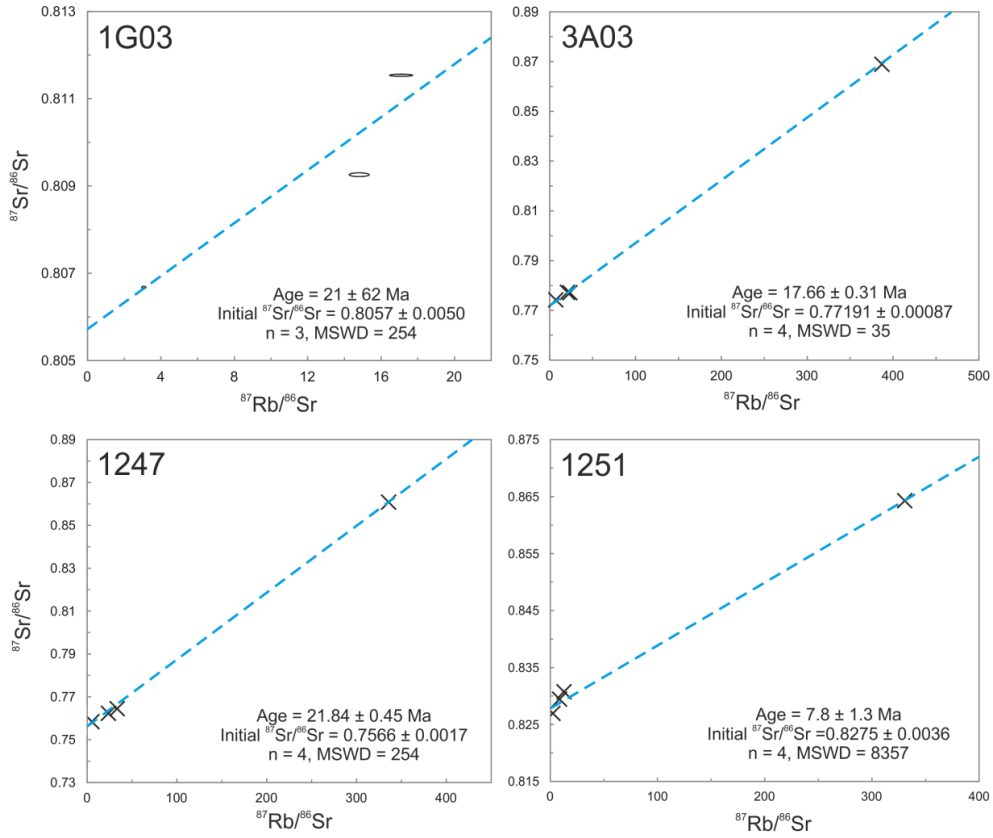

Figure 7.9: *Rb-Sr isochrons for all phases in all samples. Error ellipses are shown in 1G03, while data are marked by crosses in other samples.*

For sample 1251, the isochron age of 7.8 ± 1.3 Ma is significantly younger than the zircon U-Pb age of c. 14.0 Ma. This disparity in ages could indicate a post-crystallizational event at 7.8 Ma, which may have served to homogenise the $^{87}Sr/^{86}Sr$ ratio across all mineral phases, effectively resetting the Rb-Sr chronometer and potentially also disturbing the stable isotope systematics. 1251 is 0.4‰ lighter than all other samples in its $\delta^{87/85}Rb$ ratio, and also expresses the largest variation in $\delta^{88/86}Sr$ (2.51‰) across all mineral phases, setting this sample apart from others. Although there is limited petrographic evidence for such fluid activity, there is evidence for post-crystallizational metamorphism, with sillimanite nucleating on earlier biotite (Figure 7.10). Therefore it is possible that the young Rb-Sr isochron age could reflect the timing of a re-heating event at ~7.8 Ma, while the zircon crystallization age was unaffected by such activity. Another possibility is that some of the minerals are xenocrysts, with different chemical characteristics than their igneous counterparts, although this is unlikely given the homogeneity observed in $\delta^{87/85}Rb$ across all mineral phases.

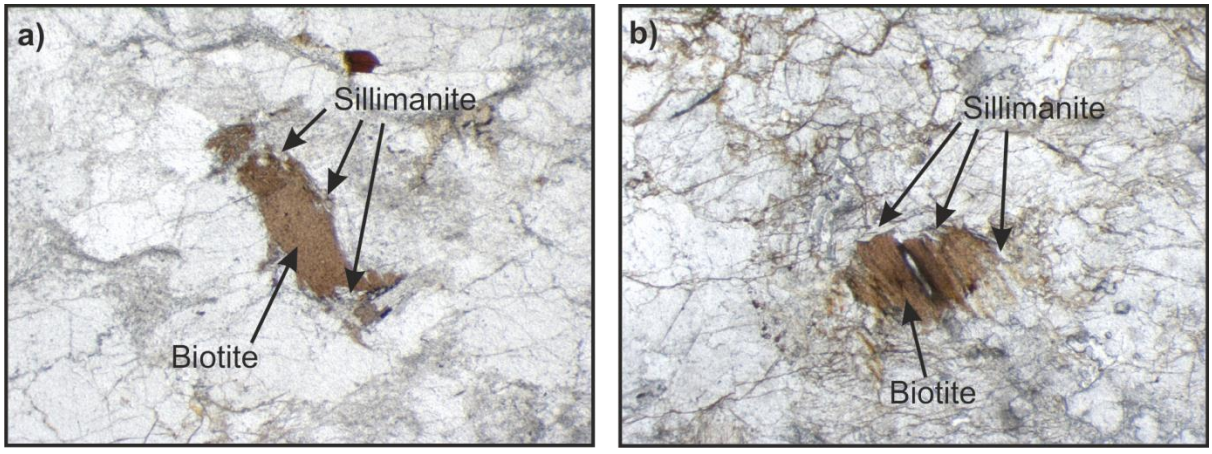

Figure 7.10: *a) and b): Examples of sillimanite growth nucleating on pre-existing biotite grains in sample 1251, providing evidence of post-crystallizational metamorphism.*

7.7. Effects of stable isotope fractionation on Rb-Sr geochronology

Stable Rb and Sr isotope variations not only provide insights into the petrogenetic origin of these rocks but also carry implications for geochronology using the Rb-Sr decay system.

One of the fundamental tenets of isochron dating in any radiogenic isotope system is that the suite of cogenetic rocks (or minerals within a rock) used to construct an isochron crystallised at the same time and with the same radiogenic isotope ratio. In other words, they should possess the same initial ratio at t = 0 and form a horizontal line on a plot of parent-daughter ratio versus radiogenic isotope ratio (Figure 7.9). If mass-dependent stable isotopic fractionation occurs during crystallisation, then this fundamental assumption is not met, and in the case of the strontium system, any measured variation in $^{88}Sr/^{86}Sr$ ratios will also be present in the radiogenic $^{87}Sr/^{86}Sr$ ratio at half the magnitude; for example, if a sample has a $\delta^{88/86}Sr$ value of +1‰, then the internal fractionation correction will ultimately lead to an underestimate of the $^{87}Sr/^{86}Sr_i$ ratio by 0.5‰. Thus, although the minerals crystallised at the same time, they will possess different true $^{87}Sr/^{86}Sr_i$ ratios.

This is shown schematically in Figure 7.11. In this example, two phases (one at low $^{87}Rb/^{86}Sr$, e.g. feldspar, and one at high $^{87}Rb/^{86}Sr$, e.g. mica) are considered, both of which have experienced some mass-dependent fractionation. During crystallization, if no stable isotope fractionation occurs, then all phases should contain identical $^{87}Sr/^{86}Sr$ ratios, as indicated by the horizontal blue line. However, if the low $^{87}Rb/^{86}Sr$ phase is enriched in lighter isotopes and the high $^{87}Rb/^{86}Sr$ phase enriched in heavier isotopes due to mass-dependent fractionation during crystallization, then the minerals define an apparently positive age, as indicated by the green line. Conversely, should the low Rb/Sr phase (feldspar) be enriched in heavier isotopes and the high Rb/Sr phase (mica) enriched in lighter isotopes, an apparently negative age would be calculated, as indicated by the red line. This initial deviation in $^{87}Sr/^{86}Sr$ ratios will cause an absolute offset from the true isochron age, regardless of the actual age of the sample.

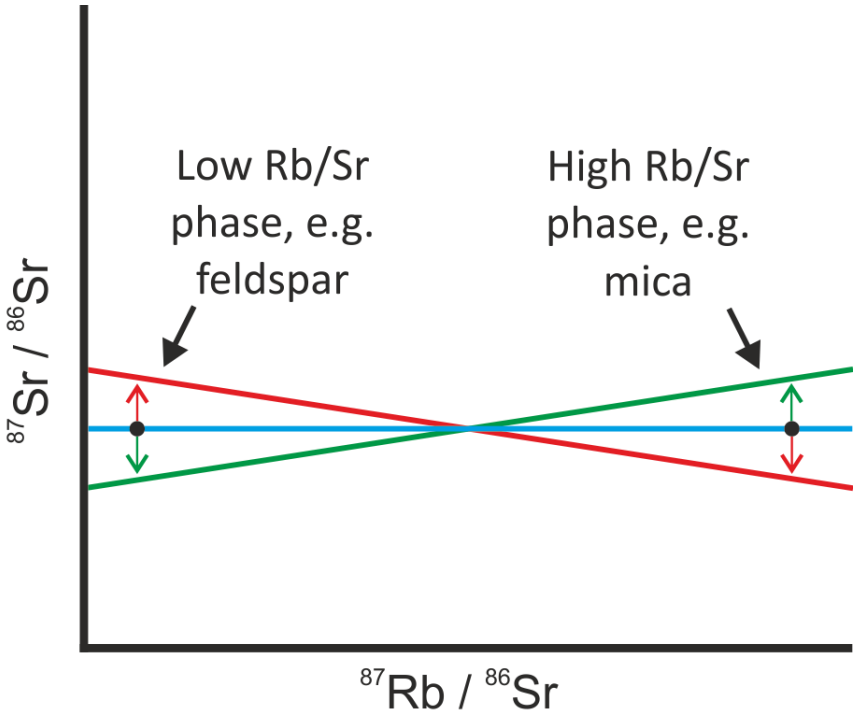

Figure 7.11: *Schematic diagram showing the effects of potential isotopic fractionation of phases during crystallization. Blue line indicates regular starting composition of different phases in a rock, while green and red lines show the effects of possible mass-dependent fractionation during crystallization.*

At face value, such variations in the true isotope ratios produced via double spiking techniques should produce inaccurate ages. However, it is worth considering in this context whether the double spike 'absolute' ratios are useful for isochron work. The radiogenic ($^{87}Sr/^{86}Sr$) ratio measured by double spike or doping methodologies includes the combination of both the radiogenic effect, and the effects of mass dependent fractionation, induced both in nature and in the mass spectrometer (Neymark et al., 2014). As mentioned earlier, the conventional method of analysing Sr isotope compositions (either by MC-ICP-MS or TIMS) is to correct instrumental mass fractionation through normalisation to a fixed $^{88}Sr/^{86}Sr$ ratio (e.g. Thirlwall, 1991). Given that this fractionation is mass-dependent, then this correction to a fixed value will correct for any mass-dependent isotope fractionation, regardless of its origin (geological or instrumental). The net effect of this correction is that the analyses defining the isochron are normalised to a common value (at t = 0, the horizontal blue line in Figure 7.11) and can therefore be used for

direct comparison with one another and used in turn to calculate an age after a period of radiogenic ingrowth has occurred.

The choice of $^{88}Sr/^{86}Sr$ value used for correction is essentially arbitrary, but the use of a value that is agreed upon in the geochronological community (Berglund and Wieser, 2011) permits ratios to be compared between different labs and instruments. However, in the context of correcting for stable isotope variations (instrumental or geological), the assumption of a fixed value could lead to a slight 'mis-correction'. This would have no effect on the slope of an isochron (and therefore the resultant age), but could have ramifications for the initial $^{87}Sr/^{86}Sr$ ratio of the rock and therefore on any chronology based on the evolution of initial ratios between rocks with disparate degrees of mass-dependent fractionation.

It is therefore recommended that for accurate internal isochron ages and chronology using only initial $^{87}Sr/^{86}Sr_i$ ratios, double spike or doping procedures are followed, but for internal isochrons, conventionally internally normalised data are sufficient.

Variations in the stable $^{87}Rb/^{85}Rb$ ratio can also have an effect on the calculated age of a sample. As ^{87}Rb decays to ^{87}Sr and causes its build up over time, any over- or under-estimation of the concentration of ^{87}Rb in a sample will cause a recorded age to be too old or young, respectively. This is because the isotope dilution (ID) calculations are based on the addition of a known amount of enriched spike (with a known isotopic composition) to a known amount of sample, where the assumption is that the Rb isotopic composition in the sample is considered as natural ($^{85}Rb/^{87}Rb$ = 2.59265, IUPAC value, Berglund and Wieser, 2011). As was shown earlier (Section 7.5), samples analysed here exhibit a range of Rb isotope ratios, and thus the assumption that the sample Rb has a fixed 'natural' composition is invalid for the purpose of the ID calculations.

In order to demonstrate these effects, data from plagioclase and muscovite (the two most disparate in their Rb/Sr ratios) of sample 3A03 were examined in detail (Table 7.4). Muscovite ^{87}Rb concentrations and $^{87}Rb/^{86}Sr$ ratios as derived from ID calculations have been tabulated

based on varying the natural $^{87}Rb/^{85}Rb$ ratio used in the ID calculations by 0.5‰ above and below the natural ratio (the maximum deviation seen in Bhutanese leucogranite samples). Simple two-point isochron ages then were calculated using the plagioclase and muscovite data.

	Plagioclase		Muscovite					
	^{87}Rb (mol/g)	$^{87}Rb/^{86}Sr$	^{87}Rb (mol/g)	$^{87}Rb/^{86}Sr$	Age (Ma)	2 s.d.	$^{87}Sr/^{86}Sr_i$	2 s.d.
Natural ratios	3.873×10^{-8}	7.483	2.000×10^{-6}	386.4	17.626	0.012	0.772268	0.000060
Plag -0.5‰, Musc +0.5‰	3.872×10^{-8}	7.480	2.006×10^{-6}	387.6	17.570	0.012	0.772275	0.000059
Plag +0.5‰, Musc -0.5‰	3.875×10^{-8}	7.485	1.993×10^{-6}	385.2	17.683	0.012	0.772262	0.000060

Table 7.4: *Variations in molar concentration of ^{87}Rb, $^{87}Rb/^{86}Sr$ ratios and age based on modelled $\delta^{87/85}Rb$ variations in mineral separates of sample 3A03. Ages were calculated using two-point isochrons between plagioclase and muscovite.*

While changing the $^{87}Rb/^{86}Sr$ ratio had limited effect on the resultant $^{87}Sr/^{86}Sr_i$ ratio, it did have a more significant effect on the slope of the isochron, and hence the age. A combination of isotopically light plagioclase and heavy muscovite caused a decrease in the calculated age by 0.056 Myr, while a similar increase in the age is seen when using heavier plagioclase and lighter muscovite. Although small, this change exceeds the nominal uncertainty on the isochrons (± 0.12 Myr) for this system and highlights the requirement of determining stable Rb isotopic signatures for accurate Rb-Sr geochronology. This is particularly true for very young and/or highly evolved rocks (e.g., Davies and Halliday, 1998).

7.8. Conclusions

1. Highly precise $^{88}Sr/^{86}Sr$, $^{87}Sr/^{86}Sr$ and $^{84}Sr/^{86}Sr$ ratios can be obtained using a double-spike TIMS method, to a precision of 0.05‰ and 0.08‰ respectively.

2. $\delta^{88/86}Sr$ values of High Himalayan leucogranites vary from +0.58 to -0.68 (a total range of 1.26‰), with samples found that are both heavier and lighter than BSE (+0.3‰). This is a greater variation than has been previously recorded in terrestrial rocks (cf. 0.5‰; Charlier et al., 2012).

3. $^{88}Sr/^{86}Sr$ and $^{84}Sr/^{86}Sr$ ratios can undergo mass-dependent fractionation during magmatic processes. Plagioclase feldspar and micas preferentially incorporate heavier Sr, whereas K-feldspars incorporate lighter Sr. Total fractionation among the minerals within a single sample can be as large as 2.51‰ $\delta^{88/86}Sr$, leading to variations in $\delta^{88/86}Sr$ measurable at the whole-rock scale.

4. Bulk variations in stable Sr signatures are able to survive multiple melting events and potentially offer a means of determining the source of a melt, particularly for sediment-derived granites.

5. Highly precise $^{87}Rb/^{85}Rb$ ratios can be determined by MC-ICP-MS using admixed Zr to a precision of 0.05‰.

6. $\delta^{87/85}Rb$ values of whole rock High Himalayan leucogranites and mineral separates vary between -0.39 and +0.11, a total variation of ~0.5‰. While this total variation is similar to that observed by Nebel et al. (2005), the increased precision of data presented here demonstrates that the $^{87}Rb/^{85}Rb$ ratio is variable in nature.

7. Rb isotopic fractionation may affect the calculated concentration of Rb in the sample. This in turn results in an over- or under-estimation of the amount of radioactive ^{87}Rb available for decay to ^{87}Sr leading to erroneous age calculations. These deviations may be greater than the uncertainty on individual age determinations.

8. Sr isotope data generated using double spike methodologies contain a mass fractionation component in addition to the radiogenic component. In geochronology, it is only of interest to compare the different degrees of ingrowth from Rb decay, and not mass fractionation processes in this context. Therefore, double spike $^{87}Sr/^{86}Sr$ data are not useful for chronological purposes, and conventional data (internally normalised to $^{86}Sr/^{88}Sr = 0.1194$) should be used instead.

9. For the correct interpretation of Rb-Sr ages derived from internal isochrons, it is important to fully understand the stable isotopic compositions of Rb and Sr within the sample. It is recommended that future Rb-Sr geochronological studies employ conventionally internally normalised Sr data for isochron work, allied to Zr-doped MC-ICP-MS for Rb data.

The fresh insights afforded by double spike methodologies demonstrate the potential for the strontium isotope system in tracking processes that cause stable isotope fractionation, in addition to the conventional use of the $^{87}Sr/^{86}Sr$ as a geochemical tracer and for high-precision geochronological work.

Chapter 8

Conclusions, synthesis and future work

8.1. Petrogenesis of leucogranites

Consistent with previous studies of the formation of the High Himalayan leucogranites, large ion lithophile element concentrations show that all leucogranites analysed in this study formed by vapour-absent muscovite melting. Crystallization temperatures, as modelled from whole-rock Zr and REE concentrations, were between 640 and 760°C, consistent both with previous studies and with the vapour-absent muscovite breakdown reaction.

Also consistent with previous studies, radiogenic Sr, Nd and Pb isotopic analyses of whole-rock leucogranites show that the majority of leucogranites fall within the GHS field, indicating that it is the likely melt source. However, some leucogranites yield Sr and Nd isotopic ratios that are more radiogenic than the GHS, with the majority of these falling into the LHS field. This suggests that for these leucogranites at least some portion of their source material was derived from the LHS.

This finding is supported by zircon isotope geochemistry. U-Pb and Hf isotopes were analysed in zircon rims from 12 leucogranites and zircon cores from 8 samples. Zircon rims recorded leucogranite crystallization ages from 31.2 Ma to 11.7 Ma, a longer period than has previously been observed in the region. Pre-Himalayan zircon cores fall into three main age categories: 550-400 Ma, 900-800 Ma and ~1800 Ma. Cores from the 550-400 Ma category typically yield

εHf_t values between -10 and +5, while 900-800 Ma cores yield more negative εHf_t values between -15 and -5.

Zircon geochemistry shows a change in source, or in the balance between contributing sources, at 17 Ma. Samples which are older tend to yield more 550-400 Ma cores, and yield εHf_{20} values between -10 and -14. Samples younger than 17 Ma yield more 900-800 Ma and ~1800 Ma zircon cores, while their zircon rims yield increasingly more negative and radiogenic εHf_{20} values, as low as -23.1 (Figure 8.1). This suggests that after 17 Ma an increasing amount of older and more radiogenic material was being melted or entrained into melts.

Zircon crystallization age and average εHf_{20} values also show correlations when plotted against whole rock εNd_i. εNd_i decreases as average zircon εHf_{20} decreases, with both values becoming more negative in younger samples. As lower εNd_i values are found only in LHS material, this finding suggests that the change in melt source may correlate with melting at the GHS-LHS boundary.

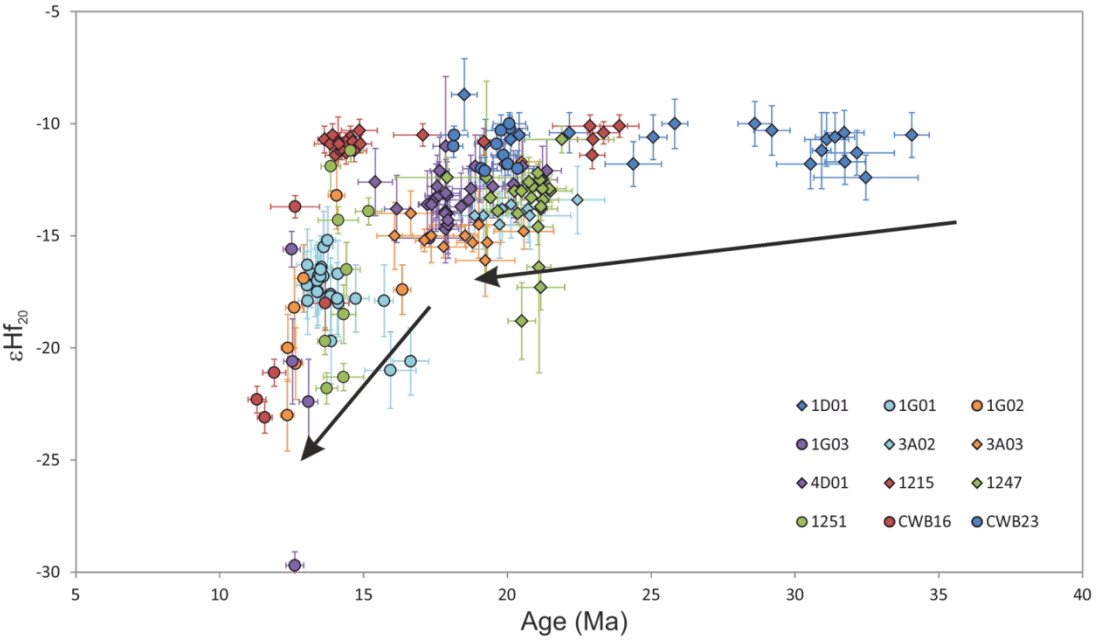

Figure 8.1: *Plot of age versus εHf_{20} values for Himalayan-aged zircon rims.*

This finding suggests that the locus of melting within the GHS dropped to the level of the Main Central Thrust (MCT) after 17 Ma, due to the increasingly more radiogenic isotope signatures in younger leucogranites. Models suggest that the GHS was extruded from deep beneath Tibet, with the LHS forming its footwall (Figure 8.2). The colder LHS cooled the lower portion of the GHS, explaining the inverted metamorphism sequence observed in structurally lower GHS metasediments (Mottram et al., 2016). The cooling effect would have decreased with depth, as the underlying LHS heats up through radioactive heat generation within the LHS and by convection from the 'hot iron' of the GHS above it. As the MCT zone heated up, the rocks around it would have acted less like a brittle fault and began to act more like a ductile fault. At this point, LHS material could easily have become entrained into the GHS and either melt or be incorporated into GHS melts, with 17 Ma marking the point where this process began. Figure 8.2 shows cross sections of the Himalaya over time, showing how this process could have occurred.

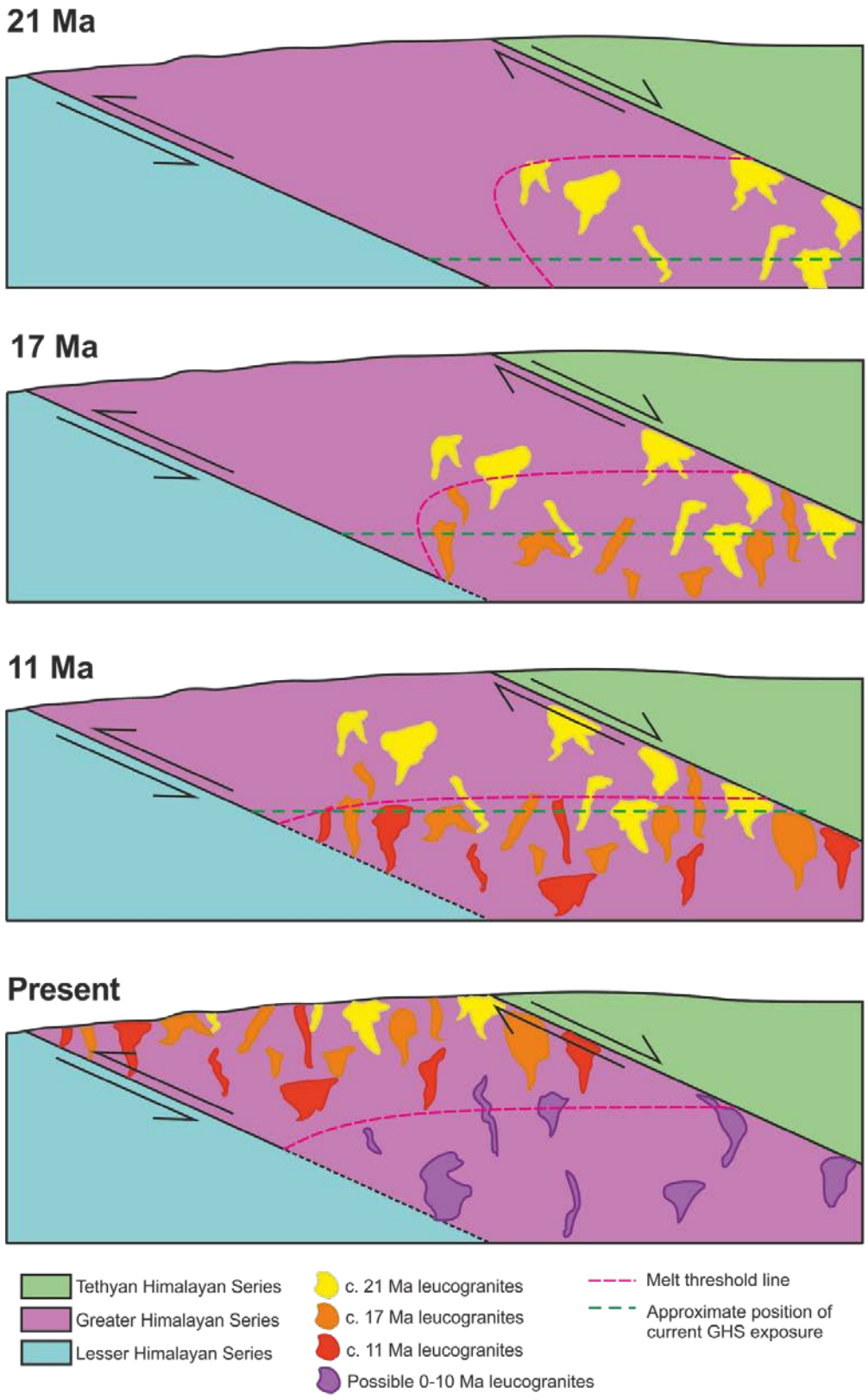

Figure 8.2: *Cartoon cross-sections of the Himalaya showing stages of evolution from 21 Ma to the present day. The movement of the upper limit of granite generation is shown, moving towards the LHS over time, with an increasing quantity of younger leucogranites generated at deeper structural levels of the GHS.*

One implication of this model is that leucogranites found in structurally-deeper parts of the GHS should tend to be younger and yield more radiogenic LHS-like isotopic values. Figure 8.3 shows that the deepest part of the GHS sampled during this study is along the Gasa – Laya transect, due to being farthest from the STD and within a large-scale synform fold (Greenwood et al., 2015). Leucogranites exposed in this transect are generally the youngest and most 'LHS-like' (in terms of isotopic characteristics) of those analysed in this study, while samples found within the STD zone typically yielded older ages and are more 'GHS-like' in their isotopic signatures. There are two major exceptions: sample 1D01 (south of Gasa) yielded an age of 31 Ma, and extreme isotope ratios that fall only in the GHS orthogneiss (as opposed to metapelite) field. Its age and petrography (presence of sillimanite and evidence of garnet resorption) suggest that this leucogranite formed from prograde melting of orthogneiss. CWB-23 (sampled near Laya) is the only sample yielding LHS Sr-Nd signatures that is older than 17 Ma (at 20 Ma). Apart from these two exceptions, there is strong correlation between leucogranite emplacement depth to age and isotopic chemistry is strong.

There are caveats to linking geochemistry to source region, however. The GHS and LHS Sr-Nd fields were constrained using samples from the central and western parts of the Himalaya, in Nepal and India. The same lithotectonic units in Bhutan, roughly 1000 km east of central Nepal, may contain Sr and Nd signatures different from those used to constrain source fields in this study. Therefore, while a change in source material after 17 Ma is suggested by these results, another possibility is that different, more radiogenic portions of the GHS were increasingly being melted over time, rather than showing increasing inclusion of LHS source material. However, given the lack of evidence of any GHS material as radiogenic as the leucogranites observed in this study, the most likely explanation is that it is LHS material that caused leucogranite Sr-Nd signatures to become more radiogenic.

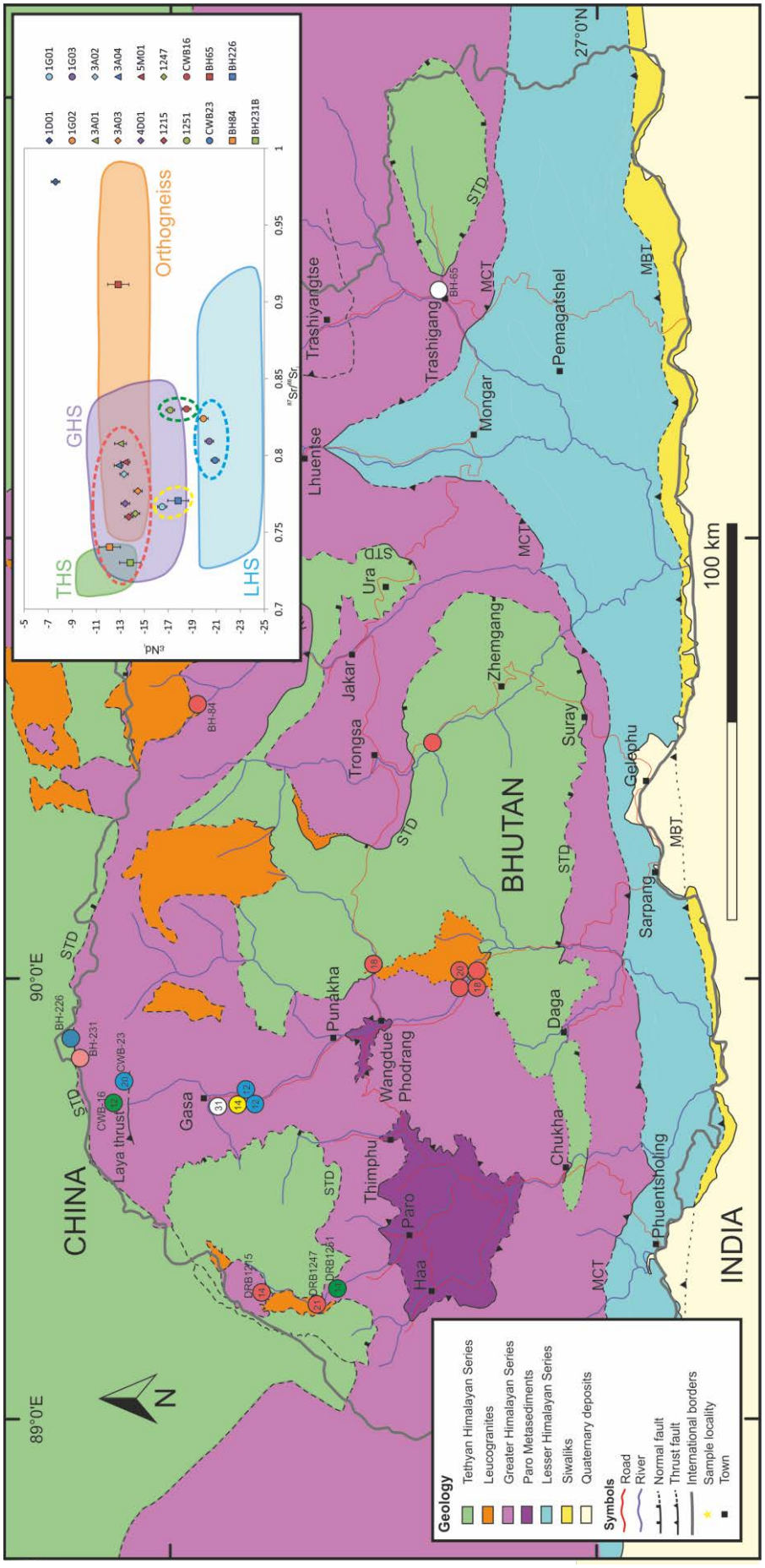

Figure 8.3: *Map of Bhutan showing samples for which whole-rock isotope data are available. Numbers within circles represent zircon crystallization age, if known. Circle colours are based on whole-rock Sr-Nd signatures, and are linked to the same-coloured dashed circles on the Sr-Nd plot (see inset). 1D01 and BH-65 are represented by white circles, as they fall outside of the main GHS and LHS fields.*

8.2. Mantle input into orogenesis

The combination of O, U-Pb and Hf isotope systematics, as derived from zircons, allows discrete contributions of mantle input into a granite to be identified. This in turn allows the quantity of mantle input during orogenic evolution to be estimated. These estimates, as derived from orogens such as the Caledonides (Appleby et al., 2010) allow the rates of crustal growth through time to be constrained (Kemp and Hawkesworth, 2006).

This study has provided conclusive isotopic proof that granite bodies may be sourced entirely from sediment, without any input from the mantle or igneous systems. The O, U-Pb, Hf data from zircons extracted from High Himalayan leucogranites has shown that these granites were sourced entirely from the metamorphic rocks in which they now sit (the GHS, with possible minor contributions from the LHS), with no input from mantle-derived sources (Figure 8.4). All zircons yield O-Hf isotopic compositions falling within the GHS field, or with more radiogenic values, with no samples lying on mixing lines with a mantle end-member. Thus the Himalayan leucogranites (virtually the only evidence for syn-orogenic magmatism in the Himalaya) contribute nothing to global crustal growth during the Himalayan orogeny.

While this is not the first evidence for pure sediment derived melts (migmatites in metasediments provide textural evidence), this study represents the first chemical evidence from a plutonic granite body using the O-Hf isotopic compositions of constituent zircons. A recommendation that follows from this work is that for future granite geochemical studies, 'end-member' S-type granites be defined as a rock with (i) zircon O-Hf isotopic signatures that lie entirely within error of those of its probable source, and (ii) where no mixing lines to mantle values are observed.

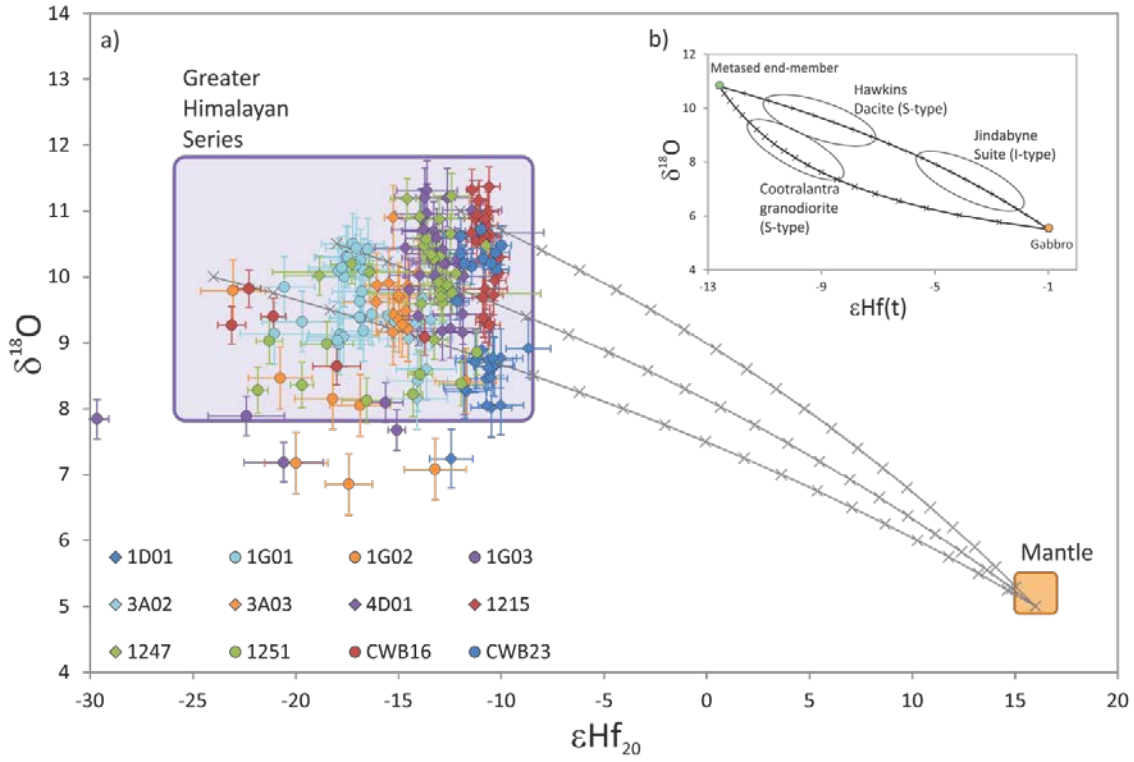

Figure 8.4: *$\delta^{18}O$-εHf_{20} isotope arrays for Oligocene to Miocene-aged zircons and zircon rims compared to possible mixing lines generated by binary mixing between potential GHS sources and the mantle (ticks show mixing at 5% intervals). The range of isotopic values from bulk rock GHS analyses (the likely source of melting) and the depleted mantle have also been plotted for reference. The GHS whole-rock εHf range is calculated from whole rock εNd (Harris and Massey, 1994) using the correlation of Vervoort and Blichert-Toft (1999). Whole-rock GHS $\delta^{18}O$ values are taken from Massey et al. (1994), and recalculated using the fractionation equation of Lackey et al. (2005) assuming 74% SiO_2 in the melt. For the mixing lines, mantle-like oxygen and hafnium isotopic values were used (Valley, 2003; Bouvier et al., 2008). The Xigaze ophiolite of southern Tibet was chosen to provide bulk-rock Hf abundances for a mantle-derived end-member of appropriate age (2.1 ppm, Pearce and Wanming, 1988; Malpas et al., 2003). There is no correlation between samples with the same symbol or colour. Error bars are 2σ for Hf and 2 s.d. for O.*

(b) Plot adapted from Kemp et al. (2006) highlighting one I-type and two S-type granites from the Lachlan fold belt, and mixing lines between potential metasedimentary and gabbroic end-members.

These findings have significant ramifications for understanding orogenic heat budgets. In the Himalaya, the majority of studies have proposed that collision occurred between 55 – 50 Ma (e.g. Najman et al., 2010), although others have suggested an age as young as ~34 Ma (Aitchison et al., 2007). Given that most High Himalayan leucogranite bodies formed at ~20 Ma, these models allow a timespan of either >30 Ma (for early Eocene collision) or ~14 Ma (for Eocene-Oligocene collision) between collision and melting. For widespread melting to have occurred in the mid-crust, temperatures must have reached at least ~700°C (Harris et al., 1995). Thermal models for orogenic evolution require at least 20 to 30 Ma between collision and melting for all realistic values of sedimentary thicknesses and heat production (England et al., 1992; Medvedev et al., 2006). Therefore the "young collision" model requires additional heat sources, such as advection from rising melts from the lower-crust or mantle, in order to shorten the timespan required for Early Miocene magmatism. This study proves that Himalayan leucogranites contain no mantle-derived input, and therefore fails to support the young collision model.

8.3. Stable isotope fractionation

The stable isotope ratios of both Sr and Rb, $^{88}Sr/^{86}Sr$ and $^{87}Rb/^{85}Rb$, respectively, have long been considered to be invariable. Recent studies, however, have shown variations in the $^{88}Sr/^{86}Sr$ isotope ratio in a variety of meteoritic and terrestrial samples (Moynier et al., 2010; Charlier et al., 2012), leading to the suggestion that variations in the $^{88}Sr/^{86}Sr$ ratio may be linked to feldspar fractionation in igneous systems (Charlier et al., 2012).

This study documents the largest stable Sr-isotope variations yet observed in terrestrial samples, with whole-rock High Himalayan leucogranites yielding $\delta^{88/86}Sr$ values between +0.58 and -0.68, a total range of 1.26‰. Larger variation is seen in mineral separates, up to 2.51‰. Consistent patterns in $\delta^{88/86}Sr$ variations are observed between the mineral phases of different samples, with K-feldspar yielding lower (and therefore are isotopically lighter) $\delta^{88/86}Sr$ values

with respect to the whole-rock, while plagioclase and micas yielded higher (are isotopically heavier) $\delta^{88/86}$Sr values than whole-rock (Figure 8.5). These data therefore suggest that mass-dependent fractionation of Sr isotopes occurs during melting and crystallization, and confirms the hypothesis that feldspar fractionation during igneous evolution causes whole-rock $\delta^{88/86}$Sr values to become lower and isotopically lighter.

While previous studies have found no deviation in the stable Rb ratio (e.g. Nebel et al., 2005), this study has found variations of up to 0.5‰ in $\delta^{87/85}$Rb values in both whole-rocks and mineral separates. Unlike Sr, no consistent patterns are observed between mineral phases and whole-rock measurements; however the findings do suggest that Rb isotopic fractionation can occur during melting and crystallization of felsic igneous rocks.

The stable Sr and Rb variations observed have ramifications for Rb-Sr geochronology. Stable Sr variations will not lead to incorrect age calculations, but may lead to inaccurate calculation of initial $^{87}Sr/^{86}Sr$ ratios. Stable Rb variations, however, will affect the calculated age of a sample, due to inaccurate calculation of isotope dilution measurements. The effect of a ± 0.5‰ variation in $\delta^{87/85}$Rb on a plagioclase-muscovite two-point isochron of sample 3A03 showed that such variations can affect the age by 0.056 Myr (0.3%), exceeding the uncertainty of each age calculation (± 0.012 Myr, 0.07%). Therefore for accurate ages and initial $^{87}Sr/^{86}Sr$ ratios, it is essential that the stable Rb and Sr isotopic ratios for all samples and mineral phases are ascertained.

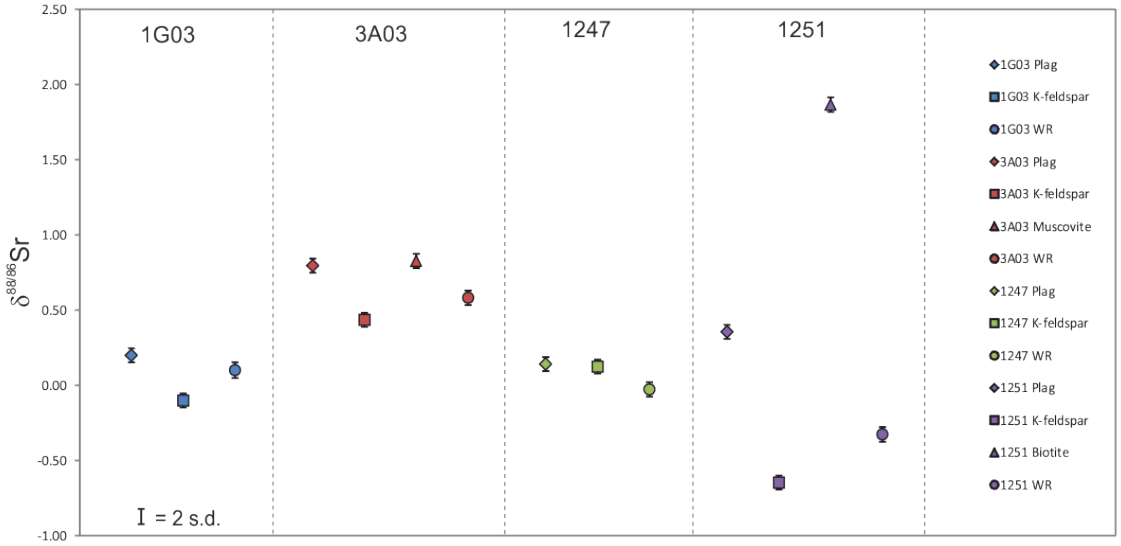

Figure 8.5: *Whole rock and mineral separate data for the four samples from which mineral separates were extracted. Significant variation occurs within all samples with the exception of 1247. In 1G03, 3A03 and 1251, plagioclase and micas are always isotopically heavier than the whole rock value, whereas K-feldspar is always isotopically lighter.*

8.4. Future work

This study has proved conclusively that the High Himalayan leucogranites represent both pure crustal melts and end-member S-type granites, with ramifications for both heat flow and timescales of collision within the Himalaya. The same combined O, U-Pb, Hf isotopic study applied to granites of other mountain belts would allow the amounts of mantle input to be calculated, and questions regarding heat flow and timescales of tectonic processes within the orogen to be addressed.

This study has also shown that stable isotope fractionation of both Sr and Rb is possible in igneous environments. For Sr, a consistent mass-dependent fractionation occurs between plagioclase, K-feldspar and mica. The consistency of this fractionation shows potential for stable Sr to be used as a tracer of igneous processes, since the whole-rock isotope signature will be a product of both source and the conditions during granite genesis. However, further work is needed to understand the stable Sr isotope signatures of the GHS, the main source of melting,

and its constituent mineral phases in order to investigate this process more thoroughly. Moreover, the causes of stable Rb fractionation remain unclear, since no consistent differences between coexisting mineral phases were observed. Further work on both source and granite is needed in order to constrain the mechanisms by which stable Rb fractionation operates.

This study has shown that 17 Ma marks a shift in leucogranite generation within the Bhutan Himalaya, as younger leucogranites start to yield more radiogenic isotope signatures. This time therefore marks a significant change in source chemistry, most likely to represent the melting or entrainment of LHS material within the High Himalayan leucogranites. In order to prove that LHS material contributed to leucogranite generation in Bhutan, further work is needed to characterise the Sr-Nd composition of both the GHS and LHS, as well as documenting their detrital zircon core age populations.

The findings made in this study regarding the age, source and location of leucogranites significantly improve our knowledge of the processes of crustal melting in the Himalaya. As leucogranites cause localised viscosity reduction, incorporating this more detailed knowledge into tectonic models of the orogen will improve our understanding of Himalayan tectonic evolution.

References

Ahmad, T., et al. 2000. Isotopic constraints on the structural relationships between the lesser Himalayan series and the high Himalayan crystalline series, Garhwal Himalaya. *Geological Society of America Bulletin,* **112,** 467-477.

Aitchison, J.C., Ali, J.R., & Davis, A.M. 2007. When and where did India and Asia collide? *Journal of Geophysical Research: Solid Earth*, **112**, B05423.

Albarède, F. 2004. The stable isotope geochemistry of copper and zinc. *Reviews in Mineralogy and Geochemistry*, **55**(1), 409-427.

Albarède, F., & Beard, B. 2004. Analytical methods for non-traditional isotopes. *Reviews in mineralogy and geochemistry*, **55**(1), 113-152.

Appleby, S. K. et al. 2010. Do S-type granites commonly sample infracrustal sources? New results from an integrated O, U–Pb and Hf isotope study of zircon. *Contributions to Mineralogy and Petrology* **160,** 115-132.

Atherton, M. P., & Ghani, A. A. 2002. Slab breakoff: a model for Caledonian, Late Granite syn-collisional magmatism in the orthotectonic (metamorphic) zone of Scotland and Donegal, Ireland. *Lithos*, **62**(3), 65-85.

Ayres, M., & Harris, N. 1997. REE fractionation and Nd-isotope disequilibrium during crustal anatexis: constraints from Himalayan leucogranites. *Chemical Geology*, **139**(1), 249-269.

Baker, J., Peate, D., Waight, T., & Meyzen, C. 2004. Pb isotopic analysis of standards and samples using a 207 Pb–204 Pb double spike and thallium to correct for mass bias with a double-focusing MC-ICP-MS. *Chemical Geology*, **211**(3), 275-303.

Bea, F., Montero, P., González-Lodeiro, F., & Talavera, C. 2007. Zircon inheritance reveals exceptionally fast crustal magma generation processes in Central Iberia during the Cambro-Ordovician. *Journal of Petrology*, **48**, 2327-2339.

Beaumont, C., Jamieson, R. A., Nguyen, M. H., & Lee, B. 2001. Himalayan tectonics explained by extrusion of a low-viscosity crustal channel coupled to focused surface denudation. *Nature*, **414**, 738-742.

Beaumont, C., Jamieson, R. A., Nguyen, M. H., & Medvedev, S. 2004. Crustal channel flows: 1. Numerical models with applications to the tectonics of the Himalayan-Tibetan orogen. *Journal of Geophysical Research: Solid Earth*, **109**(B6).

Berglund, M., & Wieser, M. E. 2011. Isotopic compositions of the elements 2009 (IUPAC Technical Report). *Pure and Applied Chemistry*, **83**(2), 397-410.

Böhm, F., Eisenhauer, A., Tang, J., Dietzel, M., Krabbenhöft, A., Kisakürek, B., & Horn, C. 2012. Strontium isotope fractionation of planktic foraminifera and inorganic calcite. *Geochimica et Cosmochimica Acta*, **93**, 300-314.

Boltwood, B. B. 1907. Ultimate disintegration products of the radioactive elements; Part II, Disintegration products of uranium. *American Journal of Science*, **134**, 78-88.

Bouvier, A., Vervoort, J. D., & Patchett, P. J. 2008. The Lu–Hf and Sm–Nd isotopic composition of CHUR: constraints from unequilibrated chondrites and implications for the bulk composition of terrestrial planets. *Earth and Planetary Science Letters*, **273,** 48-57.

Boyet, M., & Carlson, R. W. 2006. A new geochemical model for the Earth's mantle inferred from 146 Sm–142 Nd systematics. *Earth and Planetary Science Letters*, **250**(1), 254-268.

Burbidge, E. M., Burbidge, G. R., Fowler, W. A., & Hoyle, F. 1957. Synthesis of the elements in stars. *Reviews of modern physics*, **29**(4), 547.

Burchfiel, B. C., & Royden, L. H. 1985. North-south extension within the convergent Himalayan region. *Geology*, **13**(10), 679-682.

Burchfiel, B. C., Zhiliang, C., Hodges, K. V., Yuping, L., Royden, L. H., Changrong, D., & Jiene, X. 1992. The South Tibetan detachment system, Himalayan orogen: Extension contemporaneous with and parallel to shortening in a collisional mountain belt. *Geological Society of America Special Papers*, **269**, 1-41.

Cavazzini, G. 2012. Distillation law and exponential model of isotope fractionation. *International Journal of Mass Spectrometry*, **309**, 129-132.

Cawood, P. A., Johnson, M. R., & Nemchin, A. A. 2007. Early Palaeozoic orogenesis along the Indian margin of Gondwana: tectonic response to Gondwana assembly. *Earth and Planetary Science Letters*, **255**(1), 70-84.

Cerveny, P. F., Naeser, N. D., Zeitler, P. K., Naeser, C. W., & Johnson, N. M. 1988. History of uplift and relief of the Himalaya during the past 18 million years: Evidence from fission-track ages of detrital zircons from sandstones of the Siwalik Group. In *New perspectives in basin analysis* (pp. 43-61). Springer New York.

Chakungal, J., Dostal, J., Grujic, D., Duchêne, S., & Ghalley, K. S. 2010. Provenance of the Greater Himalayan sequence: Evidence from mafic granulites and amphibolites in NW Bhutan. *Tectonophysics*, **480**(1), 198-212.

Chappell, B., & White, A. 1974. Two contrasting granite types. *Pacific geology*, **8**(2), 173-174.

Chappell, B. W., & White, A. J. R. 1992. I-and S-type granites in the Lachlan Fold Belt. *Geological Society of America Special Papers*, **272**, 1-26.

Charlier, B. L. A., Ginibre, C., Morgan, D., Nowell, G. M., Pearson, D. G., Davidson, J. P., & Ottley, C. J. 2006. Methods for the microsampling and high-precision analysis of strontium and rubidium isotopes at single crystal scale for petrological and geochronological applications. *Chemical Geology*,**232**(3), 114-133.

Charlier, B. L. A., Nowell, G. M., Parkinson, I. J., Kelley, S. P., Pearson, D. G., & Burton, K. W. 2012. High temperature strontium stable isotope behaviour in the early solar system and planetary bodies. *Earth and Planetary Science Letters*, **329**, 31-40.

Clarke, F. W. 1920. The data of geochemistry. *US Geological Survey Bulletin 695*. US Government Printing Office.

Collins, W. J. 1996. Lachlan Fold Belt granitoids: products of three-component mixing. *Geological Society of America Special Papers* **315**, 171-181.

Compston, W., & Chappell, B. W. 1979. Sr-isotope evolution of granitoid source rocks. *The Earth: its origin, structure and evolution*, 377-426.

Compston, W., & Oversby, V. M. 1969. Lead isotopic analysis using a double spike. *Journal of Geophysical Research*, **74**(17), 4338-4348.

Cottle, J. M., et al. 2009. Geochronology of granulitized eclogite from the Ama Drime Massif: implications for the tectonic evolution of the South Tibetan Himalaya. *Tectonics*, **28**(1).

Dahlen, F. A. 1984. Noncohesive critical Coulomb wedges: An exact solution. *Journal of Geophysical Research: Solid Earth*, **89**(B12), 10125-10133.

Dahlen, F. A. 1990. Critical taper model of fold-and-thrust belts and accretionary wedges. *Annual Review of Earth and Planetary Sciences*, **18**, 55.

Daniel, C. G., Hollister, L. S., Parrish, R. T., & Grujic, D. 2003. Exhumation of the Main Central Thrust from lower crustal depths, eastern Bhutan Himalaya. *Journal of Metamorphic Geology*, **21**(4), 317-334.

Davies, G. F. 1981. Earth's neodymium budget and structure and evolution of the mantle. *Nature*, **290**, 208-213.

Davies, G. R., & Halliday, A. N. 1998. Development of the Long Valley rhyolitic magma system: strontium and neodymium isotope evidence from glasses and individual phenocrysts. *Geochimica et Cosmochimica Acta*, **62**(21), 3561-3574.

Davis, D., Suppe, J., & Dahlen, F. A. 1983. Mechanics of fold-and-thrust belts and accretionary wedges. *Journal of Geophysical Research: Solid Earth*, **88**(B2), 1153-1172.

de Laeter, J. R., Böhlke, J. K., De Bièvre, P., Hidaka, H., Peiser, H. S., Rosman, K. J. R., & Taylor, P. D. P. 2003. Atomic weights of the elements. Review 2000 (IUPAC Technical Report). *Pure and Applied Chemistry*, **75**(6), 683-800.

de Sigoyer, J., et al. 2000. Dating the Indian continental subduction and collisional thickening in the northwest Himalaya: Multichronology of the Tso Morari eclogites. *Geology*, **28**(6), 487-490.

Deniel, C., & Pin, C. 2001. Single-stage method for the simultaneous isolation of lead and strontium from silicate samples for isotopic measurements. *Analytica Chimica Acta*, **426**(1), 95-103.

Deniel, C., Vidal, P., Fernandez, A., Le Fort, P., & Peucat, J. J. 1987. Isotopic study of the Manaslu granite (Himalaya, Nepal): inferences on the age and source of Himalayan leucogranites. *Contributions to Mineralogy and Petrology*, **96**(1), 78-92.

Duyverman, H. J., Harris, N. B., & Hawkesworth, C. J. 1982. Crustal accretion in the Pan African: Nd and Sr isotope evidence from the Arabian Shield. *Earth and Planetary Science Letters*, **59**(2), 315-326.

England, P., Le Fort, P., Molnar, P., & Pêcher, A. 1992. Heat sources for Tertiary metamorphism and anatexis in the Annapurna-Manaslu Region central Nepal. *Journal of Geophysical Research: Solid Earth* **97,** 2107-2128.

Faure, G., & Mensing, T. M. 2005. Isotopes: principles and applications. John Wiley & Sons Inc.

Fietzke, J., & Eisenhauer, A. 2006. Determination of temperature-dependent stable strontium isotope (88Sr/86Sr) fractionation via bracketing standard MC-ICP-MS. *Geochemistry, Geophysics, Geosystems*, **7**(8).

Gansser, A. 1964. Geology of the Himalayas. Interscience Publishers London.

Gansser, A. 1983. Geology of the Bhutan Himalaya. Birkhauser Verlag Basel.

Gariépy, C., Allègre, C. J., & Xu, R. H. 1985. The Pb-isotope geochemistry of granitoids from the Himalaya-Tibet collision zone: implications for crustal evolution. *Earth and Planetary Science Letters*, **74**(2), 220-234.

Gladney, E. S., Burns, C. E., & Roelandts, I. 1983. 1982 compilation of elemental concentrations in eleven United States Geological Survey rock standards. *Geostandards Newsletter*, **7**(1), 3-6.

Goldschmidt, V.M. 1954. Geochemistry. Clarendon Press.

Govindaraju, K., Potts P. J., Webb, P. C., & Watson, J. S. 1994. 1994 report on Whin Sill Dolerite WS-E from England and Pitscurrie Microgabbro PM-S from Scotland: assessment by one hundred and four international laboratories. *Geostandards Newsletter*, **18**(2), 211-300.

Greenwood, L.V. 2013. Orogenesis in the Eastern Himalaya: A study of structure, geochronology and metamorphism in Bhutan. PhD Thesis, Department of Environment, Earth and Ecosystems, Open University, Milton Keynes.

Greenwood, L. V., Argles, T. W., Parrish, R. R., Harris, N. B., & Warren, C. 2016. The geology and tectonics of central Bhutan. *Journal of the Geological Society*, **173,** 215-238.

Griffin, W. L., Wang, X., Jackson, S. E., Pearson, N. J., O'Reilly, S. Y., Xu, X., & Zhou, X. 2002. Zircon chemistry and magma mixing, SE China: in-situ analysis of Hf isotopes, Tonglu and Pingtan igneous complexes. *Lithos*,**61**(3), 237-269.

Grujic, D., Casey, M., Davidson, C., Hollister, L. S., Kündig, R., Pavlis, T., & Schmid, S. 1996. Ductile extrusion of the Higher Himalayan Crystalline in Bhutan: evidence from quartz microfabrics. *Tectonophysics*, **260**(1), 21-43.

Grujic, D., Hollister, L. S., & Parrish, R. R. 2002. Himalayan metamorphic sequence as an orogenic channel: insight from Bhutan. *Earth and Planetary Science Letters*, **198**(1), 177-191.

Grujic, D., Warren, C. J., & Wooden, J. L. 2011. Rapid synconvergent exhumation of Miocene-aged lower orogenic crust in the eastern Himalaya.*Lithosphere*, **3**(5), 346-366.

Guillot, S., & Le Fort, P. 1995. Geochemical constraints on the bimodal origin of High Himalayan leucogranites. *Lithos*, ***35***(3), 221-234.

Guo, Z., & Wilson, M. 2012. The Himalayan leucogranites: constraints on the nature of their crustal source region and geodynamic setting. *Gondwana Research*, **22**(2), 360-376.

Haapala, I. 1997. Magmatic and postmagmatic processes in tin-mineralized granites: topaz-bearing leucogranite in the Eurajoki rapakivi granite stock, Finland. *Journal of Petrology*, **38**(12), 1645-1659.

Hanchar, J. M., & Watson, E. B. 2003. Zircon saturation thermometry. *Reviews in Mineralogy and Geochemistry*, **53,** 89-112.

Harris, N. 1981. The role of fluorine and chlorine in the petrogenesis of a peralkaline complex from Saudi Arabia. Chemical Geology, **31**, 303-310.

Harris, N. 2007. Channel flow and the Himalayan–Tibetan orogen: a critical review. *Journal of the Geological Society*, **164**(3), 511-523.

Harris, N., & Massey, J. 1994. Decompression and anatexis of Himalayan metapelites. *Tectonics*, **13**(6), 1537-1546.

Harris, N. B. W., & Inger, S. 1992. Trace element modelling of pelite-derived granites. *Contributions to Mineralogy and Petrology*, **110**(1), 46-56.

Harris, N., Ayres, M., & Massey, J. 1995. Geochemistry of granitic melts produced during the incongruent melting of muscovite: implications for the extraction of Himalayan leucogranite magmas. *Journal of Geophysical Research: Solid Earth*, **100**(B8), 15767-15777.

Harris, N., Massey, J., & Inger, S. 1993. The role of fluids in the formation of High Himalayan leucogranites. *Geological Society, London, Special Publications*, **74**(1), 391-400.

Harrison, T. M., Lovera, O. M., & Grove, M. 1997. New insights into the origin of two contrasting Himalayan granite belts. *Geology*, **25**(10), 899-902.

Harrison, T. M., Grove, M., Lovera, O. M., & Catlos, E. J. 1998. A model for the origin of Himalayan anatexis and inverted metamorphism. *Journal of Geophysical Research: Solid Earth*, **103**(B11), 27017-27032.

Healy, B., Collins, W. J., & Richards, S. W. 2004. A hybrid origin for Lachlan S-type granites: the Murrumbidgee Batholith example. *Lithos* **78**, 197-216.

Heim, A.A., & Gansser, A. 1939. Central Himalaya: Geological observations of the Swiss expedition, 1936, Hindustan Publication Corporation, India.

Hiess, J., Condon, D. J., McLean, N., & Noble, S. R. 2012. 238U/235U systematics in terrestrial uranium-bearing minerals. *Science*, **335**(6076), 1610-1614.

Hodges, K. V. 2000. Tectonics of the Himalaya and southern Tibet from two perspectives. *Geological Society of America Bulletin*, **112**(3), 324-350.

Holmes, A. 1911. The association of lead with uranium in rock-minerals, and its application to the measurement of geological time. *Proceedings of the Royal Society of London. Series A, Containing Papers of a Mathematical and Physical Character*, **85**(578), 248-256.

Holmes, A. 1913. The age of the Earth. Harper & Brothers.

Horstwood, M. S., Foster, G. L., Parrish, R. R., Noble, S. R., & Nowell, G. M. 2003. Common-Pb corrected in situ U–Pb accessory mineral geochronology by LA-MC-ICP-MS. *Journal of Analytical Atomic Spectrometry*, **18**(8), 837-846.

Hu, X., Garzanti, E., Moore, T., & Raffi, I. 2015. Direct stratigraphic dating of India-Asia collision onset at the Selandian (middle Paleocene, 59 ± 1 Ma). *Geology* **43,** 859-862.

Inger, S., & Harris, N. 1993. Geochemical constraints on leucogranite magmatism in the Langtang Valley, Nepal Himalaya. *Journal of Petrology*,**34**(2), 345-368.

Islam, R., Upadhyay, R., Ahmad, T., Thakur, V. C., & Sinha, A. K. 1999. Pan-African magmatism, and sedimentation in the NW Himalaya. *Gondwana Research*, **2**(2), 263-270.

Jackson, S.E., Pearson, N.J., Griffin, W.L., & Belousova, E.A. 2004. The application of laser ablation-inductively coupled plasma-mass spectrometry to in situ U–Pb zircon geochronology. *Chemical Geology*, **211,** 47-69.

Jamieson, R. A., Beaumont, C., Medvedev, S., & Nguyen, M. H. 2004. Crustal channel flows: 2. Numerical models with implications for metamorphism in the Himalayan-Tibetan orogen. *Journal of Geophysical Research: Solid Earth*, **109**(B6).

Jamieson, R. A., Unsworth, M. J., Harris, N. B., Rosenberg, C. L., & Schulmann, K. 2011. Crustal melting and the flow of mountains. *Elements*,**7**(4), 253-260.

Johnson, C. M., Beard, B. L., & Albarède, F. 2004. Overview and general concepts. *Reviews in Mineralogy and geochemistry*, **55(**1), 1-24.

Kavner, A., John, S. G., Sass, S., & Boyle, E. A. 2008. Redox-driven stable isotope fractionation in transition metals: Application to Zn electroplating. *Geochimica et Cosmochimica Acta*, **72(**7), 1731-1741.

Kellett, D. A., Grujic, D., Warren, C., Cottle, J., Jamieson, R., & Tenzin, T. 2010. Metamorphic history of a syn-convergent orogen-parallel detachment: The South Tibetan detachment system, Bhutan Himalaya. *Journal of Metamorphic Geology*, **28**(8), 785-808.

Kemp, A. I. S., Hawkesworth, C. J., Paterson, B. A., & Kinny, P. D. 2006. Episodic growth of the Gondwana supercontinent from hafnium and oxygen isotopes in zircon. *Nature*, **439**(7076), 580-583.

Kemp, A. I. S., et al. 2007. Magmatic and crustal differentiation history of granitic rocks from Hf-O isotopes in zircon. *Science*, **315**(5814), 980-983.

King, J.A. 2007. Crustal melting beneath southern Tibet. PhD Thesis, Department of Environment, Earth and Ecosystems, Open University, Milton Keynes.

King, J.A., Harris, N., Argles, T., Parrish, R., & Zhang, H. 2011. Contribution of crustal anatexis to the tectonic evolution of Indian crust beneath southern Tibet. *Geological Society of America Bulletin*, **123**(1-2), 218-239.

Klootwijk, C. T., Gee, J. S., Peirce, J. W., Smith, G. M., & McFadden, P. L. 1992. An early India-Asia contact: paleomagnetic constraints from Ninetyeast ridge, ODP Leg 121. *Geology*, **20**(5), 395-398.

Kohn, M. J. 2008. PTt data from central Nepal support critical taper and repudiate large-scale channel flow of the Greater Himalayan Sequence.*Geological Society of America Bulletin*, **120**(3-4), 259-273.

Lackey, J. S., Valley, J. W., & Saleeby, J. B. 2005. Supracrustal input to magmas in the deep crust of Sierra Nevada batholith: evidence from high-δ18 O zircon. *Earth and Planetary Science Letters*, **235,** 315-330.

Lakshminarayana, G. 1995. Damuda Subgroup. *The Bhutan Himalaya: A Geological Account: Geological Society of India Special Publication*. **39**, 29-33.

Larson, K. M., Bürgmann, R., Bilham, R., & Freymueller, J. T. 1999. Kinematics of the India-Eurasia collision zone from GPS measurements.*Journal of Geophysical Research: Solid Earth*, **104**(B1), 1077-1093.

Le Fort, P., Cuney, M., Deniel, C., France-Lanord, C., Sheppard, S. M. F., Upreti, B. N., & Vidal, P. 1987. Crustal generation of the Himalayan leucogranites. *Tectonophysics*, **134**(1-3), 39-57.

Lederer, G. W., Cottle, J. M., Jessup, M. J., Langille, J. M., & Ahmad, T. 2013. Timescales of partial melting in the Himalayan middle crust: insight from the Leo Pargil dome, northwest India. *Contributions to Mineralogy and Petrology*, **166**(5), 1415-1441.

Loiselle, M. C., & Wones D. R.1979. Characteristics and origin of anorogenic granites. *Geol. Soc. Am. Abstr. with Progr*. 11:468.

Long, S., & McQuarrie, N. 2010. Placing limits on channel flow: Insights from the Bhutan Himalaya. *Earth and Planetary Science Letters*, **290**(3), 375-390.

Long, S., McQuarrie, N., Tobgay, T., & Hawthorne, J. 2011. Quantifying internal strain and deformation temperature in the eastern Himalaya, Bhutan: Implications for the evolution of strain in thrust sheets. *Journal of Structural Geology*, **33**(4), 579-608.

Malpas, J., Zhou, M. F., Robinson, P. T., & Reynolds, P. H. 2003. Geochemical and geochronological constraints on the origin and emplacement of the Yarlung Zangbo ophiolites, Southern Tibet. *Geological Society, London, Special Publications*, **218,** 191-206.

Massey, J. A., Harmon, R. S., & Harris, N. B. W. 1994. Contrasting retrograde oxygen isotope exchange behaviour and implications: examples from the Langtang Valley, Nepal. *Journal of Metamorphic Geology*, **12,** 261-272.

Massey, J. A., Reddy, S. M., Harris, N. B. W., & Harmon, R. S. 1994. Correlation between melting, deformation and fluid interaction in the continental crust of the High Himalayas, Langtang Valley, Nepal. *Terra Nova*, **6,** 229-237.

McCulloch, M. T., & Chappell, B. W. 1982. Nd isotopic characteristics of S-and I-type granites. *Earth and Planetary Science Letters*, **58**(1), 51-64.

McQuarrie, N., Robinson, D., Long, S., Tobgay, T., Grujic, D., Gehrels, G., & Ducea, M. 2008. Preliminary stratigraphic and structural architecture of Bhutan: Implications for the along strike architecture of the Himalayan system. *Earth and Planetary Science Letters*, **272**(1), 105-117.

Medvedev, S., & Beaumont, C. 2006. Growth of continental plateaus by channel injection: models designed to address constraints and thermomechanical consistency. *Geological Society of London, Special Publications* **268,** 147-164.

Meija, J., Ouerdane, L., & Mester, Z. 2009. Isotope scrambling and error magnification in multiple-spiking isotope dilution. *Analytical and bioanalytical chemistry*, **394**(1), 199-205.

Montel, J. M. 1993. A model for monazite/melt equilibrium and application to the generation of granitic magmas. *Chemical Geology*, **110**(1), 127-146.

Mottram, C.M. 2014. An integrated metamorphic and isotopic study of crustal extrusion along the Main Central Thrust, Sikkim Himalaya. PhD Thesis, Department of Environment, Earth and Ecosystems, Open University, Milton Keynes.

Mottram, C. M., Argles, T. W., Harris, N. B. W., Parrish, R. R., Horstwood, M. S. A., Warren, C. J., & Gupta, S. 2014. Tectonic interleaving along the Main Central Thrust, Sikkim Himalaya. *Journal of the Geological Society*,**171**(2), 255-268.

Moynier, F., Agranier, A., Hezel, D. C., & Bouvier, A. 2010. Sr stable isotope composition of Earth, the Moon, Mars, Vesta and meteorites. *Earth and Planetary Science Letters*, **300**(3), 359-366.

Najman, Y., et al. 2010. Timing of India-Asia collision: Geological, biostratigraphic, and palaeomagnetic constraints. *Journal of Geophysical Research: Solid Earth*, **115**(B12).

Nebel, O., Mezger, K., Scherer, E. E., & Münker, C. 2005. High precision determinations of 87 Rb/85 Rb in geologic materials by MC-ICP-MS.*International Journal of Mass Spectrometry*, **246**(1), 10-18.

Nelson, K. D., et al. 1996. Partially molten middle crust beneath southern Tibet: synthesis of project INDEPTH results. *Science*, **274**, 1684-1688.

Neymark, L. A., Premo, W. R., Mel'nikov, N. N., & Emsbo, P. 2014. Precise determination of δ 88 Sr in rocks, minerals, and waters by double-spike TIMS: a powerful tool in the study of geological, hydrological and biological processes. *Journal of Analytical Atomic Spectrometry*, **29**(1), 65-75.

Nowell, G. M., Pearson, D. G., Ottley, C. J., Schweiters, J., & Dowall, D. 2003. Long-term performance characteristics of a plasma ionisation multi-collector mass spectrometer (PIMMS): the ThermoFinnigan Neptune.*Plasma Source Mass Spectrometry: Applications and Emerging Technologies. Cambridge: Royal Society of Chemistry*, 307-320.

Parkash, B., Sharma, R. P., & Roy, A. K. 1980. The Siwalik Group (molasse)—sediments shed by collision of continental plates. *Sedimentary Geology*, **25**(1), 127-159.

Parkinson, I. J., Hammond, S. J., James, R. H., & Rogers, N. W. 2007. High-temperature lithium isotope fractionation: insights from lithium isotope diffusion in magmatic systems. *Earth and Planetary Science Letters*, **257**(3), 609-621.

Parrish, R. R., & Noble, S. R. 2003. Zircon U-Th-Pb geochronology by isotope dilution—thermal ionization mass spectrometry (ID-TIMS). *Reviews in Mineralogy and Geochemistry*, **53**(1), 183-213.

Patchett, P. J. 1980a. Sr isotopic fractionation in Allende chondrules: a reflection of solar nebular processes. *Earth and Planetary Science Letters*,**50**(1), 181-188.

Patchett, P. J. 1980b. Sr isotopic fractionation in Ca-Al inclusions from the Allende meteorite. *Nature*, **283**, 438-441.

Patiño-Douce, A.E., Humphreys, E.D., & Johnston, A.D. 1990. Anatexis and metamorphism in tectonically thickened continental crust exemplified by the Sevier hinterland, western North America. *Earth and Planetary Science Letters* **97,** 290-315.

Patiño Douce, A. E., & Johnston, A. D. 1991. Phase equilibria and melt productivity in the pelitic system: implications for the origin of peraluminous granitoids and aluminous granulites. *Contributions to Mineralogy and Petrology*, **107**(2), 202-218.

Patiño Douce, A. E., & Harris, N. 1998. Experimental constraints on Himalayan anatexis. *Journal of Petrology*, **39**(4), 689-710.

Pearce, J. A., & Wanming, D. 1988. The ophiolites of the Tibetan geotraverses, Lhasa to Golmud (1985) and Lhasa to Kathmandu (1986). *Philosophical Transactions of the Royal Society of London. Series A, Mathematical and Physical Sciences*, **327,** 215-238.

Platt, J. P. 1993. Exhumation of high-pressure rocks: A review of concepts and processes. *Terra nova*, **5**(2), 119-133.

Potts, P. J., Thompson, M., Kane, J. S., Webb, P. C., & Carignan, J. 2000. GeoPT6—An international proficiency test for analytical geochemistry laboratories—Report on round 6 (OU-3: Nanhoron microgranite) and 6A (CAL-S: CRPG limestone). *Unpublished Report.*

Potts, P. J., Tindle, A. G., & Webb, P. C. 1992. Geochemical reference material compositions: rocks, minerals, sediments, soils, carbonates, refractories & ores used in research & industry. Taylor & Francis.

Ramsey, M. H., Potts, P. J., Webb, P. C., Watkins, P., Watson, J. S., & Coles, B. J. 1995. An objective assessment of analytical method precision: comparison of ICP-AES and XRF for the analysis of silicate rocks. *Chemical Geology*, **124**(1), 1-19.

Roberts, N. M., & Spencer, C. J. 2014. The zircon archive of continent formation through time. *Geological Society of London, Special Publications* **389,** 197-225.

Rosenberg, C. L., & Handy, M. R. 2005. Experimental deformation of partially melted granite revisited: implications for the continental crust. *Journal of metamorphic Geology*, **23**(1), 19-28.

Rotenberg, E., Davis, D. W., Amelin, Y., Ghosh, S., & Bergquist, B. A. 2012. Determination of the decay-constant of 87 Rb by laboratory accumulation of 87 Sr. *Geochimica et Cosmochimica Acta*, **85**, 41-57.

Royden, L.H. 1993. The steady state thermal structure of eroding orogenic belts and accretionary prisms. *Journal of Geophysical Research: Solid Earth* **98,** 4487-4507.

Rubatto, D., Chakraborty, S., & Dasgupta, S. 2013. Timescales of crustal melting in the Higher Himalayan Crystallines (Sikkim, Eastern Himalaya) inferred from trace element-constrained monazite and zircon chronology. *Contributions to Mineralogy and Petrology*, **165**(2), 349-372.

Rudge, J. F., Reynolds, B. C., & Bourdon, B. 2009. The double spike toolbox. *Chemical Geology*, **265**(3), 420-431.

Savage, P. S., Georg, R. B., Williams, H. M., Turner, S., Halliday, A. N., & Chappell, B. W. 2012. The silicon isotope composition of granites. *Geochimica et Cosmochimica Acta*, **92**, 184-202.

Schärer, U., Xu, R. H., & Allègre, C. J. 1986. U (Th) Pb systematics and ages of Himalayan leucogranites, South Tibet. *Earth and Planetary Science Letters*, **77**(1), 35-48.

Searle, M. P., Parrish, R. R., Hodges, K. V., Hurford, A., Ayres, M. W., & Whitehouse, M. J. 1997. Shisha Pangma leucogranite, south Tibetan Himalaya: field relations, geochemistry, age, origin, and emplacement. *The Journal of Geology*, **105**(3), 295-318.

Searle, M. P., Simpson, R. L., Law, R. D., Parrish, R. R., & Waters, D. J. 2003. The structural geometry, metamorphic and magmatic evolution of the Everest massif, High Himalaya of Nepal–South Tibet. *Journal of the Geological Society*, **160**(3), 345-366.

Searle, M. P., Cottle, J. M., Streule, M. J., & Waters, D. J. 2010. Crustal melt granites and migmatites along the Himalaya: melt source, segregation, transport and granite emplacement mechanisms. *Geological Society of America Special Papers*, **472**, 219-233.

Siebert, C., Nägler, T. F., & Kramers, J. D. 2001. Determination of molybdenum isotope fractionation by double-spike multicollector inductively coupled plasma mass spectrometry. *Geochemistry, Geophysics, Geosystems*, **2**(7).

Simpson, R. L., Parrish, R. R., Searle, M. P., & Waters, D. J. 2000. Two episodes of monazite crystallization during metamorphism and crustal melting in the Everest region of the Nepalese Himalaya. *Geology*, **28**(5), 403-406.

Sláma, J. et al. 2008. Plešovice zircon — A new natural reference material for U–Pb and Hf isotopic microanalysis. *Chemical Geology*, **249,** 1-35.

Soddy, F. 1913. Radioactivity. *Annual Reports on the Progress of Chemistry*, **10**, 262-288.

Spencer, C. J., Harris, R. A., & Dorais, M. J. 2012. Depositional provenance of the Himalayan metamorphic core of Garhwal region, India: Constrained by U–Pb and Hf isotopes in zircons. *Gondwana Research*,**22**(1), 26-35.

Spencer, C. J. et al. 2015. Generation and preservation of continental crust in the Grenville Orogeny. *Geoscience Frontiers*, **6,** 357–372.

Spencer, C. J., Kirkland, C. L., Taylor., R. J. M. 2016. Strategies towards robust interpretations of in situ U-Pb zircon geochronology. *Geoscience Frontiers*, **7**(4), 581-589.

Stacey, J. S., & Kramers, J. D. 1975. Approximation of terrestrial lead isotope evolution by a two-stage model. *Earth and planetary science letters*, **26(**2), 207-221.

Steiger, R., & Jäger, E. 1977. Subcommission on geochronology: convention on the use of decay constants in geo-and cosmochronology. *Earth and planetary science letters*, **36**(3), 359-362.

Stevenson, E. I. et al. 2014. Controls on stable strontium isotope fractionation in coccolithophores with implications for the marine Sr cycle. *Geochimica et cosmochimica acta*, **128**, 225-235.

Streule, M. J., Searle, M. P., Waters, D. J., & Horstwood, M. S. 2010. Metamorphism, melting, and channel flow in the Greater Himalayan Sequence and Makalu leucogranite: Constraints from thermobarometry, metamorphic modeling, and U-Pb geochronology. *Tectonics*, **29**(5).

Swapp, S. M., & Hollister, L. S. 1991. Inverted metamorphism within the Tibetan slab of Bhutan: evidence for a tectonically transported heat source. *Canadian Mineralogist.* **29**(4), 1019-1041.

Tangri, S. K. 1995. Baxa Group. *The Bhutan Himalaya: A Geological Account*. **39**, 38-58.

Taylor, S. R. 1964. Trace element abundances and the chondritic earth model. *Geochimica et Cosmochimica Acta*, **28**(12), 1989-1998.

Teng, F. Z., McDonough, W. F., Rudnick, R. L., Dalpé, C., Tomascak, P. B., Chappell, B. W., & Gao, S. 2004. Lithium isotopic composition and concentration of the upper continental crust. *Geochimica et Cosmochimica Acta*, **68**(20), 4167-4178.

Thirlwall, M. F. 1991. Long-term reproducibility of multicollector Sr and Nd isotope ratio analysis. *Chemical Geology: Isotope Geoscience section*,**94**(2), 85-104.

Thirlwall, M. F. 2000. Inter-laboratory and other errors in Pb isotope analyses investigated using a 207 Pb–204 Pb double spike. *Chemical Geology*, **163**(1), 299-322.

Thirlwall, M. F. 2002. Multicollector ICP-MS analysis of Pb isotopes using a 207 Pb-204 Pb double spike demonstrates up to 400 ppm/amu systematic errors in Tl-normalization. *Chemical Geology*, **184**(3), 255-279.

Valley, J. W. 2003. Oxygen isotopes in zircon. *Reviews in Mineralogy and Geochemistry*, **53,** 343-385.

Vervoort, J. D., & Blichert-Toft, J. 1999. Evolution of the depleted mantle: Hf isotope evidence from juvenile rocks through time. *Geochimica et Cosmochimica Acta*, **63,** 533-556.

Vidal, P., Cocherie, A., & Le Fort, P. 1982. Geochemical investigations of the origin of the Manaslu leucogranite (Himalaya, Nepal). *Geochimica et Cosmochimica Acta*, **46**(11), 2279-2292.

Vigneresse, J. L. 2004. A new paradigm for granite generation. *Transactions of the Royal Society of Edinburgh: Earth Sciences*. **95**(1-2), 11-22.

Waight, T., Baker, J., & Willigers, B. 2002. Rb isotope dilution analyses by MC-ICPMS using Zr to correct for mass fractionation: towards improved Rb–Sr geochronology?. *Chemical Geology*, **186**(1), 99-116.

Warren, C. J., Grujic, D., Kellett, D. A., Cottle, J., Jamieson, R. A., & Ghalley, K. S. 2011. Probing the depths of the India-Asia collision: U-Th-Pb monazite chronology of granulites from NW Bhutan. *Tectonics*, **30**(2).

Watson, E. B., & Harrison, T. M. 1983. Zircon saturation revisited: temperature and composition effects in a variety of crustal magma types.*Earth and Planetary Science Letters*, **64**(2), 295-304.

Watson, J. S. 1996. Fast, simple method of powder pellet preparation for X-ray fluorescence analysis. *X-Ray Spectrometry*, **25**(4), 173-174.

Weis, D., et al. 2006. High-precision isotopic characterization of USGS reference materials by TIMS and MC-ICP-MS. *Geochemistry, Geophysics, Geosystems*, **7**(8).

Wiedenbeck, M., et al. 1995. Three natural zircon standards for U-Th-Pb, Lu-Hf, trace element and REE analyses. *Geostandards Newsletter*, **19,** 1-23.

Wiedenbeck, M., et al. 2004. Further Characterisation of the 91500 Zircon Crystal. *Geostandards and Geoanalytical Research*, **28,** 9-39.

Woodhead, J.D., & Hergt, J.M. 2005. A Preliminary Appraisal of Seven Natural Zircon Reference Materials for In Situ Hf Isotope Determination. *Geostandards and Geoanalytical Research*, **29,** 183-195.

Young, E. D., Galy, A., & Nagahara, H. 2002. Kinetic and equilibrium mass-dependent isotope fractionation laws in nature and their geochemical and cosmochemical significance. *Geochimica et Cosmochimica Acta*, **66**(6), 1095-1104.

Zhang, H., et al. 2004. Causes and consequences of protracted melting of the mid-crust exposed in the North Himalayan antiform. *Earth and Planetary Science Letters*, **228**(1), 195-212.

Appendix A

Analytical techniques

A.1. Sample preparation

Slabs of each leucogranite were first sawn off using a diamond-tipped rock-saw, from which thin sections were made. Weathered surfaces were also removed from leucogranites, as well as any patches of restitic material. Samples were then broken down to ~5-10 cm pieces using either a geological hammer or a rock splitter. Pieces of rock were then crushed down to gravel using a jaw-crusher. A small amount of gravel (~20 g) from each sample was ground in a Tema agate mill to a fine powder. All elements of the Tema mill, the jaw-crusher and the blades of the rock splitter were thoroughly cleaned with distilled water between each sample. The remaining gravel was then reserved for zircon separation (see Section A.8).

A.2. Laboratory reagents

All HCl and HNO_3 used throughout this study was purified using a two-step procedure. First quartz distilled (QD) grade acid was produced by thermal distillation of analytical grade acid in a quartz still. Secondly, QD acid was thermally distilled in a Teflon still, to produced Teflon-distilled (TD) grade acid. Analytical grade HF was purified using a Teflon still to produce TD grade acid. Water was purified using a Millipore filtration system (MQ) to a resistivity of >18.4 MΩ cm. Any acid dilutions were performed using MQ grade water.

A.3. Cleaning procedures

Teflon hand-cranked beakers were cleaned as follows:

- Rinse three times with MQ H_2O and allow to dry.
- Add 1 ml TD HF and 0.1 ml TD HNO_3, seal and heat on a hotplate at 130°C overnight.
- Discard acid and rinse with MQ H_2O three times.
- Boil beakers in a vat of MQ H_2O on a hotplate set at 350°C for ~30 minutes, ensuring the H_2O does not entirely evaporate. Repeat three times, replacing the H_2O each time. Drain H_2O and allow beakers to dry.
- Add 1 ml HCl, seal and heat on a hotplate at 130°C overnight.
- Discard acid, rinse with MQ H_2O three times and leave to dry.

Pipette tips and disposable columns were cleaned as follows:

- Rinse with MQ H_2O three times.
- Boil overnight in 2% TD HNO_3 at 130°C overnight, replace acid and repeat.
- Rinse with MQ H_2O three times, and allow to dry.

High-pressure bombs were cleaned as follows:

- Metal outer jackets and plastic casings were cleaned and scrubbed with Decon 90 and sandpaper, and left to dry.
- Teflon inner capsules were rinsed with MQ H_2O three times, then boiled overnight in TD HNO_3 at 120°C.
- Drain acid and rinse with MQ H_2O. Boil inner capsules in MQ H_2O for ~30 minutes, ensuring the H_2O does not fully evaporate. Repeat three times, replacing the H_2O each time. Drain and allow to dry.
- Fill inner capsules with 500 µl TD HF and 200 µl TD HNO_3. Place in plastic casings and then into the metal outer jackets. Heat in oven overnight at 210°C.

- Allow bombs to cool entirely before opening. Drain acid from inner capsules, and then repeat twice with 700 µl HCl.
- Remove inner capsules, drain acid, rinse with MQ H_2O three times and allow to dry.

A.4. X-ray fluorescence

A.4.1. Major element analysis

In total, 36 leucogranite samples were subject to analysis of major elements concentrations and loss on ignition (LOI). Major element concentrations were determined by x-ray fluorescence (XRF) at the Open University using fused glass discs. Discs were made using pre-ignited sample powders and lithium metaborate / tetraborate flux in a 1:5 ratio by weight (0.7 g sample powder and 3.5 g flux), as described by Ramsey et al. (1995). Mixtures were melted at ~1100°C, and then fused into glass discs in a steel mould. Total LOI of volatile components (CO_2, H_2O, etc.) was measured by calculating percentage weight loss of sample powders after ignition at 1000°C for roughly 1 hour.

XRF analysis of glass discs was carried out using an ARL 8420+ dual goniometer wavelength-dispersive XRF spectrometer. Element intensity data were corrected for background and significant peak overlap interferences. Instrumental drift was corrected using drift normalisation to two standards, OU-3 and WS-E. Further information can be found in Ramsey et al. (1995). External reproducibility is better than 2.5% for elements with greater oxide concentrations than 0.30% in both OU-3 and WS-E (Table A.1). Data accuracy, by comparing average standard values to the expected concentrations, is good for all elements on both standards.

A.4.2. Trace element analysis

All 36 leucogranite samples were analysed for certain trace element abundances (Sc, V, Cr, Co, Ni, Cu, Zn, Ca, As, S, Rb, Sr, Y, Zr, Nb, Mo, Ba, Pb, Th, U). Abundances were determined by

XRF spectrometry of powder pellets, carried out at the Open University. Pellets were made by mixing approximately 0.9 ml of polyvinylpyrrolidone-methylcellulose binding solution with 9 g of sample powder, as specified by Watson (1998). The mixture was compressed at approximately 0.8 x 10^6 kPa into pellets before being dried overnight at ~100°C.

	Date of analysis												WS-E
WS-E	25/02/2013	25/02/2013	09/05/2013	09/05/2013	12/11/2013	12/11/2013	12/11/2013	12/11/2013	13/11/2013	13/11/2013	Average	2 s.d.	2 s.d. %	expected
SiO_2	51.36	51.31	51.62	51.60	51.17	51.20	51.33	51.38	51.28	51.28	51.35	0.30	0.58	51.10
TiO_2	2.44	2.43	2.45	2.44	2.42	2.42	2.40	2.43	2.42	2.43	2.43	0.03	1.09	2.43
Al_2O_3	13.93	13.94	13.92	13.90	13.79	13.80	13.92	13.92	13.98	13.94	13.90	0.12	0.87	13.78
Fe_2O_3	13.17	13.16	13.18	13.19	13.16	13.16	13.14	13.16	13.14	13.17	13.16	0.03	0.23	13.15
MnO	0.17	0.17	0.17	0.17	0.17	0.17	0.17	0.17	0.17	0.17	0.17	0.00	1.31	0.17
MgO	5.56	5.55	5.58	5.57	5.52	5.55	5.54	5.55	5.55	5.57	5.55	0.04	0.63	5.55
CaO	8.98	9.01	8.99	8.99	8.92	8.92	8.95	9.00	8.99	8.99	8.98	0.06	0.72	8.95
Na_2O	2.39	2.40	2.43	2.45	2.41	2.43	2.40	2.45	2.42	2.43	2.42	0.04	1.72	2.47
K2O	1.01	1.01	1.01	1.01	0.99	0.99	0.99	0.99	0.99	1.00	1.00	0.02	2.02	1.00
P_2O_5	0.30	0.30	0.30	0.31	0.31	0.30	0.30	0.31	0.31	0.30	0.30	0.01	2.51	0.30
LOI	0.85	0.85	0.85	0.85	0.85	0.85	0.85	0.85	0.85	0.85	0.85			0.85
Total	100.15	100.14	100.50	100.47	99.69	99.79	99.99	100.21	100.10	100.14	100.12			99.75

	Date of analysis												OU-3
OU-3	25/02/2013	25/02/2013	09/05/2013	09/05/2013	12/11/2013	12/11/2013	12/11/2013	12/11/2013	13/11/2013	13/11/2013	Average	2 s.d.	2 s.d. %	expected
SiO_2	74.12	74.19	74.16	74.06	74.08	74.04	74.33	74.37	74.26	74.18	74.18	0.23	0.31	74.09
TiO_2	0.21	0.21	0.22	0.22	0.22	0.23	0.23	0.22	0.22	0.22	0.22	0.01	4.58	0.22
Al_2O_3	11.07	11.06	10.99	10.99	11.03	11.04	11.12	11.09	11.11	11.15	11.07	0.11	0.97	11.11
Fe_2O_3	3.87	3.87	3.85	3.84	3.88	3.88	3.87	3.87	3.88	3.87	3.87	0.03	0.74	3.83
MnO	0.09	0.09	0.09	0.09	0.09	0.09	0.09	0.09	0.09	0.09	0.09	0.00	2.83	0.09
MgO	0.03	0.02	0.02	0.03	0.02	0.03	0.02	0.03	0.03	0.02	0.03	0.01	22.69	-
CaO	0.22	0.22	0.20	0.20	0.21	0.21	0.22	0.21	0.21	0.21	0.21	0.01	6.54	0.20
Na_2O	3.69	3.65	3.71	3.70	3.71	3.70	3.72	3.73	3.70	3.74	3.70	0.05	1.29	3.68
K2O	4.55	4.56	4.57	4.57	4.56	4.56	4.55	4.53	4.53	4.54	4.55	0.03	0.61	4.55
P_2O_5	0.02	0.02	0.01	0.02	0.02	0.02	0.02	0.02	0.02	0.02	0.02	0.00	11.81	-
LOI	1.82	1.82	1.82	1.82	1.82	1.82	1.82	1.82	1.82	1.82	1.82			1.82
Total	99.70	99.75	99.64	99.54	99.64	99.62	99.99	99.97	99.88	99.89	99.76			99.59

Table A.1: *Major element data and reproducibility for WS-E (top) and OU-3 (bottom), collected by XRF. All values are in weight %. Recommended values for WS-E are taken from Govindaraju et al. (1994) and for OU-3 are taken from Potts et al. (2000).*

XRF analyses were performed using the same methods detailed in A.4.1. Further information is contained in Ramsay et al. (1995). BHVO-1, DNC-1, QLO-1 and W-2 standards were used to monitor instrumental drift and precision. Long term reproducibility is better than 9% (2 s.d.) for all elements except Sc. Data accuracy, by comparing average standard values to the expected concentrations, is good for the majority of elements on all standards.

	Detection	Date of analysis									BHVO-1
BHVO-1	Limit	03/04/2013	03/04/2013	05/04/2013	05/04/2013	03/05/2013	03/05/2013	Average	2 s.d.	2 s.d. %	Expected
Rb	2	9	9	9	10	10	9	9	1	9	11
Sr	2	405	404	404	404	404	406	404	2	0	403
Y	2	29	28	28	28	29	28	28	0	1	28
Zr	2	175	172	175	174	175	173	174	3	1	179
Nb	2	20	18	19	20	20	19	19	2	8	19
Ba	12	130	140	138	138	128	131	134	10	8	139
Pb	5	-	-	-	6	-	-	6	-	-	3
Th	4	-	-	-	-	-	-	-	-	-	1
U	3	-	-	-	-	-	-	-	-	-	0
Sc	5	32	32	31	29	30	32	31	3	9	32
V	5	314	307	311	316	313	319	313	8	3	317
Cr	4	286	289	292	288	292	294	290	6	2	289
Co	2	47	47	46	46	51	47	47	4	8	45
Ni	3	121	121	119	120	121	124	121	4	3	121
Cu	3	138	136	135	138	140	139	138	3	2	136
Zn	3	112	109	112	109	108	109	110	3	3	105
Ga	3	22	22	22	23	23	22	22	1	4	21
Mo	2	-	-	-	-	-	-	-	-	-	1
As	5	-	-	-	-	-	-	-	-	-	0
S	50	213	212	216	214	209	219	214	7	3	-

	Detection	Date of analysis									W-2
W-2	Limit	03/04/2013	03/04/2013	05/04/2013	05/04/2013	03/05/2013	03/05/2013	Average	2 s.d.	2 s.d. %	Expected
Rb	2	19	20	21	21	20	21	20	1	7	20
Sr	2	199	201	201	202	201	202	201	2	1	194
Y	2	23	23	23	23	24	23	23	1	4	24
Zr	2	95	95	94	95	95	94	95	1	1	94
Nb	2	9	10	8	9	9	9	9	1	9	8
Ba	12	179	169	185	182	181	181	179	11	6	182
Pb	5	8	9	9	6	8	9	8	2	24	9
Th	4	-	-	-	-	-	-	-	-	-	2
U	3	-	-	-	-	-	-	-	-	-	1
Sc	5	39	35	36	37	39	35	37	3	9	35
V	5	261	262	256	262	253	260	259	8	3	262
Cr	4	94	97	98	94	96	95	96	3	4	93
Co	2	42	44	44	45	44	44	44	2	3	44
Ni	3	67	67	68	67	69	69	68	2	3	70
Cu	3	104	104	104	104	104	105	104	1	1	103
Zn	3	82	84	82	82	83	83	83	2	2	77
Ga	3	18	19	19	19	19	19	19	1	4	20
Mo	2	-	-	-	-	-	-	-	-	-	1
As	5	-	-	-	-	-	-	-	-	-	1
S	50	251	248	253	260	252	253	253	8	3	-

Table A.2: *Trace element data and reproducibility for BHVO-1 (above) and W-2 (below), collected by XRF. All values are in ppm. Values are not given when below the detection limit of the instrument. Expected values for BHVO-1 are taken from Potts et al. (1992), and for W-2 from Gladney et al. (1983).*

A.5. Trace element analysis by laser-ablation ICP-MS

This section describes the methods used in the analysis of all samples by laser-ablation inductively-coupled plasma mass-spectrometry (LA-ICP-MS) used for the trace element analysis of all leucogranite samples. For discussion of the comparison of ICP-MS techniques and full descriptions of the techniques used, see Appendix B).

Following major element analysis by XRF, fused glass discs were broken up, and fragments embedded in epoxy resin mounts. Mounts were then sanded down and polished in order to expose the fragments of glass disc. The surfaces of the mounts were then cleaned with ethanol prior to loading in the sample cell. Each sample was ablated in triplicate using an ESI-NWR 213 nm Nd:YAG laser under the following conditions: repetition rate of 10 Hz; line scan rate of 10 mm/minute (total line scan of approximately 50 seconds); beam diameter of 110 μm; surface fluence of approximately 12 J/cm^2; and He carrier gas flow rate of 800 mL/minute. Each line scan was pre-ablated using a 5 Hz, 6 J/cm^2, 110 μm beam. Analysis was performed using a ThermoScientific ICAP-Qc quadrupole ICP-MS using Ar carrier gas, and in KED mode. A gas blank was run at the beginning of each analytical session. NIST610 glass reference standard was used for calibration, and ^{43}Ca was used for the internal calibration. International standards WS-E, OU-3 and G-2 were run with each batch of samples to monitor data quality.

OU-3 and WS-E were used to monitor analytical uncertainty. Long term reproducibility of REEs was poor, with some elements yielding 16% uncertainty (2 s.d.). However, uncertainty within any given analytical session was typically better than 5%, and always better than 9% (2 s.d.) for all REEs on both standards (Table A.3)

OU-3	La	Ce	Pr	Nd	Sm	Eu	Gd	Tb	Dy	Ho	Er	Tm	Yb	Lu
16/12/2014	81.2	180	20.2	77.7	16.8	1.13	16.9	2.88	18.5	3.83	11.1	1.64	11.4	1.62
16/12/2014	79.5	172	19.3	76.0	17.0	1.16	15.9	2.74	18.3	3.64	11.8	1.63	11.1	1.60
16/12/2014	79.7	172	19.8	73.9	16.4	1.08	15.8	2.78	17.9	3.80	11.5	1.66	10.7	1.62
Average	80.1	174	19.7	75.9	16.7	1.12	16.2	2.80	18.2	3.76	11.5	1.64	11.1	1.62
2 s.d.	1.93	9.27	0.95	3.87	0.67	0.08	1.25	0.15	0.59	0.20	0.67	0.04	0.66	0.02
2 s.d. %	2.41	5.31	4.81	5.10	4.02	7.55	7.69	5.41	3.25	5.27	5.84	2.29	5.93	1.46
17/12/2014	72.7	173	18.2	70.7	15.6	1.01	15.7	2.58	16.5	3.43	10.7	1.49	10.1	1.43
17/12/2014	74.5	177	18.7	71.9	15.6	1.09	15.9	2.66	16.8	3.64	10.2	1.53	10.1	1.48
17/12/2014	74.6	175	18.6	74.0	15.2	1.05	16.6	2.70	16.8	3.73	11.1	1.51	10.7	1.48
Average	74.0	175	18.5	72.2	15.5	1.05	16.0	2.65	16.7	3.60	10.7	1.51	10.3	1.46
2 s.d.	2.20	4.90	0.45	3.39	0.48	0.08	0.98	0.13	0.31	0.31	0.93	0.04	0.64	0.05
2 s.d. %	2.97	2.80	2.44	4.69	3.10	7.86	6.10	4.84	1.83	8.73	8.76	2.79	6.25	3.76
18/12/2014	74.0	172	18.2	70.3	15.1	1.01	14.8	2.50	16.3	3.36	9.9	1.49	9	1.35
18/12/2014	72.2	169	18.1	71.8	15.4	1.01	14.7	2.39	15.9	3.16	9.8	1.43	9	1.33
18/12/2014	71.8	171	18.5	68.0	14.9	1.04	14.2	2.45	16.5	3.17	9.7	1.54	9	1.37
Average	72.7	171	18.3	70.0	15.1	1.02	14.6	2.45	16.3	3.23	9.8	1.48	9	1.35
2 s.d.	2.38	3.11	0.47	3.85	0.53	0.04	0.65	0.11	0.59	0.23	0.19	0.12	0.32	0.05
2 s.d. %	3.27	1.82	2.57	5.50	3.54	3.89	4.42	4.56	3.65	7.04	1.98	7.79	3.40	3.52
Long-term average	75.6	173	18.8	72.7	15.8	1	15.6	3	17.1	4	10.6	2	10.2	1
2 s.d.	7.18	6.66	1.49	6.04	1.52	0.11	1.75	0.33	1.82	0.52	1.57	0.16	1.55	0.23
2 s.d. %	9.50	3.84	7.93	8.31	9.65	10.13	11.21	12.48	10.65	14.65	14.75	10.40	15.12	15.85

WS-E	La	Ce	Pr	Nd	Sm	Eu	Gd	Tb	Dy	Ho	Er	Tm	Yb	Lu
16/12/2014	25.2	57.4	7.25	31.3	8.89	2.34	6.26	1.00	5.72	1.11	2.90	0.37	2.37	0.39
16/12/2014	25.6	56.6	7.23	30.3	8.11	2.36	6.06	0.98	5.93	1.04	2.85	0.37	2.38	0.37
16/12/2014	27.3	60.6	7.61	32.6	8.66	2.35	6.53	1.04	5.98	1.08	3.06	0.39	2.40	0.37
Average	26.1	58.2	7.36	31.4	8.56	2.35	6.28	1.01	5.88	1.07	2.93	0.38	2.38	0.38
2 s.d.	2.26	4.28	0.43	2.32	0.80	0.02	0.47	0.05	0.28	0.07	0.22	0.03	0.03	0.02
2 s.d. %	8.67	7.35	5.80	7.39	9.34	0.72	7.55	5.17	4.82	6.70	7.36	7.64	1.33	6.24
17/12/2014	26.4	57.7	7.18	31.3	8.51	2.32	6.65	1.05	5.90	1.10	2.99	0.36	2.24	0.36
17/12/2014	27.4	58.8	7.50	31.7	8.93	2.48	6.92	1.08	5.75	1.16	3.05	0.37	2.08	0.37
17/12/2014	27.3	58.7	7.51	31.4	8.93	2.29	6.72	1.05	5.80	1.11	2.97	0.39	2.21	0.34
Average	27.0	58.4	7.40	31.5	8.79	2.36	6.76	1.06	5.82	1.12	3.00	0.38	2.17	0.36
2 s.d.	1.04	1.17	0.37	0.39	0.49	0.20	0.28	0.04	0.15	0.06	0.08	0.03	0.17	0.03
2 s.d. %	3.86	2.01	4.98	1.25	5.55	8.61	4.07	3.62	2.60	5.19	2.53	7.01	7.95	7.10
18/12/2014	25.9	57.8	7.65	32.3	7.77	2.13	6.63	0.96	5.77	1.11	3.07	0.42	2.32	0.34
18/12/2014	28.0	61.5	7.70	33.1	8.36	2.15	6.94	0.97	5.77	1.15	2.83	0.45	2.20	0.35
18/12/2014	26.7	60.4	7.52	31.5	8.33	2.32	6.63	0.96	5.53	1.09	3.00	0.43	2.42	0.35
Average	26.9	59.9	7.62	32.3	8.15	2.20	6.73	0.96	5.69	1.11	2.96	0.43	2.31	0.34
2 s.d.	2.11	3.78	0.19	1.60	0.67	0.21	0.36	0.01	0.28	0.06	0.25	0.03	0.21	0.02
2 s.d. %	7.85	6.32	2.54	4.95	8.22	9.41	5.32	1.50	4.98	5.50	8.30	7.12	9.22	5.27
Long-term average	26.7	58.8	7.46	31.7	8.50	2.31	6.59	1.01	5.79	1.10	2.97	0.40	2.29	0.36
2 s.d.	1.87	3.31	0.39	1.66	0.80	0.21	0.57	0.09	0.27	0.07	0.18	0.06	0.23	0.04
2 s.d. %	7.02	5.63	5.19	5.25	9.44	9.15	8.65	8.93	4.68	6.44	6.01	15.96	9.98	10.01

Table A.3: *REE data and reproducibility for OU-3 and WS-E standards. All values are in ppm.*

A.6. Radiogenic isotope measurements (Sr and Nd by MC-ICP-MS, Pb by TIMS)

A.6.1. Dissolution procedure

In total 19 samples were analysed for their Sr and Nd isotope ratios by multi-collector (MC) ICP-MS, and Pb by TIMS. Samples were dissolved as follows:

- 0.2 g of sample was weighed in Teflon hand cranked beakers.
- Samples were dissolved in a 2 ml HF / 0.2 ml HNO_3 mix at 130°C and left overnight.
- Samples were then dried down, and redissolved in 2 ml HCl at 130°C and left overnight.
- Samples were then dried down once more, and redissolved in 1 ml 1.25 M HCl in preparation for cation column chemistry.

A.6.2. Cation column calibration

Prior to specific column chemistry for each isotope, a clean-up column of AG50W-X8 (Biorad) cation exchange resin was used to separate elements of interest from the majority of matrix elements. For this, a calibration was required. Sample 5H01 was selected due to its large Rb/Sr ratio, as separating these two elements is crucial to accurate Sr isotope analysis. During calibration, cuts were taken for every 1 ml of liquid put through the column, and analysed by ICP-MS, with the results shown in Figure A.1. Pb is the first element of interest to elute from the column in 1.25 M HCl, and the first 6 ml of acid is collected for Pb analysis. A further 24 ml 1.25 M HCl is then eluted in order to remove or collect the majority of Rb from the sample. 10 ml of 2.5 M HCl is then added and collected, which contains the majority of Sr in the sample. Finally, 5 ml 6 M HCl is passed through the column in order to collect Nd. The column procedure used throughout this study is as follows:

- Load 1 ml of clean resin in a pre-cleaned column.
- Clean the column and resin with two full column volumes of 6 M HCl, followed by two full column volumes of MQ H_2O.
- One full column volume of 1.25 M HCl is then eluted.
- The sample (dissolved in 1 ml 1.25 M HCl) is then added to the column, followed by a further 5 ml 1.25 M HCl. Collect for Pb analysis
- Elute 24 ml 1.25 M HCl
- Add 10 ml 2.5M HCl, and collect for Sr analysis.
- Add 5 ml 6 M HCl, and collect for Nd analysis.

- Clean the column and resin with three full column loads 6 M HCl, and store in clean acid.

A.6.3. Strontium column chemistry

The resultant Sr cut from the cation column chemistry was then dried down and redissolved in 1 ml 2 M HNO_3. Sr was then separated using Eichrom Sr-Spec extraction chromatographic resin. This resin was first cleaned in ~4 ml batches. Cleaning consisted of six cycles of:

- 300 ml 6 M HCl
- 300 ml MQ H_2O
- 300 ml 0.05 M HNO_3
- 300 ml MQ H_2O

The Sr-spec column procedure is as follows (modified from Deniel and Pin, 2001):

- Load 0.15 ml of cleaned resin into a pre-cleaned and fritted 1 ml pipette tip modified into a column.
- Clean resin and column with a full column volume (~1.5 ml) 6 M HCl and then two full column volumes of MQ H_2O.
- Condition the resin with 1.5 ml 2 M HNO_3.
- Load the sample (dissolved in 1 ml 2 M HNO_3) and washed on with 0.4 ml 2 M HNO_3.
- Wash with 1 ml 7 M HNO_3 and then 0.2 ml 2 M HNO_3.
- Elute with 1 ml 0.05 M HNO_3, collect this cut for Sr isotopic analysis.

Sr cuts were then dried down and re-dissolved in 1 ml 3% TD HNO_3.

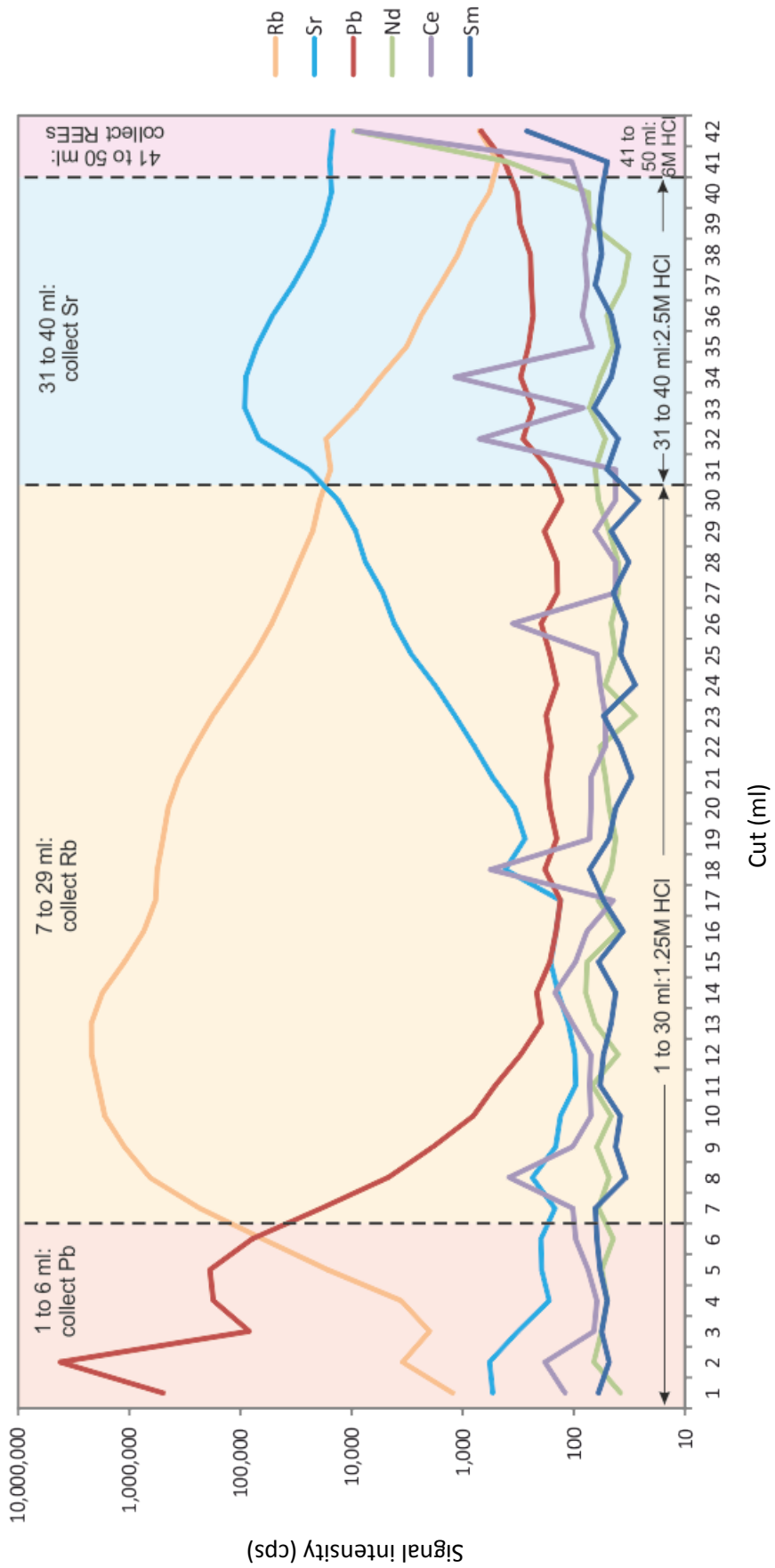

Figure A.1: *Biorad cation column calibration of selected elements.*

A.6.4. Neodymium column chemistry

Nd cuts from cation column chemistry were dried down and redissolved in 0.5 ml 0.25 M HCl. Nd was then separated out using Eichrom LN-spec resin. The Ln-spec procedure is as follows (modified from Pin and Zalduegui, 1997):

- Clean columns by rinsing with 2 ml 6M HCl, followed by 4 ml 0.25M HCl, and then an additional 1 ml 0.25M HCl.
- Load sample into the column in two batches of 0.25 ml 0.25M HCl.
- Elute a further 3.5 ml 0.25M HCl to waste.
- Add 2.5 ml 0.25M HCl, and collect for Nd analysis.
- Clean columns by rinsing 2 ml 0.75 M HCl (to elute Sm), followed by two column volumes 6M HCl.
- Prepare for storage by rinsing with one column volume 0.25M HCl, and store in 0.25M HCl.

A.6.5. Lead column chemistry

Pb cuts from cation column chemistry were dried down and redissolved in 1 ml 1M HBr. Pb was then separated out further using Biorad AG1-X8 anion exchange resin. The Pb column procedure is as follows:

- Load 0.1 ml of cleaned resin into a pre-cleaned and fritted 1 ml pipette tip modified into a column.
- Clean resin and column by washing with sequential column volumes of 6M HCl, MQ H_2O, 6M HCl, MQ H_2O.
- Rinse with one column volume 1M HBr.
- Load sample in 1 ml 1M HBr
- Elute 0.5 ml 1M HBr, followed by 1 ml 1M HBr.
- Elute two column volumes 6M HCl, collecting for Pb isotope analysis.

A.6.6. Strontium isotopic measurements by MC-ICP-MS.

Sr cuts from Sr-spec column chemistry were dried down and redissolved in 1 ml 3% HNO_3. Of this, 0.05 ml was extracted and diluted with 3% HNO_3 in order to perform a concentration check on all samples. Following this, the remaining Sr cuts were diluted with additional 3% HNO_3 to a concentration of 150 ppb Sr, and doped with Zr single element solution to a concentration of 600 ppb Zr during analytical sessions where stable Sr content was analysed.

Sr isotopes were analysed at the Open University using a Thermo-Fisher Neptune MC-ICP-MS in static low resolution mode fitted with standard H cones. A stable introductory system (SIS) was used, with a typical uptake rate of ~50 µl/min. Faraday cup configurations and any major associated interferences are shown in Table A.4.

Collector	L4	L3	L2	L1	C	H1	H2	H3	H4
Mass	^{83}Kr	^{84}Sr	^{85}Rb	^{86}Sr	^{87}Sr	^{88}Sr	^{90}Zr	^{91}Zr	^{92}Zr
Interference		^{84}Kr		^{86}Kr	^{87}Rb				

Table A.4: *Faraday cup configurations for radiogenic and stable Sr isotopic measurements by MC-ICP-MS.*

Machine gain was measured each day before analytical work began. Samples were run in 12 blocks of 10 measurements, with a 4.194 second integration time for each measured ratio. A peak centre was run at the start of each analysis, and a baseline at the start of every block. Following each sample, the machine and nebuliser were washed with 3% HNO_3 for at least 15 minutes, or until the measured blank showed no Sr spikes or washout effects.

At the start of each analytical session where stable Sr isotopes were also measured, 5-6 standards of Zr-doped NBS-987 were analysed assuming an $^{86}Sr/^{88}Sr$ ratio of 0.1194 (IUPAC value, Berglund and Wieser, 2011), in order to determine the instrumental mass bias for that analytical session. Following this, several more Zr-doped NBS-987 standards were analysed,

this time assuming the average $^{90}Zr/^{91}Zr$ determined previously to account for internal mass bias, in order to determine machine reproducibility for that day.

Isobaric interferences of Kr and Rb were monitored by measuring ^{83}Kr and ^{85}Rb, respectively. Analyses were corrected for instrumental mass fractionation using the exponential fractionation law, with the ^{86}Kr interference on ^{86}Sr stripped off iteratively, assuming an $^{86}Kr/^{83}Kr$ ratio of 0.6209 and an $^{86}Sr/^{88}Sr$ ratio of 0.1194 (Thirlwall, 1991; de Laeter et al., 2003). ^{87}Sr was corrected for ^{87}Rb interferences using an $^{85}Rb/^{87}Rb$ ratio of 2.5926 (Nebel et al., 2005).

The standard NBS-987 was utilised to ensure long term machine reproducibility across the three analytical sessions used in this study. The average $^{87}Sr/^{86}Sr$ across this period was 0.710311 ± 43 (60 ppm 2 s.d., n = 33). Though this is outside of error of the accepted TIMS value of 0.710249 ± 11 (Thirlwall, 1991) and the MC-ICP-MS value of 0.710266 ± 25 (Nowell et al., 2003), corrections were made to all data from each analytical session to bring standard data into keeping with accepted values. USGS rock standard G-2 was digested and analysed with each of the three analytical sessions, yielding an average value of 0.709723 ± 88, which is within uncertainty of the average TIMS value of 0.709770 ± 16 recorded by Weis et al. (2006).

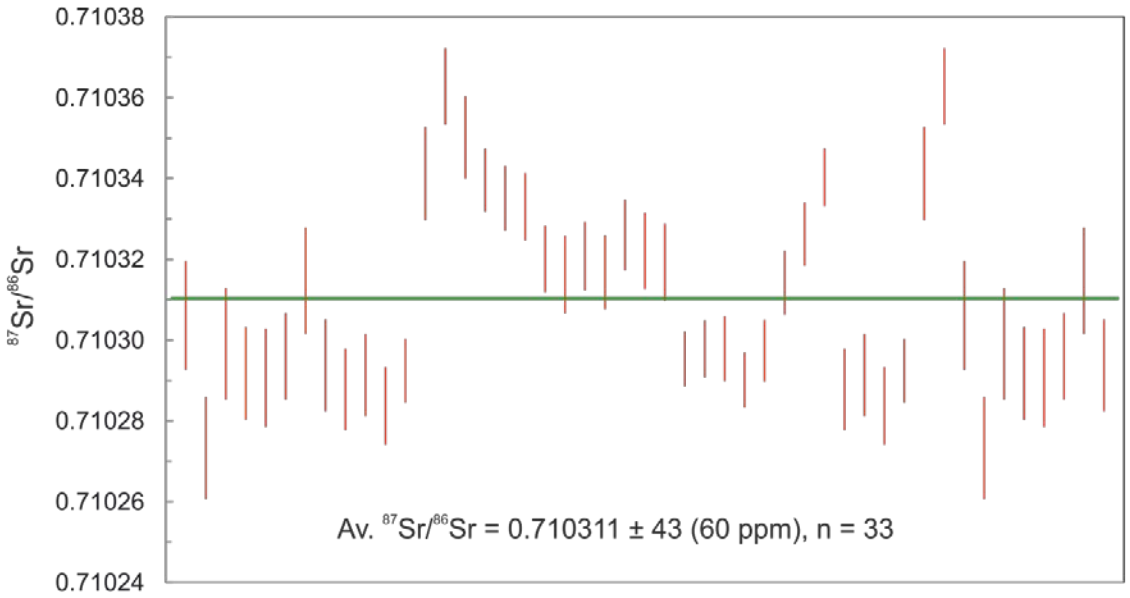

Figure A.2: *Long term standard $^{87}Sr/^{86}Sr$ ratios for NBS-987 as measured by MC-ICP-MS.*

A.6.7. Neodymium isotopic measurements by MC-ICP-MS.

Nd cuts from LN-spec column chemistry were dried down and redissolved in 1 ml 3% HNO_3. Of this, 0.05 ml was extracted and diluted with 3% HNO_3 in order to perform a concentration check on all samples. Following this, the remaining Nd cuts were diluted with additional 3% HNO_3 to a concentration of 100 ppb Nd.

Nd isotopes were analysed at the Open University using a Thermo-Fisher Neptune MC-ICP-MS in static low resolution mode fitted with standard H cones. A stable introductory system (SIS) was used, with a typical uptake rate of ~50 µl/min. Faraday cup configurations and any major associated interferences are shown in Table A.5.

Collector	L4	L3	L2	L1	C	H1	H2	H3	H4
Mass	^{140}Ce	^{142}Nd	^{143}Nd	^{144}Nd	^{145}Nd	^{146}Nd	^{147}Sm	^{148}Nd	^{150}Nd
Interference		^{142}Nd		^{144}Sm				^{148}Sm	^{150}Sm

Table A.5: *Faraday cup configurations for Nd isotopic measurements by MC-ICP-MS.*

Machine gain was measured each day before analytical work began. Samples were run in one block of 120 measurements, with a 4.194 second integration time for each measured ratio. A peak centre and a baseline were run at the start of every analysis. Following each sample, the machine and nebuliser were washed with 3% HNO_3 for at least 15 minutes, or until the measured blank showed no Nd spikes or washout effects.

Isobaric interferences of Ce and Sm were monitored by measuring ^{140}Ce and ^{147}Sm, respectively. Analyses were corrected for instrumental mass fractionation using the exponential fractionation law, with the ^{144}Sm interference on ^{144}Nd stripped off iteratively, assuming a ^{146}Nd/^{144}Nd ratio of 0.7219 and a ^{147}Sm/^{144}Sm ratio of 4.83871 (de Laeter et al., 2003). ^{148}Nd was corrected for ^{148}Sm interferences using a ^{147}Sm/^{148}Sm ratio of 1.3274, ^{150}Nd was corrected

for ^{150}Sm interferences using a ^{147}Sm/^{150}Sm ratio of 2.02703, and ^{142}Nd was corrected for ^{142}Ce interferences using a ^{140}Ce/^{142}Ce ratio of 7.97297 (de Laeter et al., 2003).

The standard J&M was utilised to ensure long term machine reproducibility across the two analytical sessions used in this study. The average ^{143}Nd/^{144}Nd across this period was 0.511810 ± 26 (50 ppm 2 s.d., n = 33). This is within uncertainty of the Open University's TIMS value of 0.511819 ± 2 (Richards et al., 2005), though all samples were corrected to account for any offset in individual analytical sessions. USGS rock standard G-2 was digested and analysed with each of the two analytical sessions, yielding an average value of 0.512229 ± 8, which is within uncertainty of the average MC-ICP-MS value of 0.512235 ± 15 recorded by Weis et al. (2006).

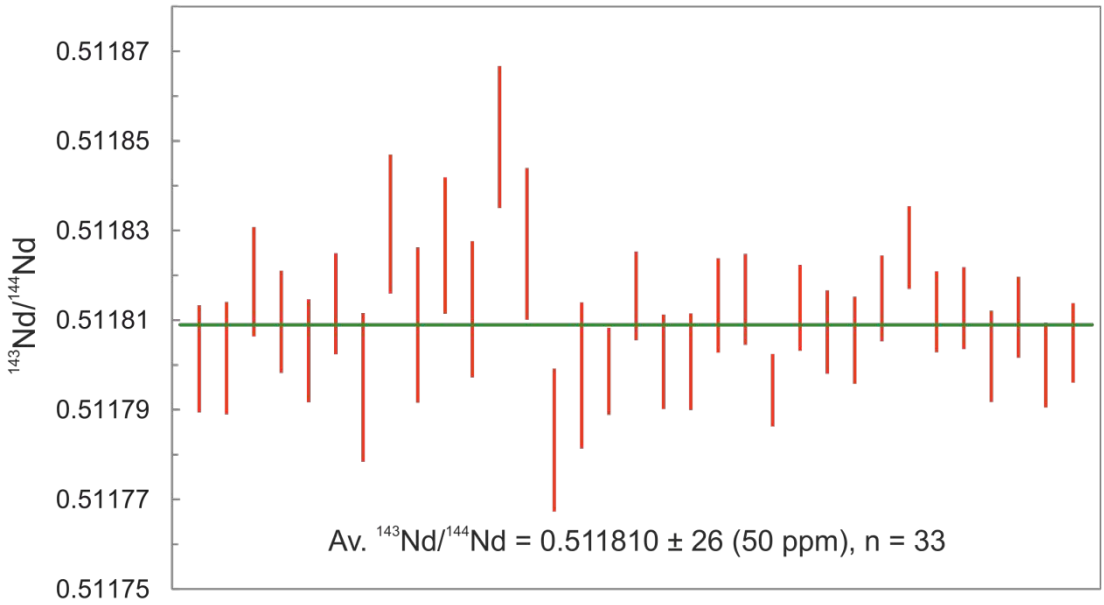

Figure A.3: *Long term standard ^{143}Nd/^{144}Nd ratios for J&M as measured by MC-ICP-MS*

A.6.8. Lead isotopic analysis by TIMS

Following Pb column chemistry, samples were dried down then redissolved in concentrated HNO_3 in order to remove all HBr. Samples were then divided into natural and double-spike

aliquots, allowing for 1000 ng Pb in each aliquot. To the DS aliquot a ^{207}Pb-^{204}Pb double-spike was added, identical in composition to that described by Thirlwall (2000). Natural and DS aliquots were then dried down and loaded onto rhenium filaments with 1 µl silica gel. Filaments were loaded into the TIMS, with natural and DS samples run in different batches.

Pb isotopic analysis was undertaken at the Open University using a Thermo-Fisher Triton TIMS. Faraday cup configurations are shown in Table A.6. Identical procedures were used for both natural and DS analyses. Samples were heated to roughly 1250°C, until at least 100 mV of ^{204}Pb (the minor isotope) was recorded, in order to ensure high accuracy and reproducibility. Data were collected in 27 blocks of 10 ratios, each with a 16 second integration. Baselines were measured prior to each block by source deflection after a 30 second pre-baseline wait time for 2 minutes.

Collector	L2	L1	C	H1	H2
Isotope	^{204}Pb	^{205}Tl	^{206}Pb	^{207}Pb	^{208}Pb

Table A.6: *Faraday cup configurations Pb isotopic measurements by TIMS.*

Deconvolution of the natural and DS samples was carried out offline using software developed by Parkinson (in-house).

NBS-981 was used as a primary standard to ensure accuracy and reproducibility throughout the study. In both batches of samples, 3-4 filaments of natural and double-spiked NBS-981 were analysed prior to samples, and deconvolved to produce isotope ratios from which reproducibility was determined. The $^{206}Pb/^{204}Pb$ ratio of NBS981 yielded average values of 16.9439 ± 8 (46 ppm 2 s.d.) and 16.9448 ± 29 (175 ppm 2 s.d.) in the two analytical sessions. The $^{207}Pb/^{204}Pb$ ratio of NBS-981 yielded average values of 15.5010 ± 30 (198 ppm 2 s.d.) and 15.5027 ± 26 (168 ppm 2 s.d.) in the two analytical sessions. The $^{208}Pb/^{204}Pb$ ratio of NBS981 yielded average values of 36.7343 ±37 (100 ppm 2 s.d.) and 36.7398 ± 74 (200 ppm 2 s.d.) in the two analytical sessions. As these values are outside of uncertainty of the accepted values

($^{206}Pb/^{204}Pb$ = 16.9409 ± 22, $^{207}Pb/^{204}Pb$ = 15.4956 ± 26, $^{206}Pb/^{204}Pb$ = 36.7228 ± 80; Thirlwall, 2000), corrections were performed on each batch of samples.

A.7. Stable isotope geochemistry (Sr by TIMS, Rb by MC-ICP-MS, Rb and Sr by ID)

Separate dissolutions were prepared for samples for which stable Rb and Sr isotopic analyses were performed. To help illustrate this, these methods are simplified into the flow chart in Figure A.4. In total, one single dissolution provides enough sample for a total of five different analyses: Rb and Sr natural analyses, double spike Sr, and Rb and Sr concentrations by ID.

Mineral separates were hand-picked from disc-milled crushate. To determine between plagioclase and K-feldspar, feldspars were mounted onto SEM stubs and analysed on a Zeiss Supra 55V SEM at the Open University to easily differentiate between the two classes of mineral.

Dissolution procedures are identical to those described in section A.6.1, with each dissolution calculated to provide at least 2100 ng Sr.

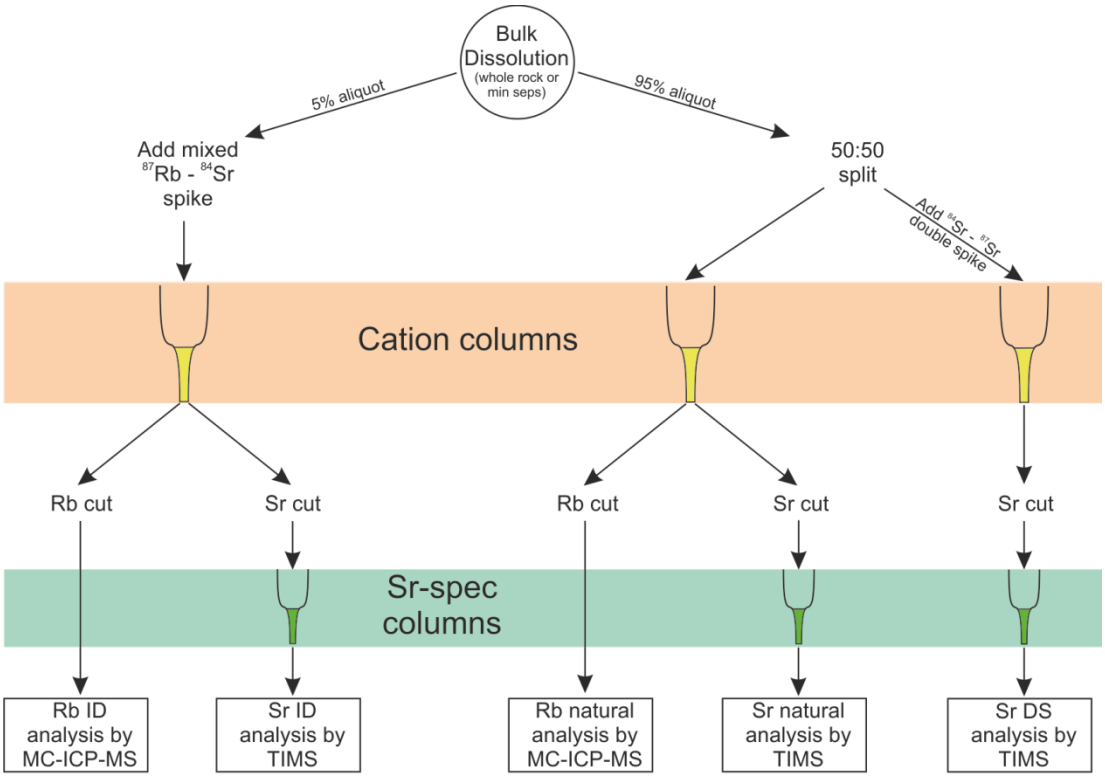

Figure A.4: *Flow diagram showing sample preparation processes in stable Sr and Rb isotopic studies.*

A.7.1. Sample aliquoting and column procedures

Following dissolution, 5% of each sample was transferred to a new beaker in preparation for ID measurements. To this aliquot, an ^{87}Rb-^{84}Sr mixed spike was added. The remaining 95% of sample was then divided into two: one for natural Rb and Sr analysis and the other for Sr DS analysis. To the latter was added an ^{87}Sr-^{84}Sr double spike.

All samples were then dried down and redissolved in 1 ml 1.25M HCl, in preparation for cation column chemistry. Cation column chemistry procedures are identical for all aliquots and are similar to those described in section A.6.2, however shall be detailed here:

- Load 1 ml of clean resin in a pre-cleaned column.
- Clean the column and resin with two full column volumes of 6 M HCl, followed by two full column volumes of MQ H_2O.
- One full column volume of 1.25 M HCl is then eluted.

- The sample (dissolved in 1 ml 1.25 M HCl) is then added to the column, followed by a further 5 ml 1.25 M HCl, eluting to waste.
- Add 24 ml 1.25 M HCl, and collect for Rb analysis.
- Add 10 ml 2.5M HCl, and collect for Sr analysis.
- Clean the column and resin with three full column loads 6 M HCl, and store in clean acid.

All aliquots were then dried down, with Rb cuts now ready for analysis. The three Sr cuts were then redissolved in 1 ml 2M HNO_3, and passed through Sr-spec columns, in the same procedure as described in section A.6.3.

A.7.2. Rb ID measurements (by MC-ICP-MS)

Rb cuts from the natural aliquot cation column were dried down and redissolved in 1 ml 3% HNO_3. Of this, 0.05 ml was extracted and diluted up to 1 ml with HNO_3, in order to perform a concentration test. All remaining sample was then diluted to a concentration of 100 ppb Rb with additional 3% HNO_3.

Rb concentrations were measured at the Open University on a Thermo-Fisher Neptune MC-ICP-MS in static low resolution mode fitted with standard H cones. A stable introductory system (SIS) was used, with a typical uptake rate of ~50 µl/min. Faraday cup configurations and any major associated interferences are shown in Table A.7.

Collector	L4	L3	L2	L1	C	H1	H2	H3	H4
Mass	^{83}Kr	^{84}Sr	^{85}Rb	^{86}Sr	^{87}Rb	^{88}Sr	^{90}Zr	^{91}Zr	^{92}Zr
Interference		^{84}Kr		^{86}Kr	^{87}Sr				

Table A.7: *Faraday cup configurations for ID and natural Rb isotopic measurements by MC-ICP-MS.*

Machine gain was measured each day before analytical work began. Samples were run in one block of 50 measurements, with a 4.194 second integration time for each measured ratio. A peak centre and a baseline measurement were run at the start of each analysis. Following each sample, the machine and nebuliser were washed with 3% HNO_3 for at least 15 minutes, or until the measured blank showed no Rb spikes or washout effects.

Rb concentrations were then calculated using known spike composition and quantity using software developed by Charlier (in-house).

A.7.3. Sr ID measurements (by TIMS)

Sr cuts from Sr-spec column chemistry were dried down and redissolved in 1 µl 16M HNO_3 and loaded onto rhenium filaments with a Ta_2O_5 activator. Sr isotopes were analysed at the Open University on a Thermo-Fisher TIMS. Faraday cup configurations are shown in Table A.8. Filaments were heated until ^{88}Sr yielded an intensity of at least 8 V, commonly this occurred at a filament temperature of roughly 1400°C.

Collector	L2	L1	C	H1	H2	H3
Mass	^{84}Sr	^{85}Rb	^{86}Sr	^{87}Sr	^{88}Sr	89

Table A.8: *Faraday cup configurations for radiogenic and stable Sr isotopic measurements by TIMS.*

A.7.4. Stable Rb isotope measurements (by MC-ICP-MS)

Rb cuts from the natural aliquot cation column were dried down and redissolved in 1 ml 3% HNO_3. Of this, 0.05 ml was extracted and diluted up to 1 ml with HNO_3, in order to perform a concentration test. All remaining sample was then diluted to a concentration of 100 ppb Rb with additional 3% HNO_3, and doped with 600 ppb Zr single element solution.

Rb isotopes were analysed at the Open University using a Thermo-Fisher Neptune MC-ICP-MS in static low resolution mode fitted with standard H cones. A stable introductory system (SIS) was used, with a typical uptake rate of ~50 µl/min. Faraday cup configurations and any major associated interferences are shown in Table A.7.

Machine gain was measured each day before analytical work began. Samples were run in one block of 120 measurements, with a 4.194 second integration time for each measured ratio. A peak centre and a baseline measurement were run at the start of each analysis. Following each sample, the machine and nebuliser were washed with 3% HNO_3 for at least 15 minutes, or until the measured blank showed no Rb spikes or washout effects.

At the start of each analytical session where stable Sr isotopes were also measured, 5-6 standards of Zr-doped NBS-984 were analysed assuming an $^{85}Rb/^{87}Rb$ ratio of 2.59265 (IUPAC value, Berglund and Wieser, 2011), in order to determine the instrumental mass bias for that analytical session. Following this, several more Zr-doped NBS-987 standards were analysed, this time assuming the average $^{90}Zr/^{91}Zr$ determined previously to account for internal mass bias, in order to determine machine reproducibility for that day.

Isobaric interferences of ^{87}Sr on ^{87}Rb and ^{86}Kr on ^{86}Sr were monitored by measuring ^{88}Sr and ^{83}Kr, respectively. Analyses were corrected for instrumental mass fractionation using the exponential fractionation law, with the ^{86}Kr interference on ^{86}Sr stripped off iteratively, assuming an $^{86}Kr/^{83}Kr$ ratio of 0.6209 and an $^{86}Sr/^{88}Sr$ ratio of 0.1194 (Thirlwall, 1991; de Laeter et al., 2003). ^{87}Rb was then corrected for ^{87}Sr interferences using an $^{87}Sr/^{88}Sr$ ratio of 0.084804 (Berglund and Wieser, 2011).

The standard NBS-984 was utilised to ensure long term machine reproducibility across the three analytical sessions used in this study. The average $^{85}Rb/^{87}Rb$ across this period was 2.59058 ± 19 (72 ppm 2 s.d., n = 46). In addition, four measurements were taken of NBS-984 doped with 1 ppb, 10 ppb and 100 ppb NBS-987 (Sr standard) in order to test the robustness of the Sr interference correction. Average measured $^{85}Rb/^{87}Rb$ values were: 1 ppb Sr = 2.590564 ± 13

(50 ppm 2 s.d.), 10 ppb = 2.590549 ± 22 (85 ppm 2 s.d.), and 100 ppb Sr = 1.590635 ± 8 (30 ppm 2 s.d.). The measured $^{85}Rb/^{87}Rb$ of both 1 ppb and 10 ppb doped NBS-984 are within uncertainty of those obtained in undoped standards, and yield similar reproducibilities, highlighting the robustness of the interfering element correction at these concentrations of Sr.

A.7.5. Stable Sr isotope measurements (by TIMS)

Natural and double spike Sr cuts from Sr-spec columns were then prepared for analysis by TIMS. Natural and double spike aliquots were treated identically, though kept separate and analysed in different analytical sessions. Aliquots were dried down before being redissolved in 1 µl 16M HNO_3 and loaded onto rhenium filaments with a Ta_2O_5 activator.

Sr isotopes were analysed at the Open University on a Thermo-Fisher TIMS. Faraday cup configurations are shown in Table A.8. Filaments were heated until ^{88}Sr yielded an intensity of at least 8 V, commonly this occurred at a filament temperature of roughly 1400°C. Data were collected in 54 blocks of 10 ratios, each with a 16 second integration. Baselines were measured by source deflection after a 30 sec pre-baseline wait time for 2 minutes after each step in the amplifier rotation. Amplifiers were cycled through each mass, with the dummy mass 89 used to fully allow discharge of the amplifier used for ^{88}Sr collection back to baseline levels, before the same amplifier then collects the smaller ^{84}Sr beam.

Deconvolution of the natural and spiked samples was carried out offline using equations outlined by Neymark et al. (2014) which involve an iterative solution using a Newton-Raphson technique. A 5000 iteration Monte-Carlo simulation (Rudge et al., 2009) was used to calculate the uncertainties for the deconvolved data.

NBS-981 was used as a primary standard to ensure accuracy and reproducibility throughout the study. In both batches of samples, 3-4 filaments of natural and double-spiked NBS-981 were analysed prior to samples, and deconvolved to produce isotope ratios from which reproducibility was determined. The average $^{87}Sr/^{86}Sr$ value for the two analytical sessions was 0.710282 ± 23 (33 ppm 2 s.d.), average $^{84}Sr/^{86}Sr$ = 0.056490 ± 5 (82 ppm 2 s.d.), and average

$^{88}Sr/^{86}Sr$ = 8.3759 ± 45 (53 ppm 2 s.d.). Of these ratios, only the $^{84}Sr/^{86}Sr$ ratio is within uncertainty of the accepted values ($^{87}Sr/^{86}Sr$ = 0.710249, $^{84}Sr/^{86}Sr$ = 0.056491, $^{88}Sr/^{86}Sr$ = 8.375209; Thirlwall, 1991; Berglund and Wieser, 2011), data were corrected to bring standard data in line with accepted values in each analytical session.

A.8. Zircon geochemistry

A.8.1. Zircon separation

Zircons were extracted from crushate reserved from milling for whole-rock geochemistry. Separation took place at NERC Isotope Geosciences Laboratory (NIGL) and consisted of several stages. Crushate was first disc milled to shear minerals apart from each other. Minerals were then sieved to ensure all minerals were between 10 µm and 355 µm, prior to the separation of heavy and light minerals on a Rogers table. Heavy fractions from the Rogers table were then magnetically separated using a Frantz magnetic separator, before the non-magnetic fraction was passed through heavy liquids (diiodomethane). Finally, zircons were hand-picked from this heavy non-magnetic fraction and mounted in 25 mm epoxy resin discs. Discs were polished to reveal an equatorial section of the zircons, and imaged by cathodoluminescence (CL) on an FEI Quanta 600 SEM at the British Geological Survey using a 10kV electron beam, a beam current of 0.2 nA and a 16 mm working distance.

A.8.2. Zircon O geochemistry

Zircons were first analysed for their O isotope geochemistry, with rims and cores targeted based on CL images. Zircon oxygen isotopes were measured on a Cameca 1270 ion microprobe at the Edinburgh Ion Microprobe Facility (EIMF), University of Edinburgh. The $^{133}Cs+$ primary ion beam was accelerated at 10 kV with a current of ~5.0 nA. Charge compensation of the Au-coated samples was accomplished using a normal incidence electron flood gun. A pre-sputtering time of 40 s was applied to remove the Au-coat with a fixed beam that produced

roughly elliptical 10 by 15 μm pits. Ions were extracted with a 10 kV voltage, and low energy secondary ions of ^{16}O and ^{18}O were selected using an energy window of 60 eV. During each analysis, the secondary beam was automatically scanned across a small field aperture for centering along the ion-optic axis, followed by scanning the entrance slit across the contrast aperture. Analyses were performed in two blocks of ten cycles with a total count time of 80 s.

Two reference zircons, 91500 (Wiedenbeck et al., 2004) and an internal standard (Laura) were analysed in the same mount as the samples. Analyses bracketed sample analyses, with an average of 10 sample analyses between each set of reference analyses. The instrumental mass fractionation factor was determined using the accepted values for the reference material (Laura $\delta^{18}O_{VSMOW}$ = 5.3 ‰, and 91500 $\delta^{18}O_{VSMOW}$ = 10.07 ‰; both measured in-house). Measured $^{18}O/^{16}O$ was normalised to Vienna Standard Mean Ocean Water compositions (VSMOW), and then corrected for instrumental mass fractionation. Standards were also used to measure and correct for drift throughout analytical sessions. Standard reproducibility was <2.5% (2 s.d.) in all analytical sessions.

A.8.3. Zircon U-Pb geochronology

Following O isotope geochemistry, all excess Au coating was removed and zircons were re-analysed on the same spot for their U-Pb ages. U-Pb analyses were conducted on a Nu Instruments Nu Plasma HR multi-collector ICP-MS (inductively coupled plasma mass spectrometer) coupled to a New Wave Research UP193ss Nd:YAG laser ablation system using a low-volume ablation cell (Horstwood et al., 2003) at the NERC Isotope Geosciences Laboratory, Keyworth, UK. Helium was used as the carrier gas through the ablation cell (at a flow rate of 0.8 l/min) with Ar makeup gas being connected via a T-piece and sourced from a Cetac Aridus I desolvating nebulizer. Laser ablation was accomplished with a 25 μm diameter spot size with a laser fluence of ~2 J/cm2 at 5 Hz for 30 s.

Masses ^{202}Hg, $^{204}Pb+Hg$, ^{206}Pb, ^{207}Pb and ^{238}U were analysed using 100 ms integration times, and ^{235}U was calculated using a $^{238}U/^{235}U$ of 137.818 (Hiess et al., 2012). The Pb/Pb and U/Pb

ratios were normalized to the bracketing primary reference zircon 91500 based on the average measured value compared to the ratio determined by ID-TIMS (Wiedenbeck et al., 1995). Secondary reference zircons GJ-1 (Jackson et al., 2004) and Plešovice (Slama et al., 2008) were used to validate the 91500 normalization. All Pb/Pb and U/Pb reference material analyses yielded an external reproducibility of < 2 % (2σ) in individual analytical sessions and long term (four analytical sessions, see Figure A.5).

Systematic uncertainties were propagated using quadratic addition incorporating the excess variance of the reference material during each analytical session, the isotopic uncertainties of the reference material as determined by ID-TIMS, long term variance of the ICP-MS, and decay constant uncertainties.

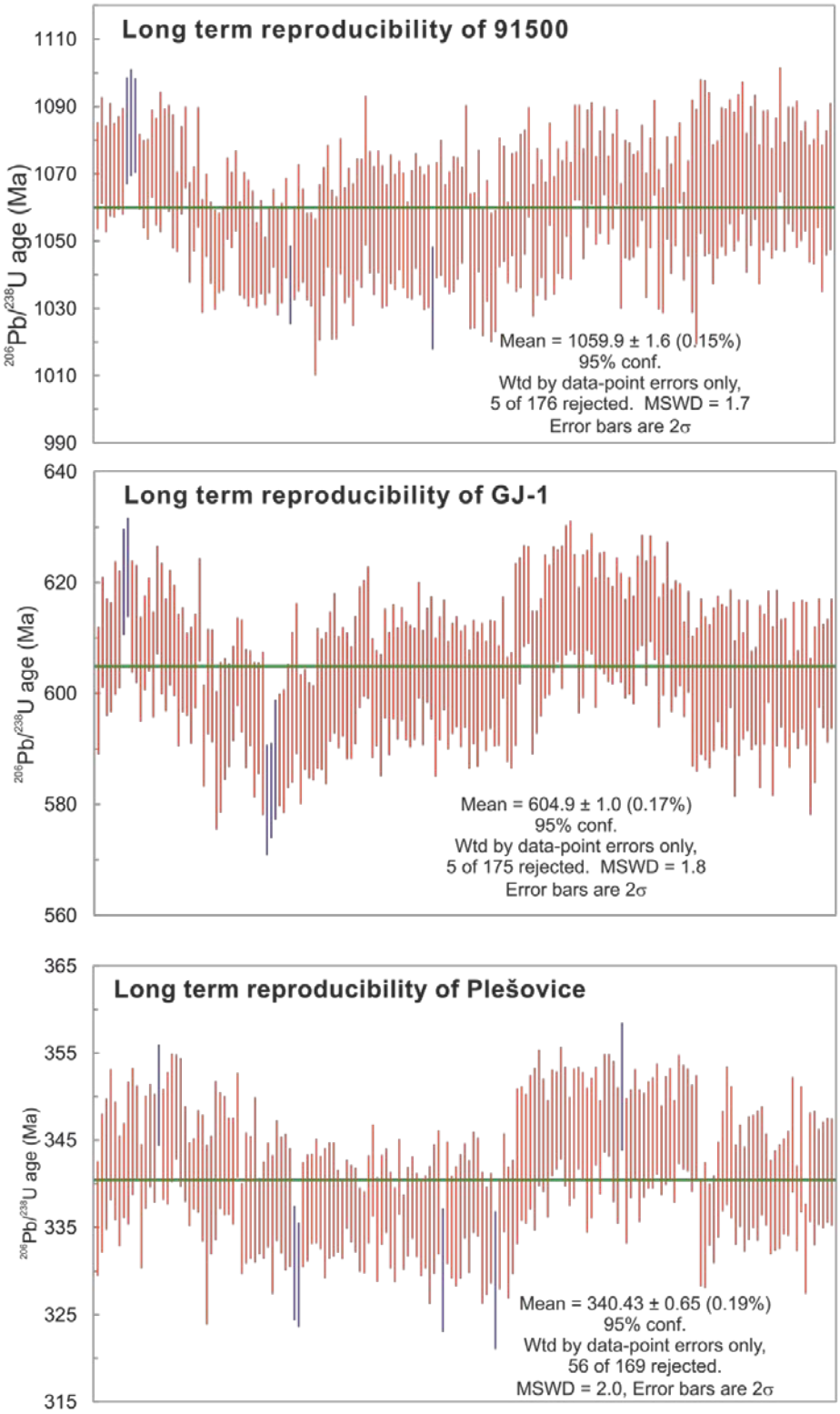

Figure A.5: *Long term reproducibility of $^{206}Pb/^{238}U$ ages of 91500, GJ-1 and Plešovice. Blue bars represent rejected data.*

A.8.4. Zircon Hf geochemistry

After U-Pb geochronology, samples were re-analysed on the same spot for their Lu-Hf isotopic composition. Lu-Hf analyses were carried out at NIGL on a Thermo Scientific Neptune Plus MC-ICP-MS coupled to a New Wave Research 193UC ArF excimer laser ablation system and the TwoVol2 cell. Helium was used as the carrier gas through the ablation cell (at a flow rate of 0.8 l/min) with Ar makeup gas being connected via a T-piece and sourced from a Cetac Aridus I desolvating nebulizer. After initial set-up and tuning, a 2% HNO3 + 0.01 molar HF solution was aspirated during the ablation analyses. The masses ^{172}Yb, ^{173}Yb, ^{175}Lu, ^{176}Hf+Yb+Lu, ^{177}Hf, ^{178}Hf , ^{179}Hf and ^{180}Hf were measured simultaneously during static 30 s ablations at 10 Hz with a 35 μm diameter spot and a fluence of 6-7 J/cm^2.

A standard–sample–standard bracketing technique, using reference zircons 'Mud Tank' (to correct ^{176}Hf/^{177}Hf, Woodhead and Hergt, 2005) and '91500' (to correct ^{176}Hf/^{177}Hf and ^{176}Lu/^{177}Hf, Hiess et al., 2012), was used to monitor accuracy and precision of internally corrected Lu and Hf isotope ratios and instrumental drift with respect to the Lu/Hf ratio. Hf reference solution JMC475 (both doped with 50 ppb Yb and undoped) was analysed during the analytical session to allow characterization of the instrument performance and validation of the ^{176}Yb interference correction. Reference zircon 'Plešovice' (Slama et al., 2008) was also used to validate normalization. Correction for ^{176}Yb on the ^{176}Hf peak was made using reverse-mass-bias correction of the ^{176}Yb/^{173}Yb ratio (0.7941) empirically derived using Hf mass bias corrected Yb-doped JMC475 solutions (Nowell and Parrish, 2001). ^{176}Lu interference on the ^{176}Hf peak was corrected by using the measured ^{175}Lu and assuming ^{176}Lu/^{175}Lu = 0.02653 and mass bias equivalent to Hf (Berglund and Wieser, 2011). Long term reproducibility was measured across five analytical sessions, with 91500 yielding an average ^{176}Hf/^{177}Hf value of 0.282297 ± 27 (95 ppm, 2 s.d., n = 99, see Figure A.6), with reproducibility in any given analytical session better than 120 ppm. Mud Tank (only used in two analytical sessions) provided an average ^{176}Hf/^{177}Hf = 0.282504 ± 27 (91 ppm, 2 s.d., n = 24). Second standard

Plešovice yielded an average $^{176}Hf/^{177}Hf$ = 0.282473 ± 19 (67 ppm, 2 s.d., n = 54, see Figure A.6).

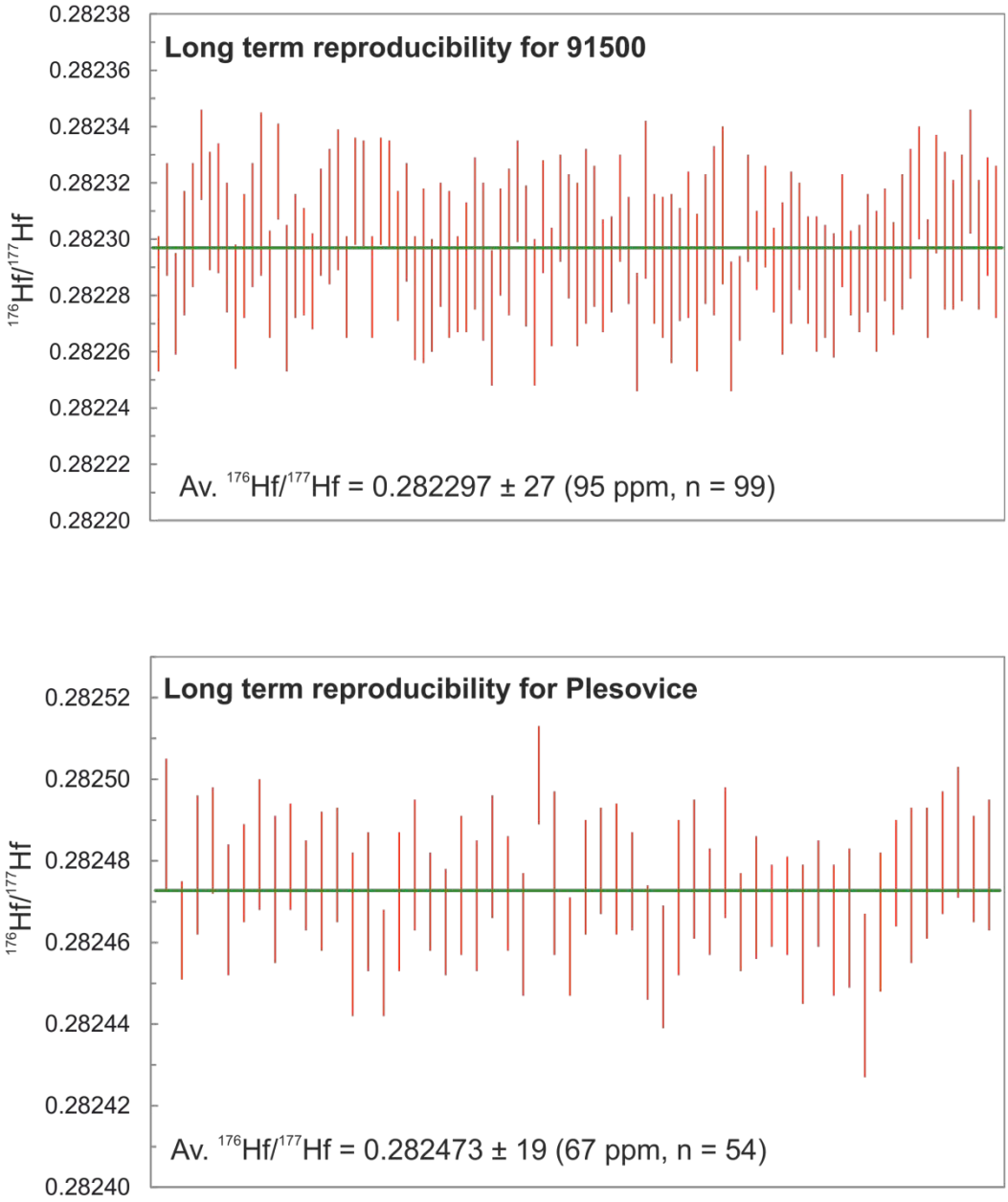

Figure A.6: *Long term $^{176}Hf/^{177}Hf$ reproducibility for 91500 and Plešovice.*

Appendix B

Comparison of techniques for the dissolution of granitic material

B.1. Introduction

One problem encountered early in this project was the question of how to dissolve granitic material for trace element and isotopic analyses. A main consideration when dealing with granites is the presence of zircon and other accessory minerals which are difficult to dissolve by conventional means (hand-cranked beaker dissolutions). Traditionally, high-pressure bomb dissolution is the standard technique for dissolving rock samples containing zircon. While the method ensures complete dissolution of zircon, it is however both time-consuming and risky in its acid usage when compared to other methods.

Zircons are a primary host of Zr, Hf and heavy REEs, while other accessory phases such as garnet and monazite may be an important residence of other REEs. Therefore if data is to be obtained that fully represents the bulk rock composition of these elements it is important that they are fully dissolved. However, one additional issue for Himalayan leucogranites is that zircons crystallize around pre-existing detrital cores, meaning that up to 90% of the zircon did not originate from Miocene melts. As such, it is arguable that excluding such cores from dissolutions would be preferable in order to gain accurate geochemical insights into Himalayan melting and granite genesis. However it is first necessary to evaluate whether or not the

dissolution of zircons has any bearing on trace element geochemical data obtained, and whether significant quantities of any elements of interest are excluded by not thoroughly dissolving zircons.

One previous study by King (2007) involving the comparison of two techniques to dissolve zircons, by hand-cranked beaker and by high pressure bomb, found that while the hand cranked beaker dissolutions were highly depleted in both Zr and Hf (both % level constituents of zircon), the type of dissolution made little difference to the REE abundances yielded by either technique.

In this experiment, I use a small selection of samples and compare trace element and REE data obtained from the two acid-digestion techniques (hand-cranked beaker and high-pressure bomb) and a third technique, involving the analysis of fluxed glass discs. The digestion of sample powders in a lithium metaborate flux is safer and quicker than the two acid digestion, as no acids are required and glass discs from major element analysis by XRF may be recycled. Such glass discs shall then be analysed by laser ablation (LA) ICP-MS.

B.2. Methods

B.2.1. Hand-cranked beaker dissolutions

Dissolutions in hand-cranked beakers used the following methods:

- 0.2 g of sample was weighed in Teflon hand cranked beakers.
- Samples were dissolved in a 2 ml HF / 0.2 ml HNO_3 mix at 130°C and left overnight.
- Samples were then dried down, and redissolved in 2 ml HCl at 130°C and left overnight.
- Samples were then dried down once more.
-

B.2.2. High-pressure bomb dissolutions

Dissolutions in high-pressure bombs used the following methods:

- 0.02 g of samples was weighed into Teflon inner capsules.
- 0.1 g (100 ul) of multi-element dope (Be, In, Rh, Tm, Re, Bi) was added to each capsule.
- 0.7 ml HF and 0.2 ml HNO_3 was added to each capsule, before the capsule was sealed, inserted into the plastic sleeve and then placed into the outer metal jacket and sealed.
- Bombs were placed in an oven at 210°C for a week
- Bombs were taken out of the oven and left to cool entirely before opening.
- Samples were pipetted out of inner capsules and into clean hand-cranked beakers to be dried down.
- Once dry, samples were redissolved in 2 ml HCl overnight.
- Samples were dried down once more, and redissolved in 2 ml HNO_3 overnight.
- Samples were then once more dried down.

B.2.3. Fluxed glass disc production

Fluxed glass discs were produced as described in Appendix A (Section A.4.1).

B.2.4. Solution ICP-MS analysis

Solutions from both hand-cranked beaker and high-pressure bomb were analysed on an Agilent 7500a quadrupole ICP-MS at the Open University. A quartz spray chamber and PFA nebuliser were used, with an uptake rate of ~500 µl/min. Count rates were typically 4 – 8 x 10^7 cps/ppm. Oxides (measured by CeO^+/Ce^+) were typically < 0.4%, and double charged species (measured by Ce^{++}/Ce^+) were < 1%.

Analyses were standardised against 5 USGS reference materials (BIR-1, W-2, BHVO-2, DNC-1 and AGV-1), while instrumental drift was monitored and corrected by measuring repeat analyses of DNC-1 every 6 unknowns.

B.2.5. LA-ICP-MS analysis

Glass discs were analysed by LA-ICP-MS on a ThermoScientific ICAP-Qc quadrupole ICP-MS at the University of Leicester. Full descriptions of this technique are described in Appendix A (Section A.5).

B.3. Results

REE concentrations (normalised to chondritic values of McDonough and Sun, 1995) plus other selected trace element data for the seven samples analysed used in the method comparison are shown in Table 3.1 (Pm is calculated from the average normalised value of Nd and Sm abundances, while Tm data for ICP-MS solutions are calculated from an average value of normalised Er and Yb). Figure 3.1 shows REE data for six samples (1D01, 1G02, 1G03, 3A02, 3A03, 3A04) repeated across different methodologies.

Table B.1: REE and selected trace element data for samples analysed by different techniques. Abundances in ppm.

		1D01			1G02	1G03	3A01		3A02		3A03		3A04
		Batch 1 Run 1	Batch 1 Run 2	Batch 2	Batch 2	Batch 2	Batch 1 Run 1	Batch 1 Run 2	Batch 1 Run 1	Batch 2	Batch 1 Run 1	Batch 1 Run 2	Batch 2
Hotplate dissolution Solution ICP-MS	La	28.7	27.0	19.8	40.8	22.0	3.55	3.43	7.63	13.0	17.4	18.6	15.5
	Ce	26.2	24.8	19.3	35.1	12.2	2.68	2.56	6.08	10.5	16.2	15.8	12.0
	Pr	21.9	20.5	15.1	26.5	15.8	2.24	2.09	4.76	8.12	11.6	11.9	9.06
	Nd	16.2	15.1	11.4	19.1	11.7	1.57	1.48	3.18	4.96	8.54	8.60	5.80
	Pm	16.5	15.3	12.2	17.9	11.4	1.92	1.81	3.87	5.25	9.00	8.98	6.49
	Sm	16.7	15.6	12.9	16.6	11.2	2.27	2.14	4.57	5.53	9.46	9.35	7.18
	Eu	6.04	5.58	5.86	7.54	3.43	1.13	1.10	0.984	0.611	4.23	4.20	1.01
	Gd	13.8	12.6	11.0	13.1	10.0	2.23	2.00	4.69	3.88	8.03	7.75	6.56
	Tb	17.3	15.1	14.0	14.6	13.0	3.59	3.12	8.55	5.88	9.66	9.16	9.63
	Dy	14.4	13.0	12.8	13.2	12.6	3.11	2.85	8.82	5.59	7.47	7.20	9.50
	Ho	11.6	10.4	10.9	11.6	11.7	2.51	2.28	7.71	4.50	5.35	5.09	8.26
	Er	10.7	9.42	9.95	11.2	11.5	2.46	2.17	8.01	4.33	4.47	4.11	8.09
	Tm	10.2	8.90	9.51	10.6	11.0	2.69	2.35	8.71	4.47	3.89	3.53	8.14
	Yb	9.76	8.38	9.07	9.95	10.47	2.93	2.52	9.41	4.62	3.31	2.96	8.18
	Lu	8.27	6.98	7.35	8.77	9.22	2.75	2.21	8.53	3.84	2.74	2.34	7.17
	Zr	0.805	0.961	0.930	9.712	16.4	0.469	0.575	3.43	9.42	3.77	3.95	1.69
	Hf	0.042	0.172	0.181	0.216	0.227	0.026	0.054	0.201	0.095	0.164	0.057	0.177
High-pressure bomb dissolution Solution ICP-MS	La	108	109	60.2	102	136	6.33	6.20	145	12.4	20.80	20.40	185
	Ce	112	114	83.3	91.5	126	4.60	4.62	118	18.7	16.07	15.97	155
	Pr	77.1	78.2	46.6	61.6	84.5	3.73	3.80	72.6	7.34	12.9	12.9	95.1
	Nd	51.9	53.4	33.8	43.3	59.7	2.60	2.63	39.9	4.50	9.36	9.31	55.5
	Pm	50.4	51.6	35.5	40.2	56.2	3.23	3.32	38.3	5.38	9.99	10.00	53.7
	Sm	48.9	49.9	37.2	37.1	52.7	3.87	4.00	36.6	6.27	10.61	10.70	51.8
	Eu	8.88	8.76	6.75	7.85	8.15	1.75	1.81	1.03	0.98	5.12	5.00	1.84
	Gd	37.1	37.3	33.6	31.5	43.5	3.97	4.02	22.5	5.73	9.35	9.39	34.6
	Tb	37.6	37.9	39.8	31.8	44.7	5.73	5.66	20.6	7.84	9.90	10.1	33.1
	Dy	32.1	32.5	37.5	30.0	42.7	5.76	5.77	14.9	7.73	8.40	8.35	26.8
	Ho	23.1	23.7	30.2	26.7	37.8	4.64	4.69	9.33	6.14	5.99	5.94	18.1
	Er	19.8	20.1	28.0	26.5	38.0	4.79	4.90	8.03	6.29	5.09	5.10	15.9
	Tm	17.5	17.7	26.5	26.0	37.0	5.31	5.37	7.86	7.39	4.50	4.49	14.4
	Yb	15.2	15.4	25.0	25.6	35.9	5.84	5.83	7.69	8.48	3.90	3.87	12.9
	Lu	11.5	12.5	21.6	22.4	31.6	5.19	5.31	7.02	7.91	3.15	3.32	10.7
	Zr	69.6	68.9	55.2	41.0	60.7	6.25	6.54	33.4	42.1	33.1	33.6	36.3
	Hf	2.89	2.99	2.35	1.42	2.06	0.335	0.349	1.50	2.19	1.27	1.32	1.78
Fluxed glass discs LA-ICP-MS	La	24.0			51.7	53.9	4.76		14.8		22.4		21.9
	Ce	24.2			42.1	47.6	3.72		12.2		18.9		17.5
	Pr	17.5			28.7	31.5	2.35		7.59		12.4		10.1
	Nd	11.9			18.0	19.2	1.35		4.14		7.72		5.53
	Pm	11.9			16.2	17.7	1.57		4.56		8.10		5.57
	Sm	11.9			14.4	16.1	1.80		4.97		8.49		5.61
	Eu	4.51			6.76	4.73	0.756		0.849		3.55		0.652
	Gd	8.22			9.62	10.6	1.27		3.28		5.06		3.57
	Tb	12.3			12.2	13.9	2.21		6.25		6.73		5.94
	Dy	12.3			12.2	14.2	2.32		7.32		5.95		6.34
	Ho	9.69			10.9	12.6	1.59		5.89		4.15		5.34
	Er	8.79			11.0	12.3	1.59		6.33		3.64		5.29
	Tm	8.01			10.3	11.6	1.59		6.86		3.08		5.15
	Yb	7.23			9.64	10.9	1.60		7.39		2.52		5.01
	Lu	6.46			10.2	10.7	1.35		6.68		2.34		4.79
	Zr	43.2			43.2	49.5	5.79		36.2		30.8		13.5
	Hf	2.21			1.81	1.99	0.31		2.17		1.37		0.73

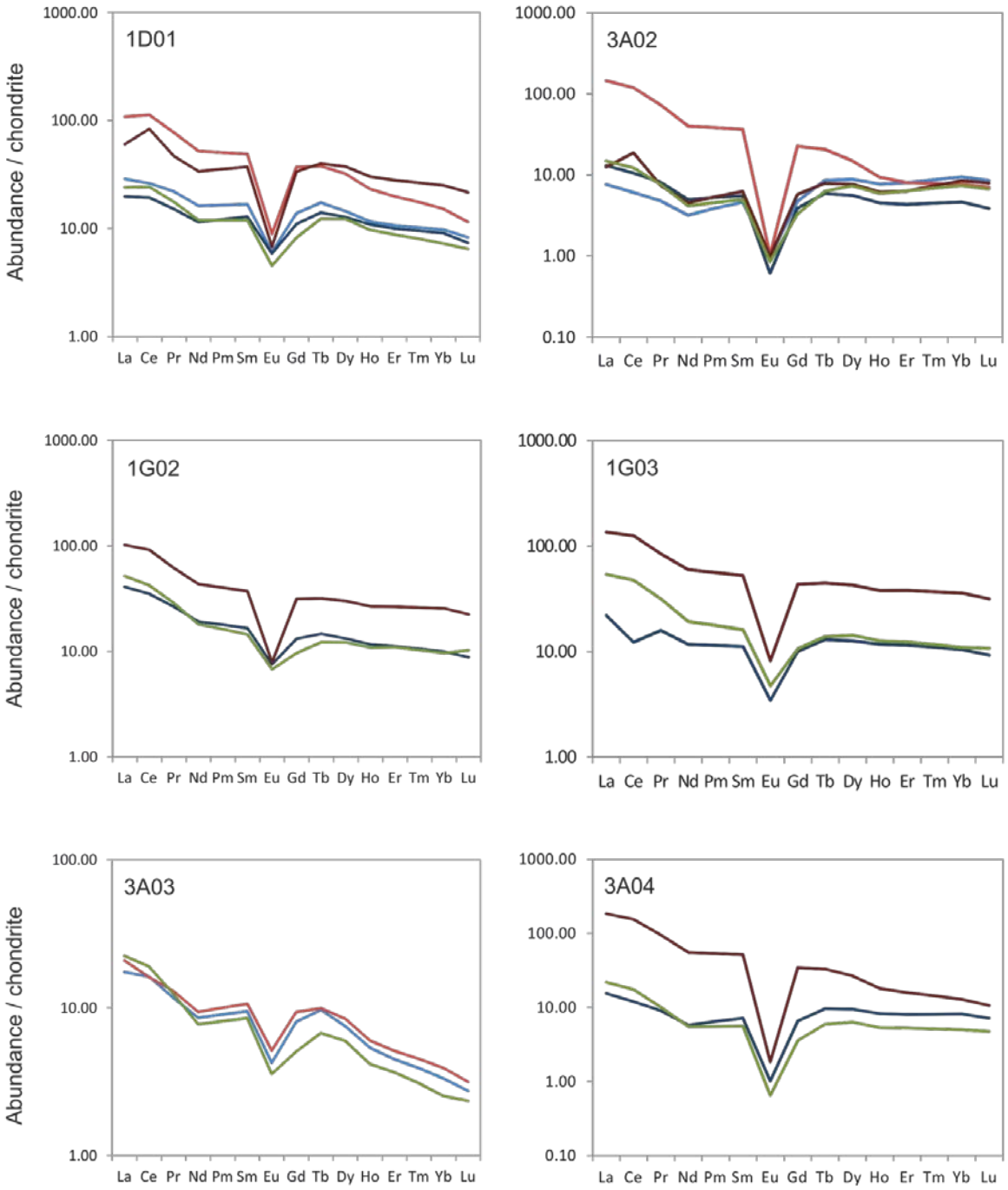

Figure B.1: *REE plots for selected samples analysed for their geochemistry by different methodologies. Pale red lines = Batch 1 high-pressure bomb dissolution, Dark red = batch 2 high-pressure bomb dissolution, Pale blue = batch 1 beaker dissolution, Dark blue = batch 2 beaker dissolution, Green = LA-ICP-MS.*

Data obtained from high-pressure bomb dissolutions are up to an order-of-magnitude higher than the same element from other methods. From Table 3.1 it is apparent that Zr and Hf (both elements present at percentage level in zircon) are found in much higher abundance in high-pressure bomb dissolutions than in the hand-cranked beaker dissolved samples. However for the REE analyses there are no obvious enrichments in HREEs relative to LREEs for the high-pressure bomb dissolutions. For two samples (3A02 and 3A04) the HREE abundances in high-pressure bomb and beaker preparations are very similar, with deviations only seen in the LREEs. All samples appear to contain higher abundances of LREEs in high-pressure bomb dissolutions than in the beaker dissolutions.

For both samples that were repeated in different batches, the REE data vary considerably. In the case of sample 1D01, the abundances obtained from the batch 1 high-pressure bomb are enriched in LREEs relative to the second batch, but depleted in HREEs. The first batch for sample 3A02 is hugely enriched in LREEs, but has a similar HREE signature. Similar differences between batches can be observed for the beaker-dissolved samples, although the magnitude of variation is far less.

REE abundances from LA-ICP-MS analyses (green lines in Figure 3.1) most closely resemble the data obtained by beaker dissolution; however the Zr and Hf concentrations are more similar to the compositions of high pressure bomb dissolutions.

B.4. Discussion

Zr and Hf abundances, two elements found in percentage level in zircon, are similar in both fluxed glass disc and high-pressure bomb dissolutions, however are far lower in hand-cranked beaker dissolutions. This suggests that beaker dissolutions do not sufficiently dissolve zircon, a finding consistent with previous studies (e.g. King, 2003). There are also differences in REE abundances using the different methodologies, as illustrated in Figure 3.1. Fluxed glass disc

concentrations are similar to those found in beaker dissolutions, however high-pressure bomb REE concentrations are typically higher.

As it is clear from both observations by SEM and Zr and Hf abundances that fluxed glass discs fully dissolve zircon and other accessory phases, it appears that zircon contributes little to the REE budget of these rocks, due to the similarity in REE concentrations between fluxed glass disc and beaker dissolutions. The higher concentrations found in high-pressure bomb dissolutions is therefore a cause for concern, as it cannot be explained by additional dissolution of accessory phases. Additionally, variations are seen in different dissolutions of the same sample by high-pressure bomb. One explanation for this could be that because of the small quantity of sample used in high-pressure bomb dissolutions (0.02 g), different aliquots may contain varying quantities of critical REE-bearing phases, despite extensive efforts to fully homogenise sample powders. Another possibility is that high-pressure bombs become increasingly difficult to clean with more use. Older bombs often contain small ridges and cracks that would potentially harbour sample material from previous dissolutions. For both batches of high-pressure bomb dissolutions, total procedural blanks were also analysed, and in both cases blank values were very low (<10 ppb for all REEs), however it could be that individual bombs are affected, rather than all of them.

As the fluxed glass disc dissolutions fully dissolve zircon and do not appear to have a problem with sample heterogeneity (0.7 g of sample is used per glass disc, as opposed to 0.02 g for high-pressure bomb), and due to the swift and safe nature of sample preparation, I conclude that this method is the most suitable and useful for the dissolution of granitic material.

B.5. Conclusions

In this study I have analysed the trace element and REE geochemistry of seven leucogranite samples in order to determine the method best suited to the investigation of granitic material. Consistent with previous investigations, it was determined that the conventional hand-cranked beaker dissolution was unsuccessful in entirely dissolving accessory phases (e.g. King, 2007). Concentrations of Zr and Hf, elements almost entirely situated within zircon, are found in far lower concentrations in the beaker dissolutions than in both high-pressure bomb dissolutions and fluxed glass discs, typically only yielding ~5-10% of the abundances.

However this lack of dissolution appears to have less of an effect on REE abundances. Hand-cranked beaker dissolutions typically yield REE abundances similar to those obtained from fluxed glass discs (confirmed by SEM observations to fully dissolve all accessory phases). Higher concentrations obtained from high-pressure bomb dissolutions are often variable between different solutions of the same sample. It was concluded that this was caused by either sample heterogeneity (based on the small amount of material dissolved by high-pressure bomb) or due to the difficulty to thoroughly clean bombs, leading to an inherent uncleanliness; or a combination of the two.

It was therefore concluded that for future geochemical studies of granitic material, laser ablation analysis of fluxed glass discs is the preferred method. This is due to the full dissolution of accessory phases that the technique offers, and the speed at which data can be acquired.

Appendix C

Sample catalogue

	Latitude		Longitude				Mineralogy												
Locality	Deg.	Mins.	Deg.	Mins.	**Sample**	**Lithology**	Qz	Ksp	Pl	Bi	Mu	Chl	Tur	Calc	Rut	Tit	Amp	Ox	Sill	Grt
1C	27	52.815	89	43.617	TH-B12- **1C01**	Leucogranite	■	■	■	■	■	■	■							
					TH-B12- **1C02**	GHS gneiss	■	■	■	■			■			■			■	
1D	27	52.774	89	43.645	TH-B12- **1D01**	Leucogranite	■	■	■	■	■	■							■	■
					TH-B12- **1D02**	GHS gneiss	■	■	■	■									■	
1G	27	51.990	89	43.587	TH-B12- **1G01**	Pegmatite	■	■	■	■	■	■			■					
					TH-B12- **1G02**	Leucogranite	■	■	■	■	■	■	■							
					TH-B12- **1G03**	Leucogranite	■	■	■	■	■	■				■				
					TH-B12- **1G04**	GHS gneiss	■	■	■	■					■			■		
					TH-B12- **1G05**	GHS calc-silicate	■	■	■	■				■		■				
					TH-B12- **1G06**	Leucogranite	■	■	■	■	■	■	■							
2A	27	49.885	89	43.695	TH-B12- **2A01**	GHS gneiss	■	■	■											
					TH-B12- **2A02**	GHS schist	■	■	■											
3A	27	15.714	90	2.223	TH-B12- **3A01**	Pegmatite	■	■	■	■	■	■								
					TH-B12- **3A02**	Leucogranite	■	■	■		■									■
					TH-B12- **3A03**	Leucogranite	■	■	■	■	■	■								
					TH-B12- **3A04**	Leucogranite	■	■	■		■		■							■
					TH-B12- **3A05**	THS schist	■	■	■	■					■	■		■		■
					TH-B12- **3A06**	THS schist	■	■	■	■	■									■
					TH-B12- **3A07**	THS schist	■	■	■	■			■							■
3B	27	13.848	90	3.744	TH-B12- **3B01**	THS phyllite	■	■	■	■		■		■						
3C	27	13.317	90	4.108	TH-B12- **3C01**	Leucogranite	■	■	■		■									■
3D	27	14.280	90	3.001	TH-B12- **3D01**	Pegmatite	■	■	■		■		■							■
					TH-B12- **3D02**	Leucogranite	■	■	■		■									
					TH-B12- **3D03**	GHS gneiss	■	■	■	■			■							■
4A	27	29.278	89	55.197	TH-B12- **4A01**	GHS gneiss	■	■	■	■	■								■	
4B	27	29.823	89	56.607	TH-B12- **4B01**	GHS gneiss	■	■	■	■	■									■
4C	27	30.232	89	59.963	TH-B12- **4C01**	Leucogranite	■	■	■	■	■									
					TH-B12- **4C02**	GHS gneiss	■	■	■		■	■							■	
4D	27	29.909	90	1.908	TH-B12- **4D01**	Leucogranite	■	■	■		■									
4G	27	31.121	90	6.248	TH-B12- **4G01**	Leucogranite	■	■	■		■		■							
4H	27	32.681	90	7.741	TH-B12- **4H01**	Leucogranite	■	■	■	■	■				■	■				
					TH-B12- **4H02**	GHS gneiss	■	■	■	■	■		■							
5C	27	17.663	90	36.490	TH-B12- **5C01**	THS phyllite	■	■	■	■	■	■								■
5H	27	21.754	90	33.463	TH-B12- **5H01**	Leucogranite	■	■	■		■		■							

	Latitude		Longitude				Mineralogy													
Locality	Deg.	Mins.	Deg.	Mins.	**Sample**	**Lithology**	Qz	Ksp	Pl	Bi	Mu	Chl	Tur	Calc	Rut	Tit	Amp	Ox	Sill	Grt
5J	27	22.102	90	32.071	TH-B12- **5J01**	Leucogranite	■	■	■		■		■							■
5L	27	25.357	90	29.557	TH-B12- **5L01**	Leucogranite	■	■	■	■	■							■		■
					TH-B12- **5L02**	GHS gneiss														
5M	27	25.036	90	29.762	TH-B12- **5M01**	Leucogranite	■	■	■		■									
					TH-B12- **5M02**	GHS schist	■	■	■	■	■	■			■	■		■		■
					TH-B12- **5M03**	GHS schist	■	■	■	■					■	■	■	■		
6A	27	25.929	90	28.604	TH-B12- **6A01**	Leucogranite	■	■	■	■	■									
6B	27	26.938	90	28.236	TH-B12- **6B01**	GHS schist	■	■	■	■								■		■
6D	27	28.285	90	29.506	TH-B12- **6D01**	GHS orthogneiss	■	■	■	■	■									
					TH-B12- **6D02**	GHS schist						■			■	■				■
6E	27	30.329	90	29.800	TH-B12- **6E01**	GHS gneiss	■	■	■	■	■									■
6F	27	30.331	90	29.415	TH-B12- **6F01**	GHS gneiss	■	■	■	■	■	■								■
					TH-B12- **6F02**	Leucogranite	■	■	■	■	■									
					TH-B12- **6F03**	GHS gneiss	■	■	■	■	■									
					TH-B12- **6F04**	GHS gneiss	■	■	■	■	■									■
6G	27	31.201	90	27.571	TH-B12- **6G01**	GHS gneiss	■	■	■	■	■									
6H	27	30.459	90	28.163	TH-B12- **6H01**	GHS gneiss	■	■	■	■	■									
	27	44.854	89	17.448	DRB **1215**	Leucogranite	■	■	■		■		■						■	
	27	41.970	89	17.573	DRB **1242**	Leucogranite	■	■	■		■								■	■
	27	41.970	89	17.573	DRB **1244**	Leucogranite	■	■	■	■	■									
	27	39.983	89	15.938	DRB **1247**	Leucogranite	■	■	■	■	■									
	27	35.181	89	17.634	DRB **1251**	Leucogranite	■	■	■	■	■	■							■	
	28	4.658	89	39.255	**CWB- 4**	Leucogranite	■	■	■	■	■	■								
	28	3.997	89	39.870	**CWB- 8**	Leucogranite	■	■	■				■							
	28	5.678	89	44.473	**CWB- 16**	Leucogranite	■	■	■	■	■	■								
	28	2.235	89	47.595	**CWB- 23**	Leucogranite	■	■	■	■	■	■								
	27	21.003	91	33.268	**BH- 65**	Leucogranite	■	■	■	■	■									■
	27	53.010	90	38.307	**BH- 84**	Leucogranite	■	■	■	■	■									
	27	22.457	91	35.839	**BH- 96**	Leucogranite	■	■	■											
	27	12.345	89	51.462	**BH- 226**	Leucogranite	■	■	■	■	■	■								
	27	10.689	89	50.485	**BH- 231a**	Leucogranite	■	■	■	■	■	■								
	27	10.689	89	50.485	**BH- 231b**	Leucogranite	■	■	■	■	■	■								
	27	11.138	89	50.186	**BH- 232**	Leucogranite	■	■	■	■	■									

Appendix D

Data tables

Contents

D.1. Whole-rock major and trace element data

Major and trace element geochemistry for Bhutanese leucogranites
Major element oxides in %, trace element abundances in ppm

	1C01	1D01	1G01	1G02	1G03	3A01	3A02	3A03	3A04	3C01	3D02	4CO1	4D01	4G01	4H01	5H01	5J01	5M01	
	Tm	Grt	Peg	Tm	2M	Peg	Grt	2M	Tm	Peg	Musc	Peg	2M	Tm	Musc	Tm	Tm	Musc	
SiO_2	73.65	77.54	70.42	73.79	73.76	72.94	74.75	73.15	74.25	70.43	75.70	76.00	75.73	73.98	75.37	73.83	74.02	74.37	SiO_2
TiO_2	0.09	0.05	0.11	0.07	0.07	0.01	0.01	0.01	0.02	0.01	0.01	0.04	0.02	0.02	0.02	0.01	0.01	0.01	TiO_2
Al_2O_3	14.39	11.95	14.96	14.15	14.21	14.96	14.37	14.81	14.61	16.54	14.75	13.03	13.74	14.68	14.42	15.03	14.80	14.58	Al_2O_3
Fe_2O_3	1.07	1.04	1.19	0.77	0.66	0.33	0.66	0.78	0.90	0.36	0.41	0.53	0.12	0.48	0.40	0.52	0.78	0.50	Fe_2O_3
MnO	0.02	0.06	0.02	0.01	0.01	0.02	0.09	0.02	0.05	0.19	0.01	0.01	0.01	0.02	0.06	0.04	0.23	0.03	MnO
MgO	0.40	0.11	0.27	0.16	0.16	0.04	0.05	0.10	0.07	0.03	0.13	0.21	0.05	0.07	0.03	0.05	0.03	0.07	MgO
CaO	2.16	0.42	0.97	0.82	0.95	0.30	0.63	0.61	0.56	0.26	0.69	0.92	1.00	0.62	0.22	0.43	0.33	0.62	CaO
Na_2O	6.19	2.63	2.41	3.67	3.97	4.83	5.63	4.77	4.83	6.23	5.33	2.77	5.01	5.18	5.11	6.20	7.47	5.61	Na_2O
K_2O	0.79	5.80	8.48	5.29	5.25	6.95	2.88	3.95	3.37	5.87	1.89	4.83	4.36	3.99	3.68	3.85	2.07	1.90	K_2O
P_2O_5	0.09	0.18	0.13	0.12	0.11	0.07	0.08	0.12	0.08	0.05	0.06	0.06	0.06	0.08	0.02	0.10	0.09	0.02	P_2O_5
Sc	2.65	3.66	1.29	3.53	5.65	0.643	0.743	0.905	0.879	0.237	0.846	3.35	0.620	1.03	0.334	0.966	0.363	0.827	Sc
Ti	646	334	738	458	460	52.3	48.5	235	98.3	28.3	229	546	138	138	125	39.7	22.3	114	Ti
V	9.50	2.98	5.57	3.58	3.02	1.17	1.39	1.87	1.13	2.62	4.87	14.9	1.55	1.60	3.01	1.45	1.55	1.59	V
Cr	11.4	11.4	5.70	13.8	9.18	4.45	17.0	6.97	10.6	6.24	9.50	15.5	13.9	12.4	20.4	5.68	9.80	5.54	Cr
Mn	169	418	92.5	71.4	87.3	133	691	124	373	1428	36.8	55.1	42.0	195	454	277	1638	185	Mn
Co	1.87	0.594	3.04	1.35	0.774	0.0880	0.205	0.183	0.185	0.145	0.479	1.07	0.231	0.577	0.201	0.0745	0.0217	6.58	Co
Ni	6.25	2.77	2.26	2.99	2.67	2.09	2.22	1.28	2.79	1.79	3.48	3.97	2.24	2.00	2.25	1.80	2.25	16.7	Ni
Cu	8.47	5.65	35.7	26.9	6.24	3.80	8.34	4.72	8.24	20.9	3.42	4.16	4.62	3.24	4.75	4.23	5.29	31.5	Cu
Zn	23.5	9.97	26.0	23.1	27.8	27.0	24.5	55.8	62.2	9.12	18.6	13.0	7.64	43.6	37.6	45.2	47.4	117	Zn
Ga	15.0	14.3	16.4	18.4	20.9	17.5	23.2	22.0	22.1	29.9	21.4	14.3	11.7	25.4	31.9	19.4	20.1	25.5	Ga
Rb	48.3	254	330	322	277	572	251	323	296	1041	168	162	143	453	547	352	273	241	Rb
Sr	89.6	62.1	181	61.0	54.6	11.4	11.5	44.1	10.2	14.1	64.0	116	121	20.2	8.80	8.50	0	12.8	Sr
Y	12.4	20.2	33.0	24.2	32.1	6.60	15.7	12.1	15.4	4.10	5.70	6.20	9.20	15.3	9.10	9.40	5.00	5.70	Y
Zr	38.5	40.9	20.5	46.3	54.3	12.5	37.8	36.4	18.6	27.0	26.3	37.3	30.1	32.4	38.6	30.8	38.6	14.6	Zr
Nb	4.90	5.00	7.40	12.9	16.1	7.90	12.4	14.5	10.4	28.7	22.6	4.40	3.00	19.2	89.6	11.3	12.7	39.3	Nb
Sn	4.39	3.09	3.77	3.80	4.58	8.74	13.63	11.9	10.7	26.3	39.2	4.31	4.92	26.9	1860	7.73	5.66	24.4	Sn
Cs	2.03	2.60	9.59	14.5	15.3	54.2	12.5	18.4	11.1	111	11.7	2.62	4.44	50.5	200	20.0	20.5	14.6	Cs
Ba	54.0	132	803	188	114	29.6	41.2	143	17.7	80.3	181	777	498	37.1	28.9	10.2	5.63	13.0	Ba
La	5.06	5.46	21.7	11.0	11.8	1.21	3.60	4.98	4.33	1.18	2.00	5.93	5.06	5.14	1.79	2.28	1.51	3.25	La
Ce	10.4	13.3	46.0	22.6	25.8	1.68	6.53	9.64	8.79	1.12	3.40	11.7	10.6	10.8	2.72	3.83	2.41	6.27	Ce
Pr	1.09	1.54	4.81	2.45	2.75	0.170	0.635	1.08	0.905	0.0734	0.364	1.23	1.09	1.20	0.242	0.336	0.295	0.564	Pr
Nd	3.84	5.55	17.67	9.21	9.70	0.637	2.17	3.99	2.76	0.181	1.09	4.00	3.87	4.09	0.995	1.07	0.53	1.70	Nd
Sm	0.999	1.87	4.31	2.42	2.97	0.224	0.862	1.26	0.868	0.0726	0.34	0.963	1.19	1.40	0.304	0.454	0.184	0.592	Sm
Eu	0.383	0.258	0.929	0.393	0.321	0.0465	0.0491	0.245	0.0560	0.0135	0.239	0.702	0.86	0.103	0.189	0.0433	0.0545	0.0802	Eu
Gd	1.12	2.48	4.78	2.85	3.09	0.527	1.24	1.77	1.31	0.0419	0.56	1.21	1.27	1.55	0.440	0.878	0.304	0.480	Gd
Tb	0.210	0.527	0.716	0.539	0.608	0.0867	0.318	0.326	0.282	0.0112	0.107	0.181	0.199	0.384	0.114	0.146	0.113	0.172	Tb
Dy	1.43	3.79	4.96	3.49	4.47	0.670	2.36	1.97	2.14	0.0709	0.666	1.40	1.02	2.47	1.11	1.01	0.539	0.597	Dy
Ho	0.242	0.631	0.909	0.747	0.843	0.0980	0.446	0.288	0.377	0.0601	0.116	0.275	0.213	0.365	0.194	0.185	0.0902	0.111	Ho
Er	0.736	1.65	2.78	2.14	2.44	0.263	1.45	0.633	1.02	0.0581	0.433	0.971	0.568	1.13	0.639	0.764	0.407	0.310	Er
Tm	0.103	0.227	0.349	0.316	0.335	0.0576	0.217	0.102	0.276	0.0104	0.0611	0.136	0.197	0.176	0.107	0.148	0.0791	0.0791	Tm
Yb	0.700	1.43	2.55	2.15	2.44	0.362	1.70	0.590	1.07	0.0780	0.426	0.805	0.450	0.876	0.923	1.06	0.560	0.260	Yb
Lu	0.0734	0.215	0.365	0.328	0.345	0.0428	0.213	0.0820	0.180	0.0121	0.0580	0.122	0.0999	0.102	0.120	0.288	0.146	0.0462	Lu
Hf	1.19	1.88	0.65	1.54	1.78	0.337	1.87	1.27	0.644	3.33	0.947	1.05	1.07	1.85	3.35	1.36	2.23	0.657	Hf
Ta	0.402	0.297	1.10	3.81	2.90	4.45	1.76	3.51	1.69	255	11.37	0.475	0.352	7.43	260	7.12	9.76	17.0	Ta
W	1.11	0.457	1.28	0.860	1.01	0.875	2.98	3.20	2.24	1.53	2.43	5.40	1.37	2.93	4.27	1.10	0.361	3.02	W
Pb	46.4	51.2	127	155	127	113	83.5	107	79.7	71.7	58.5	62.0	87.4	65.6	66.3	126	60.0	78.9	Pb
Th	4.44	7.28	15.0	10.1	8.26	0.815	2.97	3.21	4.84	4.76	1.55	3.48	2.75	5.93	6.49	20.4	1.45	4.23	Th
U	1.90	3.17	5.07	6.48	6.37	1.35	2.79	3.04	2.65	8.38	3.84	1.57	1.42	9.52	10.1	3.12	10.3	7.29	U

Major and trace element geochemistry for Bhutanese leucogranites
Major element oxides in %, trace element abundances in ppm

	6A01	6FO2	DRB-1215	DRB-1242	DRB-1244	DRB-1247	DRB-1251	CWB-10-4	CWB-10-8A	CWB-10-16	CWB-10-23	BH-65C	BH-84	BH-96	BH-226	BH-231A	BH-231B	BH-232	
	2M	Peg	Tm	2M	2M	2M	2M	2M	Tm	2M	2M	Grt	2M	Musc	2M	2M	2M	2M	
SiO_2	72.19	72.01	72.35	74.47	69.29	72.49	73.53	74.58	75.31	75.23	76.64	74.49	71.27	71.97	74.46	73.23	72.88	73.29	SiO_2
TiO_2	0.08	0.08	0.03	0.03	0.02	0.05	0.07	0.03	0.03	0.08	0.05	0.18	0.34	0.01	0.11	0.21	0.21	0.14	TiO_2
Al_2O_3	14.91	15.27	14.94	14.87	16.86	15.26	14.32	14.66	14.39	14.18	13.42	13.88	14.85	16.73	14.63	14.82	15.21	15.04	Al_2O_3
Fe_2O_3	0.72	0.63	0.43	0.49	0.17	0.72	0.85	0.40	0.41	0.93	0.78	1.86	2.95	0.08	1.14	1.62	1.67	1.32	Fe_2O_3
MnO	0.01	0.01	0.01	0.04	0.01	0.01	0.02	0.01	0.01	0.02	0.02	0.04	0.04	0.02	0.03	0.04	0.04	0.03	MnO
MgO	0.17	0.20	0.13	0.05	0.06	0.17	0.18	0.10	0.09	0.19	0.11	0.33	0.81	0.02	0.20	0.55	0.57	0.29	MgO
CaO	0.78	0.90	0.99	0.48	1.40	0.55	0.89	0.76	0.75	0.61	0.77	0.96	2.25	0.38	0.79	1.37	1.42	0.88	CaO
Na_2O	4.67	3.39	6.86	1.99	5.54	5.68	4.42	3.96	3.90	3.12	3.44	3.01	4.51	8.30	3.58	3.61	3.68	3.87	Na_2O
K_2O	4.74	6.62	3.55	7.10	6.53	4.80	5.97	5.98	5.89	5.99	5.05	4.83	2.12	2.17	4.74	4.13	3.96	4.56	K_2O
P_2O_5	0.14	0.10	0.15	0.08	0.03	0.21	0.11	0.12	0.12	0.10	0.09	0.19	0.10	0.02	0.15	0.11	0.11	0.12	P_2O_5
Sc	2.51	3.86	0.836	0.554	0.802	0.655	3.46	1.33	1.67	2.52	1.96	2.75	4.94	0.809	3.01	3.19	3.49	2.87	Sc
Ti	550	573	198	167	130	331	432	139	147	490	301	991	1948	50.5	594	1216	1217	850	Ti
V	2.61	10.9	1.63	1.88	2.96	1.90	3.59	3.22	3.56	3.72	2.26	10.6	23.4	1.63	5.31	22.7	23.6	11.7	V
Cr	8.93	5.66	9.28	6.82	7.01	28.8	9.52	9.68	17.7	12.5	18.6	14.5	24.7	6.96	9.73	35.0	35.8	17.8	Cr
Mn	88.9	51.9	49.8	319	25.1	83.8	107	63.7	77.4	175	178	232	273	104	221	272	284	191	Mn
Co	0.507	0.814	0.289	0.267	1.29	0.828	1.74	0.868	0.961	1.59	0.982	2.20	4.54	0.236	1.03	3.50	3.29	1.62	Co
Ni	3.21	1.54	1.03	1.72	4.68	7.62	2.97	4.05	6.79	7.12	3.70	2.65	5.19	5.96	3.26	12.0	9.32	5.43	Ni
Cu	6.03	5.32	3.74	6.59	21.9	6.51	18.6	6.98	7.24	15.6	8.97	2.97	3.63	4.10	2.10	3.96	4.95	4.06	Cu
Zn	46.6	15.0	44.2	27.2	6.90	69.7	12.5	15.6	20.8	34.4	29.1	32.2	33.9	8.13	43.5	62.5	58.8	45.8	Zn
Ga	20.6	15.9	20.4	26.6	19.5	23.1	17.1	18.8	20.7	17.4	15.2	19.9	18.6	26.8	21.9	22.1	22.4	21.9	Ga
Rb	311	318	209	387	182	407	231	274	268	262	236	347	163	188	334	216	219	296	Rb
Sr	80.3	87.3	54.0	57.4	404	49.6	75.9	36.6	32.5	93.4	69.4	39.0	130	66.9	94.7	199	209	210	Sr
Y	12.5	13.5	5.20	5.40	7.30	14.8	26.3	7.90	8.70	21.2	31.9	16.2	22.9	1.90	15.5	11.8	11.8	11.2	Y
Zr	48.2	58.9	26.8	20.9	20.3	32.7	40.9	23.4	24.8	41.6	34.1	73.2	154	17.7	43.8	65.1	67.1	59.9	Zr
Nb	12.4	7.50	1.90	18.0	12.9	4.10	11.3	22.6	15.6	11.2	13.6	14.6	16.0	50.6	16.4	9.04	9.08	13.3	Nb
Sn	9.88	9.39	7.29	56.9	1.04	9.57	1.96	4.55	4.95	8.96	5.15	7.01	5.73	843	12.9	4.43	7.43	10.1	Sn
Cs	11.3	7.95	8.56	25.1	16.7	52.5	4.02	5.95	5.86	10.5	7.23	11.8	10.4	36.0	37.2	11.3	18.5	32.9	Cs
Ba	261	186	89.4	114	593	129	288	79.0	75.5	380	127	183	345	138	233	376	408	526	Ba
La	7.84	7.93	3.66	1.93	3.30	4.53	10.0	2.62	2.35	8.83	9.51	20.5	33.5	0.686	12.7	19.5	18.5	16.1	La
Ce	17.2	17.3	6.59	2.93	6.14	9.53	22.2	5.09	4.70	20.9	20.5	46.6	67.8	0.442	26.6	41.3	40.6	33.4	Ce
Pr	1.81	1.83	0.654	0.295	0.583	1.19	2.33	0.506	0.535	1.72	2.24	5.03	7.34	0.0354	2.97	4.41	4.31	3.69	Pr
Nd	7.24	6.93	1.92	1.26	1.99	4.12	7.65	1.61	2.14	6.47	8.20	19.1	25.0	0.298	11.3	17.0	17.1	13.9	Nd
Sm	1.92	1.94	0.703	0.313	0.453	1.61	2.22	0.773	0.789	1.52	2.51	4.10	4.70	0.0933	2.63	3.54	3.43	3.01	Sm
Eu	0.480	0.394	0.236	0.140	0.534	0.282	0.620	0.0885	0.0794	0.509	0.366	0.479	0.692	0.110	0.376	0.620	0.603	0.526	Eu
Gd	2.12	1.86	0.611	0.444	0.534	2.06	2.29	0.915	0.930	1.83	3.60	3.75	4.04	0.213	2.49	2.66	2.59	2.63	Gd
Tb	0.343	0.361	0.135	0.206	0.142	0.414	0.409	0.174	0.215	0.521	0.830	0.607	0.631	0.0434	0.395	0.441	0.390	0.332	Tb
Dy	2.01	2.29	0.656	0.635	1.02	2.34	3.41	1.22	1.17	2.60	4.83	2.87	3.86	0.229	2.45	2.01	1.98	1.90	Dy
Ho	0.298	0.435	0.129	0.115	0.196	0.392	0.694	0.187	0.221	0.606	0.972	0.483	0.762	0.0450	0.449	0.337	0.346	0.414	Ho
Er	0.769	1.17	0.244	0.324	0.714	0.948	2.15	0.649	0.732	1.67	2.74	1.57	2.21	0.249	1.18	1.04	0.956	0.892	Er
Tm	0.0825	0.170	0.0374	0.0692	0.135	0.186	0.377	0.209	0.0987	0.483	0.397	0.201	0.320	0.0270	0.170	0.137	0.142	0.162	Tm
Yb	0.490	0.992	0.256	0.371	0.913	0.743	2.31	0.725	0.588	2.18	2.31	1.10	2.18	0.298	1.14	0.850	0.842	0.871	Yb
Lu	0.078	0.130	0.0403	0.0551	0.115	0.099	0.355	0.0797	0.0932	0.257	0.363	0.160	0.355	0.0443	0.194	0.115	0.202	0.138	Lu
Hf	1.33	2.11	0.911	0.961	1.74	1.02	1.19	0.856	1.04	1.05	1.07	2.44	4.48	2.16	1.67	2.18	2.17	2.05	Hf
Ta	0.921	0.909	0.311	7.93	15.8	0.679	2.16	10.7	5.40	2.06	2.93	2.03	1.89	145	3.06	1.00	1.02	3.01	Ta
W	3.32	5.76	0.349	2.93	0.663	1.31	0.948	2.64	2.20	1.65	2.95	1.05	1.64	1.83	5.92	0.828	1.12	3.87	W
Pb	90.5	69.8	64.3	70.1	63.5	63.9	78.6	82.2	92.1	93.0	103	32.8	18.2	20.7	59.6	62.2	58.1	88.3	Pb
Th	4.60	6.73	2.35	3.61	4.06	2.72	8.39	1.64	1.54	7.90	6.18	19.2	18.2	4.77	73.0	10.3	10.2	9.50	Th
U	3.94	1.97	7.92	10.8	10.0	5.13	3.81	8.27	6.70	3.90	14.4	4.03	3.70	8.28	10.3	5.87	5.77	8.43	U

D.1.1. XRF standard data

WS-E	Date of analysis 25/02 2013	25/02 2013	09/05 2013	09/05 2013	12/11 2013	12/11 2013	12/11 2013	12/11 2013	13/11 2013	13/11 2013	Average	2 s.d.	2 s.d. %	WS-E expected
SiO_2	51.36	51.31	51.62	51.60	51.17	51.20	51.33	51.38	51.28	51.28	51.35	0.30	0.58	51.10
TiO_2	2.44	2.43	2.45	2.44	2.42	2.42	2.40	2.43	2.42	2.43	2.43	0.03	1.09	2.43
Al_2O_3	13.93	13.94	13.92	13.90	13.79	13.80	13.92	13.92	13.98	13.94	13.90	0.12	0.87	13.78
Fe_2O_3	13.17	13.16	13.18	13.19	13.16	13.16	13.14	13.16	13.14	13.17	13.16	0.03	0.23	13.15
MnO	0.17	0.17	0.17	0.17	0.17	0.17	0.17	0.17	0.17	0.17	0.17	0.00	1.31	0.17
MgO	5.56	5.55	5.58	5.57	5.52	5.55	5.54	5.55	5.55	5.57	5.55	0.04	0.63	5.55
CaO	8.98	9.01	8.99	8.99	8.92	8.92	8.95	9.00	8.99	8.99	8.98	0.06	0.72	8.95
Na_2O	2.39	2.40	2.43	2.45	2.41	2.43	2.40	2.45	2.42	2.43	2.42	0.04	1.72	2.47
K2O	1.01	1.01	1.01	1.01	0.99	0.99	0.99	0.99	0.99	1.00	1.00	0.02	2.02	1.00
P_2O_5	0.30	0.30	0.30	0.31	0.31	0.30	0.30	0.31	0.31	0.30	0.30	0.01	2.51	0.30
LOI	0.85	0.85	0.85	0.85	0.85	0.85	0.85	0.85	0.85	0.85	0.85			0.85
Total	100.15	100.14	100.50	100.47	99.69	99.79	99.99	100.21	100.10	100.14	100.12			99.75

OU-3	Date of analysis 25/02 2013	25/02 2013	09/05 2013	09/05 2013	12/11 2013	12/11 2013	12/11 2013	12/11 2013	13/11 2013	13/11 2013	Average	2 s.d.	2 s.d. %	OU-3 expected
SiO_2	74.12	74.19	74.16	74.06	74.08	74.04	74.33	74.37	74.26	74.18	74.18	0.23	0.31	74.09
TiO_2	0.21	0.21	0.22	0.22	0.22	0.23	0.23	0.22	0.22	0.22	0.22	0.01	4.58	0.22
Al_2O_3	11.07	11.06	10.99	10.99	11.03	11.04	11.12	11.09	11.11	11.15	11.07	0.11	0.97	11.11
Fe_2O_3	3.87	3.87	3.85	3.84	3.88	3.88	3.87	3.87	3.88	3.87	3.87	0.03	0.74	3.83
MnO	0.09	0.09	0.09	0.09	0.09	0.09	0.09	0.09	0.09	0.09	0.09	0.00	2.83	0.09
MgO	0.03	0.02	0.02	0.03	0.02	0.03	0.02	0.03	0.03	0.02	0.03	0.01	22.69	-
CaO	0.22	0.22	0.20	0.20	0.21	0.21	0.22	0.21	0.21	0.21	0.21	0.01	6.54	0.20
Na_2O	3.69	3.65	3.71	3.70	3.71	3.70	3.72	3.73	3.70	3.74	3.70	0.05	1.29	3.68
K2O	4.55	4.56	4.57	4.57	4.56	4.56	4.55	4.53	4.53	4.54	4.55	0.03	0.61	4.55
P_2O_5	0.02	0.02	0.01	0.02	0.02	0.02	0.02	0.02	0.02	0.02	0.02	0.00	11.81	-
LOI	1.82	1.82	1.82	1.82	1.82	1.82	1.82	1.82	1.82	1.82	1.82			1.82
Total	99.70	99.75	99.64	99.54	99.64	99.62	99.99	99.97	99.88	99.89	99.76			99.59

BHVO-1	Detection Limit	Date of analysis 03/04/2013	03/04/2013	05/04/2013	05/04/2013	03/05/2013	03/05/2013	Average	2 s.d.	2 s.d. %	BHVO-1 Expected
Rb	2	9	9	9	10	10	9	9	1	9	11
Sr	2	405	404	404	404	404	406	404	2	0	403
Y	2	29	28	28	28	29	28	28	0	1	28
Zr	2	175	172	175	174	175	173	174	3	1	179
Nb	2	20	18	19	20	20	19	19	2	8	19
Ba	12	130	140	138	138	128	131	134	10	8	139
Pb	5	-	-	-	6	-	-	6	-	-	3
Th	4	-	-	-	-	-	-	-	-	-	1
U	3	-	-	-	-	-	-	-	-	-	0
Sc	5	32	32	31	29	30	32	31	3	9	32
V	5	314	307	311	316	313	319	313	8	3	317
Cr	4	286	289	292	288	292	294	290	6	2	289
Co	2	47	47	46	46	51	47	47	4	8	45
Ni	3	121	121	119	120	121	124	121	4	3	121
Cu	3	138	136	135	138	140	139	138	3	2	136
Zn	3	112	109	112	109	108	109	110	3	3	105
Ga	3	22	22	22	23	23	22	22	1	4	21
Mo	2	-	-	-	-	-	-	-	-	-	1
As	5	-	-	-	-	-	-	-	-	-	0
S	50	213	212	216	214	209	219	214	7	3	-

W-2	Detection Limit	Date of analysis 03/04/2013	03/04/2013	05/04/2013	05/04/2013	03/05/2013	03/05/2013	Average	2 s.d.	2 s.d. %	W-2 Expected
Rb	2	19	20	21	21	20	21	20	1	7	20
Sr	2	199	201	201	202	201	202	201	2	1	194
Y	2	23	23	23	23	24	23	23	1	4	24
Zr	2	95	95	94	95	95	94	95	1	1	94
Nb	2	9	10	8	9	9	9	9	1	9	8
Ba	12	179	169	185	182	181	181	179	11	6	182
Pb	5	8	9	9	6	8	9	8	2	24	9
Th	4	-	-	-	-	-	-	-	-	-	2
U	3	-	-	-	-	-	-	-	-	-	1
Sc	5	39	35	36	37	39	35	37	3	9	35
V	5	261	262	256	262	253	260	259	8	3	262
Cr	4	94	97	98	94	96	95	96	3	4	93
Co	2	42	44	44	45	44	44	44	2	3	44
Ni	3	67	67	68	67	69	69	68	2	3	70
Cu	3	104	104	104	104	104	105	104	1	1	103
Zn	3	82	84	82	82	83	83	83	2	2	77
Ga	3	18	19	19	19	19	19	19	1	4	20
Mo	2	-	-	-	-	-	-	-	-	-	1
As	5	-	-	-	-	-	-	-	-	-	1
S	50	251	248	253	260	252	253	253	8	3	-

D.1.2. LA-ICP-MS standard data

OU-3	La	Ce	Pr	Nd	Sm	Eu	Gd	Tb	Dy	Ho	Er	Tm	Yb	Lu
16/12/2014	81.2	180	20.2	77.7	16.8	1.13	16.9	2.88	18.5	3.83	11.1	1.64	11.4	1.62
16/12/2014	79.5	172	19.3	76.0	17.0	1.16	15.9	2.74	18.3	3.64	11.8	1.63	11.1	1.60
16/12/2014	79.7	172	19.8	73.9	16.4	1.08	15.8	2.78	17.9	3.80	11.5	1.66	10.7	1.62
Average	80.1	174	19.7	75.9	16.7	1.12	16.2	2.80	18.2	3.76	11.5	1.64	11.1	1.62
2 s.d.	1.93	9.27	0.95	3.87	0.67	0.08	1.25	0.15	0.59	0.20	0.67	0.04	0.66	0.02
2 s.d. %	2.41	5.31	4.81	5.10	4.02	7.55	7.69	5.41	3.25	5.27	5.84	2.29	5.93	1.46
17/12/2014	72.7	173	18.2	70.7	15.6	1.01	15.7	2.58	16.5	3.43	10.7	1.49	10.1	1.43
17/12/2014	74.5	177	18.7	71.9	15.6	1.09	15.9	2.66	16.8	3.64	10.2	1.53	10.1	1.48
17/12/2014	74.6	175	18.6	74.0	15.2	1.05	16.6	2.70	16.8	3.73	11.1	1.51	10.7	1.48
Average	74.0	175	18.5	72.2	15.5	1.05	16.0	2.65	16.7	3.60	10.7	1.51	10.3	1.46
2 s.d.	2.20	4.90	0.45	3.39	0.48	0.08	0.98	0.13	0.31	0.31	0.93	0.04	0.64	0.05
2 s.d. %	2.97	2.80	2.44	4.69	3.10	7.86	6.10	4.84	1.83	8.73	8.76	2.79	6.25	3.76
18/12/2014	74.0	172	18.2	70.3	15.1	1.01	14.8	2.50	16.3	3.36	9.86	1.49	9.45	1.35
18/12/2014	72.2	169	18.1	71.8	15.4	1.01	14.7	2.39	15.9	3.16	9.82	1.43	9.46	1.33
18/12/2014	71.8	171	18.5	68.0	14.9	1.04	14.2	2.45	16.5	3.17	9.68	1.54	9.18	1.37
Average	72.7	171	18.3	70.0	15.1	1.02	14.6	2.45	16.3	3.23	9.79	1.48	9.36	1.35
2 s.d.	2.38	3.11	0.47	3.85	0.53	0.04	0.65	0.11	0.59	0.23	0.19	0.12	0.32	0.05
2 s.d. %	3.27	1.82	2.57	5.50	3.54	3.89	4.42	4.56	3.65	7.04	1.98	7.79	3.40	3.52
Long-term average	75.6	173	18.8	72.7	15.8	1.06	15.6	2.63	17.1	3.53	10.6	1.55	10.2	1.48
2 s.d.	7.18	6.66	1.49	6.04	1.52	0.11	1.75	0.33	1.82	0.52	1.57	0.16	1.55	0.23
2 s.d. %	9.50	3.84	7.93	8.31	9.65	10.1	11.2	12.5	10.7	14.7	14.8	10.4	15.1	15.8

WS-E	La	Ce	Pr	Nd	Sm	Eu	Gd	Tb	Dy	Ho	Er	Tm	Yb	Lu
16/12/2014	25.2	57.4	7.25	31.3	8.89	2.34	6.26	1.00	5.72	1.11	2.90	0.37	2.37	0.39
16/12/2014	25.6	56.6	7.23	30.3	8.11	2.36	6.06	0.98	5.93	1.04	2.85	0.37	2.38	0.37
16/12/2014	27.3	60.6	7.61	32.6	8.66	2.35	6.53	1.04	5.98	1.08	3.06	0.39	2.40	0.37
Average	26.1	58.2	7.36	31.4	8.56	2.35	6.28	1.01	5.88	1.07	2.93	0.38	2.38	0.38
2 s.d.	2.26	4.28	0.43	2.32	0.80	0.02	0.47	0.05	0.28	0.07	0.22	0.03	0.03	0.02
2 s.d. %	8.67	7.35	5.80	7.39	9.34	0.72	7.55	5.17	4.82	6.70	7.36	7.64	1.33	6.24
17/12/2014	26.4	57.7	7.18	31.3	8.51	2.32	6.65	1.05	5.90	1.10	2.99	0.36	2.24	0.36
17/12/2014	27.4	58.8	7.50	31.7	8.93	2.48	6.92	1.08	5.75	1.16	3.05	0.37	2.08	0.37
17/12/2014	27.3	58.7	7.51	31.4	8.93	2.29	6.72	1.05	5.80	1.11	2.97	0.39	2.21	0.34
Average	27.0	58.4	7.40	31.5	8.79	2.36	6.76	1.06	5.82	1.12	3.00	0.38	2.17	0.36
2 s.d.	1.04	1.17	0.37	0.39	0.49	0.20	0.28	0.04	0.15	0.06	0.08	0.03	0.17	0.03
2 s.d. %	3.86	2.01	4.98	1.25	5.55	8.61	4.07	3.62	2.60	5.19	2.53	7.01	7.95	7.10
18/12/2014	25.9	57.8	7.65	32.3	7.77	2.13	6.63	0.96	5.77	1.11	3.07	0.42	2.32	0.34
18/12/2014	28.0	61.5	7.70	33.1	8.36	2.15	6.94	0.97	5.77	1.15	2.83	0.45	2.20	0.35
18/12/2014	26.7	60.4	7.52	31.5	8.33	2.32	6.63	0.96	5.53	1.09	3.00	0.43	2.42	0.35
Average	26.9	59.9	7.62	32.3	8.15	2.20	6.73	0.96	5.69	1.11	2.96	0.43	2.31	0.34
2 s.d.	2.11	3.78	0.19	1.60	0.67	0.21	0.36	0.01	0.28	0.06	0.25	0.03	0.21	0.02
2 s.d. %	7.85	6.32	2.54	4.95	8.22	9.41	5.32	1.50	4.98	5.50	8.30	7.12	9.22	5.27
Long-term average	26.7	58.8	7.46	31.7	8.50	2.31	6.59	1.01	5.79	1.10	2.97	0.40	2.29	0.36
2 s.d.	1.87	3.31	0.39	1.66	0.80	0.21	0.57	0.09	0.27	0.07	0.18	0.06	0.23	0.04
2 s.d. %	7.02	5.63	5.19	5.25	9.44	9.15	8.65	8.93	4.68	6.44	6.01	15.96	9.98	10.01

D.2. Whole-rock radiogenic isotope data

Whole-rock isotope data for Bhutanese leucogranites

	1D01	1G01	1G02	1G03	3A01	3A02	3A03	3A04	4D01	
	Grt	Peg	Tm	2M	Peg	Grt	2M	Tm	2M	
Sr method	TIMS	MC-ICP-MS	MC-ICP-MS	MC-ICP-MS	TIMS	TIMS	TIMS	TIMS	MC-ICP-MS	Sr method
$^{87}Sr/^{86}Sr$	0.978210	0.766658	0.824239	0.809263	0.807666	0.787705	0.777162	0.793745	0.768719	$^{87}Sr/^{86}Sr$
2 σ	0.000022	0.000083	0.000065	0.000066	0.000020	0.000020	0.000020	0.000020	0.000083	2 σ
$^{87}Sr/^{86}Sr_i$	0.974755	0.765154	0.819859	0.805058	0.766035	0.769610	0.771099	0.769732	0.767737	$^{87}Sr/^{86}Sr_i$
$^{143}Nd/^{144}Nd$	0.512259	0.511803	0.511616	0.511591	0.511981	0.511955	0.511896	0.511979	0.511961	$^{143}Nd/^{144}Nd$
2 σ	0.000018	0.000019	0.000019	0.000018	0.000025	0.000018	0.000018	0.000019	0.000018	2 σ
$^{143}Nd/^{144}Nd_i$	0.512234	0.511785	0.511594	0.511568	0.511956	0.511925	0.511873	0.511955	0.511936	$^{143}Nd/^{144}Nd_i$
εNd_i	-7.88	-16.65	-20.36	-20.87	-13.30	-13.91	-14.91	-13.32	-13.69	εNd_i
2 σ	0.35	0.38	0.38	0.36	0.49	0.35	0.36	0.37	0.36	2 σ
$^{206}Pb/^{204}Pb$	20.9357	19.0653		18.9813	18.9063	18.9336	18.8560	18.9507	18.9125	$^{206}Pb/^{204}Pb$
2 σ	0.0034	0.0033		0.0027	0.0032	0.0029	0.0028	0.0030	0.0033	2 σ
$^{207}Pb/^{204}Pb$	15.8922	15.7937		15.7806	15.7899	15.7945	15.7941	15.7942	15.7885	$^{207}Pb/^{204}Pb$
2 σ	0.0030	0.0030		0.0045	0.0029	0.0046	0.0046	0.0049	0.0030	2 σ
$^{208}Pb/^{204}Pb$	39.5820	39.5150		39.4232	39.5763	39.5779	39.5592	39.5714	39.6890	$^{208}Pb/^{204}Pb$
2 σ	0.0086	0.0083		0.0109	0.0082	0.0114	0.0110	0.0126	0.0083	2 σ
$^{207}Pb/^{206}Pb$	0.7591	0.8284		0.8314	0.8352	0.8342	0.8376	0.8334	0.8348	$^{207}Pb/^{206}Pb$
2 σ	0.0003	0.0003		0.0004	0.0003	0.0004	0.0004	0.0004	0.0003	2 σ
$^{206}Pb/^{204}Pb_i$	20.9156	19.0598		18.9750	18.9039	18.9269	18.8509	18.9440	18.9096	$^{206}Pb/^{204}Pb_i$
$^{207}Pb/^{204}Pb_i$	15.8920	15.7937		15.7805	15.7899	15.7944	15.7941	15.7941	15.7885	$^{207}Pb/^{204}Pb_i$
$^{208}Pb/^{204}Pb_i$	39.5669	39.5096		39.4205	39.5758	39.5755	39.5574	39.5674	39.6872	$^{208}Pb/^{204}Pb_i$
$^{207}Pb/^{206}Pb_i$	0.7598	0.8286		0.8316	0.8353	0.8345	0.8378	0.8337	0.8349	$^{207}Pb/^{206}Pb_i$

Whole-rock isotope data for Bhutanese leucogranites

	5M01	DRB1215	DRB1247	DRB1251	CW-10-16	CW-10-23	BH-65C	BH-84	BH-226	BH-231B	
	Musc	Tm	2M	2M	2M	2M	Grt	2M	2M	2M	
Sr method	MC-ICP-MS	TIMS	TIMS	TIMS	MC-ICP-MS	MC-ICP-MS	MC-ICP-MS	TIMS	MC-ICP-MS	TIMS	Sr method
$^{87}Sr/^{86}Sr$	0.795758	0.760098	0.762264	0.829544	0.830595	0.797008	0.911392	0.740317	0.770572	0.730144	$^{87}Sr/^{86}Sr$
2 σ	0.000083	0.000020	0.000020	0.000020	0.000066	0.000066	0.000083	0.000020	0.000083	0.000020	2 σ
$^{87}Sr/^{86}Sr_i$	0.780168	0.756902	0.755492	0.827016	0.828259	0.794189	0.903944	0.739281	0.767654	0.729281	$^{87}Sr/^{86}Sr_i$
$^{143}Nd/^{144}Nd$	0.511961	0.511935	0.511907	0.511758	0.511688	0.511566	0.511984	0.512021	0.511728	0.511933	$^{143}Nd/^{144}Nd$
2 σ	0.000020	0.000018	0.000018	0.000019	0.000019	0.000018	0.000045	0.000045	0.000045	0.000046	2 σ
$^{143}Nd/^{144}Nd_i$	0.511936	0.511909	0.511877	0.511736	0.511670	0.511543	0.511967	0.512005	0.511709	0.511916	$^{143}Nd/^{144}Nd_i$
εNd_i	-13.69	-14.22	-14.85	-17.59	-18.88	-21.36	-13.09	-12.35	-18.13	-14.09	εNd_i
2 σ	0.40	0.35	0.36	0.37	0.36	0.35	0.88	0.89	0.87	0.89	2 σ
$^{206}Pb/^{204}Pb$	18.5091	19.0240	18.7204	20.4498	19.8869	19.6754	19.5722	19.5125	19.4626	18.8100	$^{206}Pb/^{204}Pb$
2 σ	0.0035	0.0028	0.0027	0.0035	0.0030	0.0027	0.0038	0.0033	0.0037	0.0033	2 σ
$^{207}Pb/^{204}Pb$	15.7729	15.8034	15.7856	15.9241	15.8707	15.8583	15.8245	15.7997	15.8249	15.7617	$^{207}Pb/^{204}Pb$
2 σ	0.0034	0.0045	0.0045	0.0050	0.0046	0.0045	0.0038	0.0030	0.0036	0.0030	2 σ
$^{208}Pb/^{204}Pb$	39.0877	39.5970	39.4095	40.7662	39.8627	40.0873	39.3321	40.3560	39.8509	39.2416	$^{208}Pb/^{204}Pb$
2 σ	0.0099	0.0110	0.0109	0.0127	0.0115	0.0109	0.0114	0.0083	0.0110	0.0085	2 σ
$^{207}Pb/^{206}Pb$	0.8522	0.8307	0.8432	0.7787	0.7981	0.8060	0.8085	0.8097	0.8131	0.8379	$^{207}Pb/^{206}Pb$
2 σ	0.0003	0.0004	0.0004	0.0004	0.0004	0.0003	0.0004	0.0003	0.0003	0.0003	2 σ
$^{206}Pb/^{204}Pb_i$	18.4906	19.0064	18.7046	20.4426	19.8818	19.6468	19.5471	19.4705	19.4273	18.7900	$^{206}Pb/^{204}Pb_i$
$^{207}Pb/^{204}Pb_i$	15.7727	15.8032	15.7854	15.9241	15.8706	15.8580	15.8243	15.7993	15.8245	15.7615	$^{207}Pb/^{204}Pb_i$
$^{208}Pb/^{204}Pb_i$	39.0842	39.5953	39.4067	40.7611	39.8593	40.0833	39.2931	40.2883	39.7687	39.2300	$^{208}Pb/^{204}Pb_i$
$^{207}Pb/^{206}Pb_i$	0.8530	0.8315	0.8439	0.7790	0.7982	0.8072	0.8095	0.8114	0.8146	0.8388	$^{207}Pb/^{206}Pb_i$

D.2.1. Sr standard data (by MC-ICP-MS)

Date	Time	Analysis	$^{87}Sr/^{86}Sr$	2 se
04/06/2014	1	NBS987_1	0.710306	0.000013
04/06/2014	2	NBS987_2	0.710273	0.000013
04/06/2014	3	NBS987_3	0.710299	0.000014
04/06/2014	4	NBS987_4	0.710292	0.000011
04/06/2014	5	NBS987_5	0.710291	0.000012
04/06/2014	6	NBS987_6	0.710296	0.000011
04/06/2014	13	NBS987_7	0.710315	0.000013
04/06/2014	19	NBS987_8	0.710294	0.000011

Date	Time	Analysis	$^{87}Sr/^{86}Sr$	2 se
05/06/2014	1	NBS987_1	0.710298	0.000010
05/06/2014	2	NBS987_2	0.710291	0.000010
05/06/2014	3	NBS987_3	0.710284	0.000010
05/06/2014	4	NBS987_4	0.710292	0.000008
05/06/2014	10	NBS987_5	0.710321	0.000012
05/06/2014	16	NBS987_6	0.710353	0.000009

Date	Time	Analysis	$^{87}Sr/^{86}Sr$	2 se
06/11/2014	1	NBS987_1	0.710350	0.000010
06/11/2014	2	NBS987_2	0.710340	0.000008
06/11/2014	3	NBS987_3	0.710335	0.000008
06/11/2014	4	NBS987_4	0.710333	0.000008
06/11/2014	5	NBS987_5	0.710320	0.000008
06/11/2014	6	NBS987_6	0.710316	0.000010
06/11/2014	7	NBS987_7	0.710321	0.000008
06/11/2014	8	NBS987_8	0.710317	0.000009
06/11/2014	11	NBS987_9	0.710326	0.000009
06/11/2014	14	NBS987_10	0.710322	0.000009
06/11/2014	16	NBS987_11	0.710319	0.000010

Date	Time	Analysis	$^{87}Sr/^{86}Sr$	2 se
07/11/2014	1	NBS987_1	0.710295	0.000007
07/11/2014	2	NBS987_2	0.710298	0.000007
07/11/2014	3	NBS987_3	0.710298	0.000008
07/11/2014	4	NBS987_4	0.710290	0.000007
07/11/2014	5	NBS987_5	0.710297	0.000008
07/11/2014	8	NBS987_6	0.710314	0.000008
07/11/2014	11	NBS987_7	0.710326	0.000008
07/11/2014	17	NBS987_8	0.710340	0.000007

Date	Time	Analysis	$^{87}Sr/^{86}Sr$	2 se
16/01/2015	1	NBS987_1	0.710288	0.000010
16/01/2015	2	NBS987_2	0.710291	0.000010
16/01/2015	3	NBS987_3	0.710284	0.000010
16/01/2015	4	NBS987_4	0.710292	0.000008
16/01/2015	10	NBS987_5	0.710341	0.000012
16/01/2015	16	NBS987_6	0.710363	0.000009

Date	Time	Analysis	$^{87}Sr/^{86}Sr$	2 se
19/01/2015	1	NBS987_1	0.710306	0.000013
19/01/2015	2	NBS987_2	0.710273	0.000013
19/01/2015	3	NBS987_3	0.710299	0.000014
19/01/2015	4	NBS987_4	0.710292	0.000011
19/01/2015	5	NBS987_5	0.710291	0.000012
19/01/2015	6	NBS987_6	0.710296	0.000011
19/01/2015	13	NBS987_7	0.710315	0.000013
19/01/2015	19	NBS987_8	0.710294	0.000011

D.2.2. Nd standard data (by MC-ICP-MS)

Date	Time	Analysis	$^{143}Nd/^{144}Nd$	2 se
19/08/2014	1	J+M	0.511801	0.000012
19/08/2014	2	J+M	0.511802	0.000012
19/08/2014	3	J+M	0.511819	0.000012
19/08/2014	4	J+M	0.511810	0.000011
19/08/2014	7	J+M	0.511803	0.000011
19/08/2014	11	J+M	0.511814	0.000011

Date	Time	Analysis	$^{143}Nd/^{144}Nd$	2 se
20/08/2014	5	J+M	0.511795	0.000017
20/08/2014	6	J+M	0.511831	0.000015
20/08/2014	7	J+M	0.511809	0.000017
20/08/2014	8	J+M	0.511827	0.000015
20/08/2014	9	J+M	0.511812	0.000015
20/08/2014	12	J+M	0.511851	0.000016
20/08/2014	14	J+M	0.511827	0.000017
20/08/2014	16	J+M	0.511783	0.000016
20/08/2014	18	J+M	0.511798	0.000016

Date	Time	Analysis	$^{143}Nd/^{144}Nd$	2 se
30/10/2014	1	J+M	0.511799	0.000010
30/10/2014	2	J+M	0.511815	0.000010
30/10/2014	3	J+M	0.511801	0.000011
30/10/2014	4	J+M	0.511801	0.000011
30/10/2014	5	J+M	0.511813	0.000010
30/10/2014	8	J+M	0.511815	0.000010
30/10/2014	11	J+M	0.511794	0.000008
30/10/2014	14	J+M	0.511813	0.000010
30/10/2014	17	J+M	0.511807	0.000009

Date	Time	Analysis	$^{143}Nd/^{144}Nd$	2 se
31/10/2014	1	J+M	0.511806	0.000010
31/10/2014	2	J+M	0.511815	0.000010
31/10/2014	3	J+M	0.511826	0.000009
31/10/2014	4	J+M	0.511812	0.000009
31/10/2014	5	J+M	0.511813	0.000009
31/10/2014	6	J+M	0.511802	0.000010
31/10/2014	7	J+M	0.511811	0.000009
31/10/2014	10	J+M	0.511800	0.000009
31/10/2014	13	J+M	0.511805	0.000009

D.2.3. Pb standard data (by TIMS)

Date	Nat	DS	$^{206}Pb/^{204}Pb$	2 s.e.	$^{207}Pb/^{204}Pb$	2 s.e.	$^{208}Pb/^{204}Pb$	2 s.e.
17/09/2014	Nat1	DS1	16.9459	0.0010	15.5036	0.0010	36.7427	0.0027
17/09/2014	Nat2	DS1	16.9431	0.0009	15.5014	0.0009	36.7363	0.0024
17/09/2014	Nat3	DS1	16.9463	0.0009	15.5043	0.0009	36.7440	0.0025
17/09/2014	Nat1	DS2	16.9458	0.0009	15.5034	0.0010	36.7422	0.0026
17/09/2014	Nat2	DS2	16.9431	0.0008	15.5014	0.0009	36.7361	0.0023
17/09/2014	Nat3	DS2	16.9461	0.0008	15.5040	0.0009	36.7430	0.0024
17/09/2014	Nat1	DS3	16.9452	0.0010	15.5026	0.0010	36.7396	0.0028
17/09/2014	Nat2	DS3	16.9425	0.0009	15.5006	0.0009	36.7335	0.0026
17/09/2014	Nat3	DS3	16.9455	0.0009	15.5032	0.0009	36.7405	0.0026

Date	Nat	DS	$^{206}Pb/^{204}Pb$	2 s.e.	$^{207}Pb/^{204}Pb$	2 s.e.	$^{208}Pb/^{204}Pb$	2 s.e.
22/09/2014	Nat1	DS1	16.9440	0.0008	15.5009	0.0009	36.7340	0.0025
22/09/2014	Nat1	DS2	16.9440	0.0010	15.5010	0.0011	36.7344	0.0032
22/09/2014	Nat1	DS3	16.9443	0.0008	15.5013	0.0009	36.7354	0.0025
22/09/2014	Nat1	DS4	16.9416	0.0009	15.4976	0.0010	36.7238	0.0030
22/09/2014	Nat2	DS1	16.9435	0.0005	15.5019	0.0006	36.7343	0.0019
22/09/2014	Nat2	DS2	16.9435	0.0007	15.5019	0.0009	36.7342	0.0028
22/09/2014	Nat2	DS3	16.9438	0.0006	15.5023	0.0007	36.7355	0.0019
22/09/2014	Nat2	DS4	16.9411	0.0007	15.4986	0.0008	36.7239	0.0025
22/09/2014	Nat3	DS1	16.9443	0.0007	15.5022	0.0008	36.7357	0.0021
22/09/2014	Nat3	DS2	16.9443	0.0008	15.5022	0.0010	36.7358	0.0030
22/09/2014	Nat3	DS3	16.9445	0.0007	15.5026	0.0008	36.7370	0.0022
22/09/2014	Nat3	DS4	16.9419	0.0008	15.4989	0.0009	36.7253	0.0027
22/09/2014	Nat4	DS1	16.9433	0.0008	15.4984	0.0009	36.7307	0.0024
22/09/2014	Nat4	DS2	16.9436	0.0009	15.4987	0.0011	36.7318	0.0031
22/09/2014	Nat4	DS3	16.9437	0.0008	15.4988	0.0009	36.7322	0.0024
22/09/2014	Nat4	DS4	16.9410	0.0009	15.4952	0.0010	36.7208	0.0029

D.3. Stable isotope data

D.3.1. Whole-rock data

Stable Sr isotope data for whole rock samples

	1D 01	1G 01	1G 02	1G 03	3A 01	3A 02	3A 03	3A 04	4D 01	5M 01	
Rb ppm	254	330	322	277	572	251	323	296	143	241	Rb ppm
Sr ppm	62	181	61	55	11	12	44	10	121	13	Sr ppm
Rb/Sr	4.1	18	5.3	5.1	50	22	7.3	29	12	19	Rb/Sr
Sr method	TIM S	MC-ICP-MS	MC-ICP-MS	MC-ICP-MS	TIM S	TIM S	TIM S	TIM S	MC-ICP-MS	MC-ICP-MS	Sr method
$^{86}Sr/^{88}Sr$	0.056529	-	-	-	0.056496	0.056503	0.056457	0.056460	-	-	$^{86}Sr/^{88}Sr$
2 s.d.	0.000005	-	-	-	0.000005	0.000004	0.000004	0.000004	-	-	2 s.d.
$^{87}Sr/^{86}Sr$	0.978210	0.766658	0.824239	0.809263	0.807679	0.787705	0.777162	0.793745	0.768719	0.795758	$^{87}Sr/^{86}Sr$
2 s.d.	0.000022	0.000083	0.000065	0.000066	0.000021	0.000020	0.000020	0.000020	0.000083	0.000083	2 s.d.
$^{88}Sr/^{86}Sr$	8.36949	8.37660	8.37704	8.37605	8.37452	8.37308	8.38008	8.37964	8.37770	8.37839	$^{88}Sr/^{86}Sr$
2 s.d.	0.00044	0.00111	0.00044	0.00044	0.00044	0.00041	0.00041	0.00041	0.00111	0.00112	2 s.d.
$\delta^{84}Sr$	0.67	-	-	-	0.08	0.21	-0.60	-0.54	-	-	$\delta^{84}Sr$
2 s.d.	0.08	-	-	-	0.08	0.08	0.08	0.08	-	-	2 s.d.
$\delta^{88}Sr$	-0.68	0.17	0.22	0.10	-0.08	-0.25	0.58	0.53	0.30	0.38	$\delta^{88}Sr$
2 s.d.	0.05	0.13	0.05	0.05	0.05	0.05	0.05	0.05	0.13	0.13	2 s.d.

Stable Sr isotope data for whole rock samples

	1215	1247	1251	CWB 16	CWB 23	BH 65	BH 84	BH226	BH231	
Rb ppm	209	407	231	262	236	347	163	334	216	Rb ppm
Sr ppm	54	50	76	93	69	39	130	95	199	Sr ppm
Rb/Sr	3.9	8.2	3.0	2.8	3.4	8.9	1.3	3.5	1.1	Rb/Sr
Sr method	TIMS	TIMS	TIMS	MC-ICP-MS	MC-ICP-MS	MC-ICP-MS	TIMS	MC-ICP-MS	TIMS	Sr method
$^{84}Sr/^{86}Sr$	0.056492	0.056488	0.056507	-	-	-	0.056461	-	0.056473	$^{84}Sr/^{86}Sr$
2 s.d.	0.000004	0.000005	0.000005	-	-	-	0.000005	-	0.000005	2 s.d.
$^{87}Sr/^{86}Sr$	0.760098	0.762264	0.829544	0.830595	0.797008	0.911392	0.740317	0.770572	0.730144	$^{87}Sr/^{86}Sr$
2 s.d.	0.000020	0.000020	0.000020	0.000066	0.000066	0.000083	0.000020	0.000083	0.000020	2 s.d.
$^{88}Sr/^{86}Sr$	8.37498	8.37498	8.37248	8.37637	8.37839	8.37885	8.37927	8.37971	8.37734	$^{88}Sr/^{86}Sr$
2 s.d.	0.00041	0.00041	0.00041	0.00043	0.00043	0.00111	0.00041	0.00111	0.00041	2 s.d.
$\delta^{84}Sr$	0.01	-0.06	0.29	-	-	-	-0.53	-	-0.32	$\delta^{84}Sr$
2 s.d.	0.08	0.08	0.08	-	-	-	0.09	-	0.09	2 s.d.
$\delta^{88}Sr$	-0.03	-0.03	-0.33	0.14	0.38	0.43	0.48	0.54	0.25	$\delta^{88}Sr$
2 s.d.	0.05	0.05	0.05	0.05	0.05	0.13	0.05	0.13	0.05	2 s.d.

D.3.2. Mineral-separate data

Stable Sr and Rb isotope data for mineral separate samples

	1G03				3A03				1247				1251				
	Plag	K-spar	Whole-rock		Plag	K-spar	Musc	Whole-rock	Plag	K-spar	Musc	Whole-rock	Plag	K-spar	Biotite	Whole-rock	
Rb ppm	77	208	277		124	135	626	323	83	169	613	407	84	142	560	231	Rb ppm
Sr ppm	99	100	55		78	75	5	44	63	80	5	50	134	103	5	76	Sr ppm
Rb/Sr	0.8	2.1	5.1		1.6	1.8	134	7.3	1.3	2.1	116	8.2	0.6	1.4	114	3.0	
Sr method	TIMS	TIMS	MC-ICP-MS		TIMS	TIMS	TIMS	TIMS	TIMS	TIMS	-	TIMS	TIMS	TIMS	TIMS	TIMS	Sr method
$^{84}Sr/^{86}Sr$	0.056479	0.056487	-		0.056443	0.056465	0.056449	0.056457	0.056481	0.056485	-	0.056488	0.056470	0.056525	0.056385	0.056507	$^{84}Sr/^{86}Sr$
2 s.d.	0.000004	0.000004	-		0.000004	0.000004	0.000004	0.000004	0.000004	0.000004	-	0.000005	0.000004	0.000004	0.000005	0.000005	2 s.d.
$^{87}Sr/^{86}Sr$	0.806676	0.811537	0.809263		0.774111	0.777100	0.868988	0.777162	0.758335	0.764530	-	0.762264	0.827008	0.830912	0.864035	0.829544	$^{87}Sr/^{86}Sr$
2 s.d.	0.000020	0.000020	0.000066		0.000020	0.000020	0.000021	0.000020	0.000020	0.000020	-	0.000020	0.000020	0.000020	0.000023	0.000020	2 s.d.
$^{88}Sr/^{86}Sr$	8.376877	8.375151	8.376051		8.381870	8.378857	8.382128	8.380078	8.376386	8.376252	-	8.374978	8.378186	8.369790	8.390836	8.372478	$^{88}Sr/^{86}Sr$
2 s.d.	0.000392	0.000392	0.000441		0.000392	0.000392	0.000405	0.000408	0.000392	0.000392	-	0.000410	0.000391	0.000391	0.000405	0.000409	2 s.d.
$\delta^{84}Sr$	-0.21	-0.07	-		-0.86	-0.45	-0.74	-0.60	-0.18	-0.11	-	-0.06	-0.38	0.60	-1.87	0.29	$\delta^{84}Sr$
2 s.d.	0.07	0.07	-		0.07	0.07	0.08	0.08	0.07	0.07	-	0.08	0.07	0.07	0.09	0.08	2 s.d.
$\delta^{88}Sr$	0.20	-0.10	0.10		0.80	0.44	0.83	0.58	0.14	0.12	-	-0.03	0.36	-0.65	1.87	-0.33	$\delta^{88}Sr$
2 s.d.	0.05	0.05	0.05		0.05	0.05	0.05	0.05	0.05	0.05	-	0.05	0.05	0.05	0.05	0.05	2 s.d.
$^{87}Rb/^{85}Rb$	0.385952	0.385871	0.385971		0.385914	0.385878	0.385872	0.385875	0.385876	0.385873	0.385988	0.385920	0.386024	0.386026	0.386064	0.386016	$^{87}Rb/^{85}Rb$
2 s.d.	0.000018	0.000018	0.000017		0.000018	0.000018	0.000018	0.000017	0.000018	0.000018	0.000018	0.000017	0.000018	0.000018	0.000019	0.000017	2 s.d.
$\delta^{87}Rb$	-0.18	-0.39	-0.13		-0.28	-0.37	-0.39	-0.38	-0.38	-0.38	-0.09	-0.26	0.01	0.01	0.11	-0.01	$\delta^{87}Rb$
2 s.d.	0.05	0.05	0.04		0.05	0.05	0.05	0.04	0.05	0.05	0.05	0.04	0.05	0.05	0.05	0.04	2 s.d.

D.3.3. Rb-Sr geochronology data

Rb-Sr geochronology data

		1G03			3A03				1247				1251				
		Plag	K-spar	Whole-rock	Plag	K-spar	Musc	Whole-rock	Plag	K-spar	Musc	Whole-rock	Plag	K-spar	Biotite	Whole-rock	
	$^{87}Rb/^{86}Sr$	3.0679	17.0944	14.8063	7.4771	21.8279	387.07	21.3545	5.0616	33.0998	335.76	23.8396	2.3133	11.49	329.40	8.8950	$^{87}Rb/^{86}Sr$
	2 s.d.	0.0920	0.5128	0.4442	0.2243	0.6548	0.0271	0.6406	0.1518	0.9930	0.0319	0.7152	0.0694	0.3448	0.0368	0.2669	2 s.d.
	$^{87}Sr/^{86}Sr$	0.806676	0.811537	0.809259	0.774141	0.777100	0.868988	0.777162	0.758335	0.764530	0.860772	0.762264	0.827008	0.830912	0.864035	0.829544	$^{87}Sr/^{86}Sr$
	2 s.d.	0.000020	0.000020	0.000035	0.000020	0.000020	0.000021	0.000035	0.000020	0.000020	0.000035	0.000035	0.000020	0.000020	0.000023	0.000035	2 s.d.
	Age	-	-	-	17.59	17.72	-	17.68	21.81	22.39	-	22.24	7.91	7.34	-	7.58	Age
Two-point	2 s.d.	-	-	-	0.01	0.03	-	0.03	0.01	0.07	-	0.05	0.01	0.00	-	0.01	2 s.d.
with	$^{87}Sr/^{86}Sr_i$	-	-	-	0.772273	0.771610	-	0.771800	0.756767	0.754000	-	0.754730	0.826746	0.829714	-	0.828586	$^{87}Sr/^{86}Sr_i$
mica	2 s.d.	-	-	-	0.000060	0.000170	-	0.000170	0.000051	0.000340	-	0.000240	0.000021	0.000042	-	0.000046	2 s.d.
	Age	-	-	21	-	-	-	17.66	-	-	-	21.84	-	-	-	7.80	Age
All	2 s.d.	-	-	62	-	-	-	0.31	-	-	-	0.45	-	-	-	1.30	2 s.d.
phases	$^{87}Sr/^{86}Sr_i$	-	-	0.805700	-	-	-	0.771910	-	-	-	0.756600	-	-	-	0.827500	$^{87}Sr/^{86}Sr_i$
	2 s.d.	-	-	0.005000	-	-	-	0.000870	-	-	-	0.001700	-	-	-	0.003600	2 s.d.
	Assigned isochron age															c. 7.8 Ma	Assigned isochron age
Zircon	Age	-	-	12.52	-	-	-	c. 18 Ma	-	-	-	21.01	-	-	-	c. 14.0 Ma	Age
U-Pb	2 s.d.	-	-	0.19	-	-	-		-	-	-	0.21	-	-	-		2 s.d.

D.3.4. Sr standard data (by TIMS)

Nat	DS	$^{84}Sr/^{86}Sr$	2 s.e.	$^{87}Sr/^{86}Sr$	2 s.e.	$^{88}Sr/^{86}Sr$	2 s.e.	$d^{84}Sr$	2 s.e.	$d^{88}Sr$	2 s.e.
1	1	0.056497	0.000002	0.710297	0.000004	8.376172	0.000073	0.10	0.03	0.11	0.01
2	1	0.056488	0.000001	0.710294	0.000004	8.376222	0.000072	-0.05	0.02	0.12	0.01
3	1	0.056484	0.000001	0.710349	0.000004	8.376780	0.000072	-0.12	0.02	0.19	0.01
4	1	0.056486	0.000001	0.710306	0.000004	8.376362	0.000071	-0.09	0.02	0.14	0.01
5	1	0.056487	0.000001	0.710297	0.000004	8.376266	0.000070	-0.07	0.02	0.13	0.01
6	1	0.056489	0.000001	0.710290	0.000004	8.376182	0.000070	-0.04	0.02	0.12	0.01
1	2	0.056497	0.000002	0.710296	0.000004	8.376139	0.000075	0.11	0.03	0.11	0.01
2	2	0.056489	0.000001	0.710292	0.000004	8.376188	0.000074	-0.04	0.02	0.12	0.01
3	2	0.056484	0.000001	0.710348	0.000004	8.376746	0.000074	-0.12	0.02	0.18	0.01
4	2	0.056486	0.000001	0.710305	0.000004	8.376329	0.000072	-0.09	0.02	0.13	0.01
5	2	0.056488	0.000001	0.710296	0.000004	8.376233	0.000072	-0.06	0.02	0.12	0.01
6	2	0.056489	0.000001	0.710288	0.000004	8.376148	0.000072	-0.03	0.02	0.11	0.01
1	3	0.056500	0.000002	0.710280	0.000004	8.375766	0.000069	0.15	0.03	0.07	0.01
2	3	0.056491	0.000001	0.710276	0.000004	8.375816	0.000068	0.00	0.02	0.07	0.01
3	3	0.056487	0.000001	0.710332	0.000004	8.376374	0.000068	-0.07	0.02	0.14	0.01
4	3	0.056489	0.000001	0.710289	0.000004	8.375957	0.000067	-0.04	0.02	0.09	0.01
5	3	0.056490	0.000001	0.710280	0.000004	8.375860	0.000066	-0.02	0.02	0.08	0.01
6	3	0.056492	0.000001	0.710273	0.000004	8.375776	0.000066	0.01	0.02	0.07	0.01
1	4	0.056499	0.000002	0.710282	0.000004	8.375810	0.000071	0.15	0.03	0.07	0.01
2	4	0.056491	0.000001	0.710278	0.000004	8.375860	0.000070	0.00	0.02	0.08	0.01
3	4	0.056487	0.000001	0.710334	0.000004	8.376418	0.000070	-0.08	0.02	0.14	0.01
4	4	0.056488	0.000001	0.710291	0.000004	8.376001	0.000068	-0.05	0.02	0.09	0.01
5	4	0.056490	0.000001	0.710282	0.000004	8.375904	0.000068	-0.02	0.02	0.08	0.01
6	4	0.056491	0.000001	0.710274	0.000004	8.375820	0.000068	0.01	0.02	0.07	0.01
1	5	0.056497	0.000002	0.710293	0.000005	8.376076	0.000105	0.11	0.03	0.10	0.01
2	5	0.056489	0.000001	0.710290	0.000005	8.376125	0.000104	-0.03	0.03	0.11	0.01
3	5	0.056485	0.000001	0.710345	0.000005	8.376683	0.000104	-0.11	0.03	0.18	0.01
4	5	0.056487	0.000001	0.710302	0.000005	8.376266	0.000103	-0.08	0.02	0.13	0.01
5	5	0.056488	0.000001	0.710293	0.000005	8.376170	0.000103	-0.05	0.02	0.11	0.01
6	5	0.056490	0.000001	0.710286	0.000005	8.376085	0.000103	-0.02	0.02	0.10	0.01
1	6	0.056500	0.000002	0.710280	0.000004	8.375766	0.000070	0.15	0.03	0.07	0.01
2	6	0.056491	0.000001	0.710276	0.000004	8.375815	0.000068	0.00	0.02	0.07	0.01
3	6	0.056487	0.000001	0.710332	0.000004	8.376373	0.000069	-0.07	0.02	0.14	0.01
4	6	0.056489	0.000001	0.710289	0.000004	8.375956	0.000067	-0.04	0.02	0.09	0.01
5	6	0.056490	0.000001	0.710280	0.000004	8.375860	0.000066	-0.02	0.02	0.08	0.01
6	6	0.056492	0.000001	0.710273	0.000004	8.375775	0.000066	0.01	0.02	0.07	0.01

D.3.5. Rb standard data (by MC-ICP-MS)

Date	Analysis	Time	$^{85}Rb/^{87}Rb$	2 s.e.	2 s.d.	$d^{85}Rb$	2 s.d.	$d^{87}Rb$	2 s.d.
14/10/2015	NBS984_1	1	2.590704	0.000050	0.000124	0.07	0.05	-0.07	0.05
14/10/2015	NBS984_2	2	2.590617	0.000058	0.000127	0.03	0.05	-0.03	0.05
14/10/2015	NBS984_3	3	2.590583	0.000043	0.000121	0.02	0.05	-0.02	0.05
14/10/2015	NBS984_4	4	2.590641	0.000048	0.000123	0.04	0.05	-0.04	0.05
14/10/2015	NBS984_5	5	2.590564	0.000053	0.000125	0.01	0.05	-0.01	0.05
14/10/2015	NBS984_6	6	2.590503	0.000055	0.000126	-0.01	0.05	0.01	0.05
14/10/2015	NBS984_7	7	2.590505	0.000060	0.000128	-0.01	0.05	0.01	0.05
14/10/2015	NBS984_8	9	2.590534	0.000047	0.000123	0.00	0.05	0.00	0.05
14/10/2015	NBS984_9	11	2.590558	0.000052	0.000125	0.01	0.05	-0.01	0.05
14/10/2015	NBS984_10	13	2.590600	0.000050	0.000124	0.03	0.05	-0.03	0.05
14/10/2015	NBS984_11	15	2.590613	0.000051	0.000124	0.03	0.05	-0.03	0.05
14/10/2015	NBS984_12	17	2.590678	0.000048	0.000123	0.06	0.05	-0.06	0.05
14/10/2015	NBS984_13	19	2.590635	0.000047	0.000123	0.04	0.05	-0.04	0.05
14/10/2015	NBS984_14	21	2.590606	0.000045	0.000122	0.03	0.05	-0.03	0.05
14/10/2015	NBS984_15	23	2.590651	0.000043	0.000121	0.05	0.05	-0.05	0.05
14/10/2015	NBS984_16	25	2.590637	0.000046	0.000122	0.04	0.05	-0.04	0.05
14/10/2015	NBS984_17	28	2.590742	0.000050	0.000124	0.08	0.05	-0.08	0.05

Date	Analysis	Time	$^{85}Rb/^{87}Rb$	2 s.e.	2 s.d.	$d^{85}Rb$	2 s.d.	$d^{87}Rb$	2 s.d.
15/10/2015	NBS984_1	1	2.590633	0.000050	0.000115	0.04	0.04	-0.04	0.04
15/10/2015	NBS984_2	2	2.590638	0.000058	0.000118	0.04	0.05	-0.04	0.05
15/10/2015	NBS984_3	3	2.590588	0.000043	0.000112	0.02	0.04	-0.02	0.04
15/10/2015	NBS984_4	4	2.590515	0.000048	0.000114	-0.01	0.04	0.01	0.04
15/10/2015	NBS984_5	5	2.590541	0.000053	0.000116	0.00	0.04	0.00	0.04
15/10/2015	NBS984_6	6	2.590542	0.000055	0.000117	0.00	0.05	0.00	0.05
15/10/2015	NBS984_7	7	2.590522	0.000060	0.000119	0.00	0.05	0.00	0.05
15/10/2015	NBS984_8	8	2.590576	0.000046	0.000113	0.02	0.04	-0.02	0.04
15/10/2015	NBS984_9	10	2.590505	0.000044	0.000112	-0.01	0.04	0.01	0.04
15/10/2015	NBS984_10	12	2.590448	0.000048	0.000114	-0.03	0.04	0.03	0.04
15/10/2015	NBS984_11	14	2.590512	0.000044	0.000112	-0.01	0.04	0.01	0.04
15/10/2015	NBS984_12	16	2.590434	0.000049	0.000114	-0.04	0.04	0.04	0.04
15/10/2015	NBS984_13	18	2.590576	0.000046	0.000113	0.02	0.04	-0.02	0.04
15/10/2015	NBS984_14	20	2.590459	0.000041	0.000111	-0.03	0.04	0.03	0.04
15/10/2015	NBS984_15	22	2.590578	0.000047	0.000113	0.02	0.04	-0.02	0.04
15/10/2015	NBS984_16	24	2.590458	0.000040	0.000110	-0.03	0.04	0.03	0.04
15/10/2015	NBS984_17	27	2.590395	0.000063	0.000121	-0.05	0.05	0.05	0.05

Date	Analysis	Time	$^{85}Rb/^{87}Rb$	2 s.e.	2 s.d.	$d^{85}Rb$	2 s.d.	$d^{87}Rb$	2 s.d.
16/10/2015	NBS984_1	1	2.590521	0.000050	0.000134	0.00	0.05	0.00	0.05
16/10/2015	NBS984_2	2	2.590538	0.000058	0.000137	0.00	0.05	0.00	0.05
16/10/2015	NBS984_3	3	2.590488	0.000043	0.000131	-0.02	0.05	0.02	0.05
16/10/2015	NBS984_4	4	2.590566	0.000048	0.000133	0.01	0.05	-0.01	0.05
16/10/2015	NBS984_5	5	2.590616	0.000053	0.000135	0.03	0.05	-0.03	0.05
16/10/2015	NBS984_6	6	2.590657	0.000055	0.000136	0.05	0.05	-0.05	0.05
16/10/2015	NBS984_7	7	2.590629	0.000060	0.000138	0.04	0.05	-0.04	0.05
16/10/2015	NBS984_8	11	2.590636	0.000052	0.000135	0.04	0.05	-0.04	0.05
16/10/2015	NBS984_9	15	2.590550	0.000051	0.000134	0.01	0.05	-0.01	0.05
16/10/2015	NBS984_10	18	2.590623	0.000046	0.000132	0.04	0.05	-0.04	0.05
16/10/2015	NBS984_11	21	2.590889	0.000045	0.000132	0.14	0.05	-0.14	0.05
16/10/2015	NBS984_12	22	2.590800	0.000047	0.000133	0.10	0.05	-0.10	0.05

Date	Analysis	Time	$^{85}Rb/^{87}Rb$	2 s.e.	2 s.d.	$d^{85}Rb$	2 s.d.	$d^{87}Rb$	2 s.d.
15/10/2015	1ppb Sr	9	2.590567	0.000047	0.000113	0.01	0.04	-0.01	0.04
15/10/2015	1ppb Sr	25	2.590472	0.000046	0.000113	-0.02	0.04	0.02	0.04
16/10/2015	1ppb Sr	8	2.590623	0.000046	0.000132	0.04	0.05	-0.04	0.05
16/10/2015	1ppb Sr	12	2.590593	0.000048	0.000133	0.02	0.05	-0.02	0.05
15/10/2015	10ppb Sr	11	2.590524	0.000052	0.000115	0.00	0.04	0.00	0.04
15/10/2015	10ppb Sr	26	2.590403	0.000046	0.000113	-0.05	0.04	0.05	0.04
16/10/2015	10ppb Sr	9	2.590635	0.000047	0.000133	0.04	0.05	-0.04	0.05
16/10/2015	10ppb Sr	13	2.590633	0.000050	0.000134	0.04	0.05	-0.04	0.05
15/10/2015	100ppb Sr	10	2.590677	0.000044	0.000132	0.06	0.05	-0.06	0.05
15/10/2015	100ppb Sr	16	2.590643	0.000049	0.000133	0.04	0.05	-0.04	0.05
15/10/2015	100ppb Sr	19	2.590635	0.000047	0.000133	0.04	0.05	-0.04	0.05
16/10/2015	100ppb Sr	14	2.590584	0.000044	0.000132	0.02	0.05	-0.02	0.05
16/10/2015	AGV-1	17	2.592016	0.000048	0.000133	0.57	0.05	-0.57	0.05
16/10/2015	BCR-2	20	2.592595	0.000041	0.000131	0.80	0.05	-0.80	0.05
16/10/2015	G2	21	2.591495	0.000045	0.000113	0.37	0.04	-0.37	0.04
16/10/2015	NBS607	23	2.592236	0.000043	0.000112	0.66	0.04	-0.66	0.04

D.4. Zircon O, U-Pb, Hf data

D.4.1. Zircon rim U-Pb data

Zircon rim U-Pb data

				Data for Tera-Wasserburg plot[3]				Data for Wetherill plot[3]					Ages (Ma)[3]						
Analysis no.	f206c[1] %	^{206}Pb mV	Uppm[2]	^{238}U/^{206}Pb	1σ %	^{207}Pb/^{206}Pb	1σ %	^{207}Pb/^{235}U	1σ %	^{206}Pb/^{238}U	1σ %	Rho	^{207}Pb/^{206}Pb	2σ abs	^{206}Pb/^{238}U	2σ abs	^{207}Pb/^{235}U	2σ abs	% conc[4]
Sample: 1D01	**GPS: 27.879567 N, 89.727417 E**																		
3	bd	0.5	2494	347.9	1.2	0.0471	0.7	0.019	1.4	0.0029	1.2	0.88	54	16	19	0	19	1	98.6
5	bd	1.9	6269	249.2	0.9	0.0470	0.3	0.026	0.9	0.0040	0.9	0.93	49	8	26	0	26	0	99.1
6	bd	0.7	2880	315.3	0.9	0.0474	0.5	0.021	1.0	0.0032	0.9	0.86	69	12	20	0	21	0	98.0
9	2.5	1.0	2670	207.9	0.5	0.0475	0.7	0.031	0.8	0.0048	0.5	0.62	75	16	31	0	31	1	98.2
12	bd	0.9	2527	210.6	1.9	0.0474	0.7	0.031	2.1	0.0047	1.9	0.94	70	17	31	1	31	1	98.4
13	bd	0.9	2490	220.3	1.1	0.0473	0.7	0.030	1.3	0.0045	1.1	0.85	66	16	29	1	30	1	98.6
15	bd	0.8	2127	202.6	1.1	0.0475	0.4	0.032	1.2	0.0049	1.1	0.94	73	10	32	1	32	1	98.3
18	bd	0.7	1966	200.0	2.0	0.0497	0.5	0.034	2.1	0.0050	2.0	0.97	179	13	32	1	34	1	94.1
19	1.7	0.7	2358	263.9	2.0	0.0466	0.6	0.024	2.1	0.0038	2.0	0.96	31	15	24	1	24	1	99.8
22	bd	1.2	4917	320.0	1.2	0.0466	0.5	0.020	1.3	0.0031	1.2	0.92	27	12	20	0	20	1	99.7
23	0.2	1.8	4824	202.8	1.1	0.0474	0.4	0.032	1.2	0.0049	1.1	0.93	69	10	32	1	32	1	98.5
24	3.9	1.2	3900	256.6	1.0	0.0462	0.5	0.025	1.1	0.0039	1.0	0.90	7	11	25	0	25	1	100.8
25	0.6	12.1	31313	198.1	2.8	0.0482	0.2	0.034	2.8	0.0050	2.8	1.00	111	4	32	2	34	2	96.8
27	3	0.8	2266	224.9	1.0	0.0469	0.6	0.029	1.2	0.0044	1.0	0.87	45	14	29	1	29	1	99.4
30	bd	0.7	2718	290.4	1.6	0.0467	0.6	0.022	1.7	0.0034	1.6	0.93	31	15	22	1	22	1	99.7
31	bd	0.8	2039	206.8	1.2	0.0471	0.6	0.031	1.4	0.0048	1.2	0.91	55	13	31	1	31	1	99.1
35	bd	0.9	2240	188.7	0.9	0.0474	0.8	0.035	1.2	0.0053	0.9	0.76	71	18	34	1	35	1	98.5
38	13.5	0.7	2874	334.5	1.0	0.0467	0.4	0.019	1.1	0.0030	1.0	0.93	33	10	19	0	19	0	99.5
40	bd	1.2	3297	204.9	1.1	0.0472	0.6	0.032	1.2	0.0049	1.1	0.89	59	13	31	1	32	1	98.9
Sample: 1G01	**GPS: 27.866500 N, 89.726450 E**																		
1	1.7	4.5	18196	472.8	1.2	0.0472	0.5	0.014	1.3	0.0021	1.2	0.91	62	13	14	0	14	0	98.1
2	1.7	4.0	16101	475.7	1.3	0.0470	0.4	0.014	1.4	0.0021	1.3	0.96	48	9	14	0	14	0	98.6
3	bd	1.5	5807	468.2	1.0	0.0472	0.6	0.014	1.2	0.0021	1.0	0.84	58	15	14	0	14	0	98.2
4	1.1	3.0	12343	473.4	1.2	0.0470	0.5	0.014	1.3	0.0021	1.2	0.92	48	12	14	0	14	0	98.6
5	2	6.3	26740	497.4	0.8	0.0473	0.3	0.013	0.9	0.0020	0.8	0.94	65	8	13	0	13	0	97.9
6	bd	6.5	25916	464.8	1.6	0.0469	0.4	0.014	1.7	0.0022	1.6	0.98	43	9	14	0	14	0	98.8
11	bd	0.9	3348	437.3	1.6	0.0463	0.7	0.015	1.7	0.0023	1.6	0.91	14	17	15	0	15	1	100.1
12	bd	0.7	2285	409.7	1.0	0.0469	1.0	0.016	1.4	0.0024	1.0	0.72	45	24	16	0	16	0	98.8
13	bd	2.3	9706	480.8	1.3	0.0471	0.5	0.013	1.4	0.0021	1.3	0.94	52	11	13	0	14	0	98.5
14	1.2	2.8	11850	489.1	1.3	0.0471	0.5	0.013	1.4	0.0020	1.3	0.94	53	11	13	0	13	0	98.4
15	0.8	3.0	12218	479.7	1.3	0.0529	0.9	0.015	1.5	0.0021	1.3	0.82	326	20	13	0	15	0	87.6
16	2.5	1.9	8011	483.1	1.3	0.0474	0.5	0.014	1.4	0.0021	1.3	0.94	68	11	13	0	14	0	97.8
17	1.5	1.9	7603	464.9	1.1	0.0469	0.5	0.014	1.2	0.0022	1.1	0.92	44	12	14	0	14	0	98.8
21	2.2	1.7	5569	386.9	1.9	0.0504	1.3	0.018	2.3	0.0026	1.9	0.81	211	31	17	1	18	1	92.2
23	3.4	0.9	3361	456.0	1.3	0.0469	1.1	0.014	1.7	0.0022	1.3	0.74	44	27	14	0	14	0	98.8
24	bd	0.9	3776	493.2	1.2	0.0471	0.7	0.013	1.4	0.0020	1.2	0.87	55	17	13	0	13	0	98.3
31	bd	0.8	2642	404.0	2.8	0.0490	0.9	0.017	2.9	0.0025	2.8	0.96	146	20	16	1	17	1	94.7
32	bd	0.9	3571	456.5	0.8	0.0470	0.6	0.014	1.0	0.0022	0.8	0.83	51	13	14	0	14	0	98.5
33	bd	2.3	9750	494.1	1.4	0.0481	1.5	0.013	2.1	0.0020	1.4	0.69	103	36	13	0	14	1	96.4
34	1.1	1.4	5633	480.8	1.1	0.0468	0.6	0.013	1.3	0.0021	1.1	0.89	37	14	13	0	14	0	99.1
35	0.7	7.9	33395	493.6	1.4	0.0499	0.8	0.014	1.6	0.0020	1.4	0.86	190	19	13	0	14	0	92.9
39	10.6	1.1	4547	464.2	1.3	0.0490	1.3	0.015	1.8	0.0022	1.3	0.70	149	30	14	0	15	1	94.5
40	bd	1.5	6219	477.1	1.3	0.0467	0.7	0.013	1.5	0.0021	1.3	0.88	33	17	13	0	14	0	99.2
41	bd	1.9	8008	480.1	1.1	0.0463	0.5	0.013	1.2	0.0021	1.1	0.92	14	11	13	0	13	0	100.0
43	2.2	3.0	11889	457.1	1.3	0.0486	0.5	0.015	1.4	0.0022	1.3	0.94	127	11	14	0	15	0	95.5
44	bd	1.7	6783	476.8	1.4	0.0468	0.6	0.014	1.5	0.0021	1.4	0.92	38	15	14	0	14	0	99.0
45	1.3	6.7	27778	480.9	1.3	0.0475	0.7	0.014	1.5	0.0021	1.3	0.86	72	18	13	0	14	0	97.6
Sample: 1G02	**GPS: 27.866500 N, 89.726450 E**																		
6	bd	0.1	522	393.8	0.9	0.0495	1.7	0.017	1.9	0.0025	0.9	0.47	173	40	16	0	17	1	93.7
31	2.7	0.2	1344	521.6	1.0	0.0476	1.1	0.013	1.5	0.0019	1.0	0.65	81	27	12	0	13	0	97.2
32	bd	1.2	7958	520.9	1.0	0.0475	0.5	0.013	1.1	0.0019	1.0	0.89	75	12	12	0	13	0	97.5
33	bd	1.0	6508	509.8	1.0	0.0475	0.5	0.013	1.1	0.0020	1.0	0.91	74	12	13	0	13	0	97.5
39	bd	1.3	8282	511.4	1.2	0.0476	0.5	0.013	1.3	0.0020	1.2	0.93	80	11	13	0	13	0	97.3
40	8.3	1.0	5788	458.0	1.0	0.0474	0.4	0.014	1.1	0.0022	1.0	0.92	67	11	14	0	14	0	97.9
44	bd	1.1	7299	498.7	1.2	0.0467	0.3	0.013	1.3	0.0020	1.2	0.96	33	8	13	0	13	0	99.2
Sample: 1G03	**GPS: 27.866500 N, 89.726450 E**																		
4	7.8	0.9	4254	514.0	1.2	0.0465	0.8	0.012	1.5	0.0019	1.2	0.85	23	18	13	0	13	0	99.6
5	0.0	2.1	9750	510.7	1.2	0.0469	0.6	0.013	1.4	0.0020	1.2	0.90	44	14	13	0	13	0	98.7
18	bd	2.6	12440	515.2	1.2	0.0470	0.5	0.013	1.3	0.0019	1.2	0.91	50	13	13	0	13	0	98.5
21	2.6	0.3	1171	372.4	3.8	0.0470	1.2	0.017	3.9	0.0027	3.8	0.95	47	29	17	1	17	1	98.8
22	3.2	3.2	15070	492.2	1.2	0.0551	8.5	0.015	8.6	0.0020	1.2	0.14	418	191	13	0	16	3	84.1
Sample: 3A02	**GPS: 27.261900 N, 90.037050 E**																		
1	3.5	2.7	6752	286.8	2.1	0.0661	3.6	0.032	4.2	0.0035	2.1	0.50	809	76	22	1	32	3	70.7
2	0.6	1.9	5453	326.2	1.7	0.0588	3.2	0.025	3.7	0.0031	1.7	0.47	561	71	20	1	25	2	79.2
3	0.5	3.7	9889	310.6	1.6	0.0758	3.6	0.034	3.9	0.0032	1.6	0.42	1090	72	21	1	34	3	61.7
5	bd	3.5	10472	335.9	2.2	0.0514	1.9	0.021	2.9	0.0030	2.2	0.76	257	43	19	1	21	1	90.5
6	0.4	7.7	18824	309.7	3.4	0.0527	1.9	0.023	3.9	0.0032	3.4	0.88	317	42	21	1	24	2	88.2
7	0.6	3.3	9302	324.8	2.0	0.0554	5.6	0.024	6.0	0.0031	2.0	0.34	427	125	20	1	24	3	84.0
8	bd	3.2	8822	319.8	1.6	0.0589	2.9	0.025	3.3	0.0031	1.6	0.48	564	63	20	1	25	2	79.1
9	bd	3.1	9212	341.3	1.4	0.0605	1.6	0.024	2.2	0.0029	1.4	0.66	621	35	19	1	25	1	77.0

Zircon rim U-Pb data

Analysis no.	f206c[1] %	^{206}Pb mV	Uppm[2]	Data for Tera-Wasserburg plot[3] ^{238}U/^{206}Pb	1σ %	^{207}Pb/^{206}Pb	1σ %	Data for Wetherill plot[3] ^{207}Pb/^{235}U	1σ %	^{206}Pb/^{238}U	1σ %	Rho	Ages (Ma)[3] ^{207}Pb/^{206}Pb	2σ abs	^{206}Pb/^{238}U	2σ abs	^{207}Pb/^{235}U	2σ abs	% conc[4]
Sample: 3A03	**GPS: 27.261900 N, 90.037050 E**																		
1	1.4	3.9	11402	338.7	2.4	0.0571	3.5	0.023	4.2	0.0030	2.4	0.56	497	77	19	1	23	2	81.4
5	bd	0.4	1012	313.9	1.5	0.0473	1.1	0.021	1.8	0.0032	1.5	0.82	64	25	21	1	21	1	98.3
7	0.0	7.2	24734	400.3	1.9	0.0549	1.7	0.019	2.6	0.0025	1.9	0.75	409	38	16	1	19	1	84.6
8	2.5	4.4	14408	334.7	2.7	0.0729	3.7	0.030	4.6	0.0030	2.7	0.58	1011	75	19	1	30	3	64.0
12	1.0	6.1	19585	376.2	0.9	0.0541	2.1	0.020	2.2	0.0027	0.9	0.40	376	46	17	0	20	1	85.8
14	bd	2.7	8332	359.8	1.4	0.0504	1.6	0.019	2.1	0.0028	1.4	0.67	213	36	18	1	19	1	92.2
17	0.4	5.5	16935	386.9	3.9	0.0500	1.5	0.018	4.2	0.0026	3.9	0.93	195	36	17	1	18	1	92.8
22	bd	3.5	10415	347.3	1.1	0.0496	0.8	0.020	1.4	0.0029	1.1	0.80	178	20	19	0	20	1	93.6
25	0.0	2.6	8520	362.0	2.2	0.0567	2.8	0.022	3.6	0.0028	2.2	0.61	481	63	18	1	22	2	82.0
28	bd	4.6	13485	342.6	1.5	0.0477	0.5	0.019	1.5	0.0029	1.5	0.95	84	11	19	1	19	1	97.4
33	0.8	7.5	23496	359.5	1.7	0.0505	2.2	0.019	2.8	0.0028	1.7	0.61	219	51	18	1	19	1	91.9
34	bd	4.2	16037	371.0	2.9	0.0521	2.3	0.019	3.7	0.0027	2.9	0.78	288	53	17	1	19	1	89.2
37	bd	4.4	12577	333.4	1.2	0.0491	1.0	0.020	1.6	0.0030	1.2	0.76	150	24	19	0	20	1	94.7
40	1.4	4.1	11242	312.9	2.5	0.0580	2.3	0.026	3.4	0.0032	2.5	0.75	529	50	21	1	26	2	80.3
Sample: 4D01	**GPS: 27.493483 N, 90.031800 E**																		
1	0.2	2.3	7126	364.8	0.9	0.0469	0.7	0.018	1.1	0.0027	0.9	0.81	45	16	18	0	18	0	98.9
2	bd	2.6	8187	360.5	1.2	0.0476	1.5	0.018	1.9	0.0028	1.2	0.64	79	35	18	0	18	1	97.5
3	bd	1.2	3166	317.0	1.2	0.0549	2.0	0.024	2.3	0.0032	1.2	0.50	409	45	20	0	24	1	84.8
4	bd	0.8	2992	417.9	1.9	0.0489	1.4	0.016	2.4	0.0024	1.9	0.80	142	33	15	1	16	1	94.9
5	bd	2.9	8815	359.4	1.4	0.0472	0.7	0.018	1.5	0.0028	1.4	0.90	61	16	18	0	18	1	98.3
6	bd	5.0	17102	398.5	1.3	0.0472	0.5	0.016	1.4	0.0025	1.3	0.93	59	13	16	0	16	0	98.3
7	bd	0.6	1644	330.0	1.5	0.0632	6.5	0.026	6.7	0.0030	1.5	0.23	714	138	20	1	26	3	73.8
8	bd	1.1	3043	323.2	1.1	0.0481	0.7	0.021	1.4	0.0031	1.1	0.84	104	17	20	0	21	1	96.6
9	bd	3.2	9465	344.9	1.8	0.0467	0.6	0.019	1.9	0.0029	1.8	0.94	35	15	19	1	19	1	99.4
10	bd	1.5	3966	313.6	1.5	0.0554	4.9	0.024	5.1	0.0032	1.5	0.29	427	109	21	1	24	2	84.1
11	bd	1.4	4403	373.9	0.8	0.0466	0.9	0.017	1.2	0.0027	0.8	0.69	31	20	17	0	17	0	99.5
12	3.0	1.0	3123	367.5	0.7	0.0468	0.4	0.018	0.8	0.0027	0.7	0.84	37	11	18	0	18	0	99.2
14	4.2	1.4	4371	370.8	1.3	0.0479	0.7	0.018	1.5	0.0027	1.3	0.87	92	17	17	0	18	1	97.0
15	0.1	3.4	10577	359.7	1.3	0.0470	0.5	0.018	1.3	0.0028	1.3	0.93	48	12	18	0	18	0	98.8
16	bd	2.4	7266	350.0	1.1	0.0480	0.7	0.019	1.3	0.0029	1.1	0.82	100	17	18	0	19	0	96.7
17	0.5	1.6	4100	303.3	1.2	0.0508	2.8	0.023	3.0	0.0033	1.2	0.40	230	64	21	1	23	1	91.7
18	1.6	1.8	5850	360.6	1.3	0.0468	0.6	0.018	1.4	0.0028	1.3	0.91	38	14	18	0	18	1	99.2
19	bd	0.9	2440	318.4	0.9	0.0486	0.9	0.021	1.3	0.0031	0.9	0.68	129	22	20	0	21	1	95.6
20	bd	2.5	7742	360.7	1.2	0.0467	0.4	0.018	1.2	0.0028	1.2	0.93	36	11	18	0	18	0	99.3
21	bd	2.8	8748	365.4	1.4	0.0483	0.9	0.018	1.6	0.0027	1.4	0.84	113	21	18	0	18	1	96.2
22	bd	4.8	14805	358.8	0.8	0.0485	0.7	0.019	1.0	0.0028	0.8	0.76	123	16	18	0	19	0	95.8
24	bd	2.3	7149	366.5	1.0	0.0469	0.5	0.018	1.1	0.0027	1.0	0.89	42	12	18	0	18	0	99.0
25	bd	1.3	3799	337.9	1.6	0.0475	0.7	0.019	1.7	0.0030	1.6	0.92	76	16	19	1	19	1	97.7
27	2.4	2.0	5938	340.9	0.5	0.0543	2.1	0.022	2.1	0.0029	0.5	0.23	384	46	19	0	22	1	85.6
29	1.8	2.3	6042	301.1	1.2	0.0543	2.4	0.025	2.7	0.0033	1.2	0.44	384	54	21	1	25	1	85.7
30	bd	5.0	15598	360.8	0.9	0.0473	0.5	0.018	1.0	0.0028	0.9	0.87	62	12	18	0	18	0	98.2
31	2.4	2.5	7768	360.5	1.4	0.0470	0.6	0.018	1.5	0.0028	1.4	0.92	47	14	18	0	18	1	98.8
32	10.7	1.3	3816	343.6	1.7	0.0469	0.6	0.019	1.8	0.0029	1.7	0.95	42	14	19	1	19	1	99.1
33	bd	1.0	3177	358.9	1.4	0.0470	0.7	0.018	1.6	0.0028	1.4	0.89	51	18	18	1	18	1	98.7
Sample: 1215	**GPS: 27.747569 N, 89.290803 E**																		
1	bd	3.0	12981	472.2	0.8	0.0484	0.6	0.014	1.0	0.0021	0.8	0.82	120	14	14	0	14	0	95.7
2	6.5	3.0	11816	433.5	2.1	0.0782	9.5	0.025	9.7	0.0023	2.1	0.22	1151	188	15	1	25	5	59.6
5	2.6	2.6	10320	442.8	1.3	0.0493	1.2	0.015	1.7	0.0023	1.3	0.74	164	27	15	0	15	1	94.0
7	bd	2.7	11237	447.4	1.1	0.0482	0.8	0.015	1.3	0.0022	1.1	0.80	108	19	14	0	15	0	96.2
8	1.1	4.0	10501	280.1	1.2	0.0517	0.7	0.025	1.4	0.0036	1.2	0.86	273	16	23	1	26	1	90.0
9	bd	2.9	7575	280.4	1.0	0.0473	0.5	0.023	1.1	0.0036	1.0	0.87	63	13	23	0	23	1	98.4
14	0.2	1.3	5490	459.2	1.3	0.0471	0.8	0.014	1.5	0.0022	1.3	0.85	53	18	14	0	14	0	98.5
15	bd	0.9	3945	454.0	1.3	0.0532	3.6	0.016	3.8	0.0022	1.3	0.35	337	82	14	0	16	1	87.2
16	bd	1.8	7379	452.3	1.2	0.0472	0.6	0.014	1.3	0.0022	1.2	0.89	57	14	14	0	14	0	98.3
17	0.1	3.1	12725	447.8	1.6	0.0511	1.1	0.016	2.0	0.0022	1.6	0.82	246	26	14	0	16	1	90.7
18	1.9	5.8	23014	456.2	1.9	0.0540	4.5	0.016	4.9	0.0022	1.9	0.39	370	101	14	1	16	2	85.9
19	0.4	3.6	15316	465.2	2.0	0.0487	1.0	0.014	2.2	0.0021	2.0	0.90	134	22	14	1	15	1	95.1
20	bd	1.2	4352	377.3	3.0	0.0465	0.7	0.017	3.1	0.0027	3.0	0.97	21	16	17	1	17	1	99.9
21	bd	6.9	28078	440.2	1.2	0.0474	0.5	0.015	1.3	0.0023	1.2	0.92	70	12	15	0	15	0	97.8
22	bd	2.3	5804	281.3	2.9	0.0487	0.8	0.024	3.0	0.0036	2.9	0.97	135	18	23	1	24	1	95.5
23	bd	4.6	11568	275.6	1.2	0.0467	0.6	0.023	1.3	0.0036	1.2	0.90	36	14	23	1	23	1	99.5
24	0.9	2.5	10356	438.8	1.5	0.0618	6.2	0.019	6.3	0.0023	1.5	0.24	667	132	15	0	20	2	75.2
25	4.3	1.9	7299	432.4	1.3	0.0790	13.9	0.025	14.0	0.0023	1.3	0.09	1171	276	15	0	25	7	59.0
26	2.6	5.8	14766	269.3	1.4	0.0642	4.9	0.033	5.1	0.0037	1.4	0.28	748	102	24	1	33	3	72.8
27	bd	1.6	4546	335.5	0.6	0.0470	0.7	0.019	0.9	0.0030	0.6	0.65	50	16	19	0	19	0	98.8
29	bd	1.3	5270	455.3	1.2	0.0484	0.9	0.015	1.5	0.0022	1.2	0.79	116	21	14	0	15	0	95.9
30	bd	1.8	7666	462.5	0.9	0.0497	1.7	0.015	2.0	0.0022	0.9	0.47	179	40	14	0	15	1	93.4

Zircon rim U-Pb data

Analysis no.	f206c[1] %	^{206}Pb mV	Uppm[2]	Data for Tera-Wasserburg plot[3] ^{238}U/^{206}Pb	1σ %	^{207}Pb/^{206}Pb	1σ %	Data for Wetherill plot[3] ^{207}Pb/^{235}U	1σ %	^{206}Pb/^{238}U	1σ %	Rho	Ages (Ma)[3] ^{207}Pb/^{206}Pb	2σ abs	^{206}Pb/^{238}U	2σ abs	^{207}Pb/^{235}U	2σ abs	% conc[4]
Sample: 1247	**GPS: 27.666389 N, 89.265639 E**																		
1	0.1	15.0	42132	303.7	1.3	0.0475	0.5	0.022	1.3	0.0033	1.3	0.93	73	12	21	1	22	1	97.9
2	1.3	7.1	21274	327.4	1.0	0.0637	5.0	0.027	5.1	0.0031	1.0	0.19	733	107	20	0	27	3	73.1
3	bd	10.1	28644	308.2	1.1	0.0468	0.5	0.021	1.2	0.0032	1.1	0.91	39	12	21	0	21	1	99.3
4	1.4	5.5	15239	299.4	1.8	0.0477	0.8	0.022	1.9	0.0033	1.8	0.91	84	19	21	1	22	1	97.5
7	2.3	13.1	40327	331.6	1.6	0.0658	2.5	0.027	2.9	0.0030	1.6	0.54	799	52	19	1	27	2	70.9
8	1.5	5.0	13861	308.9	0.9	0.0524	1.7	0.023	1.9	0.0032	0.9	0.48	302	39	21	0	23	1	88.8
9	bd	3.8	10506	304.2	2.0	0.0480	0.6	0.022	2.0	0.0033	2.0	0.95	97	15	21	1	22	1	97.0
11	bd	9.0	25116	299.9	1.4	0.0468	0.5	0.022	1.4	0.0033	1.4	0.94	38	12	21	1	22	1	99.3
12	0.7	4.3	12056	303.2	0.7	0.0476	0.6	0.022	0.9	0.0033	0.7	0.79	80	13	21	0	22	0	97.6
13	bd	4.4	12231	304.5	0.7	0.0470	0.5	0.021	0.9	0.0033	0.7	0.81	50	13	21	0	21	0	98.8
14	bd	10.6	29837	305.6	1.1	0.0468	0.5	0.021	1.2	0.0033	1.1	0.92	40	11	21	0	21	1	99.3
15	bd	2.3	6130	293.9	4.1	0.0473	1.1	0.022	4.3	0.0034	4.1	0.96	66	27	22	2	22	2	98.2
19	1.3	5.3	14878	305.5	1.2	0.0471	0.5	0.021	1.3	0.0033	1.2	0.92	56	13	21	1	21	1	98.6
20	0.7	4.2	12213	314.0	1.2	0.0469	0.6	0.021	1.3	0.0032	1.2	0.90	43	14	20	0	21	1	99.1
21	bd	10.2	28626	304.0	1.3	0.0470	0.5	0.021	1.4	0.0033	1.3	0.94	49	12	21	1	21	1	98.9
22	0.2	9.3	25903	302.9	1.3	0.0527	2.7	0.024	3.0	0.0033	1.3	0.42	317	61	21	1	24	1	88.3
23	bd	7.0	20085	310.2	1.0	0.0471	0.5	0.021	1.2	0.0032	1.0	0.89	55	12	21	0	21	0	98.6
28	3.2	2.8	8260	317.8	0.6	0.0776	7.9	0.034	7.9	0.0031	0.6	0.08	1136	157	20	0	34	5	60.3
29	bd	9.1	25646	305.0	1.0	0.0491	1.2	0.022	1.6	0.0033	1.0	0.63	151	29	21	0	22	1	94.8
30	3.0	2.6	7987	334.0	4.4	0.0788	9.0	0.033	10.0	0.0030	4.4	0.44	1168	179	19	2	33	6	59.3
31	3.2	9.5	26404	304.0	0.9	0.0781	2.5	0.035	2.6	0.0033	0.9	0.34	1150	49	21	0	35	2	59.9
35	1.5	3.0	8644	314.1	1.2	0.0471	0.6	0.021	1.3	0.0032	1.2	0.90	52	13	20	0	21	1	98.8
36	2.5	3.1	8915	316.1	1.0	0.0483	1.1	0.021	1.5	0.0032	1.0	0.68	114	26	20	0	21	1	96.2
38	bd	8.3	25936	359.6	5.1	0.0471	0.5	0.018	5.1	0.0028	5.1	1.00	55	12	18	2	18	2	98.5
Sample: 1251	**GPS: 27.586353 N, 89.293903 E**																		
4	2.7	1.2	4404	446.9	1.7	0.0475	0.9	0.015	1.9	0.0022	1.7	0.88	72	21	14	0	15	1	97.7
8	3.2	1.5	5599	450.0	1.5	0.0463	0.7	0.014	1.6	0.0022	1.5	0.90	12	17	14	0	14	0	100.1
9	2.0	2.6	9284	450.2	2.4	0.0498	3.0	0.015	3.9	0.0022	2.4	0.63	187	70	14	1	15	1	93.0
11	6.4	1.2	4507	471.4	0.9	0.0471	0.6	0.014	1.1	0.0021	0.9	0.86	56	13	14	0	14	0	98.3
12	3.9	1.3	4769	464.6	1.2	0.0469	0.5	0.014	1.3	0.0022	1.2	0.94	43	11	14	0	14	0	98.8
17	bd	0.5	1656	424.3	1.5	0.0474	1.2	0.015	2.0	0.0024	1.5	0.78	67	29	15	0	15	1	97.9
21	bd	0.7	2687	469.4	1.4	0.0471	1.2	0.014	1.8	0.0021	1.4	0.75	52	28	14	0	14	0	98.5
23	bd	0.8	2933	442.7	1.5	0.0473	1.7	0.015	2.3	0.0023	1.5	0.68	66	39	15	0	15	1	97.9
25	0.3	1.8	6484	456.2	2.5	0.0477	0.8	0.014	2.6	0.0022	2.5	0.95	85	19	14	1	15	1	97.1
Sample: CWB16	**GPS: 28.094639 N, 89.741222 E**																		
5	bd	1.1	4930	510.2	3.4	0.0465	0.9	0.013	3.5	0.0020	3.4	0.97	22	21	13	1	13	1	99.7
7	bd	0.8	3582	556.9	1.1	0.0477	1.5	0.012	1.9	0.0018	1.1	0.60	84	35	12	0	12	0	97.1
11	8.8	0.4	1728	570.2	1.4	0.0468	1.9	0.011	2.3	0.0018	1.4	0.59	37	45	11	0	11	1	99.0
17	0.1	2.5	10876	541.5	1.7	0.0474	0.6	0.012	1.8	0.0018	1.7	0.94	67	14	12	0	12	0	97.8
19	5.6	2.0	7871	471.1	3.0	0.0488	0.4	0.014	3.0	0.0021	3.0	0.99	138	10	14	1	14	1	95.0
Sample: CWB23	**GPS: 28.037250 N, 89.793250 E**																		
1	bd	0.1	303	355.2	0.9	0.0504	5.4	0.020	5.4	0.0028	0.9	0.16	214	124	18	0	20	2	92.1
2	0.5	0.3	709	337.0	0.9	0.0491	2.0	0.020	2.2	0.0030	0.9	0.41	151	48	19	0	20	1	94.7
3	bd	0.9	2429	320.4	1.5	0.0473	1.0	0.020	1.8	0.0031	1.5	0.85	67	23	20	1	20	1	98.1
4	bd	0.4	1016	334.9	1.5	0.0469	1.6	0.019	2.2	0.0030	1.5	0.68	45	39	19	1	19	1	99.0
5	bd	0.9	2561	328.0	1.3	0.0474	0.9	0.020	1.6	0.0030	1.3	0.84	69	21	20	1	20	1	98.0
6	bd	0.9	2455	325.4	1.3	0.0463	0.9	0.020	1.6	0.0031	1.3	0.84	11	21	20	1	20	1	100.4
8	bd	0.6	1476	324.1	1.0	0.0467	1.1	0.020	1.5	0.0031	1.0	0.69	36	26	20	0	20	1	99.4
9	bd	0.5	1393	320.7	1.4	0.0457	1.3	0.020	1.9	0.0031	1.4	0.73	-20	32	20	1	20	1	101.7
10	bd	0.7	1814	321.6	1.3	0.0467	1.2	0.020	1.7	0.0031	1.3	0.72	31	29	20	1	20	1	99.6
13	3.4	0.9	2491	354.7	1.3	0.0472	0.8	0.018	1.5	0.0028	1.3	0.85	61	20	18	0	18	1	98.3
14	bd	0.5	1355	316.2	1.4	0.0486	1.3	0.021	1.9	0.0032	1.4	0.72	127	31	20	1	21	1	95.7

[1] Fraction of 206Pb that is common Pb
[2] Concentration uncertainty c.20%
[3] Data not corrected for common Pb
[4] Concordance calculated as (^{206}Pb-^{238}U age/^{207}Pb-^{235}U age)*100
Decay constants of Jaffey et al. 1971 used
bd = below detection; #N/A = not available

D.4.2. Zircon core U-Pb data

Zircon core U-Pb data

Analysis no.	f206c[1] %	^{206}Pb mV	Uppm[2]	Data for Tera-Wasserburg plot[3] ^{238}U/^{206}Pb	1s %	^{207}Pb/^{206}Pb	1s %	Data for Wetherill plot[3] ^{207}Pb/^{235}U	1s %	^{206}Pb/^{238}U	1s %	Rho	Ages (Ma)[3] ^{207}Pb/^{206}Pb	2s abs	^{206}Pb/^{238}U	2s abs	^{207}Pb/^{235}U	2s abs	% conc[4]
Sample: 1D01	**GPS: 27.879567 N, 89.727417 E**																		
1	0.3	4.6	2031	33.9	6.4	0.0559	0.38	0.228	6.5	0.0295	6.4	1.00	450	8	187	24	208	24	90.1
2	0.3	2.6	466	13.7	1.2	0.0578	0.31	0.582	1.3	0.0731	1.2	0.97	521	7	455	11	465	9	97.7
4	bd	9.4	3970	33.9	3.0	0.0561	0.21	0.228	3.0	0.0295	3.0	1.00	458	5	187	11	208	11	89.8
7	0.1	14.8	3907	20.4	2.9	0.0579	0.11	0.392	2.9	0.0491	2.9	1.00	527	2	309	17	336	16	92.0
8	bd	5.2	922	13.6	2.6	0.0572	0.17	0.581	2.6	0.0738	2.6	1.00	498	4	459	23	465	19	98.6
10	bd	21.8	4780	16.9	0.9	0.0584	0.10	0.477	0.9	0.0592	0.9	0.99	545	2	371	6	396	6	93.7
11	bd	2.5	551	16.8	2.0	0.0575	0.43	0.472	2.1	0.0595	2.0	0.98	512	10	373	15	392	14	95.0
20	0.4	4.2	1208	22.1	2.2	0.0575	0.30	0.359	2.3	0.0452	2.2	0.99	511	6	285	12	311	12	91.7
21	3.1	4.1	3260	61.3	3.8	0.0558	0.45	0.125	3.8	0.0163	3.8	0.99	444	10	104	8	120	9	86.9
28	bd	3.5	607	13.4	1.0	0.0577	0.24	0.593	1.1	0.0746	1.0	0.97	517	5	464	9	473	8	98.1
29	bd	5.8	999	13.2	0.9	0.0575	0.21	0.602	0.9	0.0759	0.9	0.98	512	5	472	8	478	7	98.6
32	bd	8.6	3374	30.4	1.2	0.0574	0.16	0.260	1.2	0.0329	1.2	0.99	507	3	209	5	235	5	88.8
33	0.2	7.3	1526	16.1	1.8	0.0574	0.17	0.492	1.8	0.0623	1.8	1.00	505	4	389	14	406	12	95.8
36	bd	6.3	1081	13.4	1.1	0.0577	0.21	0.593	1.1	0.0746	1.1	0.98	518	5	464	10	473	9	98.1
37	0.4	18.0	4136	17.9	1.0	0.0583	0.21	0.448	1.0	0.0557	1.0	0.98	541	5	350	6	376	6	93.1
Sample: 1G01	**GPS: 27.866500 N, 89.726450 E**																		
8	2.0	4.0	2252	66.0	2.1	0.0564	0.43	0.118	2.1	0.0151	2.1	0.98	468	9	97	4	113	5	85.7
9	bd	4.2	240	6.6	1.4	0.0730	0.64	1.530	1.5	0.1520	1.4	0.91	1015	13	912	23	942	18	96.8
27	4.1	2.2	1578	86.0	6.8	0.0560	1.34	0.090	6.9	0.0116	6.8	0.98	452	30	75	10	87	12	85.4
28	2.1	5.8	4419	91.0	2.2	0.0637	0.36	0.096	2.3	0.0110	2.2	0.99	731	8	70	3	93	4	75.4
Sample: 1G02	**GPS: 27.866500 N, 89.726450 E**																		
3	0.2	14.8	1171	6.1	1.0	0.0678	0.13	1.527	1.1	0.1634	1.0	0.99	862	3	976	19	941	13	103.7
4	bd	12.1	1303	8.2	1.7	0.0677	0.18	1.134	1.7	0.1215	1.7	0.99	860	4	739	23	770	18	96.1
5	bd	4.8	2838	44.0	4.9	0.0565	0.23	0.177	4.9	0.0227	4.9	1.00	472	5	145	14	166	15	87.6
7	0.0	20.5	2244	8.4	1.6	0.0682	0.15	1.123	1.6	0.1194	1.6	1.00	875	3	727	22	764	17	95.2
8	bd	11.9	1216	7.9	0.9	0.0674	0.13	1.180	0.9	0.1270	0.9	0.99	850	3	771	14	791	10	97.4
9	bd	14.1	1445	7.9	1.2	0.0680	0.12	1.183	1.2	0.1262	1.2	1.00	868	2	766	18	793	14	96.7
10	bd	6.0	601	7.7	1.0	0.0669	0.16	1.195	1.0	0.1296	1.0	0.99	836	3	786	15	798	11	98.4
11	bd	16.1	1720	8.2	1.0	0.0683	0.18	1.141	1.0	0.1213	1.0	0.98	877	4	738	14	773	11	95.5
12	0.9	11.1	1104	7.6	1.0	0.0677	0.18	1.222	1.0	0.1310	1.0	0.98	859	4	793	15	811	11	97.9
14	3.8	1.7	2480	110.6	2.7	0.0562	0.28	0.070	2.7	0.0090	2.7	0.99	462	6	58	3	69	4	84.4
15	0.9	4.8	1915	31.3	5.0	0.0633	0.30	0.279	5.0	0.0319	5.0	1.00	718	6	203	20	249	22	81.2
17	0.6	8.6	1030	9.5	2.0	0.0677	0.19	0.986	2.0	0.1056	2.0	1.00	860	4	647	25	697	20	92.9
19	bd	12.3	1818	11.2	3.5	0.0678	0.15	0.831	3.5	0.0889	3.5	1.00	863	3	549	37	614	32	89.4
22	0.2	7.1	1208	12.7	4.3	0.0671	0.19	0.726	4.3	0.0785	4.3	1.00	841	4	487	41	554	36	87.9
23	bd	21.2	2232	8.2	1.1	0.0681	0.14	1.141	1.1	0.1215	1.1	0.99	872	3	739	16	773	12	95.6
24	bd	0.9	41	3.3	0.8	0.1108	0.37	4.609	0.9	0.3019	0.8	0.91	1812	7	1701	24	1751	15	97.1
25	9.0	0.8	33	3.3	1.0	0.1111	0.47	4.689	1.1	0.3062	1.0	0.90	1818	8	1722	29	1765	18	97.5
26	bd	7.0	783	8.7	2.1	0.0654	0.29	1.037	2.1	0.1151	2.1	0.99	787	6	702	28	723	22	97.2
27	0.2	3.9	589	11.8	1.0	0.1102	0.42	1.289	1.1	0.0849	1.0	0.92	1803	8	525	10	841	12	62.4
34	0.3	22.7	2418	8.2	0.9	0.0684	0.08	1.147	0.9	0.1216	0.9	1.00	882	2	740	12	776	9	95.4
35	bd	19.8	2072	8.0	1.3	0.0682	0.10	1.172	1.3	0.1247	1.3	1.00	876	2	757	18	788	14	96.1
36	bd	6.8	1565	17.6	2.1	0.0571	0.16	0.447	2.1	0.0568	2.1	1.00	494	4	356	15	375	13	95.0
37	bd	27.4	3032	8.5	0.9	0.0692	0.22	1.117	0.9	0.1171	0.9	0.97	904	4	714	12	761	9	93.8
38	4.6	2.0	2623	104.2	5.8	0.0552	0.33	0.073	5.9	0.0096	5.8	1.00	420	7	62	7	72	8	86.1
42	0.6	7.2	7103	75.5	2.7	0.0645	0.14	0.118	2.7	0.0132	2.7	1.00	757	3	85	4	113	6	75.1
43	bd	14.3	1464	7.9	1.0	0.0677	0.08	1.175	1.0	0.1259	1.0	1.00	860	2	764	15	789	11	96.9
Sample: 1G03	**GPS: 27.866500 N, 89.726450 E**																		
6	0.4	5.5	659	13.2	0.9	0.0571	0.50	0.597	1.0	0.0759	0.9	0.88	494	11	472	8	475	8	99.2
8	bd	15.9	1319	8.9	3.6	0.0661	0.55	1.026	3.6	0.1126	3.6	0.99	809	12	688	47	717	37	96.0
15	bd	15.1	474	3.4	1.5	0.1101	0.46	4.400	1.5	0.2901	1.5	0.95	1800	8	1642	42	1712	25	95.9

Zircon core U-Pb data

Analysis no.	f206c[1] %	^{206}Pb mV	Uppm[2]	Data for Tera-Wasserburg plot[3] ^{238}U/^{206}Pb	1σ %	^{207}Pb/^{206}Pb	1σ %	Data for Wetherill plot[3] ^{207}Pb/^{235}U	1σ %	^{206}Pb/^{238}U	1σ %	Rho	Ages (Ma)[3] ^{207}Pb/^{206}Pb	2σ abs	^{206}Pb/^{238}U	2σ abs	^{207}Pb/^{235}U	2σ abs	% conc[4]
Sample: 3A03	**GPS: 27.261900 N, 90.037050 E**																		
2	bd	4.7	430	10.3	5.3	0.0703	0.53	0.942	5.3	0.0972	5.3	0.99	937	11	598	60	674	51	88.7
9	bd	6.0	776	14.7	3.1	0.0573	0.37	0.536	3.1	0.0679	3.1	0.99	504	8	423	26	436	22	97.1
18	0.4	17.6	1104	7.2	1.6	0.0727	0.40	1.390	1.7	0.1387	1.6	0.97	1006	8	837	26	885	20	94.6
29	bd	6.7	384	6.7	1.0	0.0717	0.36	1.467	1.1	0.1485	1.0	0.94	978	7	892	17	917	13	97.3
31	bd	4.3	2508	64.6	8.4	0.0551	0.54	0.118	8.4	0.0155	8.4	1.00	416	12	99	17	113	18	87.8
Sample: 1247	**GPS: 27.666389 N, 89.265639 E**																		
6	0.0	11.0	1347	13.2	1.5	0.0573	0.50	0.597	1.6	0.0756	1.5	0.95	503	11	470	14	475	12	98.9
10	0.2	9.1	2848	32.0	9.0	0.0562	0.51	0.242	9.0	0.0313	9.0	1.00	459	11	199	35	220	35	90.2
16	bd	9.4	1118	13.4	1.9	0.0573	0.50	0.588	2.0	0.0745	1.9	0.97	503	11	463	17	470	15	98.6
17	2.6	14.5	4596	31.2	10.6	0.1006	2.04	0.444	10.8	0.0320	10.6	0.98	1636	38	203	42	373	65	54.5
24	0.5	6.0	758	13.6	1.6	0.0570	0.53	0.578	1.7	0.0736	1.6	0.95	493	12	458	14	463	12	98.8
25	bd	5.2	1531	28.6	8.3	0.0567	0.51	0.273	8.3	0.0350	8.3	1.00	480	11	222	36	245	36	90.3
Sample: 1251	**GPS: 27.586353 N, 89.293903 E**																		
1	0.0	10.1	1053	13.1	1.0	0.0579	0.39	0.611	1.1	0.0766	1.0	0.94	527	8	476	10	484	9	98.2
2	bd	12.8	1611	15.4	3.2	0.0577	0.38	0.517	3.3	0.0650	3.2	0.99	517	8	406	25	423	22	96.0
3	0.0	34.7	4442	16.0	2.4	0.0586	0.31	0.505	2.4	0.0626	2.4	0.99	551	7	391	18	415	16	94.3
5	0.5	2.4	249	13.1	1.3	0.0576	0.41	0.606	1.4	0.0763	1.3	0.95	516	9	474	12	481	10	98.5
6	0.1	5.7	1218	25.7	5.4	0.0571	0.37	0.306	5.4	0.0389	5.4	1.00	495	8	246	26	271	25	90.8
10	0.6	11.9	1202	12.5	1.5	0.0577	0.32	0.633	1.5	0.0797	1.5	0.98	517	7	494	14	498	12	99.2
14	bd	28.5	1805	7.8	0.6	0.0685	0.36	1.207	0.7	0.1278	0.6	0.86	884	8	776	9	804	8	96.5
15	0.4	10.6	1178	13.5	1.1	0.0578	0.33	0.592	1.2	0.0743	1.1	0.96	522	7	462	10	472	9	97.9
16	0.5	21.1	3064	18.2	4.6	0.0582	0.35	0.441	4.6	0.0549	4.6	1.00	538	8	345	30	371	28	93.0
18	0.9	6.1	712	14.5	4.4	0.0591	1.30	0.560	4.6	0.0688	4.4	0.96	571	28	429	36	452	33	94.9
19	1.6	5.2	1689	40.1	2.6	0.0551	0.37	0.189	2.6	0.0249	2.6	0.99	416	8	159	8	176	8	90.2
20	bd	5.3	1401	32.4	1.5	0.0659	0.46	0.280	1.6	0.0308	1.5	0.96	804	10	196	6	251	7	78.0
22	bd	30.0	3391	14.1	1.5	0.0591	0.32	0.579	1.6	0.0711	1.5	0.98	569	7	443	13	464	12	95.5
24	bd	15.3	1634	13.4	0.7	0.0578	0.32	0.593	0.8	0.0745	0.7	0.91	522	7	463	6	473	6	97.9
Sample: CWB16	**GPS: 28.094639 N, 89.741222 E**																		
2	bd	6.3	661	12.9	1.3	0.0580	0.35	0.622	1.3	0.0778	1.3	0.96	531	8	483	12	491	10	98.3
4	bd	8.8	744	10.3	2.4	0.0632	0.82	0.848	2.5	0.0973	2.4	0.95	717	17	599	27	624	23	96.0
10	bd	3.7	1039	35.1	16.9	0.0561	1.28	0.220	16.9	0.0285	16.9	1.00	456	28	181	60	202	60	89.6
13	0.2	28.3	796	3.4	2.4	0.1159	0.31	4.684	2.4	0.2933	2.4	0.99	1894	6	1658	68	1764	39	94.0
14	1.3	4.5	1369	37.0	2.2	0.0920	1.10	0.343	2.4	0.0270	2.2	0.89	1467	21	172	7	299	13	57.5
16	0.6	19.5	2096	13.0	1.8	0.0583	0.37	0.619	1.9	0.0771	1.8	0.98	539	8	479	17	489	14	97.9

D.4.3. Zircon rim O, Hf data

Zircon rim O, Hf data

Analysis no.	$^{176}Hf/^{177}Hf$	2 s.e.	$^{176}Yb/^{177}Hf$	2 s.e.	$^{176}Lu/^{177}Hf$	2 s.e.	$^{176}Hf/^{177}Hf$ (20)	εHf (20)	2σ	2 stage T_{DM}	$^{18}O/^{16}O$	1 s.e.%	$\delta^{18}O$	2 s.d.
Sample: 1D01 GPS: 27.879567 N, 89.727417 E														
3	0.282523	0.000037	0.01304	0.00066	0.000342	0.000012	0.282523	-8.7	1.6	1448	0.0020214	0.0117	8.91	0.45
5	0.282485	0.000017	0.00866	0.00012	0.000156	0.000004	0.282485	-10.0	1.1	1523	0.0020211	0.0098	8.76	0.45
6	0.282472	0.000011	0.00366	0.00007	0.000062	0.000001	0.282472	-10.5	1.0	1549	0.0020196	0.0116	8.02	0.45
9	0.282452	0.000040	0.00536	0.00041	0.000118	0.000006	0.282452	-11.2	1.7	1588	0.0020211	0.0162	8.76	0.47
12	0.282434	0.000017	0.03460	0.00344	0.000798	0.000108	0.282434	-11.8	1.1	1624	0.0020211	0.0065	8.35	0.45
13	0.282476	0.000016	0.00569	0.00024	0.000102	0.000001	0.282476	-10.3	1.1	1541	0.0020217	0.0093	8.64	0.45
15	0.282438	0.000012	0.01257	0.00036	0.000288	0.000011	0.282438	-11.7	1.0	1616	0.0020209	0.0075	8.26	0.45
18	0.282450	0.000014	0.03264	0.00138	0.000695	0.000026	0.282450	-11.3	1.0	1592	0.0020218	0.0073	8.70	0.45
19	0.282435	0.000011	0.02110	0.00214	0.000437	0.000034	0.282435	-11.8	1.0	1622	0.0020210	0.0049	8.30	0.44
22	0.282465	0.000012	0.00525	0.00042	0.000093	0.000004	0.282465	-10.7	1.0	1562	0.0020213	0.0091	8.46	0.45
23	0.282475	0.000012	0.01149	0.00021	0.000194	0.000008	0.282475	-10.4	1.0	1543	0.0020217	0.0076	8.64	0.45
24	0.282468	0.000011	0.00511	0.00023	0.000089	0.000003	0.282468	-10.6	1.0	1556	0.0020218	0.0081	8.73	0.45
25	0.282417	0.000011	0.03221	0.00116	0.000733	0.000052	0.282417	-12.4	1.0	1657	0.0020189	0.0080	7.24	0.45
27	0.282485	0.000014	0.00581	0.00046	0.000101	0.000004	0.282485	-10.0	1.0	1523	0.0020205	0.0067	8.05	0.45
30	0.282474	0.000008	0.00898	0.00016	0.000170	0.000009	0.282474	-10.4	0.9	1545	0.0020219	0.0086	8.77	0.45
31	0.282466	0.000022	0.03587	0.00594	0.000782	0.000152	0.282466	-10.7	1.2	1561	0.0020205	0.0073	8.05	0.45
35	0.282471	0.000015	0.00823	0.00043	0.000165	0.000003	0.282471	-10.5	1.0	1551	0.0020213	0.0064	8.47	0.45
38	0.282459	0.000018	0.00847	0.00059	0.000183	0.000010	0.282459	-10.9	1.1	1574	0.0020221	0.0091	8.89	0.45
40	0.282468	0.000020	0.00430	0.00016	0.000075	0.000003	0.282468	-10.6	1.1	1556	0.0020216	0.0076	8.61	0.45
Sample: 1G01 GPS: 27.866500 N, 89.726450 E														
1	0.282330	0.000020	0.21093	0.00951	0.005460	0.000079	0.282328	-15.5	1.6	1832	0.0020226	0.0067	9.41	0.46
2	0.282303	0.000010	0.12433	0.00228	0.003355	0.000084	0.282302	-16.4	1.4	1883	0.0020239	0.0100	10.07	0.47
3	0.282338	0.000018	0.09365	0.00304	0.002624	0.000209	0.282337	-15.2	1.5	1814	0.0020224	0.0082	9.33	0.47
4	0.282291	0.000010	0.09281	0.00263	0.002341	0.000035	0.282290	-16.8	1.4	1906	0.0020225	0.0059	9.37	0.46
5	0.282290	0.000014	0.12249	0.00496	0.003066	0.000023	0.282289	-16.9	1.5	1909	0.0020225	0.0068	9.39	0.46
6	0.282270	0.000020	0.24705	0.00618	0.006259	0.000038	0.282268	-17.6	1.6	1950	0.0020237	0.0062	10.00	0.46
11	0.282263	0.000016	0.10379	0.00202	0.002843	0.000187	0.282262	-17.8	1.5	1961	0.0020219	0.0089	9.13	0.47
12	0.282261	0.000024	0.06586	0.00230	0.001813	0.000148	0.282260	-17.9	1.6	1965	0.0020215	0.0090	8.98	0.47
13	0.282290	0.000013	0.09263	0.00167	0.002826	0.000096	0.282289	-16.9	1.5	1908	0.0020228	0.0091	9.63	0.47
14	0.282295	0.000014	0.09232	0.00202	0.002474	0.000027	0.282294	-16.7	1.5	1898	0.0020238	0.0096	10.11	0.47
15	0.282291	0.000014	0.11239	0.00258	0.003002	0.000019	0.282290	-16.8	1.5	1907	0.0020241	0.0079	10.25	0.47
16	0.282284	0.000018	0.09873	0.00315	0.002978	0.000152	0.282283	-17.1	1.5	1920	0.0020239	0.0080	10.18	0.47
17	0.282268	0.000029	0.15243	0.00493	0.004249	0.000415	0.282266	-17.7	1.7	1953	0.0020217	0.0076	9.09	0.47
21	0.282186	0.000014	0.08214	0.00120	0.002223	0.000047	0.282185	-20.6	1.5	2111	0.0020231	0.0091	9.84	0.47
23	0.282259	0.000016	0.07311	0.00091	0.001902	0.000054	0.282258	-18.0	1.5	1969	0.0020215	0.0129	9.04	0.47
24	0.282260	0.000013	0.02762	0.00040	0.000736	0.000016	0.282260	-17.9	1.5	1966	0.0020236	0.0163	10.10	0.48
31	0.282172	0.000025	0.06214	0.00477	0.001976	0.000195	0.282171	-21.0	1.7	2139	0.0020216	0.0074	9.14	0.46
32	0.282295	0.000017	0.08396	0.00378	0.002609	0.000241	0.282294	-16.7	1.5	1899	0.0020217	0.0078	9.18	0.47
33	0.282280	0.000017	0.07528	0.00433	0.002289	0.000083	0.282279	-17.2	1.5	1928	0.0020243	0.0070	10.50	0.46
34	0.282285	0.000015	0.05307	0.00227	0.001681	0.000039	0.282284	-17.0	1.5	1917	0.0020242	0.0083	10.43	0.47
35	0.282307	0.000021	0.14998	0.00354	0.004454	0.000207	0.282305	-16.3	1.6	1876	0.0020222	0.0085	9.43	0.47
39	0.282211	0.000038	0.09486	0.00304	0.003361	0.000122	0.282210	-19.7	1.9	2063	0.0020219	0.0069	9.32	0.46
40	0.282293	0.000012	0.06014	0.00186	0.001766	0.000068	0.282292	-16.8	1.5	1902	0.0020228	0.0095	9.77	0.47
41	0.282271	0.000013	0.08388	0.00313	0.002127	0.000004	0.282270	-17.5	1.5	1945	0.0020238	0.0087	10.31	0.47
43	0.282266	0.000022	0.14893	0.00503	0.004919	0.000117	0.282264	-17.8	1.6	1957	0.0020235	0.0073	10.14	0.46
44	0.282301	0.000012	0.08609	0.00083	0.002389	0.000070	0.282300	-16.5	1.5	1887	0.0020240	0.0058	10.42	0.46
45	0.282275	0.000024	0.24746	0.01027	0.006350	0.000196	0.282273	-17.5	1.6	1940	0.0020238	0.0054	10.30	0.46
Sample: 1G02 GPS: 27.866500 N, 89.726450 E														
6	0.282276	0.000020	0.00495	0.00061	0.000115	0.000017	0.282276	-17.4	1.1	1934	0.0020167	0.0073	6.85	0.46
31	0.282115	0.000020	0.04840	0.00182	0.001226	0.000014	0.282115	-23.0	1.6	2249	0.0020223	0.0120	9.79	0.47
32	0.282202	0.000018	0.07486	0.00274	0.001980	0.000164	0.282201	-20.0	1.5	2080	0.0020170	0.0082	7.18	0.47
33	0.282181	0.000019	0.15232	0.00334	0.003873	0.000220	0.282180	-20.7	1.6	2122	0.0020196	0.0093	8.47	0.47
39	0.282253	0.000034	0.12412	0.00433	0.003530	0.000142	0.282252	-18.2	1.8	1981	0.0020189	0.0057	8.15	0.46
40	0.282394	0.000016	0.13864	0.00294	0.003792	0.000061	0.282393	-13.2	1.5	1705	0.0020168	0.0100	7.08	0.47
44	0.282290	0.000013	0.06702	0.00273	0.001695	0.000113	0.282289	-16.9	1.5	1908	0.0020187	0.0060	8.05	0.46
Sample: 1G03 GPS: 27.866500 N, 89.726450 E														
4	0.282180	0.000054	0.05729	0.00520	0.001925	0.000164	0.282179	-20.6	1.9	2123	0.0020140	0.0093	7.19	0.30
5	0.281923	0.000015	0.03855	0.00344	0.001261	0.000100	0.281923	-29.7	0.6	2622	0.0020153	0.0094	7.84	0.30
18	0.282320	0.000023	0.05072	0.00272	0.001501	0.000090	0.282319	-15.6	0.8	1849	0.0020158	0.0101	8.09	0.30
21	0.282335	0.000010	0.00479	0.00167	0.000163	0.000056	0.282335	-15.1	0.4	1818	0.0020149	0.0121	7.67	0.31
22	0.282130	0.000052	0.15943	0.01244	0.005064	0.000226	0.282128	-22.4	1.9	2223	0.0020153	0.0094	7.89	0.30
Sample: 3A02 GPS: 27.261900 N, 90.037050 E														
1	0.282387	0.000011	0.03477	0.00087	0.000832	0.000019	0.282387	-13.4	1.5	1717	0.0020226	0.0070	9.35	0.46
2	0.282357	0.000011	0.03782	0.00116	0.000912	0.000057	0.282357	-14.5	1.5	1776	0.0020220	0.0072	9.06	0.46
3	0.282376	0.000011	0.03509	0.00156	0.000922	0.000022	0.282376	-13.8	1.5	1738	0.0020232	0.0057	9.67	0.46
5	0.282369	0.000011	0.03867	0.00075	0.000963	0.000031	0.282369	-14.1	1.5	1752	0.0020207	0.0095	8.42	0.47
6	0.282367	0.000014	0.05740	0.00302	0.001285	0.000031	0.282367	-14.1	1.5	1756	0.0020224	0.0082	9.29	0.47
7	0.282375	0.000013	0.02818	0.00223	0.000680	0.000025	0.282375	-13.8	1.5	1740	0.0020220	0.0094	9.07	0.47
8	0.282381	0.000011	0.03639	0.00110	0.000853	0.000028	0.282381	-13.6	1.5	1728	0.0020210	0.0055	8.60	0.46
9	0.282368	0.000014	0.03629	0.00086	0.000897	0.000022	0.282368	-14.1	1.5	1754	0.0020201	0.0068	8.15	0.46

Zircon rim O, Hf data

Analysis no.	$^{176}Hf/^{177}Hf$	2 s.e.	$^{176}Yb/^{177}Hf$	2 s.e.	$^{176}Lu/^{177}Hf$	2 s.e.	$^{176}Hf/^{177}Hf$ (20)	εHf (20)	2σ	2 stage T_{DM}	$^{18}O/^{16}O$	1 s.e.%	$\delta^{18}O$	2 s.d.
Sample: 3A03 GPS: 27.261900 N, 90.037050 E														
1	0.282356	0.000015	0.07730	0.00870	0.001802	0.000136	0.282355	-14.5	1.5	1778	0.0020217	0.0078	9.86	0.49
5	0.282435	0.000014	0.02026	0.00261	0.000458	0.000073	0.282435	-11.7	1.5	1622	0.0020187	0.0082	8.42	0.49
7	0.282344	0.000012	0.07670	0.00441	0.001845	0.000066	0.282343	-15.0	1.5	1802	0.0020213	0.0090	9.68	0.49
8	0.282313	0.000020	0.16144	0.00765	0.003588	0.000123	0.282312	-16.1	1.6	1864	0.0020211	0.0076	9.61	0.49
12	0.282334	0.000015	0.06908	0.00233	0.001690	0.000037	0.282333	-15.2	0.5	1821	0.0020207	0.0065	9.42	0.49
14	0.282353	0.000012	0.04271	0.00204	0.001060	0.000038	0.282353	-14.5	0.4	1784	0.0020203	0.0104	9.21	0.50
17	0.282368	0.000029	0.06594	0.00359	0.001598	0.000100	0.282367	-14.0	1.0	1754	0.0020220	0.0106	10.06	0.50
22	0.282341	0.000013	0.05679	0.00062	0.001362	0.000021	0.282340	-15.0	0.5	1807	0.0020205	0.0126	9.35	0.50
25	0.282327	0.000013	0.07924	0.00317	0.001859	0.000054	0.282326	-15.5	0.5	1835	0.0020216	0.0110	9.91	0.50
28	0.282333	0.000012	0.06603	0.00220	0.001603	0.000036	0.282332	-15.3	0.4	1823	0.0020236	0.0082	10.90	0.49
33	0.282351	0.000020	0.12134	0.00365	0.002742	0.000081	0.282350	-14.6	0.7	1789	0.0020207	0.0100	9.48	0.49
34	0.282341	0.000034	0.12922	0.01154	0.003278	0.000404	0.282340	-15.0	1.2	1809	0.0020212	0.0115	9.72	0.50
37	0.282333	0.000021	0.07722	0.00436	0.002196	0.000163	0.282332	-15.3	0.7	1824	0.0020200	0.0111	9.16	0.50
40	0.282346	0.000023	0.11104	0.00993	0.002869	0.000188	0.282345	-14.8	0.8	1799	0.0020202	0.0087	9.27	0.49
Sample: 4D01 GPS: 27.493483 N, 90.031800 E														
1	0.282426	0.000012	0.06135	0.00156	0.001334	0.000019	0.282426	-12.1	1.5	1640	0.0020247	0.0069	10.19	0.45
2	0.282456	0.000077	0.06764	0.00320	0.002093	0.000100	0.282455	-11.0	3.1	1582	0.0020257	0.0056	10.67	0.45
3	0.282403	0.000015	0.03923	0.00358	0.000932	0.000081	0.282403	-12.9	1.5	1685	0.0020227	0.0054	9.18	0.45
4	0.282410	0.000017	0.05458	0.00180	0.001541	0.000117	0.282409	-12.6	1.5	1672	0.0020268	0.0063	11.20	0.45
5	0.282370	0.000019	0.09551	0.00594	0.002145	0.000150	0.282369	-14.0	1.6	1751	0.0020232	0.0067	9.41	0.45
6	0.282377	0.000018	0.09449	0.00395	0.002116	0.000042	0.282376	-13.8	1.5	1737	0.0020258	0.0109	10.71	0.45
7	0.282404	0.000009	0.03356	0.00166	0.000794	0.000024	0.282404	-12.8	1.4	1683	0.0020248	0.0081	10.24	0.45
8	0.282432	0.000012	0.03025	0.00112	0.000710	0.000017	0.282432	-11.8	1.5	1628	0.0020244	0.0078	10.01	0.45
9	0.282389	0.000012	0.05756	0.00334	0.001250	0.000037	0.282389	-13.4	1.5	1713	0.0020249	0.0073	10.29	0.45
10	0.282431	0.000011	0.03226	0.00183	0.000734	0.000024	0.282431	-11.9	1.5	1630	0.0020232	0.0093	9.43	0.45
11	0.282382	0.000013	0.07218	0.00247	0.001880	0.000141	0.282381	-13.6	1.5	1727	0.0020270	0.0086	11.31	0.45
12	0.282391	0.000018	0.04211	0.00169	0.001177	0.000110	0.282391	-13.3	1.5	1709	0.0020257	0.0089	10.69	0.45
14	0.282382	0.000018	0.04886	0.00064	0.001198	0.000024	0.282382	-13.6	1.5	1727	0.0020263	0.0070	10.96	0.45
15	0.282395	0.000015	0.06997	0.00392	0.001955	0.000209	0.282394	-13.2	1.5	1702	0.0020251	0.0073	10.35	0.45
16	0.282379	0.000012	0.06298	0.00195	0.001506	0.000051	0.282378	-13.7	1.5	1733	0.0020268	0.0078	11.20	0.45
17	0.282414	0.000013	0.02520	0.00115	0.000623	0.000016	0.282414	-12.5	1.5	1663	0.0020228	0.0095	9.22	0.45
18	0.282352	0.000013	0.05188	0.00166	0.001224	0.000020	0.282352	-14.7	1.5	1786	0.0020252	0.0069	10.44	0.45
19	0.282408	0.000012	0.02467	0.00101	0.000571	0.000013	0.282408	-12.7	1.5	1675	0.0020248	0.0085	10.21	0.45
20	0.282374	0.000011	0.07740	0.00191	0.001701	0.000008	0.282373	-13.9	1.5	1743	0.0020261	0.0091	10.88	0.45
21	0.282393	0.000013	0.06837	0.00374	0.001597	0.000062	0.282392	-13.2	1.5	1705	0.0020244	0.0074	10.02	0.45
22	0.282358	0.000014	0.11742	0.00514	0.002653	0.000066	0.282357	-14.5	1.5	1775	0.0020239	0.0099	9.80	0.45
24	0.282404	0.000009	0.03474	0.00047	0.000843	0.000011	0.282404	-12.8	1.4	1683	0.0020264	0.0108	11.01	0.45
25	0.282427	0.000017	0.03845	0.00104	0.000973	0.000048	0.282427	-12.0	1.5	1638	0.0020248	0.0079	10.21	0.46
27	0.282431	0.000009	0.03827	0.00137	0.000797	0.000022	0.282431	-11.9	1.4	1630	0.0020237	0.0074	9.68	0.45
29	0.282424	0.000010	0.02987	0.00052	0.000705	0.000034	0.282424	-12.1	1.4	1644	0.0020226	0.0069	9.16	0.45
30	0.282372	0.000017	0.09579	0.00208	0.002233	0.000067	0.282371	-14.0	1.5	1747	0.0020249	0.0118	10.28	0.45
31	0.282395	0.000013	0.05029	0.00040	0.001121	0.000025	0.282395	-13.1	1.5	1701	0.0020244	0.0095	10.02	0.45
32	0.282403	0.000016	0.03754	0.00356	0.000868	0.000066	0.282403	-12.9	1.5	1685	0.0020255	0.0106	10.59	0.45
33	0.282362	0.000014	0.04086	0.00179	0.001006	0.000027	0.282362	-14.3	1.5	1766	0.0020251	0.0090	10.41	0.45
Sample: 1215 GPS: 27.747569 N, 89.290803 E														
1	0.282461	0.000016	0.06232	0.00225	0.001531	0.000064	0.282460	-10.7	0.6	1571	0.0020211	0.0111	10.78	0.30
2	0.282473	0.000015	0.05239	0.00238	0.001570	0.000152	0.282472	-10.3	0.5	1548	0.0020194	0.0122	9.95	0.31
5	0.282465	0.000015	0.06528	0.00164	0.001573	0.000032	0.282464	-10.6	0.5	1563	0.0020223	0.0090	11.37	0.30
7	0.282446	0.000015	0.05694	0.00309	0.001611	0.000182	0.282445	-11.3	0.5	1601	0.0020213	0.0140	10.88	0.31
8	0.282463	0.000015	0.06687	0.00045	0.001624	0.000016	0.282462	-10.7	0.5	1567	0.0020215	0.0091	10.99	0.30
9	0.282441	0.000016	0.05189	0.00203	0.001316	0.000034	0.282441	-11.4	0.6	1611	0.0020209	0.0108	10.66	0.30
14	0.282441	0.000007	0.03548	0.00101	0.000893	0.000015	0.282441	-11.4	0.2	1610	0.0020222	0.0121	11.32	0.31
15	0.282448	0.000011	0.03800	0.00122	0.000990	0.000026	0.282448	-11.2	0.4	1597	0.0020214	0.0093	10.94	0.30
16	0.282451	0.000013	0.03885	0.00070	0.001066	0.000033	0.282451	-11.1	0.5	1591	0.0020218	0.0125	11.15	0.31
17	0.282460	0.000010	0.04369	0.00153	0.001135	0.000018	0.282460	-10.8	0.4	1573	0.0020213	0.0096	10.88	0.30
18	0.282460	0.000030	0.05434	0.00459	0.001681	0.000096	0.282459	-10.8	1.1	1573	0.0020191	0.0110	9.81	0.30
19	0.282456	0.000014	0.04746	0.00174	0.001234	0.000036	0.282456	-10.9	0.5	1581	0.0020189	0.0147	9.69	0.32
20	0.282466	0.000015	0.03725	0.00070	0.000867	0.000012	0.282466	-10.5	0.5	1561	0.0020208	0.0103	10.63	0.30
21	0.282460	0.000013	0.08957	0.00614	0.002231	0.000053	0.282459	-10.8	0.5	1574	0.0020181	0.0142	9.32	0.32
22	0.282478	0.000013	0.03856	0.00148	0.001043	0.000045	0.282478	-10.1	0.5	1537	0.0020196	0.0100	10.06	0.30
23	0.282471	0.000013	0.04721	0.00039	0.001144	0.000016	0.282471	-10.4	0.5	1551	0.0020189	0.0088	9.72	0.30
24	0.282448	0.000015	0.03902	0.00100	0.001002	0.000016	0.282448	-11.2	0.5	1597	0.0020205	0.0110	10.52	0.30
25	0.282457	0.000010	0.04233	0.00196	0.001080	0.000039	0.282457	-10.9	0.4	1579	0.0020183	0.0093	9.38	0.30
26	0.282479	0.000014	0.07575	0.00121	0.001689	0.000023	0.282478	-10.1	0.5	1536	0.0020201	0.0124	10.30	0.31
27	0.282459	0.000017	0.03877	0.00126	0.001032	0.000021	0.282459	-10.8	0.6	1575	0.0020207	0.0112	10.62	0.31
29	0.282457	0.000014	0.04259	0.00227	0.001102	0.000072	0.282457	-10.9	0.5	1579	0.0020206	0.0114	10.54	0.31
30	0.282466	0.000014	0.04236	0.00137	0.001095	0.000023	0.282466	-10.5	0.5	1561	0.0020180	0.0111	9.26	0.30

Zircon rim O, Hf data

Analysis no.	$^{176}Hf/^{177}Hf$	2 s.e.	$^{176}Yb/^{177}Hf$	2 s.e.	$^{176}Lu/^{177}Hf$	2 s.e.	$^{176}Hf/^{177}Hf$ (20)	εHf (20)	2σ	2 stage T_{DM}	$^{18}O/^{16}O$	1 s.e.%	$\delta^{18}O$	2 s.d.
Sample: 1247 GPS: 27.666389 N, 89.265639 E														
1	0.282399	0.000016	0.09091	0.00032	0.001931	0.000020	0.282398	-12.9	0.6	1694	0.0020191	0.0094	9.80	0.30
2	0.282372	0.000023	0.05098	0.00303	0.001562	0.000166	0.282371	-13.9	0.8	1747	0.0020187	0.0077	9.59	0.30
3	0.282403	0.000010	0.06242	0.00132	0.001411	0.000028	0.282402	-12.8	0.4	1685	0.0020193	0.0090	9.90	0.30
4	0.282397	0.000014	0.03053	0.00133	0.000724	0.000018	0.282397	-13.0	0.5	1697	0.0020201	0.0101	10.31	0.30
7	0.282390	0.000019	0.12755	0.00387	0.002649	0.000036	0.282389	-13.3	0.7	1712	0.0020176	0.0096	9.05	0.30
8	0.282389	0.000015	0.06649	0.00128	0.001479	0.000032	0.282388	-13.3	0.5	1713	0.0020200	0.0084	10.27	0.30
9	0.282276	0.000029	0.06413	0.00386	0.001389	0.000055	0.282275	-17.3	1.0	1935	0.0020199	0.0113	10.20	0.31
11	0.282401	0.000013	0.06841	0.00038	0.001664	0.000013	0.282400	-12.9	0.5	1690	0.0020187	0.0074	9.61	0.30
12	0.282399	0.000009	0.05323	0.00168	0.001276	0.000036	0.282399	-12.9	0.3	1693	0.0020188	0.0095	9.70	0.30
13	0.282412	0.000010	0.07025	0.00202	0.001715	0.000064	0.282411	-12.5	0.4	1668	0.0020207	0.0116	10.65	0.31
14	0.282420	0.000012	0.06773	0.00083	0.001552	0.000008	0.282419	-12.2	0.4	1652	0.0020195	0.0068	10.05	0.29
15	0.282461	0.000017	0.05844	0.00141	0.001547	0.000050	0.282460	-10.7	0.6	1571	0.0020204	0.0086	10.47	0.30
19	0.282350	0.000022	0.07379	0.00560	0.002286	0.000207	0.282349	-14.6	0.8	1790	0.0020218	0.0115	11.18	0.31
20	0.282229	0.000048	0.03661	0.00200	0.001177	0.000052	0.282229	-18.8	1.7	2027	0.0020195	0.0092	10.02	0.30
21	0.282373	0.000021	0.05536	0.00096	0.001597	0.000025	0.282372	-13.8	0.8	1745	0.0020204	0.0076	10.47	0.30
22	0.282383	0.000012	0.08094	0.00293	0.002289	0.000078	0.282382	-13.4	0.5	1725	0.0020201	0.0089	10.34	0.30
23	0.282405	0.000031	0.04827	0.00152	0.001550	0.000071	0.282404	-12.6	1.1	1682	0.0020192	0.0100	9.87	0.30
28	0.282393	0.000014	0.05141	0.00312	0.001562	0.000077	0.282392	-13.0	0.5	1705	0.0020192	0.0104	9.92	0.30
29	0.282298	0.000133	0.07387	0.00957	0.001691	0.000063	0.282297	-16.4	4.7	1892	0.0020195	0.0099	10.07	0.30
30	0.282412	0.000121	0.07543	0.00791	0.001965	0.000108	0.282411	-12.4	4.3	1668	0.0020189	0.0086	9.75	0.30
31	0.282376	0.000016	0.06580	0.00249	0.001910	0.000049	0.282375	-13.7	0.6	1739	0.0020205	0.0114	10.56	0.31
35	0.282394	0.000045	0.04916	0.00270	0.001516	0.000087	0.282393	-13.0	1.6	1703	0.0020211	0.0088	10.88	0.30
36	0.282367	0.000012	0.05243	0.00074	0.001510	0.000015	0.282366	-14.0	0.5	1756	0.0020212	0.0069	10.91	0.29
38	0.282411	0.000024	0.05196	0.00396	0.001575	0.000071	0.282410	-12.4	0.9	1670	0.0020218	0.0203	11.23	0.34
Sample: 1251 GPS: 27.586353 N, 89.293903 E														
4	0.282295	0.000034	0.11520	0.00670	0.003920	0.000280	0.282294	-16.5	1.2	1899	0.0020158	0.0090	8.12	0.34
8	0.282240	0.000036	0.09100	0.01300	0.003300	0.000430	0.282239	-18.5	1.3	2007	0.0020175	0.0069	8.98	0.34
9	0.282161	0.000018	0.11590	0.00270	0.004020	0.000076	0.282160	-21.3	0.6	2162	0.0020176	0.0096	9.03	0.34
11	0.282206	0.000016	0.12640	0.00380	0.004305	0.000088	0.282204	-19.7	0.6	2074	0.0020162	0.0089	8.36	0.34
12	0.282424	0.000030	0.04000	0.00760	0.001410	0.000240	0.282423	-11.9	1.1	1644	0.0020162	0.0070	8.38	0.34
17	0.282429	0.000017	0.02440	0.00130	0.000838	0.000041	0.282429	-13.9	0.6	1634	0.0020165	0.0104	8.52	0.35
21	0.282237	0.000014	0.07100	0.00900	0.002370	0.000190	0.282236	-21.8	0.7	2012	0.0020160	0.0104	8.28	0.35
23	0.282345	0.000016	0.05250	0.00600	0.001860	0.000210	0.282344	-11.2	0.5	1800	0.0020171	0.0077	8.85	0.34
25	0.282158	0.000013	0.10690	0.00200	0.003777	0.000050	0.282157	-14.3	0.6	2167	0.0020158	0.0092	8.22	0.34
Sample: CWB16 GPS: 28.094639 N, 89.741222 E														
5	0.282374	0.000014	0.05123	0.00275	0.001944	0.000094	0.282373	-13.7	0.5	1743	0.0020175	0.0095	9.09	0.28
7	0.282110	0.000018	0.16970	0.00928	0.005812	0.000351	0.282108	-23.1	0.7	2262	0.0020178	0.0110	9.27	0.28
11	0.282133	0.000015	0.10601	0.00746	0.003626	0.000297	0.282132	-22.3	0.6	2216	0.0020189	0.0117	9.82	0.29
17	0.282167	0.000016	0.13775	0.00869	0.004710	0.000275	0.282165	-21.1	0.6	2150	0.0020180	0.0085	9.40	0.28
19	0.282254	0.000032	0.12647	0.00701	0.004351	0.000231	0.282252	-18.0	1.2	1980	0.0020165	0.0110	8.64	0.28
Sample: CWB23 GPS: 28.037250 N, 89.793250 E														
1	0.282451	0.000014	0.00358	0.00029	0.000104	0.000011	0.282451	-11.0	0.5	1590	0.0020206	0.0116	10.72	0.28
2	0.282423	0.000014	0.01227	0.00022	0.000346	0.000009	0.282423	-12.0	0.5	1645	0.0020199	0.0142	10.36	0.29
3	0.282472	0.000016	0.00808	0.00108	0.000210	0.000032	0.282472	-10.2	0.6	1549	0.0020194	0.0100	10.12	0.28
4	0.282418	0.000015	0.01382	0.00024	0.000376	0.000006	0.282418	-12.1	0.6	1655	0.0020185	0.0095	9.63	0.28
5	0.282454	0.000016	0.00126	0.00005	0.000030	0.000001	0.282454	-10.9	0.6	1584	0.0020197	0.0064	10.28	0.27
6	0.282471	0.000018	0.00286	0.00050	0.000072	0.000012	0.282471	-10.3	0.7	1551	0.0020199	0.0102	10.37	0.28
8	0.282438	0.000017	0.00108	0.00002	0.000030	0.000000	0.282438	-11.4	0.6	1616	0.0020195	0.0085	10.16	0.28
9	0.282479	0.000012	0.00152	0.00012	0.000046	0.000003	0.282479	-10.0	0.5	1535	0.0020201	0.0139	10.48	0.29
10	0.282428	0.000013	0.00449	0.00013	0.000116	0.000004	0.282428	-11.8	0.5	1635	0.0020196	0.0112	10.20	0.28
13	0.282465	0.000012	0.00358	0.00027	0.000103	0.000009	0.282465	-10.5	0.4	1562	0.0020196	0.0073	10.21	0.27
14	0.282423	0.000024	0.00930	0.00140	0.000341	0.000058	0.282423	-12.0	0.8	1645	0.0020204	0.0112	10.61	0.28

D.4.4. Zircon core O, Hf data

Zircon core O, Hf data

Analysis no.	$^{176}Hf/^{177}Hf$	2 s.e.	$^{176}Yb/^{177}Hf$	2 s.e.	$^{176}Lu/^{177}Hf$	2 s.e.	$^{176}Hf/^{177}Hf$ (t)	eHf (t)	2s	2 stage T_{DM}	$^{18}O/^{16}O$	1 s.e.%	$d^{18}O$	2 s.d.
Sample: 1D01 GPS: 27.879567 N, 89.727417 E														
1	0.282413	0.000016	0.038946	0.003035	0.000886	0.000054	0.282410	-3.2	1.1	1665	0.00202068	0.0131	8.57	0.46
2	0.282347	0.000015	0.080327	0.004834	0.001712	0.000033	0.282335	-4.3	1.0	1795	0.00202318	0.0112	9.82	0.46
4	0.282411	0.000010	0.038117	0.002245	0.000957	0.000031	0.282407	-3.2	1.0	1669	0.00202043	0.0132	8.44	0.46
7	0.282456	0.000013	0.036834	0.001698	0.000841	0.000067	0.282452	0.0	1.0	1581	0.00202089	0.0119	8.67	0.46
8	0.282386	0.000011	0.043658	0.004519	0.001016	0.000068	0.282381	-3.2	1.0	1719	0.00202239	0.0143	9.42	0.46
10	0.282482	0.000014	0.036106	0.006195	0.000759	0.000114	0.282479	1.3	1.0	1529	0.00201989	0.0140	8.17	0.46
11	0.282386	0.000017	0.043745	0.002635	0.001086	0.000032	0.282380	-2.9	1.1	1719	0.00202342	0.0070	9.51	0.45
20	0.282358	0.000018	0.083128	0.009364	0.001759	0.000164	0.282346	-4.1	1.1	1774	0.00202244	0.0226	9.02	0.49
21	0.282419	0.000015	0.021292	0.000805	0.000474	0.000035	0.282419	-3.1	1.0	1654	0.00202058	0.0065	8.10	0.45
28	0.282331	0.000014	0.075923	0.002901	0.001623	0.000011	0.282320	-4.9	1.0	1827	0.00202410	0.0111	9.86	0.46
29	0.282428	0.000017	0.125351	0.001046	0.002814	0.000085	0.282406	-2.0	1.1	1636	0.00202141	0.0084	8.52	0.45
32	0.282415	0.000012	0.031124	0.001922	0.000668	0.000015	0.282413	-1.9	1.0	1636	0.00202299	0.0086	9.31	0.45
33	0.282430	0.000014	0.043304	0.001945	0.001027	0.000034	0.282425	-1.5	1.0	1632	0.00202179	0.0089	8.71	0.45
36	0.282388	0.000015	0.051234	0.001943	0.001112	0.000014	0.282382	-2.7	1.0	1715	0.00202250	0.0091	9.07	0.45
37	0.282384	0.000015	0.053144	0.001147	0.001183	0.000032	0.282377	-2.4	1.0	1722	0.00202297	0.0078	9.30	0.45
Sample: 1G01 GPS: 27.866500 N, 89.726450 E														
8	0.282324	0.000026	0.048823	0.000964	0.001623	0.000105	0.282317	-6.1	1.7	1836	0.00202202	0.0066	9.17	0.46
9	0.282314	0.000029	0.046352	0.002872	0.001246	0.000013	0.282297	5.5	1.7	1856	0.00201400	0.0064	5.17	0.46
27	0.282480	0.000025	0.093356	0.006442	0.002970	0.000124	0.282462	-1.4	1.7	1529	0.00201945	0.0094	8.04	0.47
28	0.282193	0.000021	0.083041	0.003384	0.002390	0.000238	0.282168	-5.5	1.6	2093	0.00202042	0.0059	8.52	0.46
Sample: 1G02 GPS: 27.866500 N, 89.726450 E														
3	0.281888	0.000016	0.035678	0.001083	0.000914	0.000041	0.281878	-12.8	1.1	2689	0.00201769	0.0071	7.31	0.46
4	0.281890	0.000020	0.047720	0.003240	0.001182	0.000032	0.281876	-13.0	1.1	2685	0.00201832	0.0113	7.63	0.47
5	0.282057	0.000015	0.038638	0.004621	0.001152	0.000060	0.282051	-15.5	1.0	2362	0.00201835	0.0068	7.65	0.46
7	0.281878	0.000018	0.090892	0.008012	0.002104	0.000109	0.281849	-13.6	1.1	2709	0.00201855	0.0098	7.76	0.47
8	0.282029	0.000020	0.032427	0.002028	0.000931	0.000029	0.282019	-8.1	1.1	2416	0.00201681	0.0088	6.89	0.47
9	0.282002	0.000017	0.046339	0.001759	0.001226	0.000078	0.281987	-8.8	1.1	2469	0.00201767	0.0101	7.33	0.47
10	0.281854	0.000015	0.031429	0.001216	0.000786	0.000037	0.281846	-14.6	1.0	2755	0.00201838	0.0071	7.69	0.46
11	0.282041	0.000022	0.055100	0.002253	0.001806	0.000162	0.282019	-7.5	1.6	2389	0.00201124	0.0084	4.13	0.47
12	0.281929	0.000018	0.032639	0.000728	0.000846	0.000024	0.281922	-11.4	1.5	2606	0.00201862	0.0091	7.82	0.47
14	0.282245	0.000011	0.046322	0.000850	0.001235	0.000014	0.282241	-9.0	1.5	1991	0.00201639	0.0071	6.71	0.46
15	0.282169	0.000016	0.044318	0.001273	0.001269	0.000056	0.282159	-6.1	1.5	2140	0.00201585	0.0092	6.45	0.47
17	0.281954	0.000018	0.050128	0.002617	0.001245	0.000069	0.281941	-10.7	1.5	2558	0.00201691	0.0083	7.01	0.47
19	0.281917	0.000012	0.051837	0.005662	0.001247	0.000096	0.281904	-11.9	1.5	2629	0.00201870	0.0101	7.92	0.47
22	0.281880	0.000021	0.055472	0.001396	0.001308	0.000031	0.281866	-13.7	1.6	2701	0.00201898	0.0069	8.07	0.46
23	0.281914	0.000022	0.098765	0.002510	0.002375	0.000059	0.281883	-12.4	1.6	2635	0.00201616	0.0081	6.67	0.47
24	0.281385	0.000018	0.016103	0.000577	0.000410	0.000003	0.281378	-9.0	1.5	3648	0.00201488	0.0105	6.04	0.47
25	0.281402	0.000021	0.016783	0.000970	0.000412	0.000010	0.281395	-8.2	1.6	3616	0.00201487	0.0091	6.04	0.47
26	0.281961	0.000023	0.050965	0.001151	0.001231	0.000020	0.281950	-12.0	1.6	2544	0.00201664	0.0073	6.92	0.46
27	0.281920	0.000039	0.096453	0.004688	0.002512	0.000284	0.281844	7.4	2.0	2624	0.00201764	0.0101	7.43	0.47
34	0.281958	0.000018	0.033187	0.000662	0.000923	0.000067	0.281949	-9.9	1.5	2550	0.00201706	0.0108	7.20	0.47
35	0.281909	0.000021	0.033832	0.001693	0.000843	0.000015	0.281902	-11.7	1.6	2645	0.00201807	0.0076	7.71	0.47
36	0.282368	0.000024	0.035074	0.004901	0.000972	0.000082	0.282366	-3.8	1.6	1750	0.00202006	0.0130	8.71	0.47
37	0.281917	0.000018	0.033465	0.001392	0.000870	0.000018	0.281909	-10.8	1.5	2629	0.00201712	0.0093	7.24	0.47
38	0.282246	0.000015	0.043747	0.000855	0.001230	0.000070	0.282243	-9.8	1.5	1989	0.00201819	0.0098	7.78	0.47
42	0.282073	0.000016	0.176588	0.003828	0.004298	0.000228	0.282021	-10.2	1.5	2327	0.00201809	0.0088	7.75	0.47
43	0.282004	0.000019	0.083165	0.002627	0.002050	0.000123	0.281978	-9.3	1.6	2461	0.00201854	0.0075	7.98	0.46
Sample: 1G03 GPS: 27.866500 N, 89.726450 E														
6	0.282330	0.000017	0.078950	0.002610	0.002634	0.000088	0.282316	-5.6	0.6	1815	0.00201702	0.0111	8.70	0.30
8	0.281909	0.000017	0.016877	0.000469	0.000638	0.000011	0.281910	-12.9	0.6	2635	0.00201342	0.0099	6.90	0.30
15	0.281620	0.000022	0.034946	0.003352	0.001131	0.000105	0.281591	-1.7	0.8	3191	0.00201550	0.0099	7.96	0.30

Zircon core O, Hf data

Analysis no.	$^{176}Hf/^{177}Hf$	2 s.e.	$^{176}Yb/^{177}Hf$	2 s.e.	$^{176}Lu/^{177}Hf$	2 s.e.	$^{176}Hf/^{177}Hf$ (20)	εHf (20)	2σ	2 stage T_{DM}	$^{18}O/^{16}O$	1 s.e.%	$\delta^{18}O$	2 s.d.
Sample: 3A03 GPS: 27.261900 N, 90.037050 E														
2	0.282152	0.000012	0.015790	0.000716	0.000381	0.000027	0.282152	-1.4	1.5	2173	0.00201899	0.0079	8.54	0.49
9	0.282441	0.000016	0.045183	0.003833	0.001129	0.000067	0.282437	-1.1	1.5	1606	0.00201701	0.0097	7.56	0.49
18	0.282320	0.000019	0.074693	0.002444	0.001840	0.000057	0.282294	5.1	0.7	1839	0.00202239	0.0110	10.27	0.50
29	0.282111	0.000017	0.030405	0.001895	0.000750	0.000038	0.282106	-2.2	0.6	2248	0.00201986	0.0099	9.05	0.49
31	0.282377	0.000017	0.076747	0.001986	0.001886	0.000067	0.282371	-5.4	0.6	1728	0.00201908	0.0124	8.67	0.50
Sample: 1247 GPS: 27.666389 N, 89.265639 E														
6	0.282433	0.000018	0.077361	0.005364	0.001835	0.000094	0.282424	-1.6	0.6	1617	0.00201889	0.0094	9.71	0.30
10	0.282359	0.000016	0.072619	0.001016	0.001770	0.000044	0.282352	-5.1	0.6	1763	0.00201855	0.0107	9.54	0.30
16	0.282284	0.000013	0.054335	0.002409	0.001788	0.000083	0.282277	-6.8	0.5	1905	0.00202019	0.0091	10.37	0.30
17	0.282063	0.000019	0.053215	0.001595	0.001748	0.000064	0.282017	9.7	0.7	2337	0.00201735	0.0113	8.95	0.31
24	0.282545	0.000055	0.049612	0.003765	0.001469	0.000056	0.282542	2.4	2.0	1391	0.00201426	0.0112	7.42	0.31
25	0.282397	0.000015	0.059406	0.003077	0.001962	0.000102	0.282390	-3.3	0.6	1683	0.00201436	0.0119	7.47	0.31
Sample: 1251 GPS: 27.586353 N, 89.293903 E														
1	0.282389	0.000020	0.043000	0.001200	0.001460	0.000020	0.282386	-2.4	0.7	1699	0.00201747	0.0097	8.96	0.34
2	0.282404	0.000017	0.063700	0.002200	0.002109	0.000053	0.282395	-2.3	0.6	1669	0.00201647	0.0084	8.46	0.34
3	0.282458	0.000016	0.055300	0.001000	0.001823	0.000039	0.282450	0.4	0.6	1563	0.00201654	0.0100	8.50	0.34
5	0.282421	0.000044	0.030400	0.004900	0.000980	0.000140	0.282423	-1.3	1.6	1636	0.00201761	0.0108	9.04	0.35
6	0.282313	0.000018	0.055100	0.003500	0.001980	0.000140	0.282306	-5.9	0.6	1848	0.00201625	0.0101	8.36	0.34
10	0.282330	0.000017	0.044100	0.002200	0.001503	0.000063	0.282327	-4.7	0.6	1815	0.00201535	0.0097	7.92	0.34
14	0.281901	0.000021	0.026300	0.001400	0.000878	0.000043	0.281897	-11.7	0.7	2651	0.00201643	0.0110	8.48	0.35
15	0.282730	0.000030	0.054300	0.004000	0.001786	0.000098	0.282724	9.5	1.1	1024	0.00201640	0.0089	8.47	0.34
16	0.282368	0.000016	0.073900	0.002300	0.002538	0.000051	0.282353	-3.3	0.6	1740	0.00201345	0.0091	7.00	0.34
18	0.282343	0.000030	0.046000	0.006700	0.001540	0.000230	0.282338	-3.1	1.1	1789	0.00201678	0.0092	8.66	0.34
19	0.282482	0.000018	0.012000	0.004100	0.000400	0.000140	0.282490	-1.2	0.6	1516	0.00201513	0.0112	7.84	0.35
20	0.282145	0.000021	0.098100	0.006700	0.003480	0.000250	0.282103	-6.2	0.7	2177	0.00201486	0.0076	7.71	0.34
22	0.282446	0.000014	0.068500	0.007600	0.002310	0.000220	0.282432	0.2	0.5	1587	0.00201590	0.0094	8.25	0.34
24	0.282358	0.000016	0.068400	0.006700	0.002190	0.000180	0.282348	-3.8	0.6	1760	0.00201674	0.0104	8.67	0.35
Sample: CWB16 GPS: 28.094639 N, 89.741222 E														
2	0.282328	0.000016	0.061255	0.002113	0.002022	0.000080	0.282318	-4.7	0.6	1819	0.00201881	0.0105	9.75	0.28
4	0.282214	0.000044	0.037680	0.001221	0.001380	0.000065	0.282206	-4.5	1.6	2042	0.00201922	0.0113	9.96	0.28
10	0.282376	0.000018	0.039864	0.001224	0.001517	0.000060	0.282374	-4.4	0.7	1725	0.00201567	0.0085	8.20	0.28
13	0.281512	0.000016	0.016390	0.000991	0.000567	0.000035	0.281502	-2.7	0.6	3397	0.00201395	0.0067	7.34	0.27
14	0.281694	0.000018	0.015957	0.001502	0.000415	0.000040	0.281693	-5.7	0.7	3049	0.00201270	0.0110	6.72	0.28
16	0.282326	0.000015	0.057775	0.001208	0.001796	0.000048	0.282318	-4.5	0.6	1823	0.00201850	0.0111	9.62	0.28

D.4.5. Zircon U-Pb 91500 standard data

							Data for Tera-Wasserberg plot				Data for Wetherill plot					Ages					
Analysis:	Date:	f206c	^{206}Pb mV	Uppm*	^{206}Pb/^{204}Pb	1σ %	^{238}U/^{206}Pb	1σ %	^{207}Pb/^{206}Pb	1σ %	^{207}Pb/^{235}U	1σ %	^{206}Pb/^{238}U	1σ %	Rho	^{207}Pb/^{206}Pb 2σ abs		^{206}Pb/^{238}U 2σ abs		^{207}Pb/^{235}U 2σ abs	
91500_01	21/2/15	0.6	1.1	76	2841	503	5.5	0.8	0.07535	0.28	1.874	0.9	0.1805	0.8	0.95	1078	6	1069	16	1072	11
91500_02	21/2/15	1.5	1.1	75	1146	186	5.5	0.8	0.07618	0.49	1.909	0.9	0.1818	0.8	0.85	1100	10	1077	16	1084	12
91500_03	21/2/15	6.0	1.1	76	280	39	5.5	0.8	0.07488	0.40	1.860	0.9	0.1803	0.8	0.90	1065	8	1068	16	1067	12
91500_04	21/2/15	-4.3	1.0	71	-395	87	5.5	0.9	0.07423	0.39	1.855	0.9	0.1813	0.9	0.91	1048	8	1074	17	1065	12
91500_05	21/2/15	-4.4	1.0	71	-389	80	5.5	0.7	0.07526	0.43	1.875	0.8	0.1807	0.7	0.86	1075	9	1071	14	1072	11
91500_06	21/2/15	3.1	1.1	79	543	100	5.5	0.7	0.07513	0.39	1.876	0.8	0.1811	0.7	0.88	1072	8	1073	14	1073	11
91500_07	21/2/15	-0.2	1.1	78	-10979	2836	5.5	0.8	0.07565	0.38	1.889	0.9	0.1812	0.8	0.90	1086	8	1074	16	1077	12
91500_08	21/2/15	-3.9	1.1	79	-434	98	5.5	0.8	0.07470	0.31	1.883	0.9	0.1829	0.8	0.93	1061	6	1083	16	1075	11
91500_09	21/2/15	-3.5	1.1	79	-484	81	5.5	0.8	0.07526	0.33	1.902	0.9	0.1833	0.8	0.92	1075	7	1085	16	1082	11
91500_10	21/2/15	-1.9	1.1	75	-884	182	5.5	0.7	0.07498	0.43	1.893	0.8	0.1832	0.7	0.85	1068	9	1084	14	1079	11
91500_11	21/2/15	5.8	1.0	74	294	45	5.5	0.6	0.07531	0.40	1.875	0.7	0.1807	0.6	0.82	1077	8	1071	11	1072	9
91500_12	21/2/15	6.3	1.1	78	267	33	5.6	0.7	0.07488	0.44	1.858	0.8	0.1800	0.7	0.83	1065	9	1067	13	1066	10
91500_13	21/2/15	1.5	1.1	80	1123	237	5.6	0.8	0.07512	0.31	1.860	0.8	0.1797	0.8	0.93	1072	6	1065	15	1067	11
91500_14	21/2/15	8.7	1.1	79	196	39	5.5	0.7	0.07496	0.39	1.876	0.8	0.1816	0.7	0.86	1067	8	1076	13	1073	10
91500_15	21/2/15	-0.7	1.1	81	-2410	312	5.5	0.8	0.07507	0.35	1.869	0.9	0.1807	0.8	0.92	1070	7	1071	16	1070	12
91500_16	21/2/15	4.4	1.1	76	386	73	5.5	1.1	0.07475	0.33	1.867	1.1	0.1812	1.1	0.95	1062	7	1073	21	1069	15
91500_17	21/2/15	-8.9	1.2	83	-191	36	5.5	0.8	0.07503	0.40	1.876	0.9	0.1814	0.8	0.88	1069	8	1074	15	1072	11
91500_18	21/2/15	0.3	1.2	83	5765	1226	5.5	0.8	0.07506	0.41	1.876	0.9	0.1814	0.8	0.89	1070	8	1075	16	1073	12
91500_19	21/2/15	-1.2	1.0	75	-1432	258	5.6	1.0	0.07453	0.36	1.850	1.1	0.1801	1.0	0.94	1056	7	1068	20	1063	14
91500_20	21/2/15	-6.2	1.2	83	-275	49	5.6	0.6	0.07459	0.47	1.835	0.8	0.1785	0.6	0.80	1057	9	1059	12	1058	10
91500_21	21/2/15	-1.0	1.2	83	-1676	248	5.5	0.7	0.07504	0.35	1.869	0.7	0.1807	0.7	0.89	1070	7	1071	13	1070	10
91500_22	21/2/15	-4.2	1.2	85	-399	74	5.5	0.6	0.07468	0.51	1.873	0.8	0.1820	0.6	0.77	1060	10	1078	12	1072	10
91500_23	21/2/15	-0.2	1.2	87	-7675	687	5.6	0.8	0.07489	0.31	1.831	0.8	0.1774	0.8	0.93	1066	6	1053	15	1057	11
91500_24	21/2/15	-2.8	1.2	89	-616	118	5.6	0.6	0.07498	0.37	1.846	0.7	0.1786	0.6	0.87	1068	8	1060	13	1062	10
91500_25	21/2/15	-0.9	1.2	88	-1917	368	5.5	0.9	0.07509	0.37	1.872	1.0	0.1809	0.9	0.92	1071	7	1072	18	1071	13
91500_26	21/2/15	0.0	1.1	80	157978	45956	5.7	0.9	0.07471	0.39	1.813	1.0	0.1761	0.9	0.91	1061	8	1046	17	1050	12
91500_27	21/2/15	2.4	1.1	77	700	94	5.6	0.6	0.07571	0.30	1.860	0.7	0.1783	0.6	0.90	1087	6	1058	12	1067	9
91500_28	21/2/15	2.3	1.1	78	743	141	5.7	0.6	0.07552	0.37	1.840	0.7	0.1768	0.6	0.86	1082	7	1050	12	1060	9
91500_29	21/2/15	3.4	1.1	79	499	124	5.7	0.8	0.07518	0.36	1.822	0.9	0.1759	0.8	0.91	1073	7	1044	15	1053	11
91500_30	21/2/15	0.1	1.2	84	11615	2052	5.7	0.6	0.07474	0.41	1.816	0.7	0.1763	0.6	0.83	1062	8	1046	12	1051	10
91500_31	21/2/15	-1.6	1.2	87	-1028	147	5.7	0.7	0.07533	0.38	1.833	0.8	0.1765	0.7	0.86	1077	8	1048	13	1057	10
91500_32	21/2/15	1.7	1.2	85	983	210	5.6	0.6	0.07460	0.46	1.842	0.8	0.1792	0.6	0.81	1058	9	1063	12	1061	10
91500_33	21/2/15	2.4	1.2	89	693	160	5.6	0.6	0.07543	0.41	1.857	0.7	0.1786	0.6	0.82	1080	8	1059	11	1066	9
91500_34	21/2/15	1.3	1.2	86	1342	212	5.6	0.6	0.07552	0.33	1.870	0.7	0.1796	0.6	0.88	1082	7	1065	12	1070	9
91500_35	21/2/15	0.2	1.1	78	7550	1313	5.7	0.7	0.07462	0.47	1.815	0.9	0.1765	0.7	0.84	1058	9	1048	14	1051	11
91500_36	21/2/15	1.9	1.1	78	893	168	5.6	1.0	0.07525	0.29	1.838	1.0	0.1772	1.0	0.96	1075	6	1052	19	1059	13
91500_37	21/2/15	-3.2	1.0	76	-535	71	5.7	1.0	0.07472	0.56	1.821	1.1	0.1768	1.0	0.87	1061	11	1049	19	1053	15
91500_38	21/2/15	-4.8	1.1	83	-354	49	5.7	0.8	0.07536	0.40	1.835	0.9	0.1767	0.8	0.90	1078	8	1049	16	1058	12
91500_39	21/2/15	3.9	1.2	88	432	73	5.7	0.7	0.07547	0.37	1.826	0.8	0.1756	0.7	0.87	1081	7	1043	13	1055	10
91500_40	21/2/15	4.2	1.2	88	408	69	5.7	0.7	0.07500	0.21	1.825	0.8	0.1766	0.7	0.96	1069	4	1048	14	1055	10
91500_41	21/2/15	5.3	1.1	82	321	60	5.7	0.5	0.07531	0.31	1.819	0.6	0.1753	0.5	0.86	1077	6	1041	10	1052	8
91500_42	21/2/15	10.4	1.1	78	162	36	5.7	0.7	0.07541	0.42	1.834	0.8	0.1764	0.7	0.84	1080	9	1047	13	1058	10
91500_43	21/2/15	-5.5	1.0	76	-310	74	5.6	0.6	0.07485	0.44	1.832	0.7	0.1776	0.6	0.81	1064	9	1054	12	1057	10
91500_44	21/2/15	-2.4	1.1	83	-696	114	5.7	0.8	0.07491	0.55	1.815	1.0	0.1758	0.8	0.83	1066	11	1044	16	1051	13
91500_45	21/2/15	3.8	1.1	83	444	47	5.7	0.8	0.07487	0.36	1.819	0.9	0.1762	0.8	0.91	1065	7	1046	15	1052	11
91500_46	21/2/15	3.5	1.1	83	489	88	5.6	0.8	0.07484	0.41	1.832	0.9	0.1776	0.8	0.88	1064	8	1054	15	1057	11
91500_47	21/2/15	6.2	1.1	86	273	71	5.7	0.6	0.07503	0.44	1.804	0.8	0.1745	0.6	0.81	1069	9	1037	12	1047	10
91500_48	21/2/15	6.4	1.2	85	264	36	5.7	0.7	0.07533	0.52	1.830	0.9	0.1763	0.7	0.81	1077	10	1046	14	1056	12
91500_49	21/2/15	0.4	1.2	87	3872	465	5.6	1.0	0.07457	0.42	1.826	1.1	0.1776	1.0	0.92	1057	8	1054	19	1055	14
91500_50	21/2/15	-5.5	1.1	84	-309	64	5.6	0.7	0.07514	0.52	1.835	0.9	0.1772	0.7	0.81	1072	10	1052	14	1058	12
91500_51	21/2/15	0.2	1.1	83	9489	1705	5.7	0.7	0.07537	0.48	1.829	0.8	0.1761	0.7	0.82	1078	10	1045	13	1056	11
91500_52	21/2/15	-1.6	1.1	81	-1069	242	5.7	0.7	0.07511	0.29	1.821	0.8	0.1759	0.7	0.93	1071	6	1044	14	1053	10

							Data for Tera-Wasserberg plot				Data for Wetherill plot					Ages					
Analysis:	Date:	f206c	^{206}Pb mV	Uppm*	^{206}Pb/^{204}Pb	1σ %	^{238}U/^{206}Pb	1σ %	^{207}Pb/^{206}Pb	1σ %	^{207}Pb/^{235}U	1σ %	^{206}Pb/^{238}U	1σ %	Rho	^{207}Pb/^{206}Pb 2σ abs		^{206}Pb/^{238}U 2σ abs		^{207}Pb/^{235}U 2σ abs	
91500_05	20/3/15	-2.9	1.2	59	-581	106	5.8	1.2	0.07490	0.38	1.795	1.3	0.1739	1.2	0.95	1066	8	1033	23	1044	17
91500_06	20/3/15	-1.3	1.4	69	-1305	201	5.7	1.2	0.07530	0.37	1.824	1.3	0.1757	1.2	0.96	1077	7	1044	23	1054	16
91500_07	20/3/15	-6.5	1.4	66	-260	41	5.6	1.0	0.07499	0.42	1.834	1.1	0.1774	1.0	0.92	1068	8	1053	19	1058	14
91500_08	20/3/15	-4.6	1.4	67	-368	62	5.6	0.9	0.07509	0.49	1.850	1.1	0.1788	0.9	0.88	1071	10	1060	18	1064	14
91500_09	20/3/15	9.8	1.5	74	173	23	5.7	1.2	0.07552	0.61	1.828	1.3	0.1756	1.2	0.88	1082	12	1043	22	1056	17
91500_10	20/3/15	10.2	1.6	77	166	41	5.7	1.1	0.07500	0.47	1.813	1.2	0.1754	1.1	0.92	1068	9	1042	21	1050	16
91500_11	20/3/15	2.9	1.7	82	580	58	5.6	1.0	0.07536	0.34	1.857	1.1	0.1788	1.0	0.95	1078	7	1060	20	1066	14
91500_12	20/3/15	0.2	1.6	78	9618	1389	5.7	0.9	0.07436	0.51	1.811	1.0	0.1767	0.9	0.87	1051	10	1049	17	1049	13
91500_13	20/3/15	-1.2	1.7	82	-1369	175	5.6	1.0	0.07533	0.55	1.841	1.1	0.1774	1.0	0.87	1077	11	1052	19	1060	15
91500_14	20/3/15	0.6	1.7	84	2766	497	5.7	1.1	0.07471	0.48	1.814	1.2	0.1762	1.1	0.92	1061	10	1046	21	1050	16
91500_15	20/3/15	-1.3	1.5	72	-1324	137	5.6	0.9	0.07479	0.51	1.836	1.1	0.1781	0.9	0.88	1063	10	1056	18	1058	14
91500_16	20/3/15	-1.4	1.6	77	-1217	165	5.6	1.0	0.07539	0.41	1.848	1.1	0.1779	1.0	0.92	1079	8	1055	19	1063	14
91500_17	20/3/15	-1.0	1.6	78	-1684	190	5.5	1.1	0.07591	0.48	1.891	1.2	0.1807	1.1	0.92	1093	10	1071	22	1078	16
91500_18	20/3/15	-2.4	1.6	78	-720	137	5.6	0.9	0.07510	0.46	1.847	1.0	0.1785	0.9	0.90	1071	9	1059	18	1062	14
91500_19	20/3/15	-1.6	1.7	84	-1085	261	5.6	1.0	0.07503	0.46	1.835	1.1	0.1775	1.0	0.91	1069	9	1053	19	1058	14
91500_20	20/3/15	0.7	1.8	86	2468	144	5.6	0.9	0.07454	0.49	1.834	1.1	0.1785	0.9	0.88	1056	10	1059	18	1058	14
91500_21	20/3/15	-0.6	1.7	80	-2698	302	5.6	1.1	0.07530	0.53	1.838	1.2	0.1771	1.1	0.90	1077	11	1051	21	1059	16
91500_22	20/3/15	-0.4	1.8	85	-4596	331	5.7	0.9	0.07535	0.38	1.835	1.0	0.1767	0.9	0.93	1078	8	1049	18	1058	13
91500_23	20/3/15	-2.8	1.8	86	-601	79	5.6	1.0	0.07457	0.57	1.830	1.1	0.1781	1.0	0.87	1057	11	1056	19	1056	15
91500_24	20/3/15	-5.8	1.3	65	-291	47	5.6	0.9	0.07528	0.59	1.840	1.1	0.1774	0.9	0.83	1076	12	1053	17	1060	14
91500_25	20/3/15	-9.5	1.5	70	-178	30	5.6	0.8	0.07484	0.42	1.839	0.9	0.1783	0.8	0.89	1064	8	1058	16	1059	12
91500_26	20/3/15	-2.3	1.5	74	-732	112	5.6	0.9	0.07495	0.54	1.833	1.0	0.1775	0.9	0.85	1067	11	1053	17	1057	14
91500_27	20/3/15	3.3	1.7	81	516	57	5.7	0.7	0.07554	0.46	1.837	0.9	0.1764	0.7	0.85	1083	9	1047	14	1059	11
91500_28	20/3/15	2.4	1.7	83	702	89	5.6	1.0	0.07475	0.42	1.826	1.1	0.1772	1.0	0.92	1062	8	1052	19	1055	14
91500_29	20/3/15	-0.2	1.8	86	-8572	1258	5.6	0.9	0.07474	0.50	1.839	1.0	0.1785	0.9	0.87	1062	10	1059	17	1060	13
91500_30	20/3/15	3.1	1.6	78	549	106	5.6	1.0	0.07466	0.56	1.826	1.1	0.1775	1.0	0.87	1059	11	1053	19	1055	15
91500_31	20/3/15	-1.5	1.7	82	-1149	179	5.7	1.0	0.07485	0.52	1.824	1.2	0.1768	1.0	0.89	1065	11	1050	20	1054	15
91500_32	20/3/15	-4.7	1.7	83	-359	59	5.6	1.1	0.07449	0.41	1.819	1.2	0.1772	1.1	0.94	1055	8	1051	21	1052	15
91500_33	20/3/15	-0.2	1.7	82	-7361	678	5.8	0.8	0.07543	0.44	1.807	0.9	0.1738	0.8	0.88	1080	9	1033	15	1048	12
91500_34	20/3/15	1.2	1.7	84	1440	345	5.6	0.9	0.07525	0.33	1.846	0.9	0.1780	0.9	0.94	1075	7	1056	17	1062	12
91500_35	20/3/15	1.6	1.8	87	1039	98	5.6	1.0	0.07568	0.44	1.864	1.1	0.1787	1.0	0.92	1087	9	1060	20	1068	15
91500_36	20/3/15	-3.1	1.4	69	-553	97	5.6	0.8	0.07475	0.48	1.825	0.9	0.1772	0.8	0.85	1062	10	1052	15	1055	12
91500_37	20/3/15	-4.4	1.5	74	-387	63	5.6	0.9	0.07513	0.54	1.836	1.1	0.1774	0.9	0.86	1072	11	1053	18	1059	14
91500_38	20/3/15	0.6	1.5	71	2641	525	5.6	1.0	0.07506	0.52	1.839	1.2	0.1778	1.0	0.89	1070	10	1055	20	1060	15
91500_39	20/3/15	2.4	1.6	76	693	96	5.6	0.9	0.07464	0.46	1.832	1.0	0.1781	0.9	0.90	1059	9	1057	18	1057	14
91500_40	20/3/15	9.2	1.6	76	185	51	5.6	0.7	0.07476	0.60	1.837	1.0	0.1783	0.7	0.77	1062	12	1058	14	1059	12
91500_41	20/3/15	-0.2	1.6	78	-9563	1268	5.5	0.8	0.07471	0.42	1.869	0.9	0.1815	0.8	0.88	1061	8	1075	15	1070	12
91500_42	20/3/15	-2.9	1.6	77	-590	92	5.7	1.0	0.07502	0.62	1.818	1.2	0.1758	1.0	0.86	1069	13	1044	20	1052	16
91500_43	20/3/15	-2.1	1.7	82	-816	98	5.7	1.0	0.07567	0.55	1.834	1.2	0.1758	1.0	0.88	1086	11	1044	20	1058	15
91500_44	20/3/15	-3.3	1.7	83	-507	55	5.6	0.9	0.07474	0.49	1.839	1.1	0.1785	0.9	0.88	1062	10	1059	18	1060	14
91500_45	20/3/15	-0.2	1.6	80	-8723	1251	5.7	1.0	0.07504	0.43	1.812	1.1	0.1753	1.0	0.92	1069	9	1041	19	1050	14
91500_46	20/3/15	-2.3	1.7	84	-732	98	5.7	0.9	0.07506	0.59	1.830	1.1	0.1769	0.9	0.85	1070	12	1050	18	1056	14
91500_47	20/3/15	-5.6	1.7	85	-300	38	5.7	1.0	0.07475	0.41	1.802	1.1	0.1749	1.0	0.92	1062	8	1039	19	1046	14
91500_48	20/3/15	-4.9	1.6	79	-343	40	5.7	0.9	0.07510	0.40	1.814	1.0	0.1753	0.9	0.92	1071	8	1041	18	1051	13
91500_49	20/3/15	-0.3	1.6	78	-5942	791	5.6	1.0	0.07452	0.48	1.838	1.1	0.1790	1.0	0.90	1055	10	1061	19	1059	14
91500_50	20/3/15	-1.4	1.7	82	-1242	135	5.6	0.9	0.07511	0.45	1.852	1.0	0.1789	0.9	0.89	1071	9	1061	17	1064	13
91500_51	20/3/15	3.2	1.7	83	535	59	5.7	0.6	0.07525	0.54	1.834	0.8	0.1768	0.6	0.75	1075	11	1050	12	1058	11
91500_52	20/3/15	2.1	1.8	86	811	98	5.6	0.8	0.07529	0.44	1.856	0.9	0.1789	0.8	0.87	1076	9	1061	15	1066	12

						Data for Tera-Wasserberg plot				Data for Wetherill plot					Ages					
Analysis: Date:	f206c	^{206}Pb mV	Uppm*	$^{206}Pb/^{204}Pb$	1σ%	$^{238}U/^{206}Pb$	1σ%	$^{207}Pb/^{206}Pb$	1σ%	$^{207}Pb/^{235}U$	1σ%	$^{206}Pb/^{238}U$	1σ%	Rho	$^{207}Pb/^{206}Pb$ 2σ abs		$^{206}Pb/^{238}U$ 2σ abs		$^{207}Pb/^{235}U$ 2σ abs	
91500_01 21/03/15	4.7	1.3	67	359	48	5.6	1.1	0.07511	0.33	1.842	1.1	0.1780	1.1	0.96	1071	7	1056	21	1061	15
91500_02 21/03/15	4.9	1.4	72	346	59	5.6	1.2	0.07479	0.38	1.840	1.2	0.1785	1.2	0.95	1063	8	1059	23	1060	16
91500_03 21/03/15	9.5	1.3	69	178	27	5.6	0.9	0.07560	0.54	1.871	1.1	0.1796	0.9	0.87	1085	11	1065	19	1071	14
91500_03 21/03/15	6.6	1.3	68	257	49	5.5	0.8	0.07538	0.78	1.882	1.1	0.1812	0.8	0.73	1079	16	1073	16	1075	15
91500_05 21/03/15	-2.9	1.4	74	-579	109	5.7	1.0	0.07544	0.43	1.834	1.1	0.1764	1.0	0.92	1080	9	1047	20	1058	14
91500_06 21/03/15	-3.5	1.5	80	-489	65	5.6	1.1	0.07513	0.36	1.842	1.2	0.1779	1.1	0.95	1072	7	1056	22	1061	15
91500_07 21/03/15	-1.1	1.6	85	-1589	168	5.6	0.9	0.07457	0.60	1.830	1.1	0.1781	0.9	0.83	1057	12	1057	17	1056	14
91500_08 21/03/15	-3.0	1.5	79	-560	93	5.7	0.9	0.07542	0.43	1.839	1.0	0.1769	0.9	0.91	1080	9	1050	18	1059	13
91500_09 21/03/15	1.7	1.6	84	986	123	5.5	0.8	0.07530	0.40	1.874	0.9	0.1805	0.8	0.89	1077	8	1070	15	1072	11
91500_10 21/03/15	-1.8	1.6	86	-959	119	5.6	0.9	0.07467	0.56	1.824	1.1	0.1772	0.9	0.85	1060	11	1052	17	1054	14
91500_11 21/03/15	1.8	1.5	76	926	138	5.6	1.0	0.07544	0.29	1.856	1.0	0.1785	1.0	0.96	1080	6	1059	19	1066	13
91500_12 21/03/15	1.7	1.6	82	1022	133	5.6	0.9	0.07553	0.35	1.853	1.0	0.1781	0.9	0.93	1083	7	1056	17	1065	13
91500_13 21/03/15	0.3	1.6	84	4862	335	5.6	0.7	0.07476	0.37	1.852	0.8	0.1797	0.7	0.89	1062	7	1065	14	1064	11
91500_14 21/03/15	-0.9	1.4	71	-1928	309	5.6	0.9	0.07428	0.44	1.822	1.0	0.1780	0.9	0.90	1049	9	1056	17	1053	13
91500_15 21/03/15	-3.3	1.5	78	-518	64	5.5	0.7	0.07468	0.50	1.870	0.9	0.1817	0.7	0.82	1060	10	1076	14	1071	12
91500_16 21/03/15	-3.3	1.5	78	-518	64	5.5	0.7	0.07468	0.50	1.870	0.9	0.1817	0.7	0.82	1060	10	1076	14	1071	12
91500_17 21/03/15	-2.7	1.4	73	-618	66	5.6	0.8	0.07508	0.34	1.851	0.9	0.1789	0.8	0.93	1071	7	1061	16	1064	12
91500_18 21/03/15	-1.8	1.5	76	-952	191	5.5	0.9	0.07481	0.65	1.865	1.1	0.1808	0.9	0.81	1063	13	1072	17	1069	14
91500_19 21/03/15	-2.2	1.5	78	-783	136	5.5	0.8	0.07466	0.28	1.869	0.8	0.1817	0.8	0.94	1059	6	1076	15	1070	11
91500_20 21/03/15	0.1	1.5	77	32658	4098	5.6	0.7	0.07546	0.26	1.863	0.7	0.1791	0.7	0.93	1081	5	1062	13	1068	9
91500_21 21/03/15	3.2	1.6	81	533	50	5.6	0.8	0.07499	0.44	1.861	0.9	0.1801	0.8	0.87	1068	9	1068	15	1068	12
91500_22 21/03/15	1.6	1.5	80	1036	145	5.5	0.7	0.07482	0.37	1.875	0.8	0.1818	0.7	0.87	1064	7	1077	13	1072	10
91500_23 21/03/15	2.0	1.5	77	847	107	5.6	0.7	0.07442	0.65	1.837	0.9	0.1791	0.7	0.72	1053	13	1062	13	1059	12
91500_24 21/03/15	-4.4	1.5	80	-386	78	5.6	0.7	0.07478	0.49	1.857	0.9	0.1801	0.7	0.83	1063	10	1068	14	1066	11
91500_25 21/03/15	0.7	1.6	82	2596	408	5.5	0.7	0.07445	0.48	1.862	0.9	0.1815	0.7	0.83	1054	10	1075	14	1068	11
91500_26 21/03/15	1.2	1.6	83	1415	181	5.7	1.0	0.07492	0.40	1.824	1.0	0.1766	1.0	0.92	1066	8	1049	19	1054	14
91500_27 21/03/15	3.5	1.7	88	483	80	5.6	0.9	0.07429	0.33	1.834	1.0	0.1792	0.9	0.94	1049	7	1062	17	1058	12
91500_28 21/03/15	3.8	1.7	90	452	34	5.6	0.9	0.07455	0.47	1.840	1.0	0.1790	0.9	0.89	1056	9	1062	17	1060	13
91500_29 21/03/15	-0.8	1.6	85	-2057	355	5.6	0.8	0.07483	0.53	1.844	0.9	0.1788	0.8	0.83	1064	11	1061	15	1061	12
91500_30 21/03/15	-0.7	1.7	89	-2553	511	5.6	0.7	0.07471	0.50	1.845	0.9	0.1792	0.7	0.82	1061	10	1063	14	1062	12
91500_31 21/03/15	-1.8	1.7	89	-917	124	5.5	0.7	0.07485	0.40	1.863	0.8	0.1806	0.7	0.87	1065	8	1070	14	1068	11
91500_32 21/03/15	1.4	1.6	83	1234	146	5.6	1.0	0.07529	0.44	1.839	1.1	0.1772	1.0	0.91	1076	9	1052	19	1059	14
91500_33 21/03/15	-0.8	1.7	87	-2042	304	5.6	0.8	0.07527	0.31	1.862	0.9	0.1795	0.8	0.94	1076	6	1064	16	1068	12
91500_34 21/03/15	-1.1	1.7	86	-1492	123	5.5	0.7	0.07480	0.28	1.876	0.8	0.1820	0.7	0.93	1063	6	1078	14	1073	10
91500_35 21/03/15	-0.9	1.6	83	-1844	133	5.7	1.1	0.07474	0.57	1.823	1.2	0.1770	1.1	0.88	1062	11	1051	21	1054	16
91500_36 21/03/15	-4.2	1.6	88	-404	53	5.7	1.0	0.07493	0.33	1.821	1.0	0.1764	1.0	0.95	1067	7	1047	19	1053	13
91500_37 21/03/15	-2.0	1.7	88	-842	93	5.6	0.8	0.07407	0.46	1.835	0.9	0.1798	0.8	0.86	1043	9	1066	15	1058	12
91500_38 21/03/15	-2.7	1.6	84	-620	79	5.6	0.8	0.07437	0.60	1.826	1.0	0.1781	0.8	0.82	1052	12	1057	16	1055	13
91500_39 21/03/15	-5.7	1.7	90	-297	32	5.6	0.8	0.07461	0.53	1.847	1.0	0.1796	0.8	0.84	1058	11	1065	16	1062	13
91500_40 21/03/15	0.6	1.7	90	2860	386	5.5	0.6	0.07463	0.25	1.863	0.7	0.1811	0.6	0.92	1059	5	1073	12	1068	9
91500_41 21/03/15	7.0	1.6	82	242	65	5.6	0.7	0.07519	0.53	1.836	0.9	0.1772	0.7	0.79	1074	11	1051	13	1058	11
91500_42 21/03/15	0.2	1.7	88	9037	1587	5.6	0.7	0.07465	0.52	1.838	0.9	0.1787	0.7	0.81	1059	10	1060	14	1059	12

						Data for Tera-Wasserberg plot				Data for Wetherill plot					Ages					
Analysis: Date:	f206c	^{206}Pb mV	Uppm*	$^{206}Pb/^{204}Pb$	1σ%	$^{238}U/^{206}Pb$	1σ%	$^{207}Pb/^{206}Pb$	1σ%	$^{207}Pb/^{235}U$	1σ%	$^{206}Pb/^{238}U$	1σ%	Rho	$^{207}Pb/^{206}Pb$ 2σ abs		$^{206}Pb/^{238}U$ 2σ abs		$^{207}Pb/^{235}U$ 2σ abs	
91500_01 03/04/15	2.5	2.2	98	683	39	5.6	1.6	0.07571	0.44	1.865	1.7	0.1788	1.6	0.97	1087	9	1060	32	1069	22
91500_02 03/04/15	-2.6	2.3	102	-651	53	5.6	1.8	0.07571	0.53	1.854	1.9	0.1777	1.8	0.96	1087	11	1054	35	1065	24
91500_03 03/04/15	-3.6	2.3	101	-475	52	5.5	1.2	0.07522	0.47	1.881	1.2	0.1815	1.2	0.93	1074	9	1075	23	1075	16
91500_04 03/04/15	-1.2	2.5	109	-1396	158	5.5	1.3	0.07538	0.58	1.879	1.4	0.1809	1.3	0.92	1079	12	1072	26	1074	19
91500_04 03/04/15	-1.3	2.4	105	-1310	154	5.5	1.2	0.07495	0.50	1.865	1.3	0.1806	1.2	0.93	1067	10	1070	24	1069	17
91500_06 03/04/15	-1.2	1.9	85	-1355	145	5.6	1.1	0.07568	0.62	1.860	1.2	0.1784	1.1	0.86	1087	12	1058	21	1067	16
91500_07 03/04/15	-1.4	2.1	91	-1250	160	5.6	0.9	0.07554	0.44	1.865	1.0	0.1791	0.9	0.90	1083	9	1062	17	1069	13
91500_08 03/04/15	-2.4	2.1	92	-702	63	5.5	1.1	0.07584	0.40	1.885	1.1	0.1804	1.1	0.94	1091	8	1069	21	1076	15
91500_09 03/04/15	-2.4	2.1	95	-714	78	5.6	1.1	0.07525	0.44	1.868	1.2	0.1801	1.1	0.93	1075	9	1068	22	1070	16
91500_10 03/04/15	-2.1	2.1	93	-795	87	5.5	0.9	0.07498	0.46	1.873	1.0	0.1812	0.9	0.90	1068	9	1074	19	1071	14
91500_11 03/04/15	-1.2	1.9	87	-1410	214	5.6	1.1	0.07444	0.42	1.848	1.1	0.1801	1.1	0.93	1053	8	1068	21	1063	15
91500_12 03/04/15	1.2	2.0	90	1442	97	5.5	1.1	0.07412	0.46	1.848	1.2	0.1809	1.1	0.92	1045	9	1072	22	1063	16
91500_13 03/04/15	3.3	2.0	90	512	43	5.5	1.0	0.07425	0.49	1.862	1.1	0.1820	1.0	0.90	1048	10	1078	20	1068	14
91500_14 03/04/15	2.2	2.0	92	763	55	5.6	1.1	0.07539	0.54	1.860	1.2	0.1790	1.1	0.89	1079	11	1061	21	1067	16
91500_15 03/04/15	1.5	2.0	91	1103	160	5.5	1.1	0.07496	0.53	1.864	1.2	0.1804	1.1	0.89	1068	11	1069	21	1068	15
91500_16 03/04/15	-0.5	2.1	91	-3514	580	5.5	0.9	0.07511	0.40	1.878	1.0	0.1814	0.9	0.92	1071	8	1075	19	1073	13
91500_17 03/04/15	-3.9	1.9	87	-439	85	5.6	1.1	0.07467	0.35	1.836	1.1	0.1784	1.1	0.95	1060	7	1058	21	1058	15
91500_18 03/04/15	-2.1	1.9	87	-822	72	5.5	1.1	0.07551	0.45	1.875	1.1	0.1802	1.1	0.92	1082	9	1068	21	1072	15
91500_19 03/04/15	1.4	1.9	86	1179	114	5.5	1.0	0.07490	0.50	1.862	1.1	0.1804	1.0	0.89	1066	10	1069	20	1068	15
91500_20 03/04/15	2.4	2.1	93	694	73	5.6	0.8	0.07516	0.40	1.854	0.9	0.1789	0.8	0.90	1073	8	1061	16	1065	12
91500_21 03/04/15	2.5	2.1	97	675	49	5.6	1.0	0.07531	0.44	1.868	1.1	0.1800	1.0	0.92	1077	9	1067	20	1070	14
91500_22 03/04/15	0.4	2.2	96	4144	626	5.5	0.9	0.07494	0.50	1.890	1.1	0.1829	0.9	0.88	1067	10	1083	19	1077	14
91500_23 03/04/15	-1.9	1.8	81	-897	118	5.6	0.8	0.07538	0.45	1.863	0.9	0.1793	0.8	0.88	1079	9	1063	16	1068	12
91500_24 03/04/15	-1.4	1.7	77	-1209	264	5.5	0.9	0.07501	0.44	1.871	1.0	0.1810	0.9	0.90	1069	9	1072	17	1071	13
91500_25 03/04/15	6.3	1.7	77	269	27	5.5	0.9	0.07514	0.61	1.872	1.1	0.1808	0.9	0.84	1072	12	1071	19	1071	15
91500_26 03/04/15	2.7	1.8	80	634	89	5.5	1.1	0.07500	0.53	1.866	1.2	0.1805	1.1	0.90	1069	11	1070	22	1069	16
91500_27 03/04/15	2.4	1.9	86	702	75	5.6	0.8	0.07461	0.50	1.850	1.0	0.1799	0.8	0.86	1058	10	1066	16	1063	13
91500_28 03/04/15	-1.0	1.7	78	-1629	78	5.5	0.8	0.07528	0.44	1.872	0.9	0.1804	0.8	0.88	1076	9	1069	16	1071	12
91500_29 03/04/15	-3.4	1.8	84	-494	30	5.6	0.9	0.07538	0.33	1.859	1.0	0.1789	0.9	0.94	1079	7	1061	17	1067	13
91500_30 03/04/15	-1.1	1.8	84	-1537	221	5.6	0.9	0.07524	0.39	1.857	1.0	0.1790	0.9	0.92	1075	8	1062	19	1066	13
91500_31 03/04/15	-5.2	1.9	84	-328	24	5.5	0.9	0.07477	0.49	1.863	1.0	0.1808	0.9	0.87	1062	10	1071	17	1068	13
91500_32 03/04/15	-1.4	1.7	80	-1237	101	5.6	1.1	0.07528	0.50	1.848	1.2	0.1781	1.1	0.91	1076	10	1057	22	1063	16
91500_33 03/04/15	-0.4	1.6	76	-4778	718	5.6	0.9	0.07531	0.44	1.863	1.0	0.1795	0.9	0.91	1077	9	1064	19	1068	14
91500_34 03/04/15	1.0	1.6	74	1645	268	5.5	1.1	0.07481	0.42	1.860	1.2	0.1804	1.1	0.94	1063	8	1069	22	1067	16

D.4.6. Zircon U-Pb Plešovice standard data

							Data for Tera-Wasserberg plot				Data for Wetherill plot					Ages					
Analysis:	Date:	f206c	^{206}Pb mV Uppm*		$^{206}Pb/^{204}Pb$	1σ%	$^{238}U/^{206}Pb$	1σ%	$^{207}Pb/^{206}Pb$	1σ%	$^{207}Pb/^{235}U$	1σ%	$^{206}Pb/^{238}U$	1σ%	Rho	$^{207}Pb/^{206}Pb$ 2σ abs		$^{206}Pb/^{238}U$ 2σ abs		$^{207}Pb/^{235}U$ 2σ abs	
Ples_01	21/02/15	4.4	1.6	395	410	28	18.7	1.0	0.05316	0.38	0.392	1.1	0.0535	1.0	0.94	336	9	336	7	336	6
Ples_02	21/02/15	-1.8	1.8	438	-1018	141	18.5	1.2	0.05335	0.39	0.398	1.3	0.0542	1.2	0.95	344	9	340	8	340	7
Ples_03	21/02/15	1.8	1.6	390	1019	137	18.3	1.1	0.05362	0.35	0.403	1.2	0.0545	1.1	0.95	355	8	342	7	344	7
Ples_04	21/02/15	1.4	2.2	511	1296	103	18.2	1.1	0.05369	0.26	0.408	1.1	0.0551	1.1	0.97	358	6	346	7	347	7
Ples_05	21/02/15	-0.3	4.1	975	-7154	382	18.3	1.0	0.05339	0.32	0.402	1.1	0.0546	1.0	0.95	345	7	343	7	343	6
Ples_06	21/02/15	-1.1	2.3	557	-1645	105	18.5	1.0	0.05336	0.24	0.397	1.0	0.0540	1.0	0.97	344	6	339	6	340	6
Ples_07	21/02/15	-1.0	2.6	627	-1876	156	18.4	0.8	0.05457	0.31	0.409	0.9	0.0544	0.8	0.93	395	7	342	5	348	5
Ples_08	21/02/15	1.0	3.2	765	1780	78	18.3	1.2	0.05333	0.30	0.402	1.3	0.0547	1.2	0.97	343	7	343	8	343	7
Ples_09	21/02/15	0.1	4.3	1008	22924	1088	18.1	1.1	0.05368	0.24	0.408	1.1	0.0551	1.1	0.98	358	5	346	7	347	6
Ples_10	21/02/15	-1.0	3.4	790	-1910	106	18.1	0.8	0.05321	0.28	0.404	0.9	0.0551	0.8	0.94	338	6	346	5	345	5
Ples_11	21/02/15	-0.6	2.4	576	-2989	233	18.6	1.1	0.05395	0.50	0.400	1.2	0.0537	1.1	0.91	369	11	337	7	341	7
Ples_12	21/02/15	0.2	2.5	582	8939	910	18.3	1.0	0.05353	0.28	0.404	1.0	0.0547	1.0	0.96	351	6	344	6	344	6
Ples_13	21/02/15	0.2	2.7	630	10510	804	18.2	0.9	0.05309	0.30	0.403	0.9	0.0551	0.9	0.95	333	7	346	6	344	5
Ples_14	21/02/15	0.3	2.8	671	6564	362	18.2	0.9	0.05324	0.26	0.402	1.0	0.0548	0.9	0.96	339	6	344	6	343	6
Ples_15	21/02/15	2.3	2.7	640	797	64	17.9	0.9	0.05350	0.30	0.412	0.9	0.0558	0.9	0.94	350	7	350	6	350	5
Ples_16	21/02/15	-1.5	2.8	663	-1178	73	18.2	0.9	0.05325	0.12	0.403	1.0	0.0549	0.9	0.99	340	3	345	6	344	6
Ples_17	21/02/15	0.1	3.9	934	15450	734	18.2	1.1	0.05579	0.29	0.423	1.2	0.0550	1.1	0.97	444	6	345	8	358	7
Ples_18	21/02/15	0.4	4.4	1035	4735	218	18.1	1.1	0.05346	0.24	0.408	1.1	0.0554	1.1	0.98	348	5	348	7	348	7
Ples_19	21/02/15	-0.2	4.4	1050	-8769	465	18.0	0.9	0.05339	0.24	0.409	0.9	0.0556	0.9	0.96	346	6	349	6	348	5
Ples_20	21/02/15	-3.0	1.9	448	-612	70	18.1	1.1	0.05305	0.51	0.404	1.2	0.0553	1.1	0.91	331	12	347	7	345	7
Ples_21	21/02/15	-4.1	1.5	351	-440	66	18.3	0.8	0.05380	0.37	0.406	0.9	0.0547	0.8	0.91	363	8	343	5	346	5
Ples_22	21/02/15	-0.1	2.0	472	-15267	1803	18.5	0.7	0.05367	0.24	0.401	0.8	0.0542	0.7	0.95	357	5	340	5	342	4
Ples_23	21/02/15	1.6	2.1	508	1146	184	18.4	0.6	0.05346	0.39	0.400	0.7	0.0543	0.6	0.84	348	9	341	4	342	4
Ples_24	21/02/15	-0.4	2.5	600	-4350	348	18.3	0.9	0.05345	0.26	0.402	0.9	0.0546	0.9	0.96	348	6	343	6	343	5
Ples_25	21/02/15	0.0	2.2	528	-55946	3521	18.4	1.1	0.05298	0.23	0.396	1.1	0.0543	1.1	0.98	328	5	341	7	339	6
Ples_26	21/02/15	3.7	2.5	624	486	42	18.8	1.6	0.05352	0.30	0.392	1.6	0.0532	1.6	0.98	351	7	334	10	336	9
Ples_27	21/02/15	4.3	2.3	559	426	37	18.5	1.0	0.05367	0.26	0.399	1.1	0.0539	1.0	0.97	357	6	339	7	341	6
Ples_29	21/02/15	-0.2	4.0	954	-8772	581	18.3	1.4	0.05348	0.34	0.402	1.4	0.0546	1.4	0.97	349	8	343	9	343	8
Ples_30	21/02/15	-0.1	5.2	1230	-12504	490	18.3	1.0	0.05411	0.28	0.409	1.0	0.0548	1.0	0.96	375	6	344	7	348	6
Ples_31	21/02/15	0.7	3.9	935	2660	148	18.3	1.0	0.05353	0.24	0.403	1.0	0.0547	1.0	0.97	351	5	343	7	344	6
Ples_32	21/02/15	0.0	4.7	1113	-91020	3351	18.4	0.8	0.05323	0.23	0.400	0.9	0.0545	0.8	0.97	339	5	342	6	341	5
Ples_33	21/02/15	1.1	4.6	1108	1615	87	18.4	0.9	0.05355	0.21	0.401	0.9	0.0544	0.9	0.98	352	5	341	6	343	5
Ples_34	21/02/15	3.0	4.4	1044	594	55	18.1	0.9	0.05538	0.36	0.422	1.0	0.0553	0.9	0.93	427	8	347	6	357	6
Ples_35	21/02/15	-0.8	1.9	452	-2234	183	18.8	0.8	0.05311	0.28	0.390	0.8	0.0533	0.8	0.94	334	6	335	5	335	5
Ples_36	21/02/15	2.0	2.1	503	927	84	18.6	1.1	0.05331	0.32	0.396	1.2	0.0539	1.1	0.96	342	7	338	7	339	7
Ples_37	21/02/15	-1.7	1.9	461	-1066	146	18.6	1.1	0.05370	0.34	0.399	1.1	0.0539	1.1	0.95	359	8	338	7	341	6
Ples_38	21/02/15	2.0	3.8	896	931	43	18.4	1.4	0.05347	0.28	0.400	1.5	0.0542	1.4	0.98	349	6	340	9	341	8
Ples_39	21/02/15	0.0	5.7	1372	89124	3182	18.7	0.7	0.05360	0.14	0.396	0.7	0.0536	0.7	0.98	354	3	336	4	338	4
Ples_41	21/02/15	1.8	1.9	465	1033	134	18.6	0.8	0.05358	0.24	0.396	0.9	0.0537	0.8	0.96	353	5	337	6	339	5
Ples_42	21/02/15	-2.3	2.1	505	-809	50	18.5	0.9	0.05290	0.34	0.393	1.0	0.0539	0.9	0.94	324	8	339	6	337	6
Ples_44	21/02/15	0.3	4.5	1078	7156	275	18.7	1.2	0.05324	0.34	0.392	1.3	0.0534	1.2	0.96	339	8	335	8	336	7
Ples_45	21/02/15	-0.6	4.7	1119	-2831	113	18.4	1.0	0.05368	0.19	0.401	1.1	0.0542	1.0	0.98	358	4	340	7	342	6
Ples_46	21/02/15	1.1	4.8	1161	1674	87	18.5	1.0	0.05346	0.21	0.397	1.0	0.0539	1.0	0.98	348	5	339	7	340	6
Ples_47	21/02/15	1.6	4.5	1095	1111	46	18.6	1.2	0.05311	0.17	0.394	1.2	0.0538	1.2	0.99	333	4	338	8	337	7
Ples_48	21/02/15	-1.5	4.6	1119	-1254	102	18.6	1.0	0.05309	0.21	0.393	1.1	0.0537	1.0	0.98	333	5	337	7	337	6
Ples_50	21/02/15	-1.6	3.0	743	-1169	72	19.0	1.0	0.05339	0.28	0.388	1.1	0.0527	1.0	0.96	345	6	331	7	333	6
Ples_51	21/02/15	-1.9	3.0	729	-946	64	19.1	0.9	0.05366	0.35	0.388	1.0	0.0525	0.9	0.93	357	8	330	6	333	6
Ples_52	21/02/15	-2.3	2.7	659	-800	83	18.7	0.9	0.05318	0.26	0.393	1.0	0.0536	0.9	0.96	337	6	336	6	336	5

							Data for Tera-Wasserberg plot				Data for Wetherill plot					Ages					
Analysis:	Date:	f206c	^{206}Pb mV Uppm*		$^{206}Pb/^{204}Pb$	1σ%	$^{238}U/^{206}Pb$	1σ%	$^{207}Pb/^{206}Pb$	1σ%	$^{207}Pb/^{235}U$	1σ%	$^{206}Pb/^{238}U$	1σ%	Rho	$^{207}Pb/^{206}Pb$ 2σ abs		$^{206}Pb/^{238}U$ 2σ abs		$^{207}Pb/^{235}U$	
Ples_05	20/03/15	-2.9	3.2	515	-625	48	18.6	0.9	0.05280	0.43	0.391	1.0	0.0537	0.9	0.91	320	10	337	6	335	
Ples_06	20/03/15	-2.0	3.2	513	-901	61	18.6	0.8	0.05319	0.41	0.395	0.9	0.0539	0.8	0.88	337	9	338	5	338	
Ples_07	20/03/15	-0.2	3.2	513	-7471	718	18.5	0.9	0.05312	0.57	0.396	1.1	0.0540	0.9	0.85	334	13	339	6	338	
Ples_08	20/03/15	-3.9	3.2	511	-470	39	18.6	0.8	0.05315	0.40	0.394	0.9	0.0538	0.8	0.90	335	9	338	5	337	
Ples_09	20/03/15	3.6	3.0	484	503	36	18.7	1.1	0.05319	0.45	0.393	1.2	0.0536	1.1	0.93	337	10	337	7	337	
Ples_10	20/03/15	3.3	3.2	517	558	40	18.6	1.0	0.05298	0.44	0.393	1.1	0.0538	1.0	0.92	328	10	338	7	337	
Ples_11	20/03/15	1.1	3.0	468	1600	133	18.6	1.0	0.05338	0.51	0.396	1.1	0.0539	1.0	0.89	345	12	338	7	339	
Ples_12	20/03/15	2.2	3.2	506	813	52	18.6	0.7	0.05323	0.45	0.394	0.8	0.0536	0.7	0.85	339	10	337	5	337	
Ples_13	20/03/15	-3.7	3.2	511	-488	45	18.7	0.7	0.05349	0.42	0.394	0.8	0.0535	0.7	0.85	350	10	336	5	338	
Ples_14	20/03/15	0.0	3.2	496	-41249	5458	18.5	0.6	0.05328	0.53	0.396	0.8	0.0540	0.6	0.75	341	12	339	4	339	
Ples_15	20/03/15	-0.5	3.2	514	-3646	192	18.6	0.7	0.05315	0.33	0.394	0.7	0.0538	0.7	0.90	335	8	338	4	337	
Ples_16	20/03/15	-1.5	3.4	541	-1185	136	18.6	0.7	0.05296	0.39	0.392	0.8	0.0537	0.7	0.88	327	9	337	5	336	
Ples_17	20/03/15	1.0	3.4	555	1829	123	18.8	0.7	0.05297	0.73	0.389	1.0	0.0533	0.7	0.71	328	16	335	5	334	
Ples_18	20/03/15	-0.4	3.4	554	-4861	351	18.8	0.7	0.05304	0.38	0.389	0.8	0.0532	0.7	0.89	331	9	334	5	334	
Ples_19	20/03/15	-0.8	3.5	562	-2203	116	18.6	0.8	0.05339	0.52	0.396	0.9	0.0539	0.8	0.82	346	12	338	5	339	
Ples_20	20/03/15	0.8	3.5	549	2174	80	18.4	0.8	0.05327	0.54	0.399	1.0	0.0544	0.8	0.82	340	12	342	5	341	
Ples_21	20/03/15	-2.1	3.2	519	-867	79	18.8	0.9	0.05321	0.45	0.391	1.0	0.0533	0.9	0.90	338	10	335	6	335	
Ples_22	20/03/15	-1.6	3.6	572	-1129	78	18.6	0.8	0.05305	0.51	0.394	0.9	0.0539	0.8	0.84	331	12	338	5	337	
Ples_23	20/03/15	-0.1	4.5	713	-17010	637	18.5	0.7	0.05318	0.48	0.396	0.9	0.0540	0.7	0.84	337	11	339	5	339	
Ples_24	20/03/15	-0.9	4.2	676	-2076	122	18.7	0.8	0.05307	0.41	0.391	0.9	0.0535	0.8	0.90	332	9	336	6	335	
Ples_25	20/03/15	-2.8	3.6	586	-640	19	18.8	0.8	0.05271	0.45	0.386	1.0	0.0532	0.8	0.88	316	10	334	5	332	
Ples_26	20/03/15	-3.8	4.4	700	-475	27	18.4	0.7	0.05310	0.50	0.397	0.8	0.0543	0.7	0.80	333	11	341	4	340	
Ples_27	20/03/15	0.3	3.3	527	6863	455	18.8	0.7	0.05336	0.59	0.392	0.9	0.0533	0.7	0.75	344	13	334	4	336	
Ples_28	20/03/15	0.2	3.3	535	10117	750	18.6	0.8	0.05340	0.47	0.395	0.9	0.0536	0.8	0.86	346	11	337	5	338	
Ples_29	20/03/15	3.4	3.3	528	538	45	18.6	0.7	0.05333	0.51	0.396	0.9	0.0539	0.7	0.81	343	12	338	5	339	
Ples_30	20/03/15	-2.8	3.3	523	-652	81	18.7	0.7	0.05309	0.44	0.392	0.9	0.0536	0.7	0.86	333	10	336	5	336	
Ples_31	20/03/15	-2.3	3.2	509	-802	55	18.8	0.8	0.05330	0.50	0.392	1.0	0.0533	0.8	0.86	342	11	335	5	336	
Ples_32	20/03/15	1.2	3.0	496	1570	137	18.7	0.8	0.05325	0.45	0.392	0.9	0.0534	0.8	0.87	340	10	336	5	336	
Ples_33	20/03/15	0.0	4.5	735	149600	10208	18.8	1.2	0.05303	0.36	0.389	1.3	0.0532	1.2	0.96	330	8	334	8	334	
Ples_34	20/03/15	-0.6	5.1	823	-3236	156	18.6	1.1	0.05323	0.35	0.394	1.2	0.0537	1.1	0.96	339	8	337	7	337	
Ples_35	20/03/15	0.1	5.0	789	22849	1213	18.5	1.1	0.05321	0.48	0.396	1.2	0.0540	1.1	0.91	338	11	339	7	339	
Ples_36	20/03/15	-1.6	3.9	630	-1113	58	19.0	1.1	0.05291	0.41	0.383	1.2	0.0525	1.1	0.94	325	9	330	7	329	
Ples_37	20/03/15	-0.8	4.3	692	-2160	93	18.6	1.1	0.05314	0.40	0.394	1.1	0.0538	1.1	0.94	335	9	338	7	337	
Ples_38	20/03/15	-2.5	4.2	664	-734	46	18.7	0.9	0.05287	0.37	0.389	1.0	0.0533	0.9	0.93	323	8	335	6	333	
Ples_39	20/03/15	0.2	3.7	589	8242	520	18.7	1.1	0.05347	0.39	0.393	1.1	0.0534	1.1	0.94	349	9	335	7	337	
Ples_40	20/03/15	-1.6	3.5	563	-1160	49	18.7	1.1	0.05297	0.50	0.391	1.2	0.0535	1.1	0.91	328	11	336	7	335	
Ples_41	20/03/15	-3.9	3.9	622	-461	49	18.5	0.8	0.05324	0.44	0.396	0.9	0.0540	0.8	0.88	339	10	339	5	339	
Ples_42	20/03/15	0.1	4.3	686	28626	1450	18.7	1.0	0.05374	0.37	0.397	1.1	0.0535	1.0	0.93	360	8	336	6	339	
Ples_43	20/03/15	-0.2	4.9	785	-8834	304	18.5	0.9	0.05294	0.38	0.395	0.9	0.0542	0.9	0.92	326	9	340	6	338	
Ples_44	20/03/15	-2.2	4.4	708	-817	65	18.5	0.9	0.05300	0.38	0.395	0.9	0.0541	0.9	0.92	329	9	340	6	338	
Ples_45	20/03/15	0.5	4.4	708	3893	165	18.8	1.2	0.05299	0.50	0.388	1.3	0.0531	1.2	0.92	328	11	334	8	333	
Ples_46	20/03/15	0.4	4.5	726	4622	207	18.8	1.0	0.05315	0.41	0.389	1.0	0.0531	1.0	0.92	335	9	333	6	334	
Ples_47	20/03/15	-0.7	4.4	709	-2767	175	18.8	1.0	0.05292	0.41	0.389	1.1	0.0533	1.0	0.92	325	9	335	6	334	
Ples_48	20/03/15	-1.3	2.9	481	-1374	64	19.1	1.2	0.05302	0.48	0.383	1.3	0.0524	1.2	0.93	330	11	329	8	329	
Ples_49	20/03/15	1.3	3.2	519	1424	89	18.8	1.0	0.05291	0.47	0.388	1.1	0.0532	1.0	0.90	325	11	334	6	333	
Ples_50	20/03/15	-0.2	3.2	505	-8441	656	18.5	0.9	0.05308	0.43	0.396	1.0	0.0542	0.9	0.90	332	10	340	6	339	
Ples_51	20/03/15	-0.6	3.5	568	-3277	173	18.8	1.2	0.05317	0.40	0.390	1.2	0.0532	1.2	0.95	336	9	334	8	334	
Ples_52	20/03/15	-0.8	3.2	515	-2326	89	18.7	1.0	0.05330	0.48	0.393	1.1	0.0535	1.0	0.90	342	11	336	7	337	

							Data for Tera-Wasserberg plot				Data for Wetherill plot					Ages					
Analysis:	Date:	f206c	^{206}Pb mV	Uppm*	$^{206}Pb/^{204}Pb$	1σ %	$^{238}U/^{206}Pb$	1σ %	$^{207}Pb/^{206}Pb$	1σ %	$^{207}Pb/^{235}U$	1σ %	$^{206}Pb/^{238}U$	1σ %	Rho	$^{207}Pb/^{206}Pb$ 2σ abs		$^{206}Pb/^{238}U$ 2σ abs		$^{207}Pb/^{235}U$ 2σ abs	
Ples_01	21/03/15	0.8	4.2	724	2411	125	18.4	1.3	0.05330	0.26	0.400	1.4	0.0545	1.3	0.98	342	6	342	9	342	8
Ples_02	21/03/15	1.2	4.3	739	1507	60	18.3	1.2	0.05304	0.26	0.400	1.2	0.0547	1.2	0.98	330	6	343	8	342	7
Ples_03	21/03/15	0.0	4.0	692	-57196	4181	18.3	1.1	0.05343	0.27	0.402	1.1	0.0546	1.1	0.97	347	6	343	7	343	7
Ples_04	21/03/15	2.7	3.6	610	677	41	18.2	1.1	0.05309	0.30	0.402	1.2	0.0549	1.1	0.97	333	7	345	8	343	7
Ples_05	21/03/15	0.8	3.2	556	2419	116	18.2	1.4	0.05329	0.35	0.403	1.4	0.0548	1.4	0.97	341	8	344	9	343	8
Ples_06	21/03/15	-1.9	3.9	655	-983	43	18.1	1.2	0.05296	0.35	0.404	1.2	0.0554	1.2	0.96	327	8	348	8	345	7
Ples_07	21/03/15	-1.3	3.3	561	-1434	81	18.2	1.0	0.05320	0.30	0.404	1.0	0.0551	1.0	0.95	337	7	346	6	344	6
Ples_08	21/03/15	0.0	3.8	647	137672	7374	18.3	1.0	0.05334	0.32	0.402	1.1	0.0546	1.0	0.95	343	7	343	7	343	6
Ples_09	21/03/15	-0.1	4.3	736	-23246	1079	18.1	0.9	0.05288	0.34	0.403	1.0	0.0553	0.9	0.94	324	8	347	6	344	6
Ples_10	21/03/15	0.0	4.1	688	36628	1384	18.1	0.8	0.05294	0.29	0.404	0.9	0.0553	0.8	0.94	326	7	347	6	344	5
Ples_11	21/03/15	-0.6	4.1	696	-3245	232	18.0	1.0	0.05382	0.32	0.413	1.0	0.0557	1.0	0.95	363	7	349	6	351	6
Ples_12	21/03/15	-1.2	3.6	608	-1569	57	18.1	1.0	0.05326	0.27	0.405	1.0	0.0552	1.0	0.97	340	6	347	7	346	6
Ples_13	21/03/15	-1.2	3.9	676	-1468	81	18.3	0.9	0.05335	0.51	0.403	1.1	0.0548	0.9	0.88	344	12	344	6	344	6
Ples_14	21/03/15	-0.8	4.7	807	-2196	79	18.1	1.1	0.05684	0.46	0.432	1.2	0.0551	1.1	0.92	485	10	346	7	364	7
Ples_15	21/03/15	-2.7	4.8	812	-681	29	18.1	0.9	0.05309	0.21	0.405	0.9	0.0554	0.9	0.97	333	5	348	6	345	5
Ples_16	21/03/15	-1.3	4.5	765	-1351	74	18.1	0.9	0.05299	0.30	0.403	1.0	0.0552	0.9	0.95	329	7	347	6	344	6
Ples_17	21/03/15	-1.0	3.3	576	-1758	139	18.3	1.2	0.05328	0.32	0.401	1.3	0.0546	1.2	0.97	341	7	343	8	342	7
Ples_18	21/03/15	2.7	2.9	491	684	59	18.2	1.2	0.05318	0.32	0.402	1.2	0.0548	1.2	0.97	337	7	344	8	343	7
Ples_19	21/03/15	2.1	3.2	545	853	66	18.0	0.8	0.05314	0.37	0.406	0.9	0.0554	0.8	0.91	335	8	348	6	346	5
Ples_20	21/03/15	-1.1	4.8	816	-1649	86	18.2	0.8	0.05311	0.30	0.401	0.9	0.0548	0.8	0.94	334	7	344	5	343	5
Ples_21	21/03/15	-1.8	4.8	802	-1030	47	18.0	0.8	0.05255	0.34	0.403	0.9	0.0557	0.8	0.93	310	8	349	6	344	5
Ples_22	21/03/15	-0.1	4.4	749	-13271	464	18.0	0.9	0.05296	0.35	0.406	0.9	0.0556	0.9	0.93	327	8	349	6	346	5
Ples_23	21/03/15	-0.1	4.4	755	-23997	1173	18.1	1.2	0.05305	0.32	0.403	1.2	0.0551	1.2	0.97	331	7	346	8	344	7
Ples_24	21/03/15	0.2	3.4	587	9573	738	18.3	1.2	0.05296	0.34	0.399	1.2	0.0547	1.2	0.96	327	8	343	8	341	7
Ples_25	21/03/15	0.5	3.8	638	3887	285	17.9	1.1	0.05300	0.29	0.409	1.1	0.0560	1.1	0.97	329	7	351	7	348	7
Ples_26	21/03/15	0.9	2.6	443	2136	142	18.4	1.2	0.05286	0.30	0.396	1.3	0.0544	1.2	0.97	323	7	341	8	339	7
Ples_27	21/03/15	2.1	2.8	483	875	53	18.2	0.9	0.05322	0.34	0.403	1.0	0.0549	0.9	0.94	338	8	345	6	344	6
Ples_28	21/03/15	0.5	3.1	530	3494	243	18.1	0.9	0.05275	0.36	0.402	1.0	0.0553	0.9	0.94	318	8	347	6	343	6
Ples_29	21/03/15	-1.3	3.8	650	-1377	90	18.3	1.1	0.05318	0.29	0.401	1.2	0.0547	1.1	0.97	337	6	343	8	342	7
Ples_30	21/03/15	-1.6	4.0	681	-1104	95	18.2	0.9	0.05303	0.30	0.401	0.9	0.0549	0.9	0.95	330	7	344	6	342	5
Ples_31	21/03/15	0.3	4.2	722	6727	270	18.2	0.9	0.05275	0.36	0.400	1.0	0.0551	0.9	0.93	318	8	346	6	342	6
Ples_32	21/03/15	-0.8	4.7	806	-2278	187	18.1	0.9	0.05293	0.27	0.402	1.0	0.0551	0.9	0.96	326	6	346	6	343	6
Ples_33	21/03/15	0.4	4.5	761	4200	141	18.1	0.9	0.05312	0.27	0.405	1.0	0.0554	0.9	0.96	334	6	347	6	346	6
Ples_34	21/03/15	0.8	4.4	747	2148	107	18.3	0.8	0.05346	0.39	0.404	0.9	0.0548	0.8	0.89	348	9	344	5	344	5
Ples_35	21/03/15	-2.5	4.2	714	-742	41	18.1	0.9	0.05276	0.36	0.401	1.0	0.0552	0.9	0.93	319	8	346	6	342	6
Ples_36	21/03/15	-0.3	4.4	742	-6340	315	18.1	1.0	0.05293	0.35	0.403	1.0	0.0553	1.0	0.94	326	8	347	6	344	6
Ples_37	21/03/15	1.4	4.0	691	1321	61	18.3	0.9	0.05289	0.29	0.399	0.9	0.0548	0.9	0.95	324	7	344	6	341	5
Ples_38	21/03/15	1.0	4.1	688	1835	133	18.0	0.9	0.05274	0.30	0.404	1.0	0.0556	0.9	0.95	317	7	349	6	344	6
Ples_39	21/03/15	-2.3	3.7	627	-776	55	18.0	0.9	0.05366	0.30	0.410	0.9	0.0554	0.9	0.95	357	7	348	6	349	5
Ples_40	21/03/15	0.6	3.4	579	2982	162	18.1	0.9	0.05286	0.27	0.403	0.9	0.0554	0.9	0.95	323	6	347	6	344	5
Ples_41	21/03/15	0.8	4.5	772	2408	91	18.2	0.9	0.05275	0.27	0.400	0.9	0.0550	0.9	0.96	318	6	345	6	342	5
Ples_42	21/03/15	1.1	4.7	805	1651	81	18.1	0.9	0.05281	0.39	0.402	1.0	0.0552	0.9	0.92	320	9	346	6	343	6

							Data for Tera-Wasserberg plot				Data for Wetherill plot					Ages					
Analysis:	Date:	f206c	^{206}Pb mV	Uppm*	$^{206}Pb/^{204}Pb$	1σ %	$^{238}U/^{206}Pb$	1σ %	$^{207}Pb/^{206}Pb$	1σ %	$^{207}Pb/^{235}U$	1σ %	$^{206}Pb/^{238}U$	1σ %	Rho	$^{207}Pb/^{206}Pb$ 2σ abs		$^{206}Pb/^{238}U$ 2σ abs		$^{207}Pb/^{235}U$ 2σ abs	
Ples_01	03/04/15	-0.7	4.5	673	-2777	173	18.8	0.9	0.05336	0.49	0.392	1.1	0.0532	0.9	0.88	344	11	334	6	336	6
Ples_02	03/04/15	-0.2	4.5	687	-9304	477	18.7	1.1	0.05324	0.38	0.392	1.2	0.0534	1.1	0.95	339	8	335	7	336	7
Ples_03	03/04/15	-0.8	4.6	687	-2417	130	18.7	0.5	0.05315	0.38	0.393	0.7	0.0536	0.5	0.82	335	9	336	4	336	4
Ples_04	03/04/15	-1.7	4.7	693	-1080	57	18.7	0.8	0.05312	0.41	0.392	0.9	0.0535	0.8	0.88	334	9	336	5	336	5
Ples_06	03/04/15	-0.4	4.3	635	-4116	208	18.5	0.8	0.05325	0.40	0.397	0.9	0.0540	0.8	0.90	339	9	339	6	339	5
Ples_07	03/04/15	-0.2	4.2	618	-11944	528	18.3	0.9	0.05323	0.42	0.400	1.0	0.0546	0.9	0.90	339	10	343	6	342	6
Ples_08	03/04/15	-0.4	4.0	592	-5118	274	18.2	1.2	0.05286	0.37	0.401	1.2	0.0551	1.2	0.96	323	8	346	8	342	7
Ples_09	03/04/15	-1.8	4.0	581	-1022	48	18.3	1.1	0.05316	0.51	0.401	1.2	0.0547	1.1	0.91	336	12	344	8	342	7
Ples_10	03/04/15	-0.6	4.3	636	-3040	176	18.5	0.9	0.05328	0.41	0.396	1.0	0.0540	0.9	0.90	341	9	339	6	339	6
Ples_11	03/04/15	0.1	4.0	598	21885	1513	18.4	0.9	0.05315	0.42	0.398	1.0	0.0543	0.9	0.90	335	10	341	6	340	6
Ples_12	03/04/15	-0.5	3.9	584	-3591	228	18.6	0.9	0.05311	0.40	0.394	1.0	0.0539	0.9	0.92	334	9	338	6	338	6
Ples_14	03/04/15	0.7	3.8	563	2557	136	18.4	1.1	0.05344	0.40	0.400	1.1	0.0543	1.1	0.94	348	9	341	7	341	7
Ples_15	03/04/15	1.9	3.8	567	953	36	18.4	1.0	0.05359	0.46	0.402	1.1	0.0544	1.0	0.90	354	10	341	6	343	6
Ples_16	03/04/15	1.4	3.7	548	1301	45	18.4	1.1	0.05335	0.44	0.399	1.2	0.0543	1.1	0.93	344	10	341	7	341	7
Ples_17	03/04/15	1.7	4.0	593	1087	39	18.3	0.9	0.05345	0.40	0.402	1.0	0.0546	0.9	0.92	348	9	343	6	343	6
Ples_18	03/04/15	-0.6	4.0	590	-2858	179	18.4	0.8	0.05316	0.34	0.397	0.9	0.0542	0.8	0.92	336	8	340	5	340	5
Ples_20	03/04/15	0.9	3.9	587	1913	99	18.6	0.8	0.05376	0.40	0.398	0.9	0.0537	0.8	0.90	361	9	337	5	340	5
Ples_21	03/04/15	1.9	4.0	605	954	59	18.6	0.9	0.05326	0.41	0.395	1.0	0.0538	0.9	0.90	340	9	338	6	338	6
Ples_22	03/04/15	2.9	4.1	624	628	17	18.5	0.9	0.05351	0.44	0.398	1.0	0.0539	0.9	0.90	351	10	339	6	340	6
Ples_23	03/04/15	-0.8	3.8	577	-2263	128	18.5	0.8	0.05336	0.40	0.398	0.9	0.0541	0.8	0.90	344	9	340	6	340	5
Ples_24	03/04/15	-0.4	3.9	582	-4250	255	18.5	0.9	0.05339	0.36	0.399	1.0	0.0542	0.9	0.93	346	8	340	6	341	6
Ples_25	03/04/15	0.5	3.7	552	3502	175	18.2	1.0	0.05336	0.47	0.405	1.1	0.0551	1.0	0.90	344	11	346	7	345	6
Ples_26	03/04/15	0.2	3.6	546	9858	337	18.6	0.7	0.05324	0.42	0.394	0.9	0.0537	0.7	0.87	339	10	337	5	337	5
Ples_27	03/04/15	1.3	3.7	556	1403	58	18.2	1.1	0.05308	0.43	0.401	1.2	0.0548	1.1	0.93	332	10	344	7	342	7
Ples_28	03/04/15	0.4	3.8	573	4442	254	18.9	0.8	0.05311	0.50	0.387	0.9	0.0529	0.8	0.85	333	11	333	5	333	5
Ples_29	03/04/15	0.1	3.7	562	18457	1303	18.4	0.9	0.05287	0.43	0.397	1.0	0.0545	0.9	0.91	323	10	342	6	339	6
Ples_30	03/04/15	-1.4	3.7	557	-1325	89	18.4	1.2	0.05327	0.41	0.398	1.2	0.0543	1.2	0.94	340	9	341	8	340	7
Ples_31	03/04/15	-0.1	3.7	558	-15469	455	18.4	0.8	0.05335	0.39	0.399	0.9	0.0543	0.8	0.91	344	9	341	6	341	5
Ples_32	03/04/15	1.1	3.9	585	1589	96	18.4	0.9	0.05360	0.35	0.401	1.0	0.0543	0.9	0.93	354	8	341	6	343	6
Ples_33	03/04/15	-0.9	3.9	593	-2068	106	18.4	0.9	0.05333	0.41	0.400	1.0	0.0544	0.9	0.91	343	9	342	6	342	6
Ples_34	03/04/15	1.7	3.8	577	1044	64	18.4	0.9	0.05348	0.39	0.401	1.0	0.0544	0.9	0.92	349	9	341	6	342	6

D.4.7. Zircon U-Pb GJ-1 standard data

							Data for Tera-Wasserberg plot				Data for Wetherill plot					Ages					
Analysis:	Date:	f206c	^{206}Pb	mV	Uppm*	$^{206}Pb/^{204}Pb$	1σ%	$^{238}U/^{206}Pb$	1σ%	$^{207}Pb/^{206}Pb$	1σ%	$^{207}Pb/^{235}U$	1σ%	$^{206}Pb/^{238}U$	1σ%	Rho	$^{207}Pb/^{206}Pb$	2σ abs	$^{206}Pb/^{238}U$	2σ abs	$^{207}Pb/^{235}U$	2σ abs
GJ-1_01	21/02/15	1.2	2.0	272	1485	114	10.2	1.0	0.06058	0.51	0.815	1.1	0.0976	1.0	0.89	624	11	600	11	605	10
GJ-1_02	21/02/15	1.4	2.1	274	1296	97	10.1	0.9	0.06026	0.28	0.826	0.9	0.0994	0.9	0.95	613	6	611	10	611	8
GJ-1_03	21/02/15	1.3	2.1	271	1352	92	10.1	0.9	0.06058	0.41	0.824	1.0	0.0987	0.9	0.91	624	9	607	11	610	9
GJ-1_04	21/02/15	0.3	2.1	274	6669	700	10.1	0.9	0.06051	0.33	0.823	0.9	0.0987	0.9	0.93	622	7	607	10	610	8
GJ-1_05	21/02/15	0.8	2.1	274	2168	240	10.0	1.0	0.05999	0.30	0.823	1.1	0.0996	1.0	0.96	603	6	612	12	610	10
GJ-1_06	21/02/15	2.5	2.2	285	707	51	10.0	0.9	0.06032	0.23	0.827	0.9	0.0995	0.9	0.97	615	5	612	11	612	9
GJ-1_07	21/02/15	-1.1	2.2	283	-1669	130	9.9	0.8	0.06020	0.28	0.838	0.9	0.1010	0.8	0.94	611	6	620	10	618	8
GJ-1_08	21/02/15	-1.5	2.2	282	-1150	82	9.9	0.8	0.06064	0.31	0.848	0.8	0.1014	0.8	0.92	626	7	623	9	623	8
GJ-1_09	21/02/15	3.5	2.2	283	508	33	10.0	0.9	0.06051	0.35	0.833	0.9	0.0999	0.9	0.93	622	7	614	10	615	9
GJ-1_10	21/02/15	1.7	2.2	285	1030	126	10.0	0.9	0.06020	0.37	0.827	1.0	0.0997	0.9	0.93	611	8	612	11	612	9
GJ-1_11	21/02/15	-2.5	2.2	298	-717	40	10.2	0.8	0.06027	0.50	0.816	1.0	0.0983	0.8	0.85	613	11	604	9	606	9
GJ-1_12	21/02/15	-1.0	2.3	297	-1759	146	10.1	0.7	0.06023	0.23	0.823	0.8	0.0991	0.7	0.95	612	5	609	8	609	7
GJ-1_13	21/02/15	2.3	2.2	294	755	95	10.0	0.7	0.06035	0.20	0.829	0.7	0.0997	0.7	0.96	616	4	612	8	613	7
GJ-1_14	21/02/15	-4.8	2.2	292	-372	26	10.2	0.8	0.05989	0.28	0.813	0.9	0.0984	0.8	0.95	600	6	605	10	604	8
GJ-1_15	21/02/15	1.0	2.2	295	1797	163	10.0	0.8	0.06038	0.38	0.836	0.9	0.1004	0.8	0.91	617	8	617	10	617	8
GJ-1_16	21/02/15	0.2	2.3	300	7353	551	10.0	1.0	0.05985	0.18	0.821	1.0	0.0995	1.0	0.98	598	4	612	12	609	9
GJ-1_17	21/02/15	-0.5	2.3	294	-3454	264	10.1	0.9	0.06023	0.30	0.820	0.9	0.0987	0.9	0.95	612	6	607	10	608	8
GJ-1_18	21/02/15	-1.8	2.3	298	-1002	51	10.0	0.9	0.06037	0.36	0.828	1.0	0.0996	0.9	0.93	617	8	612	10	613	9
GJ-1_19	21/02/15	-0.7	2.3	303	-2716	182	10.1	0.9	0.06047	0.25	0.827	0.9	0.0992	0.9	0.96	621	5	610	10	612	8
GJ-1_20	21/02/15	0.3	2.3	312	5642	491	10.2	1.0	0.06026	0.22	0.813	1.1	0.0979	1.0	0.98	613	5	602	12	604	10
GJ-1_21	21/02/15	-0.8	2.3	308	-2157	273	10.1	0.8	0.06046	0.31	0.821	0.9	0.0986	0.8	0.93	620	7	606	9	609	8
GJ-1_22	21/02/15	-2.8	2.3	302	-642	43	10.2	0.6	0.06076	0.33	0.822	0.7	0.0981	0.6	0.89	631	7	603	7	609	7
GJ-1_23	21/02/15	-1.5	2.3	308	-1219	91	10.2	0.9	0.06026	0.33	0.812	1.0	0.0978	0.9	0.94	613	7	601	10	604	9
GJ-1_24	21/02/15	-2.7	2.4	321	-667	81	10.1	0.7	0.06040	0.36	0.820	0.8	0.0985	0.7	0.90	618	8	606	8	608	7
GJ-1_25	21/02/15	-2.9	2.4	304	-616	41	10.0	0.8	0.05998	0.33	0.828	0.9	0.1001	0.8	0.92	603	7	615	9	612	8
GJ-1_26	21/02/15	2.6	2.3	305	671	87	10.4	0.8	0.06033	0.17	0.800	0.8	0.0962	0.8	0.98	615	4	592	9	597	7
GJ-1_27	21/02/15	2.0	2.4	320	894	104	10.2	0.8	0.06030	0.30	0.814	0.9	0.0979	0.8	0.94	614	6	602	9	605	8
GJ-1_28	21/02/15	0.5	2.3	311	3249	394	10.2	0.9	0.06046	0.40	0.815	1.0	0.0978	0.9	0.91	620	9	601	10	605	9
GJ-1_29	21/02/15	1.5	2.3	312	1219	115	10.5	1.1	0.05993	0.25	0.789	1.1	0.0955	1.1	0.98	601	5	588	12	590	10
GJ-1_30	21/02/15	1.5	2.4	323	1214	96	10.4	1.2	0.06047	0.28	0.802	1.2	0.0962	1.2	0.97	620	6	592	14	598	11
GJ-1_31	21/02/15	1.7	2.4	319	1053	69	10.3	1.0	0.06007	0.22	0.801	1.0	0.0968	1.0	0.98	606	5	595	11	597	9
GJ-1_32	21/02/15	2.5	2.3	312	718	53	10.3	0.8	0.06012	0.32	0.803	0.9	0.0969	0.8	0.93	608	7	596	9	598	8
GJ-1_33	21/02/15	3.8	2.4	313	469	65	10.3	0.7	0.06029	0.32	0.811	0.8	0.0975	0.7	0.92	614	7	600	9	603	7
GJ-1_34	21/02/15	0.0	2.3	306	-53095	5337	10.2	0.7	0.05981	0.30	0.812	0.8	0.0985	0.7	0.92	597	7	606	8	604	7
GJ-1_35	21/02/15	0.5	2.3	313	3368	250	10.2	0.9	0.06044	0.31	0.817	0.9	0.0981	0.9	0.94	619	7	603	10	606	9
GJ-1_36	21/02/15	-0.8	2.3	307	-2286	217	10.3	0.9	0.06000	0.32	0.803	1.0	0.0971	0.9	0.95	604	7	597	11	598	9
GJ-1_37	21/02/15	-2.9	2.4	318	-603	63	10.3	0.7	0.06031	0.27	0.809	0.8	0.0974	0.7	0.94	615	6	599	9	602	7
GJ-1_38	21/02/15	3.1	2.2	297	566	68	10.4	1.1	0.06080	0.33	0.808	1.1	0.0964	1.1	0.96	632	7	593	12	601	10
GJ-1_39	21/02/15	-1.0	2.2	306	-1822	192	10.3	0.9	0.06027	0.23	0.804	0.9	0.0968	0.9	0.97	613	5	596	10	599	8
GJ-1_40	21/02/15	5.1	2.1	289	347	33	10.4	1.3	0.06037	0.25	0.801	1.3	0.0963	1.3	0.98	617	5	593	15	598	12
GJ-1_41	21/02/15	-0.8	2.2	303	-2169	243	10.6	0.9	0.06021	0.40	0.782	1.0	0.0943	0.9	0.91	611	9	581	10	587	9
GJ-1_42	21/02/15	-3.0	2.2	306	-582	41	10.6	0.8	0.06045	0.40	0.788	0.9	0.0946	0.8	0.89	620	9	582	9	590	8
GJ-1_43	21/02/15	3.1	2.3	309	577	44	10.5	1.0	0.06037	0.25	0.795	1.0	0.0955	1.0	0.97	617	5	588	11	594	9
GJ-1_44	21/02/15	-0.7	2.2	303	-2540	248	10.4	0.9	0.05999	0.37	0.792	1.0	0.0958	0.9	0.93	603	8	590	10	592	9
GJ-1_45	21/02/15	-1.4	2.2	304	-1223	111	10.4	1.0	0.06046	0.28	0.798	1.0	0.0958	1.0	0.96	620	6	590	11	596	9
GJ-1_46	21/02/15	-0.5	2.3	313	-3238	185	10.4	1.0	0.06025	0.43	0.802	1.1	0.0965	1.0	0.92	612	9	594	11	598	10
GJ-1_47	21/02/15	-1.2	2.3	306	-1465	131	10.3	1.2	0.06021	0.51	0.806	1.3	0.0971	1.2	0.92	611	11	597	14	600	12
GJ-1_48	21/02/15	1.3	2.3	310	1373	128	10.2	1.2	0.05994	0.32	0.810	1.2	0.0980	1.2	0.97	601	7	603	14	602	11
GJ-1_49	21/02/15	-4.7	2.2	300	-380	32	10.4	1.0	0.06040	0.38	0.800	1.1	0.0961	1.0	0.94	618	8	592	12	597	10
GJ-1_50	21/02/15	-1.8	2.2	295	-988	69	10.3	0.8	0.05997	0.25	0.799	0.8	0.0967	0.8	0.95	602	5	595	9	597	8
GJ-1_51	21/02/15	-2.5	2.2	292	-698	50	10.4	0.8	0.06023	0.38	0.800	0.9	0.0964	0.8	0.89	612	8	593	9	597	8
GJ-1_52	21/02/15	-0.5	2.2	297	-3734	317	10.4	0.8	0.06025	0.30	0.800	0.8	0.0963	0.8	0.93	613	6	593	9	597	7

							Data for Tera-Wasserberg plot				Data for Wetherill plot					Ages					
Analysis:	Date:	f206c	^{206}Pb	mV	Uppm*	$^{206}Pb/^{204}Pb$	1σ%	$^{238}U/^{206}Pb$	1σ%	$^{207}Pb/^{206}Pb$	1σ%	$^{207}Pb/^{235}U$	1σ%	$^{206}Pb/^{238}U$	1σ%	Rho	$^{207}Pb/^{206}Pb$	2σ abs	$^{206}Pb/^{238}U$	2σ abs	$^{207}Pb/^{235}U$	2σ abs
GJ-1_05	20/03/15	-1.1	3.3	288	-1591	136	10.3	1.1	0.06000	0.50	0.805	1.2	0.0974	1.1	0.91	603	11	599	13	600	11
GJ-1_06	20/03/15	-1.7	3.3	293	-1058	99	10.3	1.0	0.06010	0.44	0.805	1.1	0.0972	1.0	0.92	607	9	598	12	600	10
GJ-1_07	20/03/15	-2.0	3.5	313	-874	58	10.3	1.2	0.06044	0.41	0.809	1.3	0.0971	1.2	0.95	620	9	597	14	602	11
GJ-1_08	20/03/15	-0.5	3.5	302	-3403	228	10.2	1.0	0.06000	0.45	0.811	1.1	0.0981	1.0	0.92	604	10	603	12	603	10
GJ-1_09	20/03/15	1.0	3.4	301	1774	104	10.2	1.1	0.05984	0.42	0.812	1.2	0.0985	1.1	0.93	598	9	605	13	604	11
GJ-1_10	20/03/15	1.2	3.5	299	1450	149	10.2	0.9	0.06027	0.39	0.811	1.0	0.0976	0.9	0.91	613	8	600	10	603	9
GJ-1_11	20/03/15	1.0	3.4	302	1830	107	10.2	0.9	0.05992	0.37	0.808	0.9	0.0979	0.9	0.92	601	8	602	10	602	8
GJ-1_12	20/03/15	1.9	3.4	301	922	92	10.3	1.0	0.06049	0.35	0.813	1.1	0.0975	1.0	0.94	621	8	600	11	604	10
GJ-1_13	20/03/15	-0.3	3.3	288	-6194	441	10.3	0.9	0.06046	0.43	0.810	1.0	0.0973	0.9	0.90	620	9	598	10	603	9
GJ-1_14	20/03/15	1.0	3.2	283	1810	113	10.2	1.0	0.05984	0.39	0.808	1.1	0.0979	1.0	0.93	598	8	602	12	601	10
GJ-1_15	20/03/15	0.6	3.2	281	2928	280	10.1	0.9	0.06032	0.53	0.823	1.1	0.0990	0.9	0.87	615	11	608	11	610	10
GJ-1_16	20/03/15	0.0	3.5	308	93353	6513	10.1	0.9	0.06032	0.43	0.825	1.0	0.0992	0.9	0.90	615	9	610	10	611	9
GJ-1_17	20/03/15	2.0	3.6	313	873	60	10.1	1.0	0.06010	0.50	0.823	1.1	0.0994	1.0	0.90	607	11	611	12	610	10
GJ-1_18	20/03/15	-0.3	3.7	325	-6903	348	10.3	0.9	0.06034	0.37	0.810	1.0	0.0974	0.9	0.93	616	8	599	11	602	9
GJ-1_19	20/03/15	3.2	3.6	320	550	22	10.3	0.8	0.05988	0.37	0.804	0.8	0.0974	0.8	0.90	599	8	599	9	599	8
GJ-1_20	20/03/15	0.7	3.6	316	2419	88	10.3	1.0	0.06020	0.46	0.804	1.1	0.0969	1.0	0.90	611	10	596	11	599	10
GJ-1_21	20/03/15	2.2	3.4	294	807	36	10.2	0.9	0.06005	0.46	0.815	1.0	0.0985	0.9	0.88	605	10	605	10	605	9
GJ-1_22	20/03/15	1.2	3.3	292	1537	68	10.3	1.0	0.06013	0.54	0.808	1.1	0.0975	1.0	0.87	608	12	600	11	601	10
GJ-1_23	20/03/15	-1.3	3.4	296	-1396	64	10.2	0.9	0.06017	0.34	0.817	1.0	0.0985	0.9	0.93	610	7	606	10	606	9
GJ-1_24	20/03/15	-2.9	3.5	310	-618	30	10.2	0.9	0.06003	0.40	0.810	1.0	0.0979	0.9	0.91	605	9	602	10	602	9
GJ-1_25	20/03/15	-1.2	3.5	310	-1457	70	10.2	0.9	0.05977	0.44	0.811	1.0	0.0984	0.9	0.90	595	9	605	10	603	9
GJ-1_26	20/03/15	-0.7	3.4	300	-2395	217	10.2	0.9	0.06022	0.33	0.813	1.0	0.0979	0.9	0.94	612	7	602	11	604	9
GJ-1_27	20/03/15	-1.2	3.5	310	-1450	174	10.2	1.0	0.06010	0.50	0.810	1.1	0.0978	1.0	0.89	607	11	601	11	602	10
GJ-1_28	20/03/15	-1.9	3.4	307	-917	50	10.2	0.9	0.06028	0.42	0.813	1.0	0.0978	0.9	0.90	614	9	602	10	604	9
GJ-1_29	20/03/15	0.4	3.6	308	4690	409	10.1	0.9	0.06023	0.40	0.823	1.0	0.0992	0.9	0.91	612	9	610	10	610	9
GJ-1_30	20/03/15	1.5	3.3	291	1147	86	10.2	0.9	0.06028	0.32	0.812	1.0	0.0977	0.9	0.94	614	7	601	10	603	9
GJ-1_31	20/03/15	-1.6	3.6	310	-1105	87	10.1	0.7	0.06012	0.53	0.818	0.9	0.0987	0.7	0.81	608	11	607	9	607	8
GJ-1_32	20/03/15	-1.8	3.5	304	-967	73	10.1	1.0	0.06006	0.42	0.816	1.0	0.0986	1.0	0.91	606	9	606	11	606	10
GJ-1_33	20/03/15	0.5	3.5	313	3820	301	10.3	1.1	0.06032	0.40	0.807	1.2	0.0971	1.1	0.94	615	9	598	12	601	11
GJ-1_34	20/03/15	1.7	3.6	312	1051	60	10.2	1.0	0.05986	0.45	0.809	1.1	0.0980	1.0	0.91	599	10	603	11	602	10
GJ-1_35	20/03/15	2.6	3.5	298	695	53	10.1	0.9	0.06007	0.40	0.817	0.9	0.0987	0.9	0.91	606	9	607	10	607	9
GJ-1_36	20/03/15	-0.1	3.6	320	-31693	2028	10.3	0.8	0.06009	0.38	0.807	0.9	0.0975	0.8	0.91	607	8	600	10	601	8
GJ-1_37	20/03/15	-1.3	3.5	310	-1315	98	10.2	0.9	0.06031	0.35	0.815	0.9	0.0980	0.9	0.93	615	8	603	10	605	8
GJ-1_38	20/03/15	-0.9	3.5	305	-1977	175	10.2	0.9	0.05994	0.37	0.811	0.9	0.0982	0.9	0.92	602	8	604	10	603	8
GJ-1_39	20/03/15	-1.3	3.4	299	-1408	62	10.2	0.9	0.05998	0.39	0.807	1.0	0.0977	0.9	0.92	603	8	601	10	601	9
GJ-1_40	20/03/15	1.3	3.3	290	1386	143	10.2	0.8	0.06042	0.33	0.816	0.9	0.0981	0.8	0.92	618	7	603	9	606	8
GJ-1_41	20/03/15	0.1	3.4	298	12685	758	10.3	0.9	0.05985	0.36	0.801	1.0	0.0971	0.9	0.93	598	8	597	11	597	9
GJ-1_42	20/03/15	-0.7	3.5	308	-2632	151	10.2	1.0	0.06020	0.47	0.812	1.1	0.0979	1.0	0.90	611	10	602	11	604	10
GJ-1_43	20/03/15	-0.3	3.5	305	-5098	320	10.3	1.1	0.05991	0.32	0.804	1.1	0.0974	1.1	0.96	600	7	599	12	599	10
GJ-1_44	20/03/15	1.7	3.4	301	1031	70	10.2	0.8	0.06018	0.35	0.813	0.9	0.0980	0.8	0.92	610	8	603	10	604	8
GJ-1_45	20/03/15	-1.6	3.5	307	-1143	71	10.3	0.9	0.06000	0.46	0.806	1.0	0.0975	0.9	0.88	604	10	600	10	600	9
GJ-1_46	20/03/15	-0.8	3.4	299	-2246	153	10.2	0.9	0.06006	0.51	0.812	1.0	0.0981	0.9	0.86	606	11	603	10	604	9
GJ-1_47	20/03/15	0.2	3.5	307	8767	385	10.2	1.0	0.05988	0.35	0.808	1.0	0.0978	1.0	0.94	599	8	602	11	601	9
GJ-1_48	20/03/15	-2.8	3.4	301	-625	43	10.3	0.8	0.06002	0.34	0.806	0.9	0.0975	0.8	0.92	604	7	600	9	600	8
GJ-1_50	20/03/15	-1.0	3.4	295	-1787	106	10.1	0.8	0.05951	0.56	0.812	1.0	0.0990	0.8	0.82	586	12	608	9	603	9
GJ-1_51	20/03/15	-0.2	3.2	282	-9808	667	10.3	0.8	0.05994	0.35	0.802	0.9	0.0971	0.8	0.92	601	8	597	9	598	8
GJ-1_52	20/03/15	-0.4	3.5	306	-4181	262	10.3	0.9	0.06013	0.40	0.804	1.0	0.0970	0.9	0.92	608	9	597	10	599	9

							Data for Tera-Wasserberg plot				Data for Wetherill plot					Ages					
Analysis:	Date:	f206c	^{206}Pb	mV	Uppm*	^{206}Pb/^{204}Pb	1σ%	^{238}U/^{206}Pb	1σ%	^{207}Pb/^{206}Pb	1σ%	^{207}Pb/^{235}U	1σ%	^{206}Pb/^{238}U	1σ%	Rho	^{207}Pb/^{206}Pb	2σ abs	^{206}Pb/^{238}U	2σ abs	^{207}Pb/^{235}U	2σ abs
GJ-1_01	21/03/15	1.9	3.1	295	958	81	10.1	1.4	0.05999	0.34	0.816	1.5	0.0987	1.4	0.97	603	7	607	16	606	13
GJ-1_02	21/03/15	2.2	3.2	297	793	54	10.0	1.0	0.06037	0.30	0.830	1.0	0.0998	1.0	0.95	617	7	613	11	614	9
GJ-1_03	21/03/15	1.3	3.2	301	1364	86	9.9	0.8	0.06029	0.22	0.835	0.8	0.1005	0.8	0.96	614	5	618	9	617	7
GJ-1_04	21/03/15	0.3	3.2	302	6631	384	9.9	0.7	0.06012	0.41	0.833	0.9	0.1006	0.7	0.88	608	9	618	9	615	8
GJ-1_05	21/03/15	-0.8	3.2	305	-2204	104	10.2	1.1	0.06011	0.24	0.811	1.1	0.0979	1.1	0.98	607	5	602	13	603	10
GJ-1_06	21/03/15	0.5	3.2	309	3647	349	10.2	1.0	0.05984	0.43	0.810	1.0	0.0982	1.0	0.91	598	9	604	11	602	9
GJ-1_07	21/03/15	2.1	3.3	311	858	57	10.1	0.9	0.06006	0.37	0.817	1.0	0.0987	0.9	0.93	606	8	606	11	606	9
GJ-1_08	21/03/15	-0.4	3.2	301	-5011	560	10.0	1.1	0.06012	0.35	0.825	1.2	0.0996	1.1	0.95	608	8	612	13	611	11
GJ-1_09	21/03/15	2.5	3.2	306	710	61	10.1	1.0	0.05974	0.46	0.819	1.1	0.0995	1.0	0.91	594	10	611	12	608	10
GJ-1_10	21/03/15	-0.9	3.3	310	-1955	128	10.0	1.0	0.05993	0.32	0.827	1.0	0.1001	1.0	0.95	601	7	615	11	612	9
GJ-1_11	21/03/15	-4.6	3.3	308	-386	37	10.0	0.9	0.05992	0.26	0.828	0.9	0.1002	0.9	0.96	601	6	616	10	612	8
GJ-1_12	21/03/15	0.2	3.3	310	9897	504	10.0	1.1	0.06025	0.38	0.829	1.2	0.0999	1.1	0.95	613	8	614	13	613	11
GJ-1_13	21/03/15	-1.6	3.3	311	-1106	77	9.9	1.0	0.06038	0.28	0.838	1.0	0.1007	1.0	0.96	617	6	619	12	618	9
GJ-1_14	21/03/15	-2.8	3.3	308	-625	29	9.9	1.0	0.06027	0.33	0.838	1.0	0.1009	1.0	0.95	613	7	619	12	618	10
GJ-1_15	21/03/15	-0.5	3.4	313	-3793	175	10.0	0.8	0.06035	0.49	0.834	0.9	0.1003	0.8	0.84	616	11	616	9	616	8
GJ-1_16	21/03/15	-0.5	3.3	316	-3482	211	10.1	1.0	0.05974	0.32	0.814	1.0	0.0989	1.0	0.95	594	7	608	11	605	9
GJ-1_17	21/03/15	0.4	3.3	309	4148	431	10.0	1.1	0.06044	0.33	0.830	1.2	0.0996	1.1	0.96	620	7	612	13	613	11
GJ-1_18	21/03/15	-0.6	3.3	316	-2806	195	10.0	0.8	0.06033	0.26	0.835	0.8	0.1004	0.8	0.95	615	6	617	9	616	7
GJ-1_19	21/03/15	-0.9	3.3	311	-1911	151	9.9	0.9	0.05988	0.37	0.830	1.0	0.1006	0.9	0.93	599	8	618	11	614	9
GJ-1_20	21/03/15	-0.3	3.4	320	-5389	544	10.1	1.0	0.05970	0.37	0.815	1.1	0.0991	1.0	0.94	593	8	609	12	605	10
GJ-1_21	21/03/15	-0.3	3.3	311	-6982	326	10.0	0.9	0.06012	0.31	0.829	0.9	0.1001	0.9	0.95	608	7	615	10	613	9
GJ-1_22	21/03/15	2.0	3.4	320	885	92	10.0	0.9	0.05997	0.51	0.827	1.1	0.1000	0.9	0.88	603	11	615	11	612	10
GJ-1_23	21/03/15	-3.1	3.4	320	-566	31	10.0	0.8	0.05966	0.25	0.818	0.8	0.0995	0.8	0.95	591	5	611	9	607	8
GJ-1_24	21/03/15	1.3	3.4	318	1337	86	10.1	0.8	0.06001	0.38	0.822	0.8	0.0993	0.8	0.89	604	8	610	9	609	8
GJ-1_25	21/03/15	1.0	3.4	315	1831	169	10.0	0.9	0.05960	0.23	0.821	0.9	0.1000	0.9	0.97	589	5	614	10	609	8
GJ-1_26	21/03/15	-0.3	3.4	318	-6648	519	10.0	0.8	0.05986	0.34	0.821	0.9	0.0996	0.8	0.93	599	7	612	10	609	8
GJ-1_27	21/03/15	2.1	3.4	319	855	51	10.1	0.8	0.05971	0.21	0.814	0.8	0.0989	0.8	0.97	593	5	608	9	605	7
GJ-1_28	21/03/15	1.3	3.4	322	1340	110	10.1	0.9	0.05970	0.29	0.817	1.0	0.0993	0.9	0.95	593	6	610	11	606	9
GJ-1_29	21/03/15	-0.8	3.5	329	-2295	113	10.1	0.8	0.05977	0.44	0.814	0.9	0.0989	0.8	0.88	595	10	608	10	605	9
GJ-1_30	21/03/15	0.3	3.4	324	5907	346	10.0	0.7	0.05964	0.45	0.824	0.9	0.1003	0.7	0.85	590	10	616	9	611	8
GJ-1_31	21/03/15	-1.7	3.5	322	-1060	86	9.9	0.8	0.05968	0.35	0.828	0.9	0.1007	0.8	0.92	592	8	619	10	613	8
GJ-1_32	21/03/15	-0.4	3.3	313	-3993	317	10.0	1.0	0.05990	0.41	0.823	1.0	0.0997	1.0	0.92	600	9	613	11	610	10
GJ-1_33	21/03/15	-0.6	3.3	312	-3175	222	9.9	0.8	0.05982	0.37	0.831	0.9	0.1008	0.8	0.91	597	8	619	10	614	8
GJ-1_34	21/03/15	0.4	3.4	318	4099	337	10.0	0.8	0.05968	0.32	0.824	0.9	0.1002	0.8	0.93	592	7	615	9	610	8
GJ-1_35	21/03/15	2.3	3.4	319	776	43	10.2	1.0	0.05935	0.31	0.806	1.1	0.0985	1.0	0.96	580	7	606	12	600	10
GJ-1_36	21/03/15	-2.1	3.4	318	-845	58	10.1	0.9	0.05964	0.34	0.815	0.9	0.0992	0.9	0.93	590	7	610	10	605	8
GJ-1_37	21/03/15	1.3	3.4	313	1389	96	10.0	0.9	0.05936	0.31	0.822	0.9	0.1005	0.9	0.94	580	7	617	10	609	8
GJ-1_38	21/03/15	-2.5	3.4	319	-721	43	10.1	1.0	0.05947	0.38	0.810	1.0	0.0989	1.0	0.93	584	8	608	11	603	9
GJ-1_39	21/03/15	-2.9	3.3	317	-609	68	10.1	0.9	0.05977	0.38	0.817	1.0	0.0992	0.9	0.92	595	8	610	10	607	9
GJ-1_40	21/03/15	0.9	3.3	315	2033	132	10.1	0.8	0.05965	0.49	0.817	0.9	0.0993	0.8	0.85	591	11	611	9	606	9
GJ-1_41	21/03/15	0.7	3.3	319	2387	177	10.2	0.7	0.06011	0.20	0.814	0.8	0.0983	0.7	0.97	607	4	604	9	605	7
GJ-1_42	21/03/15	2.0	3.3	315	901	46	10.1	0.8	0.05982	0.20	0.817	0.8	0.0991	0.8	0.97	597	4	609	9	607	7

							Data for Tera-Wasserberg plot				Data for Wetherill plot					Ages					
Analysis:	Date:	f206c	^{206}Pb	mV	Uppm*	^{206}Pb/^{204}Pb	1σ%	^{238}U/^{206}Pb	1σ%	^{207}Pb/^{206}Pb	1σ%	^{207}Pb/^{235}U	1σ%	^{206}Pb/^{238}U	1σ%	Rho	^{207}Pb/^{206}Pb	2σ abs	^{206}Pb/^{238}U	2σ abs	^{207}Pb/^{235}U	2σ abs
GJ-1_01	03/04/15	-1.4	3.6	304	-1229	63	10.3	1.0	0.06037	0.39	0.810	1.1	0.0973	1.0	0.94	617	8	599	12	602	10
GJ-1_02	03/04/15	-0.4	4.0	332	-4097	251	10.3	1.1	0.06033	0.40	0.809	1.2	0.0974	1.1	0.94	615	9	599	13	602	11
GJ-1_03	03/04/15	0.2	3.8	305	10133	414	10.2	1.2	0.06037	0.41	0.816	1.3	0.0981	1.2	0.95	617	9	603	14	606	12
GJ-1_04	03/04/15	0.2	4.2	343	7331	217	10.2	1.1	0.06021	0.37	0.811	1.2	0.0977	1.1	0.95	611	8	601	13	603	11
GJ-1_05	03/04/15	-1.5	3.8	314	-1156	70	10.3	1.1	0.06022	0.37	0.809	1.2	0.0975	1.1	0.95	612	8	600	13	602	11
GJ-1_06	03/04/15	-1.8	3.3	276	-997	46	10.2	1.1	0.06014	0.44	0.812	1.2	0.0980	1.1	0.93	609	9	603	13	604	11
GJ-1_07	03/04/15	-2.1	3.5	282	-850	64	10.1	1.0	0.06032	0.47	0.820	1.1	0.0986	1.0	0.90	615	10	606	11	608	10
GJ-1_08	03/04/15	-1.9	3.2	259	-945	65	10.2	1.1	0.05936	0.52	0.802	1.2	0.0981	1.1	0.91	580	11	603	13	598	11
GJ-1_09	03/04/15	-1.3	3.2	267	-1372	125	10.2	1.1	0.06016	0.39	0.813	1.2	0.0980	1.1	0.94	609	8	603	13	604	11
GJ-1_10	03/04/15	-1.3	3.5	283	-1365	67	10.1	0.9	0.05997	0.41	0.817	1.0	0.0989	0.9	0.91	602	9	608	11	607	9
GJ-1_11	03/04/15	-0.2	4.0	331	-8337	327	10.3	1.2	0.06030	0.41	0.804	1.3	0.0968	1.2	0.95	614	9	595	14	599	12
GJ-1_12	03/04/15	-0.3	3.8	314	-6873	390	10.2	1.2	0.06021	0.39	0.813	1.3	0.0980	1.2	0.95	611	8	603	14	604	12
GJ-1_13	03/04/15	1.8	3.6	298	1006	43	10.2	0.8	0.05971	0.46	0.805	1.0	0.0978	0.8	0.88	593	10	601	10	599	9
GJ-1_14	03/04/15	0.6	3.6	293	2774	192	10.2	1.0	0.05980	0.50	0.811	1.1	0.0984	1.0	0.90	596	11	605	12	603	10
GJ-1_15	03/04/15	1.7	3.5	285	1045	56	10.3	0.8	0.06028	0.37	0.808	0.9	0.0973	0.8	0.90	613	8	599	9	602	8
GJ-1_16	03/04/15	1.1	3.5	290	1602	119	10.3	0.8	0.06012	0.53	0.808	0.9	0.0975	0.8	0.83	608	11	600	9	601	8
GJ-1_17	03/04/15	-1.9	3.6	301	-933	72	10.3	1.4	0.06009	0.37	0.807	1.5	0.0974	1.4	0.97	607	8	599	16	601	13
GJ-1_18	03/04/15	2.0	3.6	295	874	49	10.2	1.0	0.05993	0.41	0.809	1.1	0.0980	1.0	0.93	601	9	603	12	602	10
GJ-1_19	03/04/15	-0.9	3.8	311	-1918	94	10.1	0.9	0.06003	0.40	0.819	1.0	0.0990	0.9	0.91	605	9	608	10	607	9
GJ-1_20	03/04/15	1.1	3.6	301	1597	158	10.3	1.3	0.05998	0.39	0.802	1.4	0.0970	1.3	0.96	603	8	597	15	598	13
GJ-1_21	03/04/15	-0.9	3.5	293	-1895	132	10.2	1.2	0.06009	0.35	0.814	1.3	0.0983	1.2	0.96	607	8	605	14	605	12
GJ-1_22	03/04/15	2.4	3.5	288	725	31	10.2	0.8	0.05985	0.44	0.810	1.0	0.0982	0.8	0.89	598	9	604	10	602	9
GJ-1_23	03/04/15	0.1	3.8	319	18073	1388	10.2	1.0	0.06091	0.46	0.822	1.1	0.0979	1.0	0.91	636	10	602	12	609	10
GJ-1_24	03/04/15	-2.4	3.6	301	-752	68	10.3	0.8	0.06057	0.40	0.809	0.9	0.0969	0.8	0.90	624	9	596	10	602	8
GJ-1_25	03/04/15	-1.0	3.8	313	-1841	159	10.2	1.0	0.05961	0.50	0.808	1.1	0.0983	1.0	0.90	590	11	605	12	601	10
GJ-1_26	03/04/15	0.9	3.4	287	2089	133	10.3	0.8	0.05962	0.37	0.800	0.9	0.0974	0.8	0.90	590	8	599	9	597	8
GJ-1_27	03/04/15	-0.4	3.6	298	-4640	361	10.2	1.0	0.06045	0.40	0.820	1.1	0.0984	1.0	0.93	620	9	605	12	608	10
GJ-1_28	03/04/15	1.5	3.6	300	1167	115	10.2	1.1	0.05974	0.54	0.808	1.2	0.0982	1.1	0.90	594	12	604	13	601	11
GJ-1_29	03/04/15	2.9	3.6	309	620	58	10.4	1.2	0.06058	0.43	0.803	1.3	0.0962	1.2	0.94	624	9	592	14	599	12
GJ-1_30	03/04/15	1.2	3.7	313	1519	134	10.3	1.2	0.06014	0.34	0.806	1.3	0.0972	1.2	0.96	609	7	598	14	600	12
GJ-1_31	03/04/15	1.1	3.6	299	1606	83	10.1	0.9	0.05980	0.38	0.814	0.9	0.0988	0.9	0.91	596	8	607	10	605	8
GJ-1_32	03/04/15	-0.6	3.6	304	-3015	157	10.2	0.8	0.06007	0.41	0.812	0.9	0.0981	0.8	0.89	606	9	603	9	604	8
GJ-1_33	03/04/15	-2.6	3.4	290	-679	40	10.2	1.0	0.06049	0.36	0.816	1.0	0.0979	1.0	0.94	621	8	602	11	606	9
GJ-1_34	03/04/15	-0.5	3.6	302	-3584	200	10.2	1.0	0.06003	0.41	0.815	1.1	0.0985	1.0	0.93	605	9	605	12	605	10

D.4.8. Zircon O isotope standard data

Date	Time	Analysis	$^{16}O/^{18}O$	% s.e.	18/16	% s.e.	16 cps	% s.e.	18 cps	% s.e.	$d^{18}O$ measured	Std at Time	$d^{18}O$ corrected	1 s.d.
02/12/2013	1	91500_1	494.62	0.0109	0.0020218	0.0109	3.08E+09	0.25	6.22E+06	0.25	9.95	2.022E-03	9.88	0.05
02/12/2013	2	91500_2	494.76	0.0101	0.0020212	0.0101	3.07E+09	0.30	6.21E+06	0.30	9.66	2.022E-03	9.60	0.05
02/12/2013	3	91500_3	494.55	0.0097	0.0020220	0.0097	3.08E+09	0.28	6.22E+06	0.28	10.08	2.022E-03	10.02	0.04
02/12/2013	4	91500_4	494.55	0.0070	0.0020221	0.0070	3.10E+09	0.27	6.26E+06	0.27	10.09	2.022E-03	10.03	0.03
02/12/2013	5	91500_5	494.34	0.0108	0.0020229	0.0108	3.06E+09	0.24	6.19E+06	0.24	10.52	2.022E-03	10.46	0.05
02/12/2013	6	91500_6	494.64	0.0086	0.0020217	0.0086	3.04E+09	0.29	6.16E+06	0.28	9.90	2.022E-03	9.84	0.04
02/12/2013	7	91500_7	494.68	0.0063	0.0020215	0.0063	3.05E+09	0.28	6.16E+06	0.28	9.82	2.022E-03	9.76	0.03
02/12/2013	8	91500_8	494.61	0.0100	0.0020218	0.0100	3.05E+09	0.28	6.16E+06	0.28	9.97	2.022E-03	9.92	0.04
02/12/2013	9	91500_9	494.49	0.0090	0.0020223	0.0090	3.04E+09	0.24	6.15E+06	0.25	10.22	2.022E-03	10.17	0.04
02/12/2013	10	91500_10	494.52	0.0100	0.0020222	0.0100	3.02E+09	0.22	6.10E+06	0.22	10.15	2.022E-03	10.10	0.04
02/12/2013	16	91500_11	494.41	0.0046	0.0020226	0.0046	3.04E+09	0.21	6.15E+06	0.21	10.37	2.022E-03	10.33	0.02
02/12/2013	17	91500_12	494.23	0.0094	0.0020234	0.0094	3.04E+09	0.22	6.15E+06	0.22	10.74	2.022E-03	10.71	0.04
02/12/2013	18	91500_13	494.49	0.0113	0.0020223	0.0113	3.06E+09	0.27	6.19E+06	0.28	10.21	2.022E-03	10.17	0.05
02/12/2013	19	91500_14	494.58	0.0093	0.0020219	0.0093	3.10E+09	0.27	6.26E+06	0.28	10.03	2.022E-03	10.00	0.04
02/12/2013	20	91500_15	494.48	0.0071	0.0020223	0.0071	3.13E+09	0.31	6.33E+06	0.32	10.24	2.022E-03	10.21	0.03
02/12/2013	31	91500_16	494.49	0.0076	0.0020223	0.0076	3.04E+09	0.26	6.15E+06	0.27	10.21	2.022E-03	10.20	0.03
02/12/2013	32	91500_17	494.57	0.0112	0.0020220	0.0112	3.05E+09	0.29	6.16E+06	0.30	10.04	2.022E-03	10.03	0.05
02/12/2013	33	91500_18	494.64	0.0103	0.0020217	0.0103	3.06E+09	0.26	6.19E+06	0.27	9.90	2.022E-03	9.89	0.05
02/12/2013	34	91500_19	494.53	0.0092	0.0020221	0.0092	3.03E+09	0.25	6.12E+06	0.25	10.13	2.022E-03	10.12	0.04
02/12/2013	35	91500_20	494.35	0.0102	0.0020229	0.0102	2.97E+09	0.18	6.01E+06	0.18	10.49	2.022E-03	10.49	0.05
02/12/2013	46	91500_21	494.77	0.0097	0.0020211	0.0097	2.90E+09	0.32	5.85E+06	0.31	9.64	2.022E-03	9.66	0.04
02/12/2013	47	91500_22	494.63	0.0069	0.0020217	0.0069	2.90E+09	0.27	5.85E+06	0.27	9.91	2.022E-03	9.94	0.03
02/12/2013	48	91500_23	494.43	0.0077	0.0020225	0.0077	2.88E+09	0.24	5.83E+06	0.24	10.32	2.022E-03	10.35	0.03
02/12/2013	49	91500_24	494.49	0.0069	0.0020223	0.0069	2.84E+09	0.22	5.74E+06	0.22	10.21	2.022E-03	10.24	0.03
02/12/2013	50	91500_25	494.64	0.0082	0.0020217	0.0082	2.83E+09	0.26	5.72E+06	0.27	9.91	2.022E-03	9.93	0.04
02/12/2013	64	91500_26	494.76	0.0119	0.0020212	0.0120	2.75E+09	0.24	5.55E+06	0.24	9.67	2.022E-03	9.72	0.05
02/12/2013	65	91500_27	494.51	0.0083	0.0020222	0.0083	2.72E+09	0.22	5.49E+06	0.22	10.16	2.022E-03	10.22	0.04
02/12/2013	66	91500_28	494.53	0.0101	0.0020221	0.0101	2.74E+09	0.24	5.55E+06	0.25	10.12	2.022E-03	10.18	0.05
02/12/2013	67	91500_29	494.65	0.0100	0.0020216	0.0100	2.74E+09	0.30	5.53E+06	0.30	9.88	2.022E-03	9.95	0.04
02/12/2013	68	91500_30	494.68	0.0089	0.0020215	0.0089	2.74E+09	0.25	5.54E+06	0.25	9.81	2.022E-03	9.88	0.04
02/12/2013	79	91500_31	494.52	0.0091	0.0020221	0.0091	2.73E+09	0.24	5.53E+06	0.24	10.14	2.022E-03	10.22	0.04
02/12/2013	80	91500_32	494.50	0.0117	0.0020222	0.0117	2.70E+09	0.24	5.45E+06	0.24	10.19	2.022E-03	10.27	0.05
02/12/2013	81	91500_33	494.64	0.0113	0.0020217	0.0113	2.70E+09	0.17	5.45E+06	0.17	9.90	2.022E-03	9.99	0.05
02/12/2013	82	91500_34	494.68	0.0111	0.0020215	0.0111	2.72E+09	0.24	5.49E+06	0.24	9.83	2.022E-03	9.92	0.05

Date	Time	Analysis	$^{16}O/^{18}O$	% s.e.	18/16	% s.e.	16 cps	% s.e.	18 cps	% s.e.	$d^{18}O$ measured	Std at Time	$d^{18}O$ corrected	1 s.d.
03/12/2013	1	91500_1	494.10	0.0060	0.0020239	0.0060	3.76E+09	0.37	7.60E+06	0.37	4.92	2.024E-03	9.95	0.03
03/12/2013	2	91500_2	493.93	0.0078	0.0020246	0.0078	3.73E+09	0.35	7.56E+06	0.35	5.25	2.024E-03	10.29	0.03
03/12/2013	3	91500_3	493.83	0.0065	0.0020250	0.0065	3.72E+09	0.33	7.53E+06	0.33	5.46	2.024E-03	10.51	0.03
03/12/2013	4	91500_4	494.00	0.0082	0.0020243	0.0082	3.72E+09	0.37	7.53E+06	0.37	5.10	2.024E-03	10.15	0.04
03/12/2013	5	91500_5	494.03	0.0095	0.0020242	0.0095	3.74E+09	0.39	7.57E+06	0.39	5.05	2.024E-03	10.10	0.04
03/12/2013	6	91500_6	494.02	0.0077	0.0020242	0.0077	3.71E+09	0.38	7.51E+06	0.38	5.08	2.024E-03	10.13	0.03
03/12/2013	7	91500_7	493.94	0.0071	0.0020245	0.0071	3.67E+09	0.34	7.43E+06	0.35	5.23	2.024E-03	10.29	0.03
03/12/2013	8	91500_8	493.91	0.0045	0.0020247	0.0045	3.69E+09	0.32	7.46E+06	0.32	5.30	2.024E-03	10.37	0.02
03/12/2013	9	91500_9	494.13	0.0066	0.0020238	0.0066	3.70E+09	0.36	7.49E+06	0.36	4.85	2.024E-03	9.92	0.03
03/12/2013	10	91500_10	494.05	0.0071	0.0020241	0.0071	3.70E+09	0.38	7.48E+06	0.38	5.01	2.024E-03	10.09	0.03
03/12/2013	16	91500_11	494.10	0.0054	0.0020239	0.0054	3.73E+09	0.35	7.55E+06	0.35	4.92	2.024E-03	10.02	0.02
03/12/2013	17	91500_12	494.23	0.0048	0.0020234	0.0048	3.71E+09	0.39	7.50E+06	0.38	4.65	2.024E-03	9.76	0.02
03/12/2013	18	91500_13	494.23	0.0053	0.0020233	0.0053	3.71E+09	0.38	7.51E+06	0.38	4.64	2.024E-03	9.76	0.02
03/12/2013	19	91500_14	494.26	0.0059	0.0020232	0.0059	3.71E+09	0.41	7.50E+06	0.41	4.58	2.024E-03	9.70	0.03
03/12/2013	20	91500_15	494.14	0.0087	0.0020237	0.0087	3.66E+09	0.32	7.42E+06	0.33	4.82	2.024E-03	9.95	0.04
03/12/2013	61	91500_16	494.20	0.0091	0.0020235	0.0091	3.50E+09	0.37	7.08E+06	0.37	10.06	2.024E-03	10.04	0.04
03/12/2013	62	91500_17	494.18	0.0095	0.0020236	0.0095	3.50E+09	0.39	7.07E+06	0.39	10.10	2.024E-03	10.09	0.04
03/12/2013	63	91500_18	494.34	0.0072	0.0020229	0.0072	3.49E+09	0.40	7.06E+06	0.40	9.77	2.024E-03	9.76	0.03
03/12/2013	64	91500_19	494.16	0.0058	0.0020237	0.0058	3.49E+09	0.38	7.06E+06	0.38	10.15	2.024E-03	10.14	0.03
03/12/2013	65	91500_20	494.00	0.0084	0.0020243	0.0084	3.44E+09	0.35	6.96E+06	0.35	10.48	2.024E-03	10.47	0.04
03/12/2013	76	91500_21	494.30	0.0055	0.0020231	0.0055	3.45E+09	0.37	6.98E+06	0.37	9.86	2.023E-03	9.91	0.02
03/12/2013	77	91500_22	494.38	0.0068	0.0020227	0.0068	3.44E+09	0.38	6.96E+06	0.39	9.69	2.023E-03	9.75	0.03
03/12/2013	78	91500_23	494.15	0.0056	0.0020237	0.0056	3.41E+09	0.36	6.89E+06	0.36	10.16	2.023E-03	10.22	0.03
03/12/2013	79	91500_24	494.14	0.0079	0.0020237	0.0079	3.32E+09	0.31	6.71E+06	0.32	10.19	2.023E-03	10.25	0.04
03/12/2013	80	91500_25	494.30	0.0070	0.0020231	0.0070	3.32E+09	0.39	6.72E+06	0.39	9.86	2.023E-03	9.93	0.03
03/12/2013	96	91500_26	494.24	0.0084	0.0020233	0.0084	3.33E+09	0.39	6.74E+06	0.39	9.98	2.023E-03	10.13	0.04
03/12/2013	97	91500_27	494.10	0.0082	0.0020239	0.0082	3.30E+09	0.30	6.68E+06	0.30	10.26	2.023E-03	10.42	0.04
03/12/2013	98	91500_28	494.34	0.0100	0.0020229	0.0100	3.27E+09	0.37	6.62E+06	0.37	9.78	2.023E-03	9.94	0.04
03/12/2013	99	91500_29	494.49	0.0078	0.0020223	0.0078	3.25E+09	0.35	6.58E+06	0.35	9.46	2.023E-03	9.63	0.03
03/12/2013	100	91500_30	494.34	0.0071	0.0020229	0.0071	3.17E+09	0.33	6.42E+06	0.33	9.77	2.023E-03	9.94	0.03
03/12/2013	116	91500_31	494.32	0.0068	0.0020230	0.0068	3.39E+09	0.33	6.86E+06	0.33	9.82	2.023E-03	10.08	0.03
03/12/2013	117	91500_32	494.38	0.0071	0.0020227	0.0071	3.38E+09	0.38	6.84E+06	0.38	9.69	2.023E-03	9.95	0.03
03/12/2013	118	91500_33	494.31	0.0081	0.0020230	0.0081	3.30E+09	0.38	6.68E+06	0.39	9.83	2.023E-03	10.09	0.04
03/12/2013	119	91500_34	494.23	0.0092	0.0020234	0.0092	3.31E+09	0.36	6.69E+06	0.36	10.01	2.023E-03	10.27	0.04
03/12/2013	120	91500_35	494.17	0.0060	0.0020236	0.0060	3.34E+09	0.39	6.76E+06	0.39	10.13	2.023E-03	10.40	0.03
03/12/2013	136	91500_36	494.39	0.0084	0.0020227	0.0084	3.20E+09	0.32	6.48E+06	0.32	9.67	2.023E-03	10.03	0.04
03/12/2013	137	91500_37	494.40	0.0087	0.0020226	0.0087	3.16E+09	0.32	6.39E+06	0.32	9.64	2.023E-03	10.00	0.04
03/12/2013	138	91500_38	494.21	0.0076	0.0020234	0.0076	3.13E+09	0.28	6.34E+06	0.28	10.03	2.023E-03	10.39	0.03
03/12/2013	139	91500_39	494.28	0.0081	0.0020231	0.0081	3.11E+09	0.33	6.29E+06	0.33	9.89	2.023E-03	10.26	0.04
03/12/2013	140	91500_40	494.56	0.0070	0.0020220	0.0070	3.08E+09	0.31	6.23E+06	0.32	9.33	2.023E-03	9.70	0.03

Date	Time	Analysis	$^{16}O/^{18}O$	% s.e.	18/16	% s.e.	16 cps	% s.e.	18 cps	% s.e.	$d^{18}O$ measured	Std at Time	$d^{18}O$ corrected	1 s.d.
04/12/2013	**1**	91500_1	493.90	0.0072	0.0020247	0.0072	3.28E+09	0.41	6.63E+06	0.41	10.17	2.025E-03	**10.13**	**0.03**
04/12/2013	**2**	91500_2	493.96	0.0073	0.0020245	0.0073	3.31E+09	0.42	6.69E+06	0.42	10.06	2.025E-03	**10.02**	**0.03**
04/12/2013	**3**	91500_3	494.09	0.0120	0.0020239	0.0120	3.30E+09	0.43	6.67E+06	0.43	9.79	2.025E-03	**9.75**	**0.05**
04/12/2013	**4**	91500_4	494.06	0.0064	0.0020241	0.0064	3.30E+09	0.44	6.68E+06	0.44	9.86	2.025E-03	**9.82**	**0.03**
04/12/2013	**5**	91500_5	493.93	0.0084	0.0020246	0.0084	3.30E+09	0.44	6.67E+06	0.44	10.11	2.025E-03	**10.08**	**0.04**
04/12/2013	**6**	91500_6	493.91	0.0066	0.0020247	0.0066	3.32E+09	0.41	6.71E+06	0.41	10.17	2.025E-03	**10.13**	**0.03**
04/12/2013	**7**	91500_7	494.05	0.0081	0.0020241	0.0081	3.34E+09	0.43	6.76E+06	0.43	9.88	2.025E-03	**9.85**	**0.04**
04/12/2013	**8**	91500_8	494.14	0.0116	0.0020237	0.0116	3.32E+09	0.41	6.72E+06	0.41	9.69	2.025E-03	**9.65**	**0.05**
04/12/2013	**9**	91500_9	493.97	0.0077	0.0020244	0.0077	3.30E+09	0.44	6.68E+06	0.43	10.03	2.025E-03	**10.00**	**0.03**
04/12/2013	**10**	91500_10	493.84	0.0086	0.0020250	0.0086	3.29E+09	0.41	6.65E+06	0.41	10.31	2.025E-03	**10.27**	**0.04**
04/12/2013	**21**	91500_11	493.88	0.0106	0.0020248	0.0106	3.38E+09	0.43	6.85E+06	0.42	10.21	2.025E-03	**10.18**	**0.05**
04/12/2013	**22**	91500_12	494.03	0.0107	0.0020242	0.0107	3.40E+09	0.44	6.88E+06	0.44	9.92	2.025E-03	**9.89**	**0.05**
04/12/2013	**23**	91500_13	493.90	0.0059	0.0020247	0.0059	3.36E+09	0.44	6.81E+06	0.44	10.19	2.025E-03	**10.16**	**0.03**
04/12/2013	**24**	91500_14	493.90	0.0104	0.0020247	0.0104	3.36E+09	0.45	6.81E+06	0.44	10.19	2.025E-03	**10.16**	**0.05**
04/12/2013	**25**	91500_15	493.80	0.0088	0.0020251	0.0088	3.35E+09	0.44	6.79E+06	0.43	10.38	2.025E-03	**10.35**	**0.04**
04/12/2013	**39**	91500_16	493.88	0.0066	0.0020248	0.0066	3.37E+09	0.43	6.82E+06	0.43	10.23	2.025E-03	**10.21**	**0.03**
04/12/2013	**40**	91500_17	493.84	0.0102	0.0020249	0.0102	3.27E+09	0.45	6.62E+06	0.45	10.30	2.025E-03	**10.28**	**0.05**
04/12/2013	**41**	91500_18	493.99	0.0082	0.0020243	0.0082	3.36E+09	0.47	6.81E+06	0.46	9.99	2.025E-03	**9.97**	**0.04**
04/12/2013	**42**	91500_19	493.96	0.0078	0.0020245	0.0078	3.37E+09	0.42	6.82E+06	0.42	10.06	2.025E-03	**10.04**	**0.03**
04/12/2013	**43**	91500_20	493.95	0.0083	0.0020245	0.0083	3.35E+09	0.44	6.78E+06	0.44	10.08	2.025E-03	**10.06**	**0.04**
04/12/2013	**54**	91500_21	493.69	0.0082	0.0020255	0.0082	3.40E+09	0.42	6.88E+06	0.42	10.60	2.025E-03	**10.59**	**0.04**
04/12/2013	**55**	91500_22	494.00	0.0082	0.0020243	0.0082	3.43E+09	0.45	6.94E+06	0.44	9.97	2.025E-03	**9.96**	**0.04**
04/12/2013	**56**	91500_23	493.83	0.0070	0.0020250	0.0070	3.40E+09	0.45	6.88E+06	0.45	10.32	2.025E-03	**10.30**	**0.03**
04/12/2013	**57**	91500_24	493.85	0.0067	0.0020249	0.0067	3.38E+09	0.43	6.85E+06	0.42	10.29	2.025E-03	**10.27**	**0.03**
04/12/2013	**58**	91500_25	493.70	0.0080	0.0020255	0.0080	3.40E+09	0.41	6.88E+06	0.40	10.59	2.025E-03	**10.58**	**0.04**
04/12/2013	**75**	91500_26	493.97	0.0082	0.0020244	0.0082	3.28E+09	0.43	6.64E+06	0.43	10.03	2.024E-03	**10.03**	**0.04**
04/12/2013	**76**	91500_27	494.00	0.0097	0.0020243	0.0097	3.29E+09	0.44	6.67E+06	0.43	9.98	2.024E-03	**9.98**	**0.04**
04/12/2013	**77**	91500_28	493.91	0.0071	0.0020247	0.0071	3.34E+09	0.45	6.76E+06	0.45	10.16	2.024E-03	**10.15**	**0.03**
04/12/2013	**78**	91500_29	493.96	0.0106	0.0020245	0.0106	3.42E+09	0.48	6.92E+06	0.47	10.06	2.024E-03	**10.06**	**0.05**
04/12/2013	**94**	91500_30	494.14	0.0076	0.0020237	0.0076	3.07E+09	0.40	6.22E+06	0.40	9.70	2.024E-03	**9.70**	**0.03**
04/12/2013	**95**	91500_31	494.09	0.0067	0.0020239	0.0067	3.06E+09	0.44	6.20E+06	0.44	9.80	2.024E-03	**9.80**	**0.03**
04/12/2013	**96**	91500_32	493.90	0.0085	0.0020247	0.0085	3.10E+09	0.42	6.28E+06	0.42	10.18	2.024E-03	**10.18**	**0.04**
04/12/2013	**97**	91500_33	493.99	0.0105	0.0020243	0.0105	3.16E+09	0.43	6.40E+06	0.43	9.99	2.024E-03	**10.00**	**0.05**
04/12/2013	**98**	91500_34	494.21	0.0121	0.0020234	0.0121	3.20E+09	0.45	6.47E+06	0.44	9.54	2.024E-03	**9.55**	**0.05**
04/12/2013	**105**	91500_35	493.93	0.0053	0.0020246	0.0053	3.22E+09	0.43	6.52E+06	0.43	10.12	2.024E-03	**10.13**	**0.02**
04/12/2013	**106**	91500_36	493.88	0.0069	0.0020248	0.0069	3.24E+09	0.44	6.57E+06	0.43	10.21	2.024E-03	**10.22**	**0.03**
04/12/2013	**107**	91500_37	493.97	0.0099	0.0020244	0.0099	3.25E+09	0.43	6.57E+06	0.43	10.05	2.024E-03	**10.05**	**0.04**
04/12/2013	**108**	91500_38	493.90	0.0064	0.0020247	0.0064	3.24E+09	0.44	6.56E+06	0.43	10.17	2.024E-03	**10.18**	**0.03**
04/12/2013	**109**	91500_39	494.00	0.0110	0.0020243	0.0110	3.22E+09	0.42	6.52E+06	0.42	9.98	2.024E-03	**9.99**	**0.05**

Date	Time	Analysis	$^{16}O/^{18}O$	% s.e.	18/16	% s.e.	16 cps	% s.e.	18 cps	% s.e.	$d^{18}O$ measured	Std at Time	$d^{18}O$ corrected	1 s.d.
05/12/2013	**1**	Laura_1	497.48	0.0088	0.0020101	0.0088	3.34E+09	0.53	6.72E+06	0.52	0.19	2.010E-03	**5.24**	**0.04**
05/12/2013	**2**	Laura_2	497.54	0.0090	0.0020099	0.0090	3.34E+09	0.53	6.71E+06	0.53	0.08	2.010E-03	**5.13**	**0.04**
05/12/2013	**3**	Laura_3	497.61	0.0120	0.0020096	0.0120	3.36E+09	0.53	6.74E+06	0.52	-0.07	2.010E-03	**4.99**	**0.05**
05/12/2013	**4**	Laura_4	497.48	0.0107	0.0020102	0.0107	3.32E+09	0.48	6.68E+06	0.47	0.20	2.010E-03	**5.26**	**0.05**
05/12/2013	**5**	Laura_5	497.42	0.0115	0.0020104	0.0115	3.26E+09	0.38	6.56E+06	0.38	0.30	2.010E-03	**5.36**	**0.05**
05/12/2013	**6**	Laura_6	497.50	0.0082	0.0020101	0.0082	3.25E+09	0.52	6.53E+06	0.52	0.16	2.010E-03	**5.22**	**0.04**
05/12/2013	**7**	Laura_7	497.43	0.0104	0.0020103	0.0104	3.25E+09	0.55	6.54E+06	0.54	0.29	2.010E-03	**5.36**	**0.05**
05/12/2013	**8**	Laura_8	497.46	0.0128	0.0020102	0.0128	3.24E+09	0.54	6.51E+06	0.53	0.23	2.010E-03	**5.30**	**0.06**
05/12/2013	**9**	Laura_9	497.47	0.0122	0.0020102	0.0122	3.19E+09	0.52	6.41E+06	0.51	0.20	2.010E-03	**5.27**	**0.05**
05/12/2013	**10**	Laura_10	497.57	0.0134	0.0020098	0.0134	3.21E+09	0.50	6.44E+06	0.49	0.01	2.010E-03	**5.07**	**0.06**
05/12/2013	**21**	Laura_11	497.51	0.0100	0.0020100	0.0100	3.28E+09	0.54	6.59E+06	0.53	5.24	2.010E-03	**5.21**	**0.04**
05/12/2013	**22**	Laura_12	497.50	0.0092	0.0020100	0.0092	3.30E+09	0.54	6.64E+06	0.53	5.25	2.010E-03	**5.22**	**0.04**
05/12/2013	**23**	Laura_13	497.41	0.0084	0.0020104	0.0084	3.26E+09	0.50	6.55E+06	0.49	5.43	2.010E-03	**5.40**	**0.04**
05/12/2013	**24**	Laura_14	497.48	0.0089	0.0020101	0.0089	3.21E+09	0.49	6.45E+06	0.48	5.29	2.010E-03	**5.26**	**0.04**
05/12/2013	**25**	Laura_15	497.40	0.0116	0.0020105	0.0116	3.18E+09	0.54	6.40E+06	0.53	5.46	2.010E-03	**5.43**	**0.05**
05/12/2013	**36**	Laura_16	497.36	0.0090	0.0020106	0.0090	3.09E+09	0.46	6.22E+06	0.46	5.53	2.010E-03	**5.51**	**0.04**
05/12/2013	**37**	Laura_17	497.49	0.0101	0.0020101	0.0101	3.12E+09	0.51	6.27E+06	0.50	5.28	2.010E-03	**5.27**	**0.05**
05/12/2013	**38**	Laura_18	497.35	0.0101	0.0020107	0.0101	3.08E+09	0.53	6.20E+06	0.52	5.55	2.010E-03	**5.54**	**0.05**
05/12/2013	**39**	Laura_19	497.35	0.0087	0.0020107	0.0087	3.10E+09	0.49	6.23E+06	0.48	5.56	2.010E-03	**5.54**	**0.04**
05/12/2013	**56**	Laura_20	497.35	0.0078	0.0020106	0.0078	3.09E+09	0.51	6.22E+06	0.51	5.55	2.010E-03	**5.55**	**0.03**
05/12/2013	**57**	Laura_21	497.38	0.0102	0.0020105	0.0102	3.04E+09	0.50	6.12E+06	0.49	5.50	2.010E-03	**5.50**	**0.05**
05/12/2013	**58**	Laura_22	497.37	0.0128	0.0020106	0.0128	3.01E+09	0.46	6.06E+06	0.45	5.52	2.010E-03	**5.52**	**0.06**
05/12/2013	**59**	Laura_23	497.53	0.0075	0.0020099	0.0075	2.95E+09	0.52	5.93E+06	0.52	5.20	2.010E-03	**5.21**	**0.03**
05/12/2013	**60**	Laura_24	497.44	0.0129	0.0020103	0.0129	2.98E+09	0.54	5.99E+06	0.53	5.37	2.010E-03	**5.38**	**0.06**
05/12/2013	**76**	Laura_25	497.49	0.0112	0.0020101	0.0112	2.90E+09	0.48	5.83E+06	0.47	5.27	2.010E-03	**5.30**	**0.05**
05/12/2013	**77**	Laura_26	497.50	0.0094	0.0020101	0.0094	2.85E+09	0.52	5.73E+06	0.52	5.26	2.010E-03	**5.28**	**0.04**
05/12/2013	**78**	Laura_27	497.52	0.0102	0.0020100	0.0102	2.84E+09	0.54	5.70E+06	0.53	5.22	2.010E-03	**5.25**	**0.05**
05/12/2013	**79**	Laura_28	497.47	0.0102	0.0020102	0.0102	2.86E+09	0.54	5.75E+06	0.53	5.32	2.010E-03	**5.34**	**0.05**
05/12/2013	**95**	Laura_29	497.46	0.0090	0.0020102	0.0090	3.06E+09	0.52	6.14E+06	0.52	5.33	2.010E-03	**5.37**	**0.04**
05/12/2013	**96**	Laura_30	497.63	0.0091	0.0020095	0.0091	3.07E+09	0.53	6.17E+06	0.52	4.99	2.010E-03	**5.03**	**0.04**
05/12/2013	**97**	Laura_31	497.46	0.0110	0.0020102	0.0110	3.07E+09	0.56	6.17E+06	0.56	5.32	2.010E-03	**5.37**	**0.05**
05/12/2013	**98**	Laura_32	497.41	0.0117	0.0020104	0.0117	3.08E+09	0.50	6.19E+06	0.49	5.42	2.010E-03	**5.47**	**0.05**
05/12/2013	**99**	Laura_33	497.52	0.0115	0.0020100	0.0115	3.09E+09	0.50	6.20E+06	0.50	5.22	2.010E-03	**5.27**	**0.05**
05/12/2013	**115**	Laura_34	497.53	0.0090	0.0020099	0.0090	3.24E+09	0.52	6.51E+06	0.52	5.19	2.010E-03	**5.25**	**0.04**
05/12/2013	**116**	Laura_35	497.63	0.0079	0.0020095	0.0079	3.26E+09	0.50	6.55E+06	0.49	4.99	2.010E-03	**5.05**	**0.04**
05/12/2013	**117**	Laura_36	497.62	0.0105	0.0020096	0.0105	3.29E+09	0.52	6.60E+06	0.52	5.02	2.010E-03	**5.08**	**0.05**
05/12/2013	**118**	Laura_37	497.55	0.0106	0.0020098	0.0106	3.21E+09	0.45	6.46E+06	0.45	5.14	2.010E-03	**5.21**	**0.05**
05/12/2013	**119**	Laura_38	497.50	0.0100	0.0020101	0.0100	3.18E+09	0.52	6.39E+06	0.51	5.26	2.010E-03	**5.32**	**0.04**
05/12/2013	**133**	Laura_39	497.51	0.0122	0.0020100	0.0122	3.03E+09	0.53	6.09E+06	0.53	0.13	2.010E-03	**5.32**	**0.05**
05/12/2013	**134**	Laura_40	497.42	0.0087	0.0020104	0.0087	3.03E+09	0.52	6.09E+06	0.51	0.30	2.010E-03	**5.49**	**0.04**
05/12/2013	**135**	Laura_41	497.49	0.0109	0.0020101	0.0109	3.07E+09	0.57	6.17E+06	0.56	0.18	2.010E-03	**5.36**	**0.05**
05/12/2013	**136**	Laura_42	497.58	0.0102	0.0020097	0.0102	3.10E+09	0.54	6.23E+06	0.54	-0.01	2.010E-03	**5.17**	**0.05**
05/12/2013	**137**	Laura_43	497.56	0.0120	0.0020098	0.0120	3.10E+09	0.56	6.24E+06	0.55	0.03	2.010E-03	**5.22**	**0.05**

Date	Time	Analysis	$^{16}O/^{18}O$	% s.e.	18/16	% s.e.	16 cps	% s.e.	18 cps	% s.e.	$d^{18}O$ measured	Std at Time	$d^{18}O$ corrected	1 s.d.
06/12/2013	1	Laura_1	497.45	0.0096	0.0020103	0.0096	2.98E+09	0.53	6.00E+06	0.53	5.43	2.010E-03	**5.32**	**0.04**
06/12/2013	2	Laura_2	497.52	0.0075	0.0020100	0.0075	2.98E+09	0.53	5.99E+06	0.52	5.29	2.010E-03	**5.18**	**0.03**
06/12/2013	3	Laura_3	497.40	0.0060	0.0020105	0.0060	2.94E+09	0.50	5.91E+06	0.50	5.52	2.010E-03	**5.42**	**0.03**
06/12/2013	4	Laura_4	497.49	0.0075	0.0020101	0.0075	2.94E+09	0.50	5.91E+06	0.50	5.35	2.010E-03	**5.25**	**0.03**
06/12/2013	5	Laura_5	497.62	0.0101	0.0020095	0.0101	2.97E+09	0.58	5.96E+06	0.58	5.07	2.010E-03	**4.97**	**0.05**
06/12/2013	6	Laura_6	497.44	0.0120	0.0020103	0.0120	3.01E+09	0.55	6.06E+06	0.54	5.43	2.010E-03	**5.34**	**0.05**
06/12/2013	7	Laura_7	497.50	0.0088	0.0020101	0.0088	3.02E+09	0.54	6.08E+06	0.53	5.33	2.010E-03	**5.23**	**0.04**
06/12/2013	8	Laura_8	497.43	0.0075	0.0020103	0.0075	3.02E+09	0.49	6.07E+06	0.48	5.46	2.010E-03	**5.38**	**0.03**
06/12/2013	9	Laura_9	497.41	0.0109	0.0020104	0.0109	3.06E+09	0.54	6.16E+06	0.54	5.50	2.010E-03	**5.41**	**0.05**
06/12/2013	10	Laura_10	497.55	0.0098	0.0020098	0.0098	3.06E+09	0.51	6.15E+06	0.51	5.21	2.010E-03	**5.13**	**0.04**
06/12/2013	11	Laura_11	497.48	0.0096	0.0020101	0.0096	3.05E+09	0.50	6.13E+06	0.50	5.36	2.010E-03	**5.28**	**0.04**
06/12/2013	12	Laura_12	497.48	0.0085	0.0020101	0.0085	3.02E+09	0.50	6.08E+06	0.50	5.36	2.010E-03	**5.28**	**0.04**
06/12/2013	13	Laura_13	497.45	0.0091	0.0020102	0.0091	3.04E+09	0.52	6.11E+06	0.52	5.41	2.010E-03	**5.34**	**0.04**
06/12/2013	14	Laura_14	497.56	0.0112	0.0020098	0.0112	3.04E+09	0.52	6.11E+06	0.52	5.20	2.010E-03	**5.13**	**0.05**
06/12/2013	15	Laura_15	497.39	0.0092	0.0020105	0.0092	3.01E+09	0.52	6.04E+06	0.51	5.54	2.010E-03	**5.47**	**0.04**
06/12/2013	26	Laura_16	497.46	0.0096	0.0020102	0.0096	2.98E+09	0.53	5.99E+06	0.53	5.41	2.010E-03	**5.36**	**0.04**
06/12/2013	27	Laura_17	497.41	0.0117	0.0020104	0.0117	2.97E+09	0.49	5.98E+06	0.49	5.51	2.010E-03	**5.46**	**0.05**
06/12/2013	28	Laura_18	497.33	0.0079	0.0020107	0.0079	2.96E+09	0.50	5.95E+06	0.49	5.66	2.010E-03	**5.61**	**0.04**
06/12/2013	29	Laura_19	497.41	0.0110	0.0020104	0.0110	2.96E+09	0.50	5.95E+06	0.50	5.51	2.010E-03	**5.46**	**0.05**
06/12/2013	30	Laura_20	497.45	0.0130	0.0020103	0.0130	2.92E+09	0.45	5.86E+06	0.45	5.42	2.010E-03	**5.38**	**0.06**
06/12/2013	41	Laura_21	497.57	0.0104	0.0020098	0.0104	3.01E+09	0.53	6.05E+06	0.52	5.18	2.010E-03	**5.16**	**0.05**
06/12/2013	42	Laura_22	497.56	0.0097	0.0020098	0.0097	2.99E+09	0.51	6.01E+06	0.51	5.19	2.010E-03	**5.18**	**0.04**
06/12/2013	43	Laura_23	497.56	0.0105	0.0020098	0.0105	2.98E+09	0.52	6.00E+06	0.52	5.20	2.010E-03	**5.19**	**0.05**
06/12/2013	44	Laura_24	497.63	0.0076	0.0020095	0.0076	2.93E+09	0.49	5.89E+06	0.48	5.07	2.010E-03	**5.06**	**0.03**
06/12/2013	45	Laura_25	497.51	0.0116	0.0020100	0.0116	2.95E+09	0.56	5.92E+06	0.55	5.29	2.010E-03	**5.28**	**0.05**
06/12/2013	63	Laura_26	497.54	0.0096	0.0020099	0.0096	2.64E+09	0.39	5.31E+06	0.39	5.24	2.010E-03	**5.27**	**0.04**
06/12/2013	64	Laura_27	497.54	0.0111	0.0020099	0.0111	2.54E+09	0.38	5.10E+06	0.38	5.24	2.010E-03	**5.28**	**0.05**
06/12/2013	65	Laura_28	497.58	0.0145	0.0020097	0.0145	2.49E+09	0.46	5.00E+06	0.45	5.15	2.010E-03	**5.19**	**0.06**
06/12/2013	66	Laura_29	497.42	0.0111	0.0020104	0.0111	2.41E+09	0.50	4.84E+06	0.49	5.47	2.010E-03	**5.51**	**0.05**
06/12/2013	67	Laura_30	497.49	0.0092	0.0020101	0.0092	2.39E+09	0.49	4.79E+06	0.49	5.34	2.010E-03	**5.38**	**0.04**
06/12/2013	84	Laura_31	497.55	0.0066	0.0020098	0.0066	2.51E+09	0.54	5.04E+06	0.53	5.22	2.010E-03	**5.30**	**0.03**
06/12/2013	85	Laura_32	497.57	0.0085	0.0020098	0.0085	2.50E+09	0.50	5.02E+06	0.50	5.18	2.010E-03	**5.26**	**0.04**
06/12/2013	86	Laura_33	497.47	0.0140	0.0020102	0.0140	2.49E+09	0.50	5.00E+06	0.49	5.39	2.010E-03	**5.47**	**0.06**
06/12/2013	87	Laura_34	497.46	0.0087	0.0020102	0.0087	2.47E+09	0.49	4.97E+06	0.49	5.40	2.010E-03	**5.49**	**0.04**
06/12/2013	88	Laura_35	497.53	0.0113	0.0020099	0.0113	2.49E+09	0.50	5.00E+06	0.49	5.25	2.010E-03	**5.34**	**0.05**
06/12/2013	106	Laura_36	497.65	0.0093	0.0020095	0.0093	2.53E+09	0.46	5.09E+06	0.46	5.03	2.010E-03	**5.15**	**0.04**
06/12/2013	107	Laura_37	497.57	0.0086	0.0020098	0.0086	2.54E+09	0.49	5.10E+06	0.49	5.19	2.010E-03	**5.31**	**0.04**
06/12/2013	108	Laura_38	497.55	0.0112	0.0020099	0.0112	2.51E+09	0.49	5.04E+06	0.48	5.23	2.010E-03	**5.36**	**0.05**
06/12/2013	110	Laura_39	497.56	0.0100	0.0020098	0.0100	2.50E+09	0.41	5.02E+06	0.40	5.21	2.010E-03	**5.34**	**0.04**
06/12/2013	118	Laura_40	497.64	0.0100	0.0020095	0.0100	2.85E+09	0.58	5.72E+06	0.58	5.05	2.010E-03	**5.20**	**0.04**
06/12/2013	119	Laura_41	497.55	0.0099	0.0020098	0.0099	2.93E+09	0.58	5.90E+06	0.57	5.22	2.010E-03	**5.37**	**0.04**
06/12/2013	120	Laura_42	497.56	0.0064	0.0020098	0.0064	3.13E+09	0.57	6.29E+06	0.57	5.20	2.010E-03	**5.36**	**0.03**
06/12/2013	121	Laura_43	497.66	0.0098	0.0020094	0.0098	3.41E+09	0.65	6.86E+06	0.65	5.00	2.010E-03	**5.16**	**0.04**
06/12/2013	122	Laura_44	497.67	0.0097	0.0020093	0.0097	3.58E+09	0.59	7.20E+06	0.58	4.97	2.010E-03	**5.13**	**0.04**

D.4.9. Hf isotope 91500 standard data

Date	Analysis	$^{176}Hf/^{177}Hf$	2 s.e.	$^{178}Hf/^{177}Hf$	2 s.e.	$^{176}Yb/^{177}Hf$	2 s.e.	$^{176}Lu/^{177}Hf$	2 s.e.	Total Hf	2 s.e.
07/04/2014	91500_1	0.282277	0.000024	1.467155	0.000054	0.011379	0.00039	0.000313	0.000001	10.5	0.20
07/04/2014	91500_2	0.282307	0.000020	1.467234	0.000048	0.011603	0.00038	0.000309	0.000001	10.7	0.18
07/04/2014	91500_3	0.282277	0.000018	1.467257	0.000036	0.011633	0.00038	0.000309	0.000001	10.8	0.20
07/04/2014	91500_4	0.282295	0.000022	1.467234	0.000044	0.010721	0.00027	0.000310	0.000002	9.11	0.24
07/04/2014	91500_5	0.282305	0.000022	1.467254	0.000064	0.010691	0.00027	0.000312	0.000001	9.45	0.22
07/04/2014	91500_6	0.282330	0.000016	1.467268	0.000056	0.010784	0.00014	0.000319	0.000004	10.0	0.29
07/04/2014	91500_7	0.282310	0.000021	1.467254	0.000044	0.009746	0.00031	0.000282	0.000000	10.3	0.18
07/04/2014	91500_8	0.282311	0.000023	1.467270	0.000065	0.010068	0.00020	0.000301	0.000001	10.1	0.30
07/04/2014	91500_9	0.282297	0.000023	1.467229	0.000043	0.012070	0.00025	0.000360	0.000002	8.96	0.23
07/04/2014	91500_10	0.282276	0.000022	1.467235	0.000055	0.010983	0.00014	0.000326	0.000005	9.09	0.27
07/04/2014	91500_11	0.282294	0.000022	1.467267	0.000033	0.012163	0.00031	0.000357	0.000001	9.00	0.21
07/04/2014	91500_12	0.282305	0.000022	1.467264	0.000054	0.012254	0.00034	0.000354	0.000002	8.79	0.06
07/04/2014	91500_13	0.282316	0.000029	1.467288	0.000056	0.011833	0.00029	0.000357	0.000002	8.89	0.19
07/04/2014	91500_14	0.282284	0.000019	1.467246	0.000055	0.012079	0.00031	0.000361	0.000002	8.94	0.10

Date	Analysis	$^{176}Hf/^{177}Hf$	2 s.e.	$^{178}Hf/^{177}Hf$	2 s.e.	$^{176}Yb/^{177}Hf$	2 s.e.	$^{176}Lu/^{177}Hf$	2 s.e.	Total Hf	2 s.e.
08/04/2014	91500_1	0.282324	0.000017	1.467251	0.000052	0.012290	0.00024	0.000348	0.000004	9.89	0.30
08/04/2014	91500_2	0.282279	0.000026	1.467238	0.000042	0.009507	0.00022	0.000270	0.000002	10.3	0.26
08/04/2014	91500_3	0.282294	0.000022	1.467235	0.000042	0.010724	0.00026	0.000303	0.000001	10.4	0.21
08/04/2014	91500_4	0.282292	0.000019	1.467236	0.000059	0.011002	0.00025	0.000314	0.000001	10.2	0.25
08/04/2014	91500_5	0.282285	0.000017	1.467249	0.000042	0.011058	0.00027	0.000311	0.000001	10.7	0.18
08/04/2014	91500_6	0.282306	0.000019	1.467207	0.000041	0.012859	0.00040	0.000369	0.000002	9.82	0.30
08/04/2014	91500_7	0.282308	0.000024	1.467251	0.000053	0.012658	0.00031	0.000361	0.000001	10.0	0.34
08/04/2014	91500_8	0.282314	0.000025	1.467284	0.000044	0.012126	0.00019	0.000356	0.000001	10.0	0.34
08/04/2014	91500_9	0.282283	0.000018	1.467211	0.000043	0.012110	0.00033	0.000352	0.000001	9.63	0.24
08/04/2014	91500_10	0.282317	0.000019	1.467251	0.000055	0.012045	0.00020	0.000348	0.000000	9.81	0.28
08/04/2014	91500_11	0.282316	0.000019	1.467217	0.000054	0.011511	0.00022	0.000336	0.000001	9.88	0.26
08/04/2014	91500_12	0.282283	0.000018	1.467211	0.000043	0.012110	0.00033	0.000352	0.000001	9.63	0.24
08/04/2014	91500_13	0.282317	0.000019	1.467251	0.000055	0.012045	0.00020	0.000348	0.000000	9.81	0.28
08/04/2014	91500_14	0.282316	0.000019	1.467217	0.000054	0.011511	0.00022	0.000336	0.000001	9.88	0.26
08/04/2014	91500_15	0.282294	0.000023	1.467213	0.000049	0.011826	0.00032	0.000338	0.000000	10.5	0.18
08/04/2014	91500_16	0.282306	0.000021	1.467216	0.000045	0.012060	0.00032	0.000336	0.000001	10.5	0.14
08/04/2014	91500_17	0.282279	0.000022	1.467266	0.000046	0.011856	0.00029	0.000336	0.000001	10.5	0.17
08/04/2014	91500_18	0.282287	0.000031	1.467230	0.000058	0.011677	0.00028	0.000347	0.000001	8.85	0.06
08/04/2014	91500_19	0.282280	0.000020	1.467202	0.000042	0.012128	0.00029	0.000358	0.000002	8.73	0.06
08/04/2014	91500_20	0.282298	0.000022	1.467201	0.000060	0.010879	0.00011	0.000320	0.000005	9.02	0.06
08/04/2014	91500_21	0.282291	0.000026	1.467240	0.000044	0.009934	0.00032	0.000292	0.000001	9.35	0.08
08/04/2014	91500_22	0.282284	0.000017	1.467290	0.000053	0.010421	0.00026	0.000307	0.000001	9.26	0.09
08/04/2014	91500_23	0.282290	0.000023	1.467205	0.000050	0.010566	0.00024	0.000310	0.000002	9.36	0.08
08/04/2014	91500_24	0.282302	0.000027	1.467241	0.000044	0.012389	0.00026	0.000362	0.000002	9.46	0.06
08/04/2014	91500_25	0.282292	0.000028	1.467321	0.000065	0.008522	0.00027	0.000254	0.000001	9.49	0.09
08/04/2014	91500_26	0.282272	0.000024	1.467275	0.000040	0.010114	0.00023	0.000300	0.000001	9.52	0.10
08/04/2014	91500_27	0.282299	0.000019	1.467239	0.000064	0.009992	0.00023	0.000294	0.000000	9.94	0.14
08/04/2014	91500_28	0.282299	0.000026	1.467231	0.000041	0.009794	0.00020	0.000290	0.000000	9.98	0.21
08/04/2014	91500_29	0.282317	0.000018	1.467264	0.000047	0.009876	0.00018	0.000291	0.000000	9.93	0.20
08/04/2014	91500_30	0.282294	0.000025	1.467306	0.000047	0.011802	0.00025	0.000350	0.000001	9.29	0.07
08/04/2014	91500_31	0.282274	0.000026	1.467258	0.000048	0.011336	0.00025	0.000336	0.000002	9.33	0.11
08/04/2014	91500_32	0.282308	0.000020	1.467288	0.000060	0.009883	0.00018	0.000291	0.000002	9.62	0.08

Date	Analysis	$^{176}Hf/^{177}Hf$	2 s.e.	$^{178}Hf/^{177}Hf$	2 s.e.	$^{176}Yb/^{177}Hf$	2 s.e.	$^{176}Lu/^{177}Hf$	2 s.e.	Total Hf	2 s.e.
09/04/2014	91500_1	0.282283	0.000021	1.467251	0.000054	0.011611	0.00025	0.000333	0.000001	9.48	0.36
09/04/2014	91500_2	0.282311	0.000019	1.467136	0.000042	0.010093	0.00023	0.000290	0.000001	9.47	0.35
09/04/2014	91500_3	0.282301	0.000022	1.467255	0.000057	0.010863	0.00017	0.000315	0.000001	9.48	0.34
09/04/2014	91500_4	0.282291	0.000029	1.467248	0.000059	0.011051	0.00020	0.000317	0.000000	9.60	0.32
09/04/2014	91500_5	0.282301	0.000031	1.467207	0.000070	0.012210	0.00023	0.000357	0.000001	8.35	0.17
09/04/2014	91500_6	0.282301	0.000025	1.467250	0.000038	0.011633	0.00009	0.000341	0.000003	8.36	0.15
09/04/2014	91500_7	0.282287	0.000020	1.467129	0.000046	0.008540	0.00021	0.000253	0.000002	8.57	0.14
09/04/2014	91500_8	0.282291	0.000017	1.467168	0.000056	0.011886	0.00023	0.000338	0.000001	10.0	0.29
09/04/2014	91500_9	0.282311	0.000019	1.467290	0.000054	0.011018	0.00026	0.000314	0.000002	10.1	0.23
09/04/2014	91500_10	0.282296	0.000019	1.467241	0.000048	0.010620	0.00017	0.000304	0.000001	10.0	0.29
09/04/2014	91500_11	0.282267	0.000021	1.467256	0.000041	0.010490	0.00005	0.000310	0.000004	8.75	0.29
09/04/2014	91500_12	0.282314	0.000028	1.467215	0.000056	0.010027	0.00013	0.000297	0.000000	8.97	0.29
09/04/2014	91500_13	0.282293	0.000023	1.467247	0.000066	0.010329	0.00011	0.000308	0.000000	9.02	0.28
09/04/2014	91500_14	0.282290	0.000025	1.467225	0.000061	0.010380	0.00013	0.000305	0.000000	9.65	0.31
09/04/2014	91500_15	0.282286	0.000030	1.467250	0.000070	0.010318	0.00013	0.000304	0.000000	9.63	0.33
09/04/2014	91500_16	0.282291	0.000020	1.467218	0.000068	0.010514	0.00013	0.000307	0.000000	9.51	0.31
09/04/2014	91500_17	0.282298	0.000026	1.467230	0.000068	0.010548	0.00008	0.000315	0.000001	8.66	0.27
09/04/2014	91500_18	0.282281	0.000028	1.467251	0.000062	0.010535	0.00009	0.000316	0.000001	8.66	0.23
09/04/2014	91500_19	0.282300	0.000023	1.467290	0.000074	0.010488	0.00010	0.000316	0.000001	8.72	0.22
09/04/2014	91500_20	0.282303	0.000030	1.467239	0.000056	0.010437	0.00014	0.000309	0.000000	8.51	0.12
09/04/2014	91500_21	0.282312	0.000028	1.467265	0.000054	0.010417	0.00016	0.000310	0.000000	8.37	0.12
09/04/2014	91500_22	0.282269	0.000023	1.467252	0.000063	0.010376	0.00018	0.000311	0.000000	8.31	0.10

Date	Analysis	$^{176}Hf/^{177}Hf$	2 s.e.	$^{178}Hf/^{177}Hf$	2 s.e.	$^{176}Yb/^{177}Hf$	2 s.e.	$^{176}Lu/^{177}Hf$	2 s.e.	Total Hf	2 s.e.
17/07/2014	91500_1	0.282279	0.000015	1.467236	0.000054	0.009036	0.00009	0.000312	0.000003	11.1	0.29
17/07/2014	91500_2	0.282311	0.000019	1.467230	0.000040	0.008638	0.00013	0.000298	0.000004	11.6	0.32
17/07/2014	91500_3	0.282296	0.000014	1.467283	0.000032	0.008615	0.00015	0.000298	0.000006	11.7	0.31
17/07/2014	91500_4	0.282308	0.000018	1.467275	0.000045	0.008795	0.00008	0.000303	0.000002	11.5	0.30
17/07/2014	91500_5	0.282289	0.000015	1.467250	0.000045	0.008818	0.00008	0.000301	0.000003	11.8	0.35
17/07/2014	91500_6	0.282286	0.000027	1.467201	0.000056	0.008493	0.00020	0.000294	0.000005	12.2	0.38
17/07/2014	91500_7	0.282297	0.000027	1.467279	0.000052	0.008468	0.00024	0.000288	0.000008	12.1	0.27
17/07/2014	91500_8	0.282301	0.000019	1.467250	0.000057	0.008438	0.00020	0.000292	0.000006	12.2	0.29
17/07/2014	91500_9	0.282289	0.000019	1.467306	0.000085	0.008519	0.00027	0.000293	0.000010	12.1	0.29
17/07/2014	91500_10	0.282284	0.000024	1.467147	0.000135	0.008358	0.00024	0.000293	0.000006	12.0	0.35
17/07/2014	91500_11	0.282285	0.000020	1.467262	0.000060	0.008647	0.00019	0.000296	0.000005	12.6	0.36
17/07/2014	91500_12	0.282280	0.000022	1.467283	0.000041	0.008794	0.00013	0.000295	0.000004	12.8	0.39
17/07/2014	91500_13	0.282303	0.000020	1.467230	0.000050	0.009067	0.00011	0.000301	0.000003	10.6	0.31
17/07/2014	91500_14	0.282288	0.000015	1.467215	0.000042	0.008753	0.00008	0.000299	0.000002	12.2	0.33
17/07/2014	91500_15	0.282286	0.000019	1.467277	0.000058	0.008765	0.00008	0.000302	0.000002	11.6	0.29
17/07/2014	91500_16	0.282295	0.000021	1.467286	0.000050	0.008769	0.00020	0.000297	0.000003	11.7	0.41
17/07/2014	91500_17	0.282285	0.000025	1.467249	0.000051	0.008515	0.00023	0.000288	0.000007	13.0	0.35
17/07/2014	91500_18	0.282298	0.000020	1.467215	0.000040	0.008508	0.00026	0.000292	0.000010	12.4	0.29
17/07/2014	91500_19	0.282286	0.000020	1.467199	0.000048	0.008585	0.00022	0.000295	0.000008	12.5	0.26

Date	Analysis	$^{176}Hf/^{177}Hf$	2 s.e.	$^{178}Hf/^{177}Hf$	2 s.e.	$^{176}Yb/^{177}Hf$	2 s.e.	$^{176}Lu/^{177}Hf$	2 s.e.	Total Hf	2 s.e.
08/12/2014	91500_1	0.282299	0.000024	-	-	-	-	0.000311	0.000000	-	-
08/12/2014	91500_2	0.282309	0.000023	-	-	-	-	0.000311	0.000001	-	-
08/12/2014	91500_3	0.282320	0.000020	-	-	-	-	0.000311	0.000001	-	-
08/12/2014	91500_4	0.282286	0.000021	-	-	-	-	0.000311	0.000001	-	-
08/12/2014	91500_5	0.282316	0.000021	-	-	-	-	0.000311	0.000001	-	-
08/12/2014	91500_6	0.282303	0.000028	-	-	-	-	0.000311	0.000000	-	-
08/12/2014	91500_7	0.282298	0.000023	-	-	-	-	0.000311	0.000001	-	-
08/12/2014	91500_8	0.282304	0.000026	-	-	-	-	0.000311	0.000001	-	-
08/12/2014	91500_9	0.282324	0.000022	-	-	-	-	0.000311	0.000000	-	-
08/12/2014	91500_10	0.282298	0.000023	-	-	-	-	0.000311	0.000000	-	-
08/12/2014	91500_11	0.282308	0.000021	-	-	-	-	0.000311	0.000001	-	-
08/12/2014	91500_12	0.282299	0.000027	-	-	-	-	0.000311	0.000001	-	-

D.4.10. Hf isotope Plešovice standard data

Date	Analysis	$^{176}Hf/^{177}Hf$	2 s.e.	$^{178}Hf/^{177}Hf$	2 s.e.	$^{176}Yb/^{177}Hf$	2 s.e.	$^{176}Lu/^{177}Hf$	2 s.e.	Total Hf	2 s.e.
07/04/2014	Plesovice	0.282489	0.000016	1.467231	0.000041	0.007148	0.00018	0.000134	0.000001	18.4	0.51
07/04/2014	Plesovice	0.282463	0.000012	1.467234	0.000039	0.006715	0.00024	0.000126	0.000001	18.6	0.53
07/04/2014	Plesovice	0.282479	0.000017	1.467202	0.000046	0.007608	0.00011	0.000143	0.000001	17.8	0.31
07/04/2014	Plesovice	0.282485	0.000013	1.467229	0.000043	0.006392	0.00022	0.000124	0.000000	19.8	0.41
07/04/2014	Plesovice	0.282468	0.000016	1.467231	0.000027	0.005308	0.00014	0.000107	0.000000	18.9	0.45
07/04/2014	Plesovice	0.282477	0.000012	1.467210	0.000032	0.006454	0.00009	0.000127	0.000001	17.6	0.55
07/04/2014	Plesovice	0.282484	0.000016	1.467285	0.000037	0.005369	0.00019	0.000104	0.000000	17.2	0.43
07/04/2014	Plesovice	0.282473	0.000018	1.467226	0.000039	0.005165	0.00014	0.000101	0.000000	17.2	0.49

Date	Analysis	$^{176}Hf/^{177}Hf$	2 s.e.	$^{178}Hf/^{177}Hf$	2 s.e.	$^{176}Yb/^{177}Hf$	2 s.e.	$^{176}Lu/^{177}Hf$	2 s.e.	Total Hf	2 s.e.
08/04/2014	Plesovice	0.282481	0.000013	1.467242	0.000040	0.004807	0.00013	0.000091	0.000000	19.6	0.64
08/04/2014	Plesovice	0.282474	0.000011	1.467265	0.000028	0.005614	0.00007	0.000110	0.000001	19.8	0.86
08/04/2014	Plesovice	0.282475	0.000017	1.467233	0.000031	0.007415	0.00010	0.000144	0.000001	19.8	0.91
08/04/2014	Plesovice	0.282479	0.000014	1.467287	0.000051	0.007048	0.00007	0.000136	0.000001	19.5	0.89
08/04/2014	Plesovice	0.282462	0.000020	1.467280	0.000035	0.006516	0.00008	0.000123	0.000001	19.4	0.88
08/04/2014	Plesovice	0.282470	0.000017	1.467251	0.000041	0.006568	0.00012	0.000125	0.000000	18.9	0.42
08/04/2014	Plesovice	0.282455	0.000013	1.467214	0.000034	0.007168	0.00008	0.000136	0.000001	19.0	0.55
08/04/2014	Plesovice	0.282470	0.000017	1.467252	0.000030	0.006988	0.00010	0.000134	0.000001	19.2	0.55
08/04/2014	Plesovice	0.282479	0.000016	1.467265	0.000032	0.007132	0.00013	0.000137	0.000001	20.8	0.66
08/04/2014	Plesovice	0.282470	0.000012	1.467259	0.000031	0.007430	0.00010	0.000144	0.000001	21.0	0.69
08/04/2014	Plesovice	0.282465	0.000013	1.467214	0.000037	0.007335	0.00009	0.000141	0.000001	20.4	0.63
08/04/2014	Plesovice	0.282474	0.000017	1.467198	0.000037	0.006522	0.00012	0.000127	0.000000	18.9	0.45
08/04/2014	Plesovice	0.282469	0.000016	1.467206	0.000037	0.005997	0.00012	0.000119	0.000000	19.0	0.51
08/04/2014	Plesovice	0.282481	0.000015	1.467259	0.000035	0.004845	0.00009	0.000095	0.000001	18.1	0.39
08/04/2014	Plesovice	0.282472	0.000014	1.467264	0.000035	0.007046	0.00009	0.000135	0.000001	19.8	0.70
08/04/2014	Plesovice	0.282462	0.000015	1.467234	0.000036	0.006816	0.00009	0.000134	0.000000	19.7	0.70
08/04/2014	Plesovice	0.282501	0.000012	1.467232	0.000031	0.007003	0.00010	0.000139	0.000001	20.1	0.57

Date	Analysis	$^{176}Hf/^{177}Hf$	2 s.e.	$^{178}Hf/^{177}Hf$	2 s.e.	$^{176}Yb/^{177}Hf$	2 s.e.	$^{176}Lu/^{177}Hf$	2 s.e.	Total Hf	2 s.e.
09/04/2014	Plesovice	0.282477	0.000020	1.467282	0.000038	0.006367	0.00007	0.000124	0.000000	18.1	0.71
09/04/2014	Plesovice	0.282459	0.000012	1.467272	0.000039	0.006650	0.00002	0.000129	0.000001	18.3	0.62
09/04/2014	Plesovice	0.282476	0.000014	1.467204	0.000036	0.006045	0.00003	0.000118	0.000000	18.8	0.68
09/04/2014	Plesovice	0.282480	0.000013	1.467245	0.000038	0.006412	0.00002	0.000123	0.000000	18.5	0.69
09/04/2014	Plesovice	0.282478	0.000016	1.467235	0.000026	0.005052	0.00008	0.000100	0.000000	17.5	0.55
09/04/2014	Plesovice	0.282475	0.000012	1.467247	0.000032	0.004799	0.00009	0.000095	0.000000	17.4	0.45
09/04/2014	Plesovice	0.282460	0.000014	1.467232	0.000025	0.004910	0.00004	0.000098	0.000001	17.7	0.60
09/04/2014	Plesovice	0.282454	0.000015	1.467211	0.000037	0.006131	0.00004	0.000121	0.000000	18.8	0.69
09/04/2014	Plesovice	0.282471	0.000019	1.467266	0.000051	0.006307	0.00004	0.000125	0.000000	19.0	0.61
09/04/2014	Plesovice	0.282478	0.000017	1.467280	0.000038	0.005984	0.00002	0.000118	0.000001	19.1	0.69
09/04/2014	Plesovice	0.282470	0.000013	1.467235	0.000037	0.006578	0.00009	0.000131	0.000001	19.9	0.78
09/04/2014	Plesovice	0.282482	0.000016	1.467235	0.000038	0.006024	0.00007	0.000120	0.000000	20.2	0.85
09/04/2014	Plesovice	0.282465	0.000012	1.467250	0.000038	0.005706	0.00004	0.000113	0.000000	20.1	0.77

Date	Analysis	$^{176}Hf/^{177}Hf$	2 s.e.	$^{178}Hf/^{177}Hf$	2 s.e.	$^{176}Yb/^{177}Hf$	2 s.e.	$^{176}Lu/^{177}Hf$	2 s.e.	Total Hf	2 s.e.
17/07/2014	Plesovice	0.282471	0.000015	1.467250	0.000028	0.005440	0.00010	0.000129	0.000002	22.4	0.44
17/07/2014	Plesovice	0.282469	0.000010	1.467247	0.000031	0.005550	0.00010	0.000131	0.000002	23.3	0.52
17/07/2014	Plesovice	0.282469	0.000012	1.467308	0.000031	0.005713	0.00009	0.000134	0.000002	23.2	0.49
17/07/2014	Plesovice	0.282462	0.000017	1.467304	0.000033	0.006014	0.00010	0.000141	0.000002	23.2	0.53
17/07/2014	Plesovice	0.282472	0.000013	1.467244	0.000029	0.006961	0.00012	0.000160	0.000003	23.1	0.55
17/07/2014	Plesovice	0.282463	0.000016	1.467230	0.000034	0.006879	0.00009	0.000159	0.000002	23.1	0.59
17/07/2014	Plesovice	0.282466	0.000017	1.467272	0.000044	0.006044	0.00010	0.000139	0.000002	23.5	0.51
17/07/2014	Plesovice	0.282447	0.000020	1.467271	0.000042	0.005838	0.00011	0.000135	0.000002	23.8	0.50
17/07/2014	Plesovice	0.282465	0.000017	1.467282	0.000035	0.005773	0.00014	0.000132	0.000002	22.9	0.56
17/07/2014	Plesovice	0.282477	0.000013	1.467277	0.000037	0.006758	0.00022	0.000156	0.000005	23.3	0.69

Appendix E

Cathodoluminescence images of zircons

E.1. Key

Red circles denote 10 µm SIMS spots for oxygen isotope analysis. Yellow circles denote 20 µm LA-MC-ICP-MS spots for U-Pb dating. Blue circles denote 35 µm LA-MC-ICP-MS spots for Lu-Hf isotope analysis. Red numbers indicate the analysis number for all analyses on the same spot. A scale bar is provided in every image.

E.2. 1D01

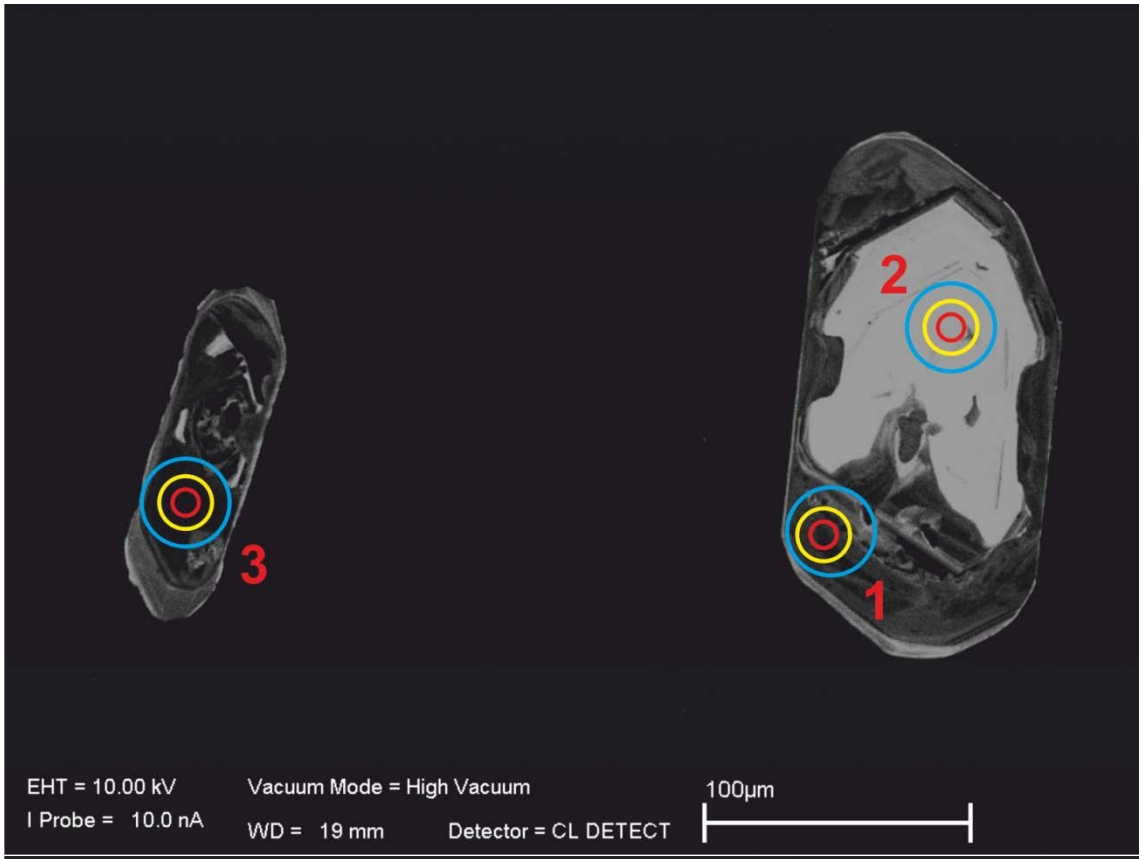
2
3
1
EHT = 10.00 kV
I Probe = 10.0 nA
Vacuum Mode = High Vacuum
WD = 19 mm
Detector = CL DETECT
100µm

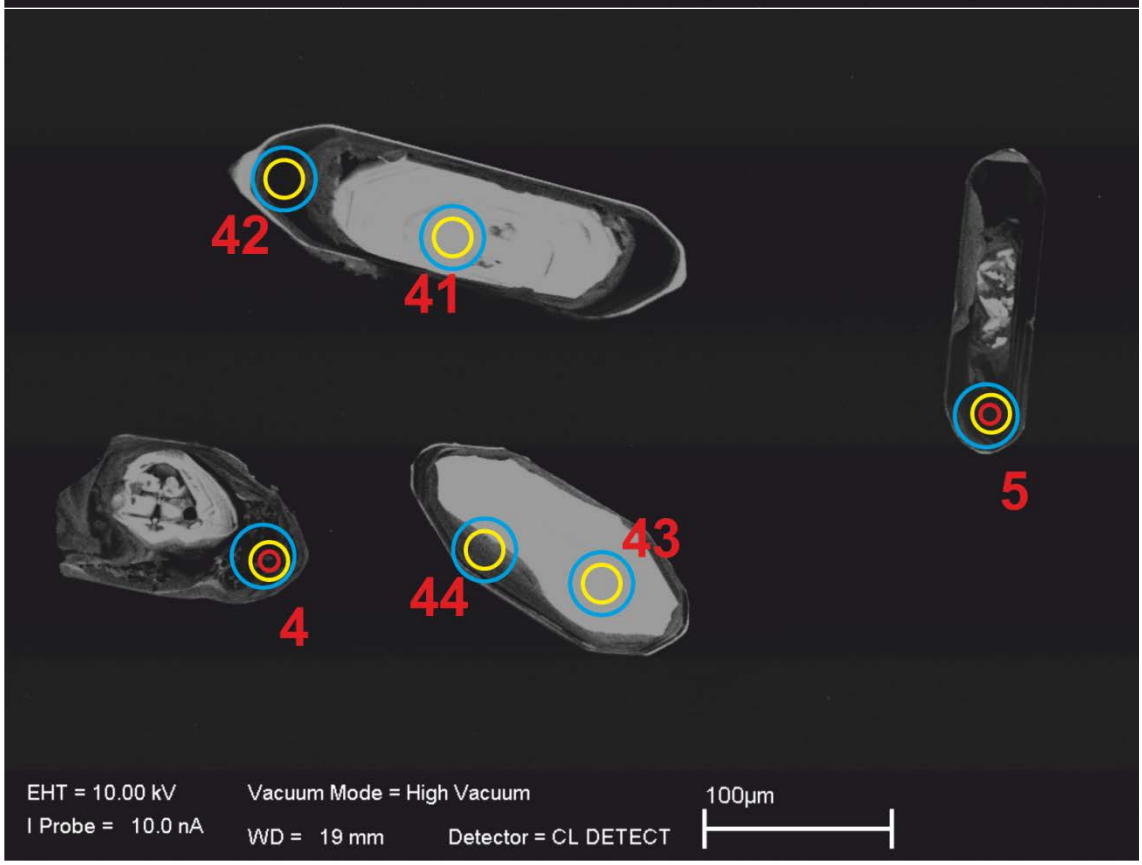
42
41
5
4
44
43
EHT = 10.00 kV
I Probe = 10.0 nA
Vacuum Mode = High Vacuum
WD = 19 mm
Detector = CL DETECT
100µm


6
7
45
EHT = 10.00 kV
I Probe = 10.0 nA
Vacuum Mode = High Vacuum
WD = 19 mm
Detector = CL DETECT
100µm
8
10
9
EHT = 10.00 kV
I Probe = 10.0 nA
Vacuum Mode = High Vacuum
WD = 19 mm
Detector = CL DETECT
100µm

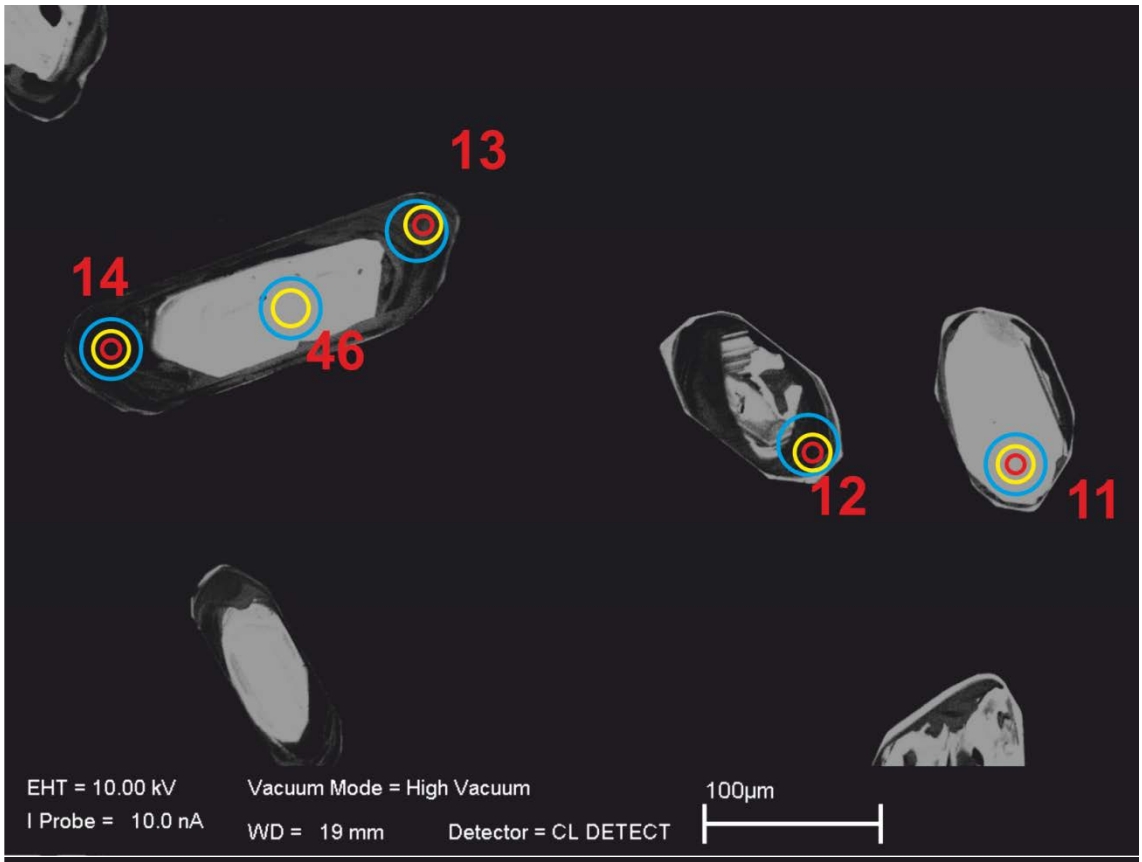
13
14
46
12
11
EHT = 10.00 kV
I Probe = 10.0 nA
Vacuum Mode = High Vacuum
WD = 19 mm
Detector = CL DETECT
100µm

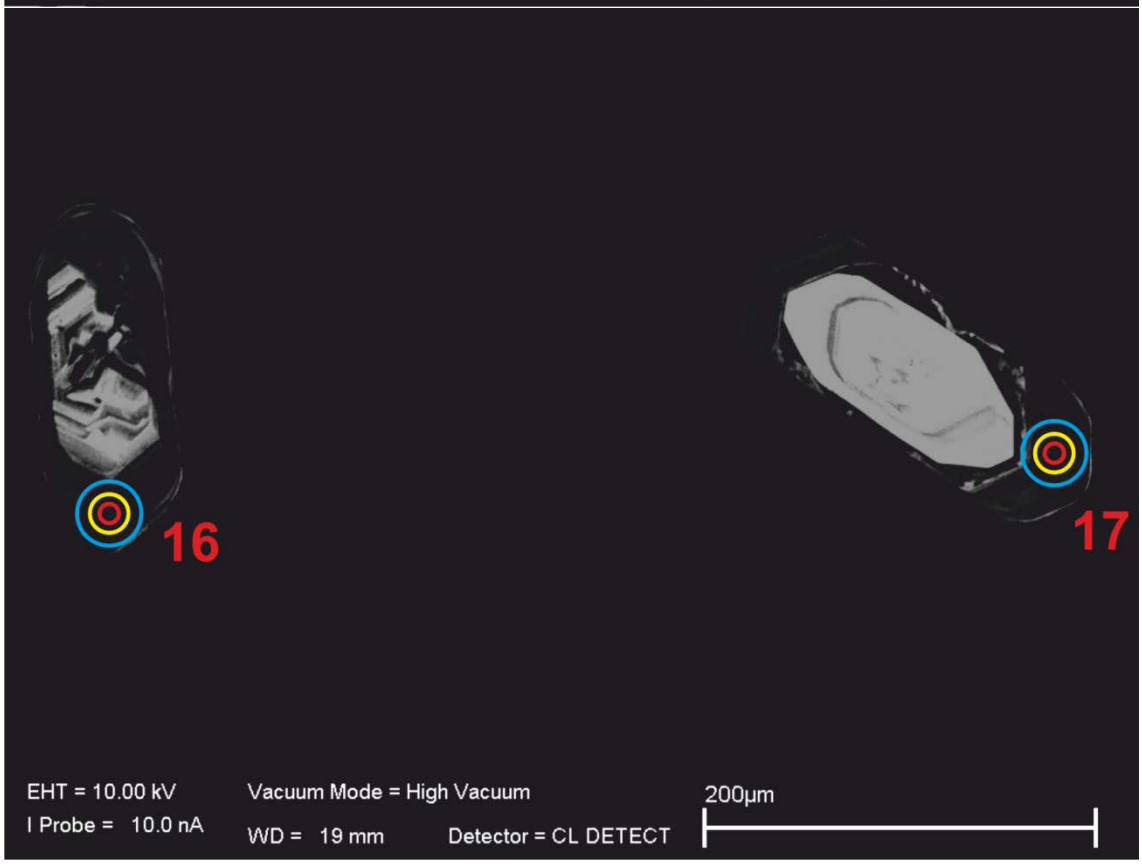
16
17
EHT = 10.00 kV
I Probe = 10.0 nA
Vacuum Mode = High Vacuum
WD = 19 mm
Detector = CL DETECT
200µm

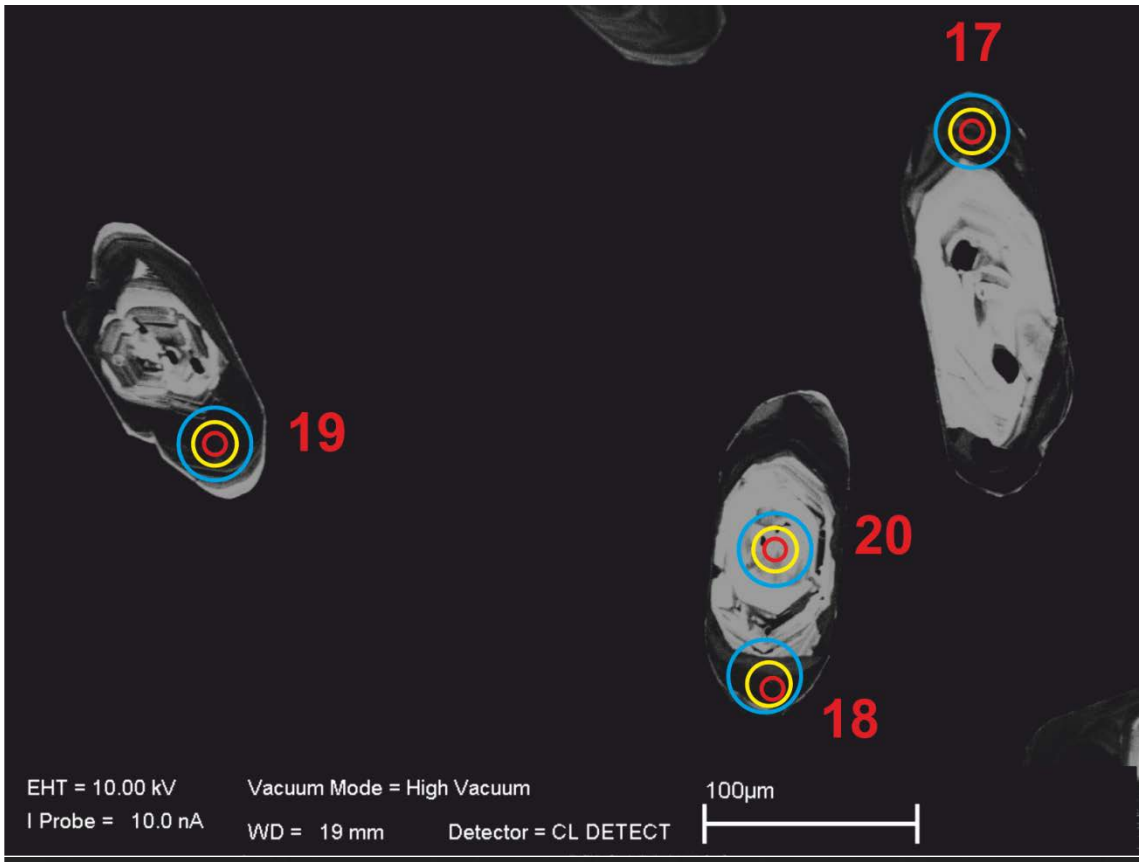
17
19
20
18
EHT = 10.00 kV
I Probe = 10.0 nA
Vacuum Mode = High Vacuum
WD = 19 mm
Detector = CL DETECT
100µm

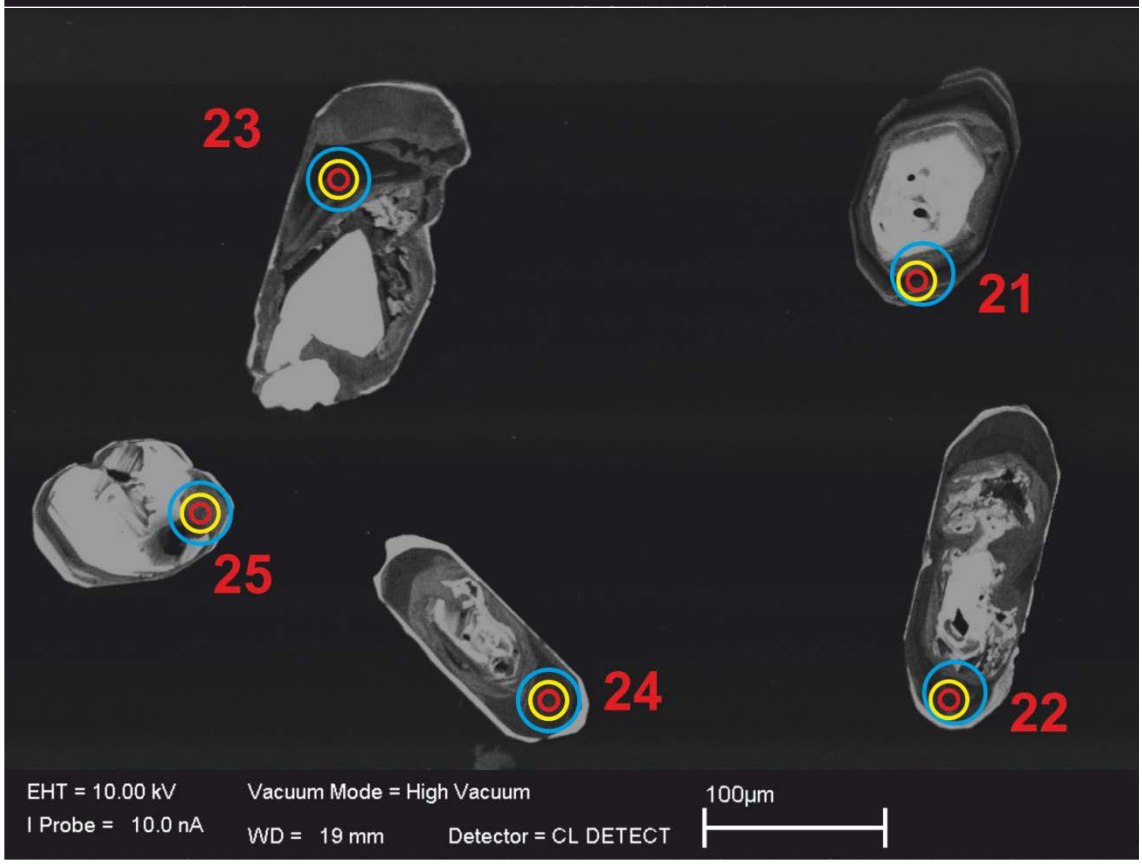
23
21
25
24
22
EHT = 10.00 kV
I Probe = 10.0 nA
Vacuum Mode = High Vacuum
WD = 19 mm
Detector = CL DETECT
100µm

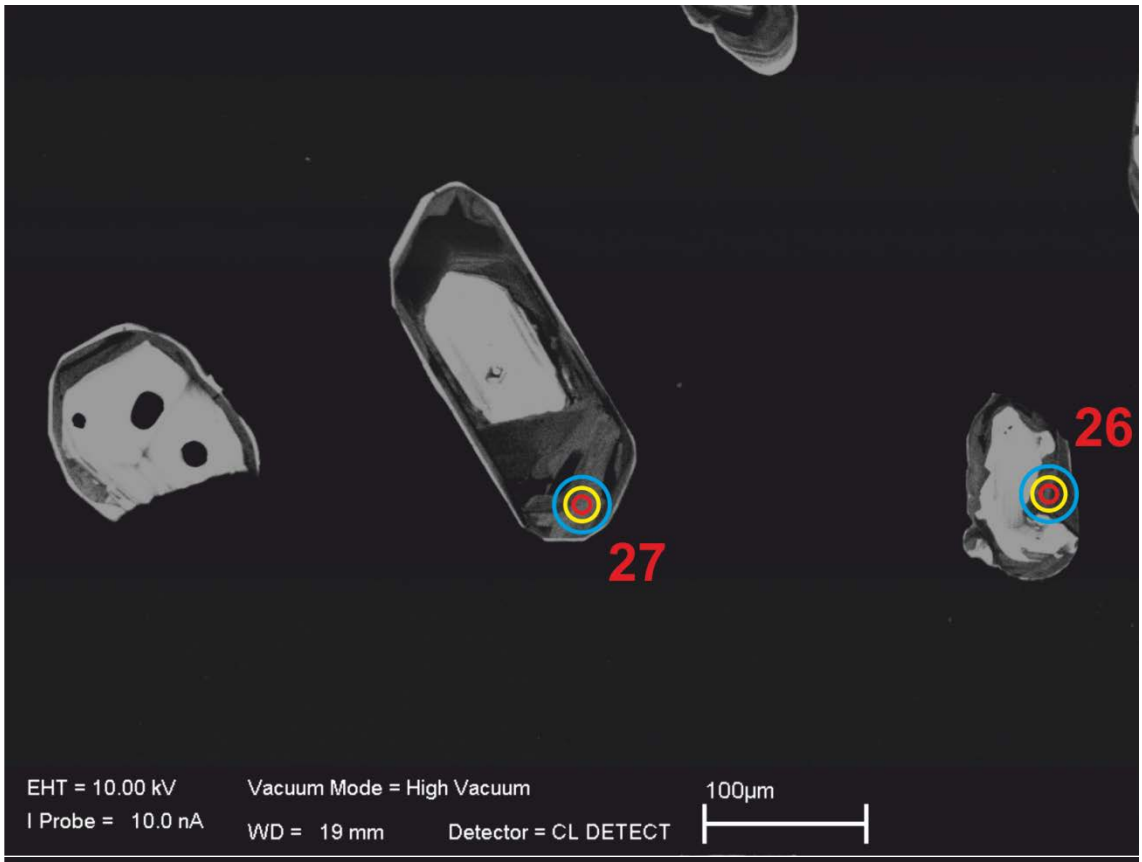
26
27
EHT = 10.00 kV
I Probe = 10.0 nA
Vacuum Mode = High Vacuum
WD = 19 mm
Detector = CL DETECT
100µm

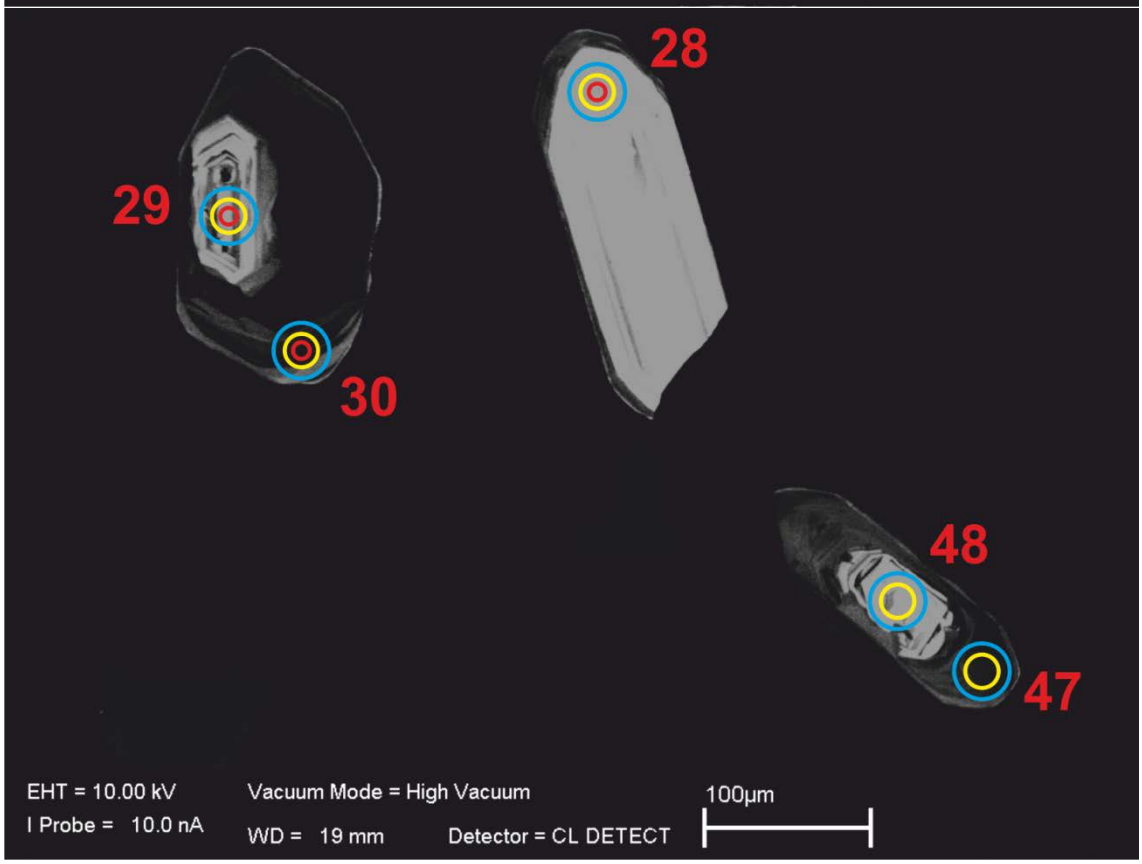
28
29
30
48
47
EHT = 10.00 kV
I Probe = 10.0 nA
Vacuum Mode = High Vacuum
WD = 19 mm
Detector = CL DETECT
100µm

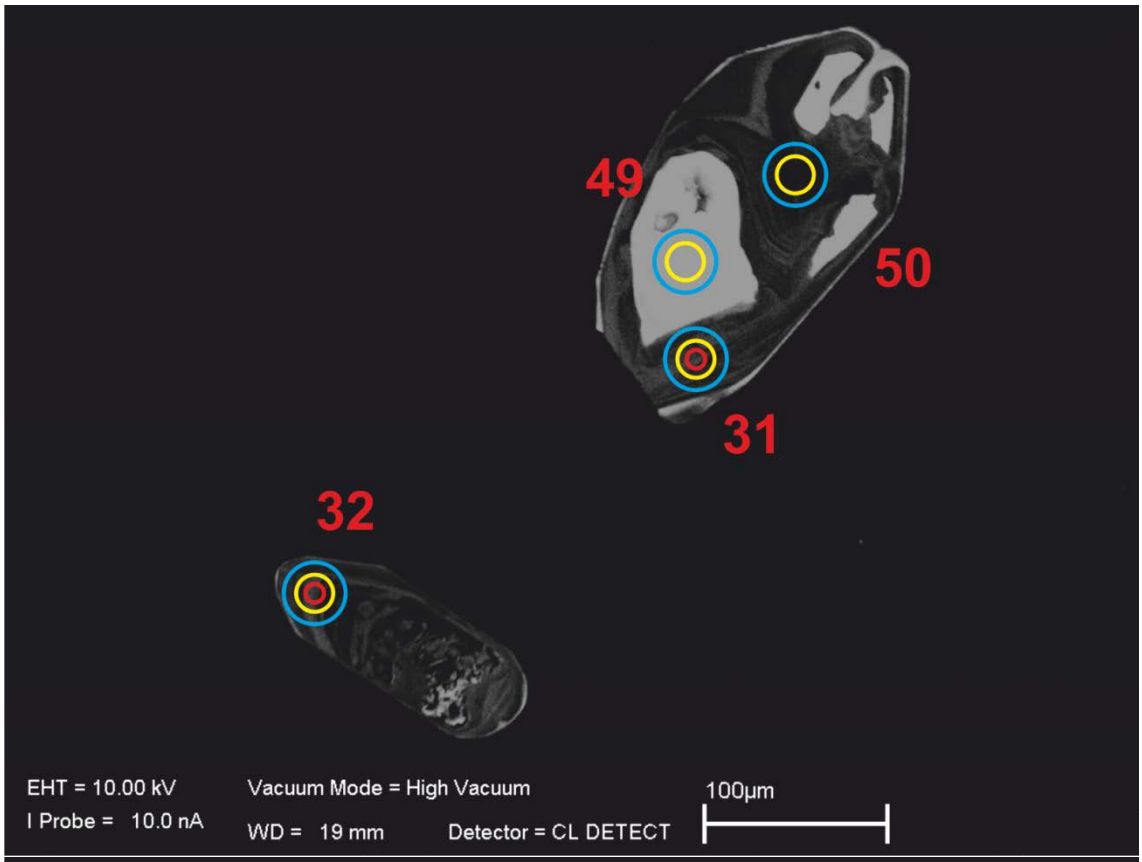
49
50
31
32
EHT = 10.00 kV
I Probe = 10.0 nA
Vacuum Mode = High Vacuum
WD = 19 mm
Detector = CL DETECT
100µm

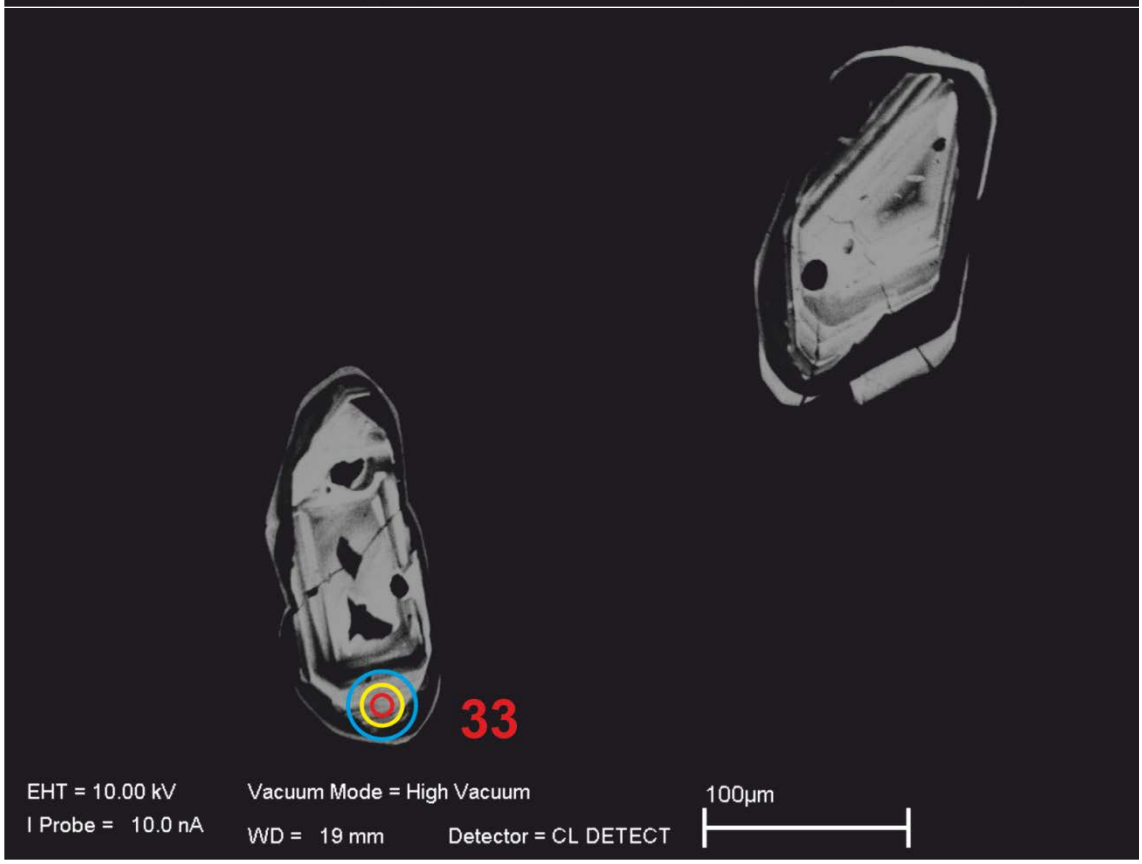
33
EHT = 10.00 kV
I Probe = 10.0 nA
Vacuum Mode = High Vacuum
WD = 19 mm
Detector = CL DETECT
100µm

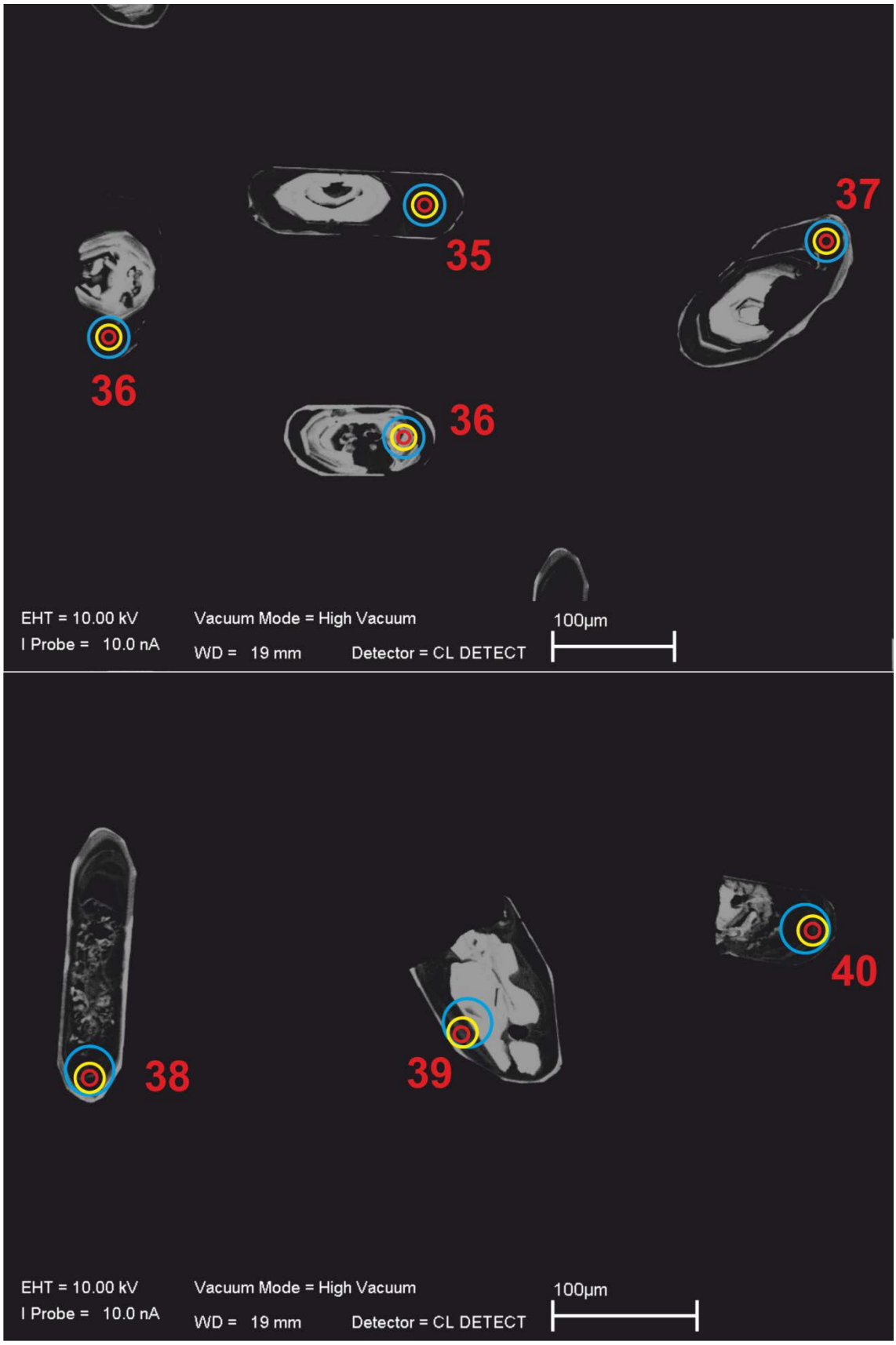
35
37
36
36
EHT = 10.00 kV
I Probe = 10.0 nA
Vacuum Mode = High Vacuum
WD = 19 mm
Detector = CL DETECT
100µm
38
39
40
EHT = 10.00 kV
I Probe = 10.0 nA
Vacuum Mode = High Vacuum
WD = 19 mm
Detector = CL DETECT
100µm

E.3. 1G01

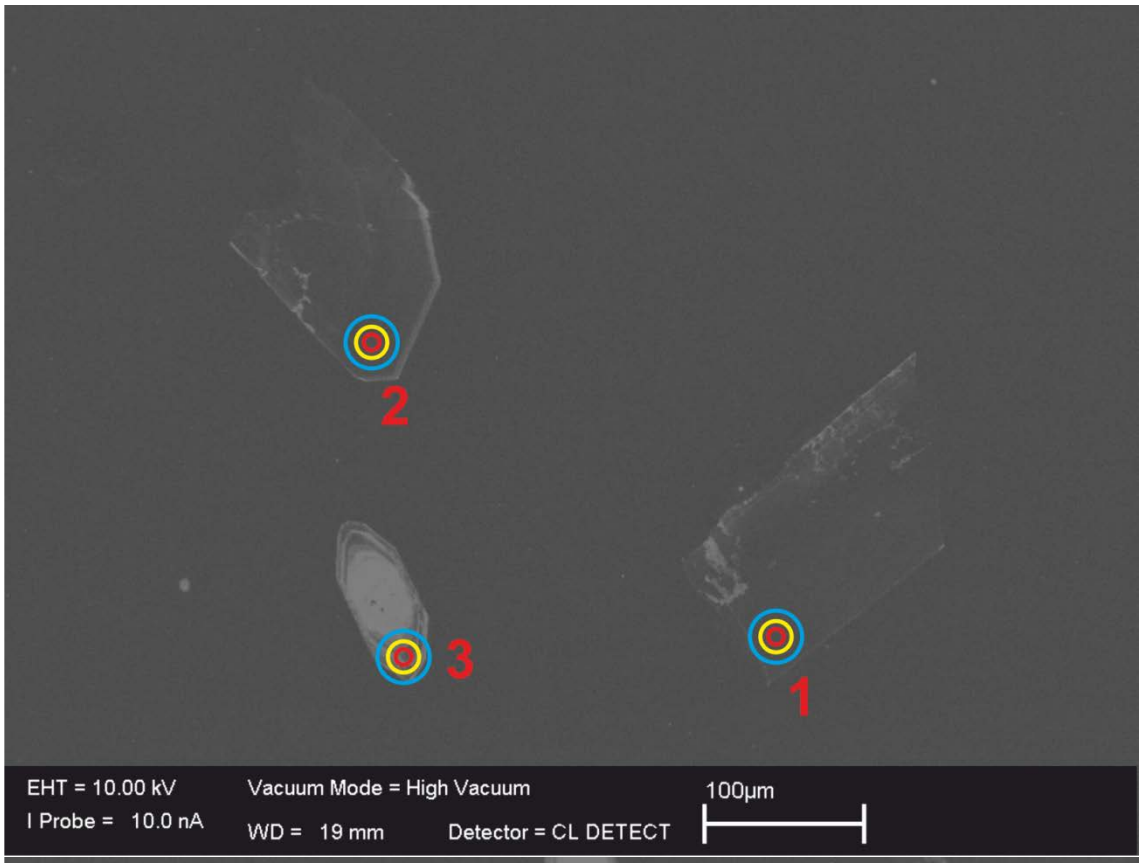
2
3
1
EHT = 10.00 kV
I Probe = 10.0 nA
Vacuum Mode = High Vacuum
WD = 19 mm
Detector = CL DETECT
100µm

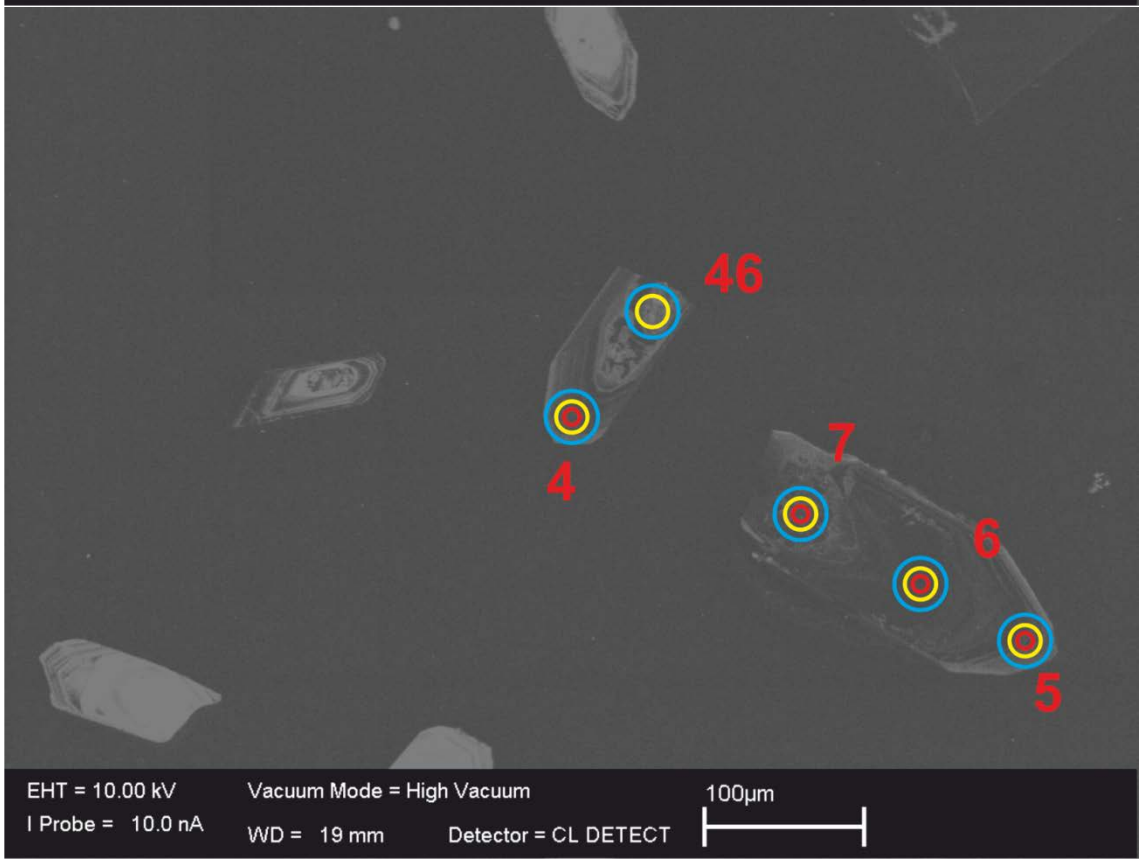
46
4
7
6
5
EHT = 10.00 kV
I Probe = 10.0 nA
Vacuum Mode = High Vacuum
WD = 19 mm
Detector = CL DETECT
100µm

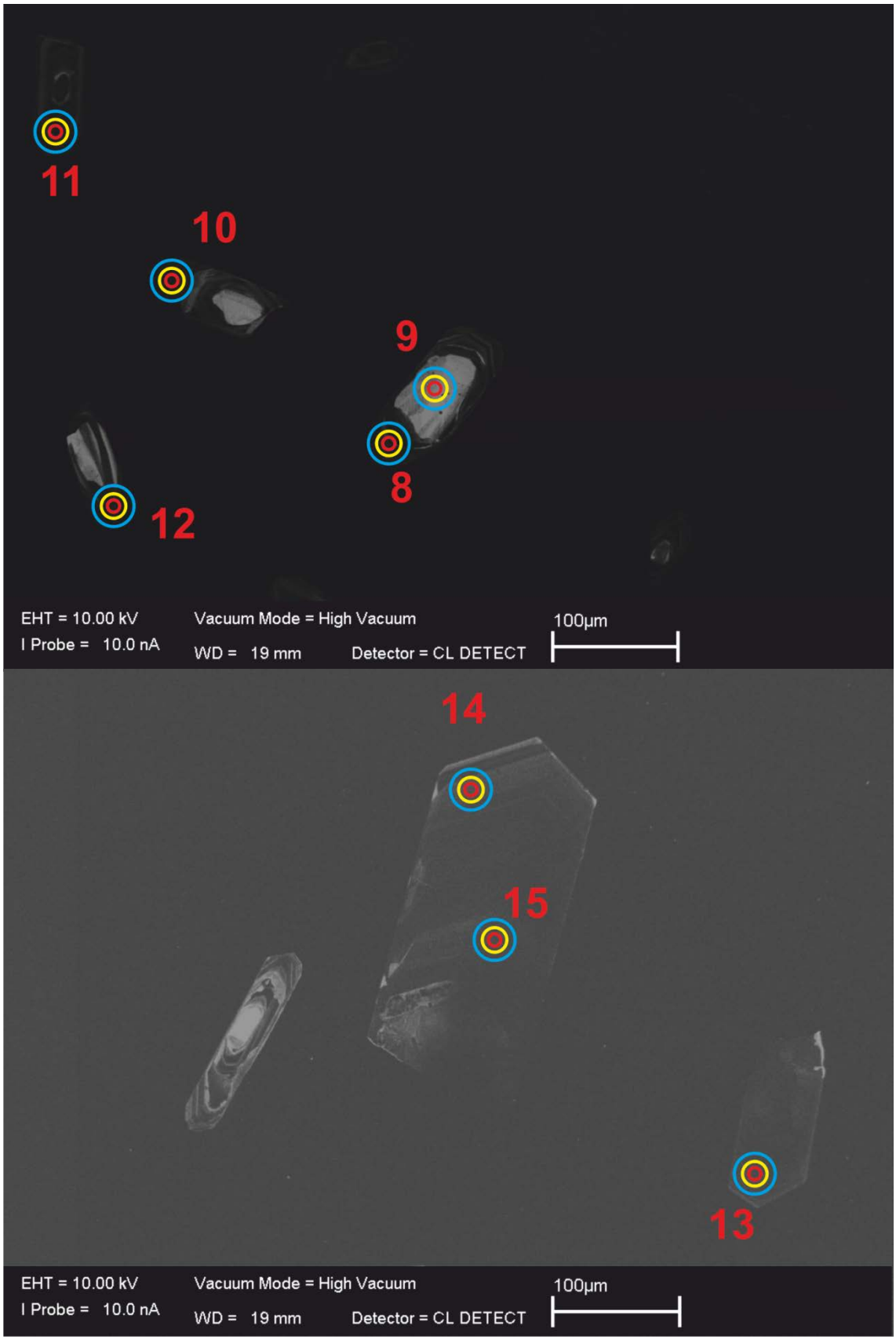
11
10
9
8
12
EHT = 10.00 kV
I Probe = 10.0 nA
Vacuum Mode = High Vacuum
WD = 19 mm
Detector = CL DETECT
100µm
14
15
13
EHT = 10.00 kV
I Probe = 10.0 nA
Vacuum Mode = High Vacuum
WD = 19 mm
Detector = CL DETECT
100µm

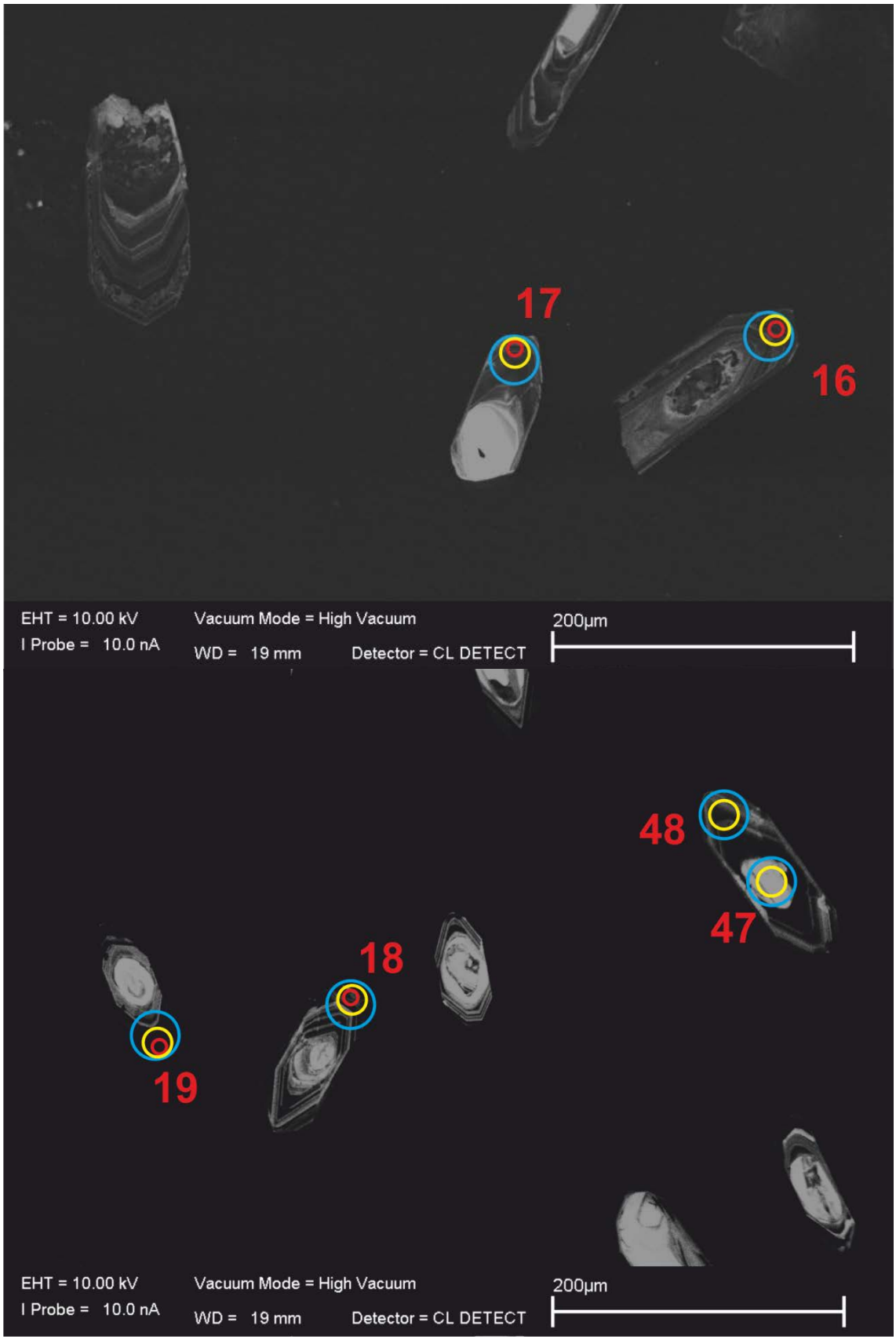
17
16
EHT = 10.00 kV
I Probe = 10.0 nA
Vacuum Mode = High Vacuum
WD = 19 mm
Detector = CL DETECT
200µm
48
47
18
19
EHT = 10.00 kV
I Probe = 10.0 nA
Vacuum Mode = High Vacuum
WD = 19 mm
Detector = CL DETECT
200µm

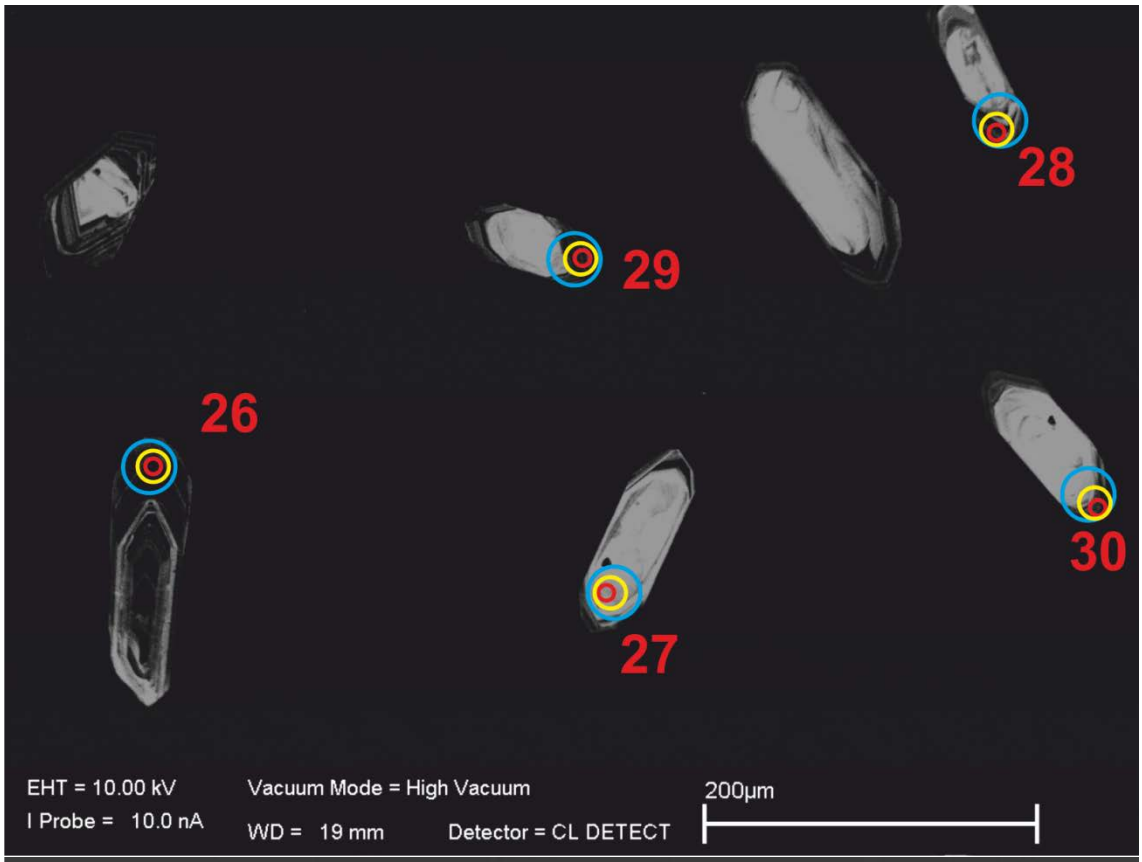
28
29
26
30
27
EHT = 10.00 kV
I Probe = 10.0 nA
Vacuum Mode = High Vacuum
WD = 19 mm
Detector = CL DETECT
200µm

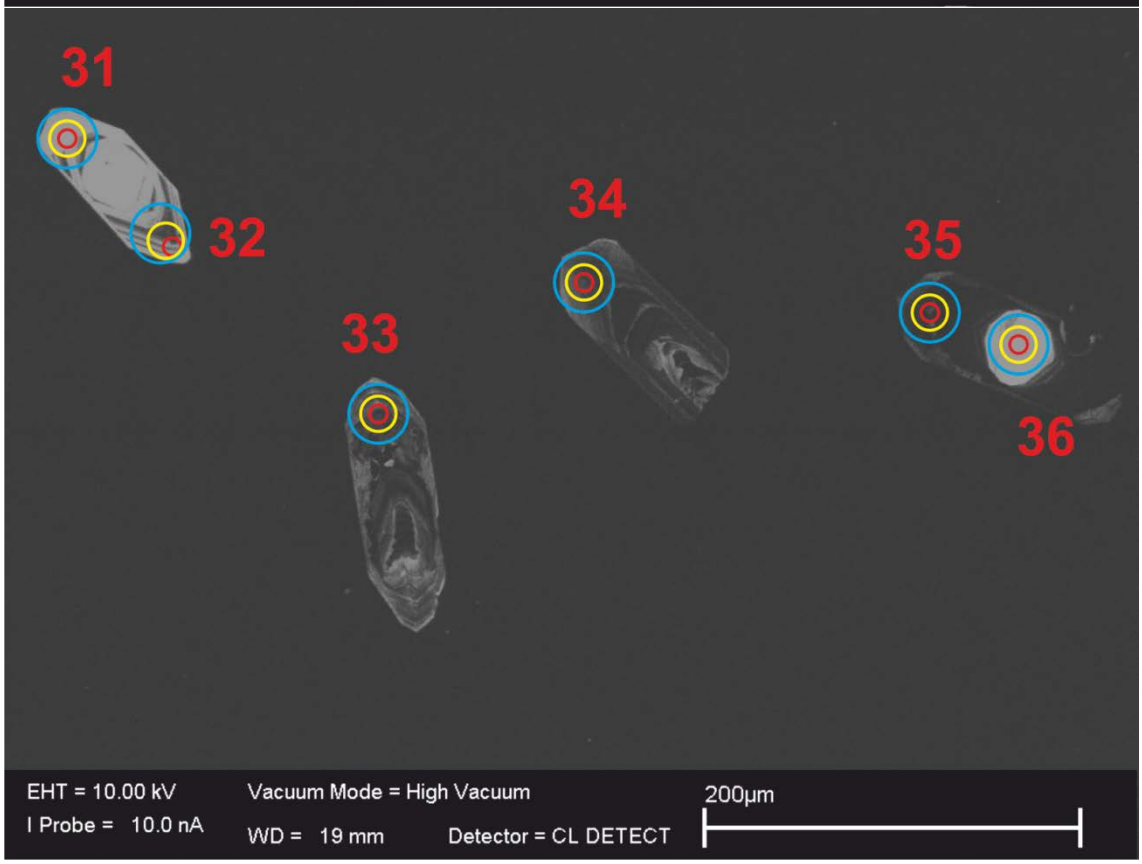
31
32
34
35
33
36
EHT = 10.00 kV
I Probe = 10.0 nA
Vacuum Mode = High Vacuum
WD = 19 mm
Detector = CL DETECT
200µm


50
38
36
37
EHT = 10.00 kV
I Probe = 10.0 nA
Vacuum Mode = High Vacuum
WD = 19 mm
Detector = CL DETECT
200µm

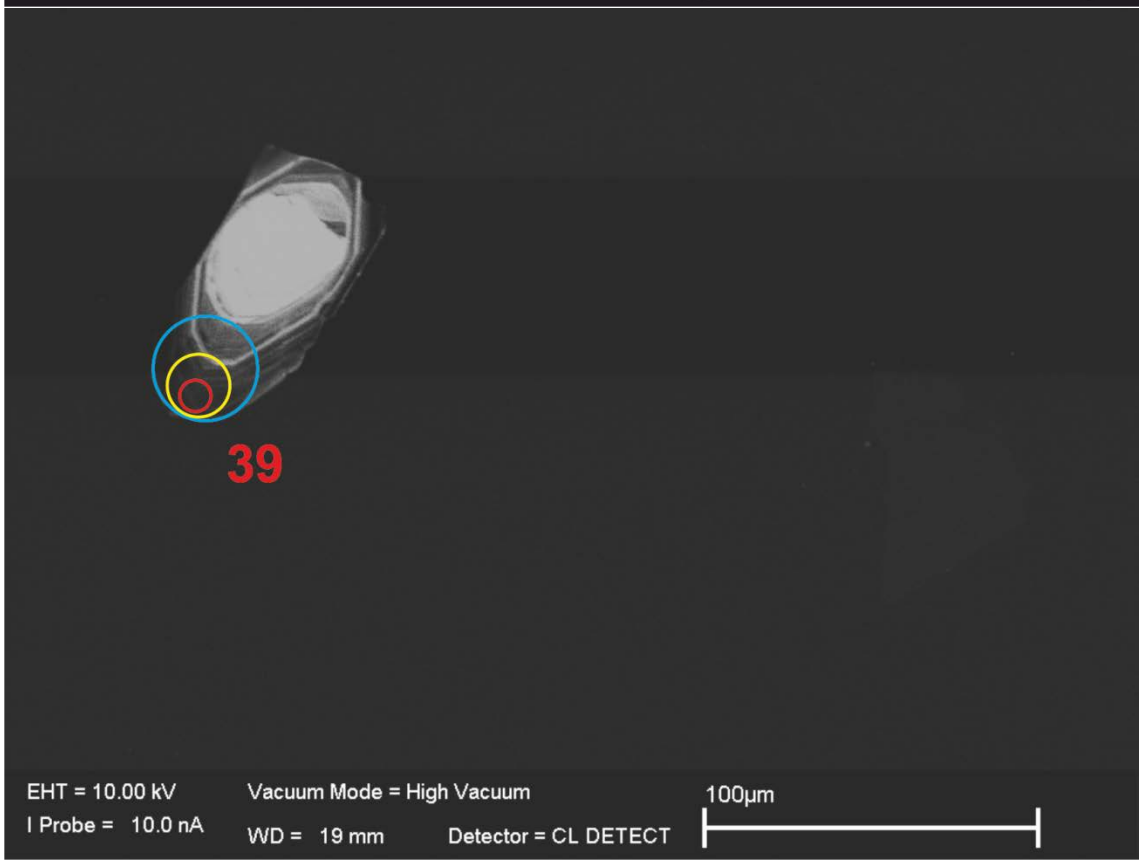
39
EHT = 10.00 kV
I Probe = 10.0 nA
Vacuum Mode = High Vacuum
WD = 19 mm
Detector = CL DETECT
100µm

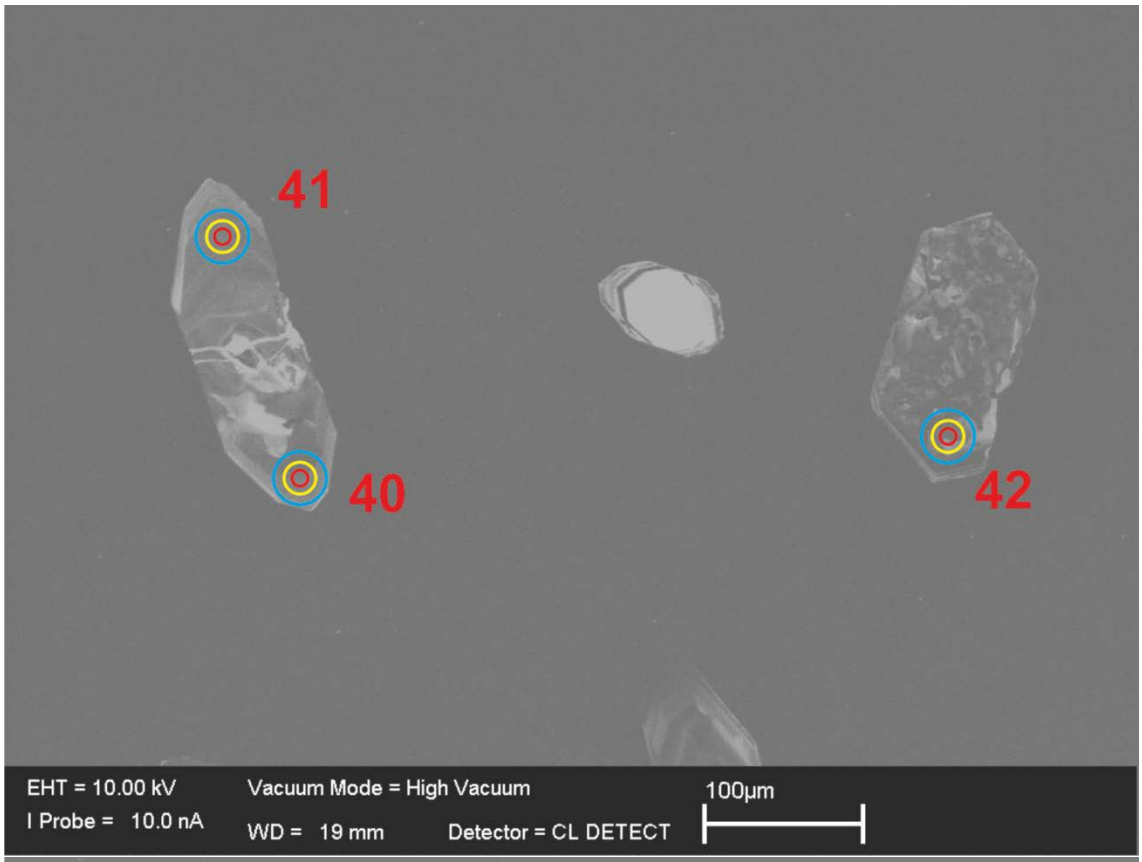
41
40
42
EHT = 10.00 kV
I Probe = 10.0 nA
Vacuum Mode = High Vacuum
WD = 19 mm
Detector = CL DETECT
100µm

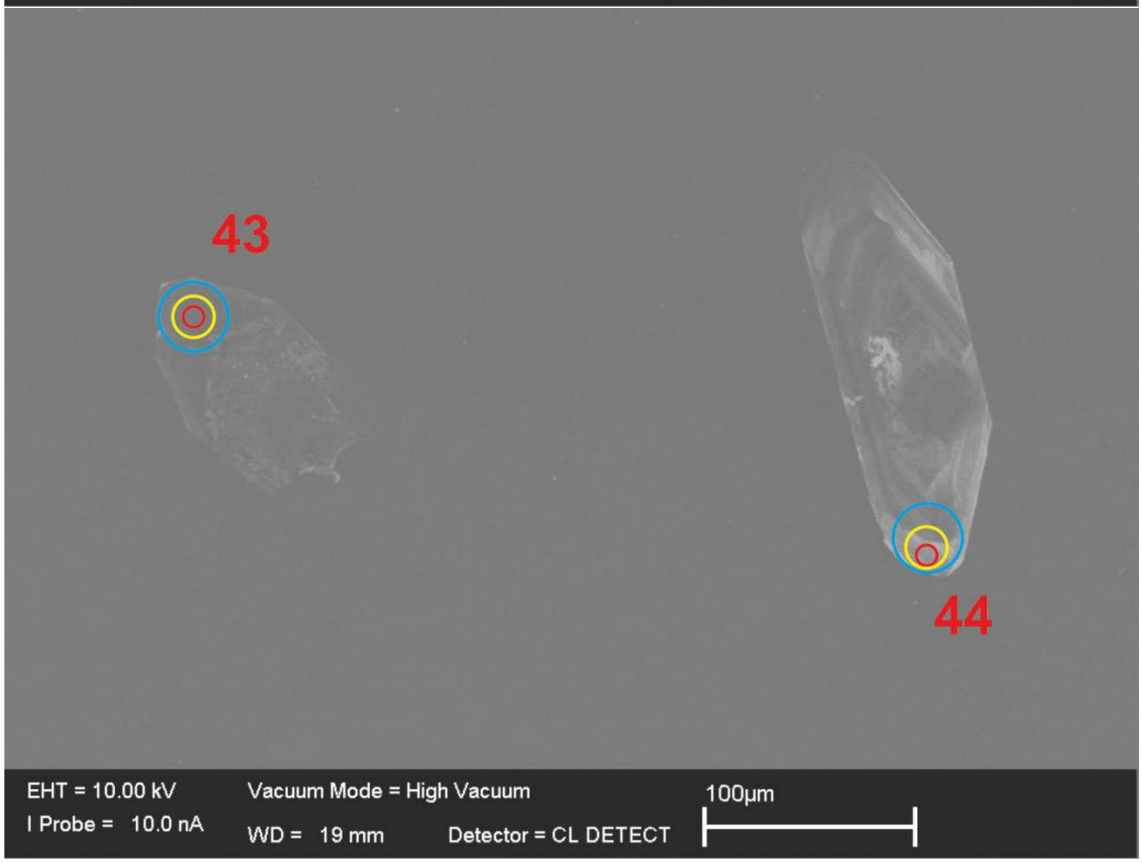
43
44
EHT = 10.00 kV
I Probe = 10.0 nA
Vacuum Mode = High Vacuum
WD = 19 mm
Detector = CL DETECT
100µm

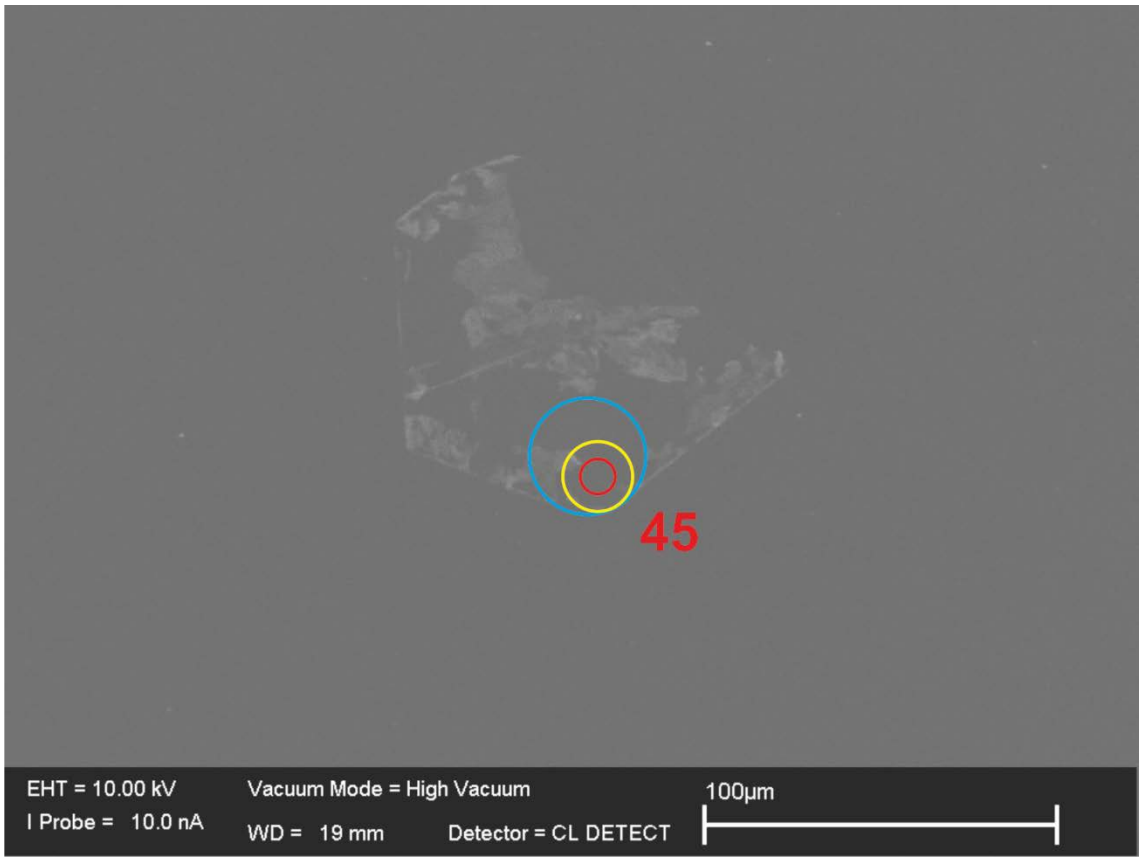
45
EHT = 10.00 kV
I Probe = 10.0 nA
Vacuum Mode = High Vacuum
WD = 19 mm
Detector = CL DETECT
100µm

E.4. 1G02

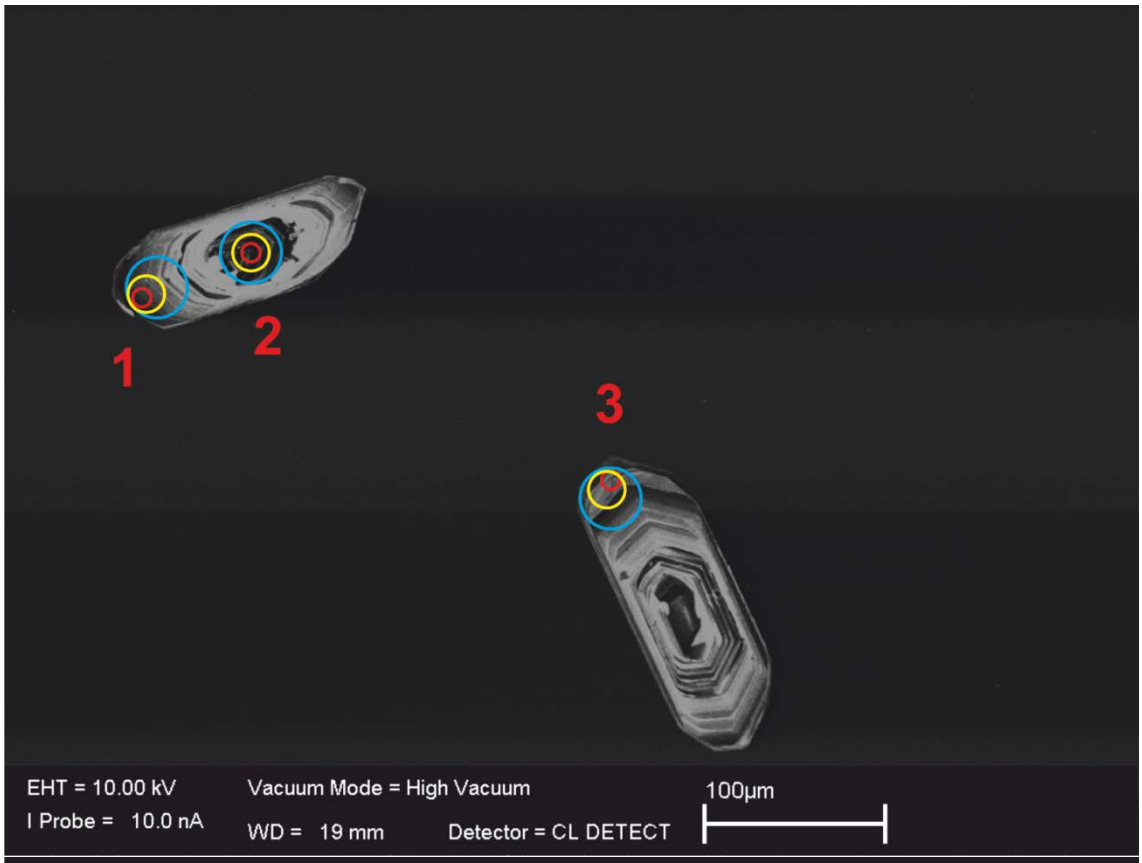
1
2
3
EHT = 10.00 kV
I Probe = 10.0 nA
Vacuum Mode = High Vacuum
WD = 19 mm
Detector = CL DETECT
100µm

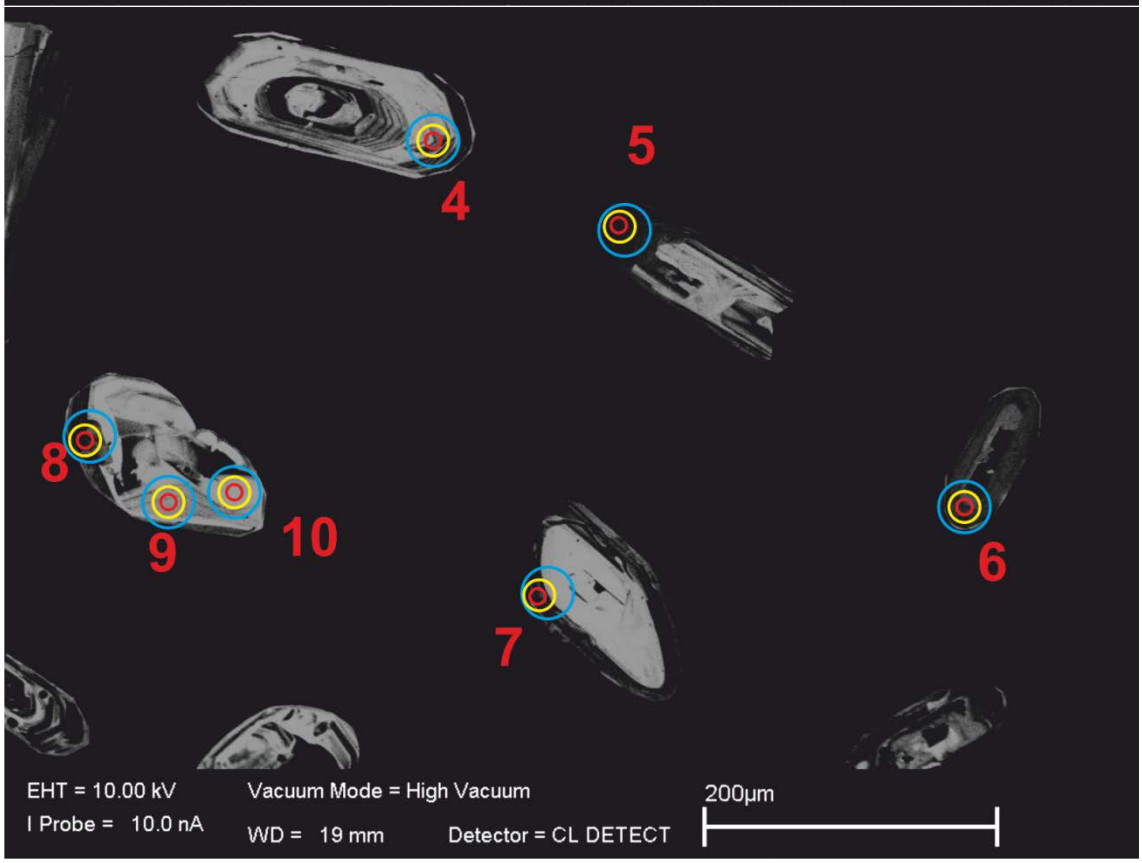
4
5
8
9
10
6
7
EHT = 10.00 kV
I Probe = 10.0 nA
Vacuum Mode = High Vacuum
WD = 19 mm
Detector = CL DETECT
200µm

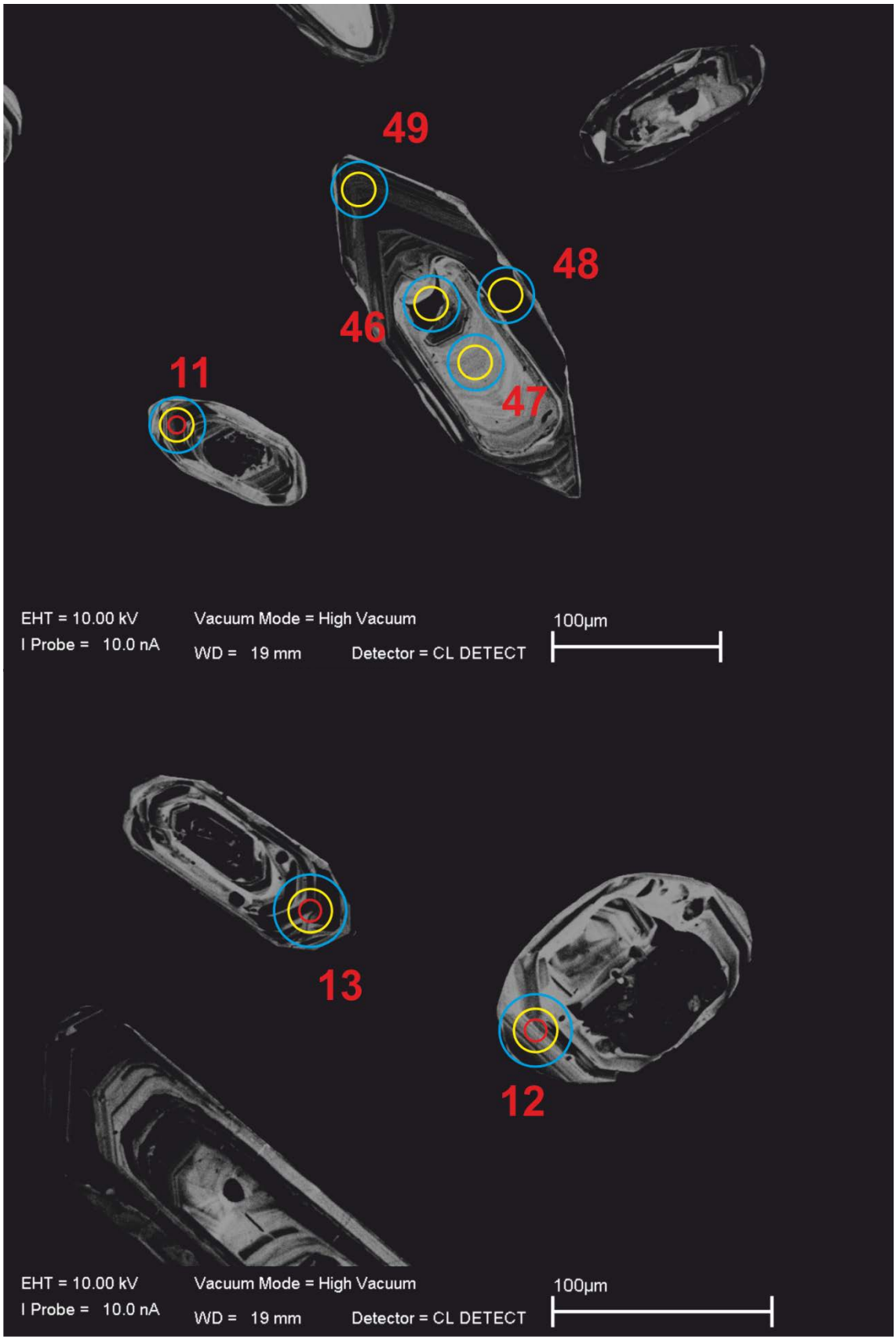
49
48
46
47
11
EHT = 10.00 kV
I Probe = 10.0 nA
Vacuum Mode = High Vacuum
WD = 19 mm
Detector = CL DETECT
100µm
13
12
EHT = 10.00 kV
I Probe = 10.0 nA
Vacuum Mode = High Vacuum
WD = 19 mm
Detector = CL DETECT
100µm

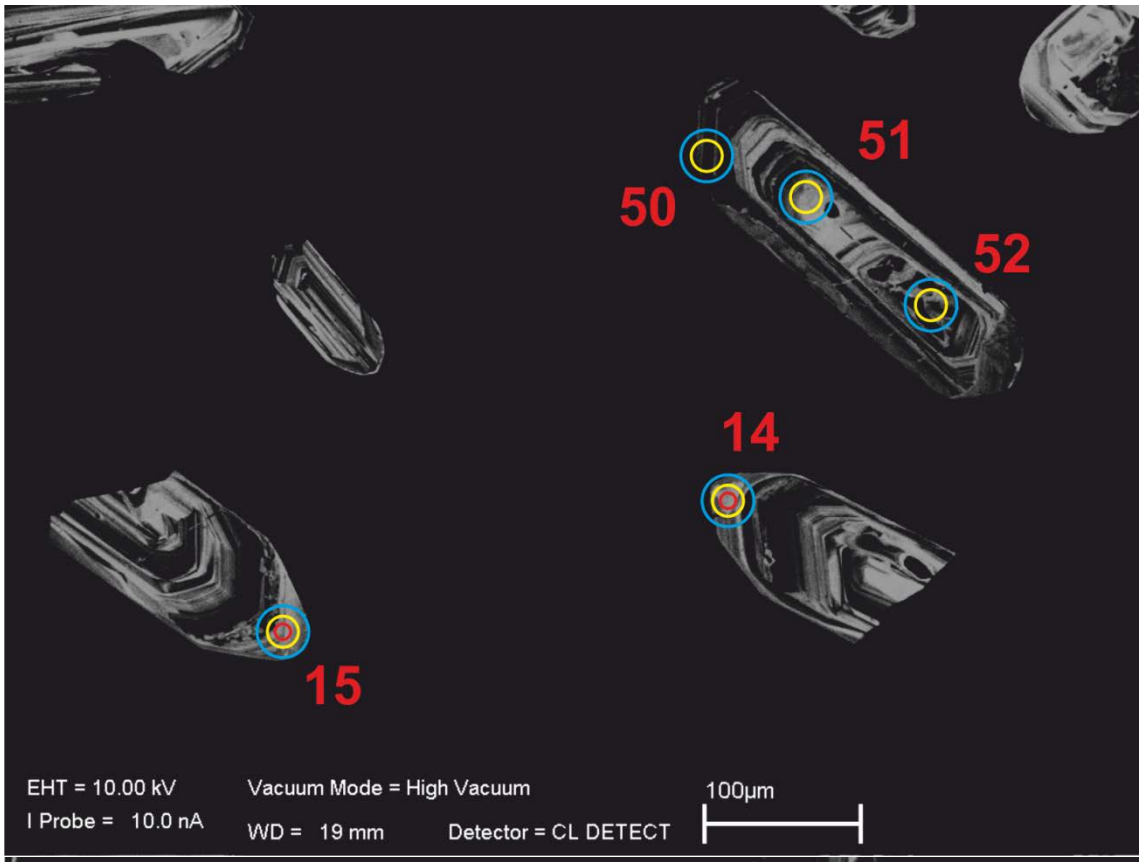
51
50
52
14
15
EHT = 10.00 kV
I Probe = 10.0 nA
Vacuum Mode = High Vacuum
WD = 19 mm
Detector = CL DETECT
100µm

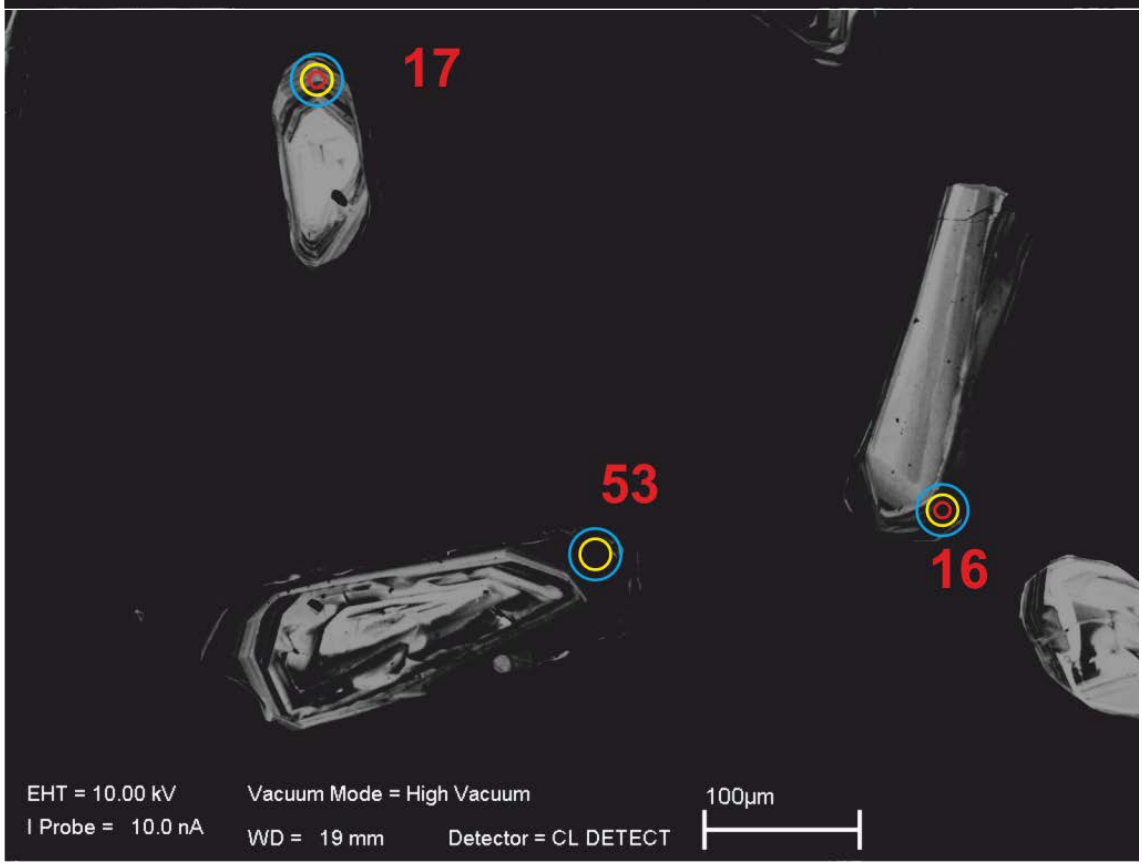
17
53
16
EHT = 10.00 kV
I Probe = 10.0 nA
Vacuum Mode = High Vacuum
WD = 19 mm
Detector = CL DETECT
100µm

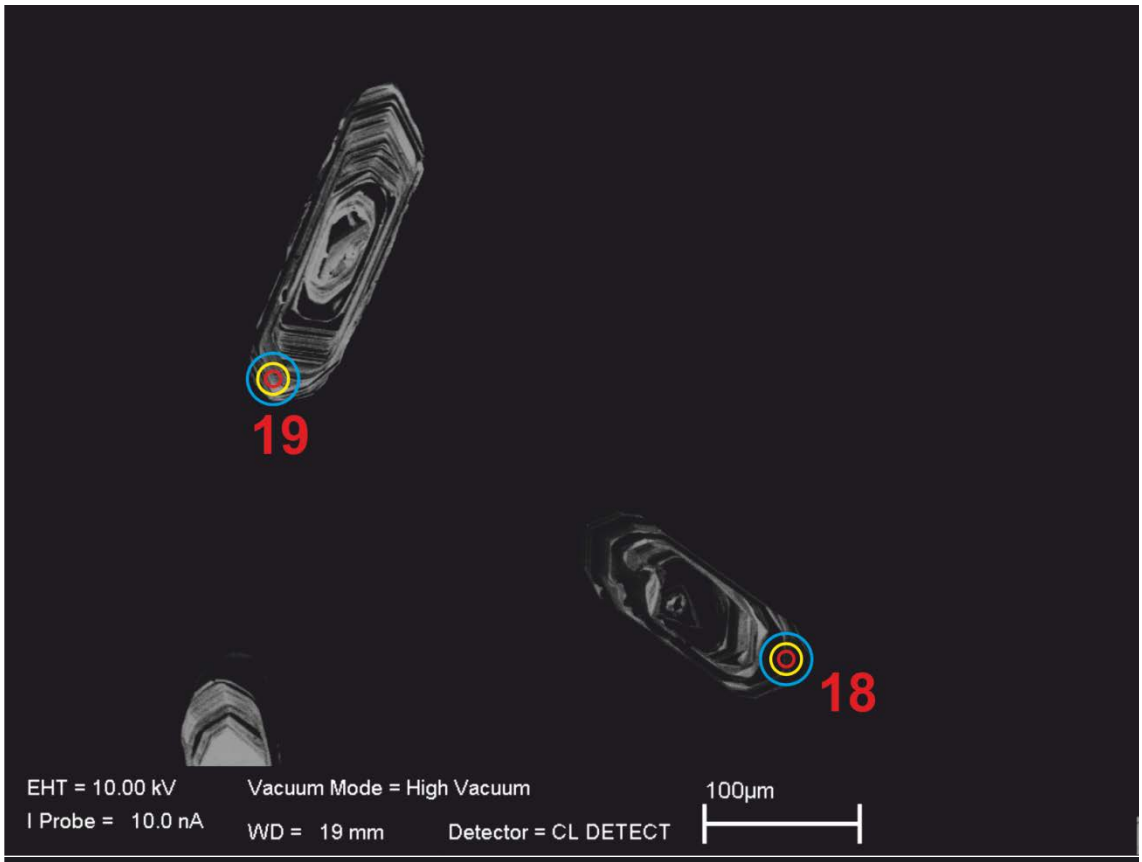
19
18
EHT = 10.00 kV
I Probe = 10.0 nA
Vacuum Mode = High Vacuum
WD = 19 mm
Detector = CL DETECT
100µm

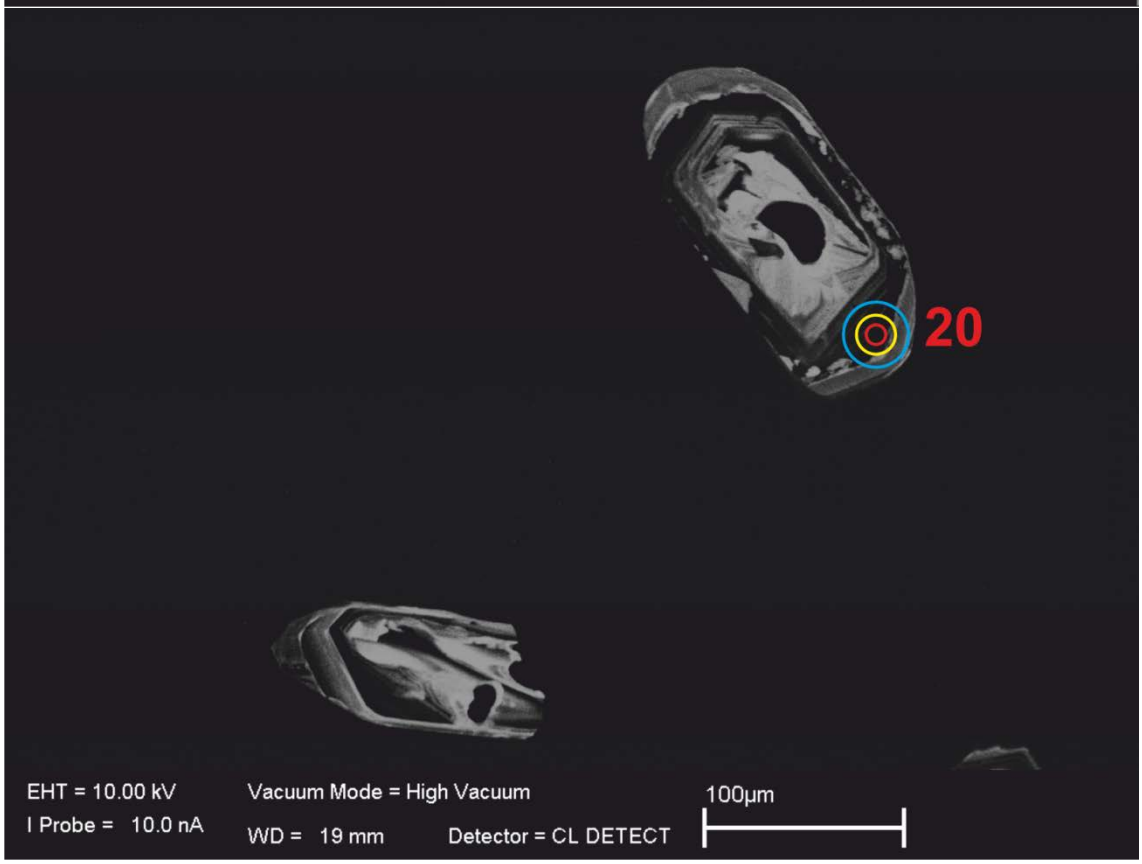
20
EHT = 10.00 kV
I Probe = 10.0 nA
Vacuum Mode = High Vacuum
WD = 19 mm
Detector = CL DETECT
100µm

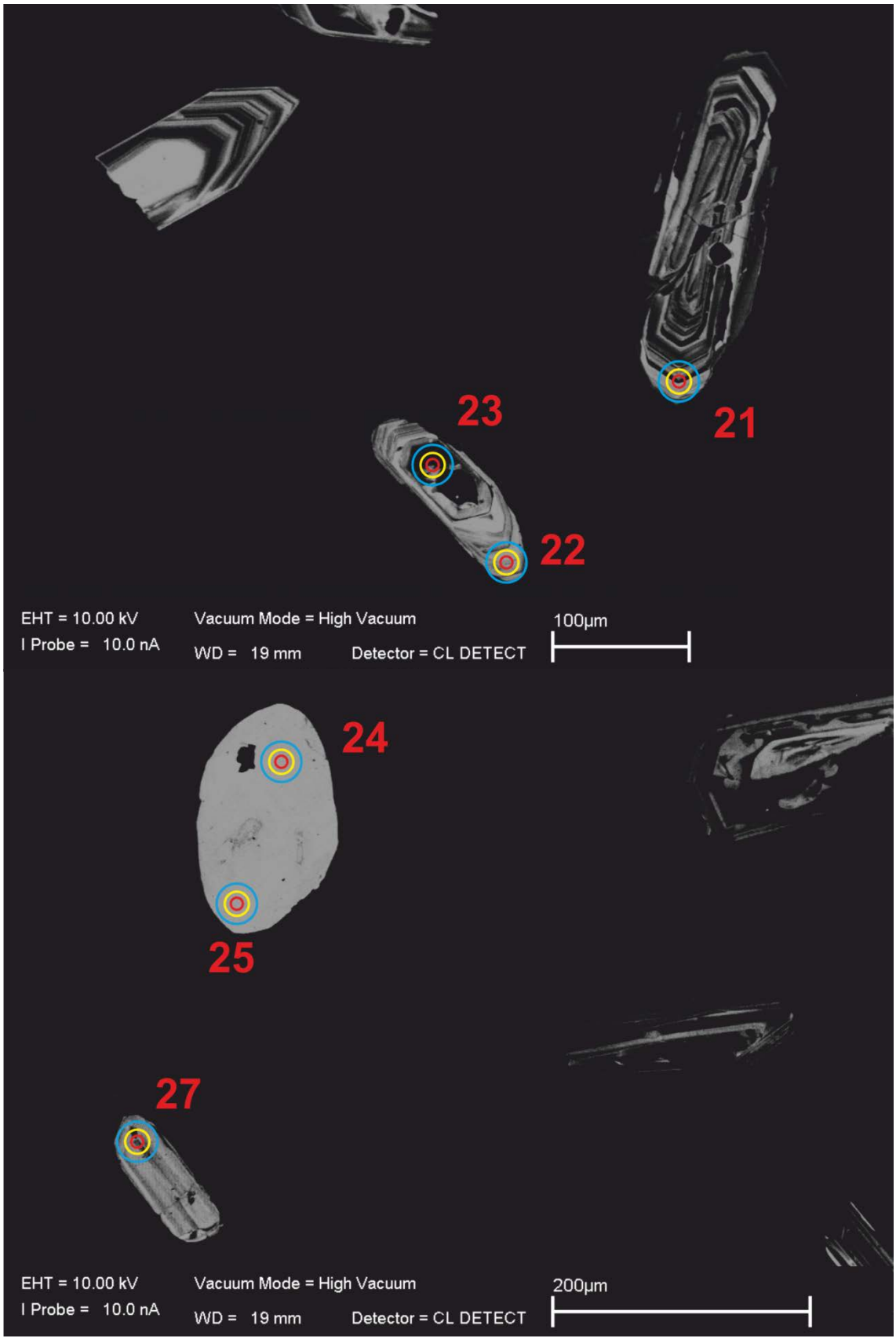
23
21
22
EHT = 10.00 kV
I Probe = 10.0 nA
Vacuum Mode = High Vacuum
WD = 19 mm
Detector = CL DETECT
100µm
24
25
27
EHT = 10.00 kV
I Probe = 10.0 nA
Vacuum Mode = High Vacuum
WD = 19 mm
Detector = CL DETECT
200µm

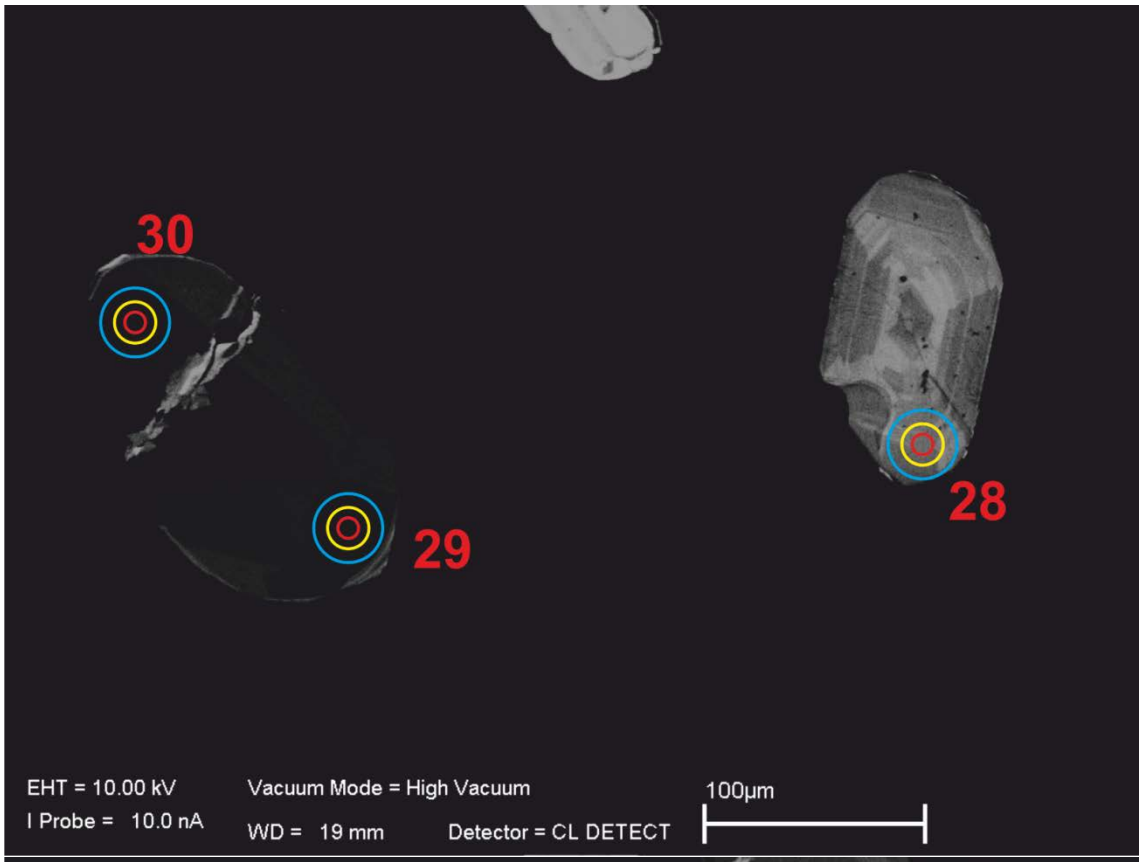
30
29
28
EHT = 10.00 kV
I Probe = 10.0 nA
Vacuum Mode = High Vacuum
WD = 19 mm
Detector = CL DETECT
100µm

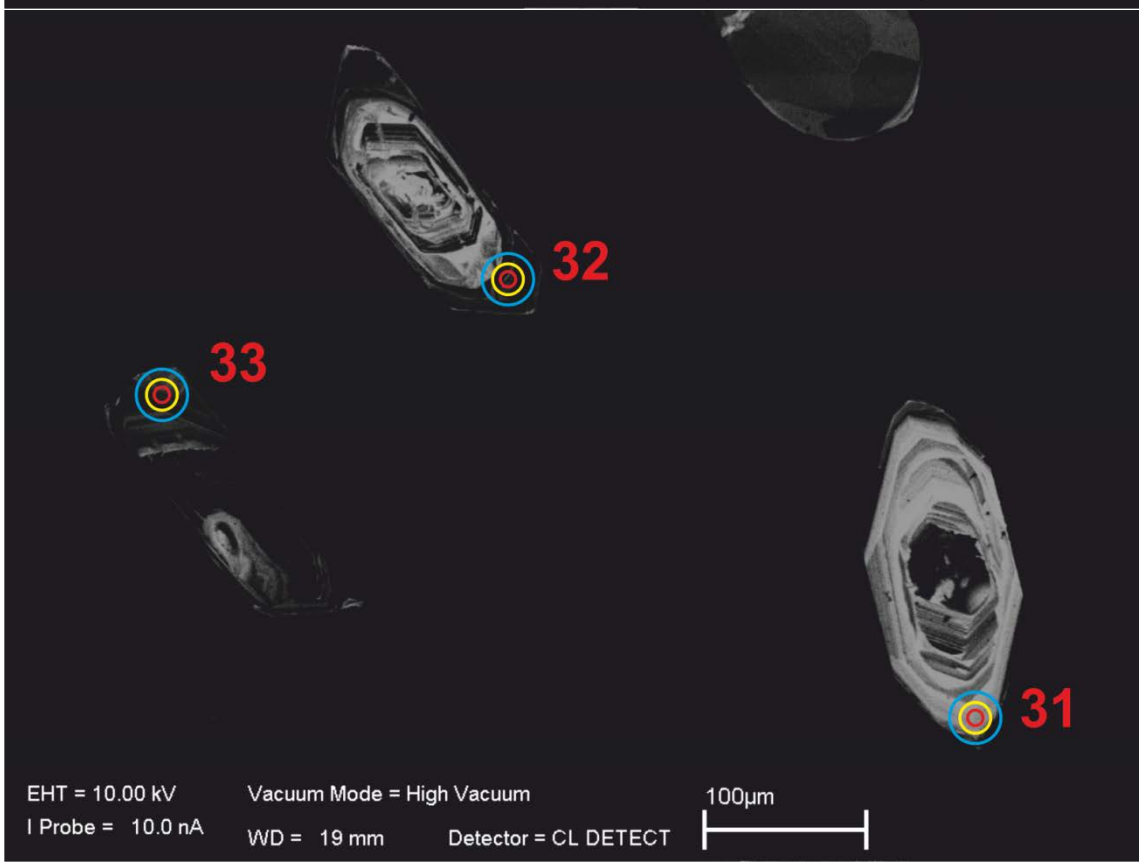
32
33
31
EHT = 10.00 kV
I Probe = 10.0 nA
Vacuum Mode = High Vacuum
WD = 19 mm
Detector = CL DETECT
100µm

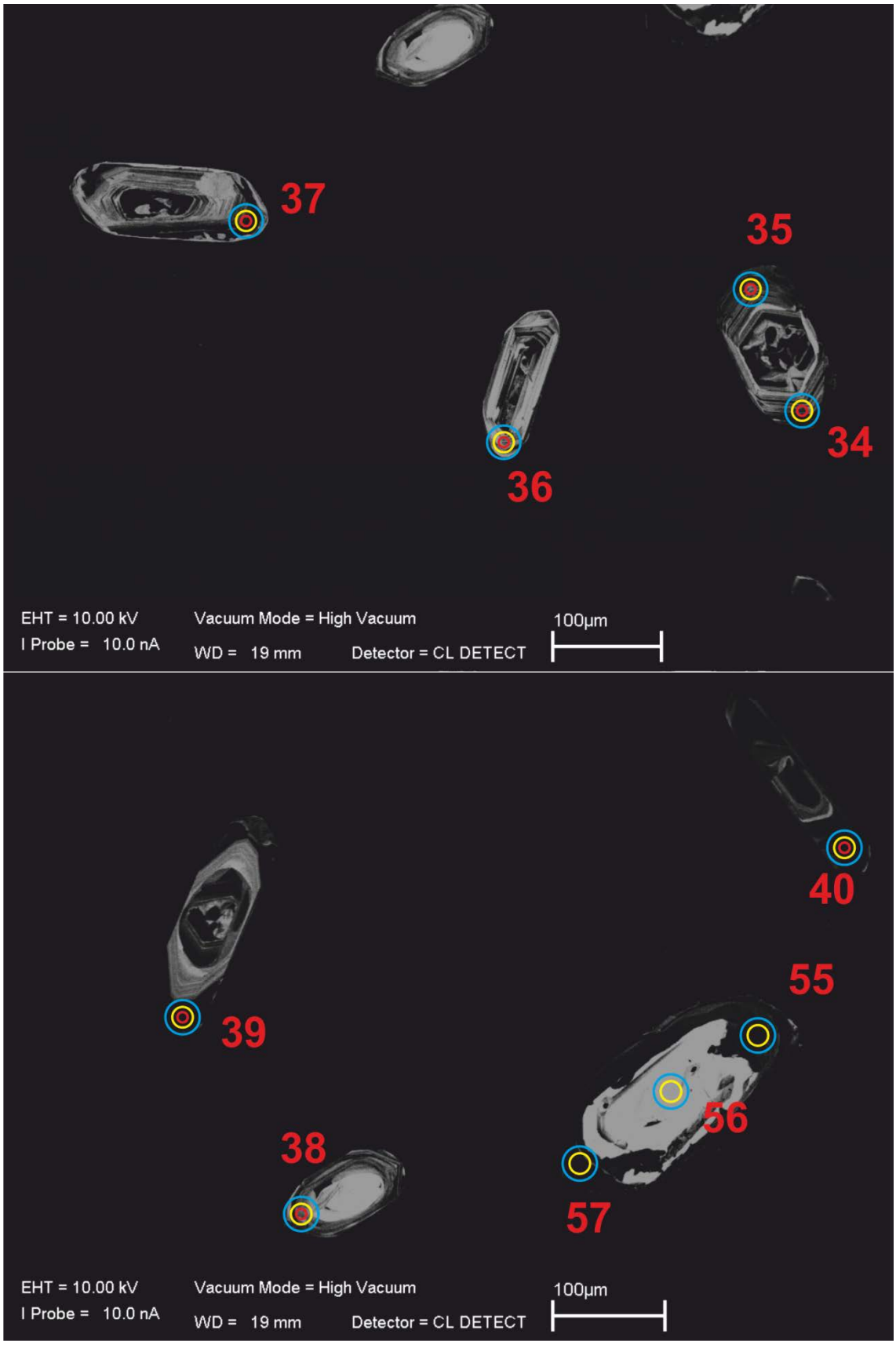
37
35
34
36
EHT = 10.00 kV
I Probe = 10.0 nA
Vacuum Mode = High Vacuum
WD = 19 mm
Detector = CL DETECT
100µm
40
55
39
56
38
57
EHT = 10.00 kV
I Probe = 10.0 nA
Vacuum Mode = High Vacuum
WD = 19 mm
Detector = CL DETECT
100µm

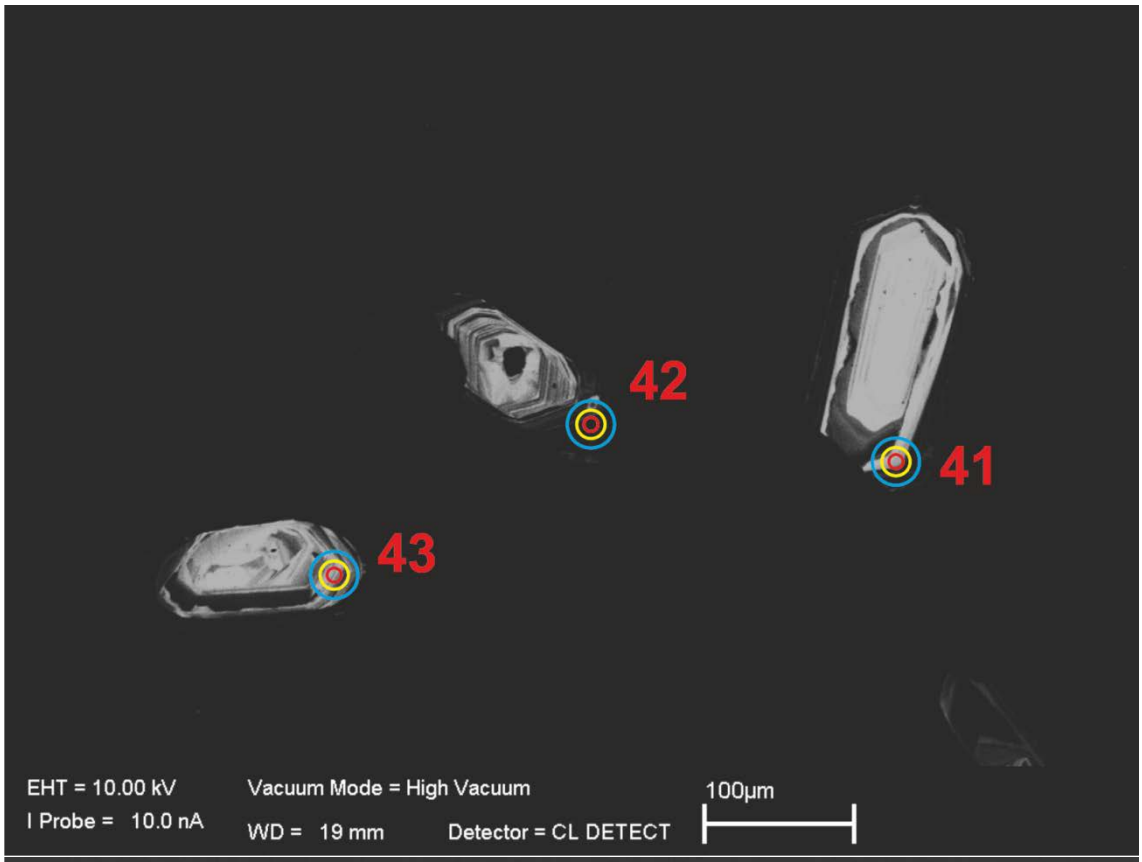
42
41
43
EHT = 10.00 kV
I Probe = 10.0 nA
Vacuum Mode = High Vacuum
WD = 19 mm
Detector = CL DETECT
100µm

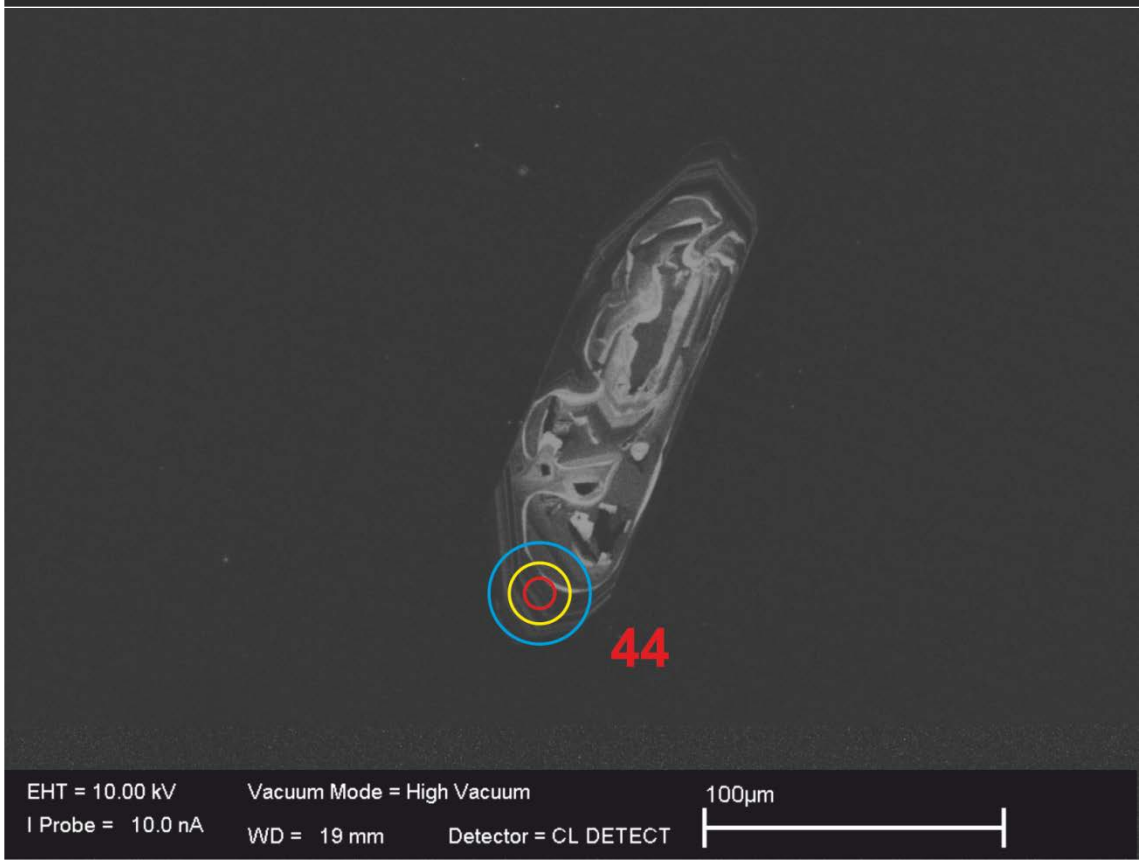
44
EHT = 10.00 kV
I Probe = 10.0 nA
Vacuum Mode = High Vacuum
WD = 19 mm
Detector = CL DETECT
100µm

E.5. 1G03

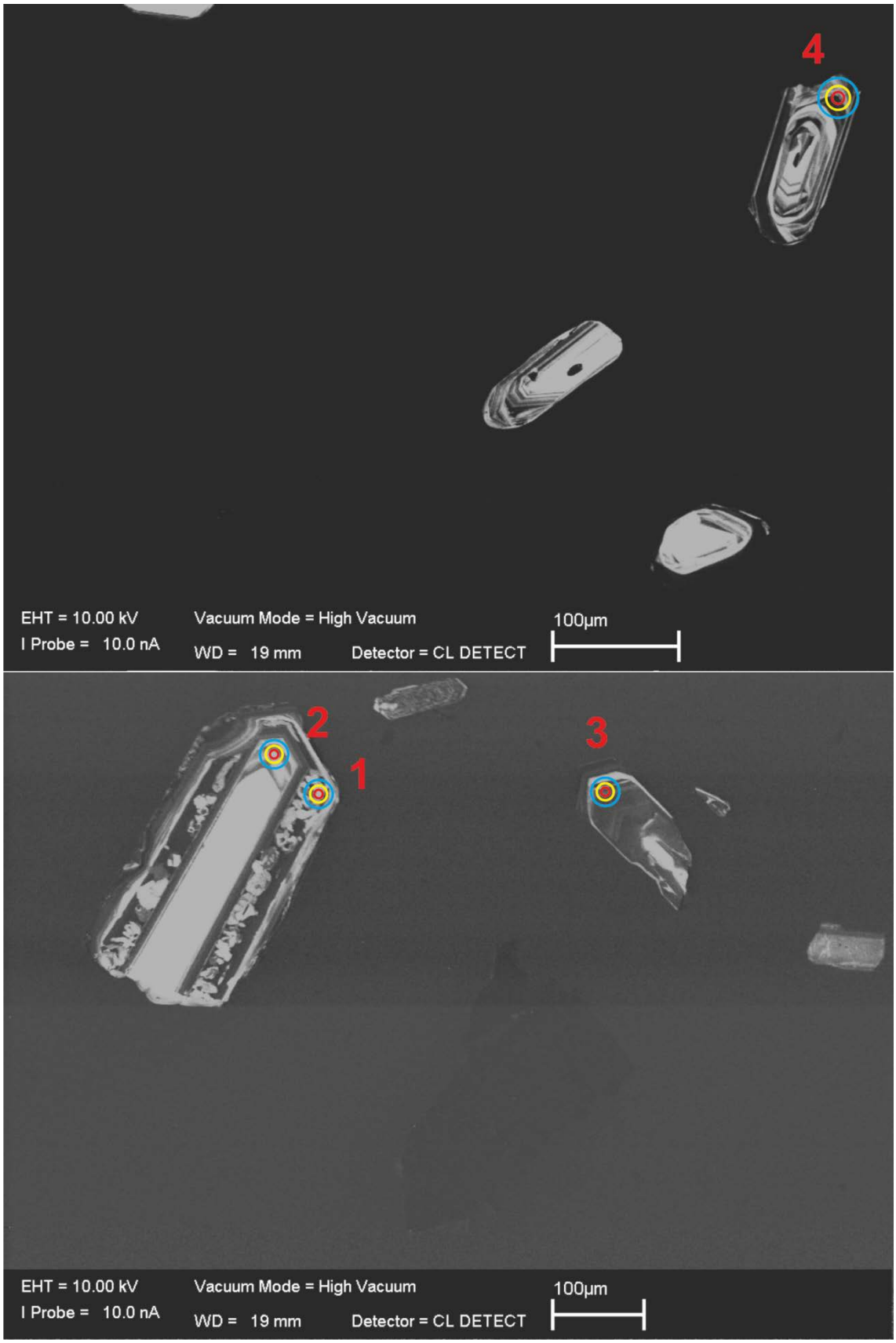
4
EHT = 10.00 kV
I Probe = 10.0 nA
Vacuum Mode = High Vacuum
WD = 19 mm
Detector = CL DETECT
100µm
2
1
3
EHT = 10.00 kV
I Probe = 10.0 nA
Vacuum Mode = High Vacuum
WD = 19 mm
Detector = CL DETECT
100µm

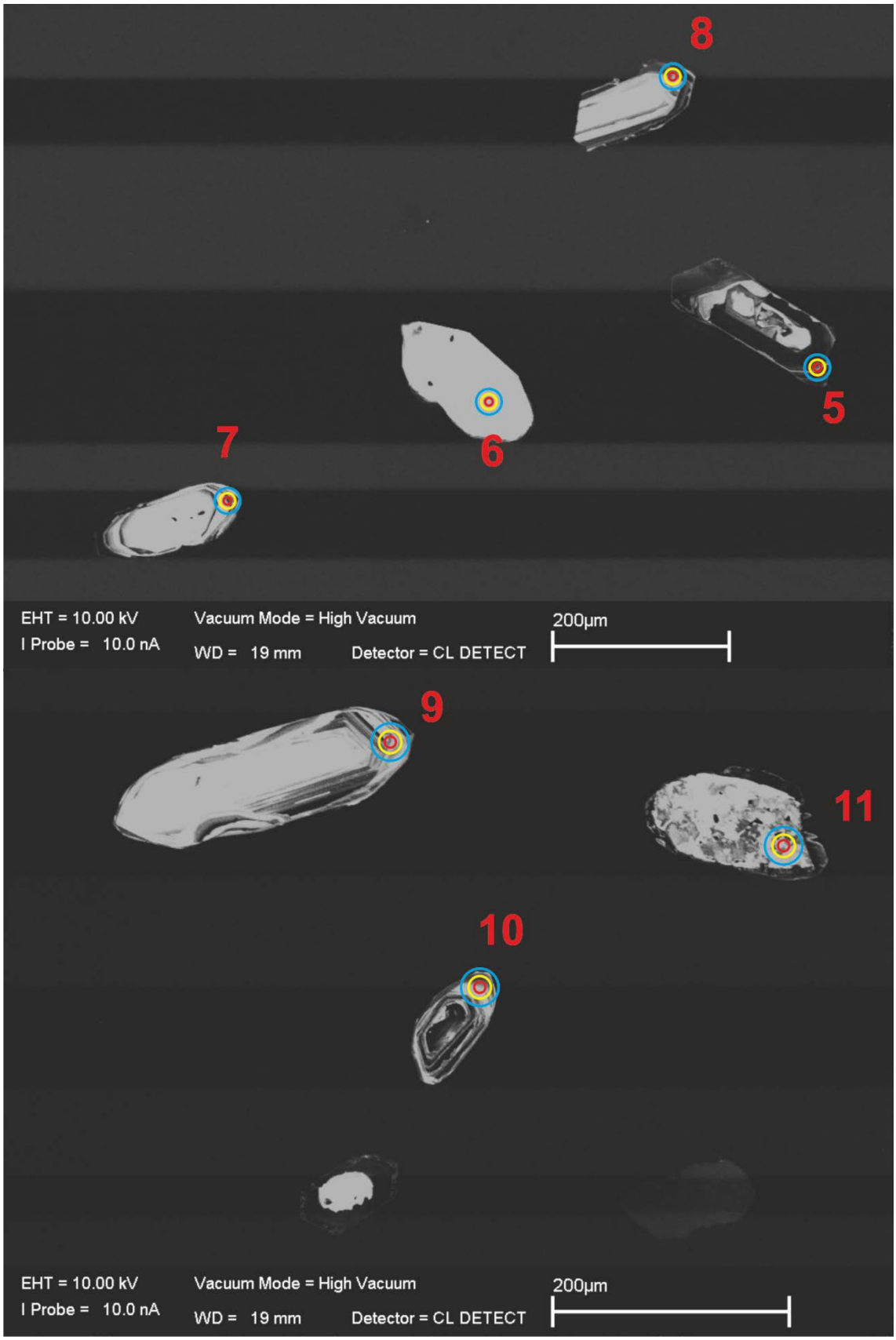
8
5
6
7
EHT = 10.00 kV
I Probe = 10.0 nA
Vacuum Mode = High Vacuum
WD = 19 mm
Detector = CL DETECT
200µm
9
11
10
EHT = 10.00 kV
I Probe = 10.0 nA
Vacuum Mode = High Vacuum
WD = 19 mm
Detector = CL DETECT
200µm

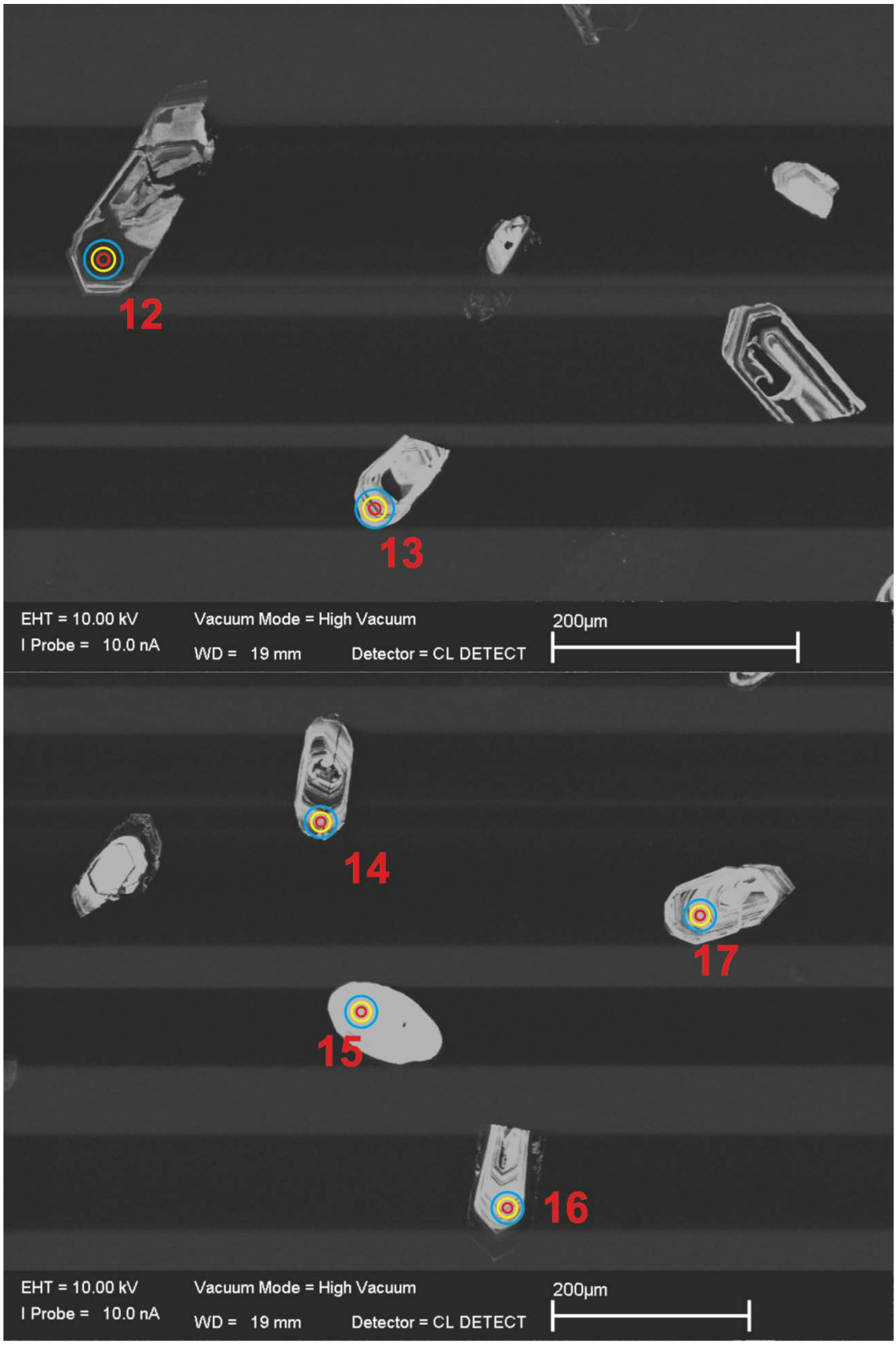
12
13
EHT = 10.00 kV
I Probe = 10.0 nA
Vacuum Mode = High Vacuum
WD = 19 mm
Detector = CL DETECT
200µm
14
17
15
16
EHT = 10.00 kV
I Probe = 10.0 nA
Vacuum Mode = High Vacuum
WD = 19 mm
Detector = CL DETECT
200µm

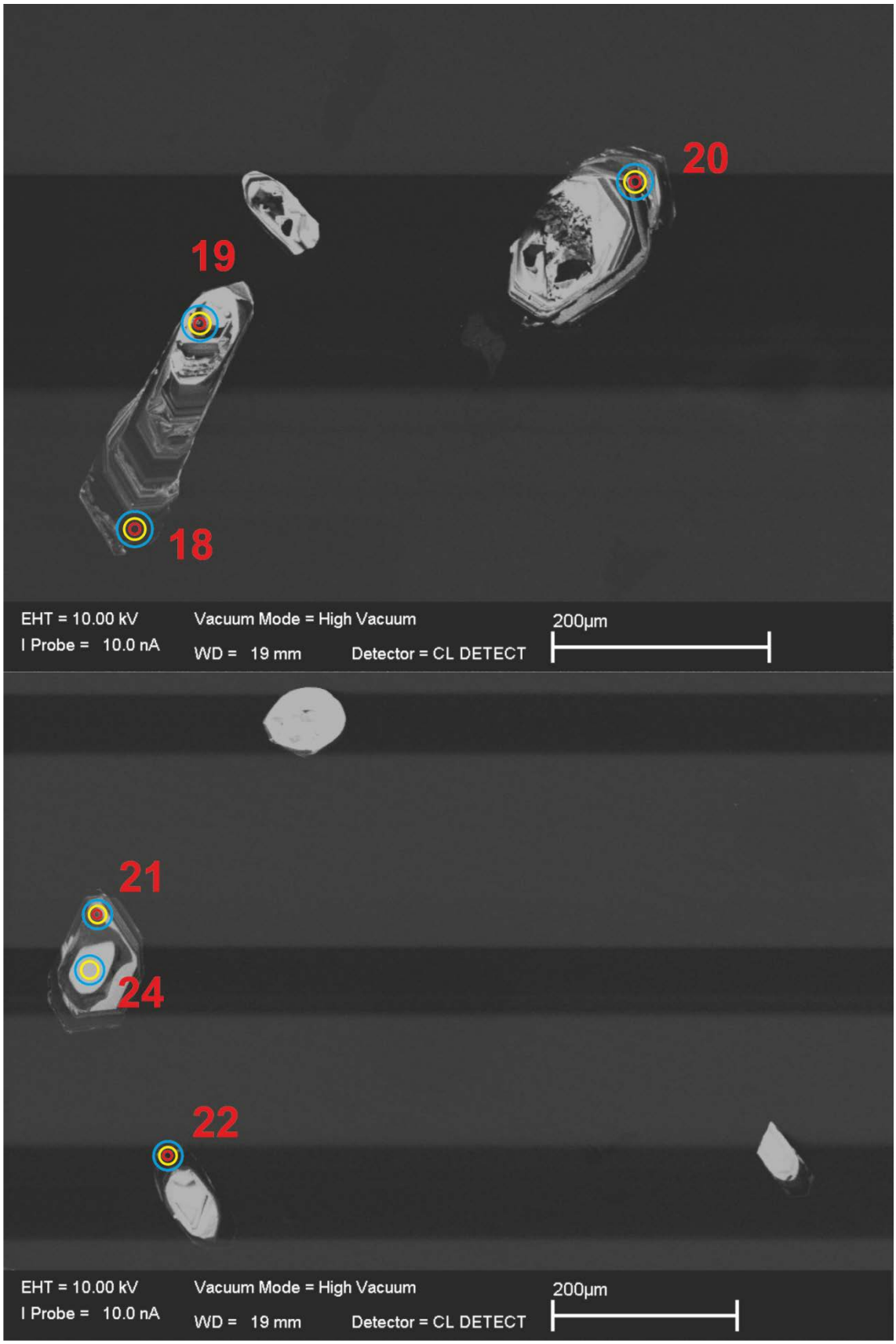
20
19
18
EHT = 10.00 kV
I Probe = 10.0 nA
Vacuum Mode = High Vacuum
WD = 19 mm
Detector = CL DETECT
200µm
21
24
22
EHT = 10.00 kV
I Probe = 10.0 nA
Vacuum Mode = High Vacuum
WD = 19 mm
Detector = CL DETECT
200µm

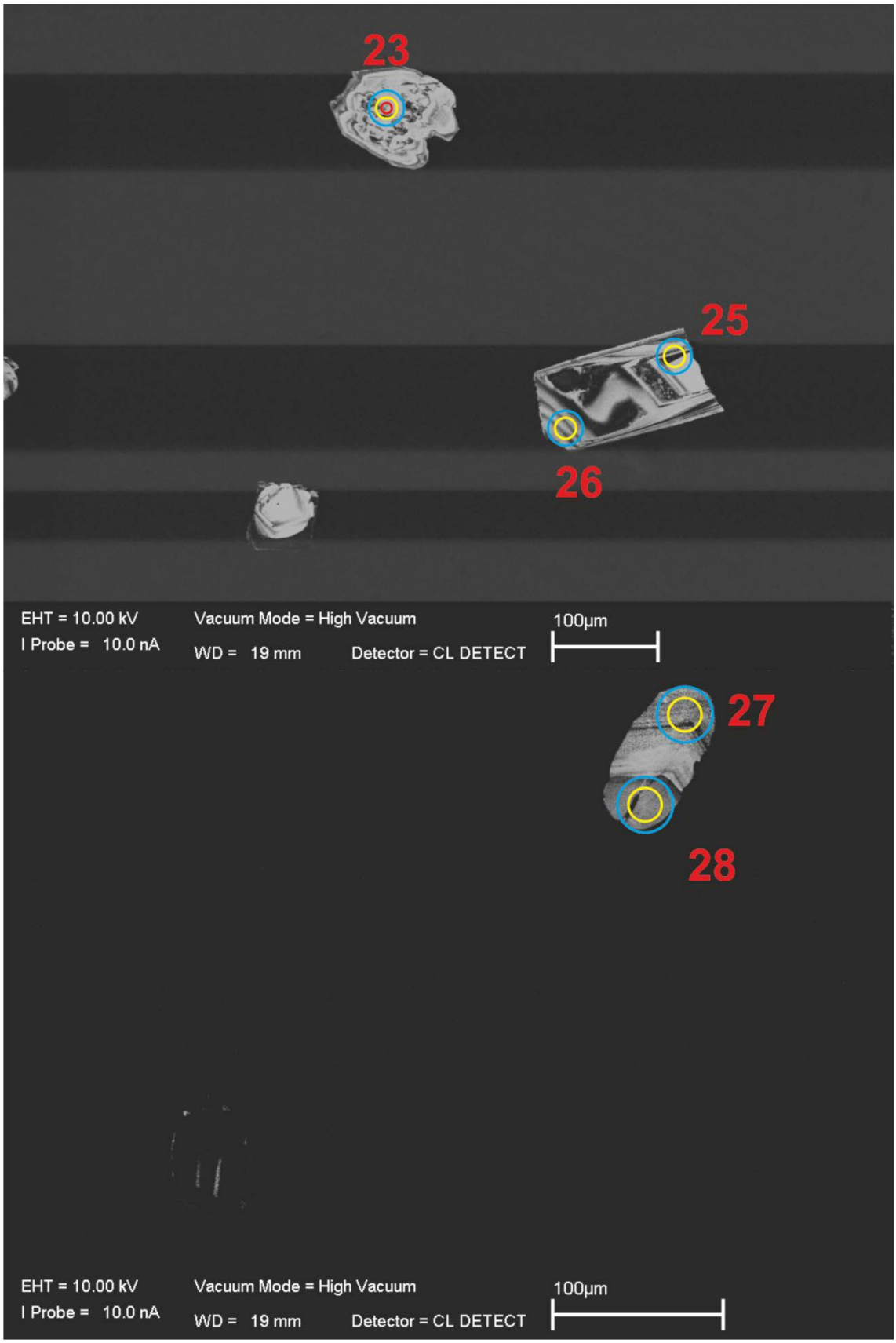
23
25
26
EHT = 10.00 kV
I Probe = 10.0 nA
Vacuum Mode = High Vacuum
WD = 19 mm
Detector = CL DETECT
100µm
27
28
EHT = 10.00 kV
I Probe = 10.0 nA
Vacuum Mode = High Vacuum
WD = 19 mm
Detector = CL DETECT
100µm

E.6. 3A02

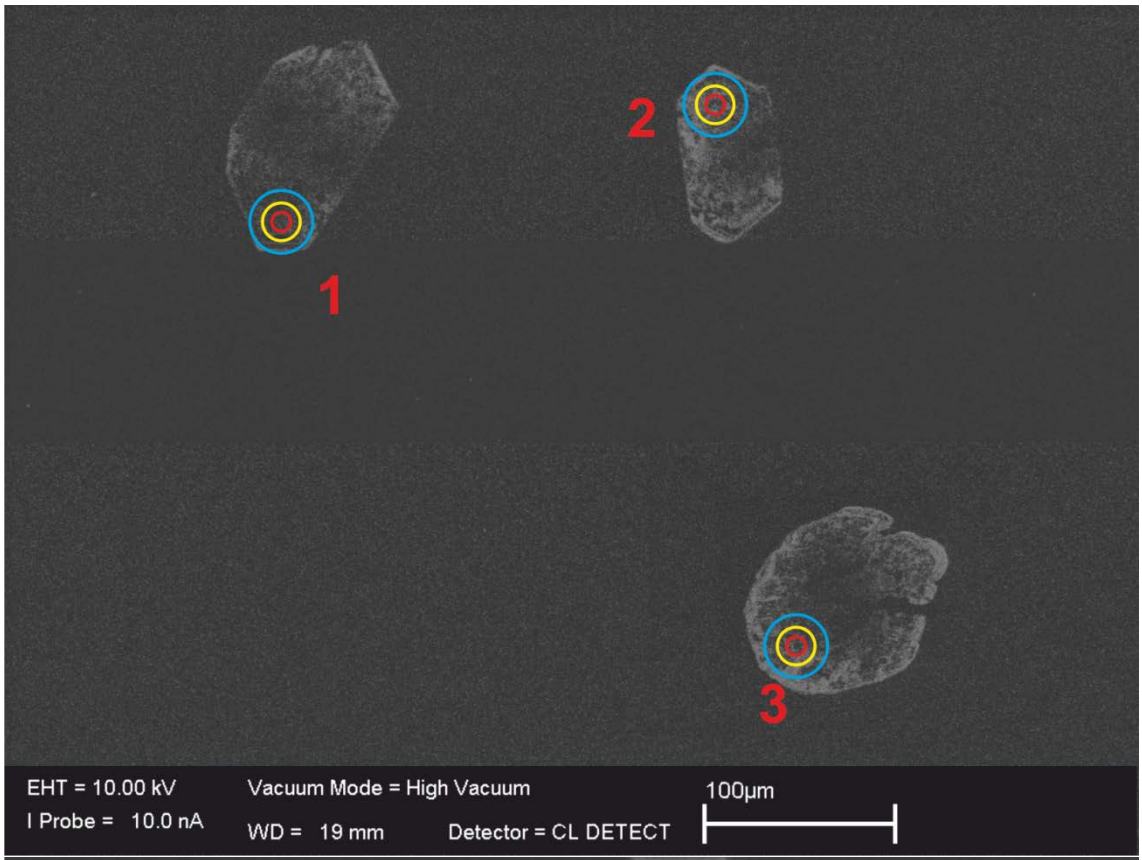
2
1
3
EHT = 10.00 kV
I Probe = 10.0 nA
Vacuum Mode = High Vacuum
WD = 19 mm
Detector = CL DETECT
100µm

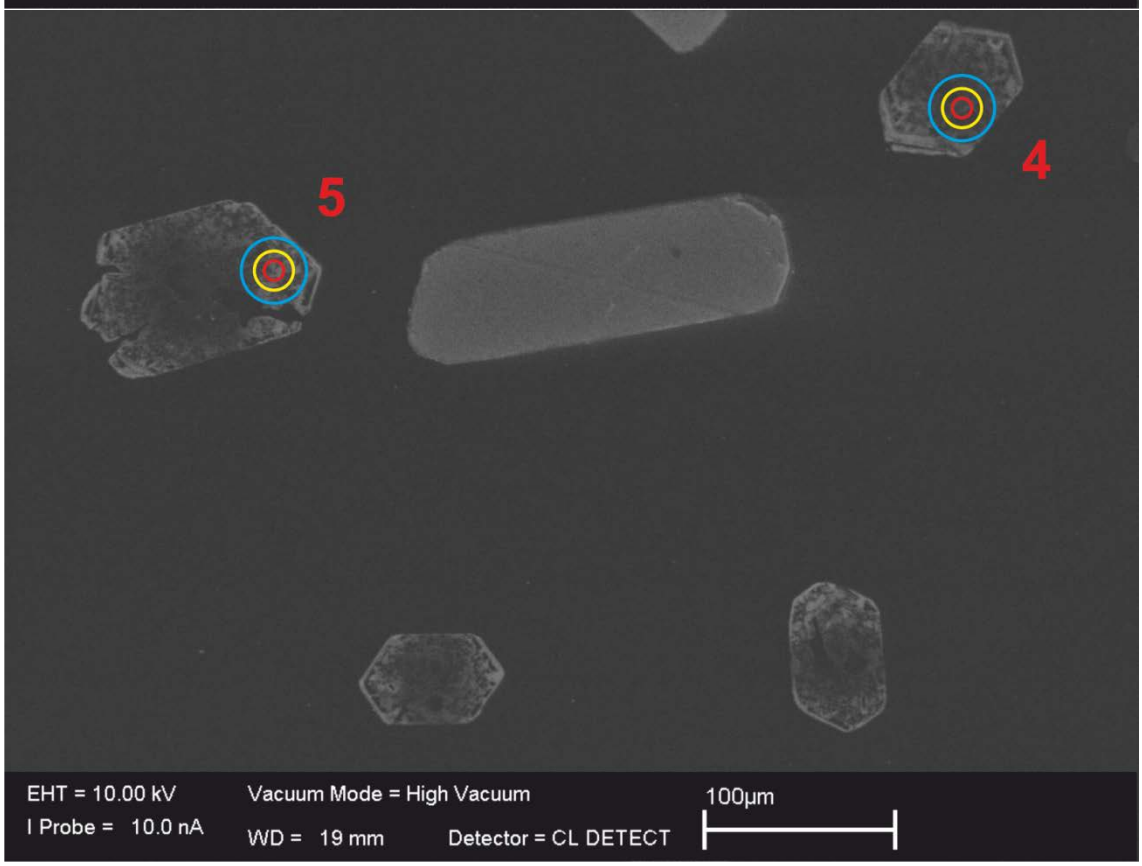
4
5
EHT = 10.00 kV
I Probe = 10.0 nA
Vacuum Mode = High Vacuum
WD = 19 mm
Detector = CL DETECT
100µm

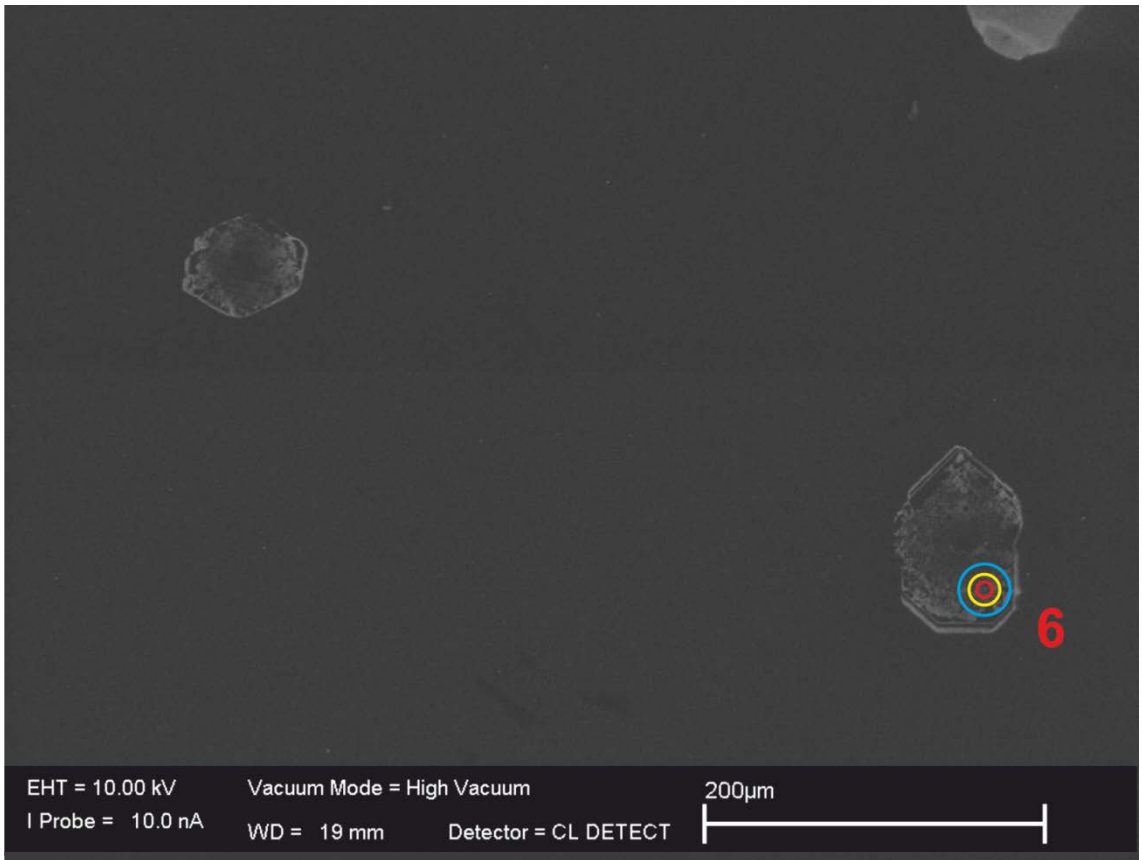
6
EHT = 10.00 kV
I Probe = 10.0 nA
Vacuum Mode = High Vacuum
WD = 19 mm
Detector = CL DETECT
200µm

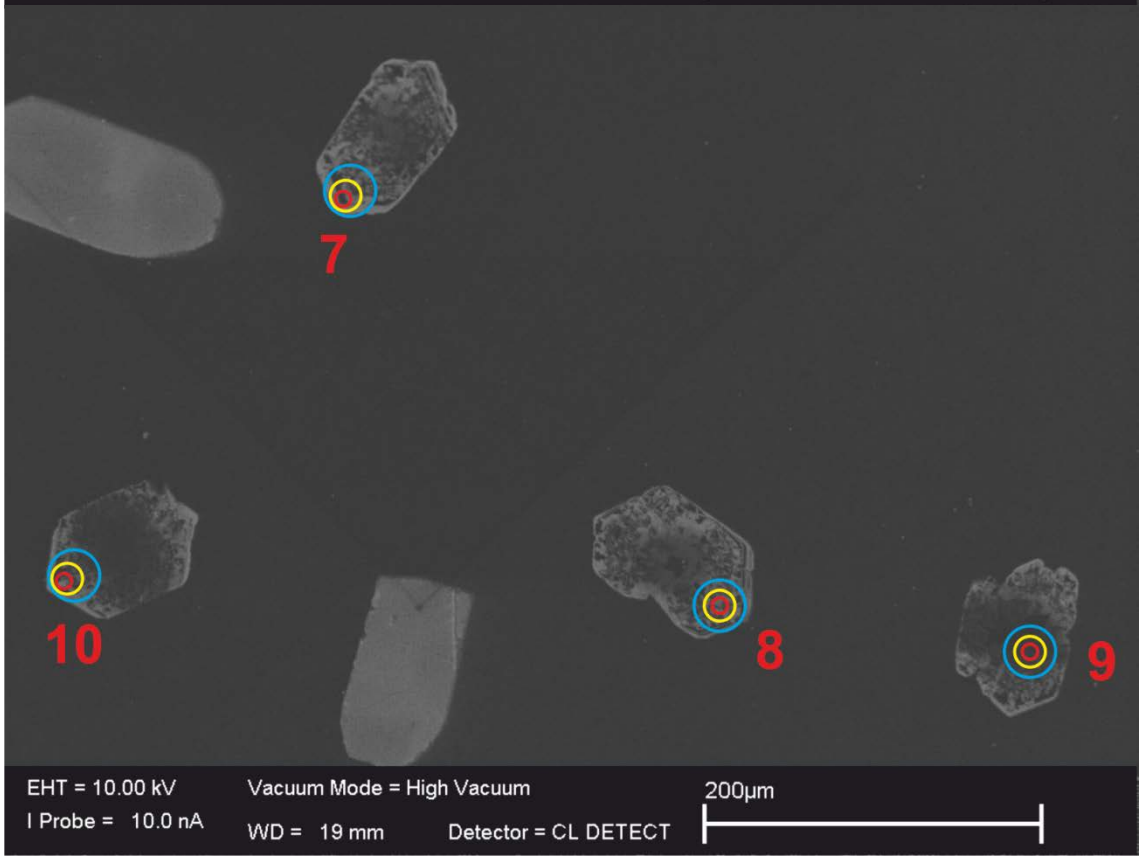
7
10
8
9
EHT = 10.00 kV
I Probe = 10.0 nA
Vacuum Mode = High Vacuum
WD = 19 mm
Detector = CL DETECT
200µm

E.7. 3A03

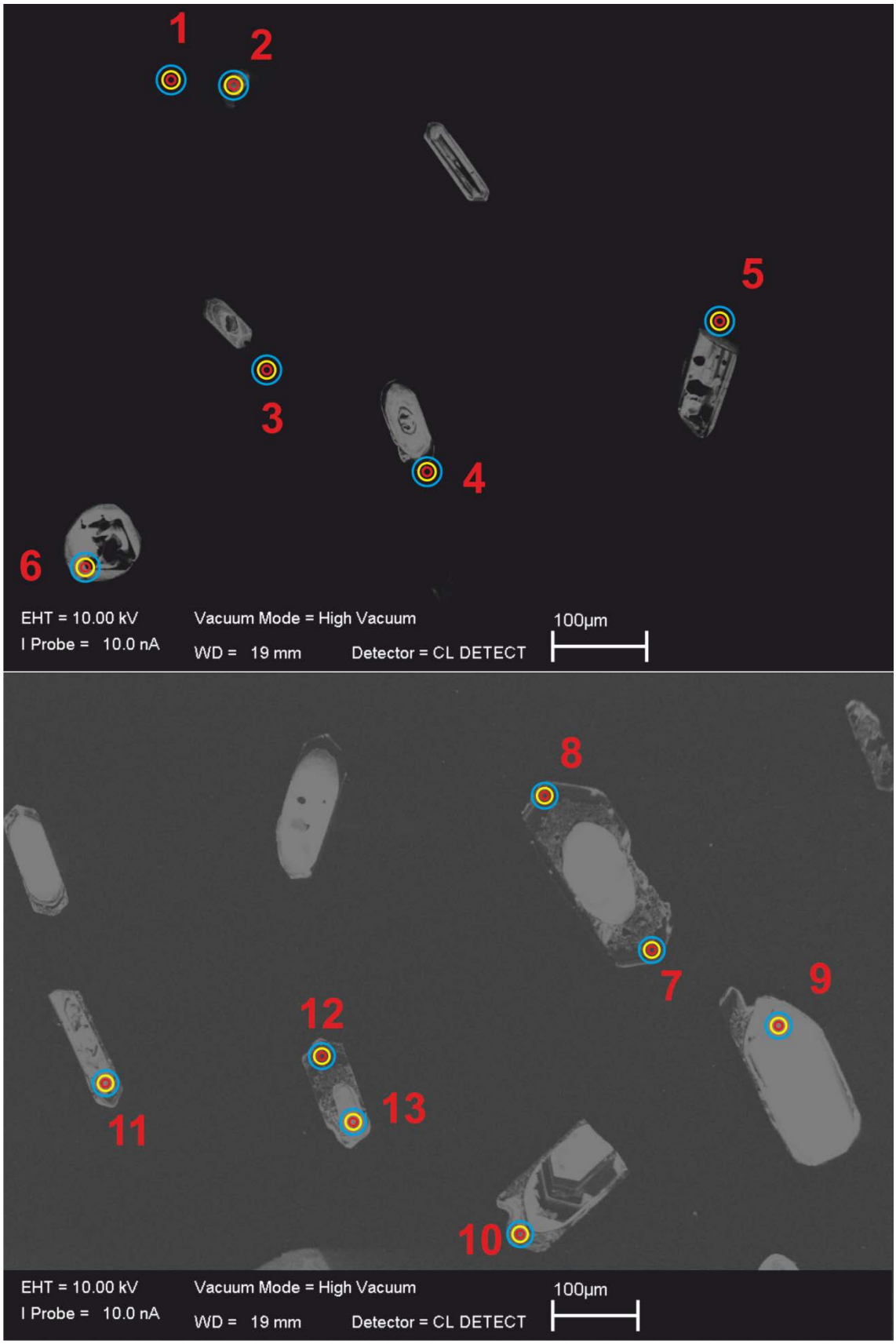
1
2
3
4
5
6
EHT = 10.00 kV
I Probe = 10.0 nA
Vacuum Mode = High Vacuum
WD = 19 mm
Detector = CL DETECT
100µm
8
7
9
12
13
11
10
EHT = 10.00 kV
I Probe = 10.0 nA
Vacuum Mode = High Vacuum
WD = 19 mm
Detector = CL DETECT
100µm

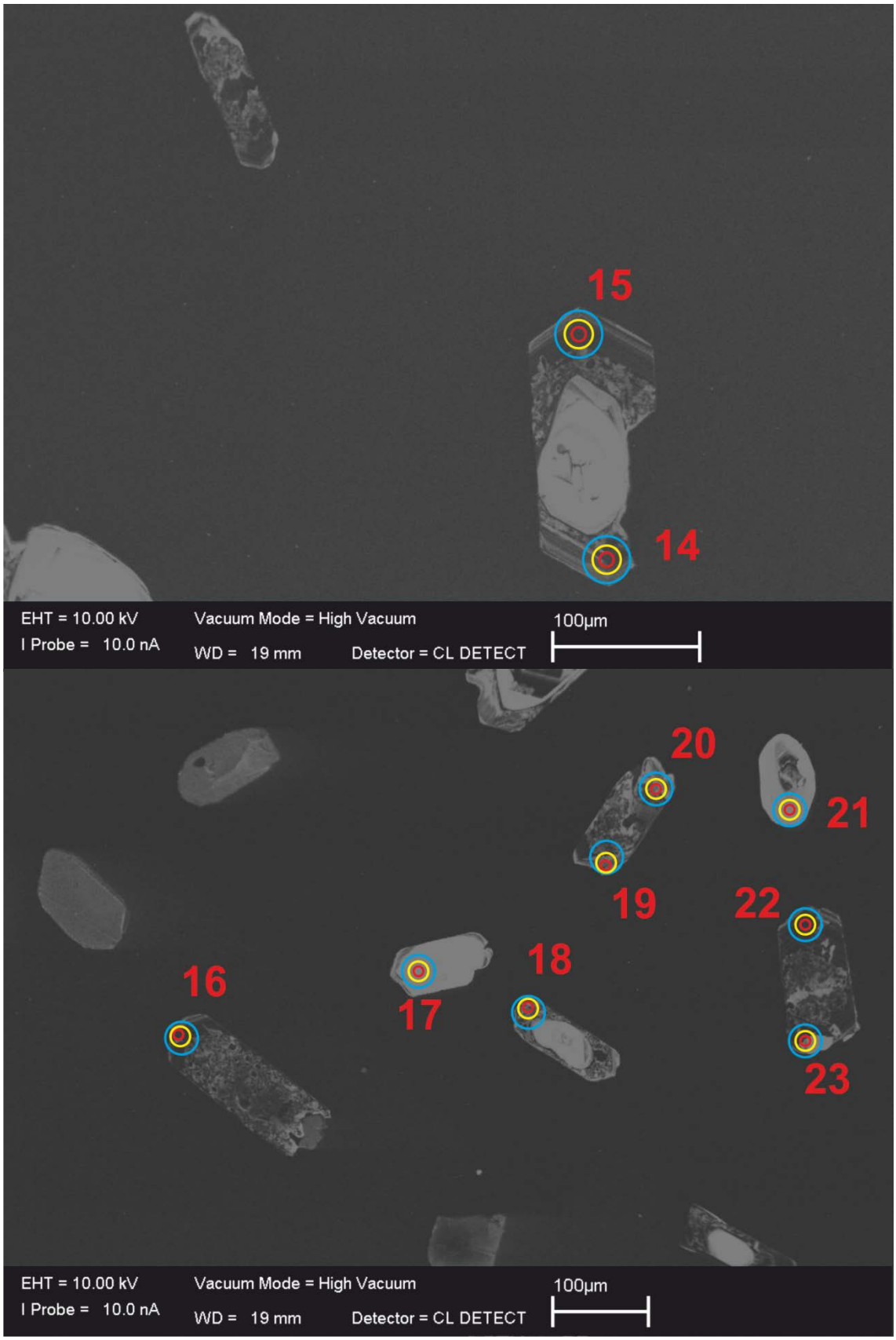
15
14
EHT = 10.00 kV
I Probe = 10.0 nA
Vacuum Mode = High Vacuum
WD = 19 mm
Detector = CL DETECT
100µm
20
21
19
22
18
16
17
23
EHT = 10.00 kV
I Probe = 10.0 nA
Vacuum Mode = High Vacuum
WD = 19 mm
Detector = CL DETECT
100µm

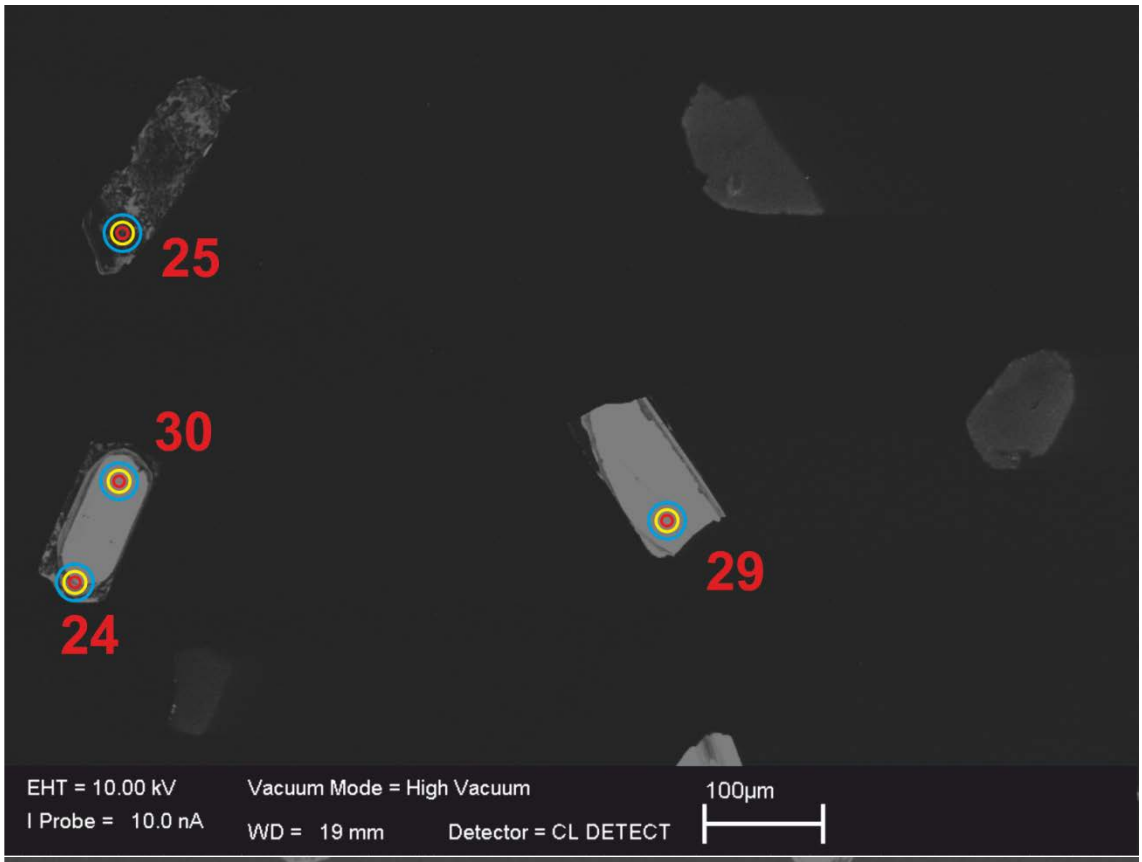
25
30
24
29
EHT = 10.00 kV
I Probe = 10.0 nA
Vacuum Mode = High Vacuum
WD = 19 mm
Detector = CL DETECT
100µm

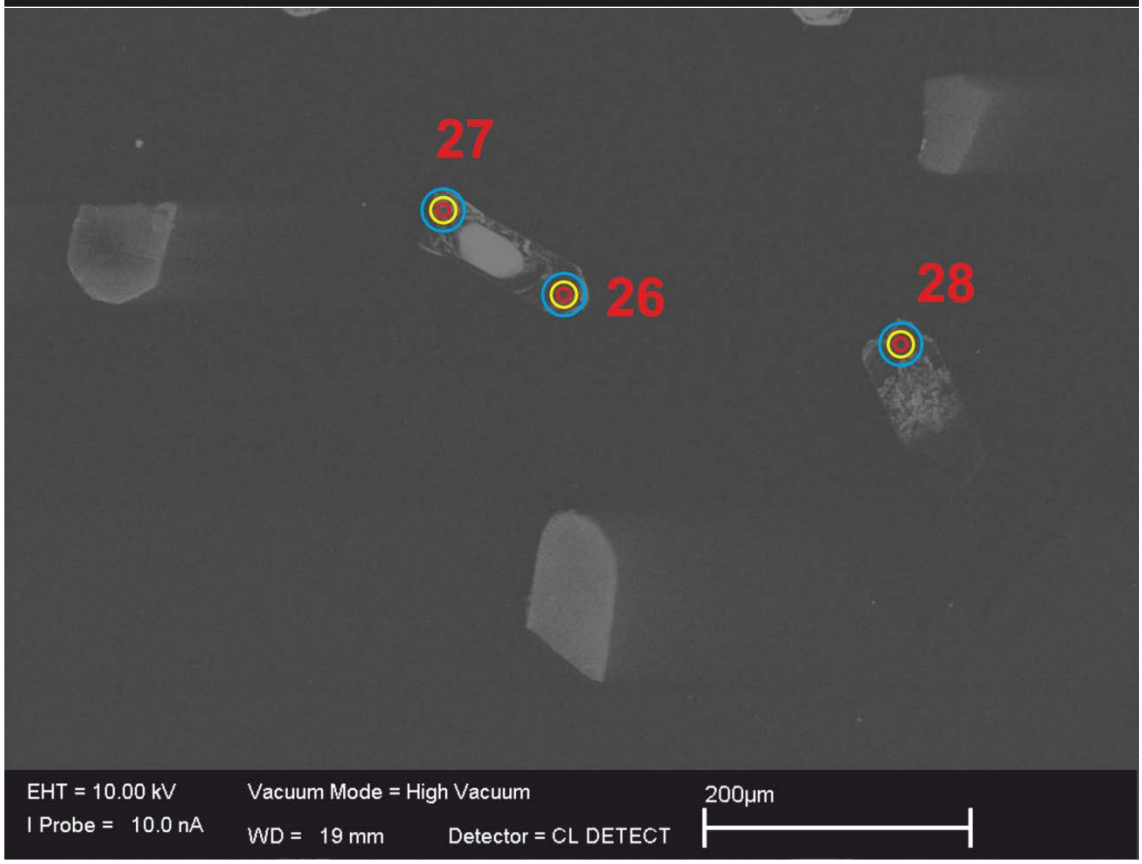
27
26
28
EHT = 10.00 kV
I Probe = 10.0 nA
Vacuum Mode = High Vacuum
WD = 19 mm
Detector = CL DETECT
200µm

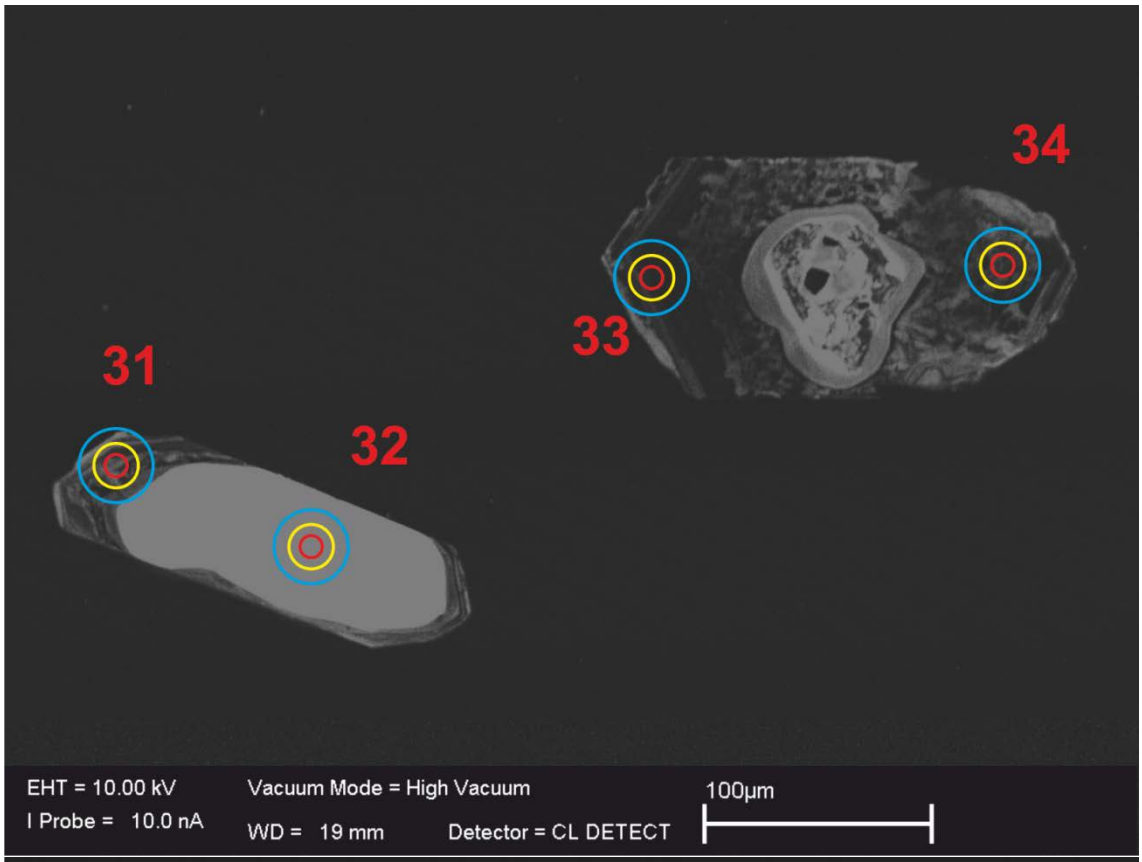
34
33
31
32
EHT = 10.00 kV
I Probe = 10.0 nA
Vacuum Mode = High Vacuum
WD = 19 mm
Detector = CL DETECT
100µm

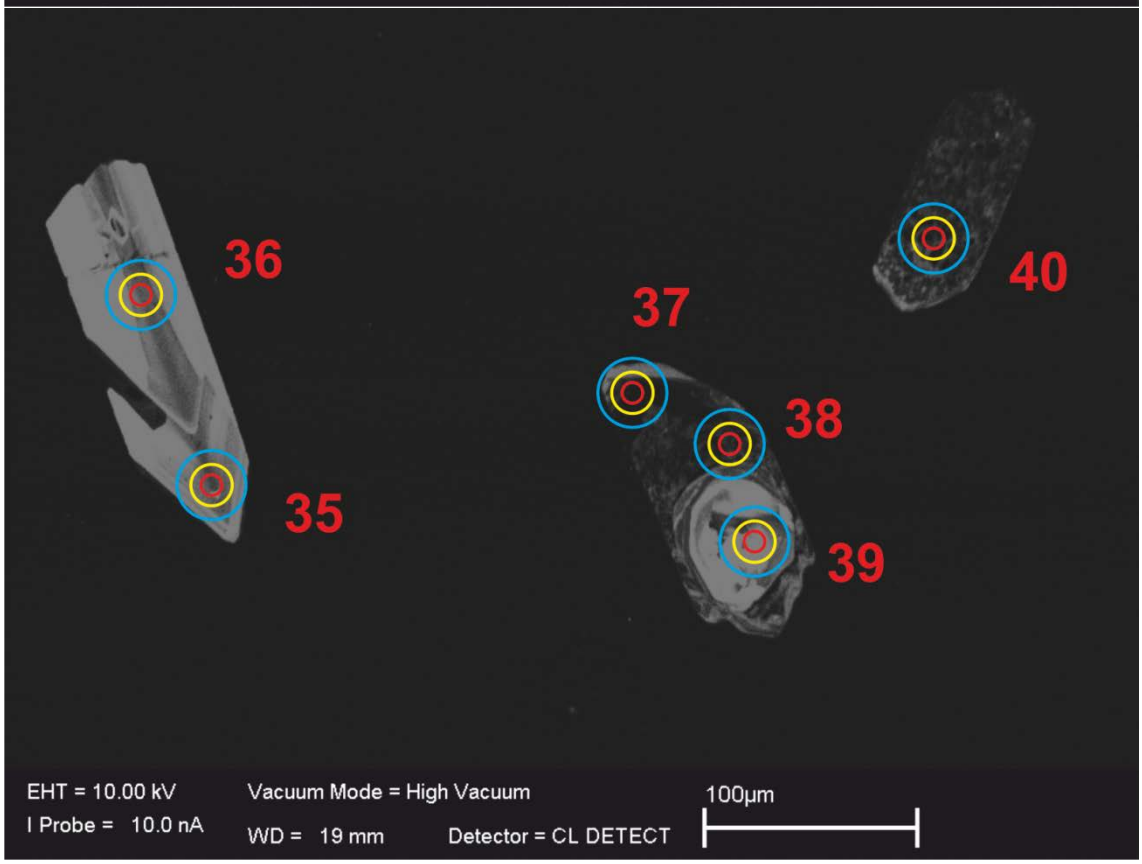
36
40
37
38
35
39
EHT = 10.00 kV
I Probe = 10.0 nA
Vacuum Mode = High Vacuum
WD = 19 mm
Detector = CL DETECT
100µm

E.8. 4D01

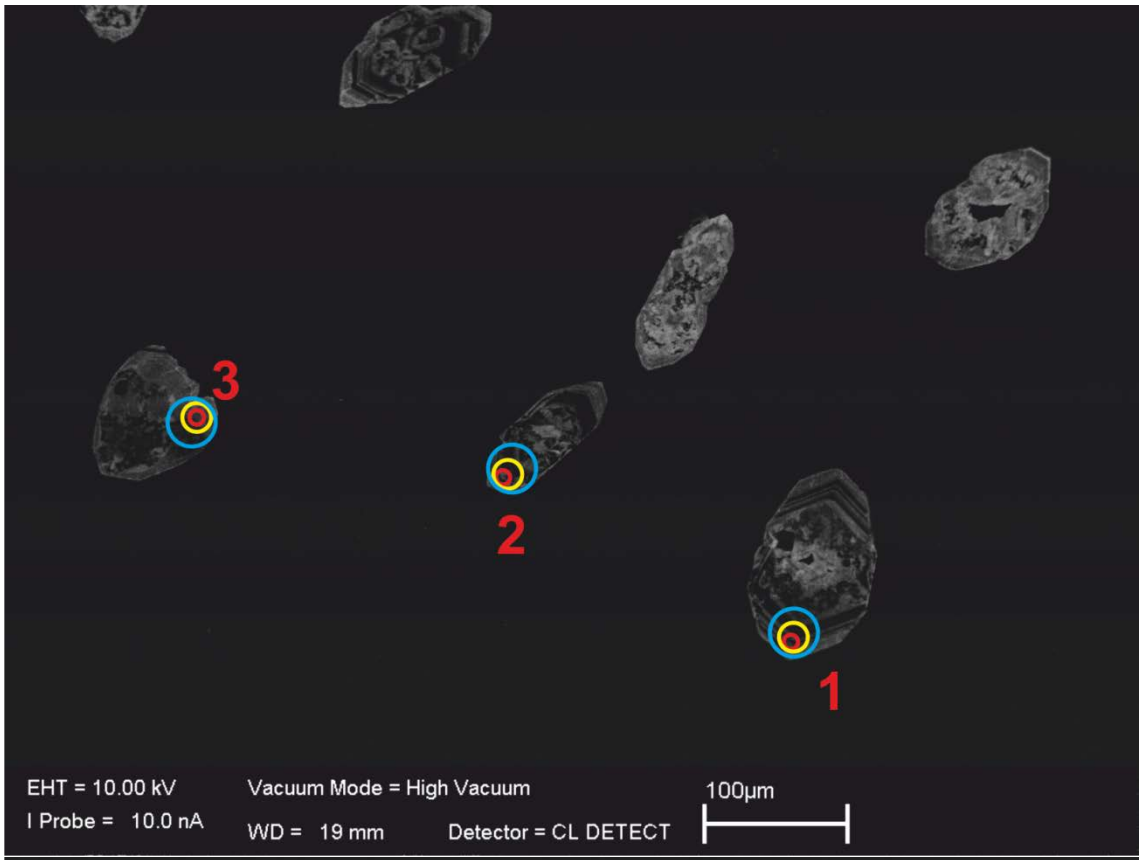
3
2
1
EHT = 10.00 kV
I Probe = 10.0 nA
Vacuum Mode = High Vacuum
WD = 19 mm
Detector = CL DETECT
100µm

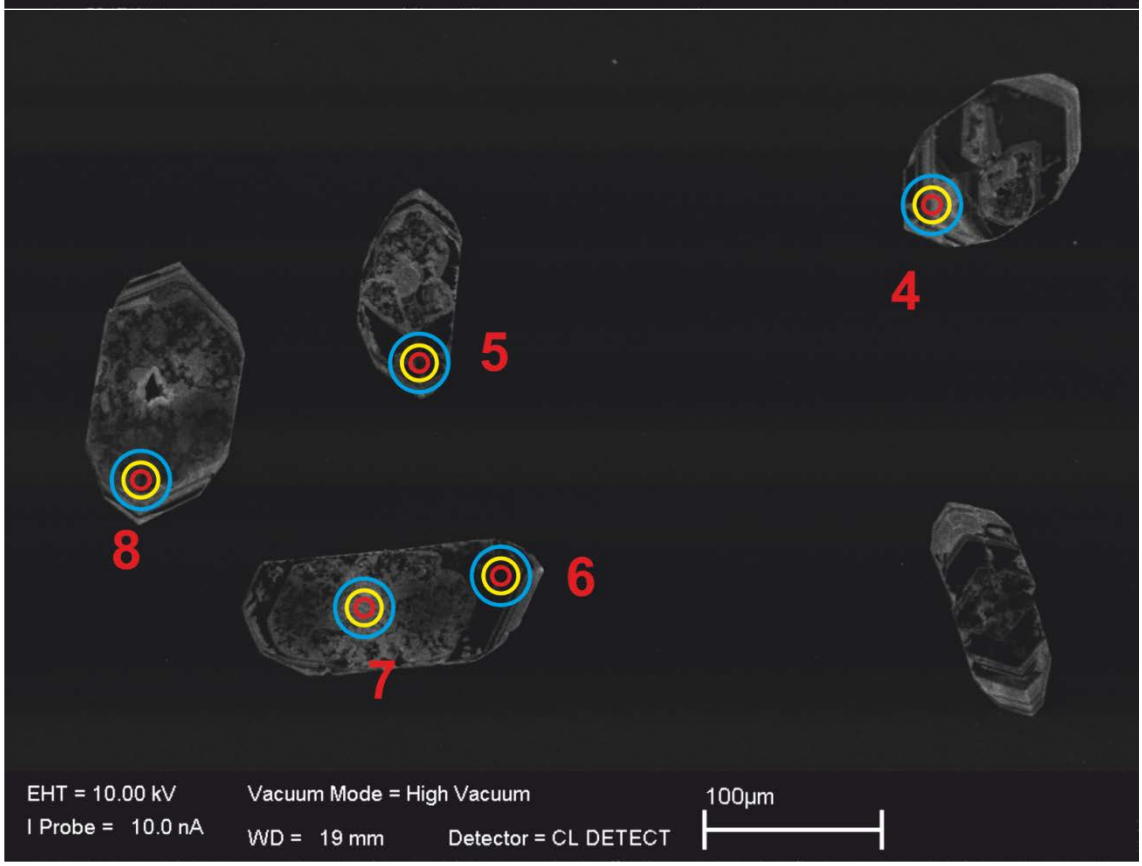
4
5
8
6
7
EHT = 10.00 kV
I Probe = 10.0 nA
Vacuum Mode = High Vacuum
WD = 19 mm
Detector = CL DETECT
100µm

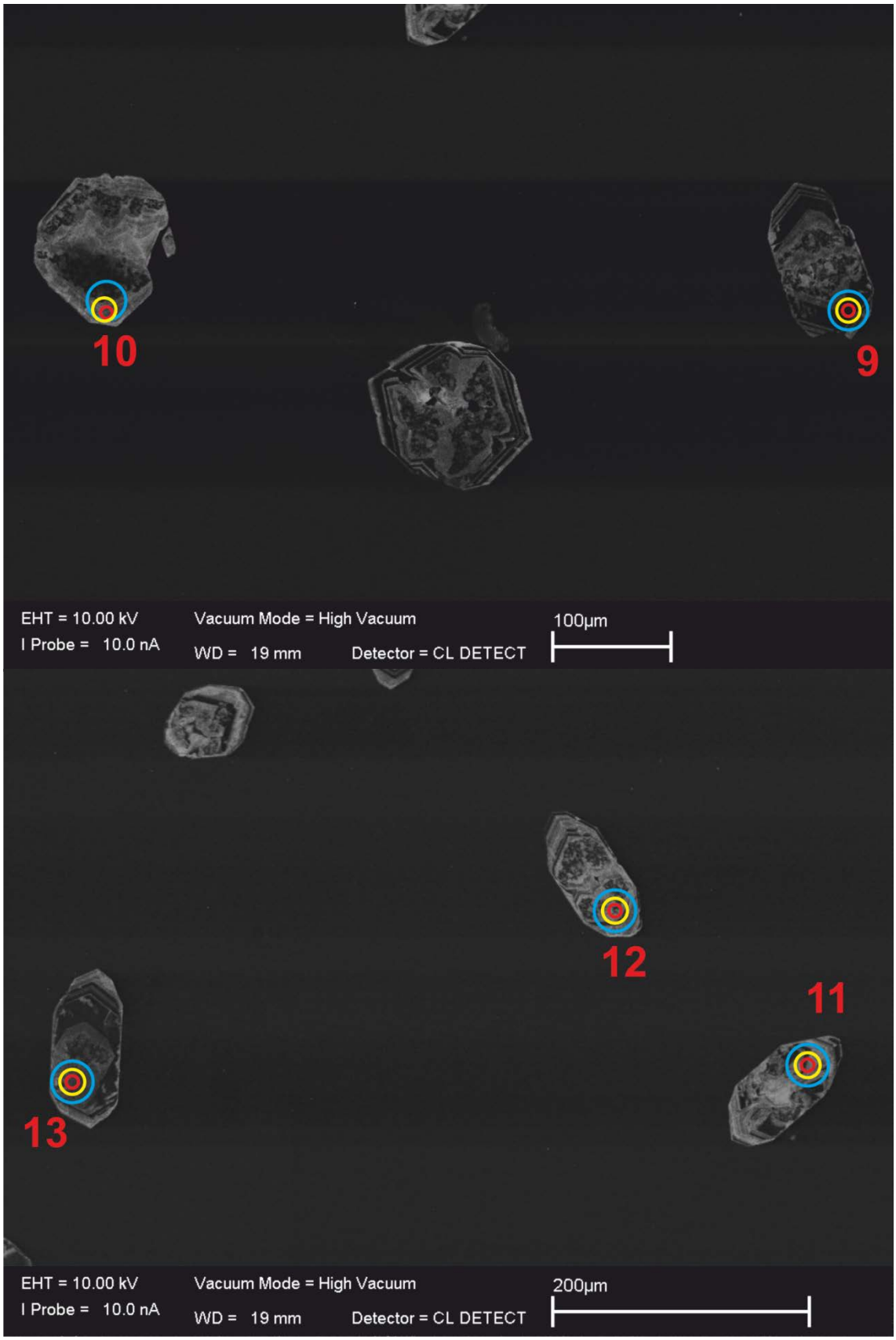
10
9
EHT = 10.00 kV
I Probe = 10.0 nA
Vacuum Mode = High Vacuum
WD = 19 mm
Detector = CL DETECT
100µm
12
11
13
EHT = 10.00 kV
I Probe = 10.0 nA
Vacuum Mode = High Vacuum
WD = 19 mm
Detector = CL DETECT
200µm

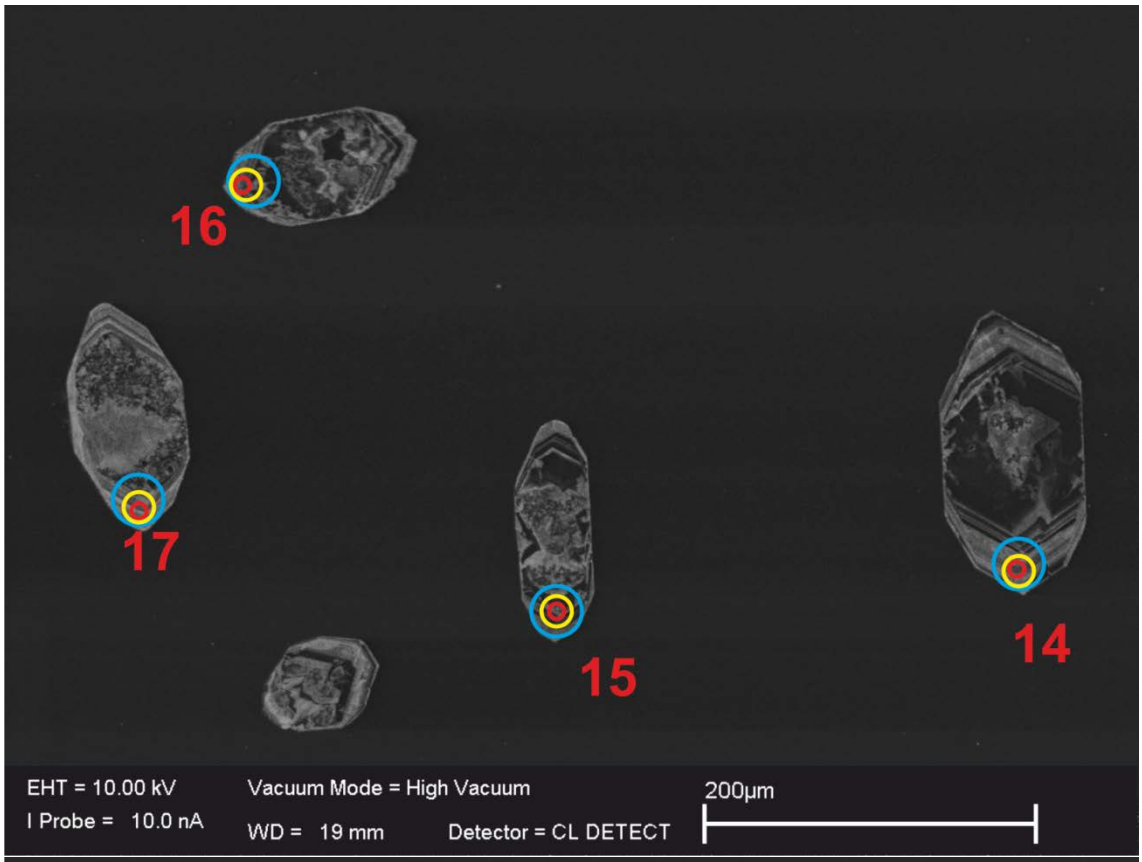
16
17
15
14
EHT = 10.00 kV
I Probe = 10.0 nA
Vacuum Mode = High Vacuum
WD = 19 mm
Detector = CL DETECT
200µm

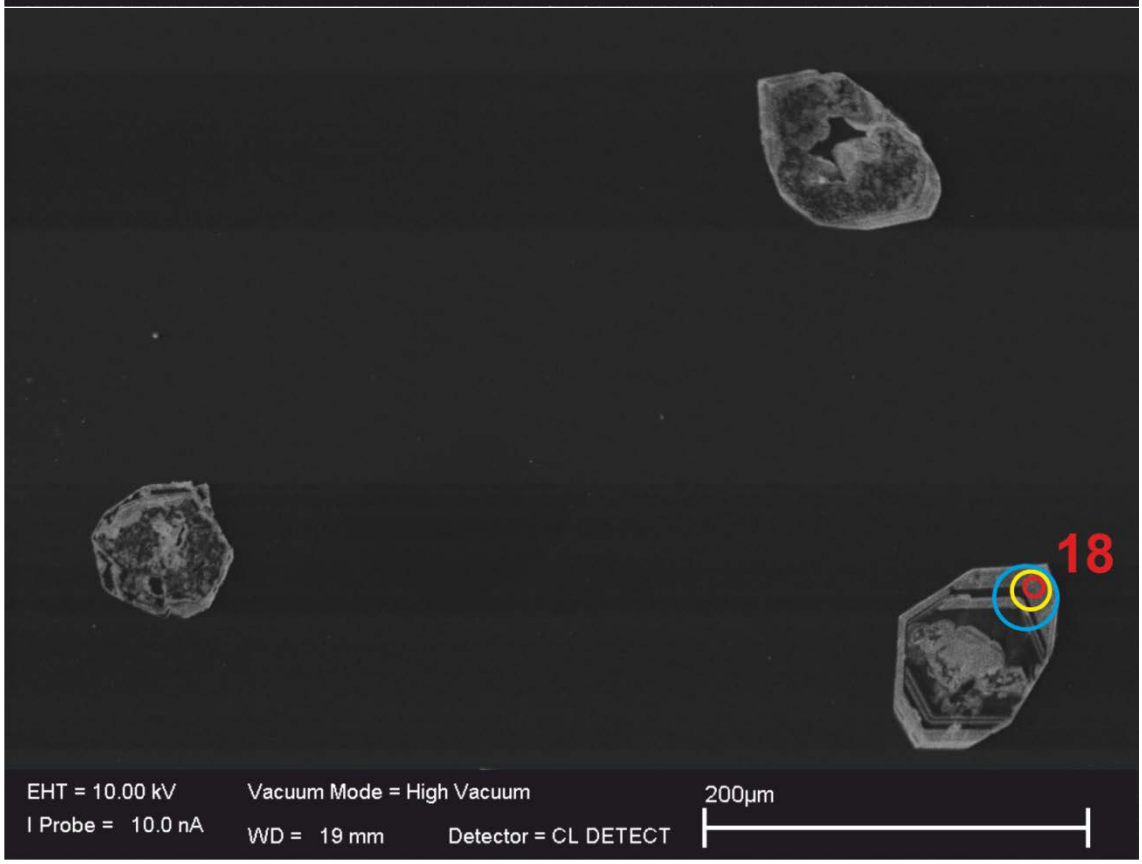
18
EHT = 10.00 kV
I Probe = 10.0 nA
Vacuum Mode = High Vacuum
WD = 19 mm
Detector = CL DETECT
200µm

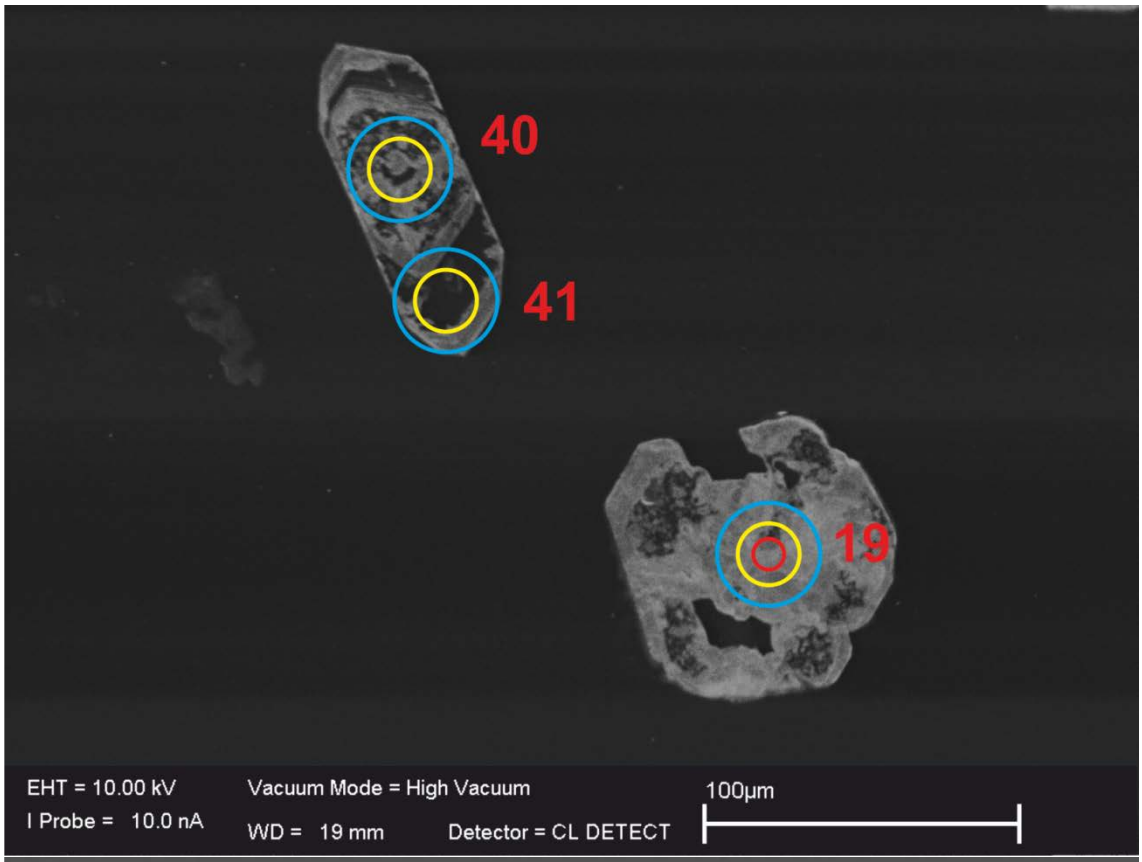
40
41
19
EHT = 10.00 kV
I Probe = 10.0 nA
Vacuum Mode = High Vacuum
WD = 19 mm
Detector = CL DETECT
100µm

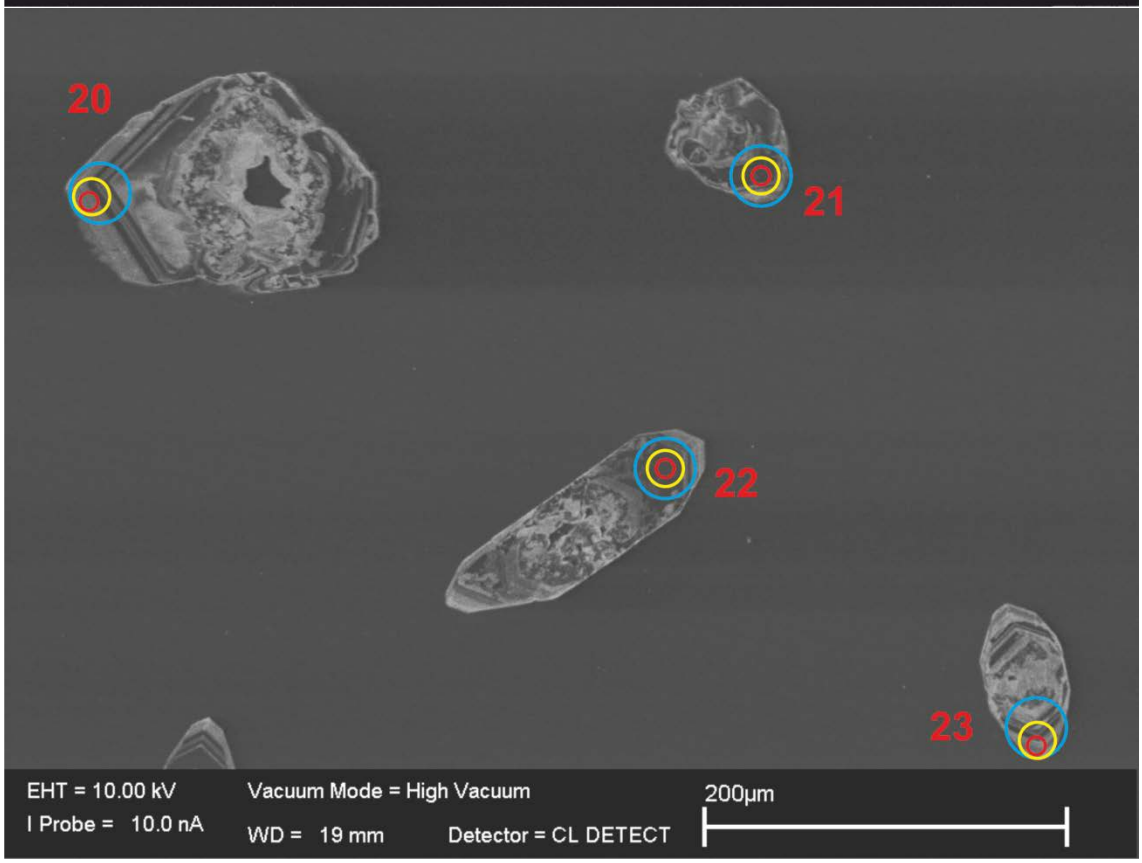
20
21
22
23
EHT = 10.00 kV
I Probe = 10.0 nA
Vacuum Mode = High Vacuum
WD = 19 mm
Detector = CL DETECT
200µm

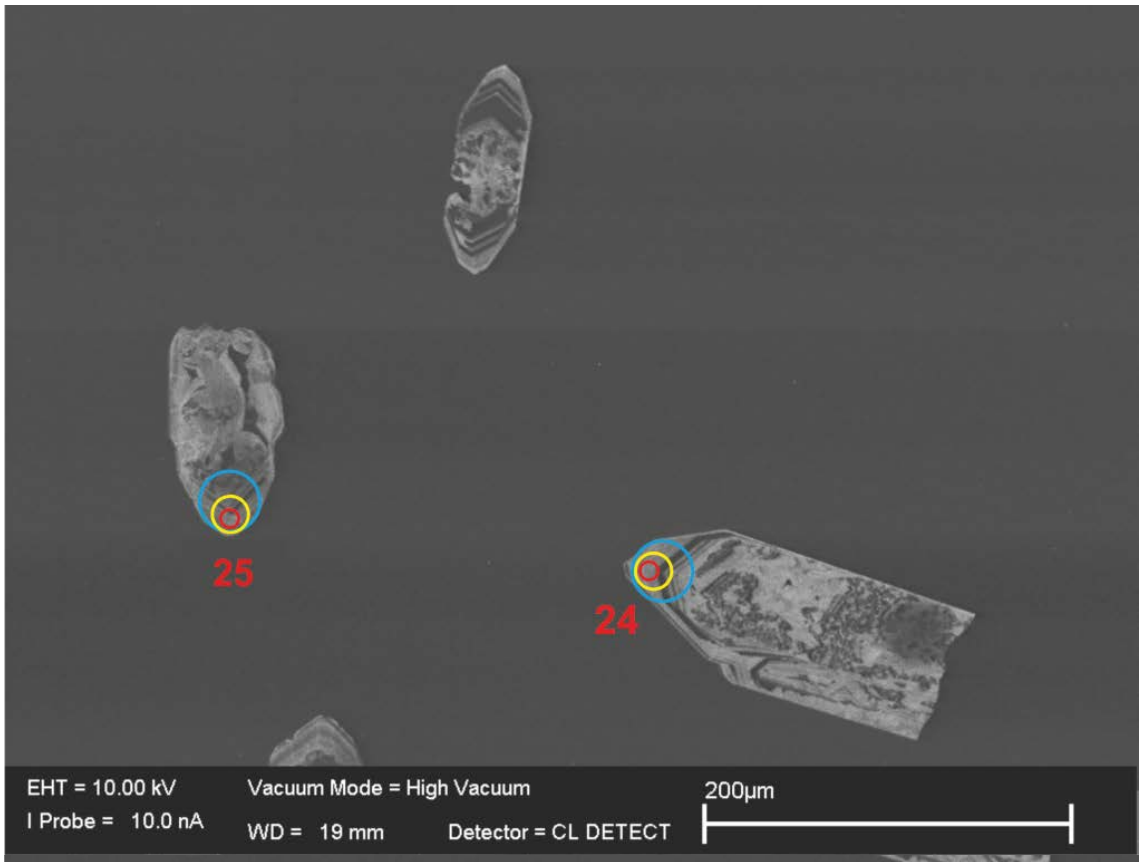
25
24
EHT = 10.00 kV
I Probe = 10.0 nA
Vacuum Mode = High Vacuum
WD = 19 mm
Detector = CL DETECT
200µm

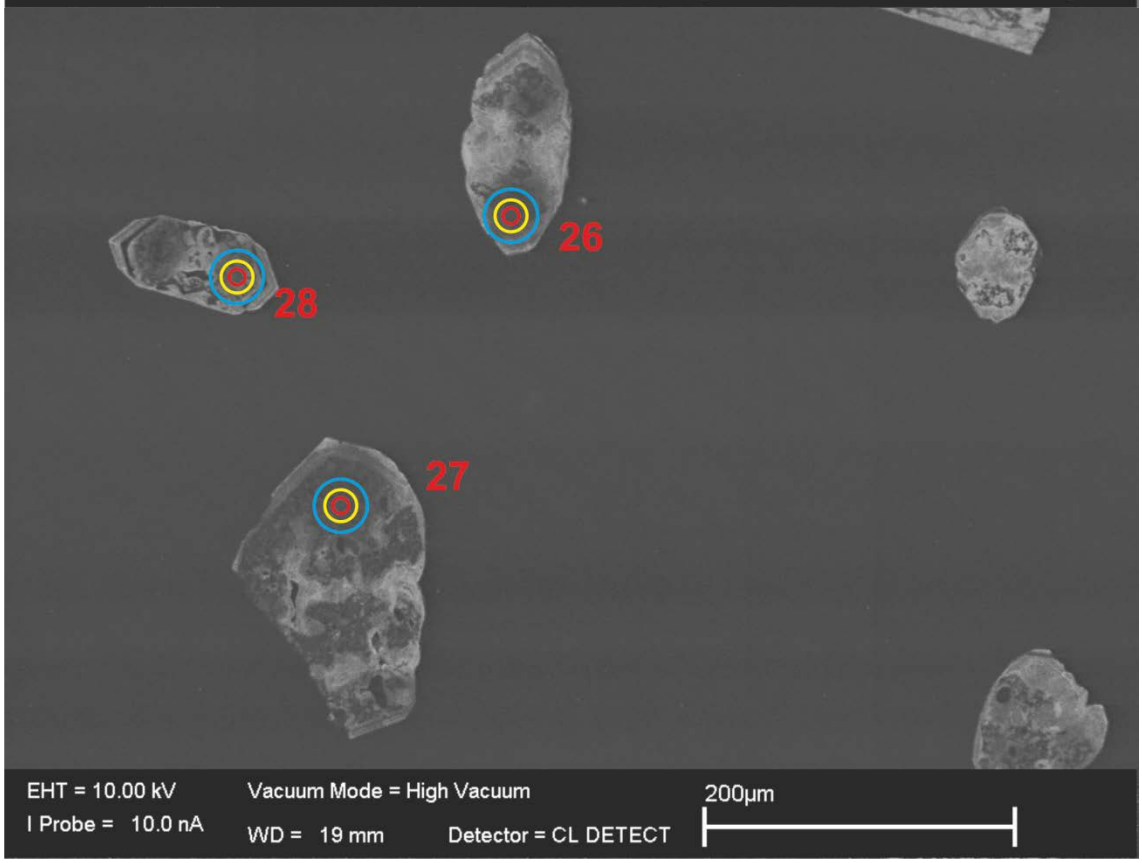
26
28
27
EHT = 10.00 kV
I Probe = 10.0 nA
Vacuum Mode = High Vacuum
WD = 19 mm
Detector = CL DETECT
200µm

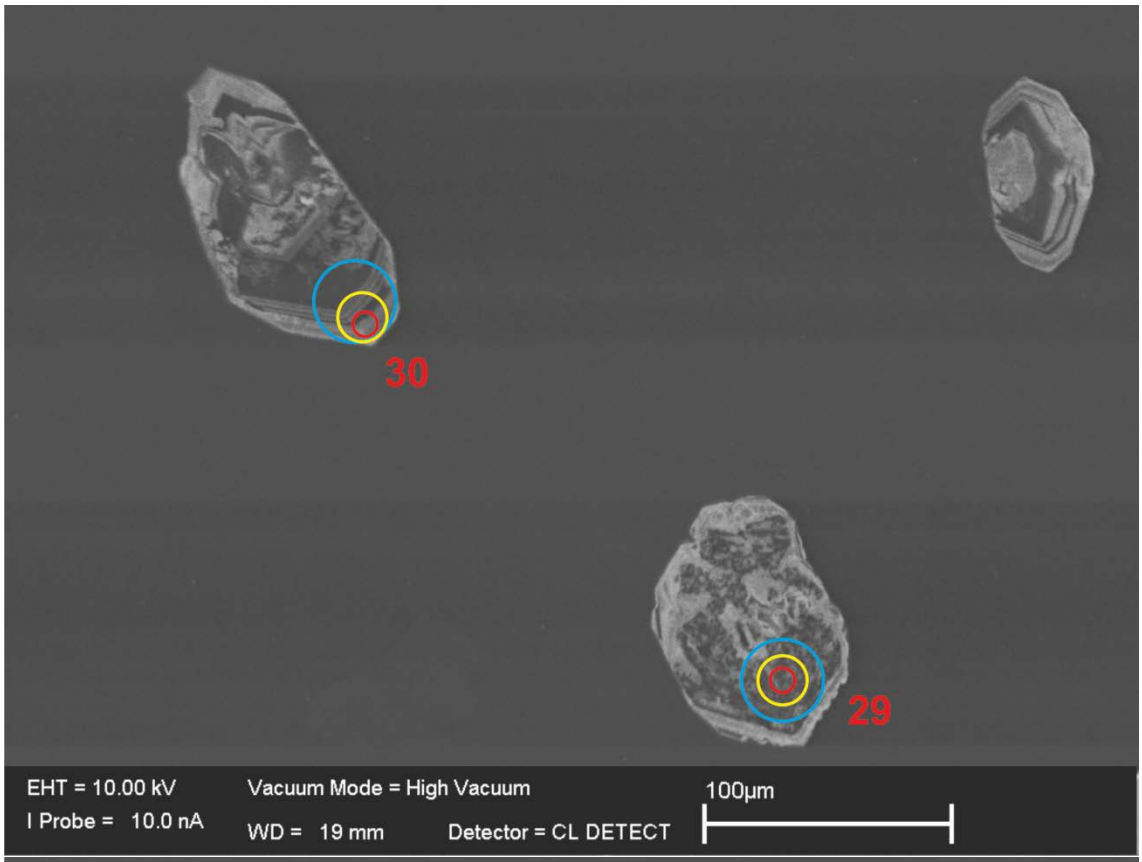
30
29
EHT = 10.00 kV
I Probe = 10.0 nA
Vacuum Mode = High Vacuum
WD = 19 mm
Detector = CL DETECT
100µm

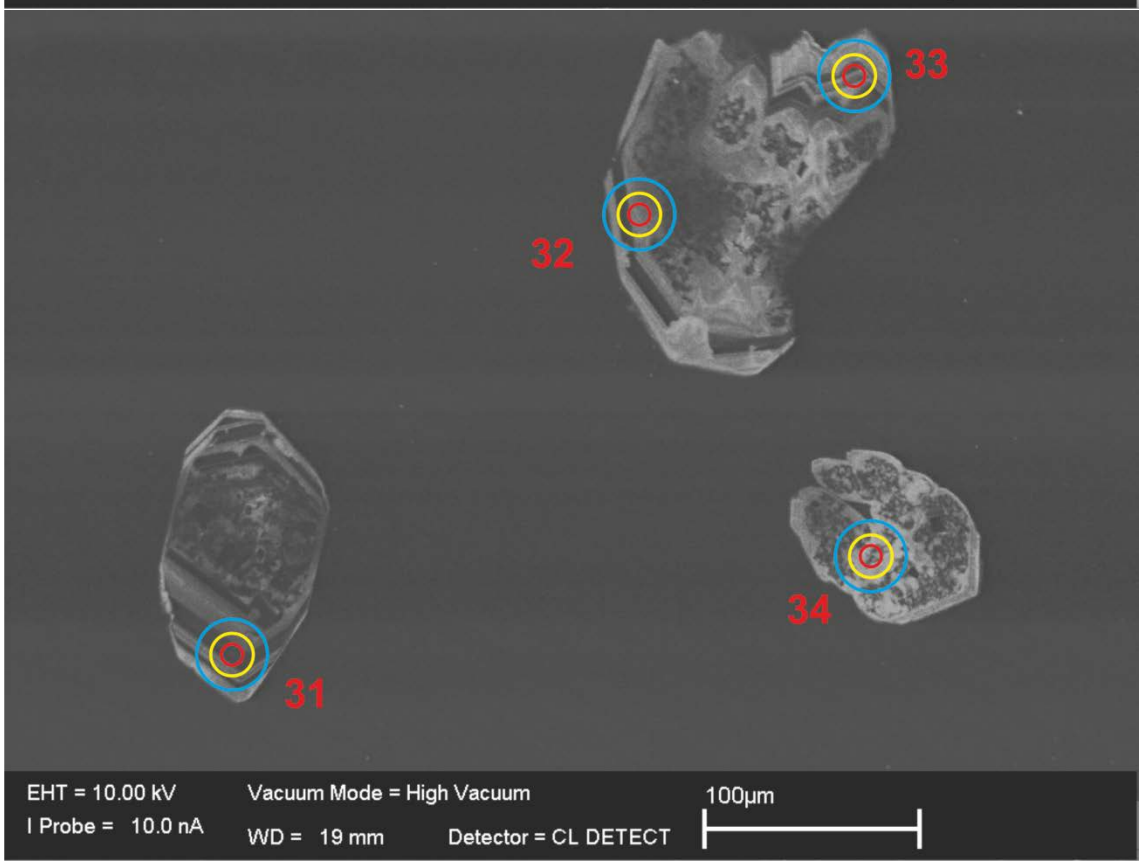
33
32
31
34
EHT = 10.00 kV
I Probe = 10.0 nA
Vacuum Mode = High Vacuum
WD = 19 mm
Detector = CL DETECT
100µm

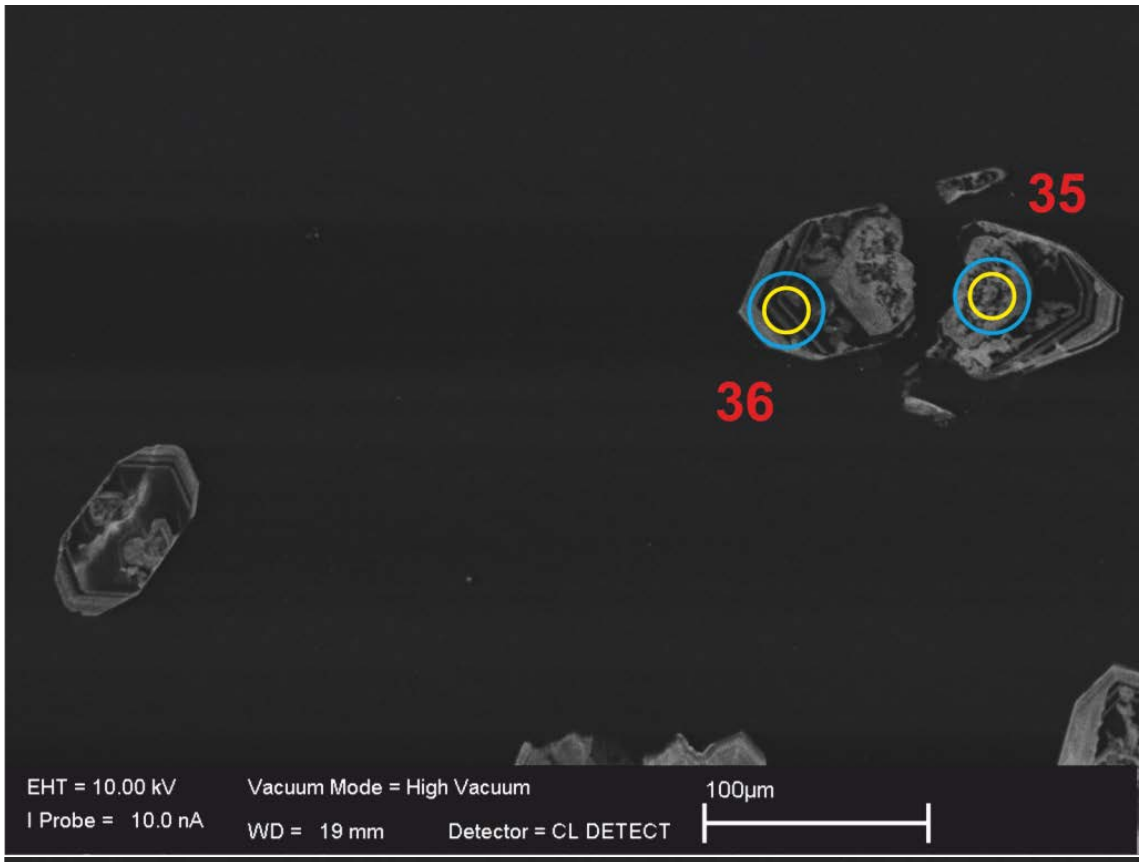
35
36
EHT = 10.00 kV
I Probe = 10.0 nA
Vacuum Mode = High Vacuum
WD = 19 mm
Detector = CL DETECT
100µm

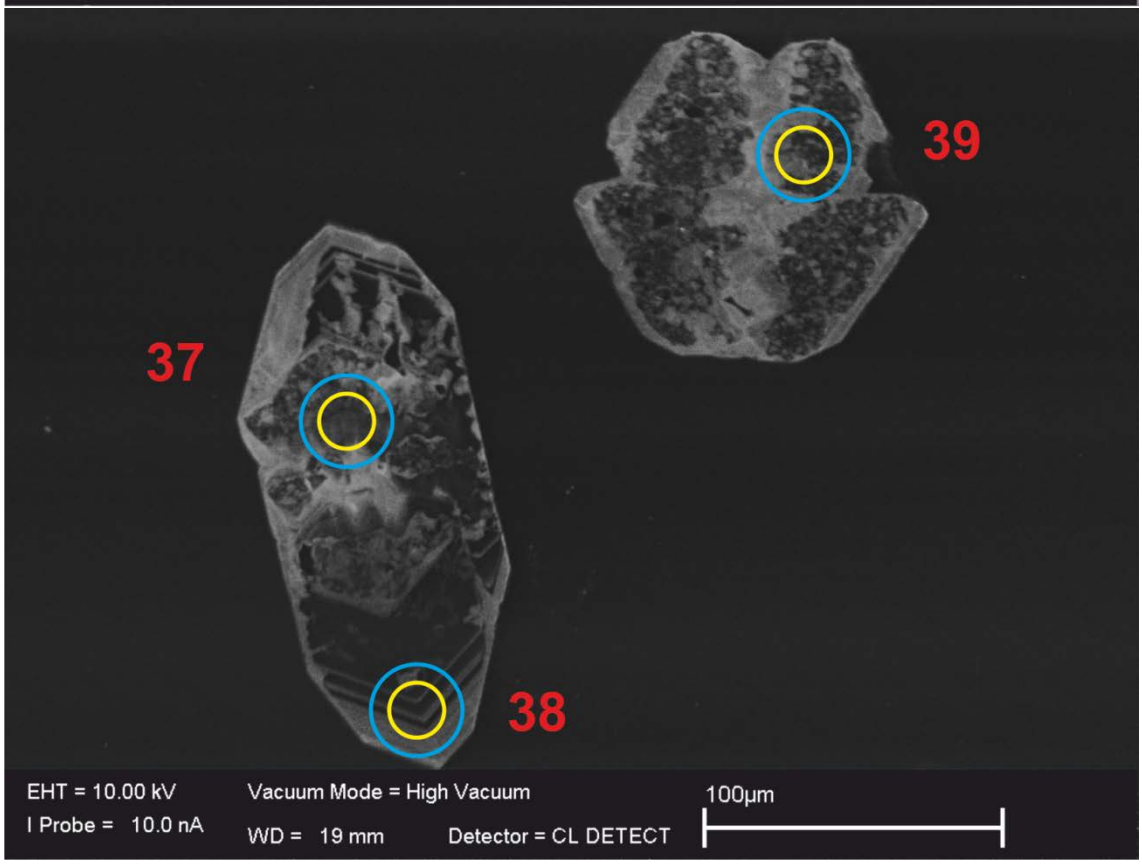
39
37
38
EHT = 10.00 kV
I Probe = 10.0 nA
Vacuum Mode = High Vacuum
WD = 19 mm
Detector = CL DETECT
100µm

E.9. DRB1215

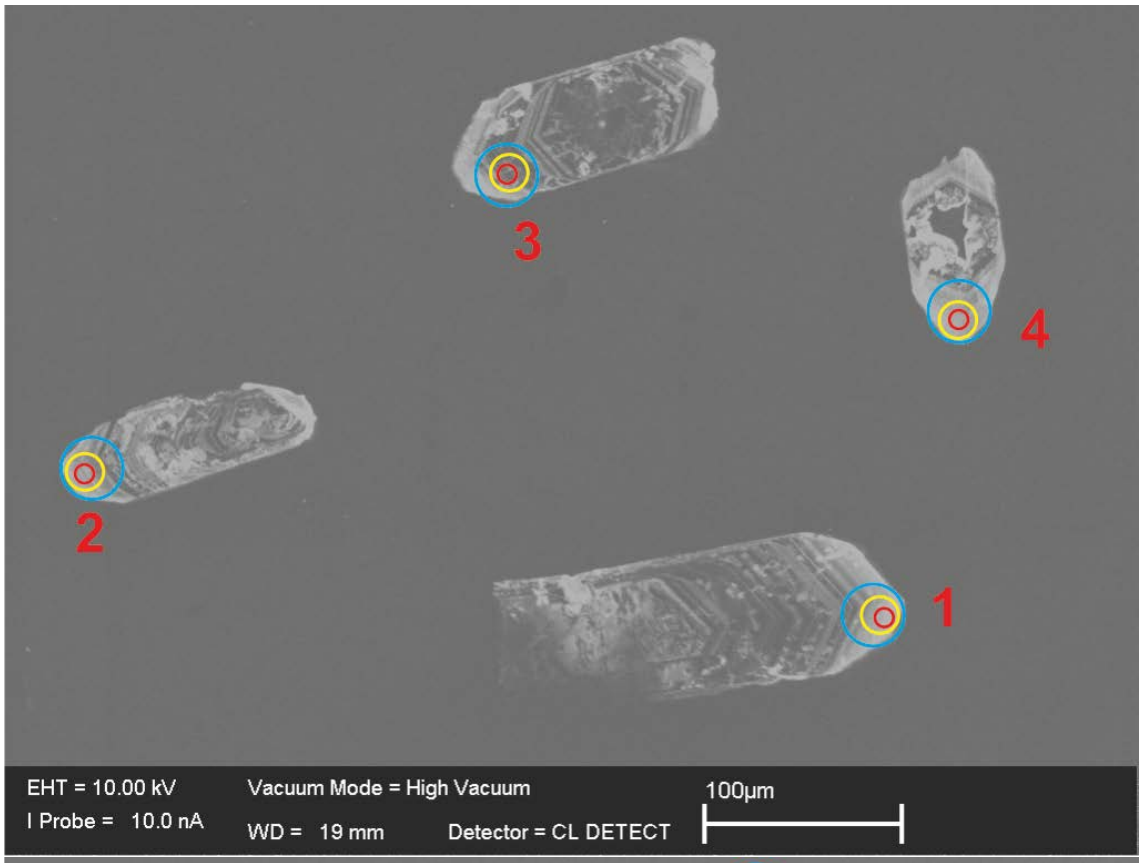
3
4
2
1
EHT = 10.00 kV
I Probe = 10.0 nA
Vacuum Mode = High Vacuum
WD = 19 mm
Detector = CL DETECT
100µm

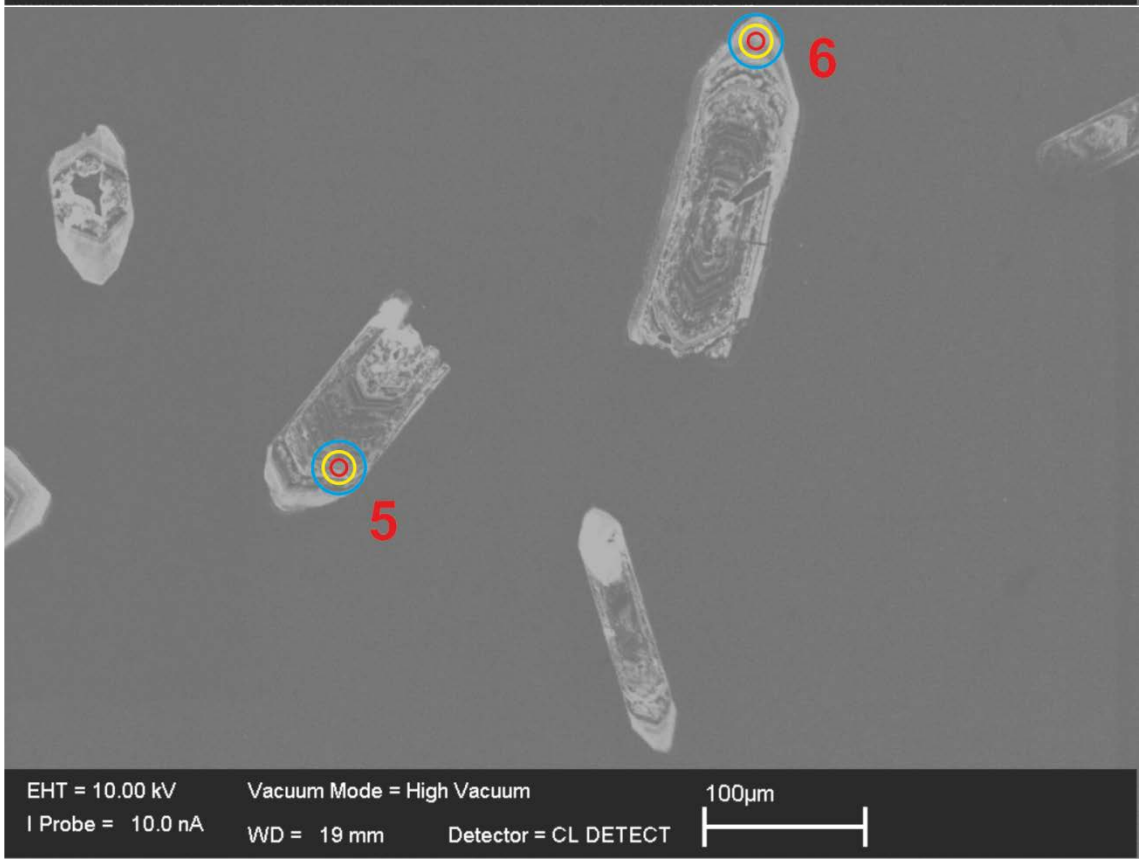
6
5
EHT = 10.00 kV
I Probe = 10.0 nA
Vacuum Mode = High Vacuum
WD = 19 mm
Detector = CL DETECT
100µm

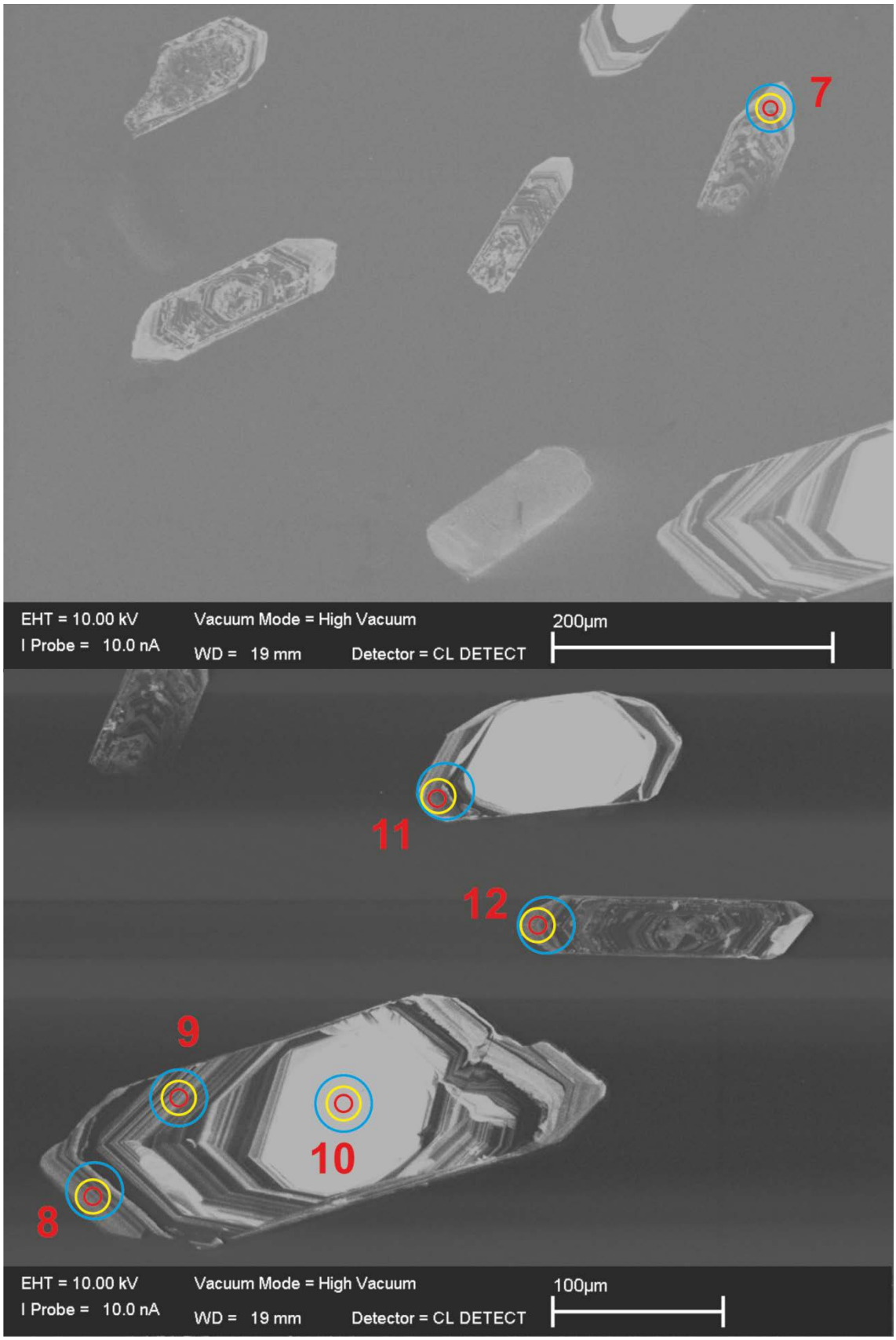
7
EHT = 10.00 kV
I Probe = 10.0 nA
Vacuum Mode = High Vacuum
WD = 19 mm
Detector = CL DETECT
200µm
11
12
9
10
8
EHT = 10.00 kV
I Probe = 10.0 nA
Vacuum Mode = High Vacuum
WD = 19 mm
Detector = CL DETECT
100µm

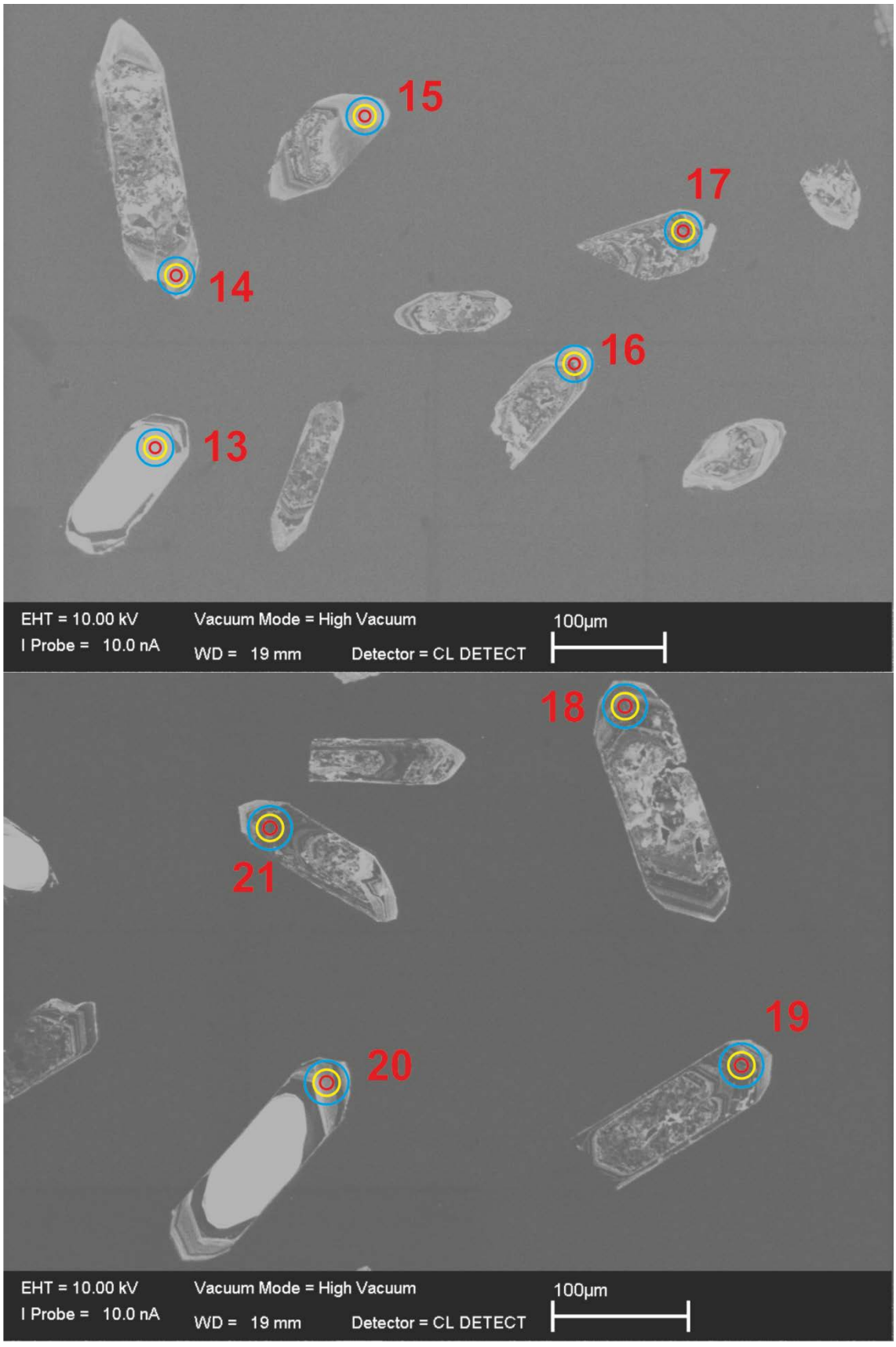
15
17
14
16
13
EHT = 10.00 kV
I Probe = 10.0 nA
Vacuum Mode = High Vacuum
WD = 19 mm
Detector = CL DETECT
100µm
18
21
19
20
EHT = 10.00 kV
I Probe = 10.0 nA
Vacuum Mode = High Vacuum
WD = 19 mm
Detector = CL DETECT
100µm

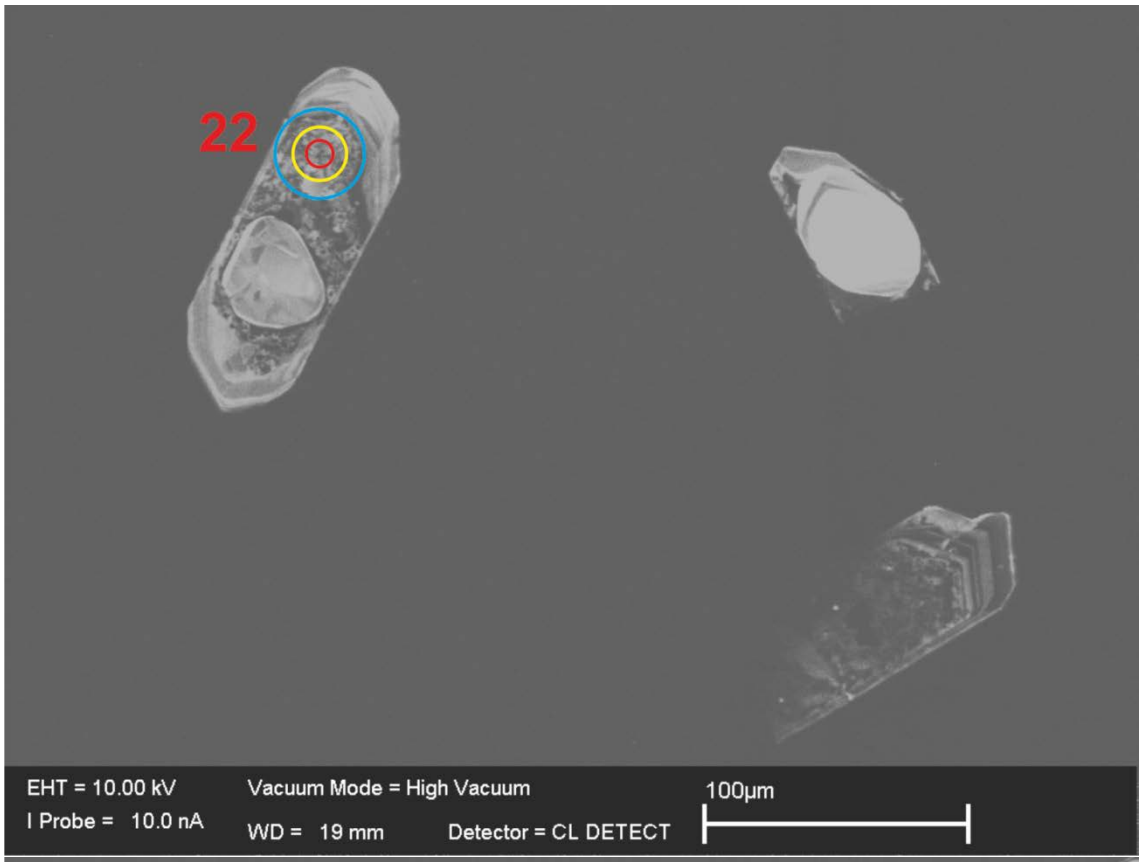
22
EHT = 10.00 kV
I Probe = 10.0 nA
Vacuum Mode = High Vacuum
WD = 19 mm
Detector = CL DETECT
100µm

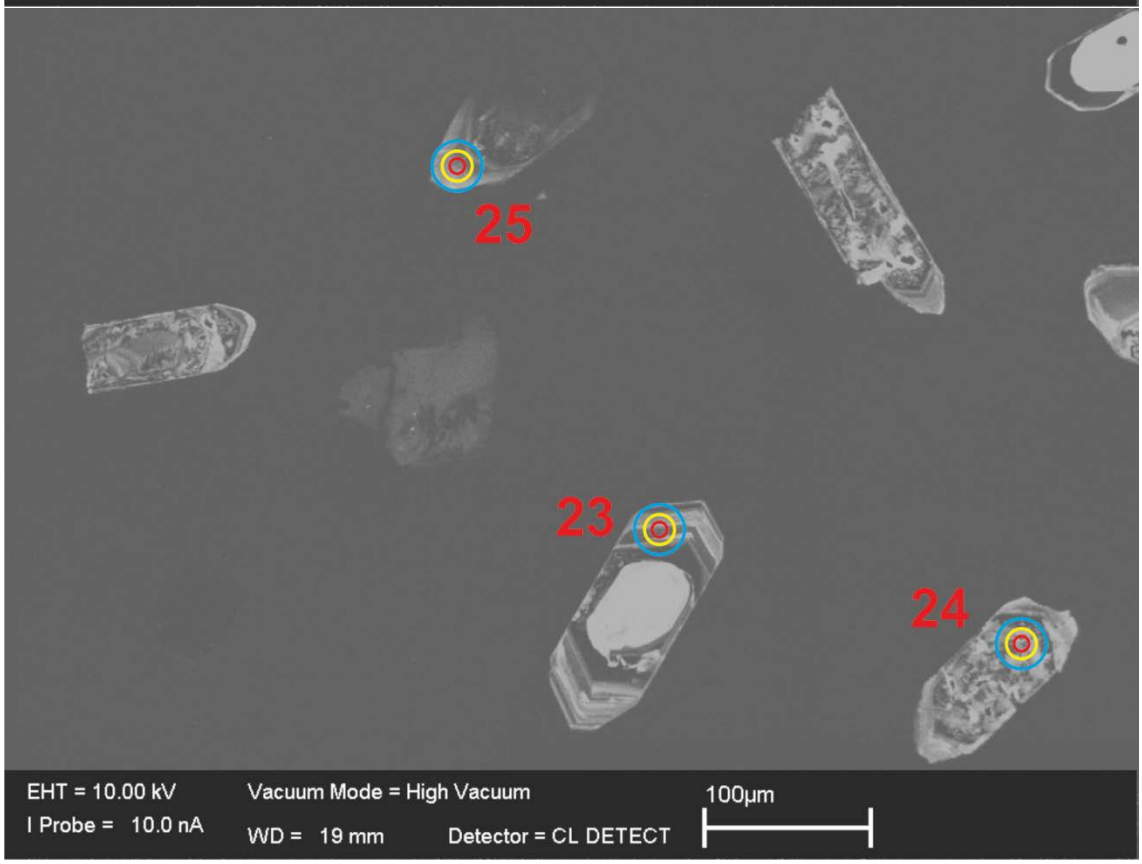
25
23
24
EHT = 10.00 kV
I Probe = 10.0 nA
Vacuum Mode = High Vacuum
WD = 19 mm
Detector = CL DETECT
100µm

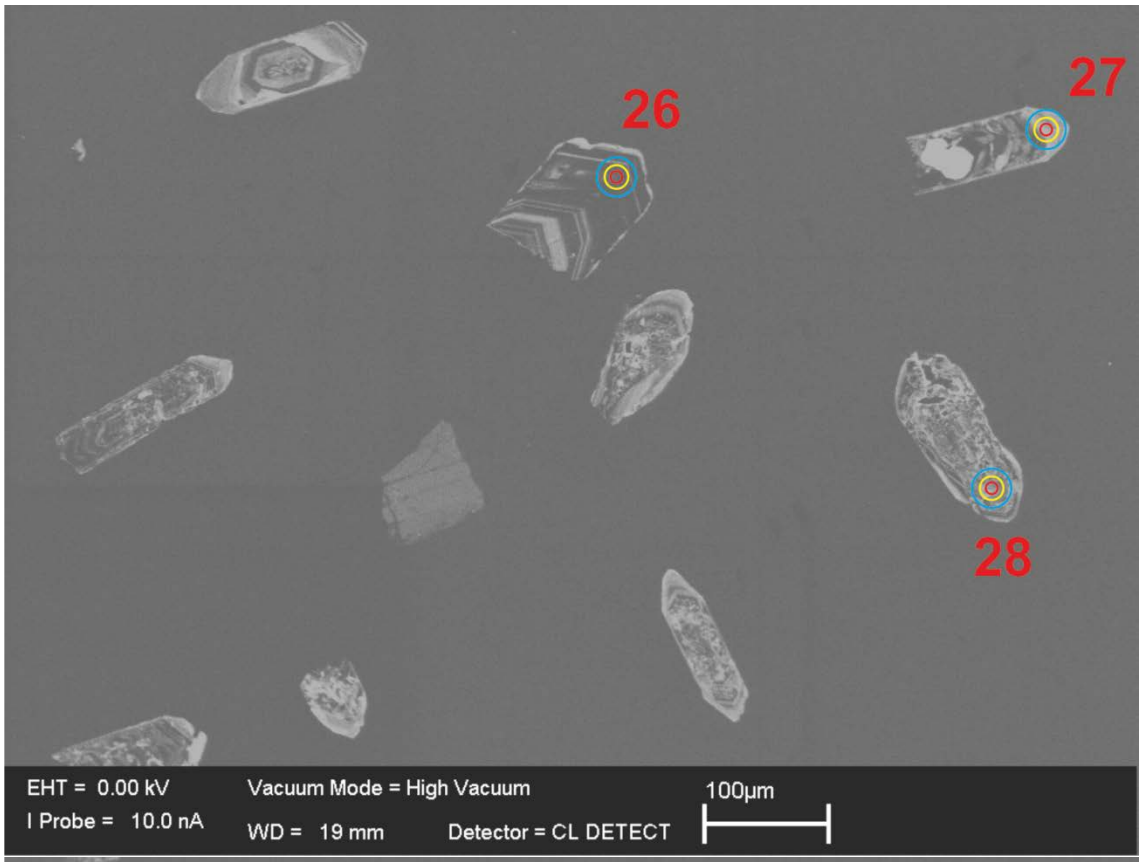
26
27
28
EHT = 0.00 kV
I Probe = 10.0 nA
Vacuum Mode = High Vacuum
WD = 19 mm
Detector = CL DETECT
100µm

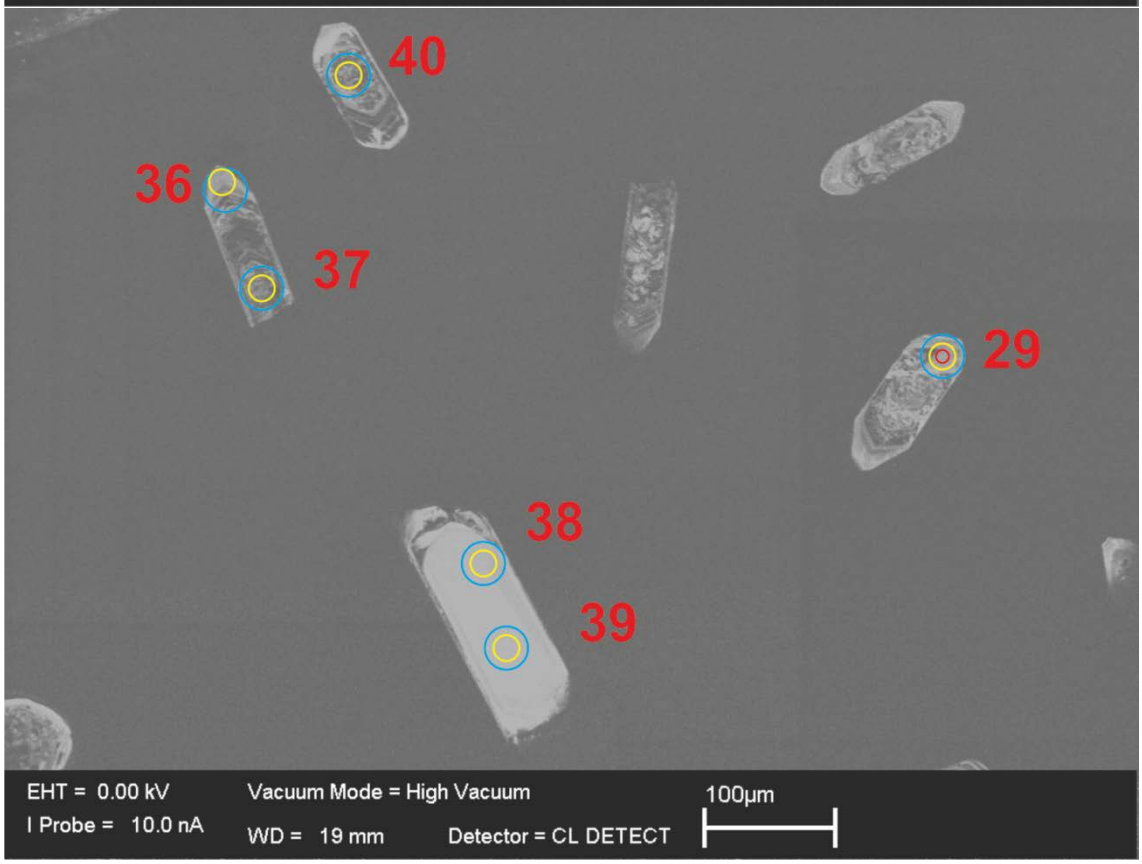
40
36
37
29
38
39
EHT = 0.00 kV
I Probe = 10.0 nA
Vacuum Mode = High Vacuum
WD = 19 mm
Detector = CL DETECT
100µm

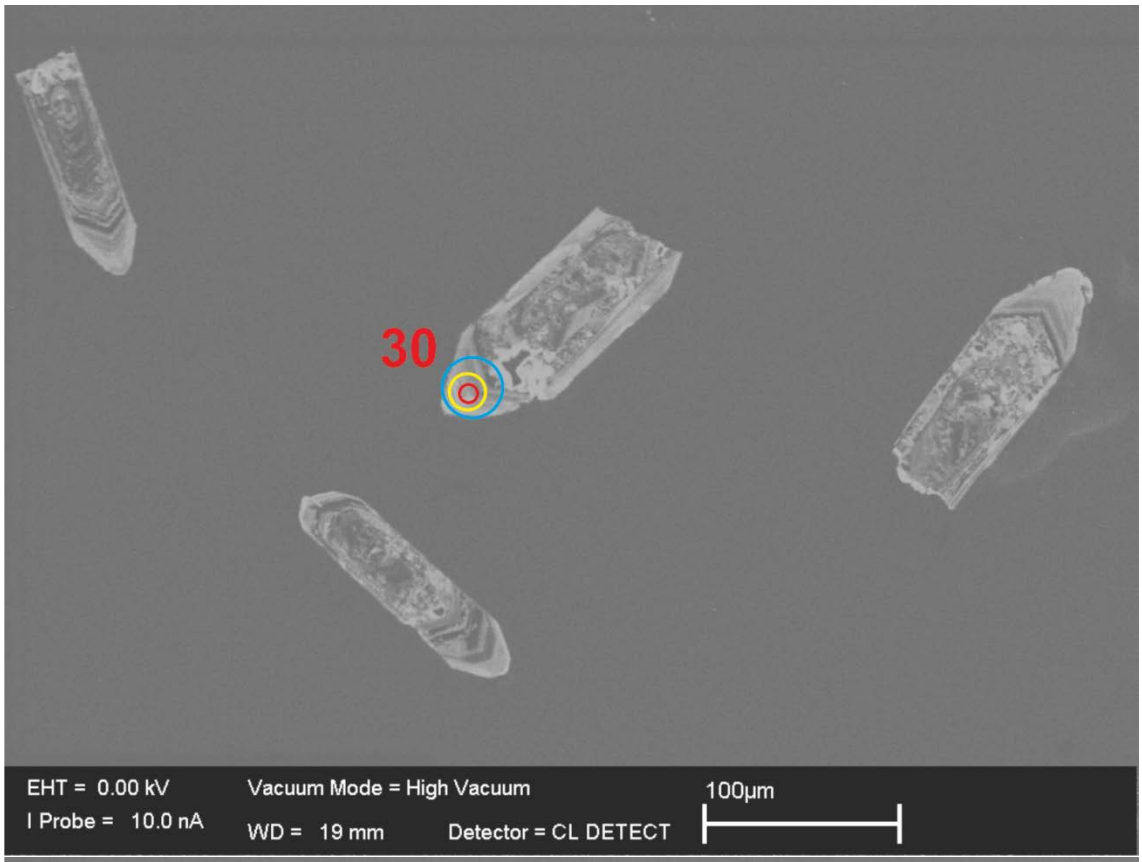
30
EHT = 0.00 kV
I Probe = 10.0 nA
Vacuum Mode = High Vacuum
WD = 19 mm
Detector = CL DETECT
100µm

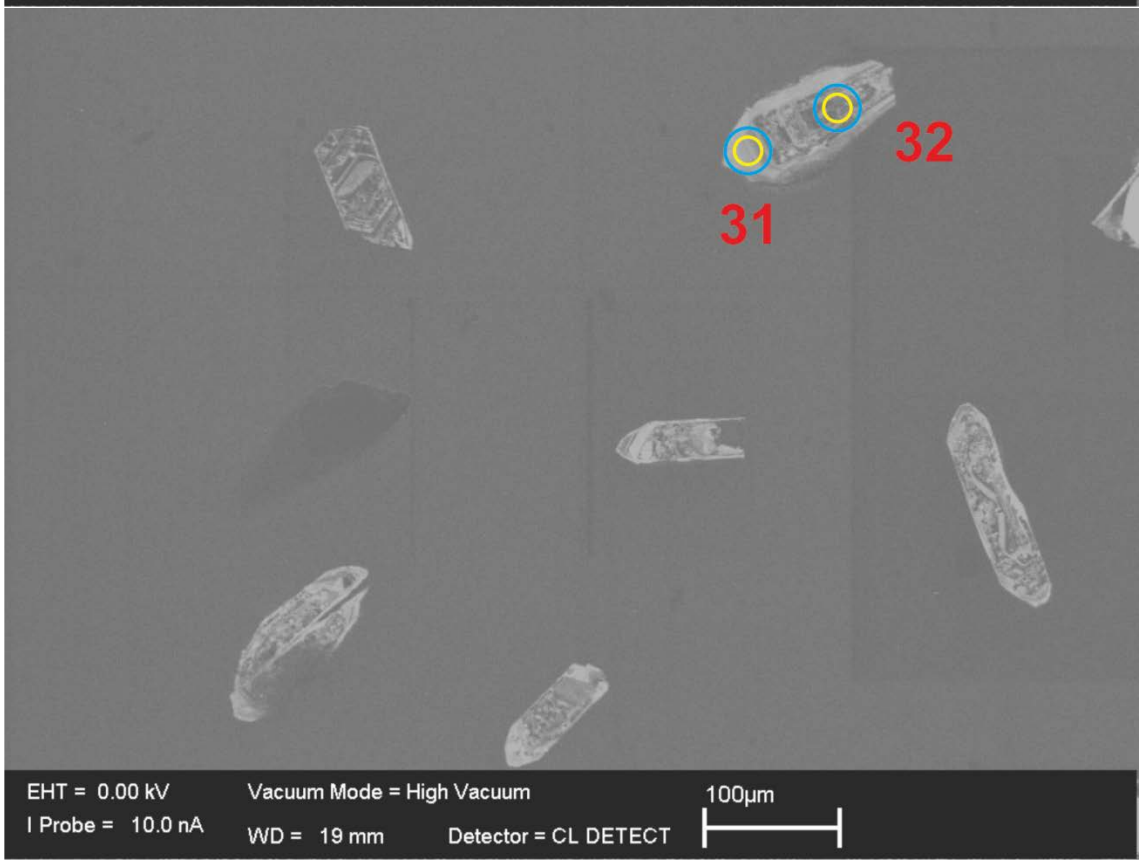
32
31
EHT = 0.00 kV
I Probe = 10.0 nA
Vacuum Mode = High Vacuum
WD = 19 mm
Detector = CL DETECT
100µm

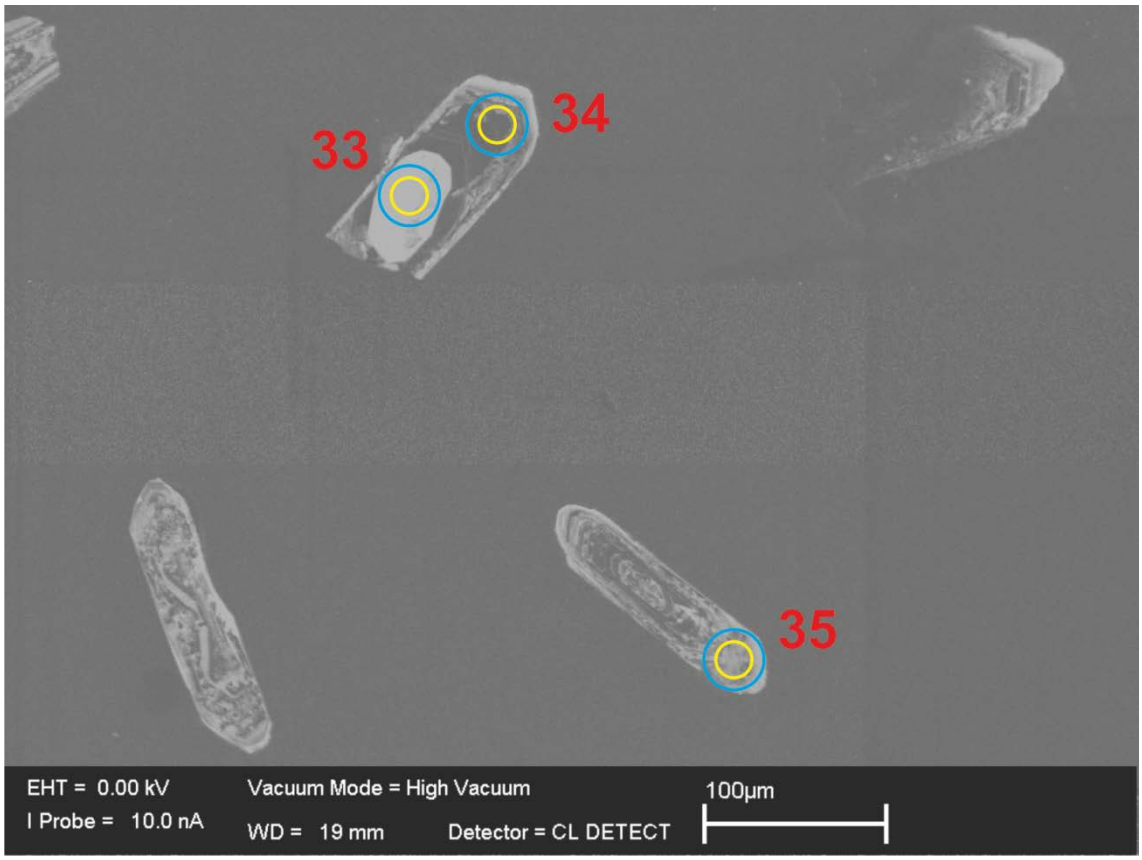
33
34
35
EHT = 0.00 kV
I Probe = 10.0 nA
Vacuum Mode = High Vacuum
WD = 19 mm
Detector = CL DETECT
100µm

E.10. DRB1247

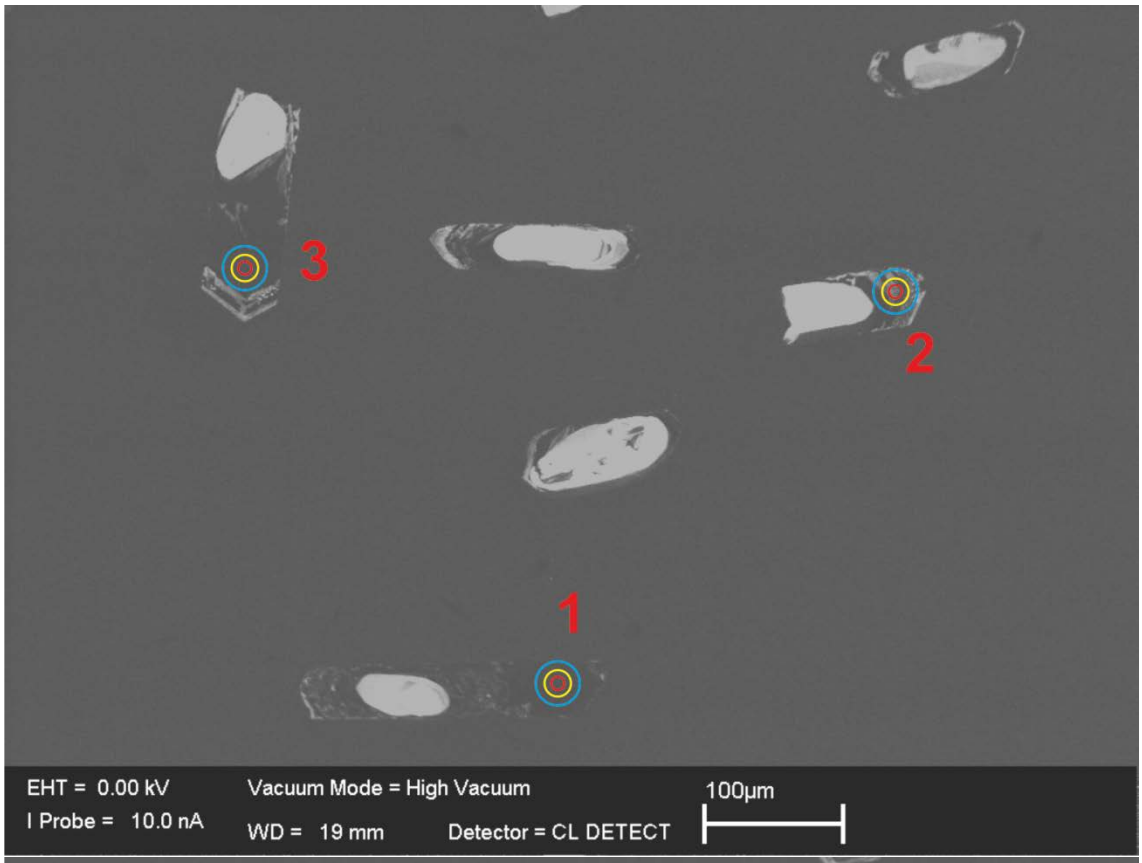
3
2
1
EHT = 0.00 kV
I Probe = 10.0 nA
Vacuum Mode = High Vacuum
WD = 19 mm
Detector = CL DETECT
100µm

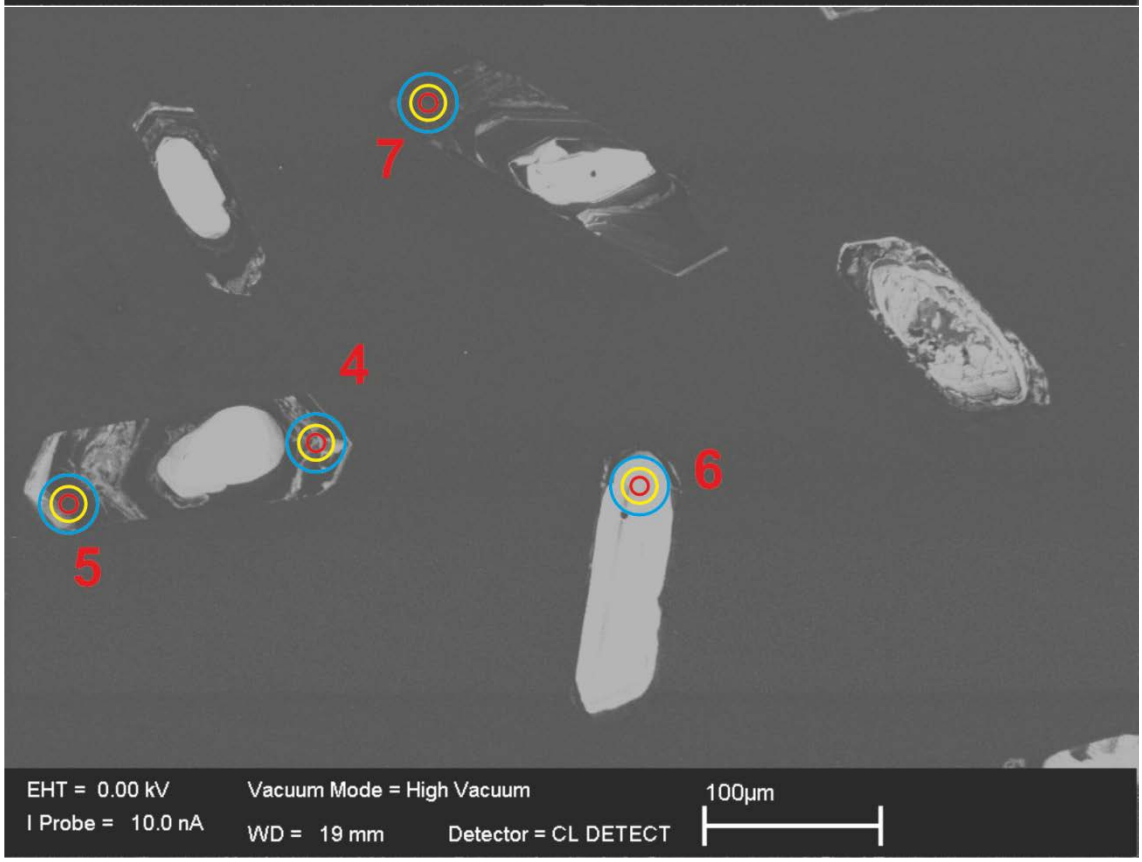
7
4
6
5
EHT = 0.00 kV
I Probe = 10.0 nA
Vacuum Mode = High Vacuum
WD = 19 mm
Detector = CL DETECT
100µm

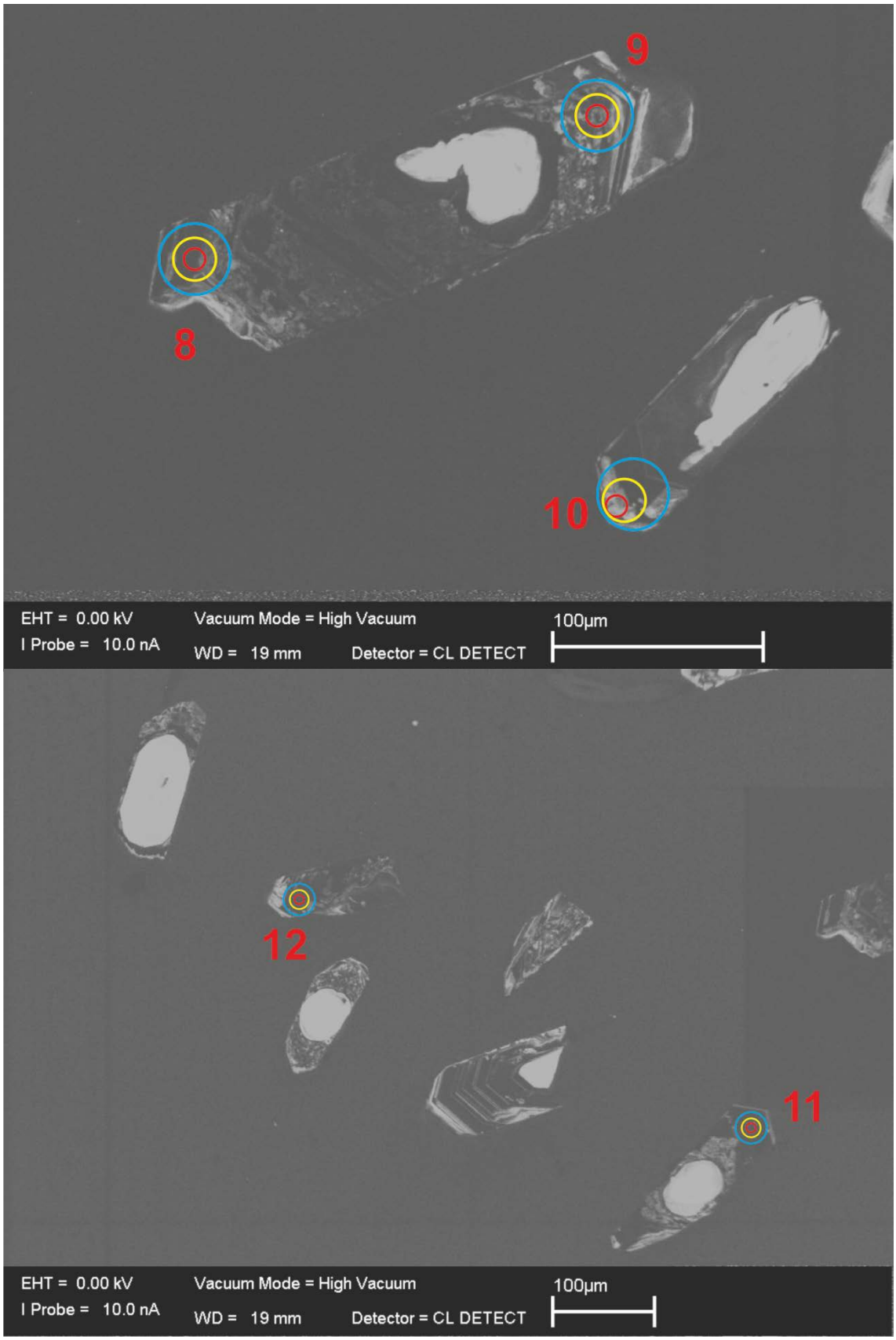
9
8
10
EHT = 0.00 kV
I Probe = 10.0 nA
Vacuum Mode = High Vacuum
WD = 19 mm
Detector = CL DETECT
100µm
12
11
EHT = 0.00 kV
I Probe = 10.0 nA
Vacuum Mode = High Vacuum
WD = 19 mm
Detector = CL DETECT
100µm

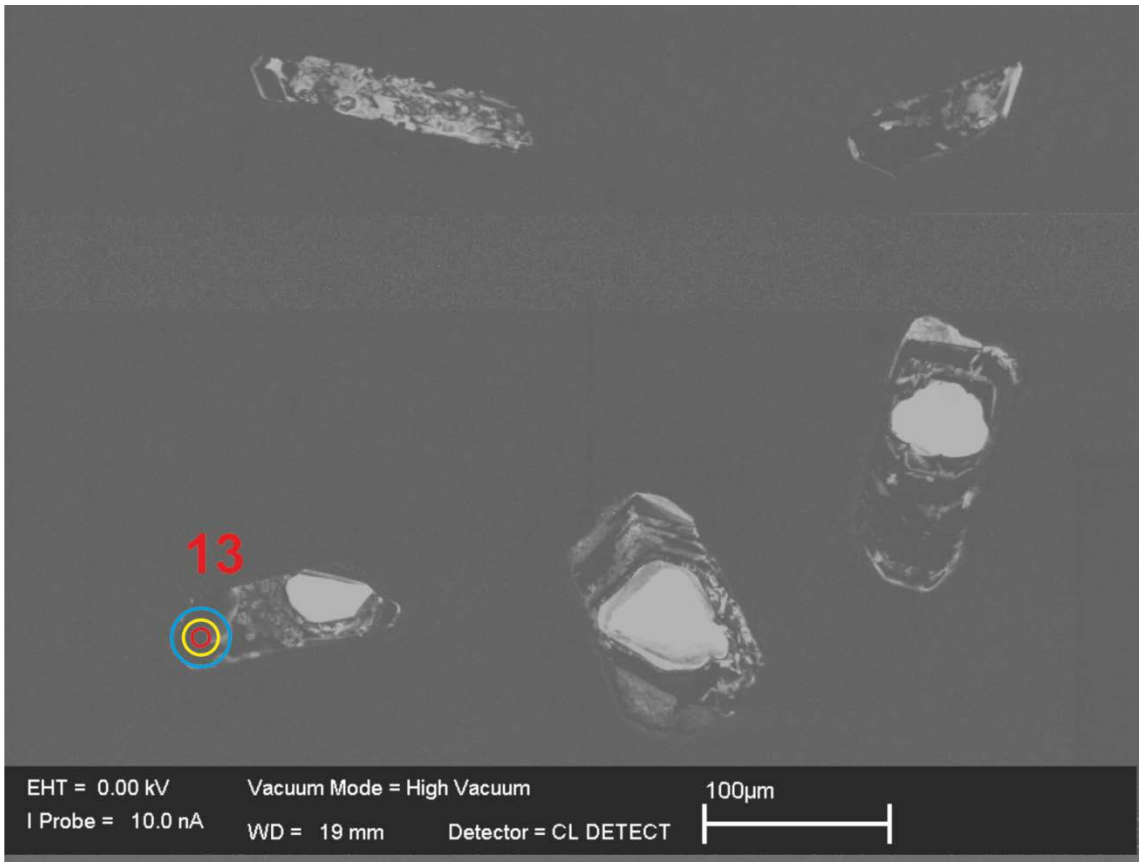
13
EHT = 0.00 kV
I Probe = 10.0 nA
Vacuum Mode = High Vacuum
WD = 19 mm
Detector = CL DETECT
100µm

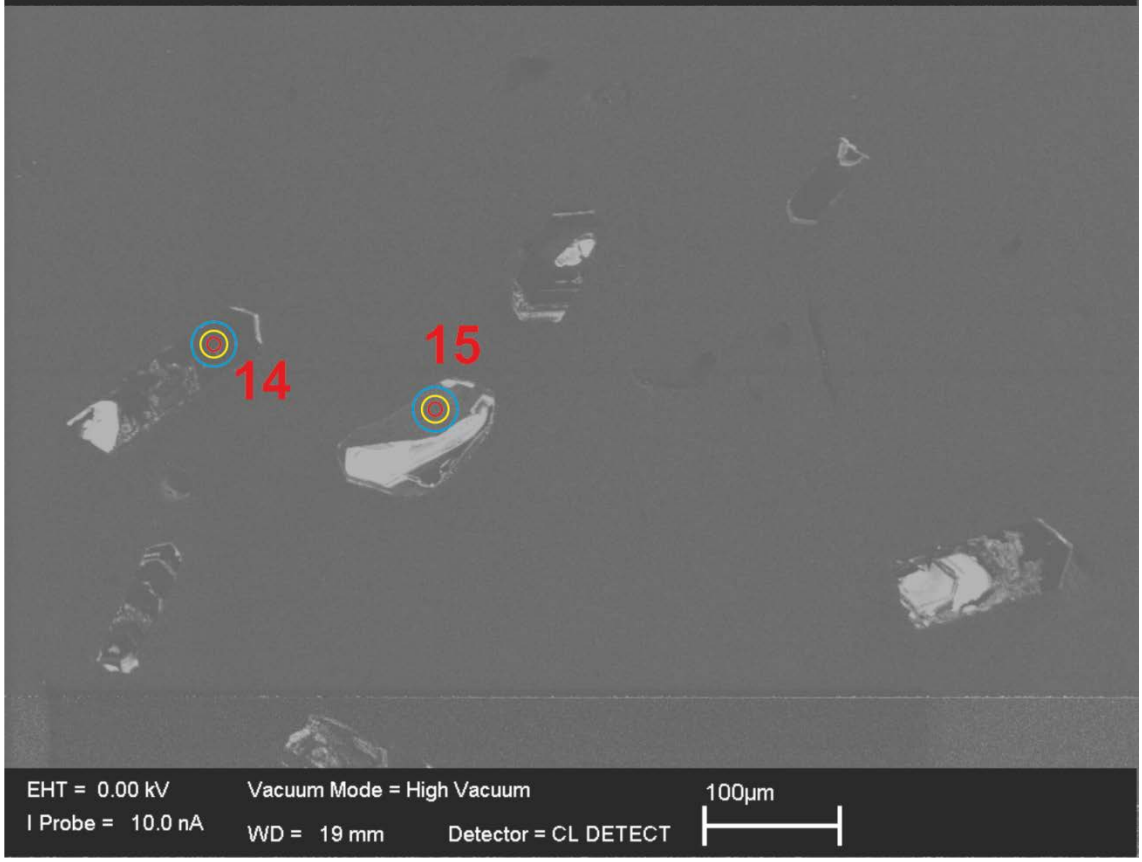
14
15
EHT = 0.00 kV
I Probe = 10.0 nA
Vacuum Mode = High Vacuum
WD = 19 mm
Detector = CL DETECT
100µm

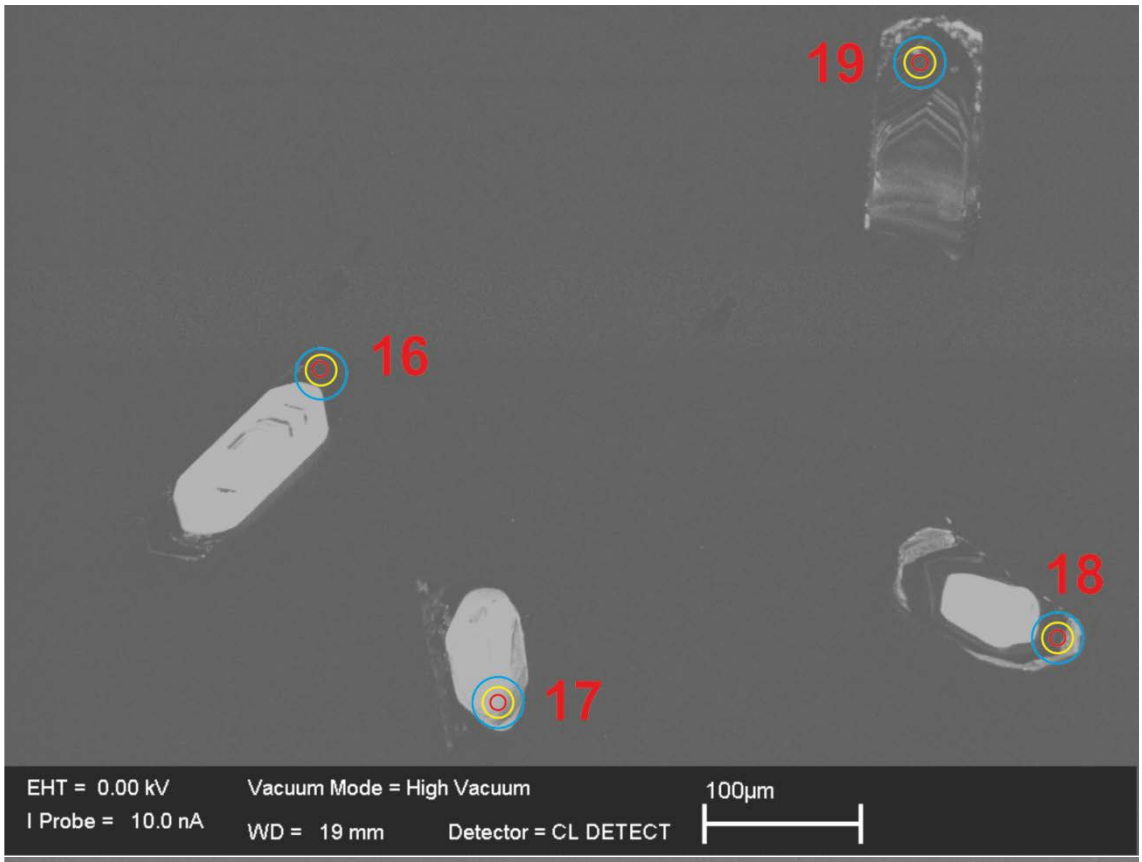
19
16
18
17
EHT = 0.00 kV
I Probe = 10.0 nA
Vacuum Mode = High Vacuum
WD = 19 mm
Detector = CL DETECT
100µm

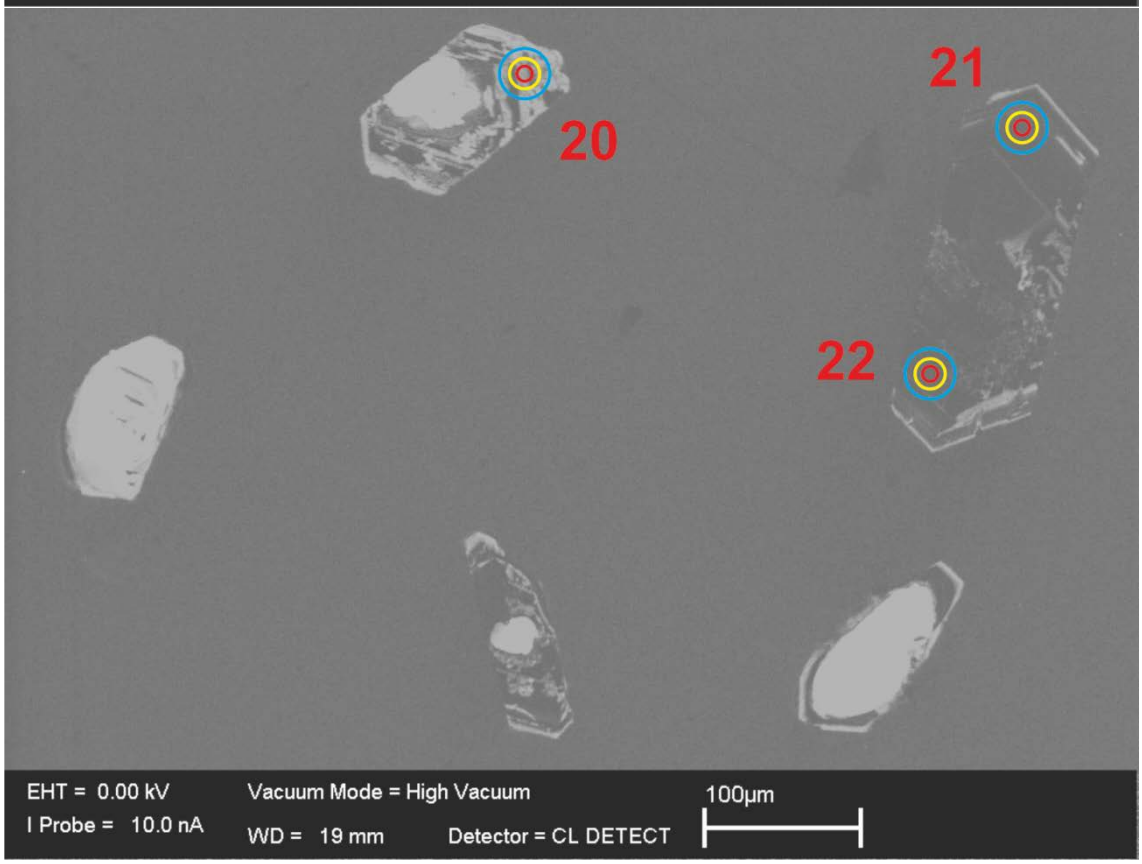
20
21
22
EHT = 0.00 kV
I Probe = 10.0 nA
Vacuum Mode = High Vacuum
WD = 19 mm
Detector = CL DETECT
100µm

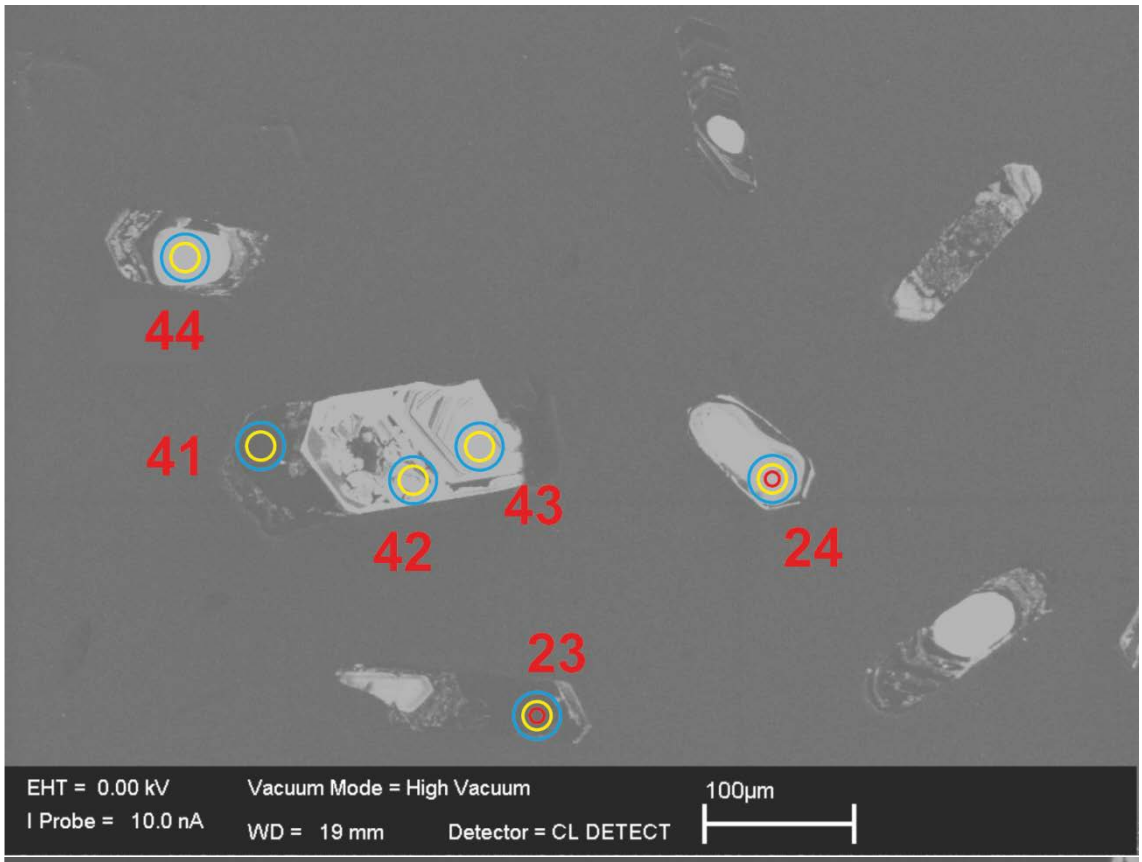
44
41
43
42
24
23
EHT = 0.00 kV
I Probe = 10.0 nA
Vacuum Mode = High Vacuum
WD = 19 mm
Detector = CL DETECT
100µm

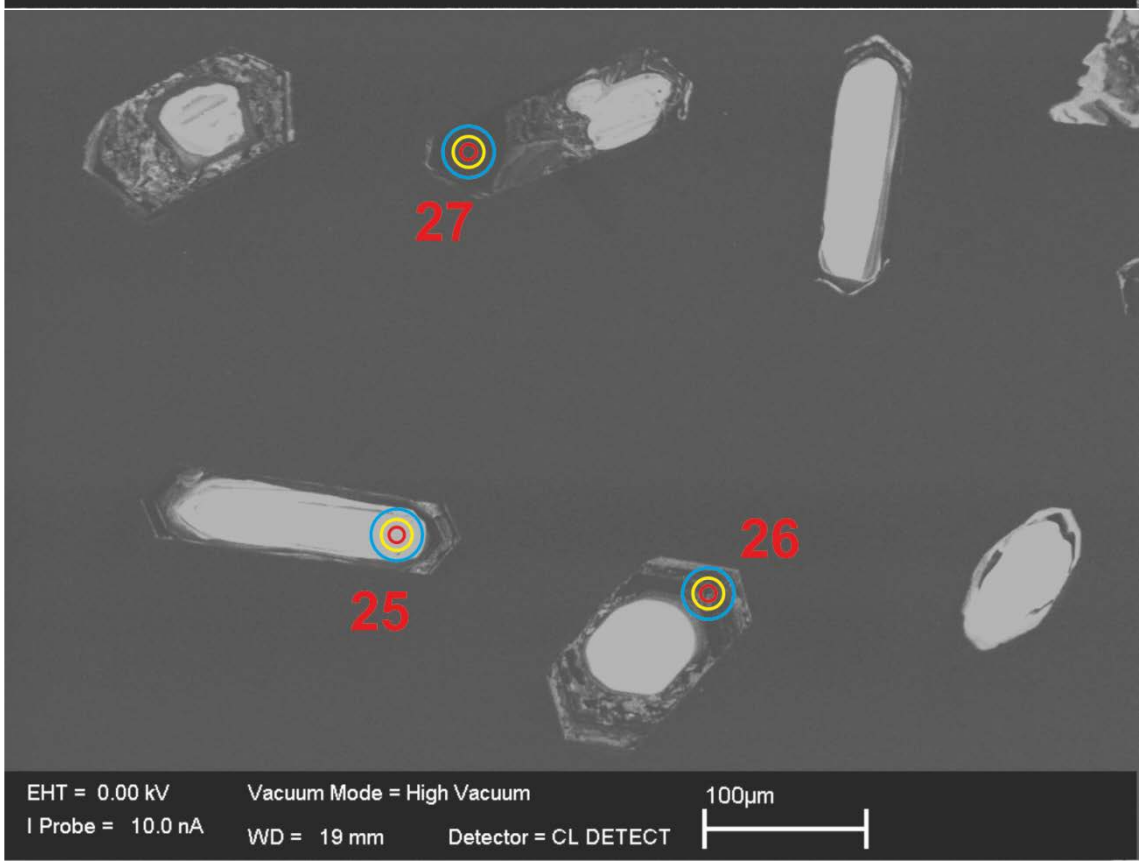
27
26
25
EHT = 0.00 kV
I Probe = 10.0 nA
Vacuum Mode = High Vacuum
WD = 19 mm
Detector = CL DETECT
100µm

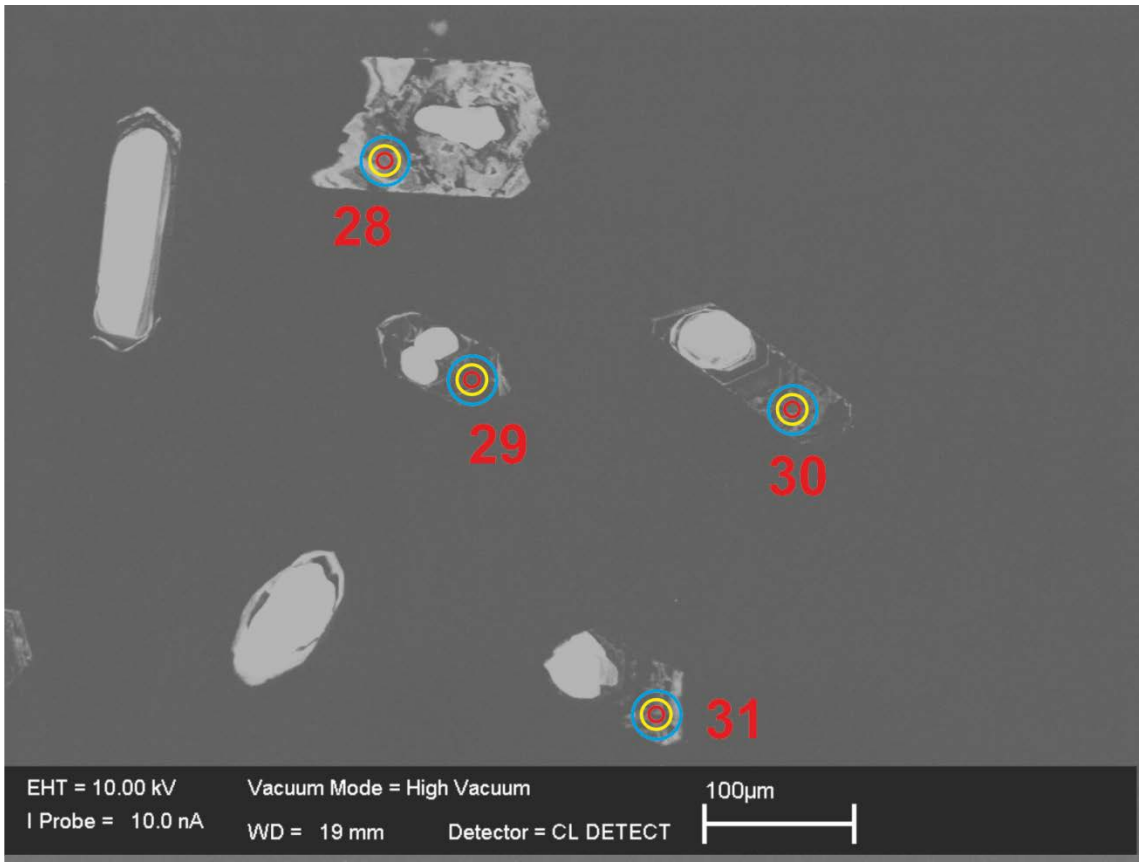
28
29
30
31
EHT = 10.00 kV
I Probe = 10.0 nA
Vacuum Mode = High Vacuum
WD = 19 mm
Detector = CL DETECT
100µm

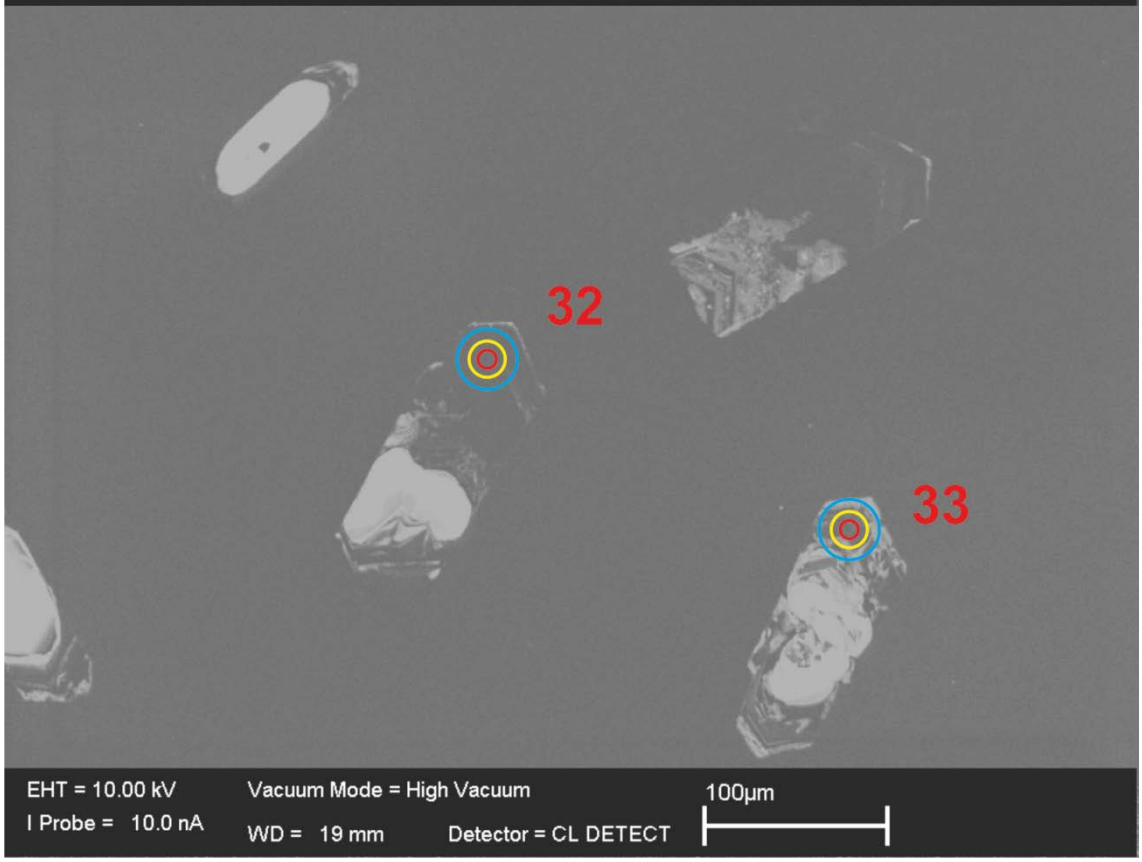
32
33
EHT = 10.00 kV
I Probe = 10.0 nA
Vacuum Mode = High Vacuum
WD = 19 mm
Detector = CL DETECT
100µm

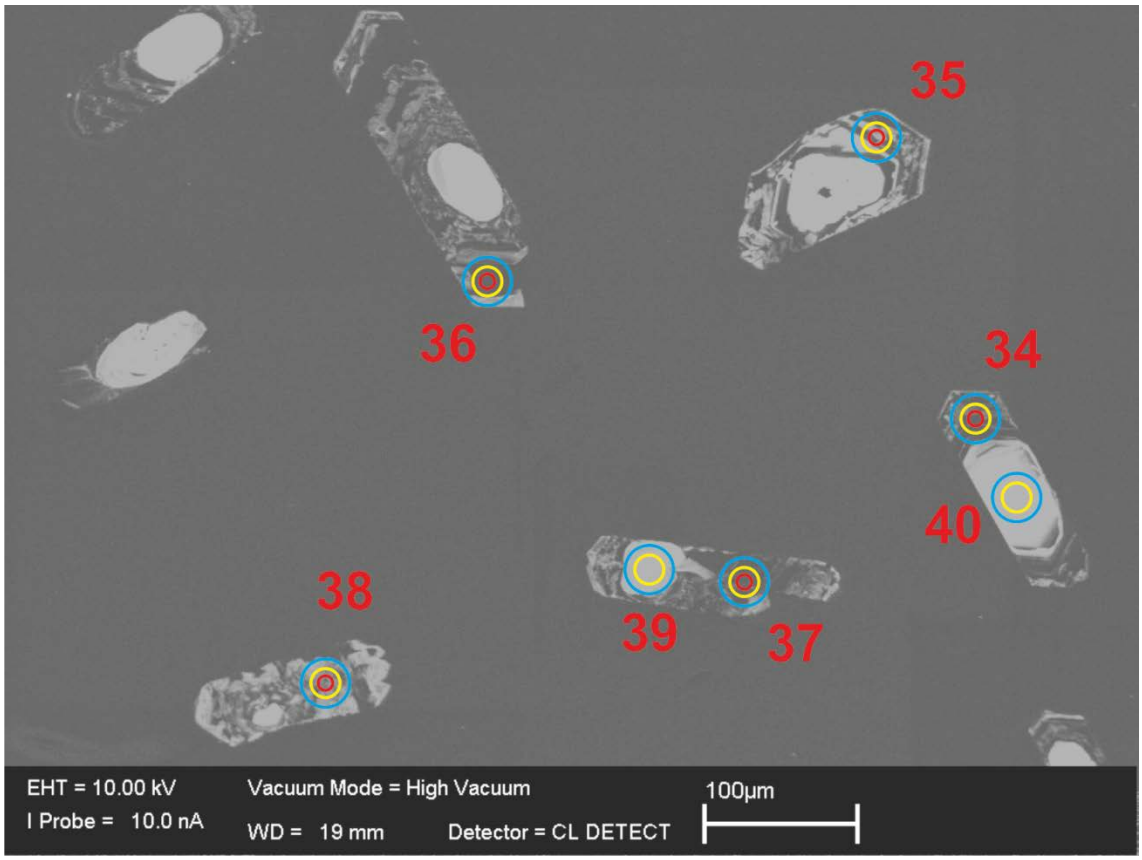
35
36
34
40
38
39
37
EHT = 10.00 kV
I Probe = 10.0 nA
Vacuum Mode = High Vacuum
WD = 19 mm
Detector = CL DETECT
100µm

E.11. DRB1251

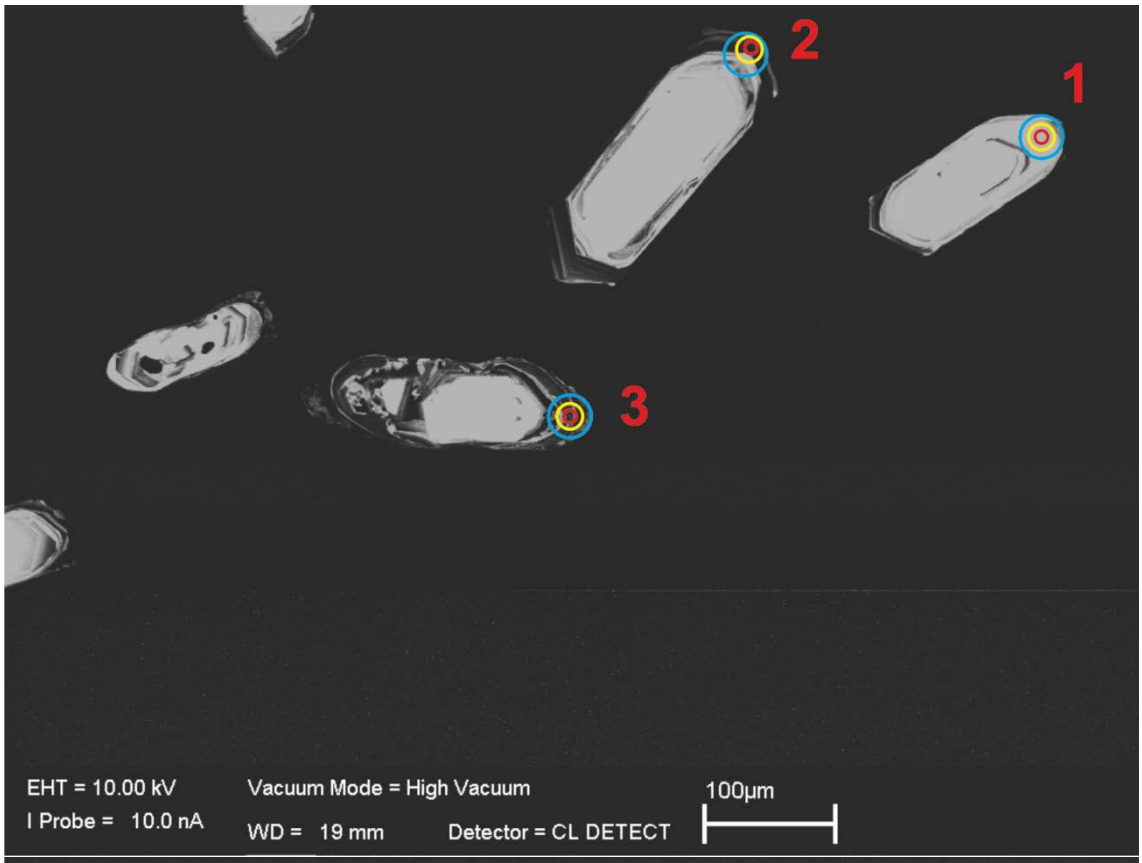
2
1
3
EHT = 10.00 kV
I Probe = 10.0 nA
Vacuum Mode = High Vacuum
WD = 19 mm
Detector = CL DETECT
100µm

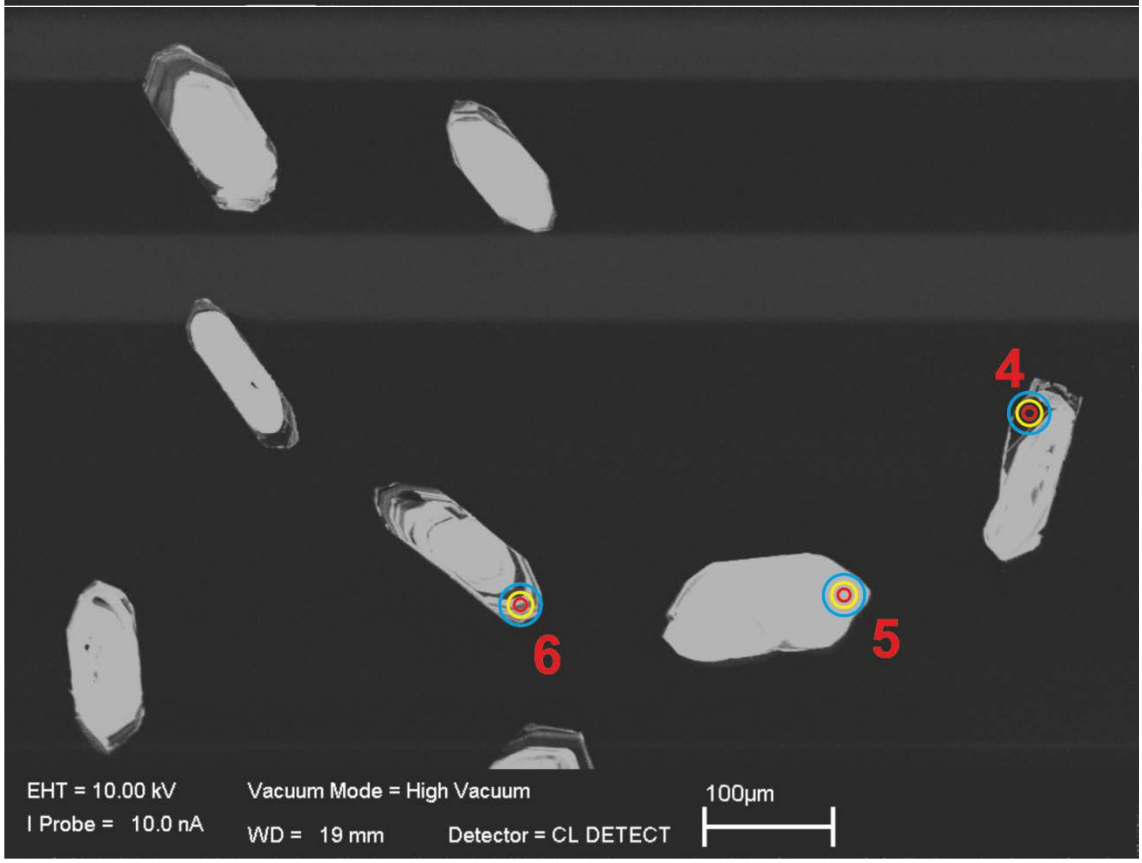
4
6
5
EHT = 10.00 kV
I Probe = 10.0 nA
Vacuum Mode = High Vacuum
WD = 19 mm
Detector = CL DETECT
100µm

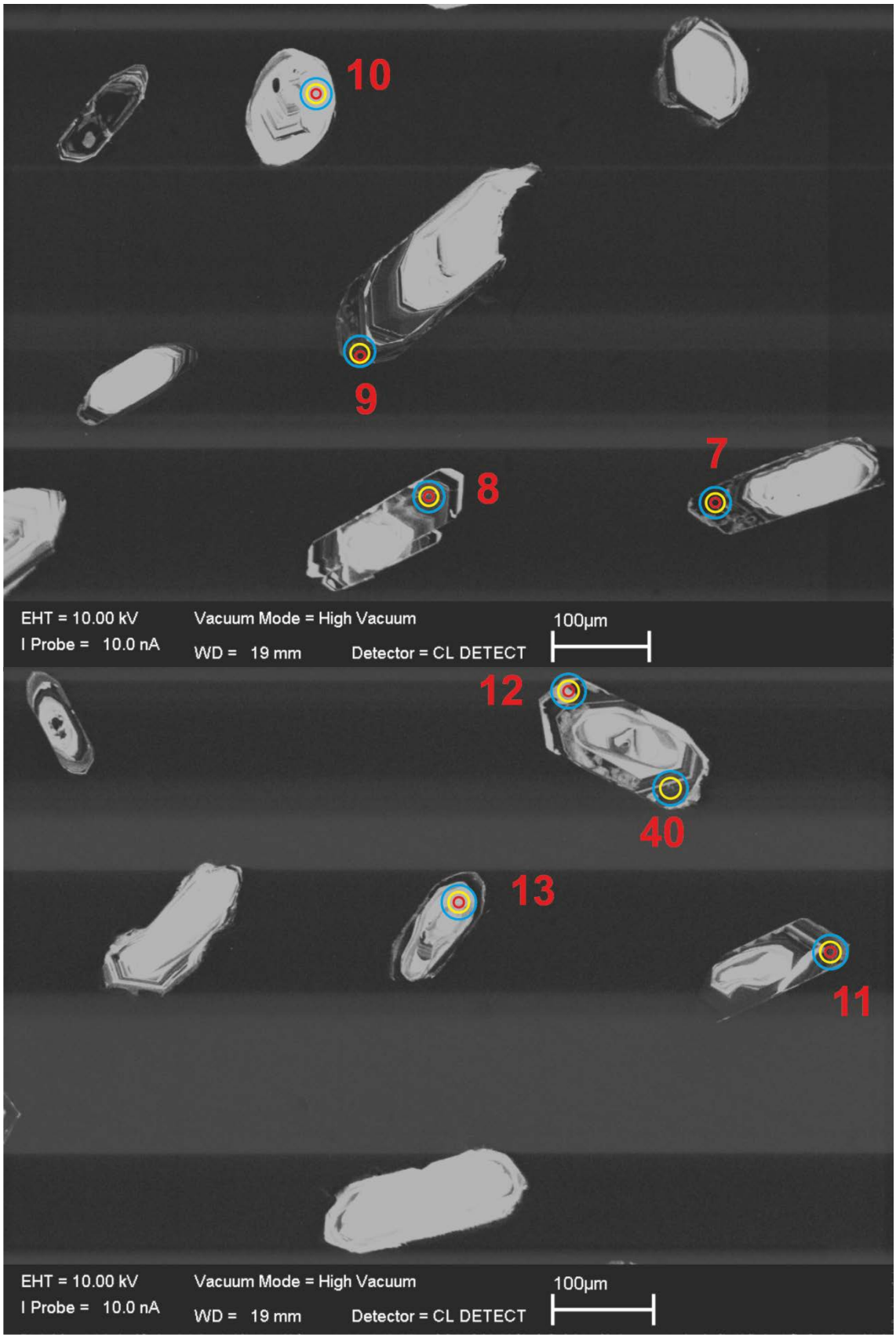
10
9
8
7
EHT = 10.00 kV
I Probe = 10.0 nA
Vacuum Mode = High Vacuum
WD = 19 mm
Detector = CL DETECT
100µm
12
40
13
11
EHT = 10.00 kV
I Probe = 10.0 nA
Vacuum Mode = High Vacuum
WD = 19 mm
Detector = CL DETECT
100µm

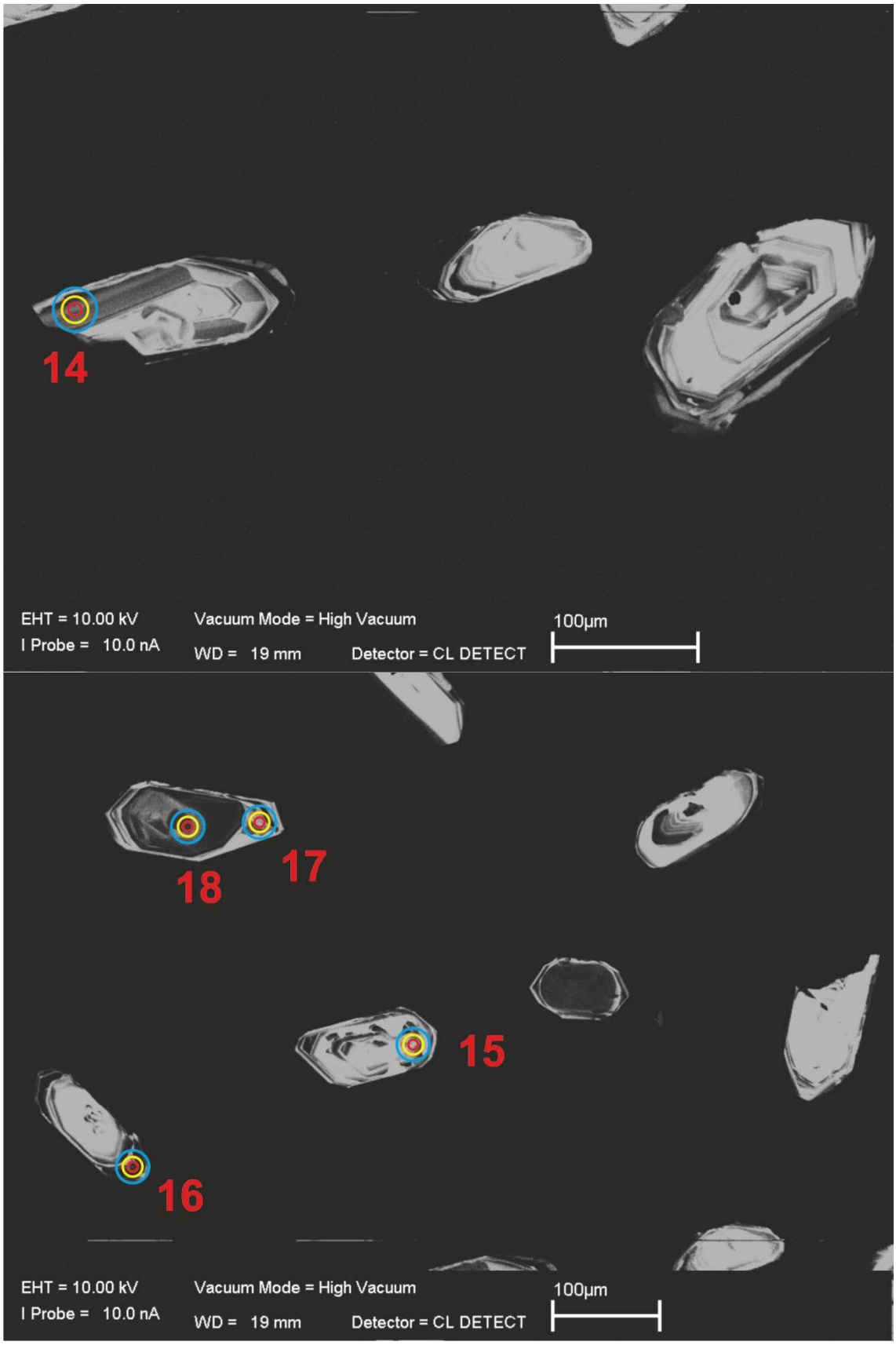
14
EHT = 10.00 kV
I Probe = 10.0 nA
Vacuum Mode = High Vacuum
WD = 19 mm
Detector = CL DETECT
100µm
18
17
15
16
EHT = 10.00 kV
I Probe = 10.0 nA
Vacuum Mode = High Vacuum
WD = 19 mm
Detector = CL DETECT
100µm

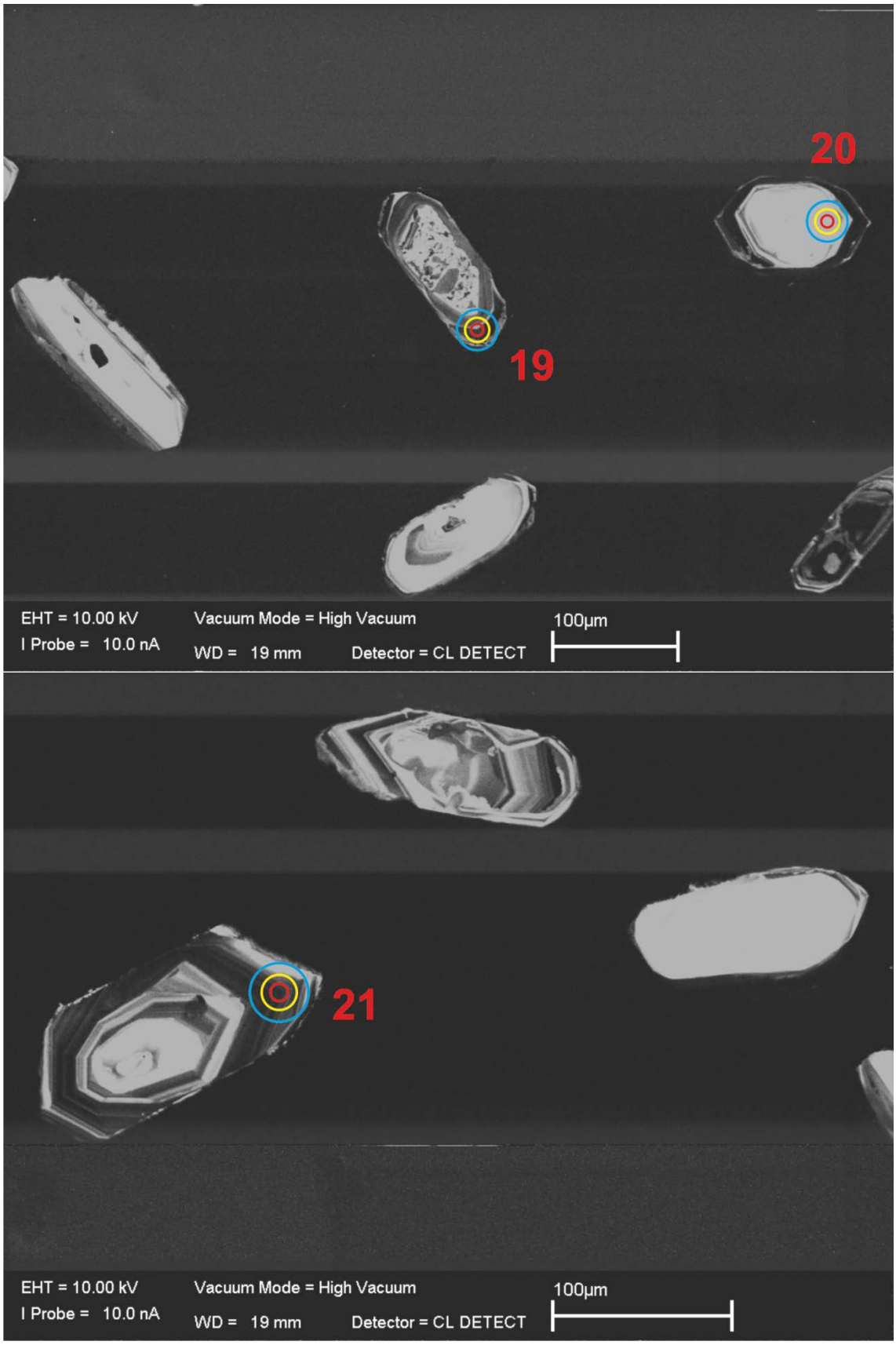
20
19
EHT = 10.00 kV
I Probe = 10.0 nA
Vacuum Mode = High Vacuum
WD = 19 mm
Detector = CL DETECT
100µm
21
EHT = 10.00 kV
I Probe = 10.0 nA
Vacuum Mode = High Vacuum
WD = 19 mm
Detector = CL DETECT
100µm

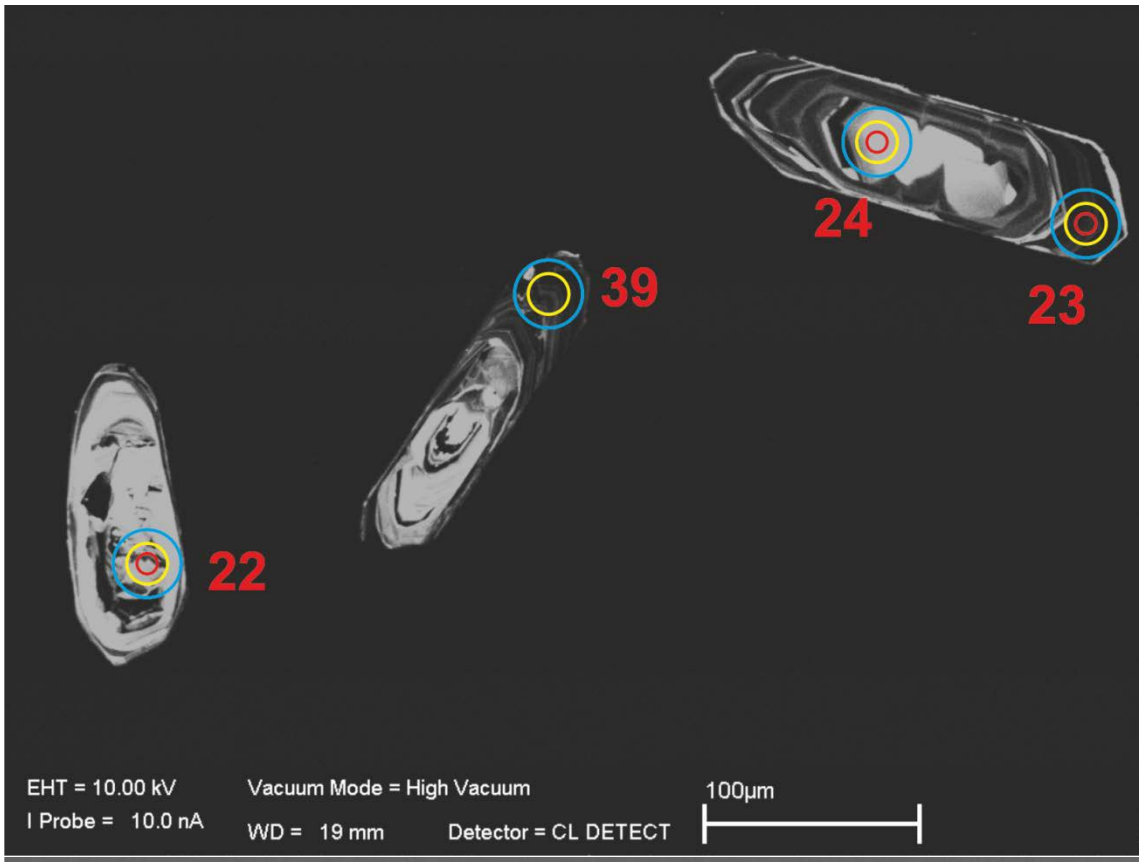
24
23
39
22
EHT = 10.00 kV
I Probe = 10.0 nA
Vacuum Mode = High Vacuum
WD = 19 mm
Detector = CL DETECT
100µm

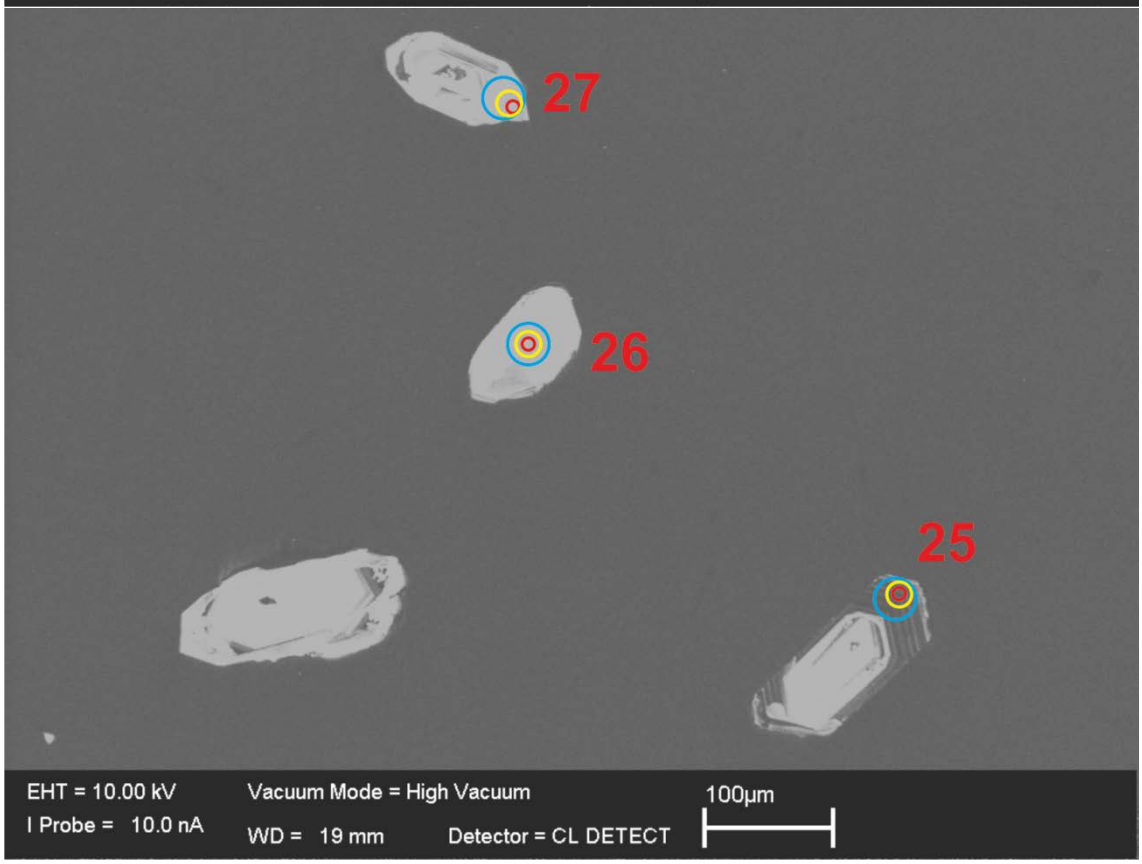
27
26
25
EHT = 10.00 kV
I Probe = 10.0 nA
Vacuum Mode = High Vacuum
WD = 19 mm
Detector = CL DETECT
100µm

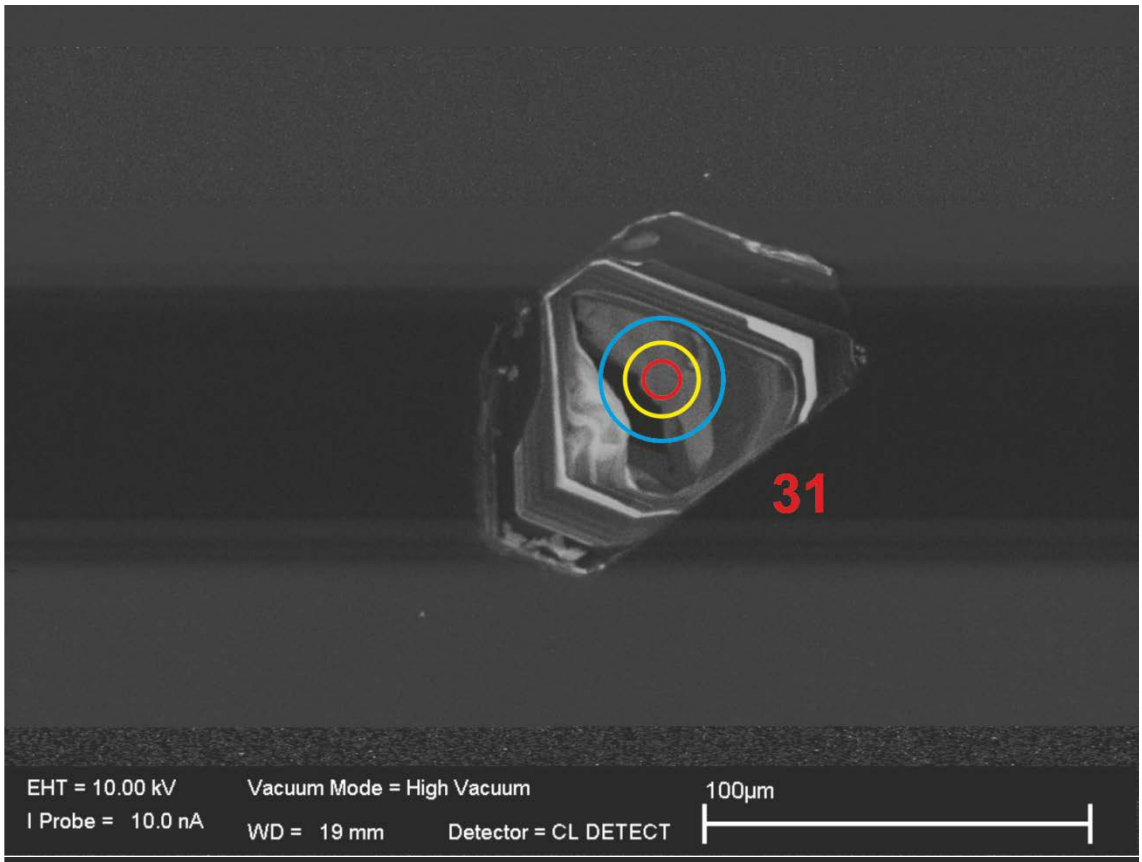
31
EHT = 10.00 kV
I Probe = 10.0 nA
Vacuum Mode = High Vacuum
WD = 19 mm
Detector = CL DETECT
100µm

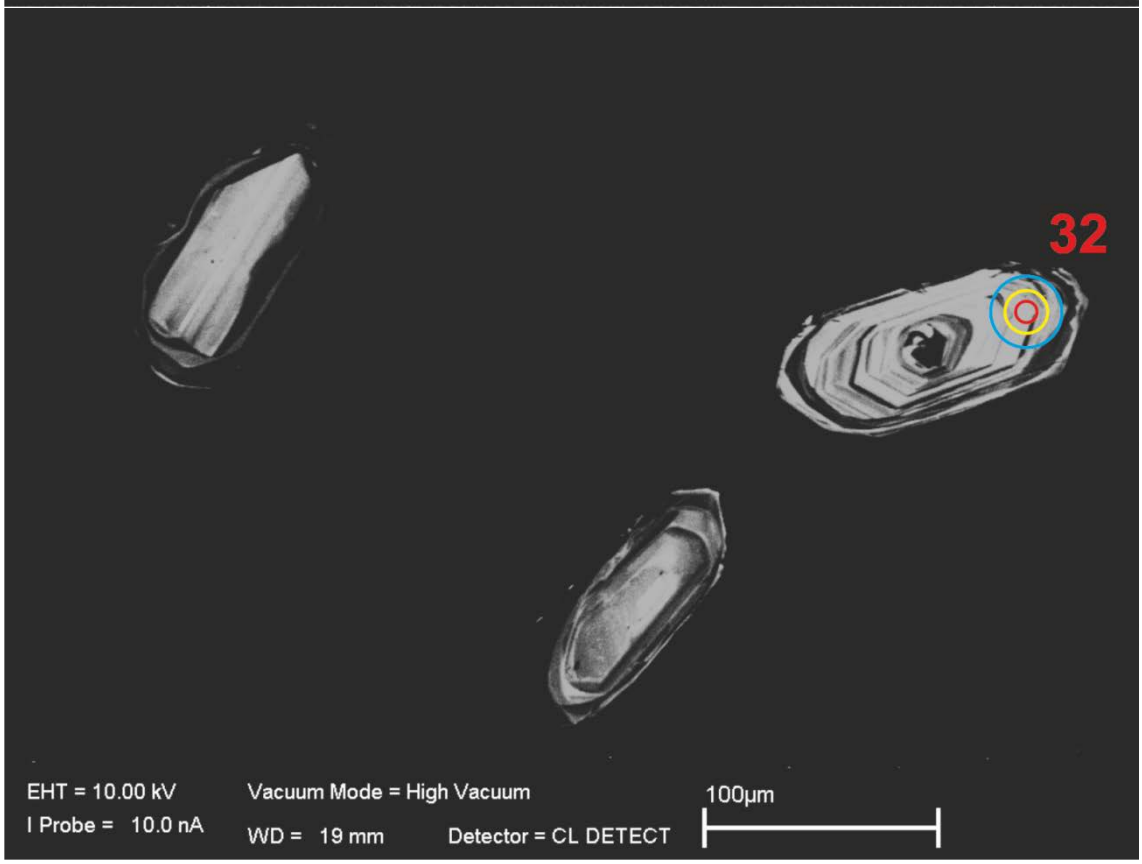
32
EHT = 10.00 kV
I Probe = 10.0 nA
Vacuum Mode = High Vacuum
WD = 19 mm
Detector = CL DETECT
100µm

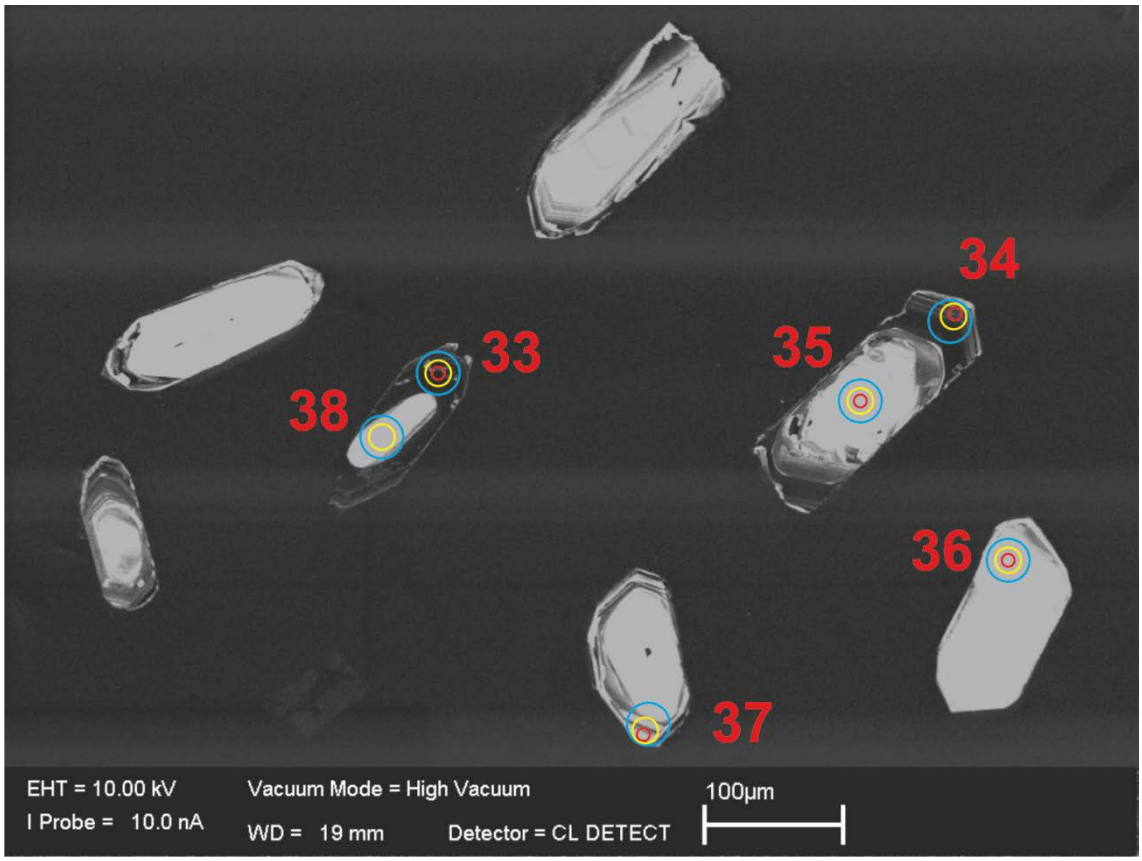
34
35
33
38
36
37
EHT = 10.00 kV
I Probe = 10.0 nA
Vacuum Mode = High Vacuum
WD = 19 mm
Detector = CL DETECT
100µm

E.12. CWB-10-16

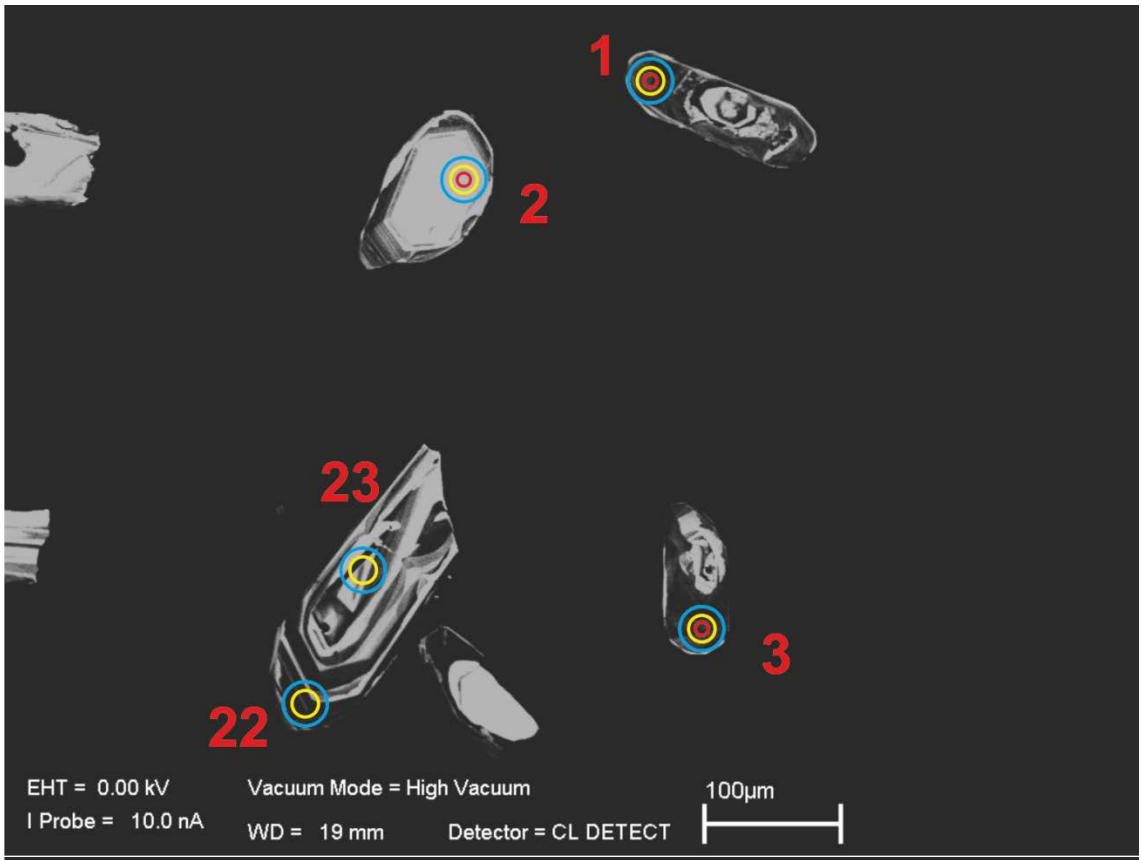
1
2
23
3
22
EHT = 0.00 kV
I Probe = 10.0 nA
Vacuum Mode = High Vacuum
WD = 19 mm
Detector = CL DETECT
100µm

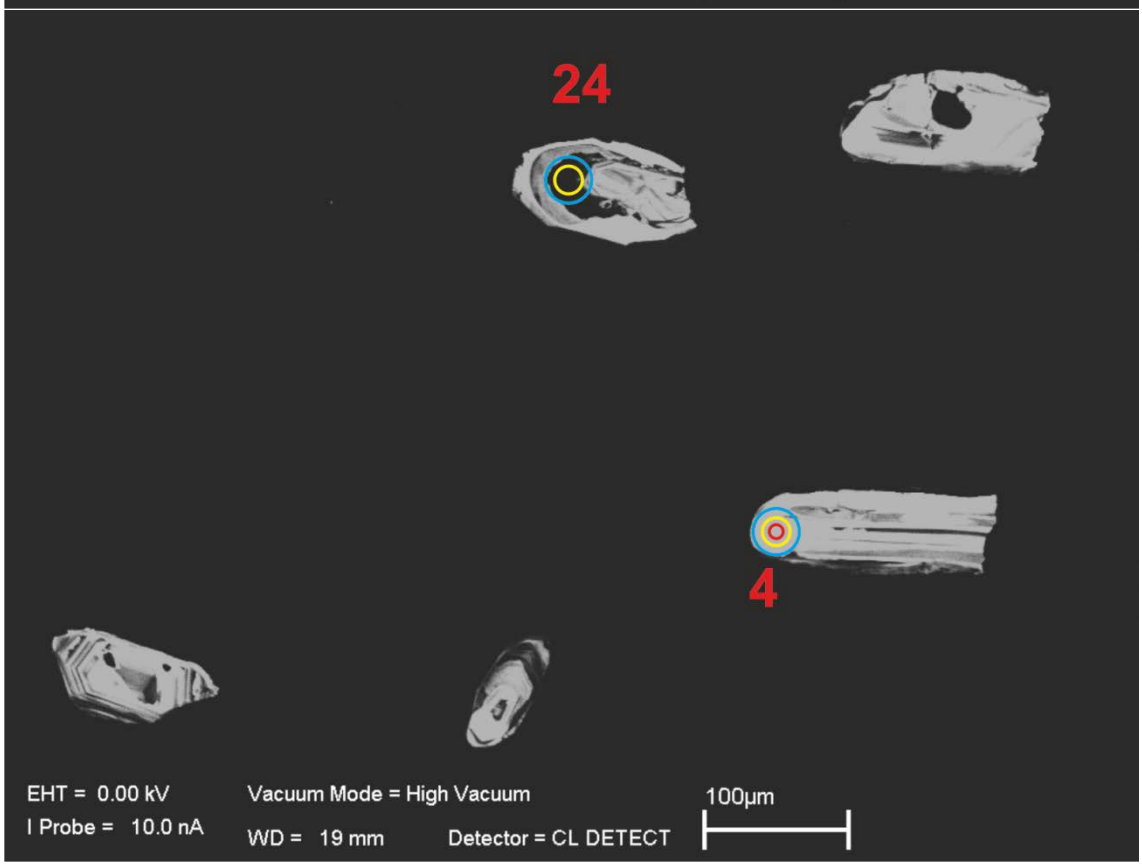
24
4
EHT = 0.00 kV
I Probe = 10.0 nA
Vacuum Mode = High Vacuum
WD = 19 mm
Detector = CL DETECT
100µm

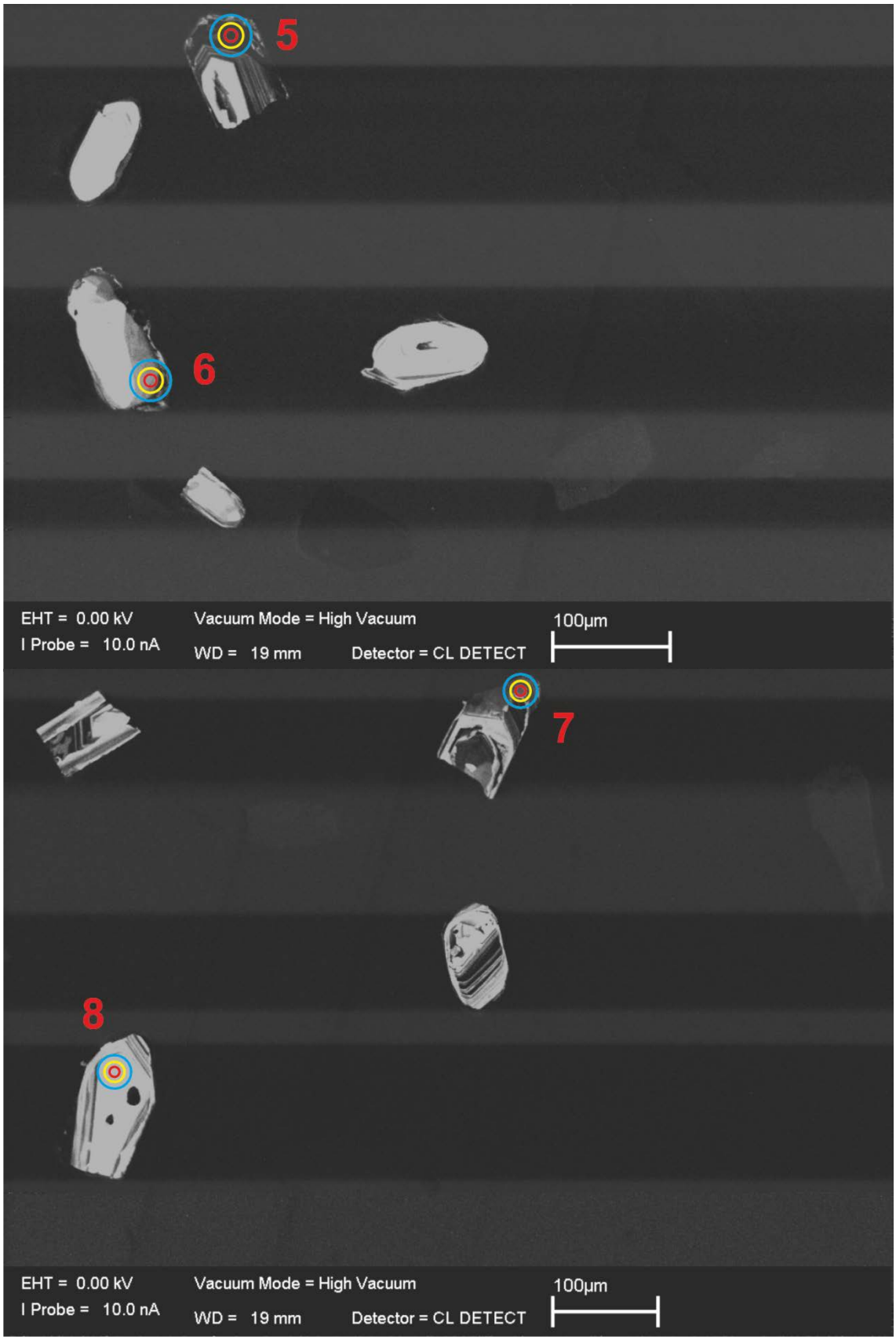
5
6
EHT = 0.00 kV
I Probe = 10.0 nA
Vacuum Mode = High Vacuum
WD = 19 mm
Detector = CL DETECT
100µm
7
8
EHT = 0.00 kV
I Probe = 10.0 nA
Vacuum Mode = High Vacuum
WD = 19 mm
Detector = CL DETECT
100µm

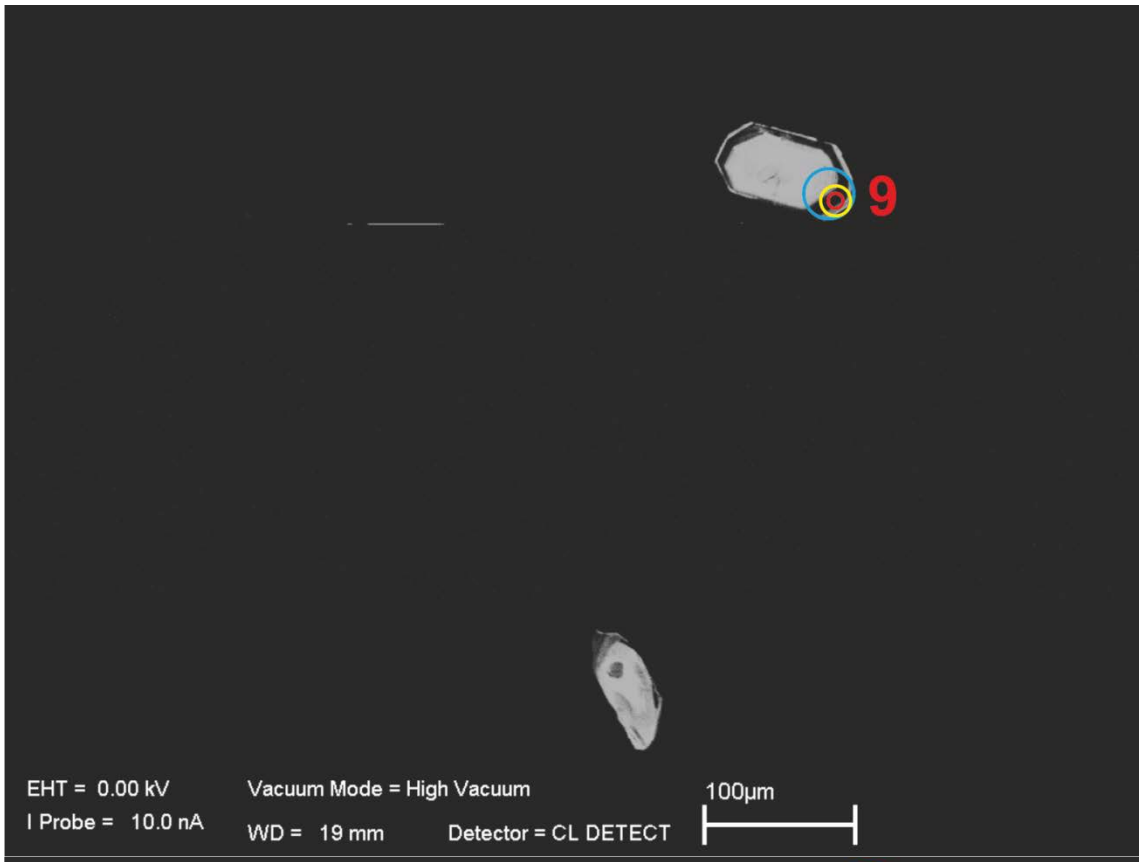
9
EHT = 0.00 kV
I Probe = 10.0 nA
Vacuum Mode = High Vacuum
WD = 19 mm
Detector = CL DETECT
100µm

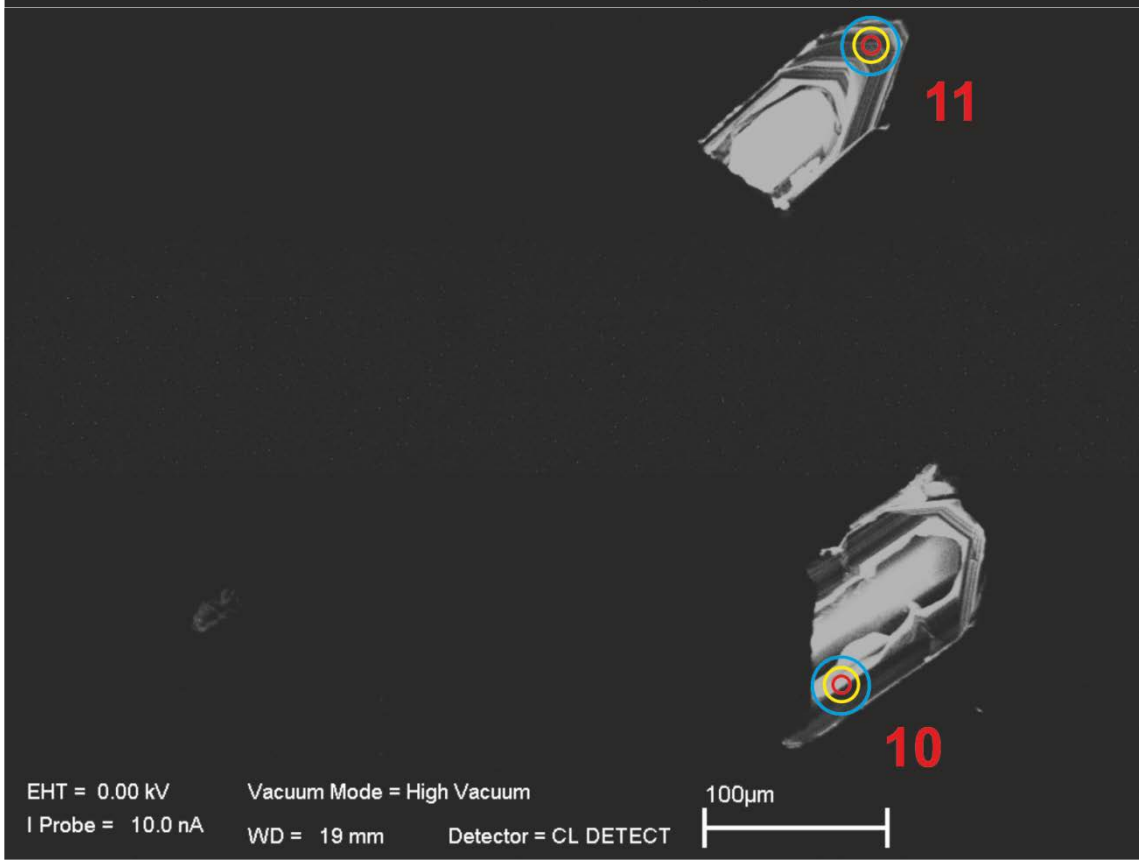
11
10
EHT = 0.00 kV
I Probe = 10.0 nA
Vacuum Mode = High Vacuum
WD = 19 mm
Detector = CL DETECT
100µm

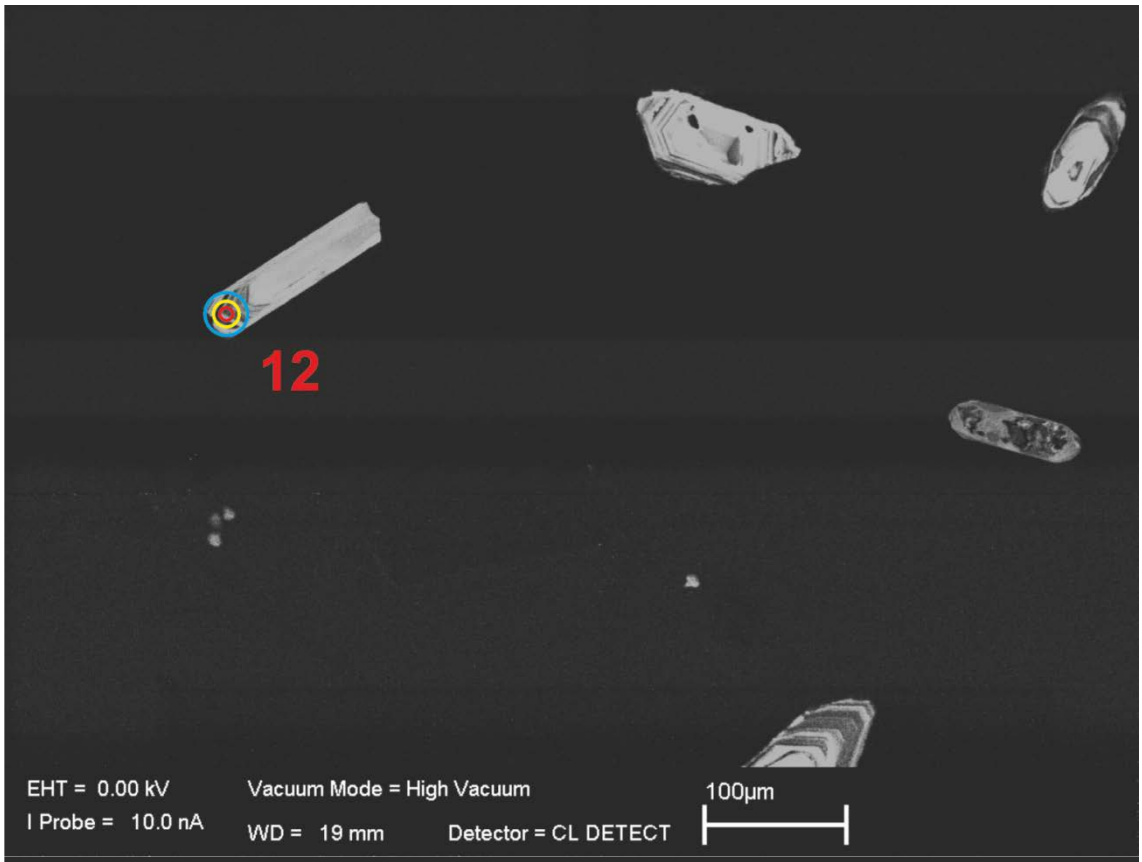
12
EHT = 0.00 kV
I Probe = 10.0 nA
Vacuum Mode = High Vacuum
WD = 19 mm
Detector = CL DETECT
100µm

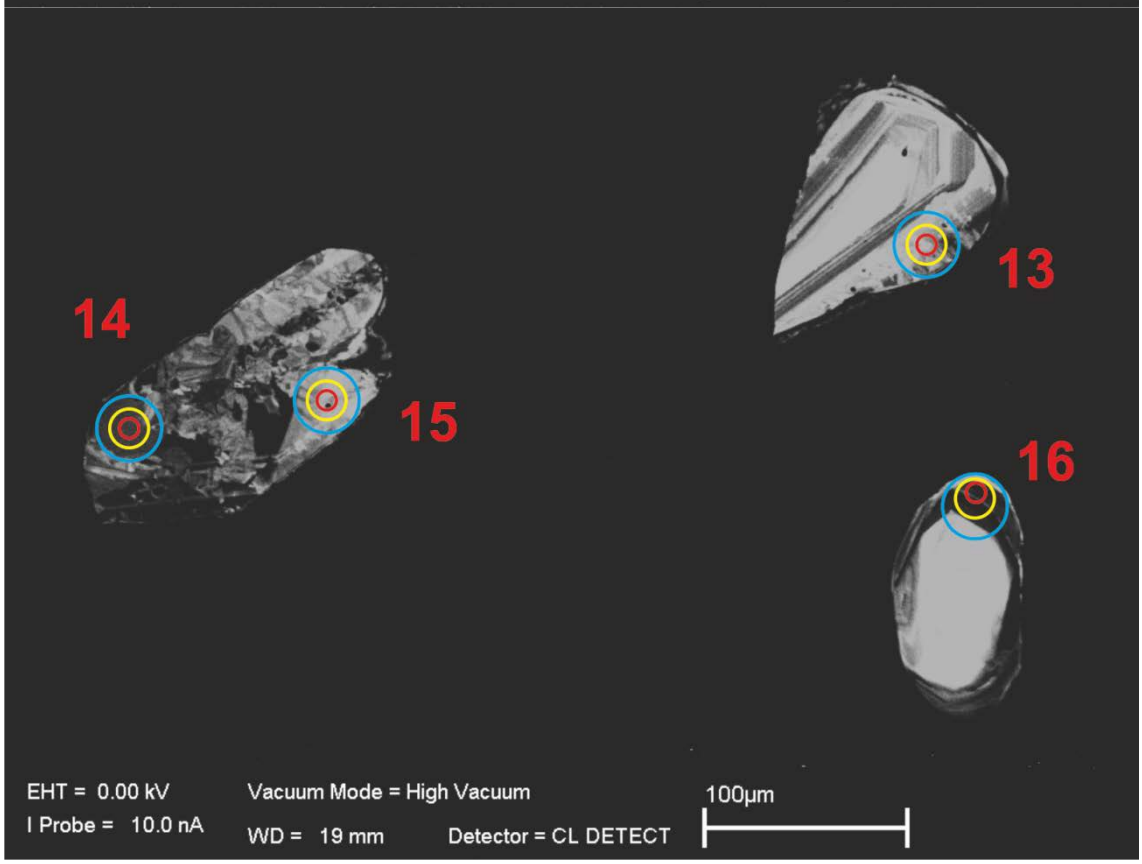
13
14
15
16
EHT = 0.00 kV
I Probe = 10.0 nA
Vacuum Mode = High Vacuum
WD = 19 mm
Detector = CL DETECT
100µm

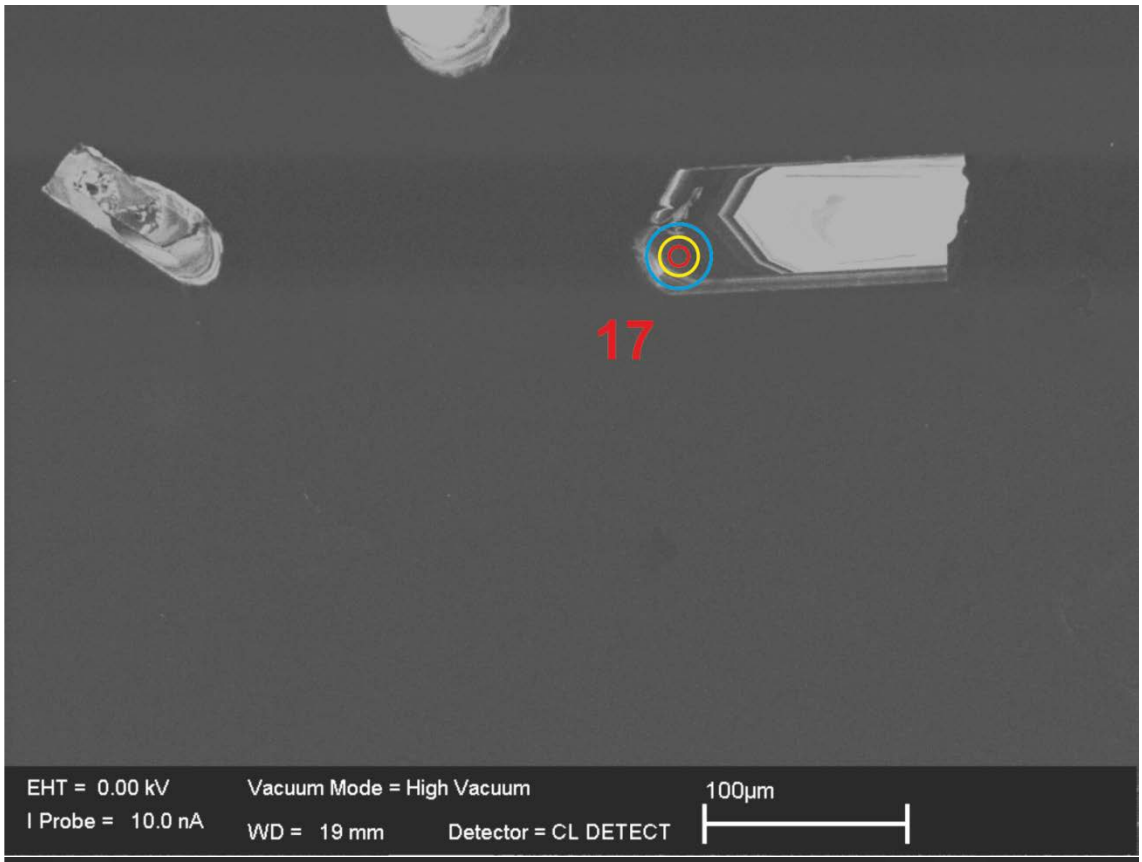
17
EHT = 0.00 kV
I Probe = 10.0 nA
Vacuum Mode = High Vacuum
WD = 19 mm
Detector = CL DETECT
100µm

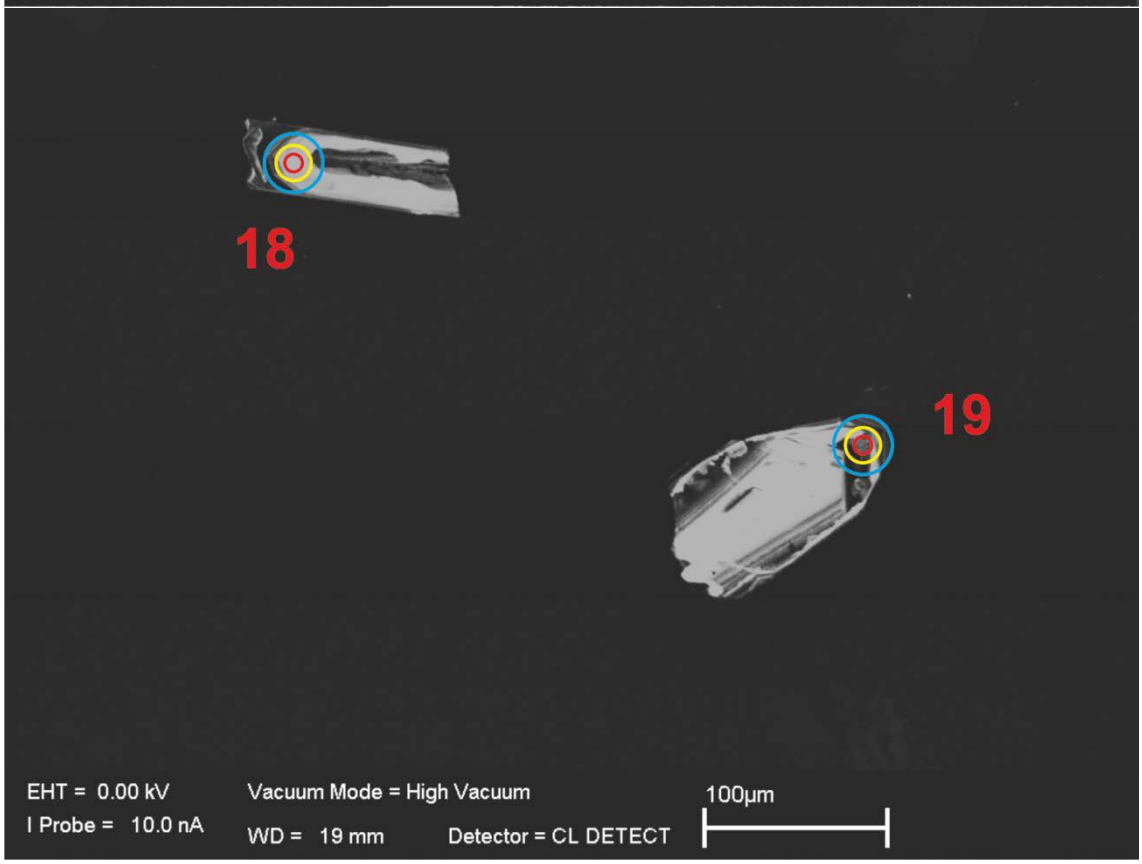
18
19
EHT = 0.00 kV
I Probe = 10.0 nA
Vacuum Mode = High Vacuum
WD = 19 mm
Detector = CL DETECT
100µm

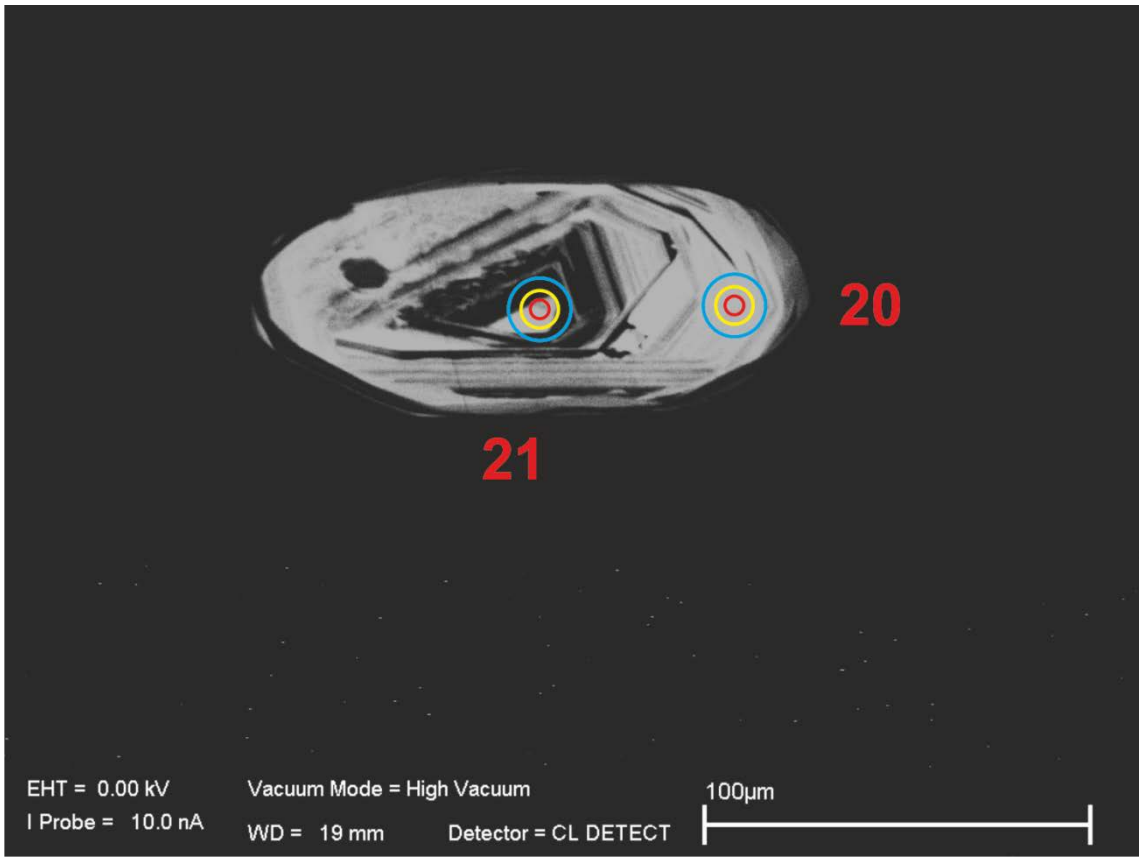
20
21
EHT = 0.00 kV
I Probe = 10.0 nA
Vacuum Mode = High Vacuum
WD = 19 mm
Detector = CL DETECT
100µm

E.3. CWB-10-23

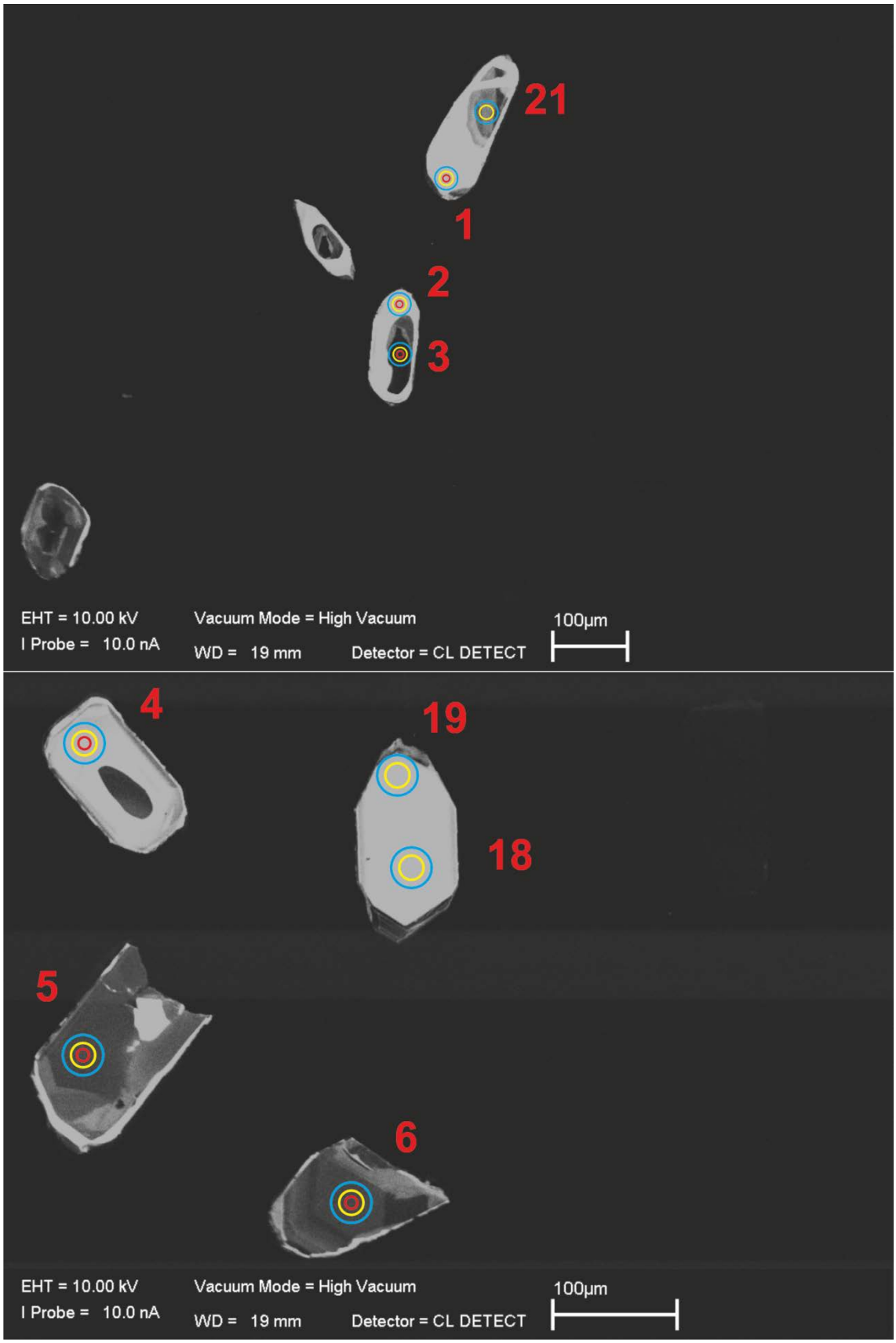
21
1
2
3
EHT = 10.00 kV
I Probe = 10.0 nA
Vacuum Mode = High Vacuum
WD = 19 mm
Detector = CL DETECT
100µm
4
19
18
5
6
EHT = 10.00 kV
I Probe = 10.0 nA
Vacuum Mode = High Vacuum
WD = 19 mm
Detector = CL DETECT
100µm

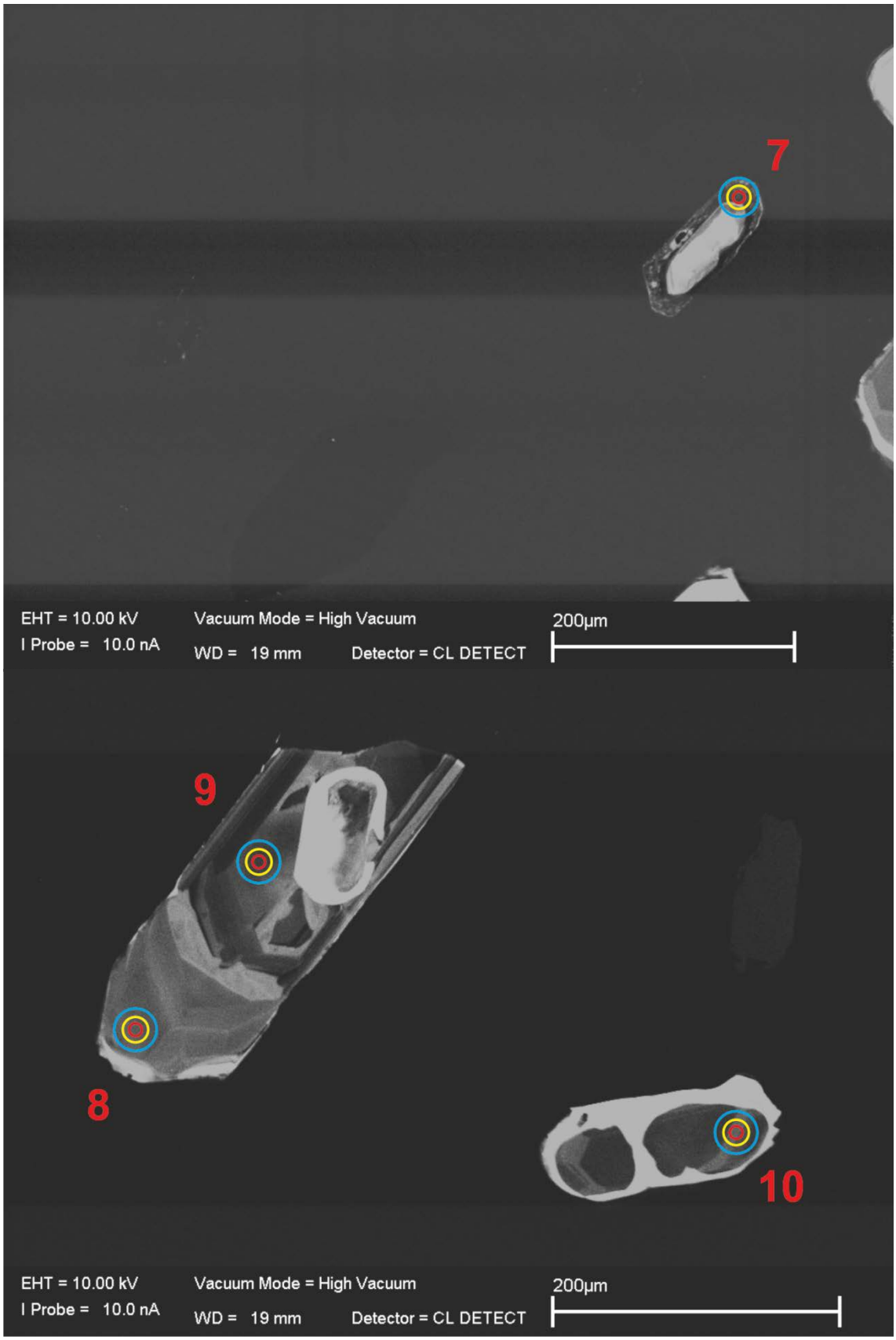
7
EHT = 10.00 kV
I Probe = 10.0 nA
Vacuum Mode = High Vacuum
WD = 19 mm
Detector = CL DETECT
200µm
9
8
10
EHT = 10.00 kV
I Probe = 10.0 nA
Vacuum Mode = High Vacuum
WD = 19 mm
Detector = CL DETECT
200µm

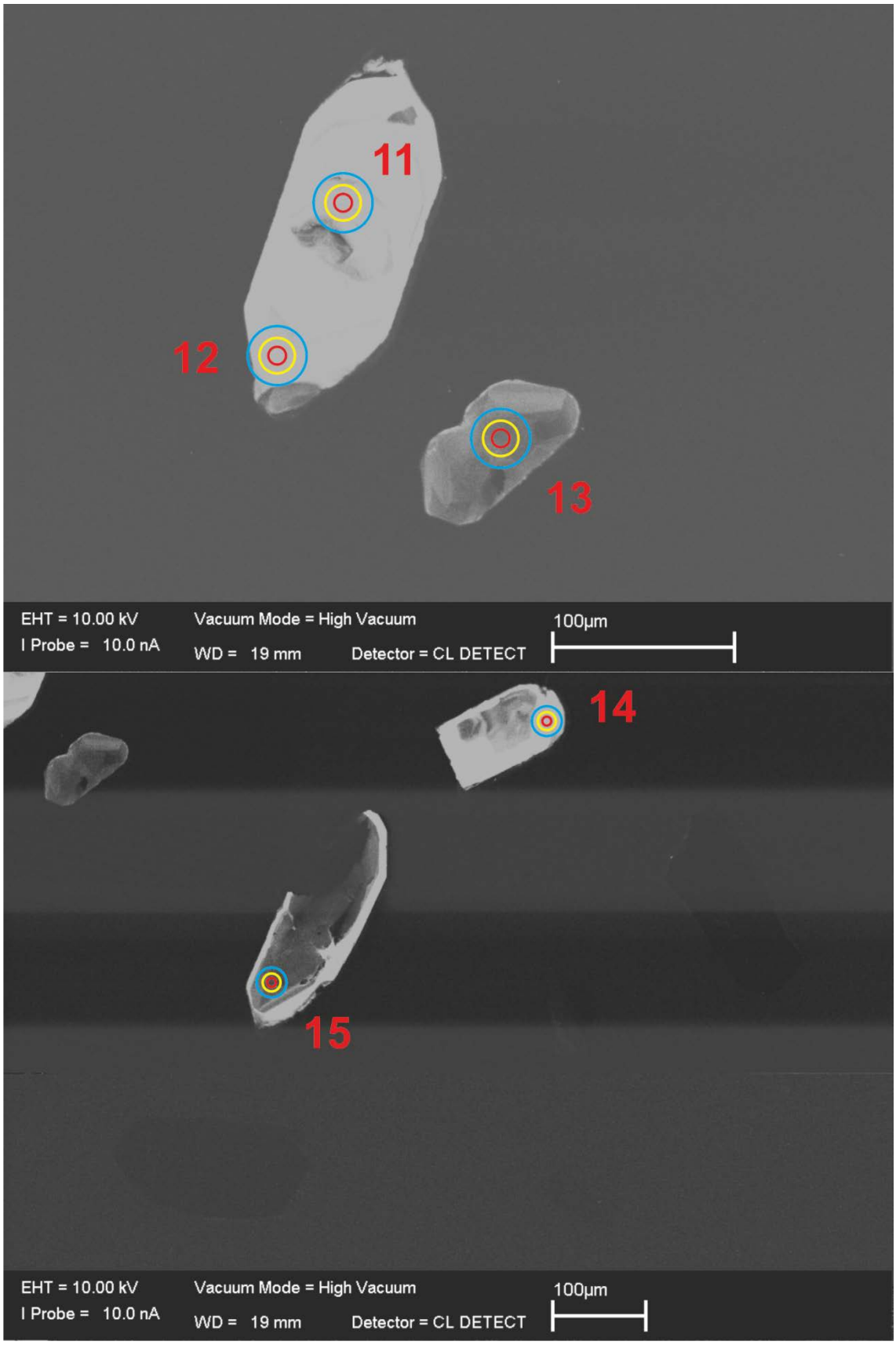
11
12
13
EHT = 10.00 kV
I Probe = 10.0 nA
Vacuum Mode = High Vacuum
WD = 19 mm
Detector = CL DETECT
100µm
14
15
EHT = 10.00 kV
I Probe = 10.0 nA
Vacuum Mode = High Vacuum
WD = 19 mm
Detector = CL DETECT
100µm

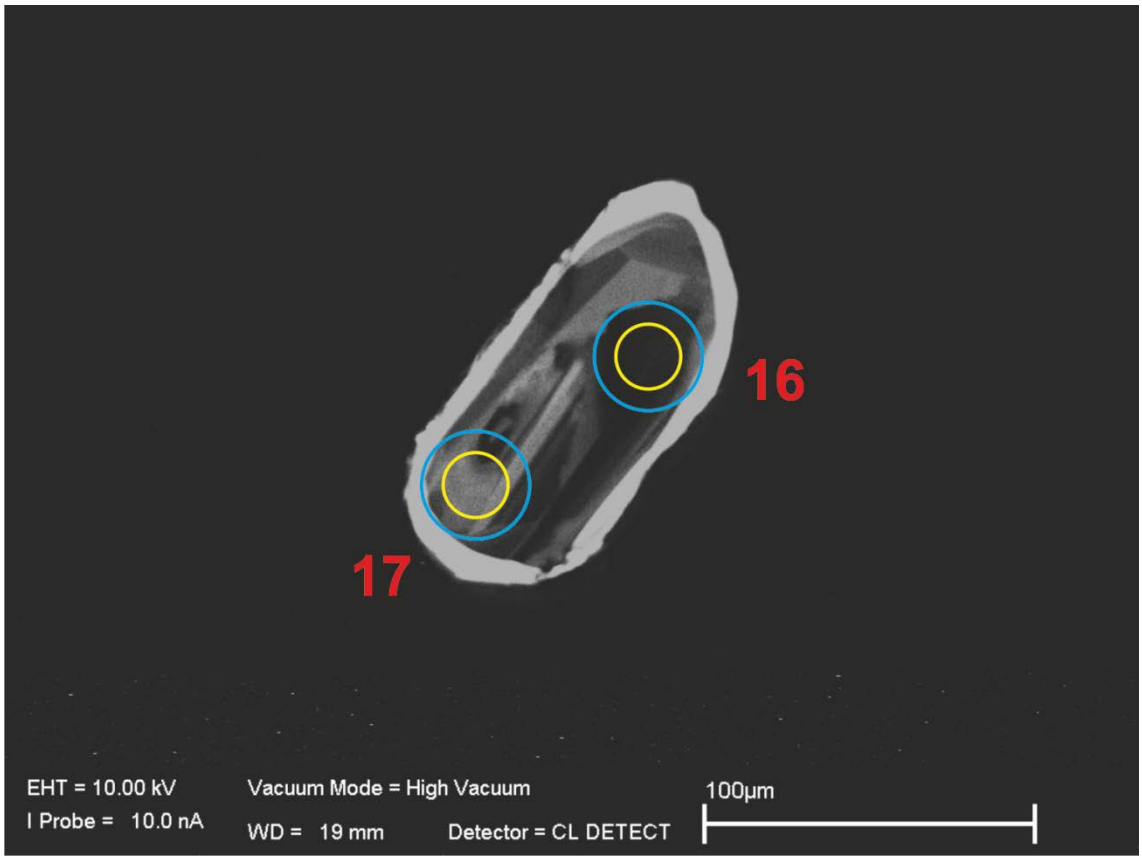
16
17
EHT = 10.00 kV
I Probe = 10.0 nA
Vacuum Mode = High Vacuum
WD = 19 mm
Detector = CL DETECT
100µm